GRAVITY GRADIENT STABILIZATION SYSTEM for the

APPLICATIONS TECHNOLOGY SATELLITE

DOCUMENT NO. 65SD4201
10 JANUARY 1965

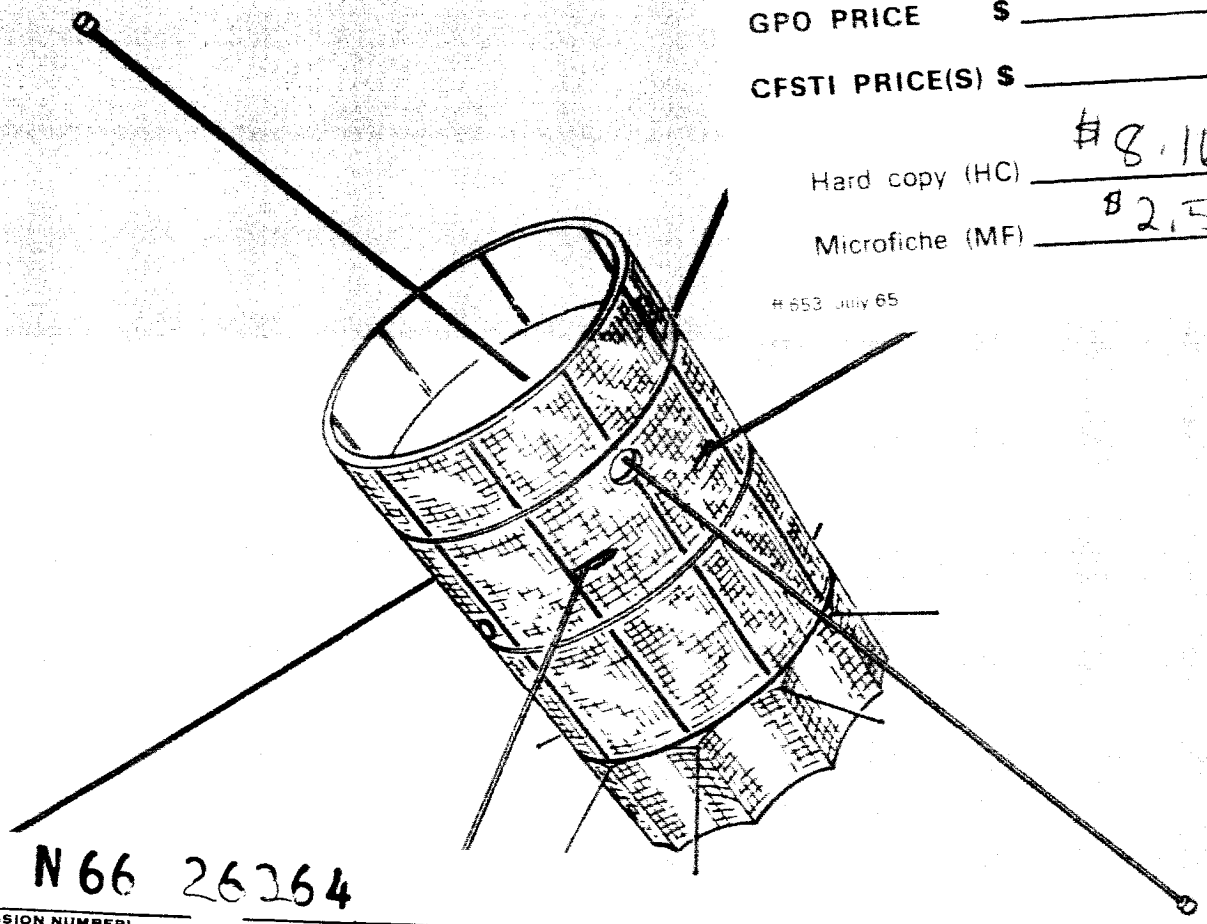
GPO PRICE $ _____

CFSTI PRICE(S) $ _____

Hard copy (HC) $8.16

Microfiche (MF) $2.50

653 July 65

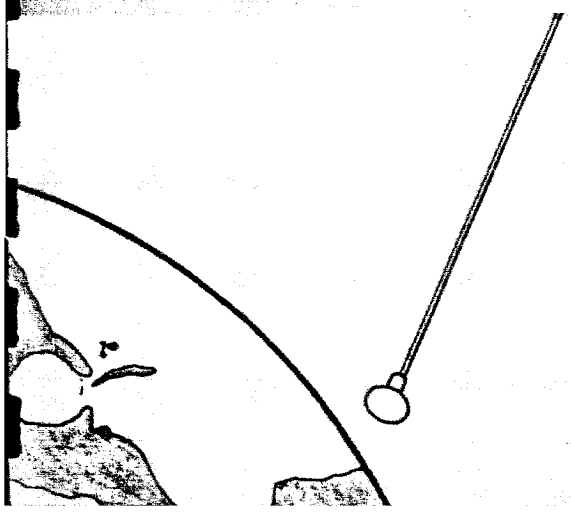


N66 26264
(ACCESSION NUMBER)
(THRU)
577
(PAGES)
1
(CODE)
CR 75709
(NASA CR OR TMX OR AD NUMBER)
31
(CATEGORY)
FACILITY FORM 602

SECOND QUARTERLY PROGRESS REPORT

NASA CONTRACT NAS 5—9042

GENERAL ELECTRIC
SPACECRAFT DEPARTMENT



DOCUMENT No. 65SD4201
10 JANUARY 1965

GRAVITY GRADIENT STABILIZATION SYSTEM

FOR THE

APPLICATIONS TECHNOLOGY SATELLITE

SECOND QUARTERLY PROGRESS REPORT

1 October through 31 December 1964

CONTRACT No. NAS 5-9042

FOR THE

National Aeronautics and Space Administration

John M. Thole
ATS TECHNICAL OFFICER

APPROVED BY 

R. J. KATUCKI, MANAGER
PASSIVE ATTITUDE CONTROL PROGRAMS

GENERAL ELECTRIC
SPACECRAFT DEPARTMENT
A Department of the Missile and Space Division
Valley Forge Space Technology Center
P. O. Box 8555 • Philadelphia, Penna. 19101

CONTENTS

Section		Page
1	INTRODUCTION	1-1
2	TECHNICAL DISCUSSION	2-1
	2.1 System Analysis and Integration	2-1
	2.1.1 Description of Mathematical Model	2-1
	2.1.2 Preliminary Performance Predictions	2-1
	2.1.3 Attitude Sensor System Error Analysis	2-49
	2.1.4 Data Correlation Procedures	2-50
	2.1.5 Analytical Studies and Results	2-50
	2.1.5.1 Isolated Effect of Boom Thermal Bending	2-50
	2.1.5.2 Capture Studies	2-51
	2.1.5.3 Inversion Studies	2-52
	2.1.5.4 Orbital Equations for Eccentricity Maneuvers	2-61
	2.1.5.5 Variation of Damper with Boom Position	2-75
	2.1.5.6 Effect of Spring Constant on Damping Performance of MAGGE	2-76
	2.1.6 System Requirements for TV	2-77
	2.1.7 Boom Thermal Bending Studies	2-88
	2.1.8 Gravity Correction for Thermal Bending Tests	2-90
	2.1.9 Boom Dynamics Studies	2-94
	2.1.10 Testing	2-95
	2.1.10.1 Thermal Test Requirements	2-95
	2.1.10.2 Vibration Test Requirements	2-97
	2.2 Boom Subsystem	2-100
	2.2.1 150-Foot Rod Configuration	2-102
	2.2.2 Lubrication Requirements	2-103
	2.2.3 Motor Selection	2-107
	2.2.4 Potentiometer Boom Length Indicator	2-110
	2.2.5 100-Foot Stop	2-110
	2.2.6 Microswitch Functions	2-110
	2.2.7 Boom Electrical Isolation	2-111
	2.2.8 Tip Target Configuration	2-111
	2.2.9 Clutch Design	2-112
	2.2.10 Damper Boom Release Monitor	2-112

CONTENTS (Continued)

Section		Page
2.3	Combination Passive Damper	2-113
2.3.1	Introduction	2-113
2.3.1.1	Basic CPD Functional Description	2-113
2.3.1.2	Chronological Summary of Major Events During Reporting Period	2-114
2.3.2	Design Effort	2-115
2.3.2.1	General	2-115
2.3.2.2	Damper Configuration Currently Proposed	2-118
2.3.2.3	Diaphragm Analysis	2-125
2.3.3	Development Engineering Activities	2-132
2.3.3.1	Diamagnetic Torsional Restraint for Eddy-Current Damper	2-132
2.3.3.2	Diamagnetic Suspension	2-137
2.3.3.3	Eddy-Current Damper	2-142
2.3.3.4	Hysteresis Damper	2-142
2.3.3.5	Caging	2-152
2.3.3.6	Instrumentation	2-153
2.3.3.7	Magnetic Dipole	2-153
2.3.4	Sub-Contract Activities	2-155
2.3.4.1	Hysteresis Damper (STL)	2-155
2.3.4.2	Angle Detector (DPC)	2-155
2.3.4.3	Solenoid (DRC)	2-155
2.3.5	Test Equipment Progress	2-156
2.4	Attitude Sensor Subsystem	2-159
2.4.1	Subsystem Description	2-159
2.4.2	Power Control Unit	2-161
2.4.2.1	Summary	2-161
2.4.2.2	General Discription	2-161
2.4.2.3	Electrical Design	2-161
2.4.2.4	Mechanical Design	2-171
2.4.3	Solar Aspect Sensor	2-177
2.4.4	TV Camera Subsystem	2-185

CONTENTS (Continued)

Section			Page
	2.4.4.1	Summary	2-185
	2.4.4.2	Standby Filament Power	2-185
	2.4.4.3	A Slow Scan Version of the TV Camera Subsystem	2-187
	2.4.4.4	Available Readout Accuracy of TV Camera Subsystem	2-192
	2.4.4.5	Testing, TV Camera	2-195
	2.4.5	Infrared Earth Sensor	2-198
	2.4.6	RF Attitude Sensor	2-199
	2.4.6.1	Introduction	2-199
	2.4.6.2	Electrical Design	2-200
	2.4.6.3	Mechanical Design	2-237
2.5		Reliability	2-245
	2.5.1	Parts, Materials and Standards	2-245
	2.5.1.1	Documentation	2-245
	2.5.1.2	Part Tasks	2-246
	2.5.2	Parts Program	2-247
2.6		Quality Control	2-256
	2.6.1	Primary and Secondary Boom Subsystems	2-256
	2.6.2	Combination Passive Damper	2-256
	2.6.3	RF Attitude Sensor	2-257
	2.6.4	Solar Aspect Sensor	2-258
2.7		Manufacturing	2-260
	2.7.1	Power Control Units	2-260
	2.7.2	Process Development	2-260
	2.7.3	Make or Buy Structure	2-261
2.8		Materials Research and Development	2-262
3		NEW TECHNOLOGIES	3-1
4		BIBLIOGRAPHY	4-1
5		GLOSSARY	5-1

CONTENTS (Continued)

Appendices		Page
A	Satellite Attitude Determination Via On-Board Earth Detector and Radio Sensor Information	A-1
B	Satellite Attitude Determination Via On-Board Radio Sensor Measurements, Two Ground Transmitter Stations	B-1
C	Analysis of the Proposed Solar Aspect System	C-1
D	ATS Solar Torque	D-1
E	Stiffness Matrix for an Element of the Gravity Gradient Rod	E-1
F	Signal-to-Noise Calculations for the TV Camera Subsystem	F-1
G	Systems Error Analysis, RF Attitude Sensor	G-1
H	Effect of Short Term Stability on Digital Phase Measurement	H-1
I	RF Attitude Sensor Application of ATS Project Approved Parts	I-1

LIST OF ILLUSTRATIONS

Figure		Page
2.1.2-1	MAGGE 19-Degree Half Angle Steady State	2- 7
2.1.2-2	MAGGE 11-Degree Half Angle Steady State	2- 9
2.1.2-3	MAGGE 31-Degree Half Angle Steady State	2-11
2.1.2-4	MAGGE 19-Degree Half Angle, 10,000 Pole-CM on Roll Axis	2-13
2.1.2-5	MAGGE 11-Degree Half Angle, 10,000 Pole-CM on Roll Axis	2-15
2.1.2-6	MAGGE 31-Degree Half Angle, 10,000 Pole-CM on Roll Axis	2-17
2.1.2-7	MAGGE 19-Degree Half Angle, 20,000 Pole-CM on Yaw Axis	2-19
2.1.2-8	MAGGE 31-Degree Half Angle, 20,000 Pole-CM on Yaw Axis	2-21
2.1.2-9	MAGGE 19-Degree Half Angle, C.P. Boom Extended 15 Feet	2-23
2.1.2-10	MAGGE 19-Degree Half Angle, C.P. Boom Extended 30 Feet	2-25
2.1.2-11	MAGGE 11-Degree Half Angle, C.P. Boom Extended 15 Feet	2-27
2.1.2-12	MAGGE 11-Degree Half Angle, C.P. Boom Fully Extended (30 Feet)	2-29
2.1.2-13	MAGGE 31-Degree Half Angle, C.P. Boom Extended 15 Feet	2-31
2.1.2-14	MAGGE 31-Degree Half Angle, C.P. Boom Extended 30 Feet on Pitch Axis	2-33
2.1.2-15	MAGGE 19-Degree Half Angle Transient	2-35
2.1.2-16	MAGGE 11-Degree Half Angle Transient	2-37
2.1.2-17	MAGGE 31-Degree Half Angle Transient	2-39

LIST OF ILLUSTRATIONS (Continued)

Figure		Page
2.1.2-18	SAGGE 19-Degree Half Angle Steady State	2-41
2.1.2-19	SAGGE 19-Degree Half Angle, 10,000 Pole-CM on Roll Axis	2-43
2.1.2-20	SAGGE 19-Degree Half Angle C.P. Boom Extended 30 Feet	2-45
2.1.2-21	SAGGE 19-Degree Half Angle Transient	2-47
2.1.5-1	Effect on Thermal Bending, MAGGE	2-53
2.1.5-2	Effect on Thermal Bending, SAGGE	2-55
2.1.5.2-1	Capture of MAGGE	2-57
2.1.5.2-2	Capture of MAGGE	2-58
2.1.5.3-1	Variation of Angular Overshoot with Thrust Level, MAGGE Configuration	2-62
2.1.5.3-2	Allowable Variation in Torque Level, MAGGE Configuration	2-63
2.1.5.3-3	Nominal Torque Level as a Function of Allowable Overshoot, MAGGE Configuration	2-64
2.1.5.3-4	Pitch Performance for Constant Maneuver Time, Maneuver Time = 2.50 Hours	2-65
2.1.5.3-5	Pitch Performance for Constant Maneuver Time, Maneuver Time = 2.30 Hours	2-66
2.1.5.3-6	Pitch Performance for Constant Maneuver Time, Maneuver Time = 2.00 Hours	2-67
2.1.5.3-7	Thrust Level as a Function of Required Torque, Level Aim - 29 Inches	2-68
2.1.5.6-1	Transient Performance of MAGGE, Spring Constant 20% Low	2-78
2.1.5.6-2	Transient Performance of MAGGE, Spring Constant Normal	2-79
2.1.5.6-3	Transient Performance of MAGGE, Spring Constant 20% High	2-80

LIST OF ILLUSTRATIONS (Continued)

Figure		Page
2.2-1	Split Series GJY Motor Characteristics	2-108
2.2-2	Shunt GJY Motor Characteristics	2-109
2.3-1	"Rough" Working Model	2-116
2.3-2	Damper Configuration	2-119
2.3-3	Corrugated Belleville Washer	2-127
2.3-4	Clutch Washer	2-129
2.3-5	Load Deflection Characteristics and Maximum Stresses (Cases 1, 2)	2-129
2.3-6	Load Deflection Characteristics and Maximum Stresses (Cases 3, 4)	2-130
2.3-7	Back-to-Back Fluted Diaphragm	2-131
2.3-8	Belleville Washer with Fingers	2-131
2.3-8A	CPD with Diamagnetic Torsional Restraint (GE Dwg SK56130-808-38)	2-133
2.3-9	Test Fixture	2-136
2.3-10	Definition of Magnet Side	2-141
2.3-11	Suspension Load Capacity vs Initial Air Gap Setting	2-141
2.3-12	Test Setup for Eddy-Current Damper	2-143
2.3-13	Torsion Wire Suspension Test Fixture	2-152
2.3-14	Magnetic Mock-up	2-154
2.4-1	Gravity Gradient Stabilization System Attitude Sensor Subsystem	2-160
2.4.2-1	Squib Driver Schematic	2-163
2.4.2-2	Oscilloscope of Preliminary Squib Driver Tests (Sweep Rate = 200 msec/cm)	2-164
2.4.2-3	Solenoid Driver Schematic	2-165
2.4.2-4	Motor Driver	2-166
2.4.2-5	Motor Field Driver	2-167
2.4.2-6	-5 Volt Power Supply	2-169
2.4.2-7	Current Sensor Schematic	2-170
2.4.2-8	A-C Power Supply	2-172

LIST OF ILLUSTRATIONS (Continued)

Figure		Page
2.4.2-9	Ladder Switch	2-173
2.4.2-10	Power Control Unit Breadboard	2-176
2.4.2-11	PCU Test Rack	2-177
2.4.3-1	SAS Geometry	2-180
2.4.3-2	Brightness Definition	2-181
2.4.3-3	Infinitesimal Earth Area (dA_C) Illuminated by Entire Sun	2-182
2.4.4-1	TVCS Video Bandwidth (mc) versus Frame Rate (fps)	2-189
2.4.4-2	TVCS Received Signal/Noise	2-189
2.4.4-3	Horizontal Readout Accuracy versus Overall Equivalent Video Bandwidth	2-194
2.4.4-4	Composite Response of Three Video Responses Having -3 db Points at 8, 5, and 4.3 mc	2-195
2.4.4-5	Composite Response of Three Video Responses Having -3 db Points at 5.6, 4 and 2.5 mc	2-196
2.4.4-6	Signal Ratio versus Target Type	2-196
2.4.4-7	Relative Signal veruss Sun Angle	2-197
2.4.4-8	Signal Ratio versus Sun Angle	2-197
2.4.5-1	Temperature Measuring Circuits for Infrared Earth Sensor	2-199
2.4.6-1	RF Attitude Sensor Mockup	2-201
2.4.6-2	RF Attitude Sensor Block Diagram	2-202
2.4.6-3	75.76 Mc IF Schematic	2-204
2.4.6-4	Receiver IF Filter	2-205
2.4.6-5	Last IF Amplifier - Detector	2-206
2.4.6-6	10 Kc Filter	2-208
2.4.6-7	Limiters Schematic	2-210
2.4.6-8	Acquisition Control	2-211

LIST OF ILLUSTRATIONS (Continued)

Figure		Page
2.4.6-9	Sweep Circuit	2-213
2.4.6-10	Multiplier Block Diagram	2-214
2.4.6-11	X2 Circuit Schematic	2-215
2.4.6-12	X4 Circuit Schematic	2-217
2.4.6-13	X6 Circuit Schematic	2-218
2.4.6-14	227.8 Mc Amplifier Circuit Schematic	2-220
2.4.6-15	2.56 Mc Oscillator and Buffer	2-222
2.4.6-16	Digital Data Collection	2-224
2.4.6-17	Data Timing Diagram	2-224
2.4.6-18	8-Bit Counter	2-227
2.4.6-19	8-Bit Counter	2-229
2.4.6-20	256 Divider and Phase Detectors	2-231
2.4.6-21	3-Channel Summer	2-233
2.4.6-22	Chopper Amplifier	2-233
2.4.6-23	Power Supply	2-237
2.4.6-24	RF Altitude Sensor Packaging	2-238
2.5-1	GE Missile and Space Quality Purchase Part Specifications (MSQ)	2-250
2.5-2	Flow Chart - Part Type Quailification	2-253
2.5-3	Flow for Screening Parts	2-254
2.5-4	Flow for Adding Parts to Approved Parts List, 490L106	2-255

LIST OF TABLES

Table		Page
2.1-1	Computer Program Comparison	2- 2
2.1-2	GAPS III Subroutines	2- 3
2.1.6-1	TV System Parametric Requirements	2- 84
2.1.6-2	TV System Measurement Sequence	2- 85
2.2-1	Tip Mass Weight Per Rod	2-102
2.2-2	Promising Lubricant Selection	2-106
2.2-3	Microswitch Functions	2-111
2.4.6-1	75 Mc IF Measurements	2-204
2.4.6-2	Frequency Multiplier Specification	2-214
2.4.6-3	Specification of X2 Module	2-216
2.4.6-4	X4 Circuit Specification	2-216
2.4.6-5	X6 and X6 Amplifier Specifications	2-219
2.4.6-6	Multiplier Specification	2-219
2.4.6-7	Output Voltage vs. Number of Channels on as A Function of Temperature	2-234

ABSTRACT

The Second Quarterly Progress Report describes the continuation of effort by General Electric toward the development of the Gravity Gradient Stabilization System for the NASA/ATS Program. This report covers the period from October 1 through December 31, 1964.

The capability of the proposed Gravity Gradient System (G^2S/ATS) Mathematical Model is compared with the current GE/GAPS III Program. Computer runs are included which were made on the GAPS III using the present vehicle design. These runs show the effect on performance of various disturbances with the assumptions that the X-rods and damper boom pass through the vehicle center of mass.

Studies made during the quarter include computer runs comparing the performance of eddy current damping with hysteresis damping, isolated effect of boom thermal bending, capture studies, and attitude error sensing analysis.

Items investigated in the Primary Boom Subsystem include lubricant selection, relative rod length and the advantage of shunt wound motors for scissoring and boom extension. Electrical isolation of the booms from their supporting structure were investigated; and functions have been assigned for the microswitches used throughout the Boom Subsystems.

Laboratory tests were conducted in support of engineering evaluation on diamagnetic torsional restraint, eddy current and hysteresis damping, and torsion wire suspension.

Preliminary circuit and package designs were made and updated to meet requirements of the Power Control Unit. A final report of the work performed on the development of the RF Attitude Sensor prior to its termination is included.

1. INTRODUCTION

1.1 PURPOSE

The purpose of this report is to document the technical progress made during the period from October 1, 1964 to December 31, 1964 in the design and development of Gravity Gradient Stabilization Systems for the Applications Technology Satellite Program.

1.2 PROGRAM CONTRACT SCOPE

Under Contract NAS-5-9042, the Spacecraft Department of the General Electric Company has contracted to provide Gravity Gradient Stabilization Systems for three Applications Technology Satellites: one to be orbited at 6000 nautical miles and two to be orbited at synchronous altitude. The gravity gradient stabilization systems will consist of the stabilizing booms and dampers, attitude sensors, and power control and interface electronics.

2. TECHNICAL DISCUSSION

2.1 SYSTEM ANALYSIS AND INTEGRATION

2.1.1 DESCRIPTION OF MATHEMATICAL MODELS

The proposed Gravity Gradient System/ATS (G^2S/ATS) Math Model can best be described by comparison with the current GE/GAPS III Program and the current version of the RAND Program as utilized by NASA/GSFC. The original RAND program, generated in June, 1963, has been modified by NASA/GSFC and HAC to include the capabilities listed in Table 2.1-1. An implicit statement of complexity and inherent program capability, for GAPS III, is contained in the list of GAPS III subroutines of Table 2.1-2. The GAPS III input routine requires the specification of 121 parameters. Priority efforts have been placed on the G^2S/ATS Math Model development.

2.1.2 PRELIMINARY PERFORMANCE PREDICTIONS

As a preliminary estimate of the MAGGE and SAGGE performance, several computer runs were made on GAPS III using the present vehicle design parameters. These runs contain all the error sources (orbit eccentricity, thermal bending, solar torque, magnetic dipole, etc.) the limitation being that the X-rods and the damper rods pass through the vehicle center of mass. As a consequence, the effect of the offset of the damper cannot currently be evaluated in GAPS III. However, a two-inch misalignment between the system center of mass and the central body center of pressure was included. For these runs, the sun was placed in the orbit plane since the most accurate solar reflectivity information is for the sun normal to the cylinder axis. Thermal bending has been included in

TABLE 2.1-1. COMPUTER PROGRAM COMPARISON

	RAND PROGRAM* with NASA/GSFC Modification	GAPS III	G^2S/ATS MATH MODEL
Gravity Grad. Torques	Constant Inertia	Time Varying Mom. & Prods. Of Inertia	Same
Orbit	Elliptical Keplerian Orbit No Perturbations	Sun Rotation - Earth Shadow	Sun Rotation Earth Shadow With Penumbra Precession Of Line Of Nodes
Solar Torques	(Body and Straight Rods Added By HAC)	Closed Cylinder Moving C.M.	ATS Config. Body Shadow On Rods Variation In Solar Cell ρ With Incidence <
Magnetics	(Added By Goddard)	Spherical Harmonics Of Tilted Off-Axix Dipole	Modified Harmonic Expans. Approx. Solar Wind Effects.
Thermal Bending And Rod Geometry	(Fixed Radius of Curvature Added By Goddard)	Planar Circ. Bending Solar Torques & Moments Of Inertia Integrated Along Rods. Rods Planar And Intersecting.	Poly. Fit To Rod Data, Individual Rods, Penumbra Effects, Thermal Time Lag, Gravity Bending.
Damper Models	Rate Damping - Hard Stops (Hysteresis Damping Added By Goddard)	Rate Damping - Non Linear Spring Rates Calculates Cocking Torques on Damper Suspension.	Rate & Hysteresis Damping, Non-Linear Spring and Hard Stops. Calculates Forces And Cocking Torques On Damper Suspension
Additional Features	(Flywheel Simulation Added By Goddard)	Inversion Capability Using Thrusters	Includes Thruster, Flywheel, More Flexible Integration Routine, Controllable Magnetic Dipole, Scissoring Dynamics, Rod Retraction And Extension

*Original Rand Program generated June, 1963

TABLE 2.1-2. GAPS III SUBROUTINES

1. INVERT — Flywheel & Thruster Inversion Routine
2. MAGFLD — Calculates Magnetic Field
3. MAGTOR — Calculates Torque on Vehicle Dipole
4. CTRMSS — Calculates Position of C.M.
5. SOLTOR — Calculates Solar Torque
6. MATRX — Calculates Matrix Elements (Veh. Fr., Sun Rod Fr. & etc.)
7. AUTO — Step Size Selection
8. ORBIT — Keplerian Orbit Calculations
9. MOMIN — Moments of Inertia-Straight Rods
10. GRATOR — Grav. Grad. Torques
11. DERIV. — Calculates Body Accelerations & Euler Angle Rates
12. TERM — Stop Integration at Req'd Time
13. MAIN — Basic Control of Program
14. INITIA — Initialization
15. VCINIT — Calculates Constants for Vehicle
16. INPUT — Input
17. PWER — Power Series for Thermal Bending
18. ROD 3
19. ROD 2
20. ROD 1

    (18–20) Rod Shape, Tip Mass Location, Moments of Inertia for Rods
21. OUT — Output
22. NOL 3 — Integration Routine

this run and it is assumed that the rods are straight in the earth's shadow (i.e., initially curved rods are not considered). The residual magnetic dipole of both the SAGGE and MAGGE vehicles was assumed to be approximately 800 pole-cm and, for generality, 410 pole-cm was placed on the pitch axis, 600 pole-cm was placed on the roll axis, and 300 pole-cm was placed on the yaw axis.

The eccentricity for all the MAGGE runs was selected to be .015 and for the SAGGE runs it was assumed to be .003.

2.1.2.1 MAGGE

With the above combination of error sources, the steady state performance of MAGGE with a 19 degree half angle (between the rods), an 11 degrees half angle, and a 31 degree half angle are shown in Figures 2.1.2-1, -2, and -3 respectively. The 19 and 11 degree configurations have comparable performance (2 degrees in pitch, 0.4 degrees in roll, and 8 degrees in yaw), but the 31 degree configuration has very poor performance (8 degree pitch, 2 degrees roll and 18 degrees yaw). Both the 11 and 31 degree configurations have crab angles and these are marked for reference. The pointing accuracy in yaw has been measured with respect to this angle.

During the course of the mission several experiments have been considered, among which are turning on a magnetic dipole, and extending a center of pressure boom. Figures 2.1.2-4 through 2.1.2-6 show the performance of MAGGE when a 10,000 pole-cm magnetic dipole is placed on the roll axis. As with the steady state runs, the best pitch and roll performance is shown by the 11 degree and 19 degree configurations Figures 2.1.2-4 and -5. However, the worst yaw performance is exhibited by the 11 degree configuration, and the best by the 31 degree configuration. It is apparent that, as the half angle is increased, the yaw restoring torque is increased. All the errors are large, however, and it is apparent that they would be easily distinguishable from the normal steady state oscillations.

Figures 2.1.2-7 and -8 show the effect of a 20,000 pole-cm magnetic dipole on yaw. A large dipole was placed on this axis because the effect of a "yaw dipole" is less than that of a "roll dipole". The pitch and roll performance of the 31 degree configuration is very poor and the pitch oscillations are large enough to "tumble" yaw. There is a very evident roll bias as would be expected from the position of the vehicle dipole and the magnetic lines of flux. This roll bias is also evident on the 19 degree configuration. Difficulties with the magnetic tape from the computer prevented the plotting of the 11 degree configuration, but the errors were 6.5 degree in pitch, 6 degrees in roll, and 12 degrees in yaw.

An additional experiment to be performed is the extension of a center of pressure boom to cause a significant solar torque. Computer runs were made for each MAGGE configuration with the rod fully extended, and the rod half extended. Figures 2.1.2-9 through -14 inclusive show the results. Inadvertently, the C.P. Boom was positioned such that the yaw solar torque cancelled the other disturbance sources. This is particularly evident in Figures 2.1.2-1, -9 and -10. In Figure 2.1.2-9, the sinusoidal motion of yaw (Figure 2.1.2-1) virtually disappears, and in Figure 2.1.2-10, the motion is again sinusoidal, but has a 180-degree phase shift with respect to Figure 2.1.2-1. The same effect can be seen in Figures 2.1.2-2, -11 and -12 for the 11 degree configuration except that the effect of the C.P. Boom is more pronounced than for the 19 degree configuration, and the error sources do not quite cancel. The effect on the 31 degree configuration is small (Figures 2.1.2-3, -13 and -14).

In view of the performance of the satellite with the C.P. Boom extended, it is recommended that a longer boom be employed. It is also possible to wait for a more propitious time to deploy the rods, but this would require waiting until a particular combination of orbital parameters occurred.

The transient performances of the vehicles were checked and the results are shown in Figures 2.1.2-15, -16 and -17. The transitions are not significantly affected

by the presence of the external disturbance sources. The 31 degree configuration damped to steady state quickly because of the high steady state error. The initial conditions for the transient runs have been taken from a capture run and differ from initial conditions used for similar runs presented in the first quarterly report.

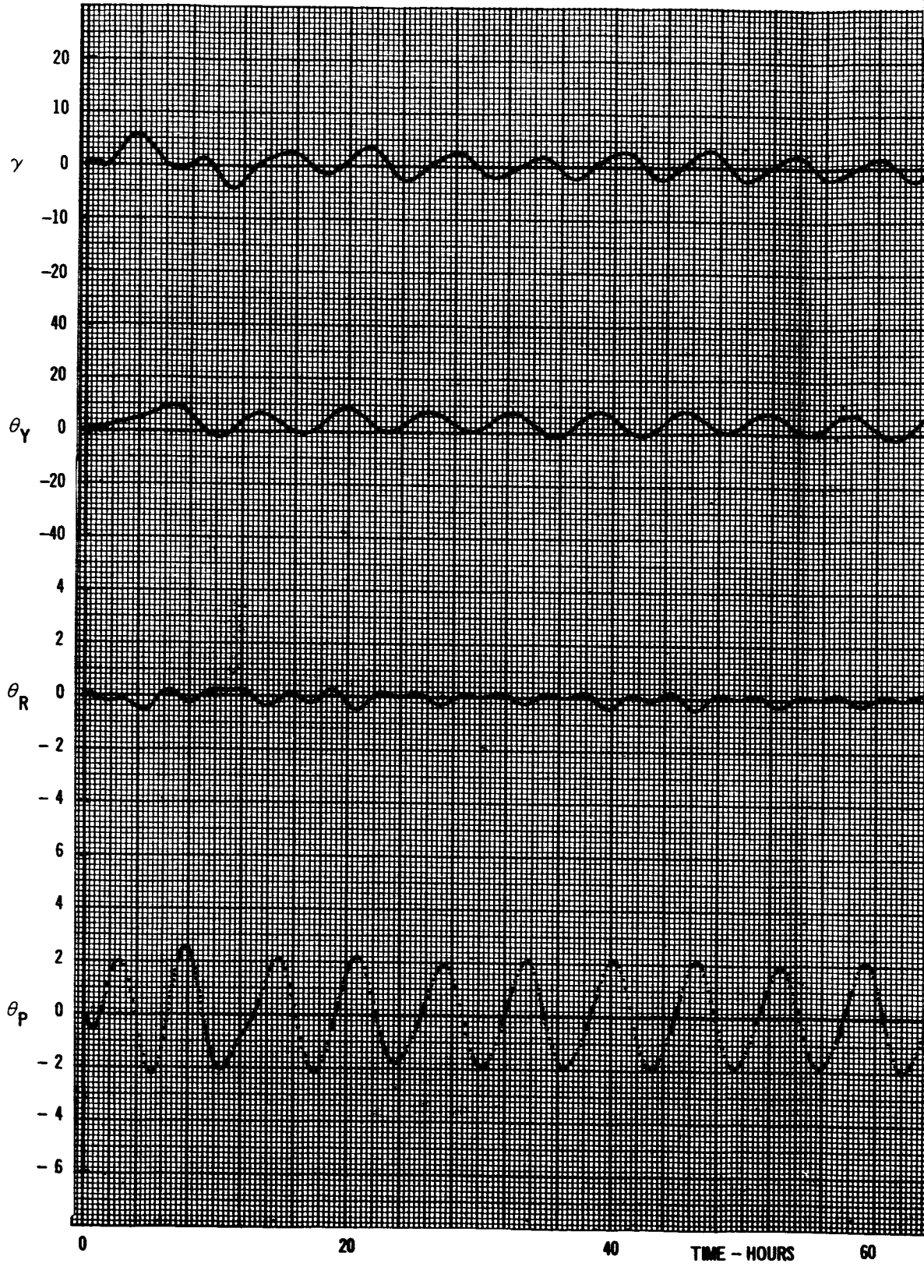
2.1.2.2 SAGGE

The performance of SAGGE, with the same error sources as MAGGE, was also checked. The magnitude and orientation of the magnetic dipole was retained but the eccentricity was reduced from the .015 value for MAGGE to .003, as mentioned earlier. The 2-inch C.P./CM misalignment was also retained. The steady state performance is shown in Figure 2.1.2-18. Note that with the reduced eccentricity, and the effect of the magnetic dipole reduced by the large moment of inertia of the SAGGE system, the pointing accuracy of SAGGE is as good as MAGGE. The largest error disturbances for this run is thermal bending, which has its greatest torque in pitch at twice orbital frequency. As a consequence the vehicle is oscillating at this frequency with only a small error.

A 10,000 pole-cm magnet was placed on the roll axis, and the results are shown in Figure 2.1.2-19. The greatest effect is in yaw, which has rotated almost 140 degrees. The vehicle is undoubtedly magnetically oriented in yaw. Pitch and roll show an increase in error but not a large one. (The results of this run differ from the results shown in the first quarterly report because of an error in the calculation of the orbital angle in GAPS III for the original runs).

Figure 2.1.2-20 shows the effect of extending a 30-foot C.P. Boom. The yaw error has increased considerably and there is no "masking" by the other disturbances. Note that the primary frequency of oscillation is orbital which is characteristic of solar torque.

The transient performance of SAGGE is shown in Figure 2.1.2-21. As with MAGGE the transient behavior is not significantly affected by the presence of the external disturbances.


20
10
γ 0
-10
-20
40
20
θY 0
-20
-40
4
2
θR 0
- 2
- 4
6
4
2
θP 0
- 2
- 4
- 6
0
20
40
TIME - HOURS
60

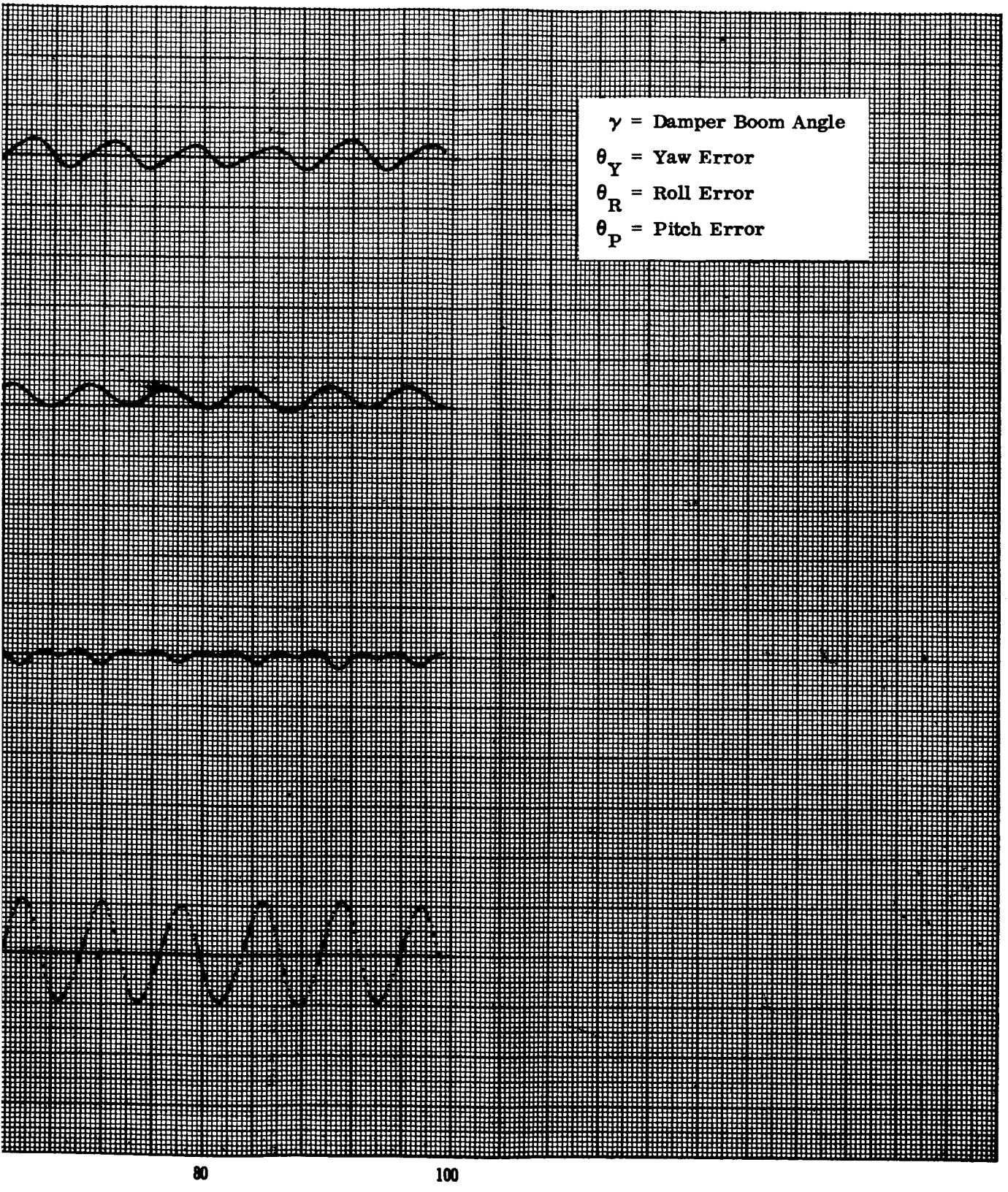
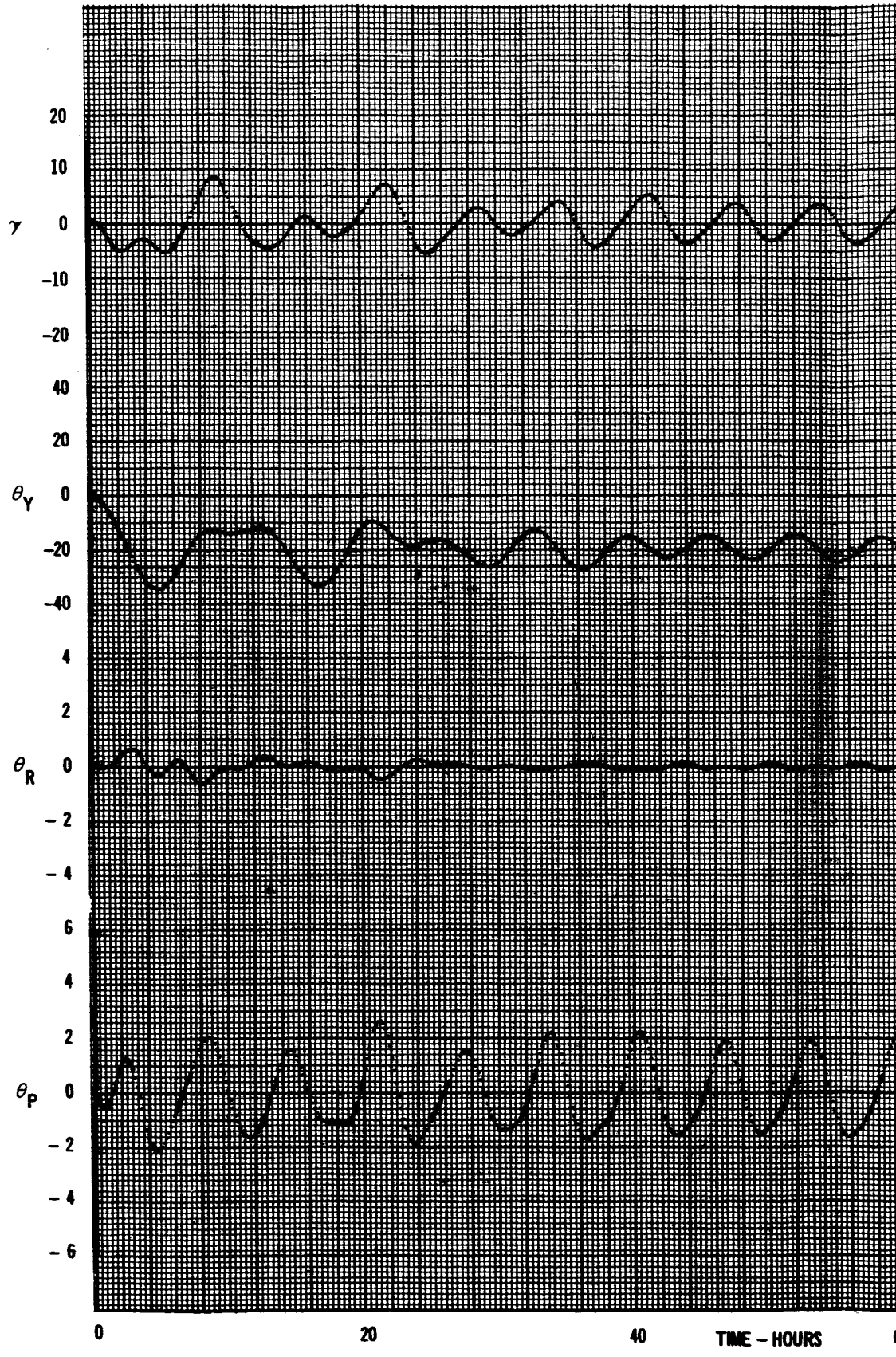


Figure 2.1.2-1. MAGGE, 19 Degree Half Angle, Steady State


20
10
γ 0
-10
-20
40
20
θY 0
-20
-40
4
2
θR 0
- 2
- 4
6
4
2
θP 0
- 2
- 4
- 6
0
20
40
TIME – HOURS

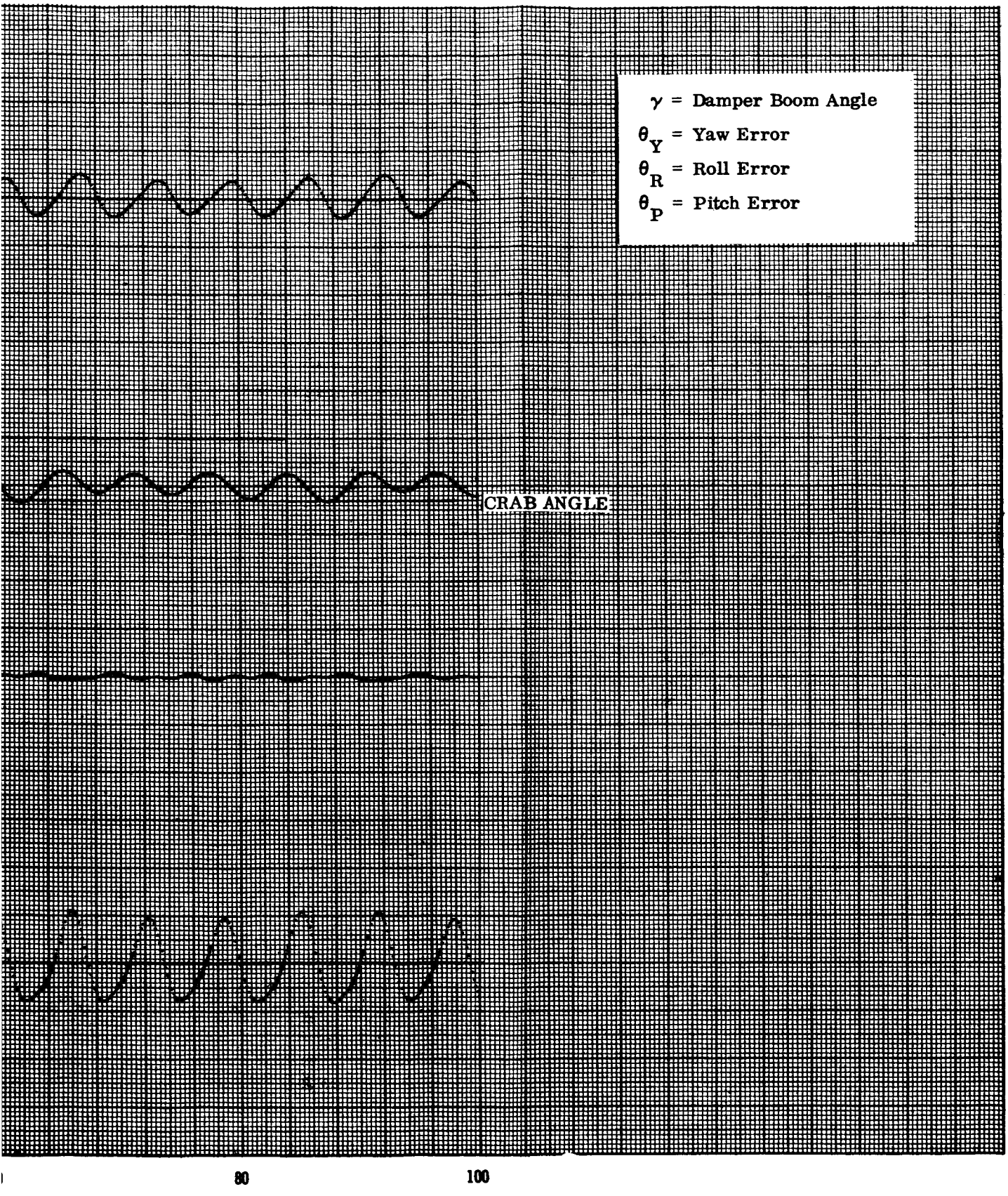
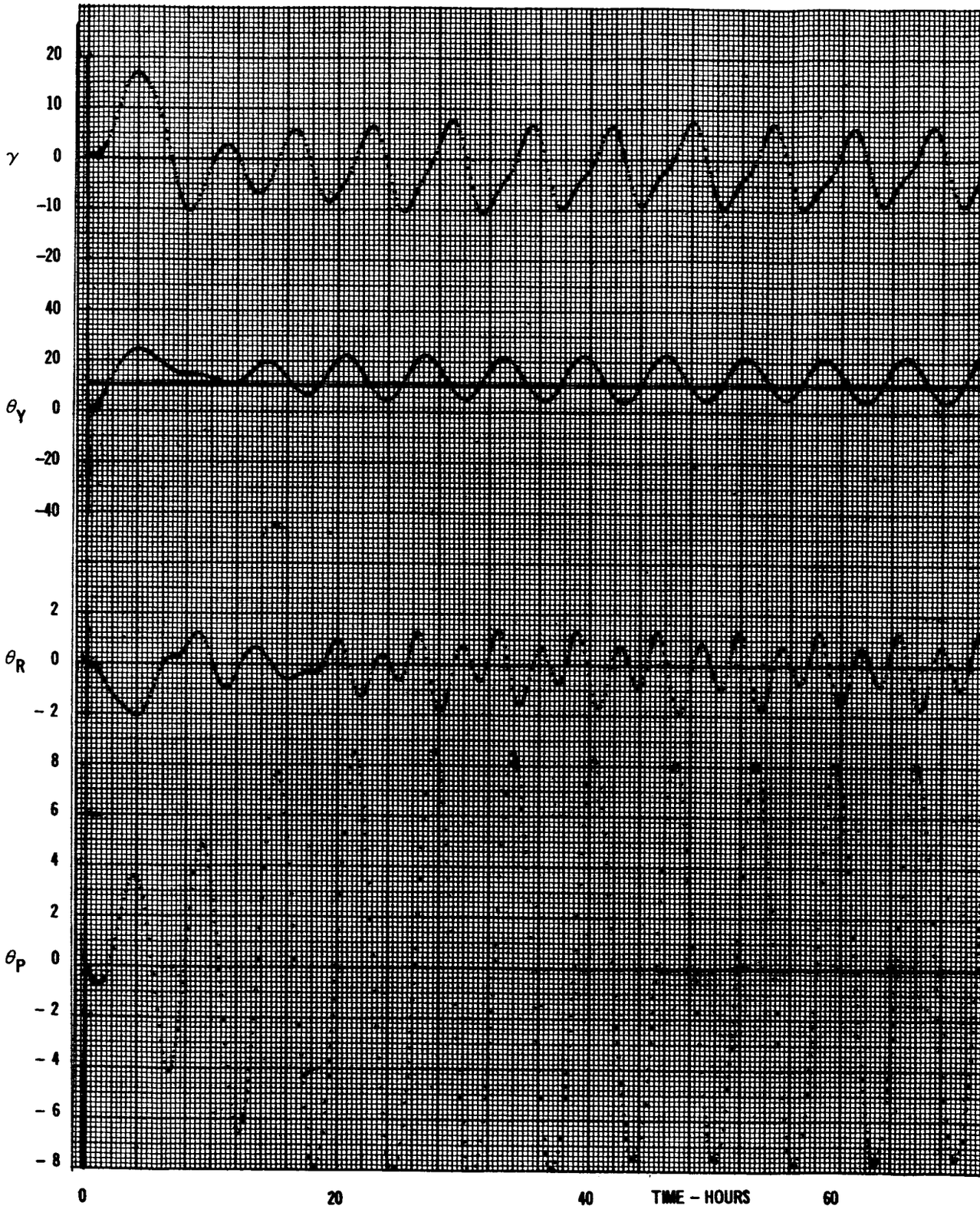


Figure 2.1.2-2. MAGGE, 11 Degree Half Angle, Steady State


20
10
γ 0
-10
-20
40
20
θY 0
-20
-40
2
θR 0
- 2
8
6
4
2
θP 0
- 2
- 4
- 6
- 8
0
20
40
TIME – HOURS
60

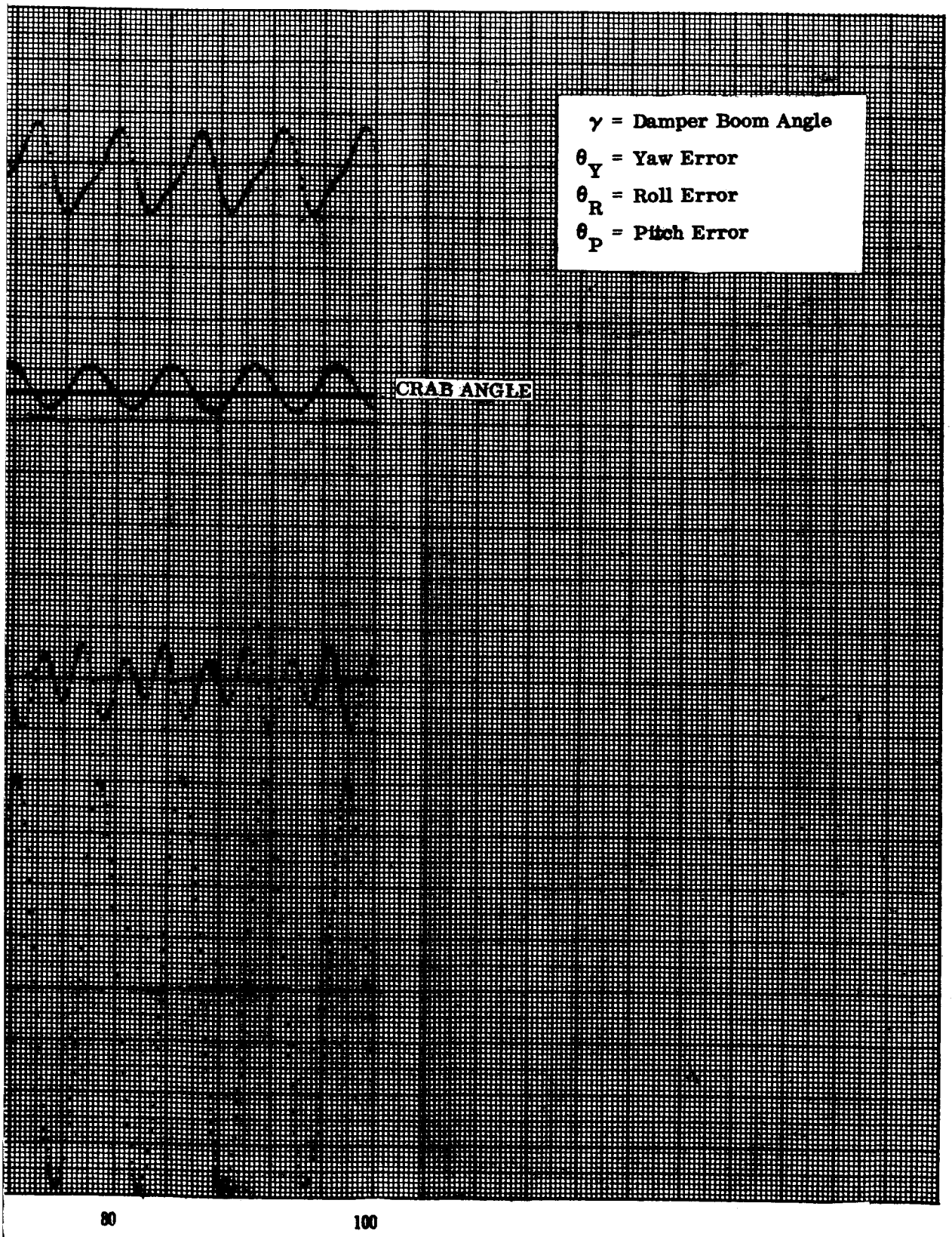
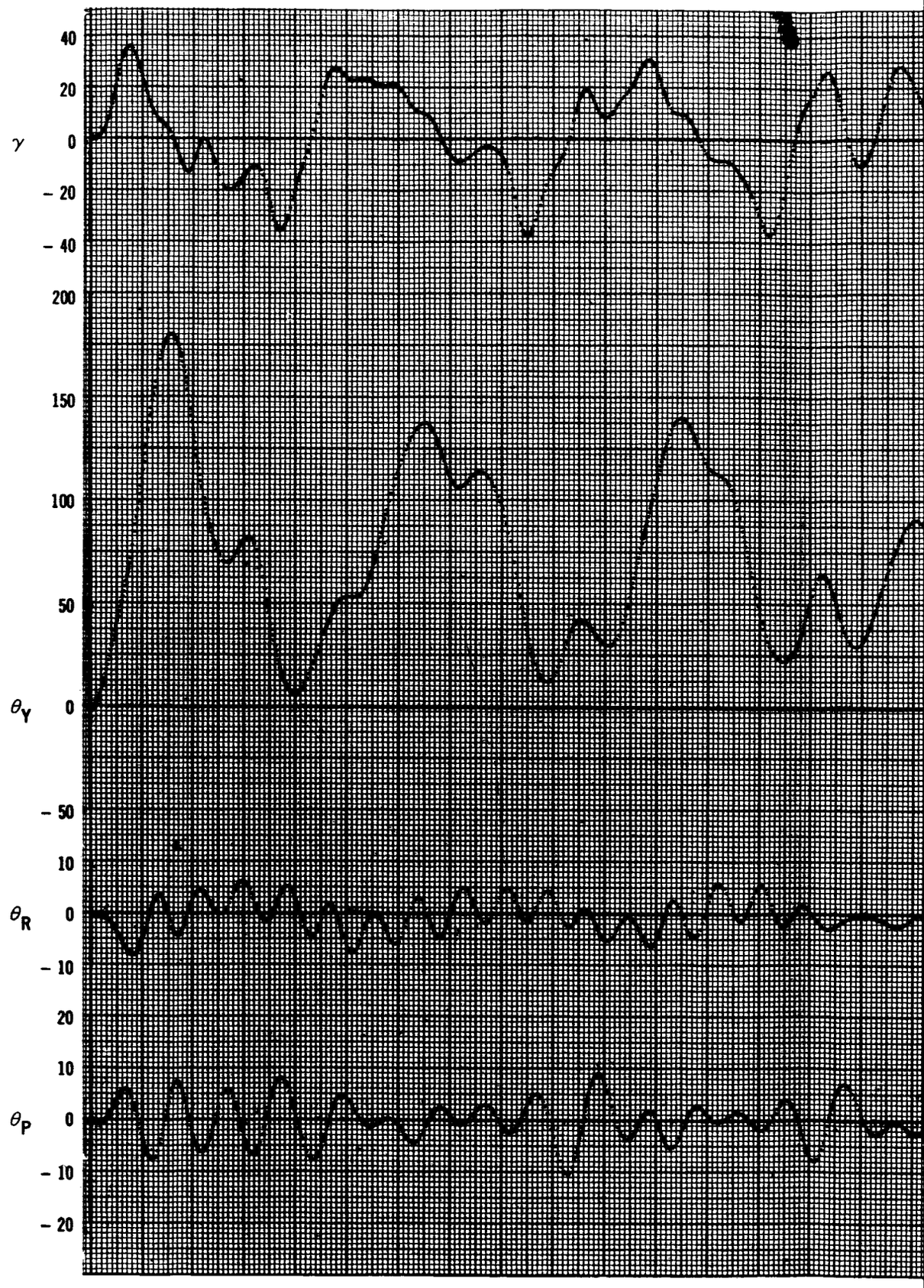


Figure 2.1.2-3. MAGGE, 31 Degree Half Angle, Steady State


40
20
γ 0
– 20
– 40
200
150
100
50
θY 0
– 50
10
θR 0
– 10
20
10
θP 0
– 10
– 20
0
20
40
60

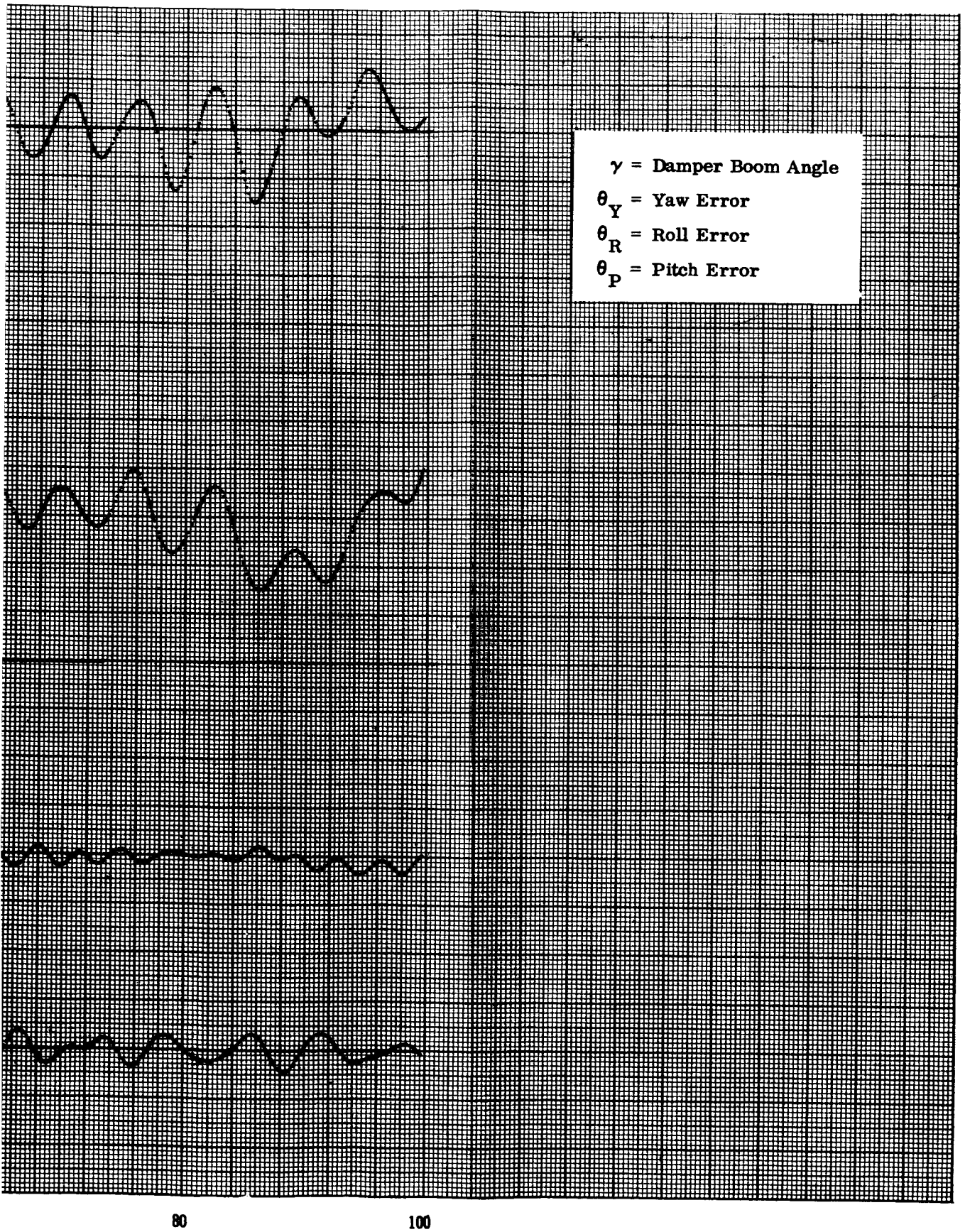
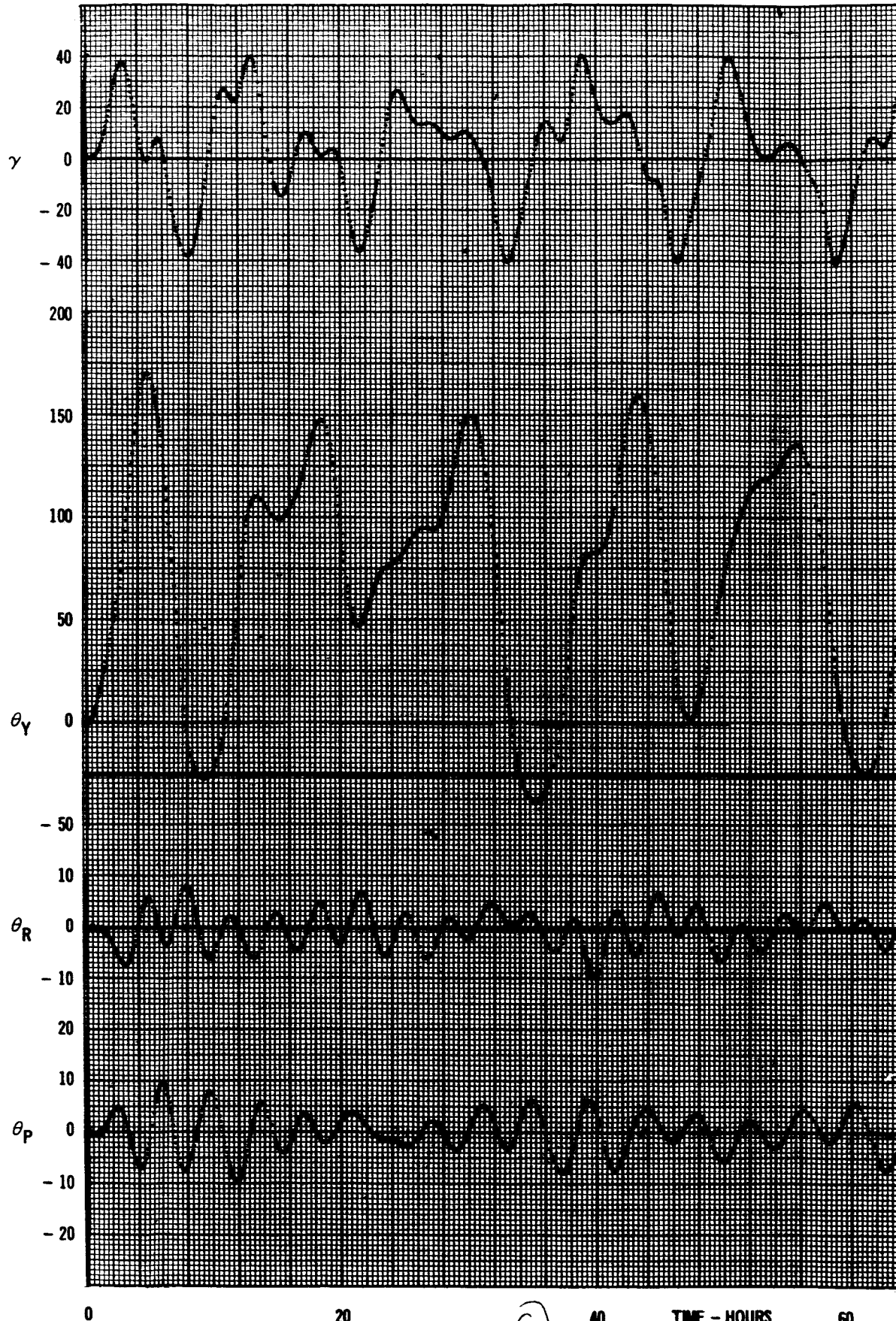


Figure 2.1.2-4. MAGGE, 19 Degree Half Angle, 10,000 Pole-CM on Roll Axis


40
20
γ 0
- 20
- 40
200
150
100
50
θY 0
- 50
10
θR 0
- 10
20
10
θP 0
- 10
- 20
0
20
40
TIME - HOURS
60

2-15

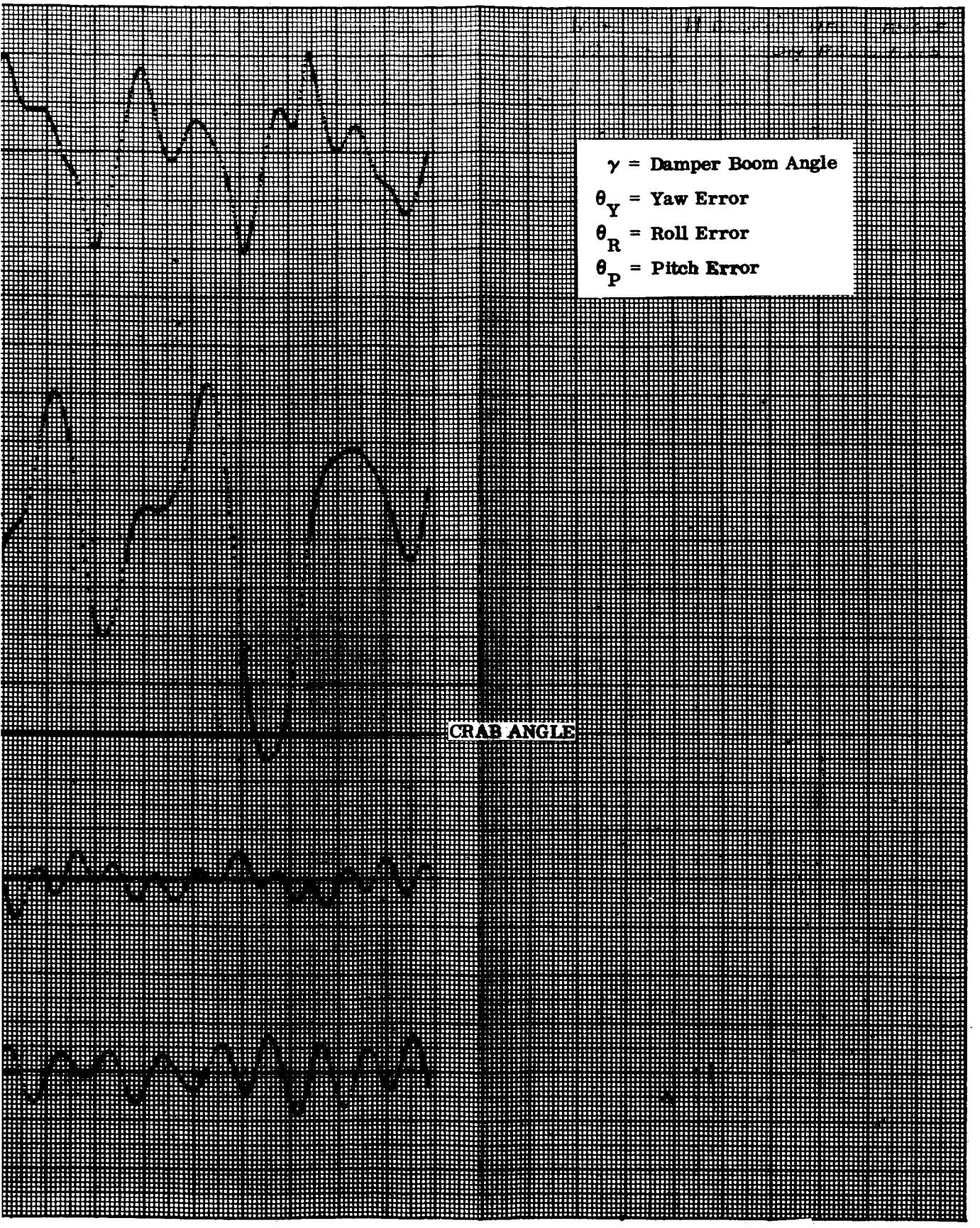
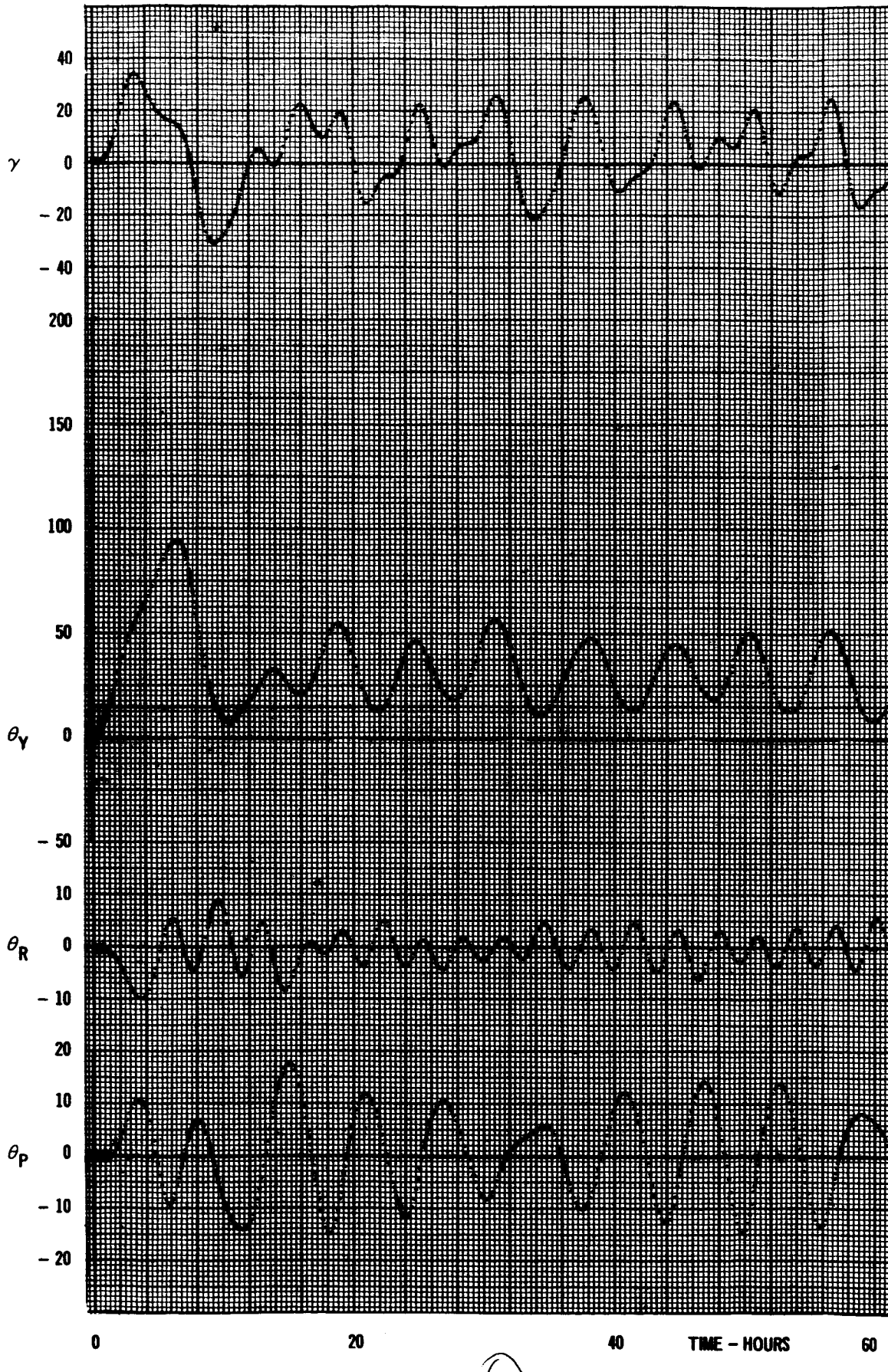


Figure 2.1.2-5. MAGGE, 11 Degree Half Angle, 10,000 Pole-CM on Role Axis


40
20
γ 0
– 20
– 40
200
150
100
50
θY 0
– 50
10
θR 0
– 10
20
10
θP 0
– 10
– 20
0
20
40
TIME – HOURS
60

10

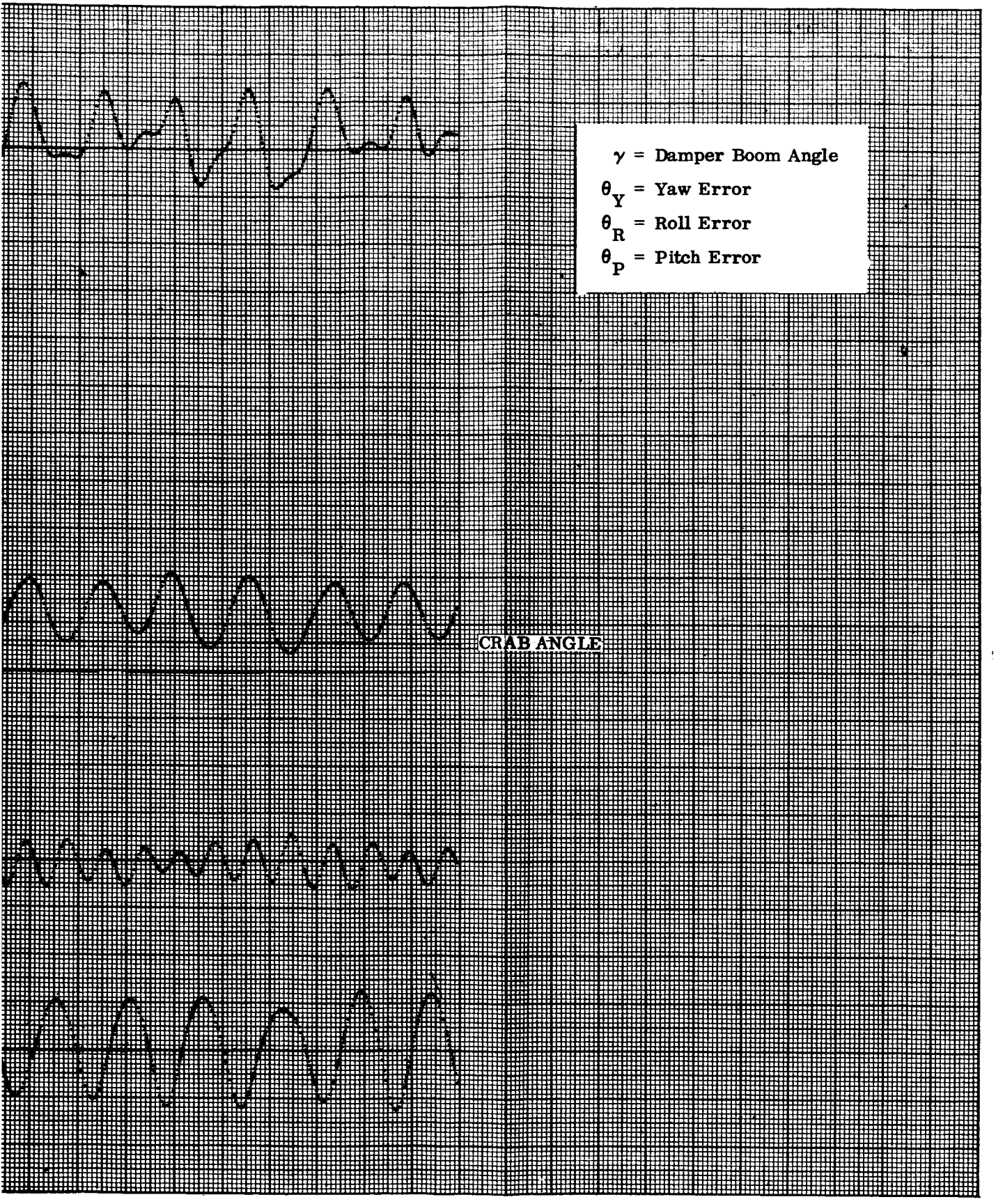
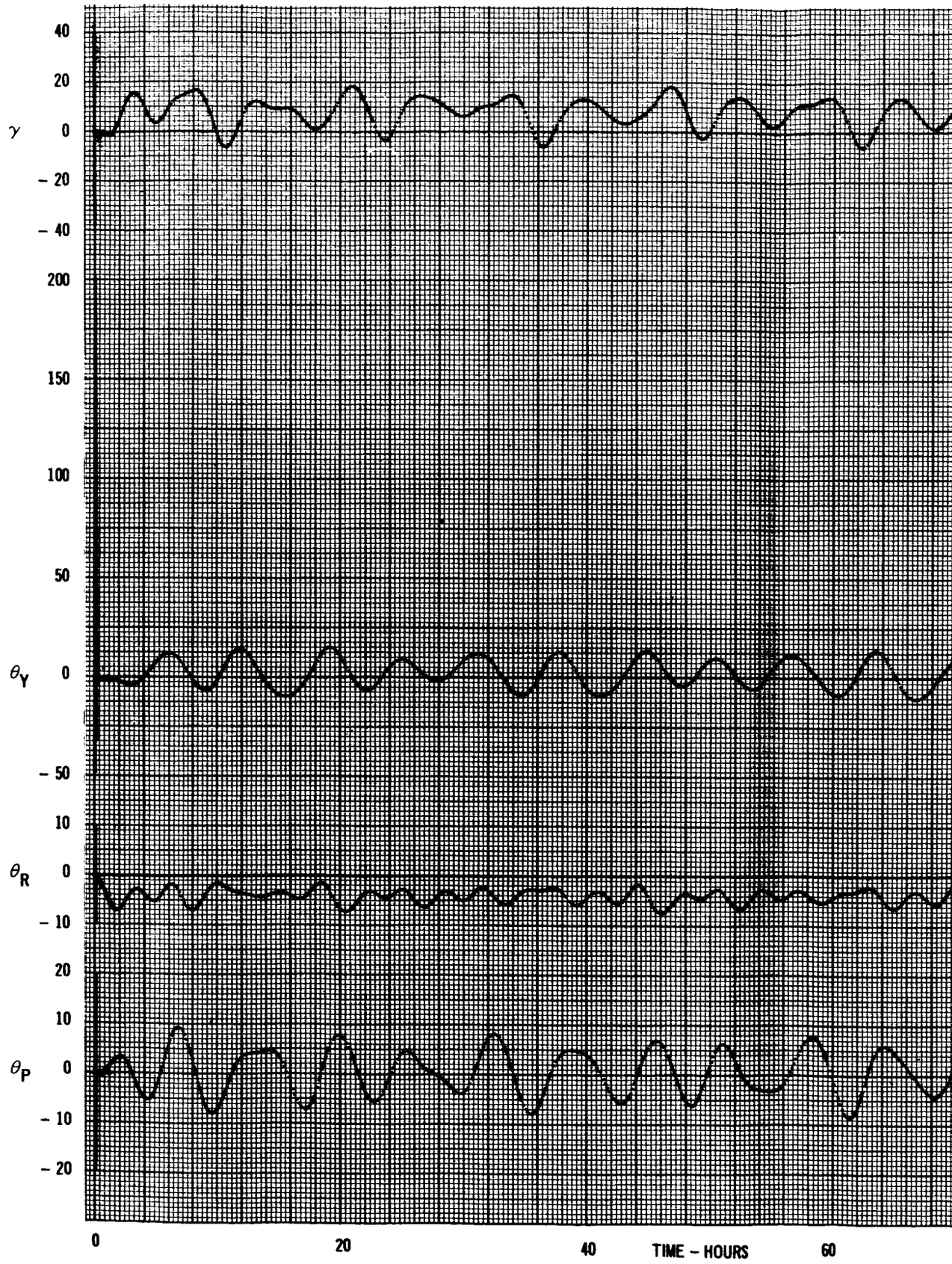


Figure 2.1.2-6. MAGGE, 31 Degree Half Angle, 10,000 Pole-CM on Roll Axis


40
20
γ 0
– 20
– 40
200
150
100
50
θY 0
– 50
10
θR 0
– 10
20
10
θP 0
– 10
– 20
0
20
40
TIME – HOURS
60

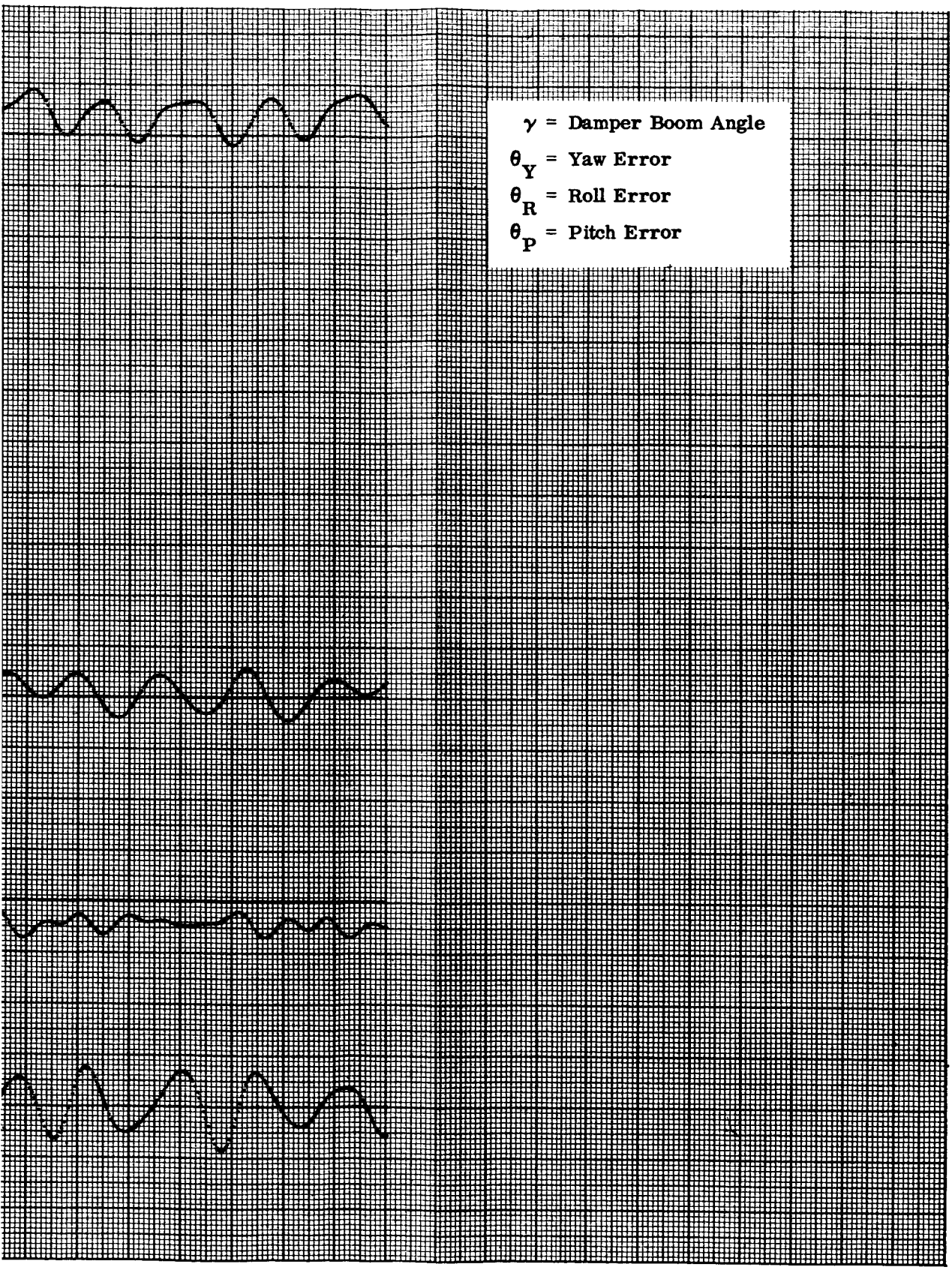
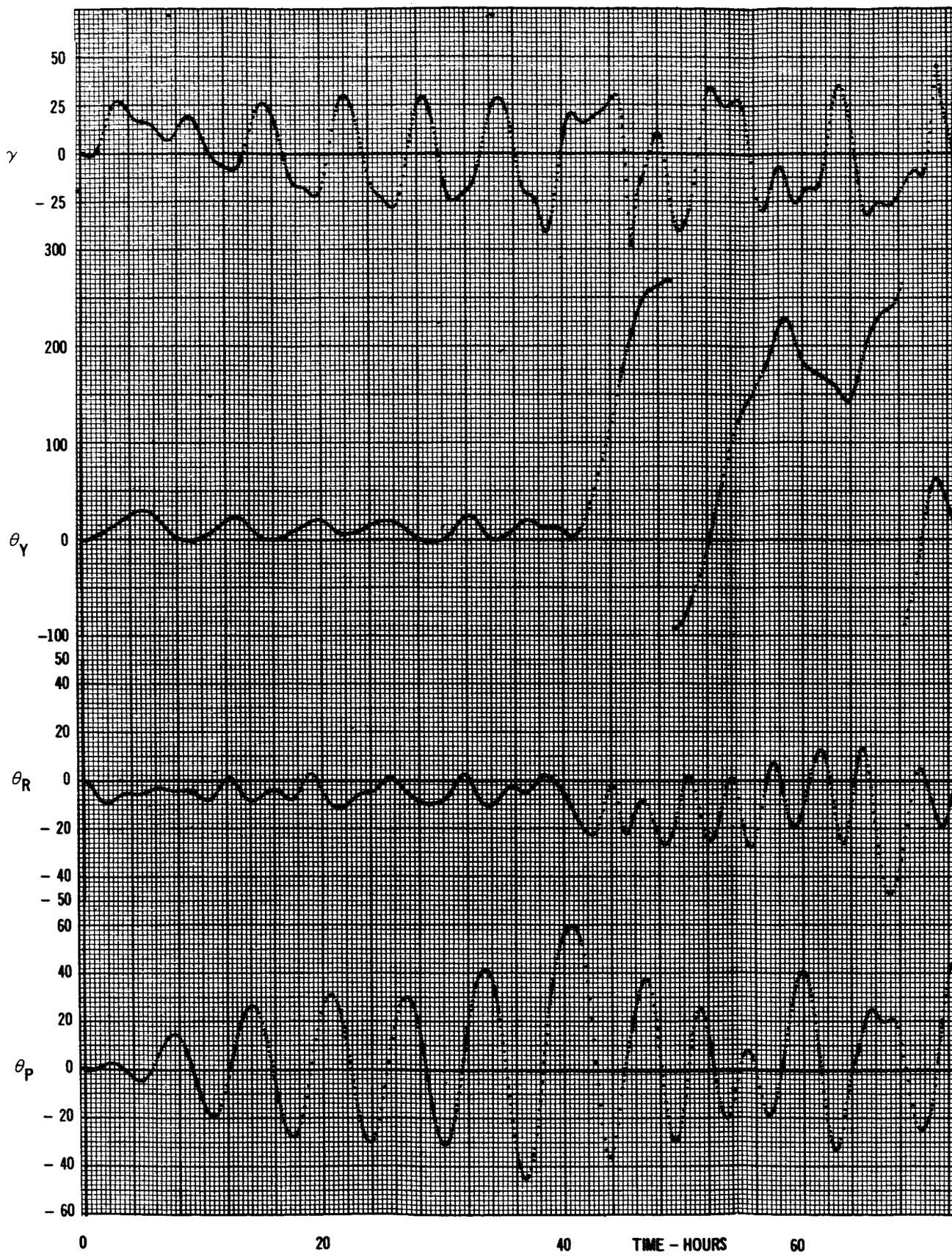


Figure 2.1.2-7. MAGGE, 19 Degree Half Angle, 20,000 Pole-CM on Yaw Axis


50
25
γ 0
– 25
300
200
100
θY 0
–100
50
40
20
θR 0
– 20
– 40
– 50
60
40
20
θP 0
– 20
– 40
– 60
0
20
40
TIME – HOURS
60

210

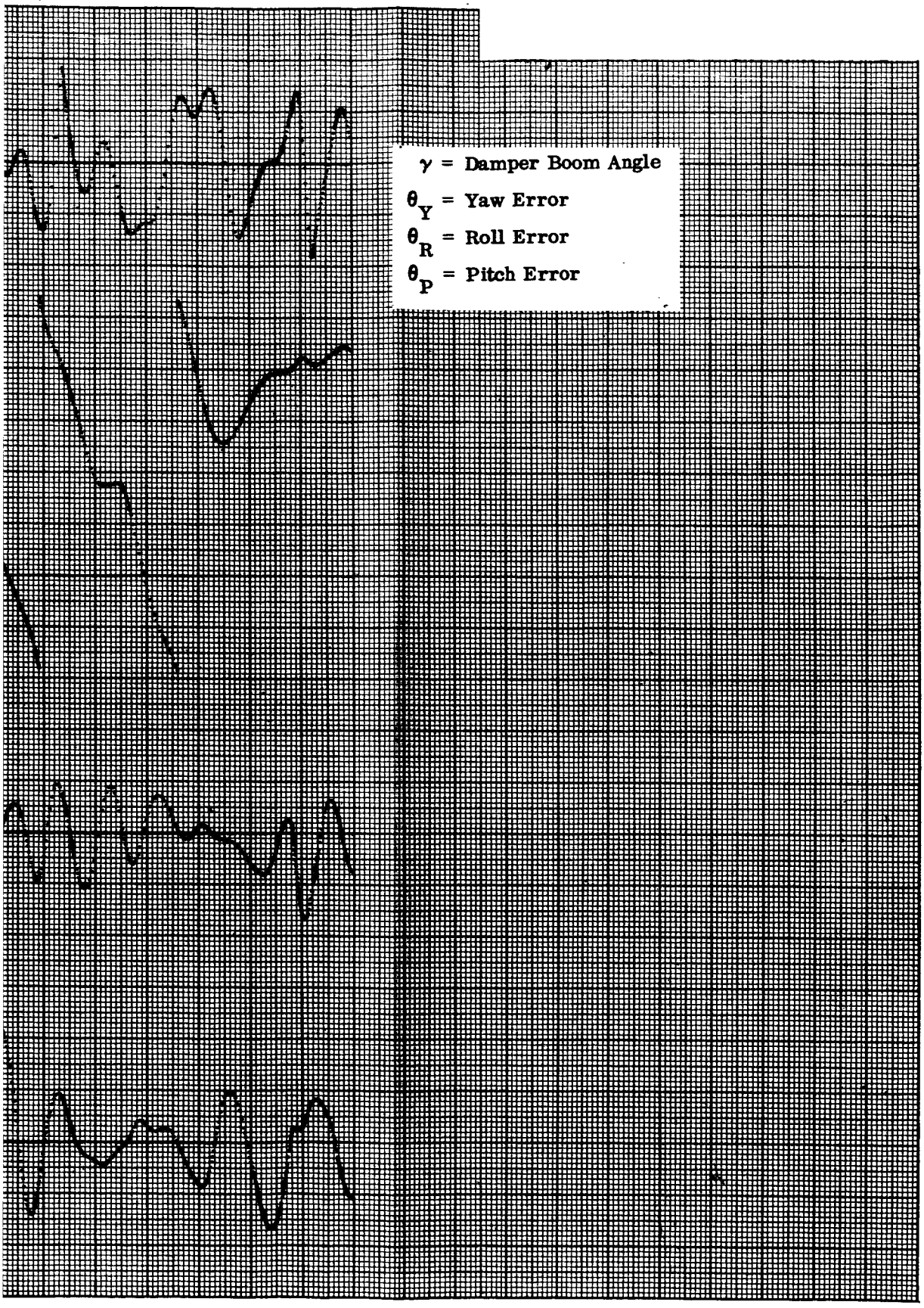
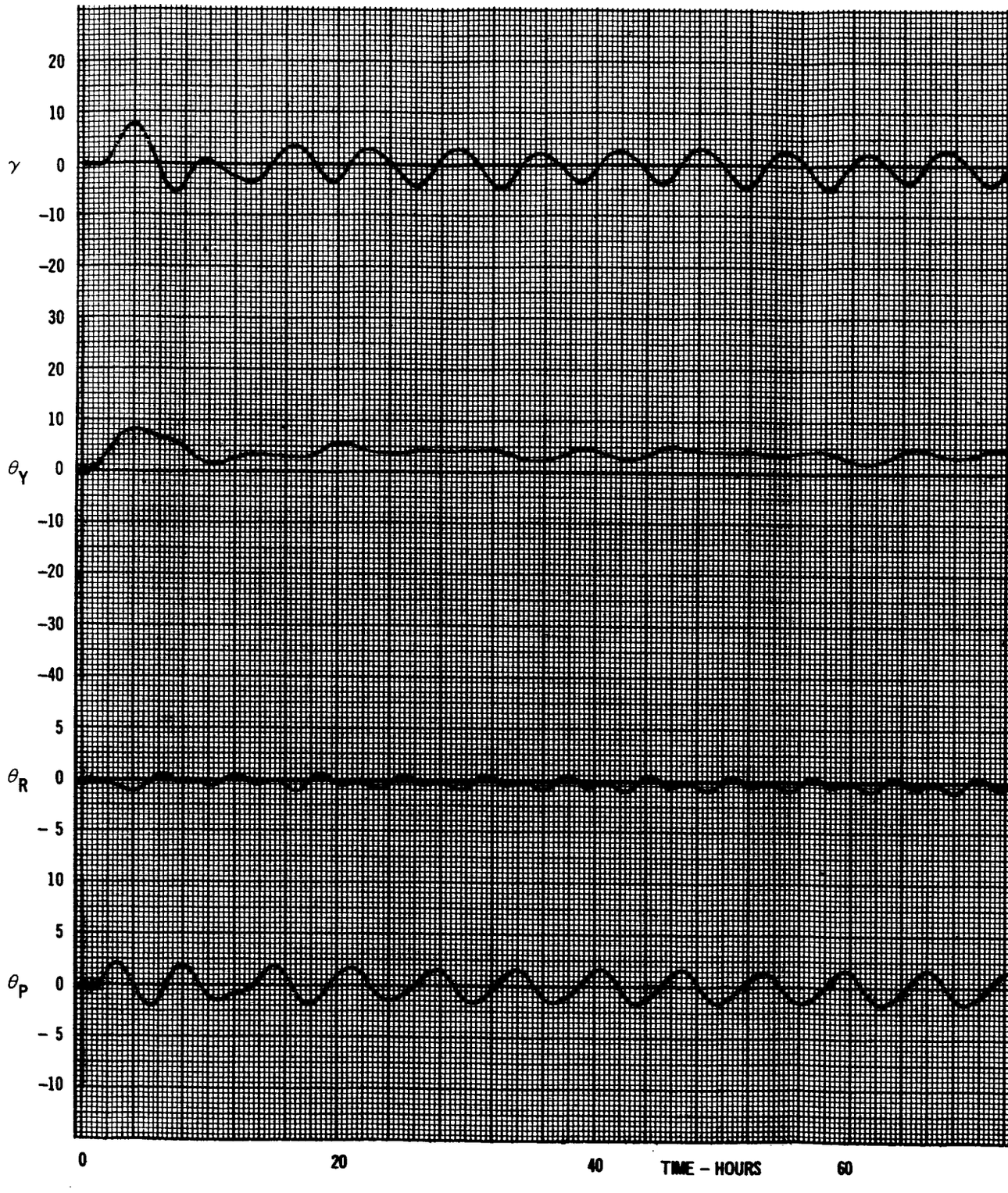


Figure 2.1.2-8. MAGGE, 31 Degree Half Angle, 20,000 Pole-CM on Yaw Axis


20
10
γ 0
-10
-20
30
20
10
θY 0
-10
-20
-30
-40
5
θR 0
- 5
10
5
θP 0
- 5
-10
0
20
40
TIME – HOURS
60

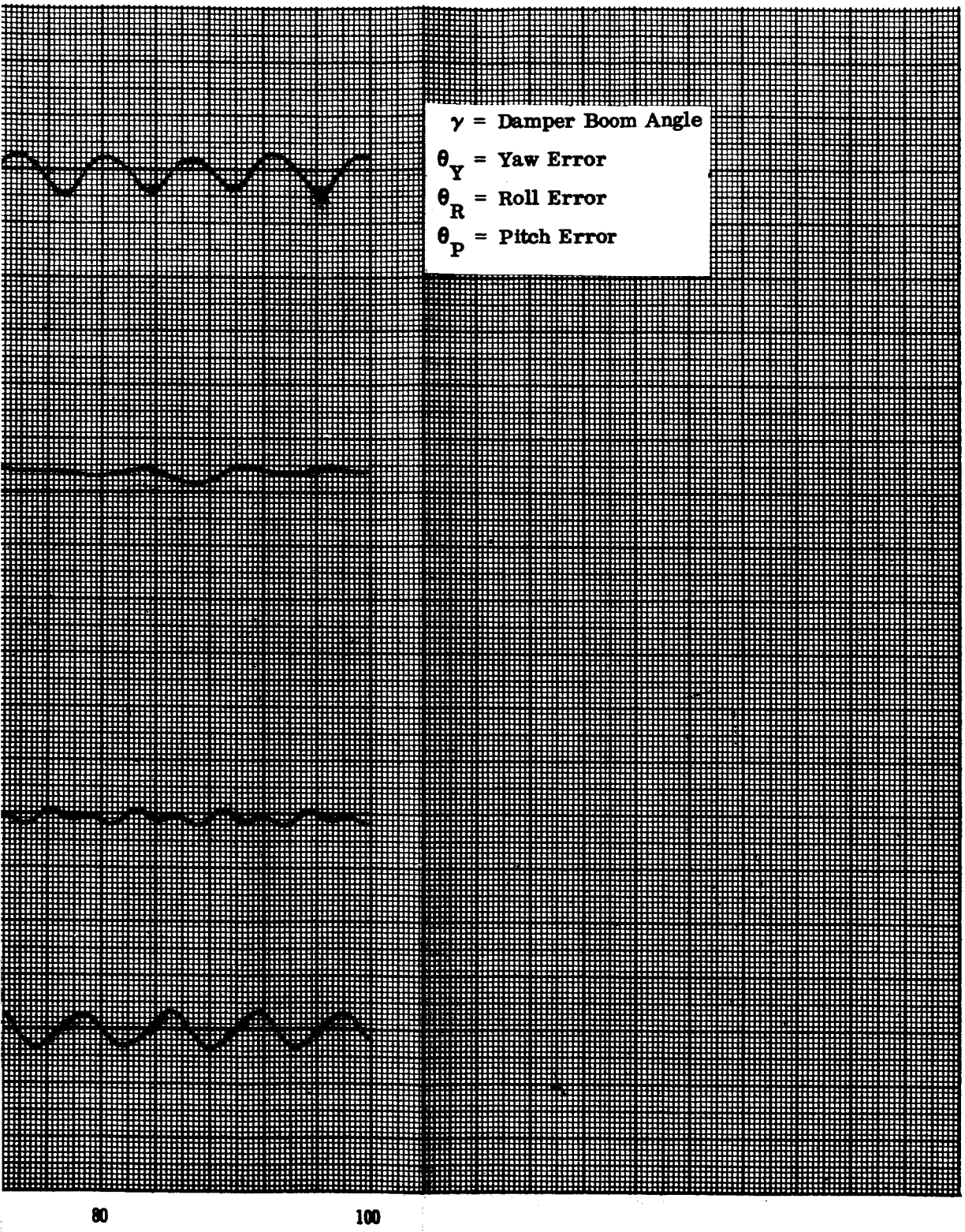
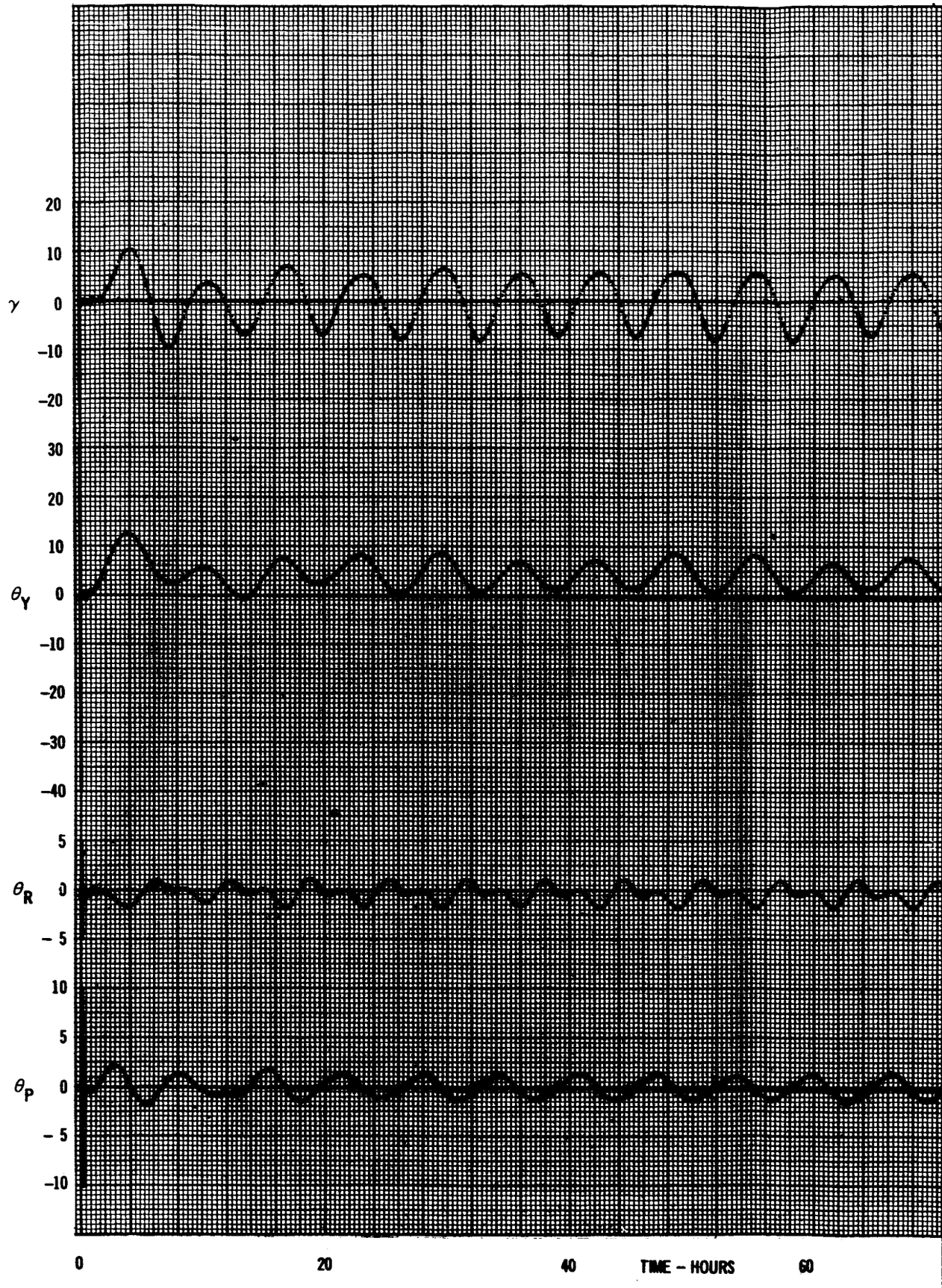


Figure 2.1.2-9. MAGGE, 19 Degree Half Angle, C.P. Boom Extended 15 Ft.


20
10
γ 0
-10
-20
30
20
10
θY 0
-10
-20
-30
-40
5
θR 0
- 5
10
5
θP 0
- 5
-10
0
20
40
TIME – HOURS
60

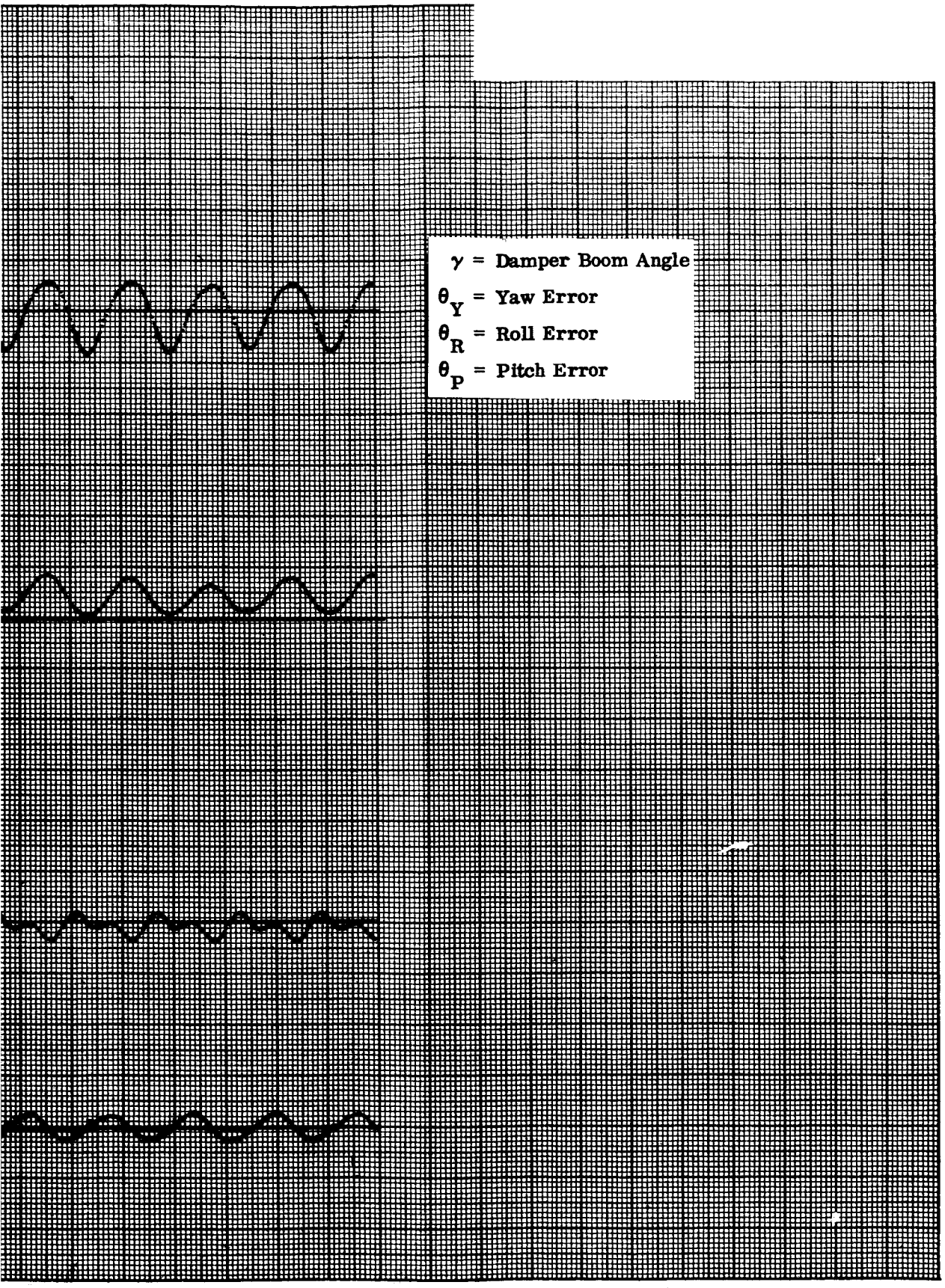
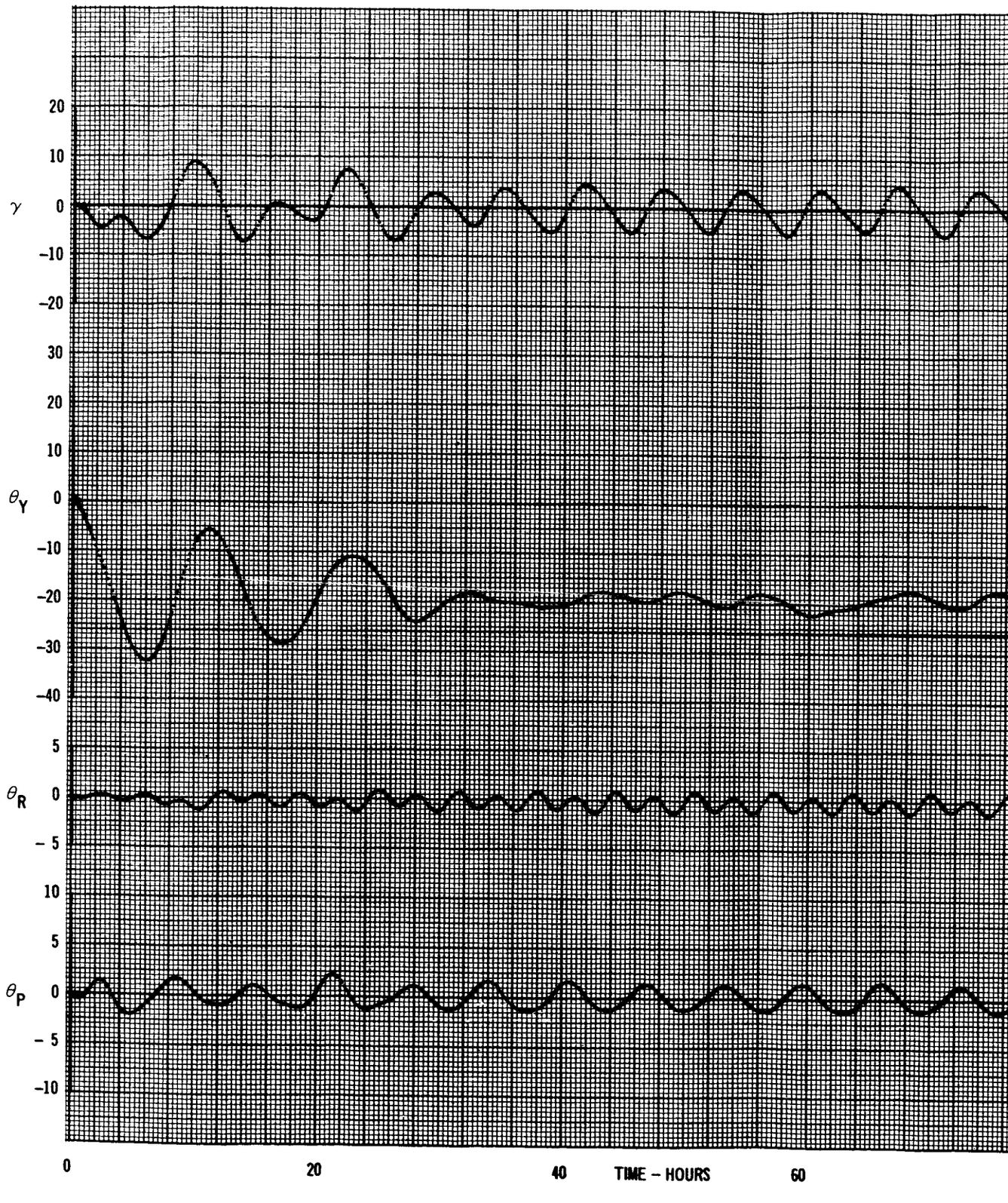


Figure 2.1.2-10. MAGGE, 19 Degree Half Angle, C.P. Boom Extended 30 Ft.


20
10
γ 0
−10
−20
30
20
10
θY 0
−10
−20
−30
−40
5
θR 0
− 5
10
5
θP 0
− 5
−10
0
20
40
TIME – HOURS
60

270

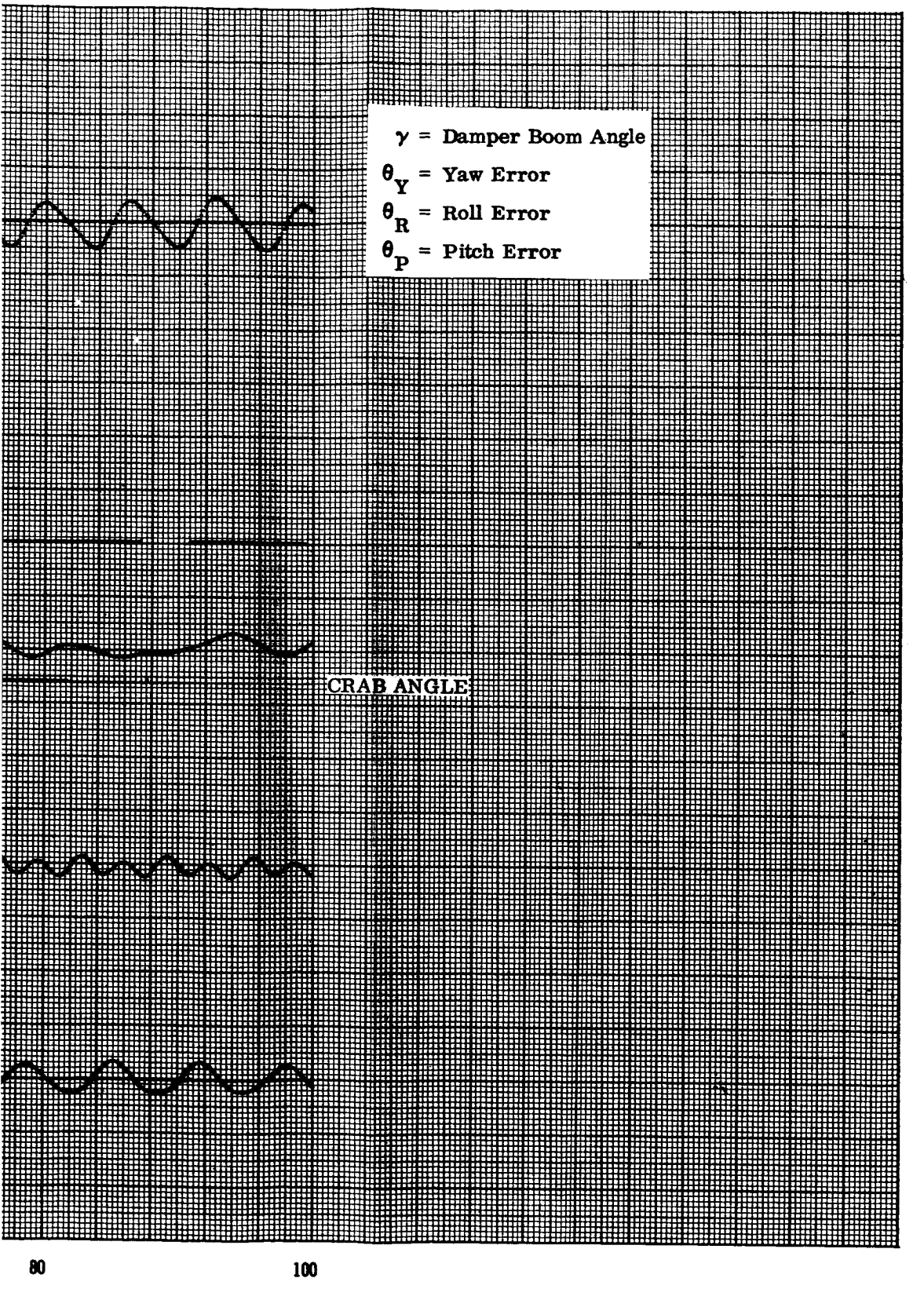
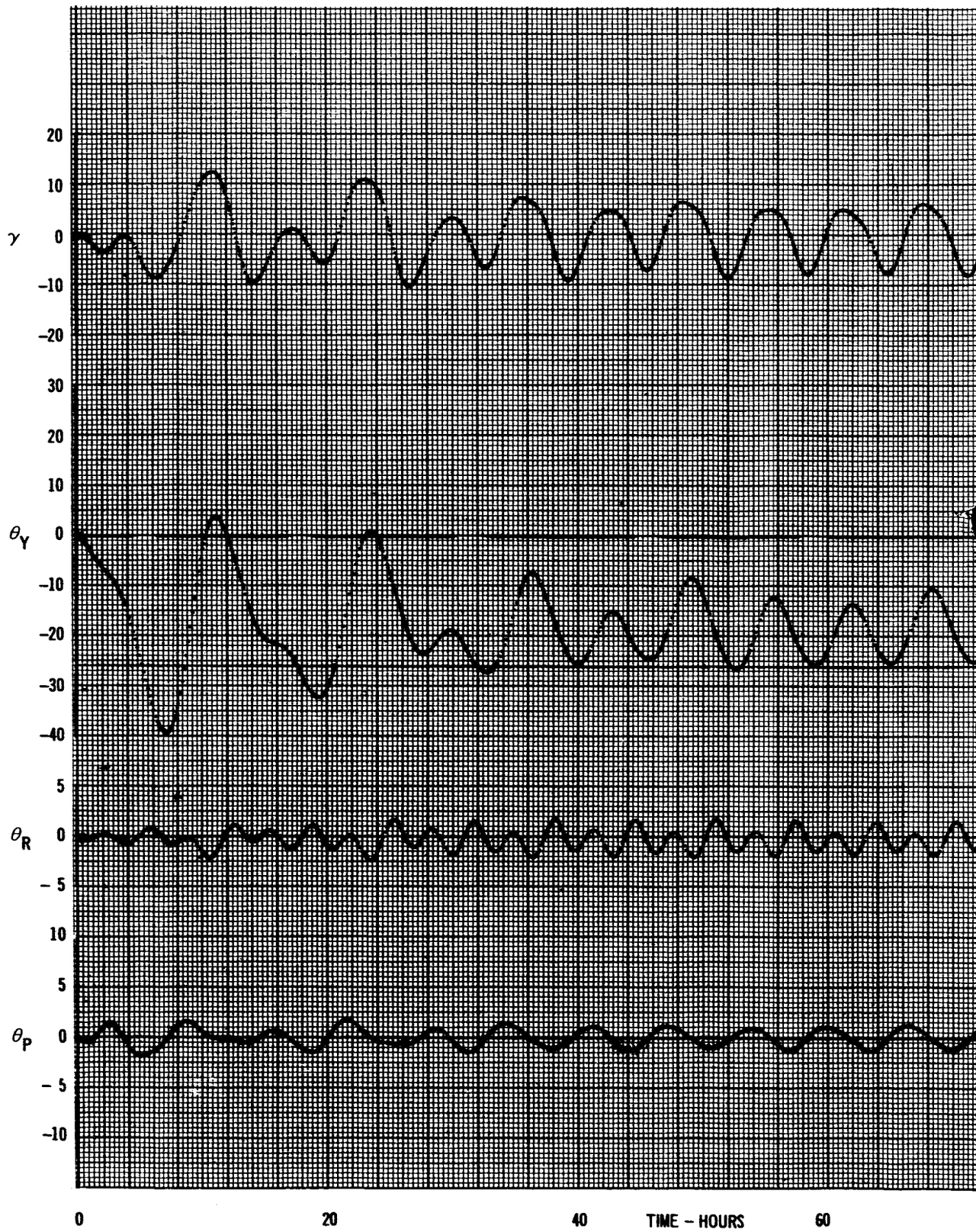


Figure 2.1.2-11. MAGGE, 11 Degree Half Angle, C.P. Boom Extended 15 Ft.


20
10
γ 0
-10
-20
30
20
10
θY 0
-10
-20
-30
-40
5
θR 0
- 5
10
5
θP 0
- 5
-10
0
20
40
TIME – HOURS
60

290

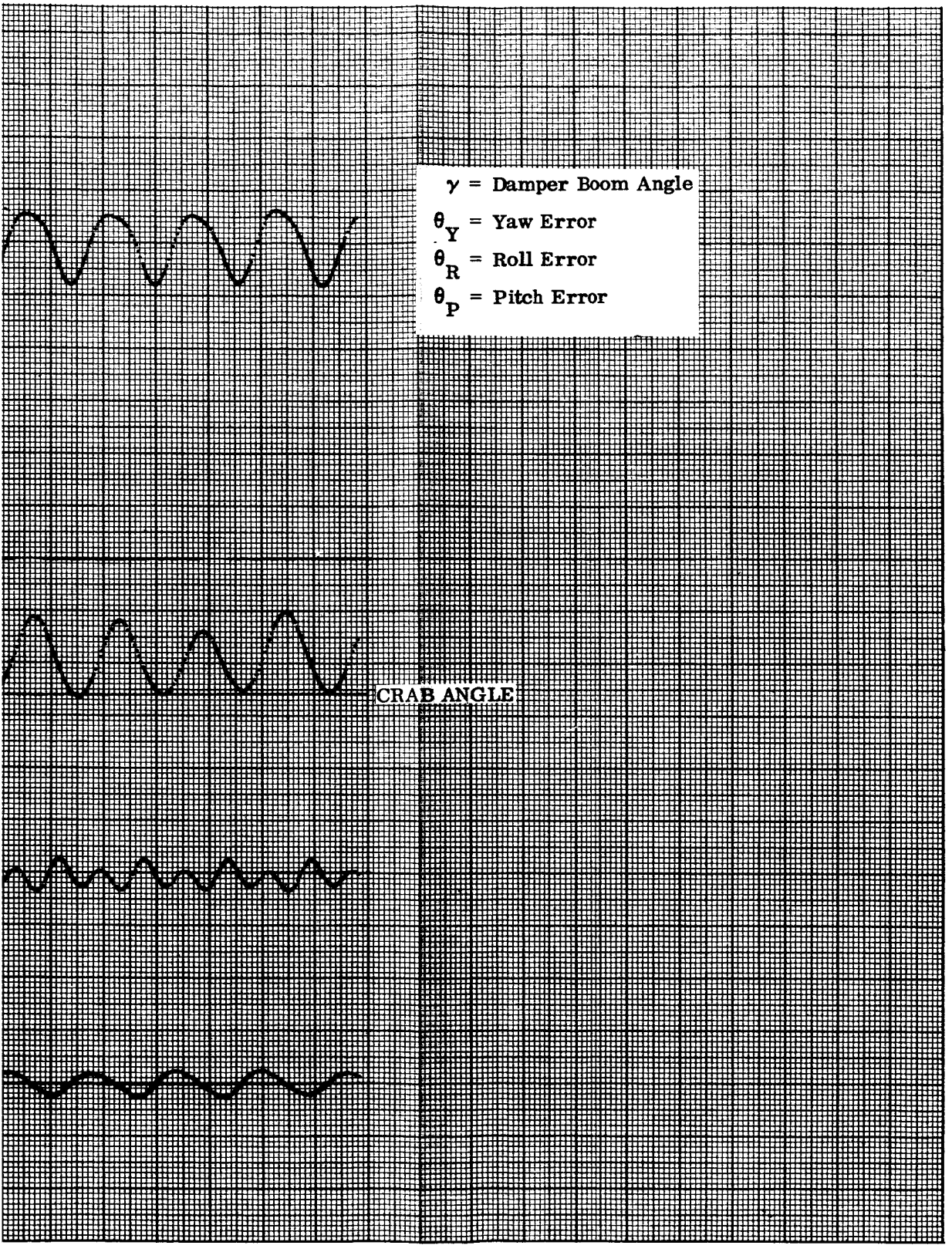
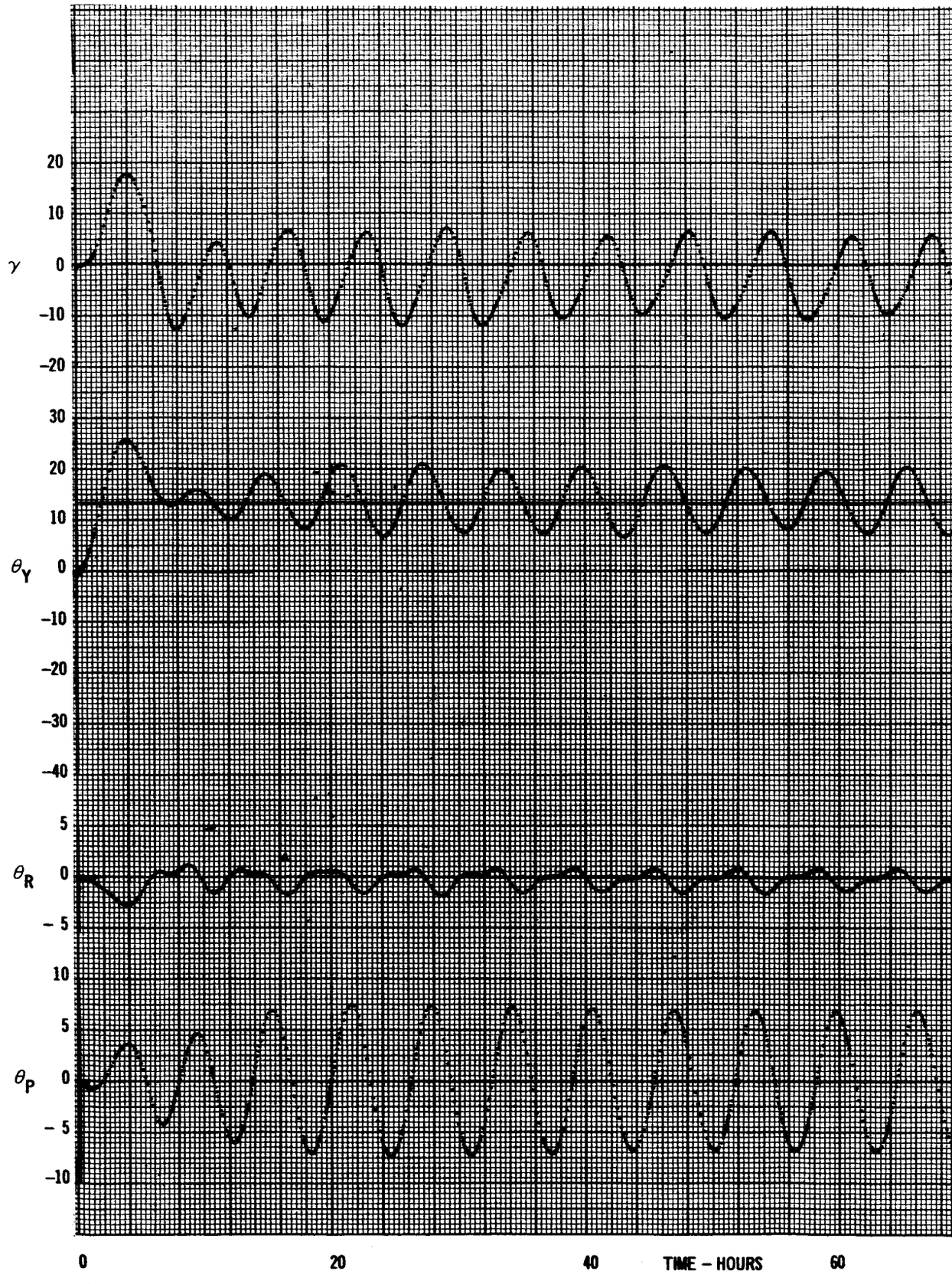


Figure 2.1.2-12. MAGGE, 11 Degree Half Angle, C.P. Boom Fully Extended - 30 Ft.


20
10
γ 0
-10
-20
30
20
10
θY 0
-10
-20
-30
-40
5
θR 0
- 5
10
5
θP 0
- 5
-10
0
20
40
TIME – HOURS
60

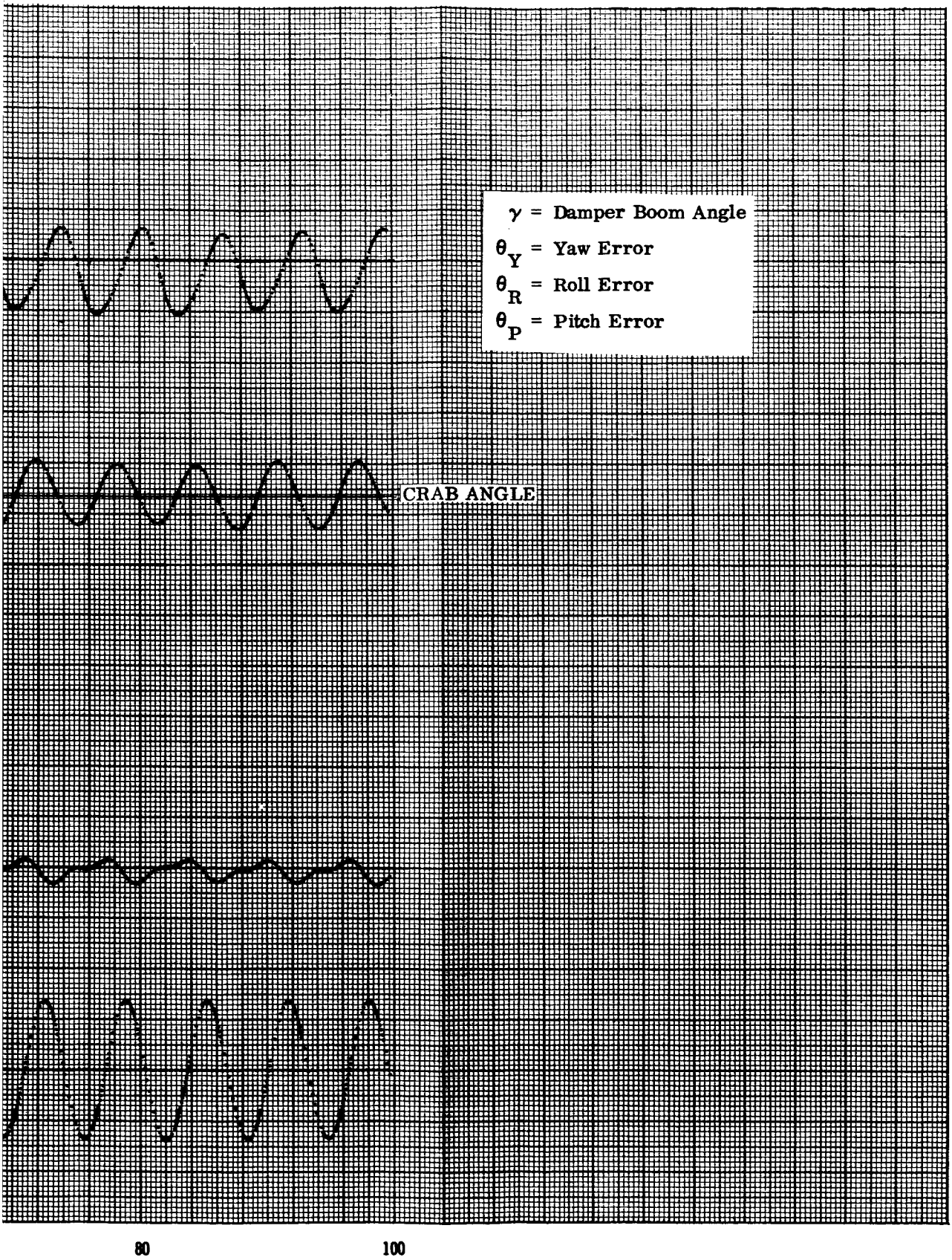
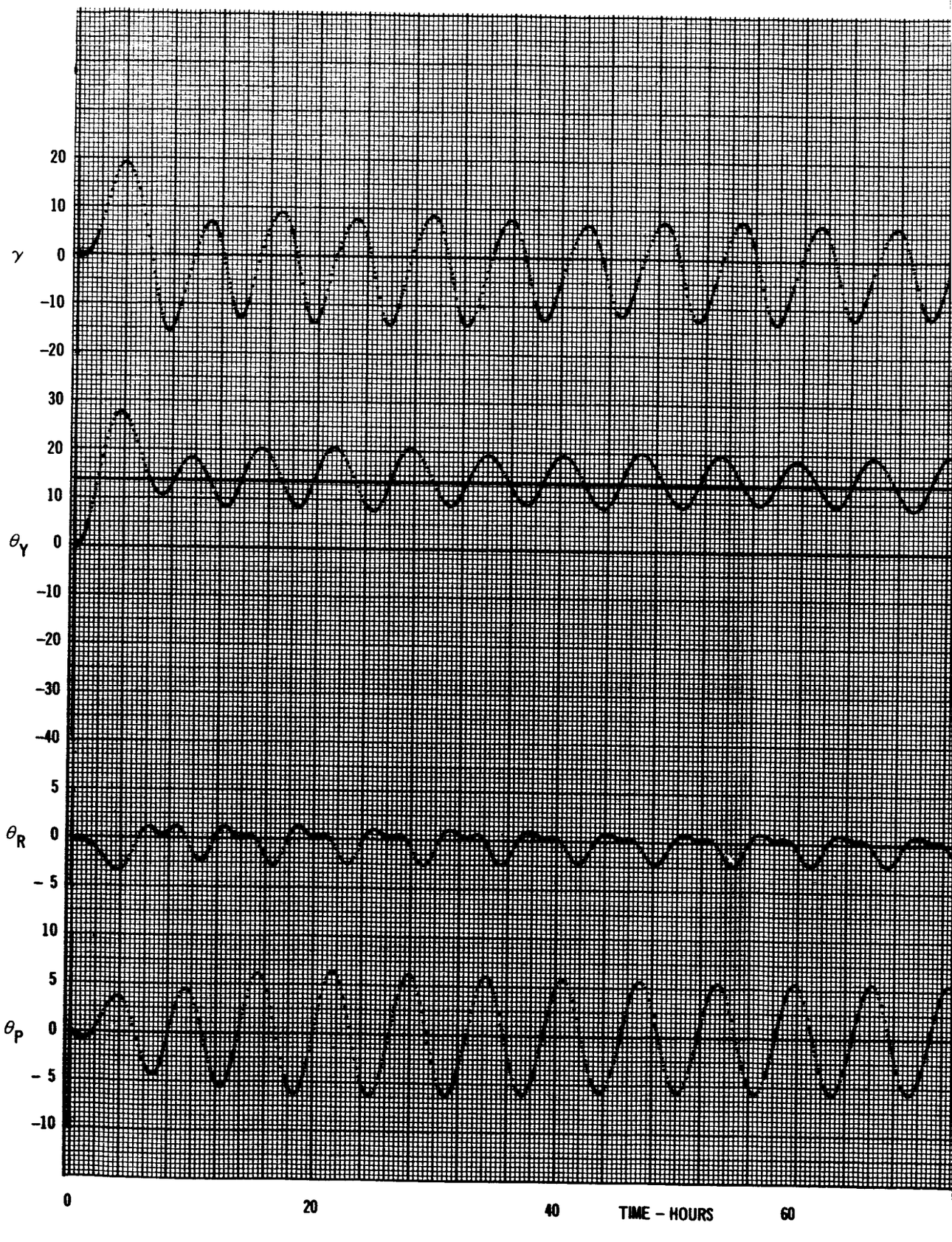


Figure 2.1.2-13. MAGGE, 31 Degree Half Angle, C.P. Boom Extended 15 Ft.


20
10
γ 0
-10
-20
30
20
10
θY 0
-10
-20
-30
-40
5
θR 0
- 5
10
5
θP 0
- 5
-10
0
20
40
TIME – HOURS
60

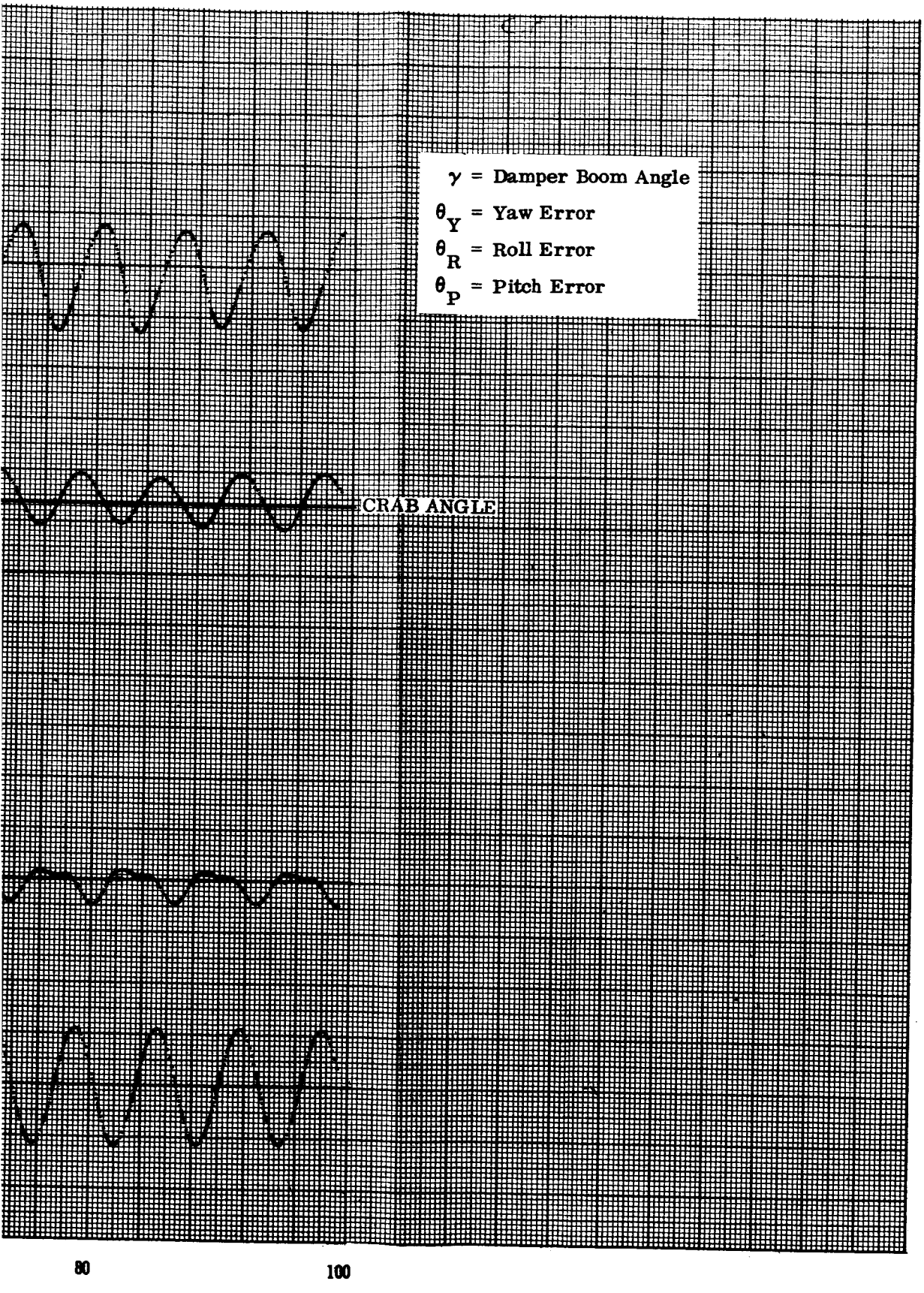
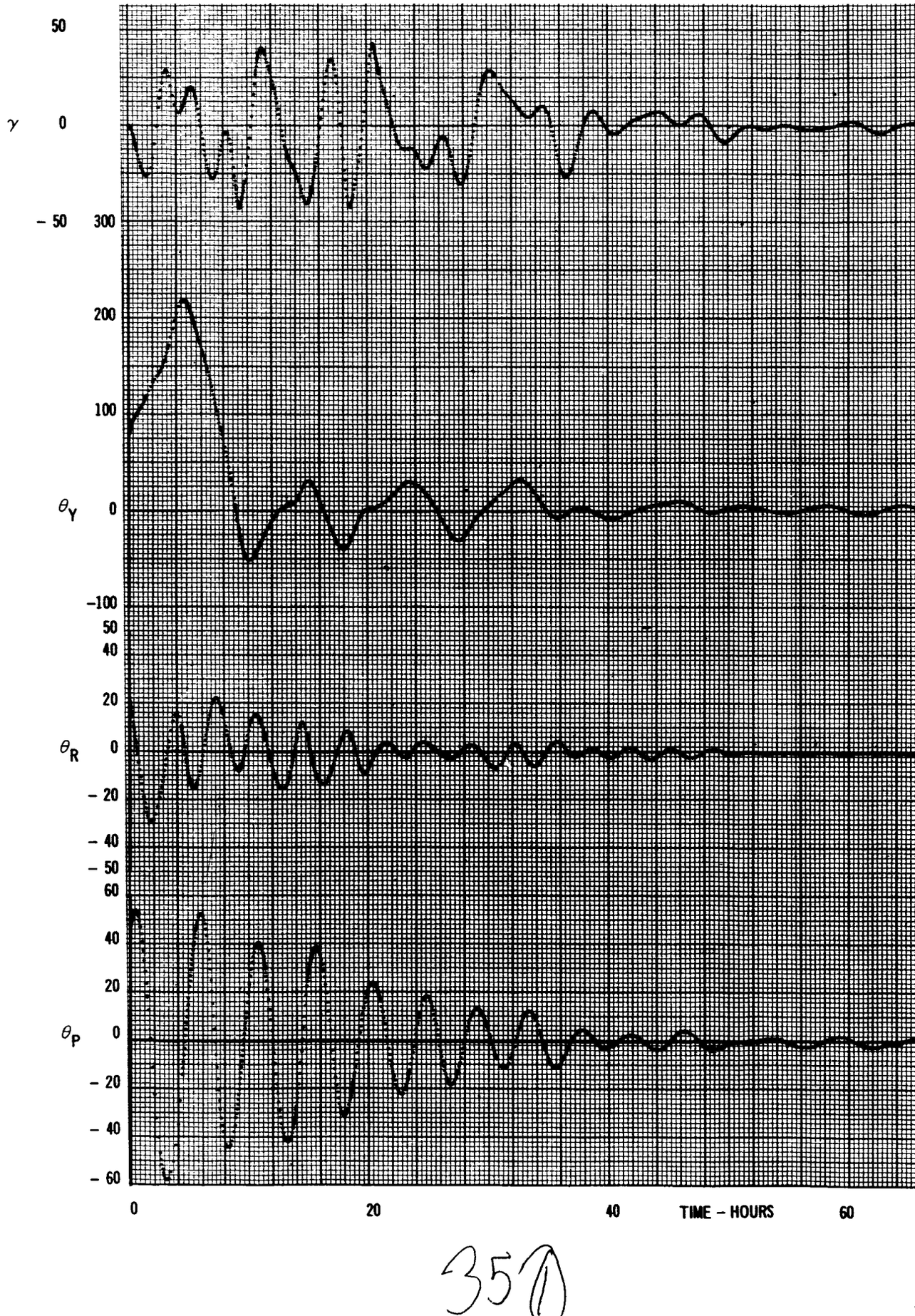


Figure 2.1.2-14. MAGGE, 31 Degree Half Angle, C.P. Extended 30 Ft. on Pitch Axis


50
γ 0
– 50
300
200
100
θY 0
–100
50
40
20
θR 0
– 20
– 40
– 50
60
40
20
θP 0
– 20
– 40
– 60
0
20
40
TIME – HOURS
60

350

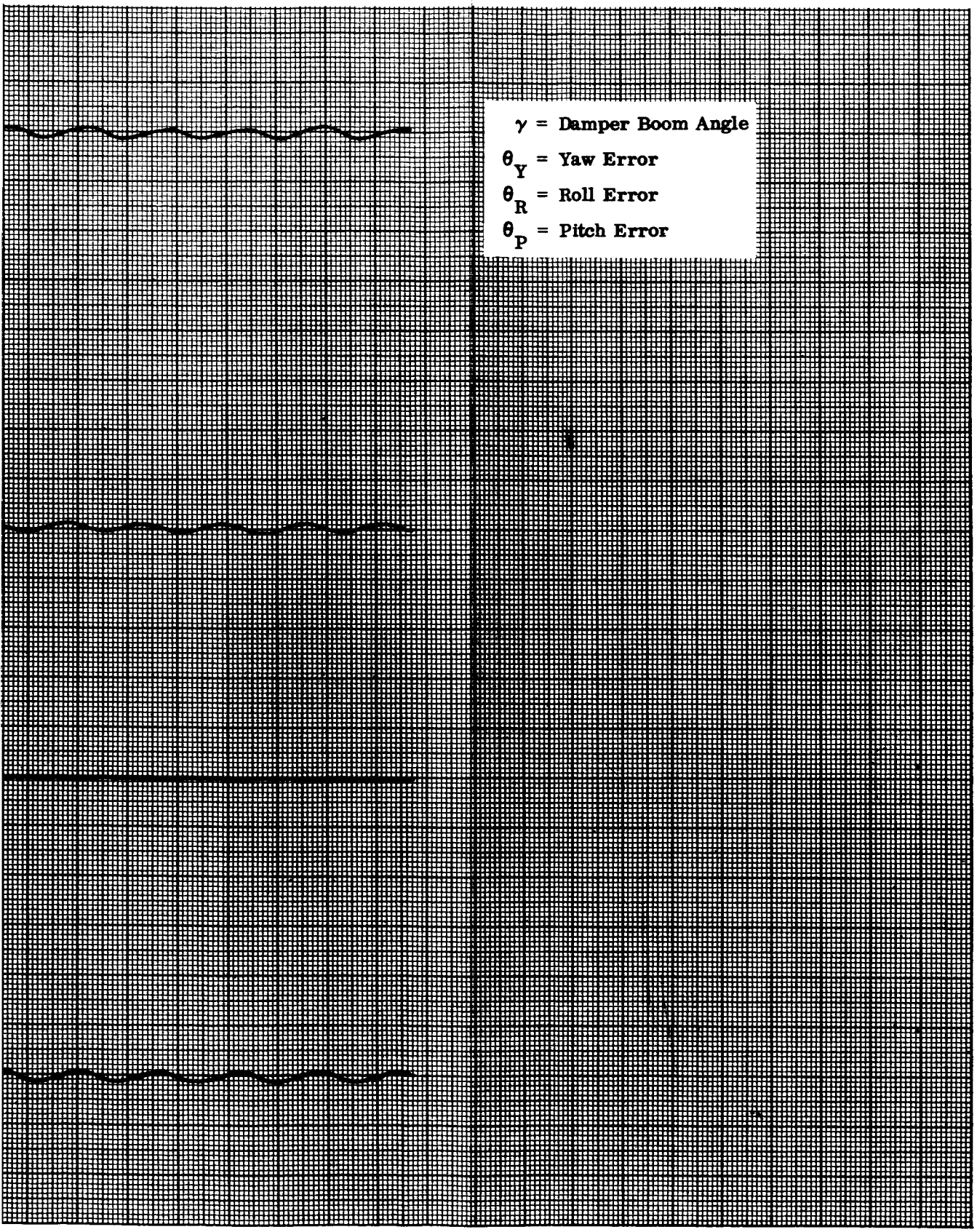
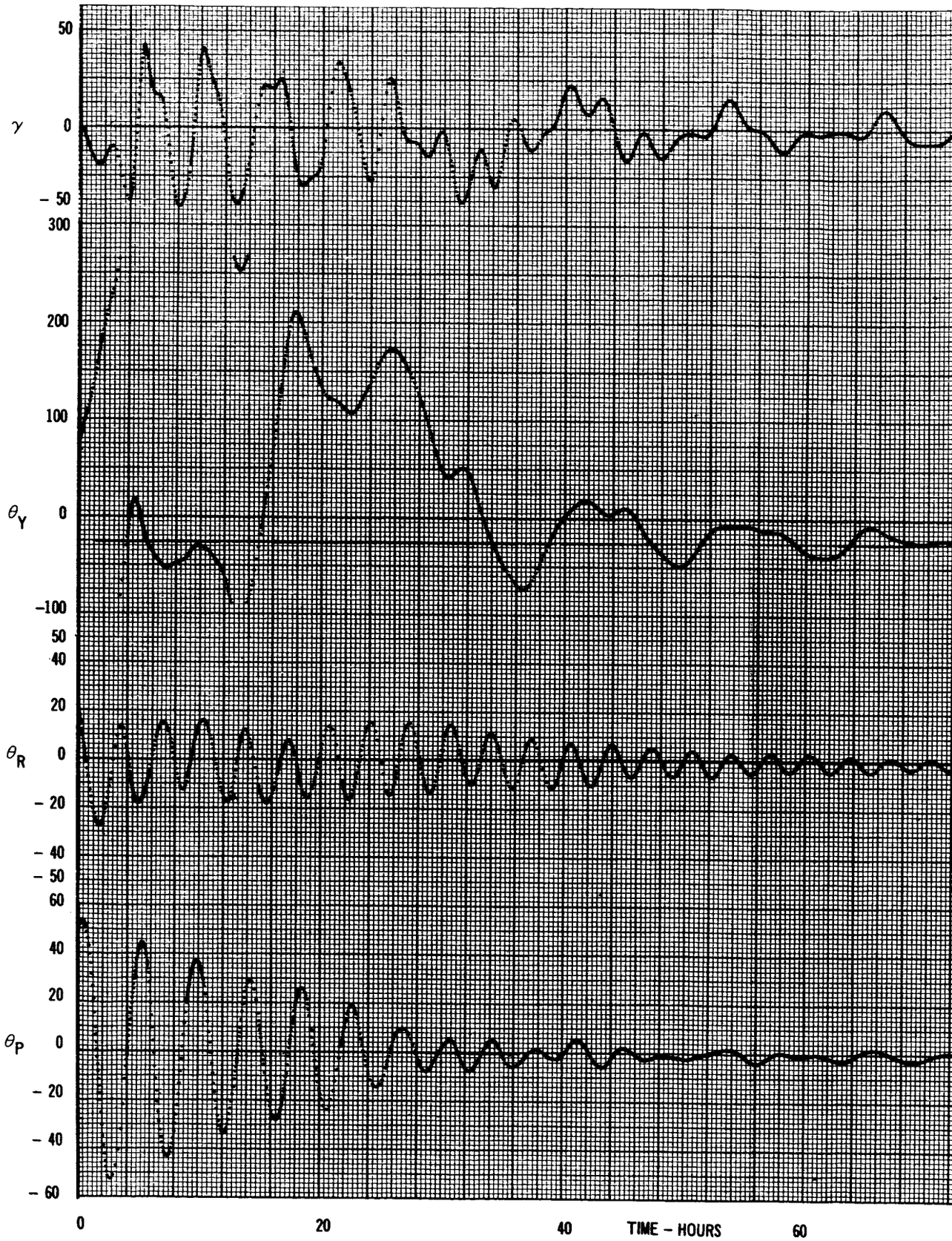


Figure 2.1.2-15. MAGGE, 19 Degree Half Angle, Transient


50
γ 0
– 50
300
200
100
θY 0
–100
50
40
20
θR 0
– 20
– 40
– 50
60
40
20
θP 0
– 20
– 40
– 60
0
20
40
TIME – HOURS
60

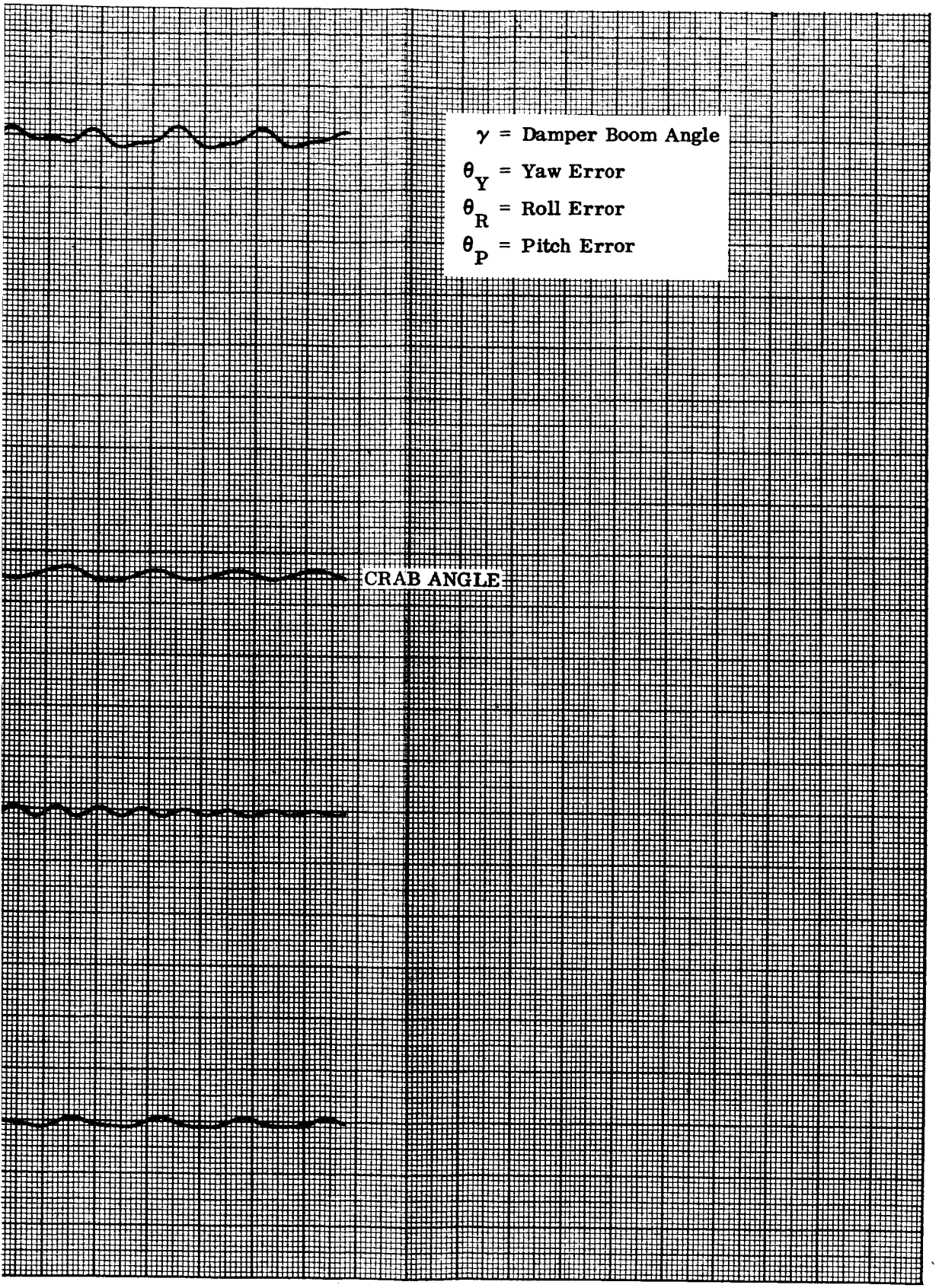
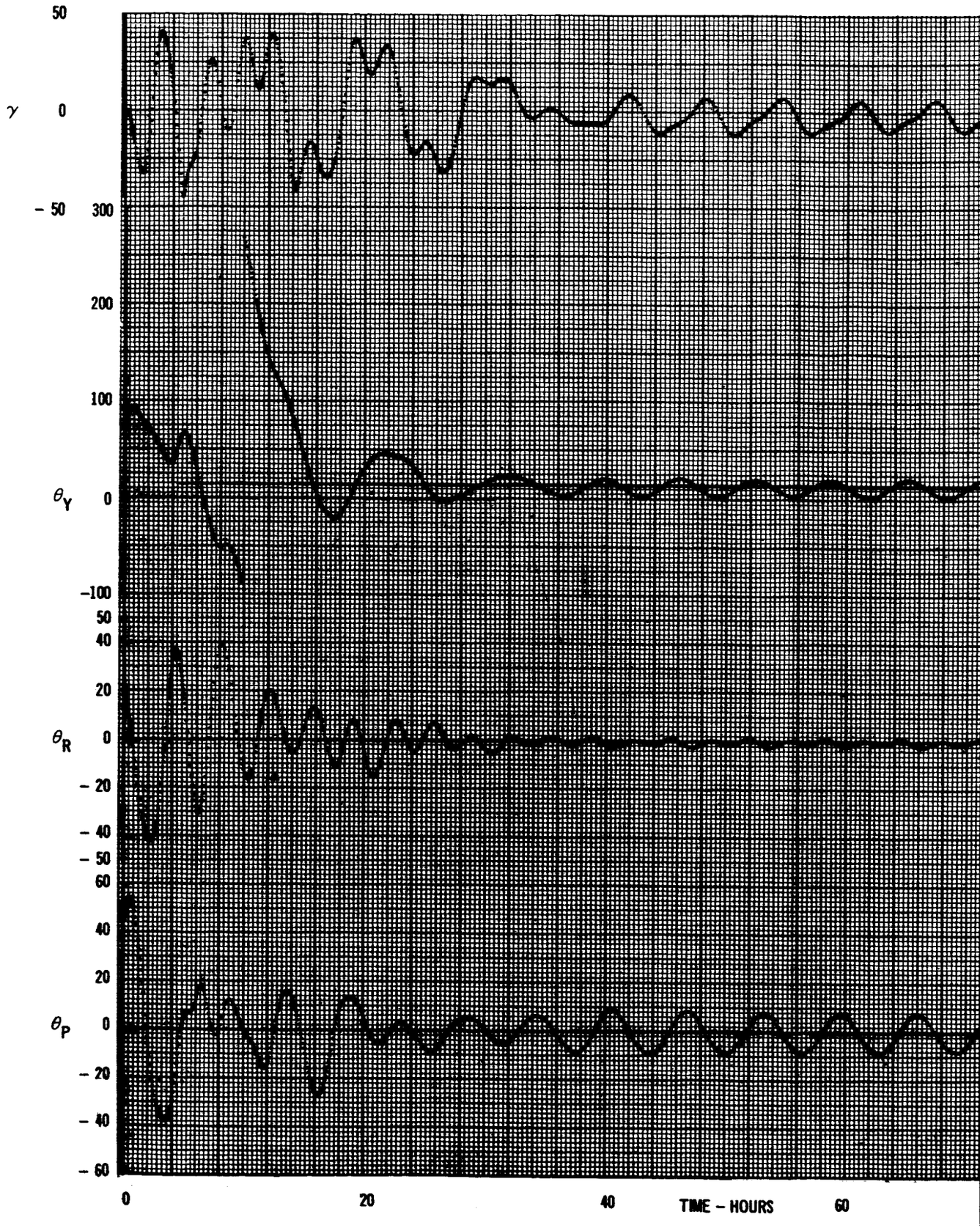


Figure 2.1.2-16. MAGGE, 11 Degree Half Angle, Transient


50
γ 0
– 50
300
200
100
θY 0
–100
50
40
20
θR 0
– 20
– 40
– 50
60
40
20
θP 0
– 20
– 40
– 60
0
20
40
TIME – HOURS
60

990

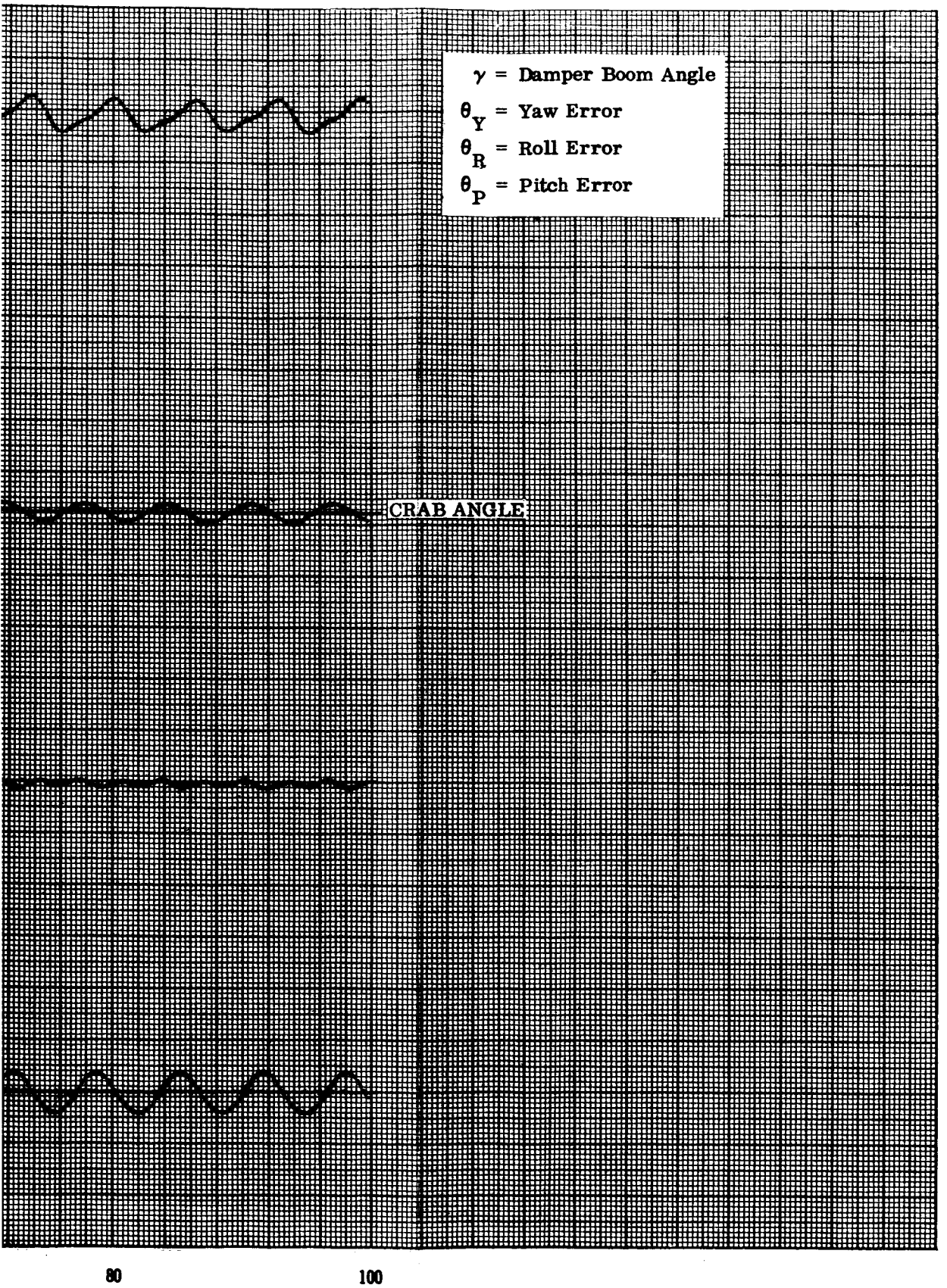
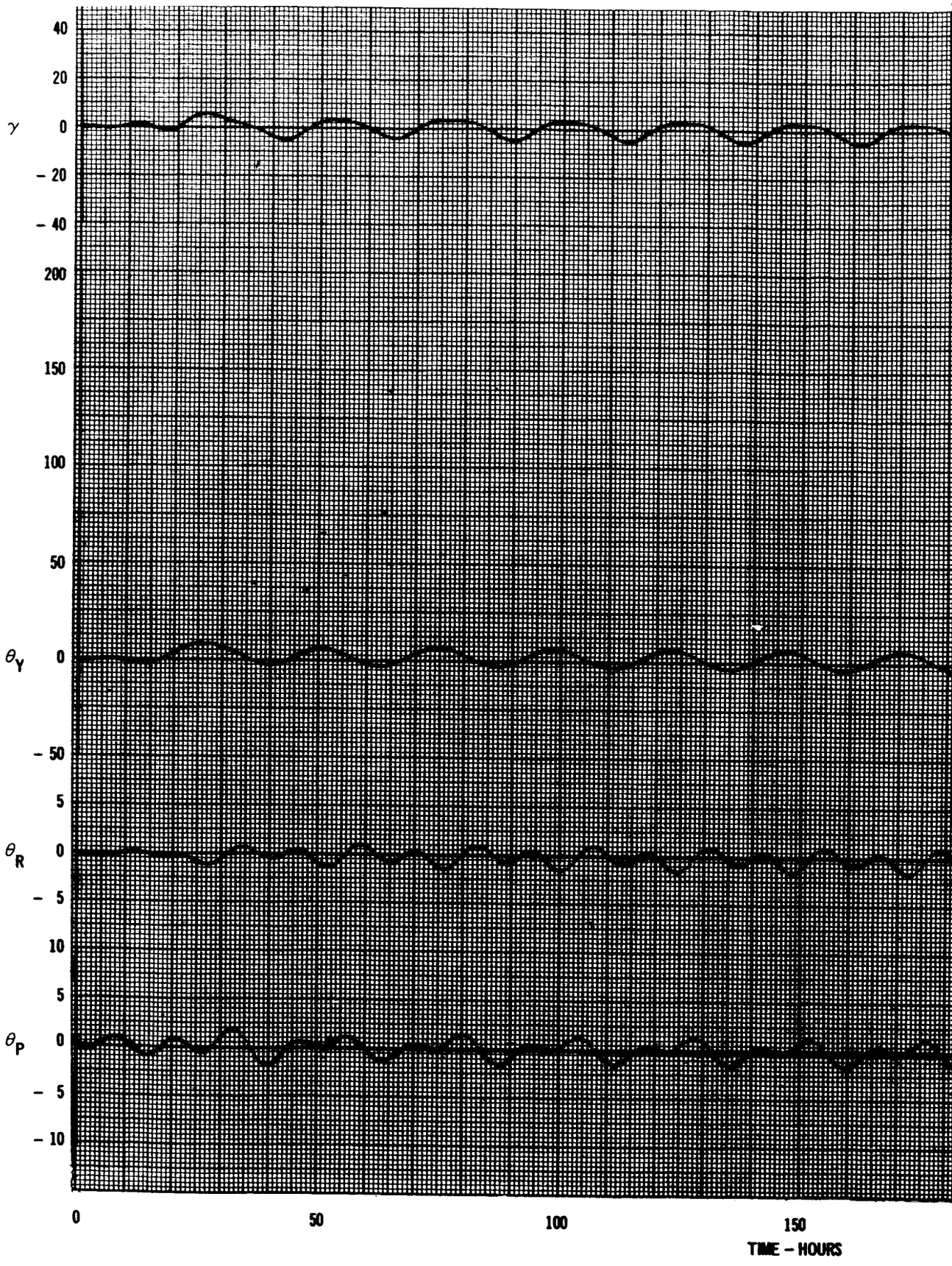


Figure 2.1.2-17. MAGGE, 31 Degree Half Angle, Transient


40
20
γ 0
– 20
– 40
200
150
100
50
θY 0
– 50
5
θR 0
– 5
10
5
θP 0
– 5
– 10
0
50
100
150
TIME – HOURS

410

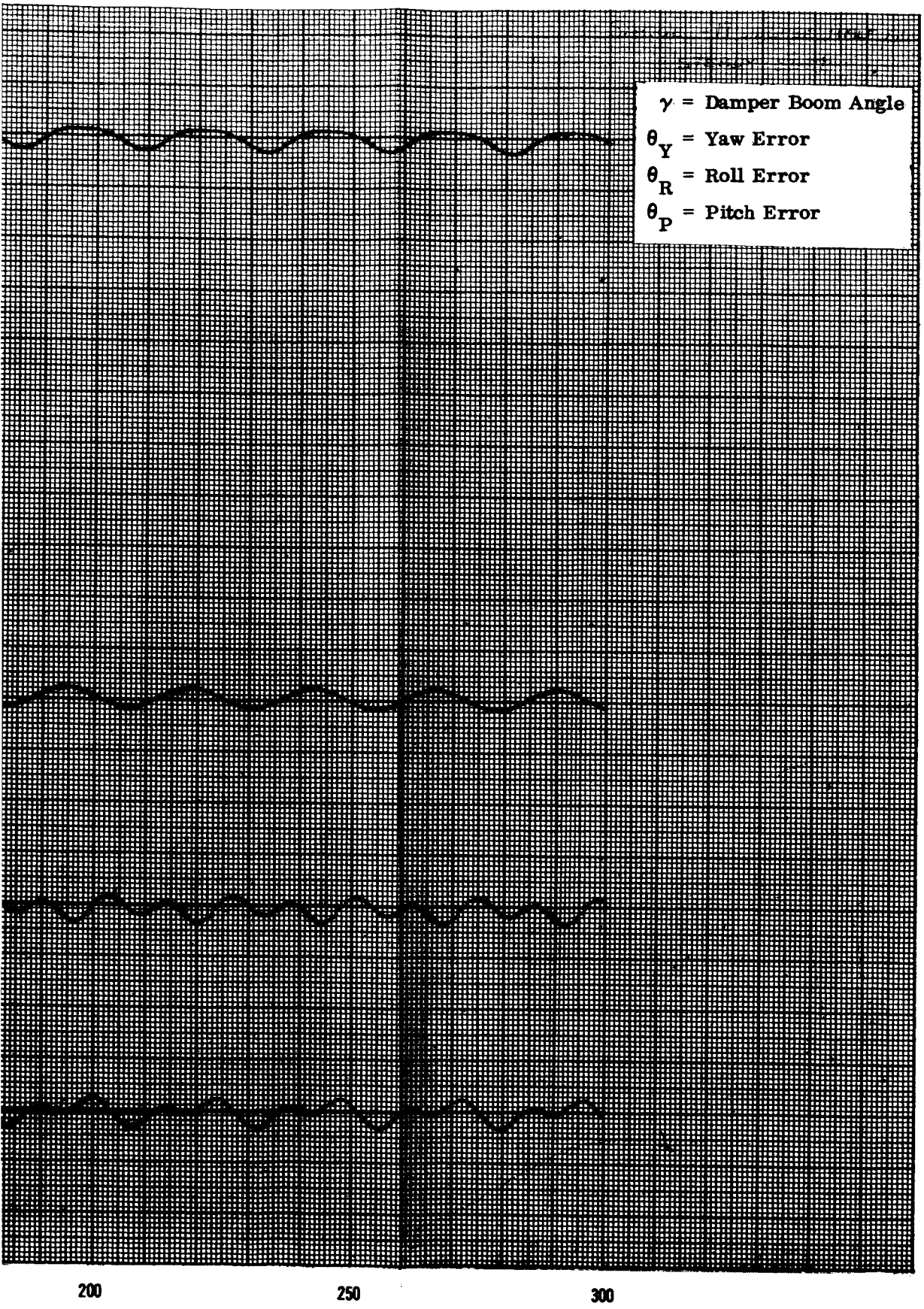


Figure 2.1.2-18. SAGGE, 19 Degree Half Angle, Steady State


40
20
γ
0
– 20
– 40
200
150
100
50
θY
0
– 50
5
θR
0
– 5
10
5
θP
0
– 5
– 10
0
50
100
150
TIME – HOURS

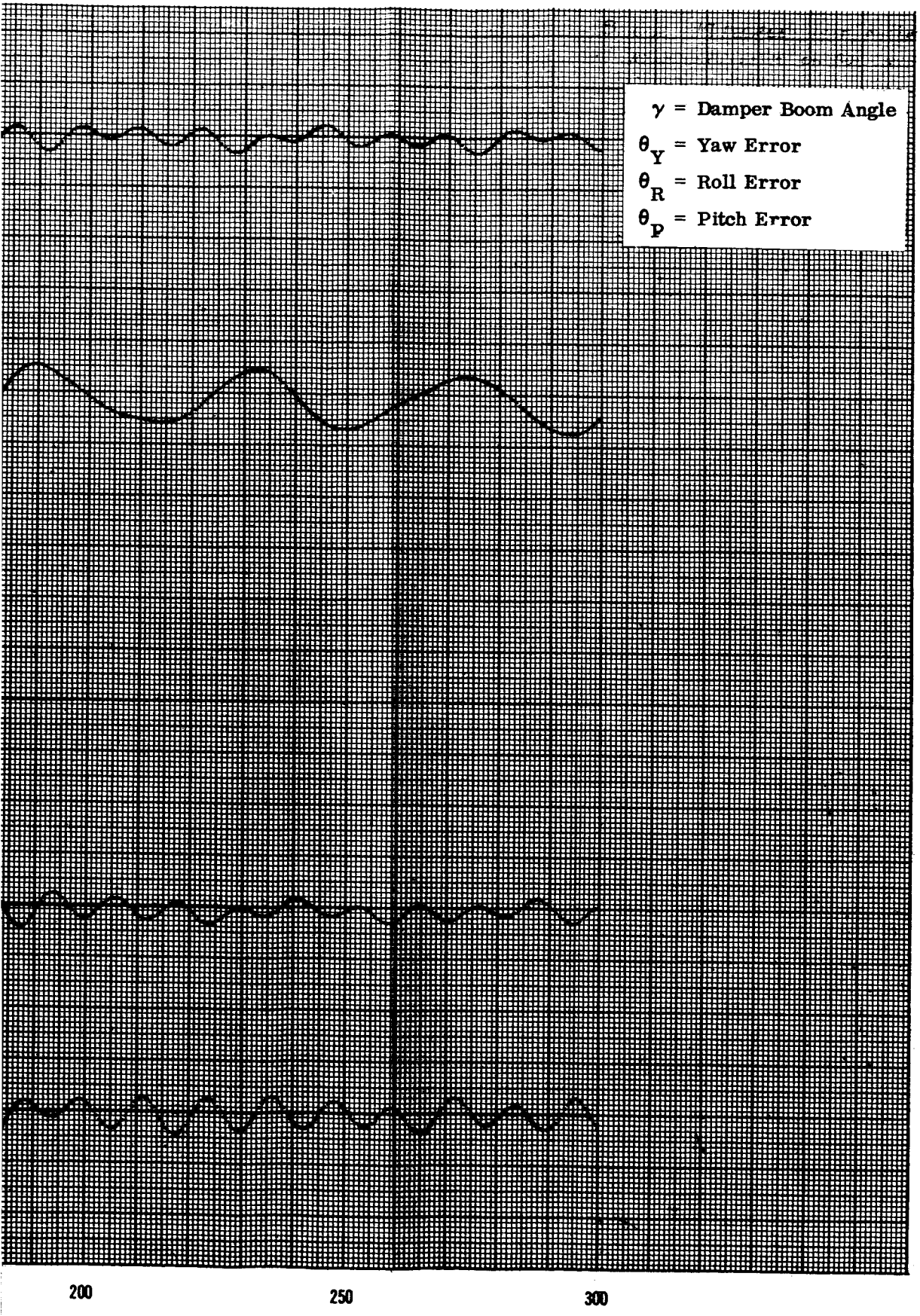
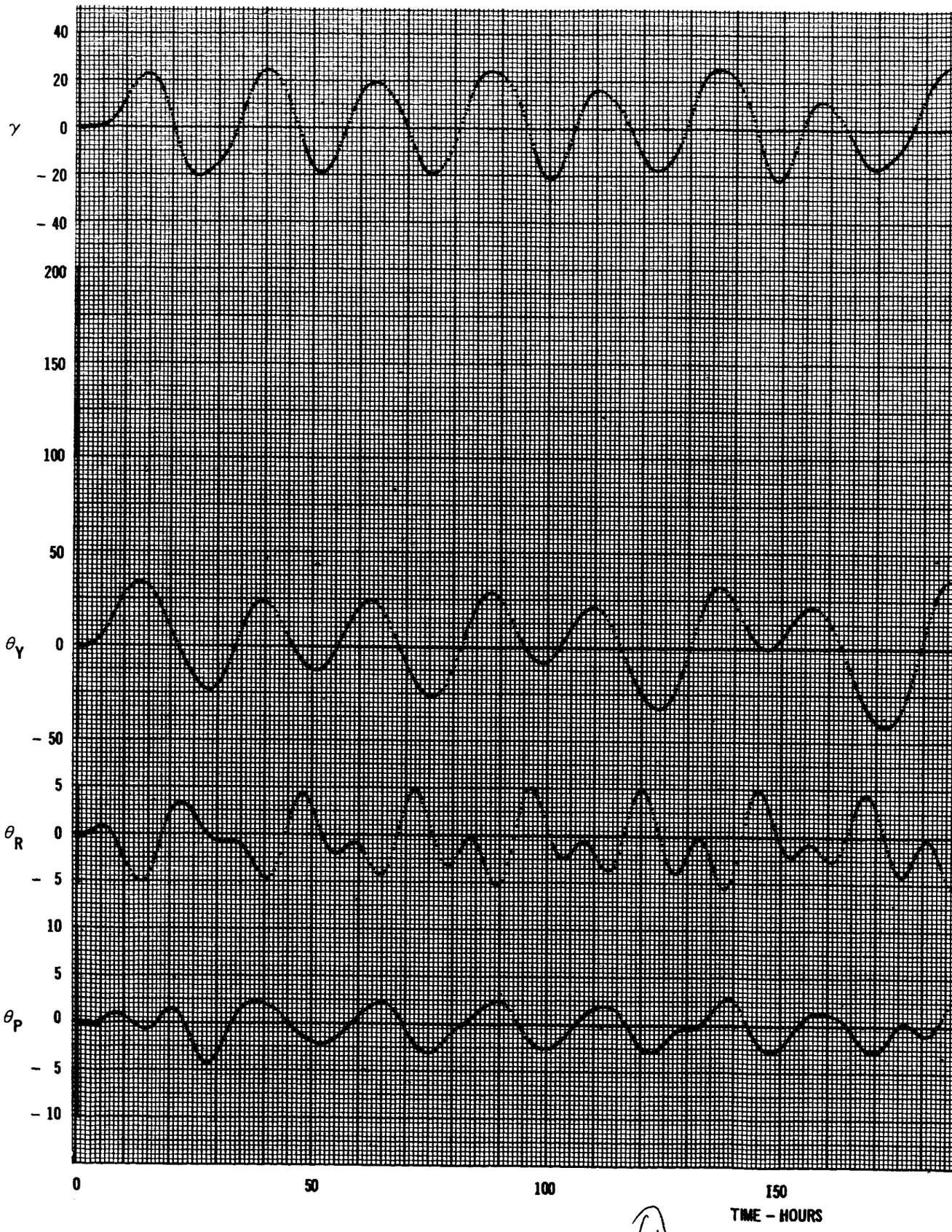


Figure 2.1.2-19. SAGGE, 19 Degree Half Angle, 10,000 Pole-CM on Roll Axis


40
20
γ
0
– 20
– 40
200
150
100
50
θY
0
– 50
5
θR
0
– 5
10
5
θP
0
– 5
– 10
0
50
100
150
TIME – HOURS

450

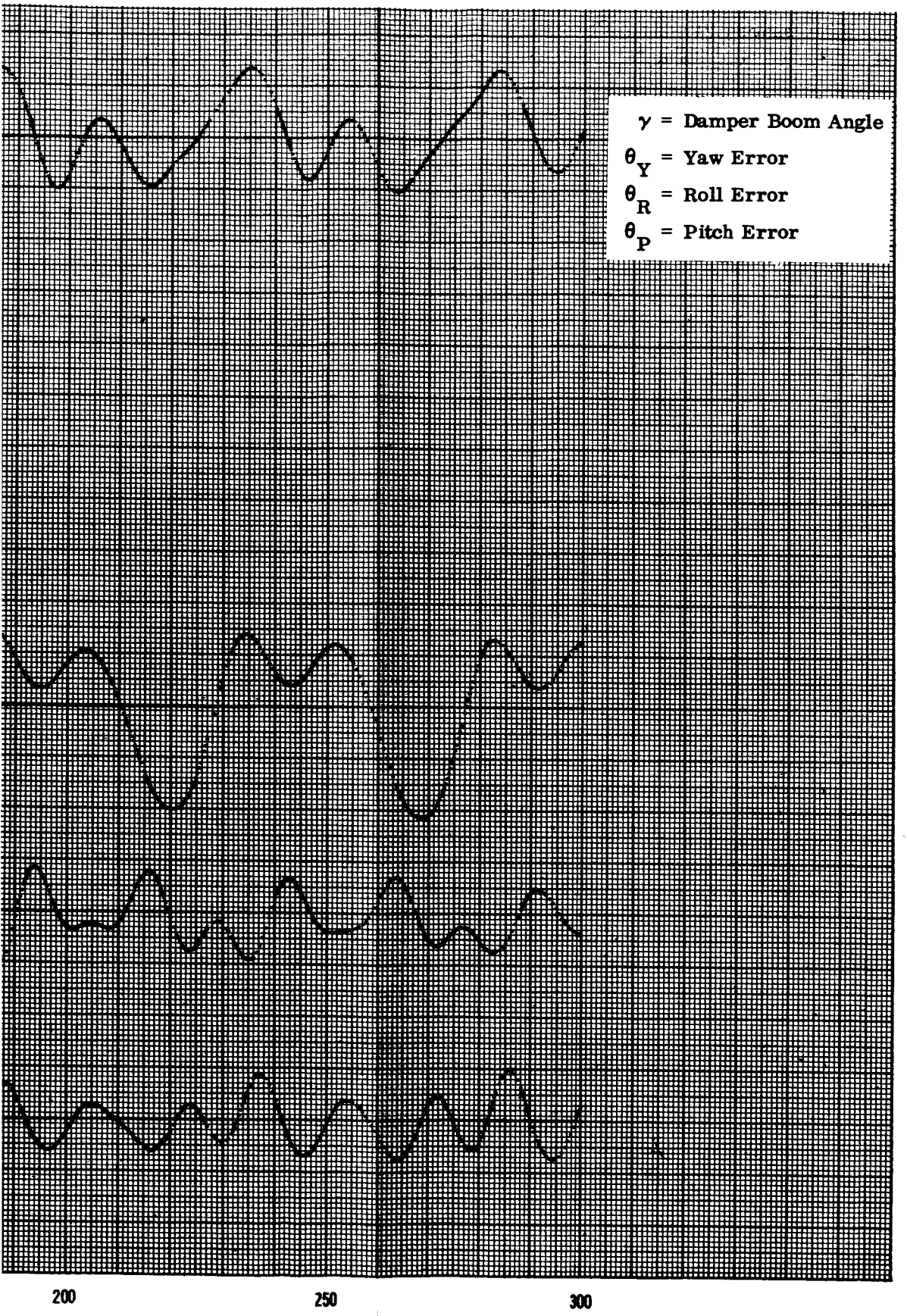


Figure 2.1.2-20. SAGGE, 19 Degree Half Angle, C.P. Boom Extended 30 Ft.


40
20
γ 0
- 20
- 40
250
200
150
100
50
θY 0
- 50
40
20
θR 0
- 20
- 40
60
40
20
θP 0
- 20
- 40
- 60
0
50
100
150
TIME - HOURS

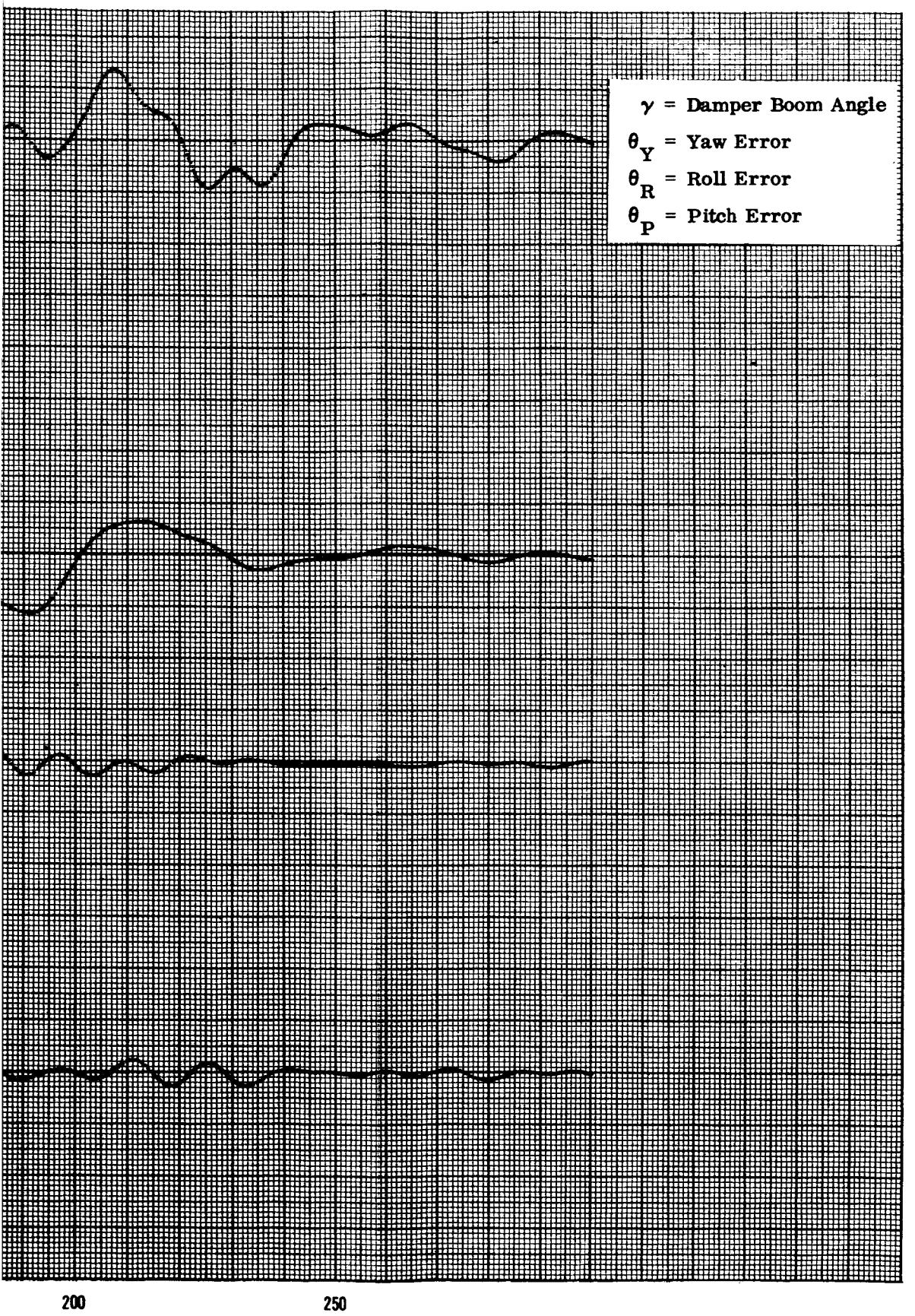


Figure 2.1.2-21. SAGGE, 19 Degree Half Angle, Transient

2.1.3 ATTITUDE SENSOR SYSTEM ERROR ANALYSIS

The final results of the attitude sensor system error analyses are critical to basic decisions affecting the future course of the ATS Program. A definitized orbit test plan, for example, cannot be developed until the philosophy pertaining to post-launch data correlation is firmly established. But the establishment of realistic data correlation goals is a direct function of the capabilities of the spacecraft attitude sensing system. The definitization of the orbit test plan has ramifications throughout the ATS Program:

1. It establishes the requirements for special-purpose hardware such as the C. P. Boom, the magnetic torquing coils, large angle displacement torque generators, retractable and extendable booms, boom scissoring devices, combination dampers, etc.
2. It establishes the data rate requirements and, hence, affects duty cycles, power requirements, and component life and reliability.
3. It affects the requirements and development plans for the attitude Determination Program and the Data Correlation Program.

This was recognized early in the program and a plan of analysis was established starting with an analysis of the sensors about which most was known. These were the RF sensor and the IR sensor, with plans to analyze these sensors in conjunction with the sun sensor when complete information on the sun sensor became available. First results are included as Appendices A and B. Appendix A cover the RF sensor/IR sensor combination and Appendix B covers the RF sensor working in conjunction with two ground stations. A third analysis, covering the RF sensor/sun sensor combination, was stopped at the time that the RF sensor was removed from the program. In its place was substituted an analysis of the sun sensor working in conjunction with a proposed system for measuring the polarization of incoming RF energy from spacecraft antennas. This effort is still in progress with subsequent analytical work to be devoted to the sun sensor working in conjunction with (1) the TV camera (2) an earth albedo sensor (3) an earth IR sensor (4) an earth horizon scanner and (5) a magnetometer. Appendix C contains the pertinent equations for the sun sensor.

Once the system error analysis is complete, realistic decisions on data correlation procedures can be made and the requirements of the Orbit Test Plan definitized.

2.1.4 DATA CORRELATION PROCEDURES

As discussed in paragraph 2.1.3, realistic decisions on data correlation procedures must await the completion of sensor system error analyses. Based on results to date, however, the ultimate accuracy of the sensor system appears to be inadequate for the reproduction of performance as predicted in paragraph 2.1.2. The implications, therefore, point towards a less sophisticated approach to data correlation than was originally conceived. Correlation of statistically determined "envelopes", either manually or automatically, with an accompanying trend analysis appears both useful and realistic. However, this may not be sufficient to meet the desired goals of the ATS Program. This area will come under close scrutiny during the next 3 months of the program.

2.1.5 ANALYTICAL STUDIES AND RESULTS

2.1.5.1 Isolated Effect of Boom Thermal Bending

The attitude errors caused by gravity gradient rod thermal bending were determined using the GAPS III, three-axis computer program. The configurations chosen were the nominal designs for the 6000 nm and synchronous orbit flights.

	MAGGE	SAGGE
Primary rod length - ft	100	100
Primary rod tip mass - lbs	2.5	10
Damper rod length tip to tip - ft	90	90
Damper rod tip mass - lbs	1.91	7.53
X-boom half angle - deg	19	19

The sun was positioned in the orbit plane in order to cause maximum errors. To eliminate solar pressure torques not caused by rod bending the vehicle center of mass and the damper hinge point were located in the plane of the X-booms. There was no CP-CM offset.

Figures 2.1.5.1-1 and 2.1.5.1-2 show the results of the computer runs. Pitch and roll errors are sinusoidal at twice orbital rate. Yaw errors result primarily from cross-coupling. The steady-state yaw offset shown is not the result of thermal bending but results from the definition of zero yaw error. The roll axis of the vehicle is nominally defined to be 20.6 degrees from the plane of the X-booms. However, the principal axes of the two configurations are located such that for MAGGE the offset is -20.1 degrees and for SAGGE the offset is -21 degrees. This introduces a $+0.5^{o}$ bias in MAGGE and a -0.4^{o} bias in SAGGE. These biases have been removed in the data that follows.

	MAGGE	SAGGE
Pitch	$\pm 0.19^{o}$	$\pm 0.73^{o}$
Roll	$\pm 0.25^{o}$	$\pm 1.19^{o}$
Yaw	$\pm 0.05^{o}$	$\pm 0.32^{o}$

2.1.5.2 Capture Studies

In the previous capture studies (reference First Quarterly Report), a pitch down rate bias and a negative position (pitch up) bias were suggested to insure the capture of MAGGE in the rightside up position. Since that time, a study has been conducted using a time delay between the time of separation from the booster and the time of rod deployment to avoid collision of the rods and the booster. The inclusion of the time delay causes a significant problem since the ability of the satellite to capture with no time delay was somewhat marginal. After applying a 20-second time delay the vehicle was found to tumble (Figure 2.1.5.2-1). The vehicle stabilized upside down because part of the energy of the pitch motion was transferred to roll motion and the energy in each axis is insufficient to cause it

to tumble. The inversion, however, is not certain, since if the separation rate is backwards (for example) the vehicle will capture right side up (Figure 2.1.5.2-2). Note that while the vehicle position after rod deployment is symmetrical with respect to zero for both positive and negative rate uncertainty, the final rate after rod deployment is not. This can be corrected with careful selection of an initial bias rate and position before rod extension which will be done after selection of a nominal delay time.

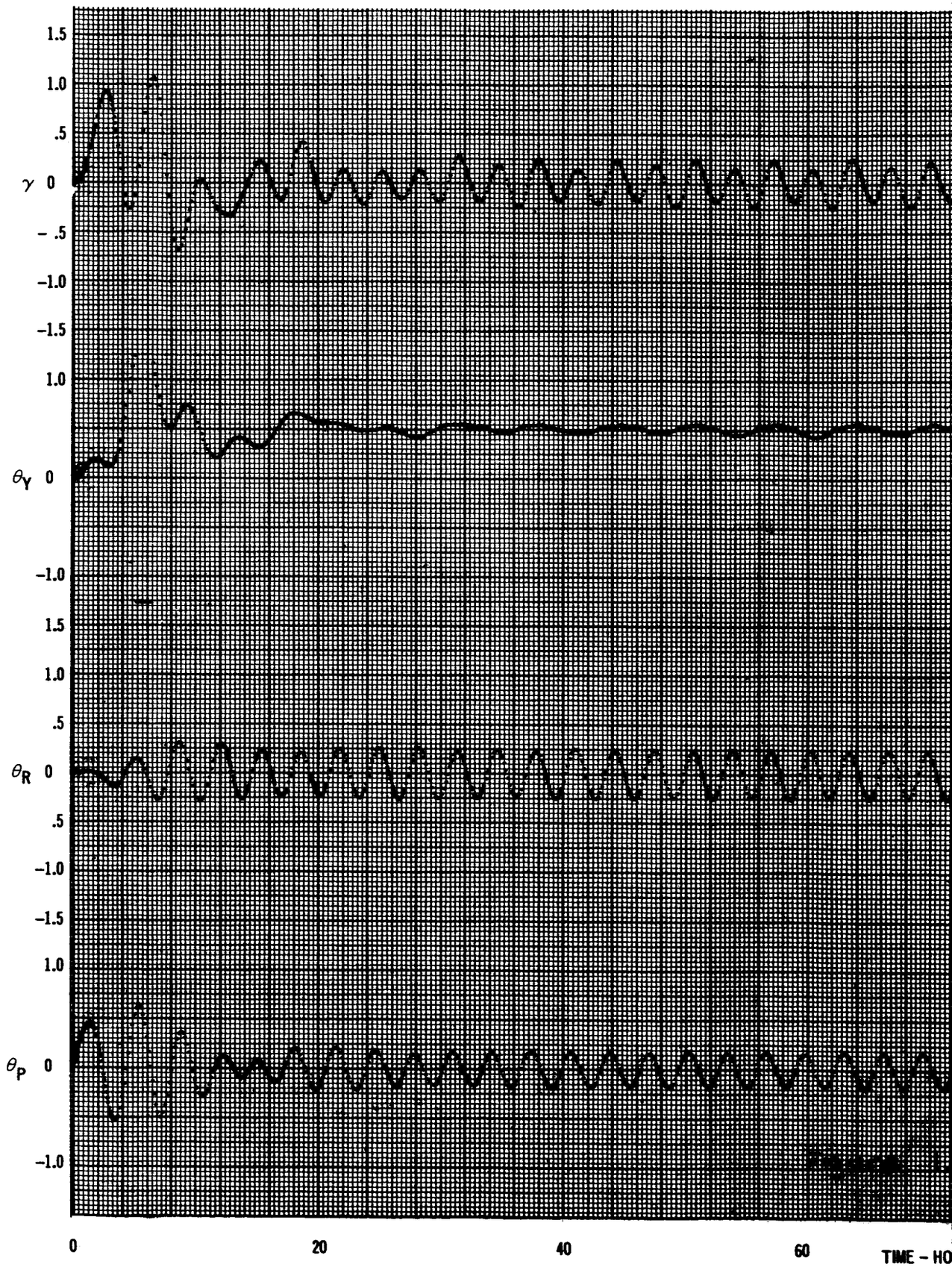
Further computer runs were made with shorter delay times and it was found that a 12-second delay was acceptable. However, when the new (and higher) initial moments of inertia of the vehicle body were introduced ($\approx$75 slug-ft^2), the vehicle did not capture after a 12-second delay. A zero delay time run was made with the new moments of inertia, and the vehicle did capture, but with an oscillation of 75 degrees, indicating a marginal capture situation.

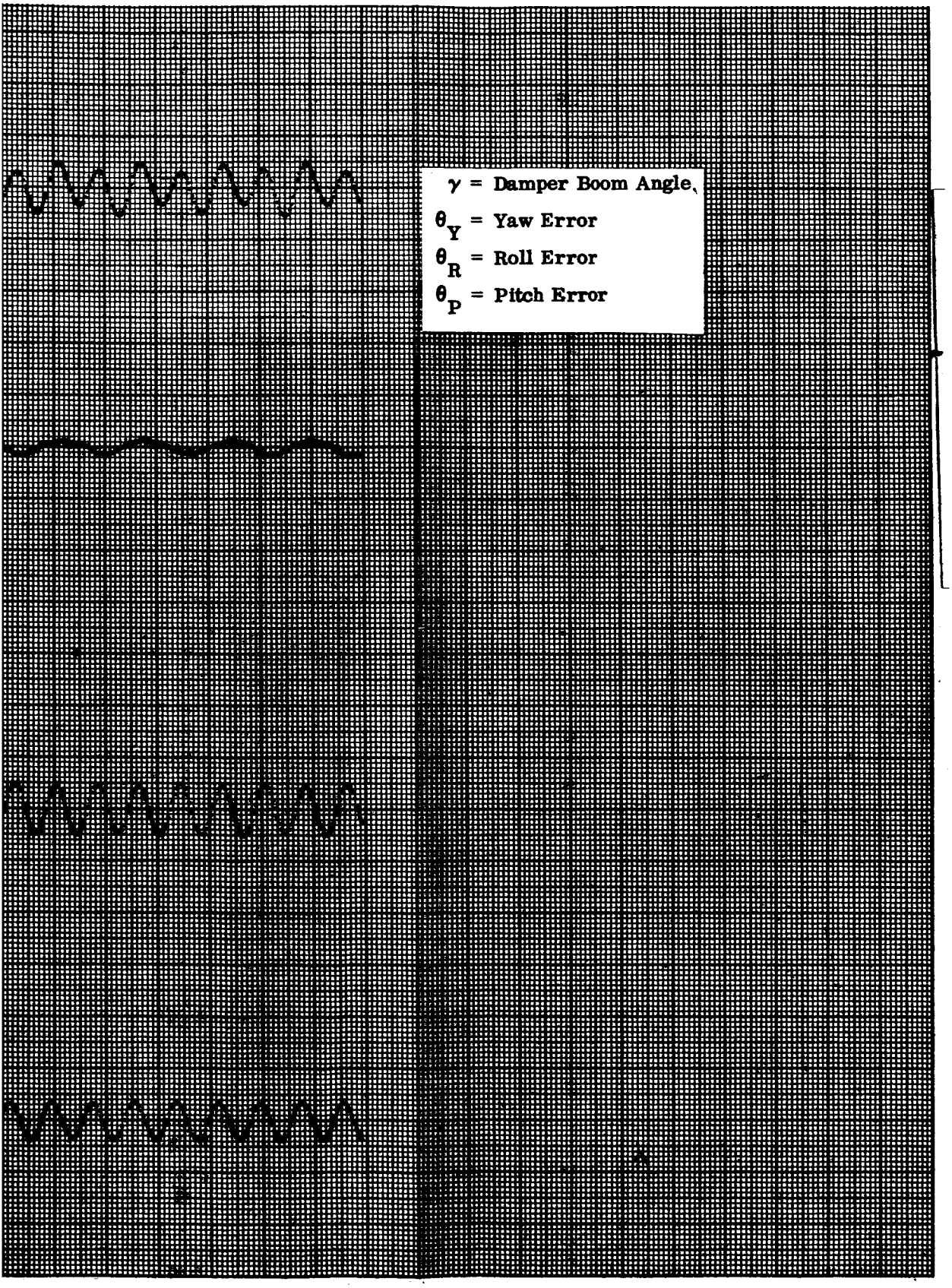
It is evident from the runs that the permissible delay time will be short, and if the time is not acceptable from the "booster collision" standpoint, other techniques such as a larger moment of inertia must be evaluated. In this connection it is recommended that the secondary boom be deployed at the same time as the X-rods to help the moment of inertia growth. (The damper need not be uncaged until later.) This will improve pitch and roll slightly, and will reduce the yaw rate should the residual separation rate appear on yaw. This was done on all the runs made for this capture study. Further study is in progress.

2.1.5.3 Inversion Studies

The inversion maneuver for ATS and the selected on-time of the thrusters, based on a nominal thrust of 2.10 pounds was discussed in Reference Items 13 of Section 4.* The results of the study indicated that the total time for the maneuver of this thrust level was approximately 3.40 hours. Subsequent to this analysis, the maximum ground station coverage of the satellite was specified to be 2.50 hours and the desirability

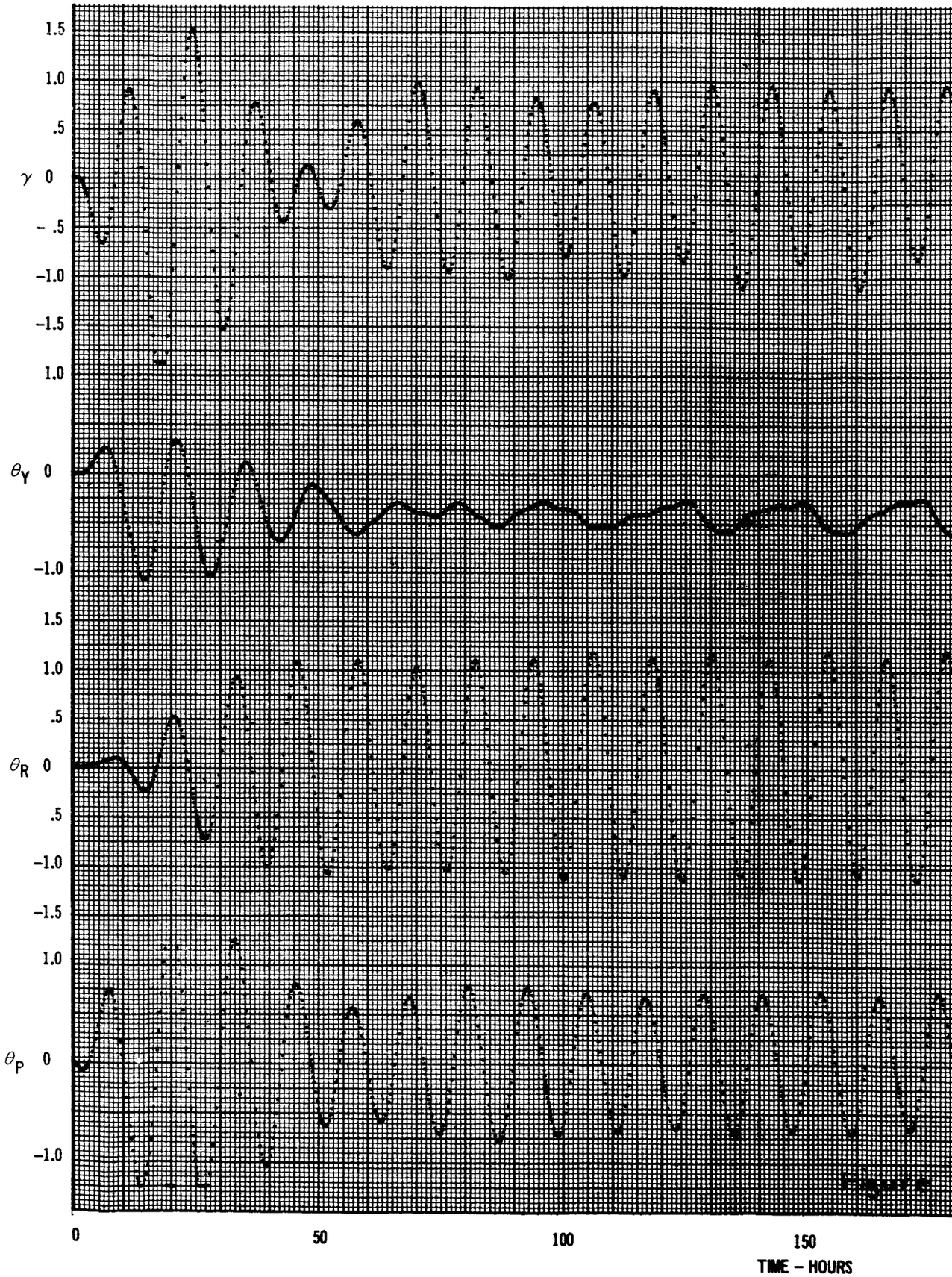
*All item references are shown in the Bibliography, Section 4.


1.5
1.0
.5
γ 0
- .5
-1.0
-1.5
1.0
θY 0
-1.0
1.5
1.0
.5
θR 0
.5
-1.0
-1.5
1.0
θP 0
-1.0
0
20
40
60
TIME - HO



URS 80 100

Figure 2.1.5-1. Effects on Thermal Bending MAGGE


1.5
1.0
.5
γ 0
– .5
–1.0
–1.5
1.0
θY 0
–1.0
1.5
1.0
.5
θR 0
.5
–1.0
–1.5
1.0
θP 0
–1.0
0
50
100
150
TIME – HOURS

9-55

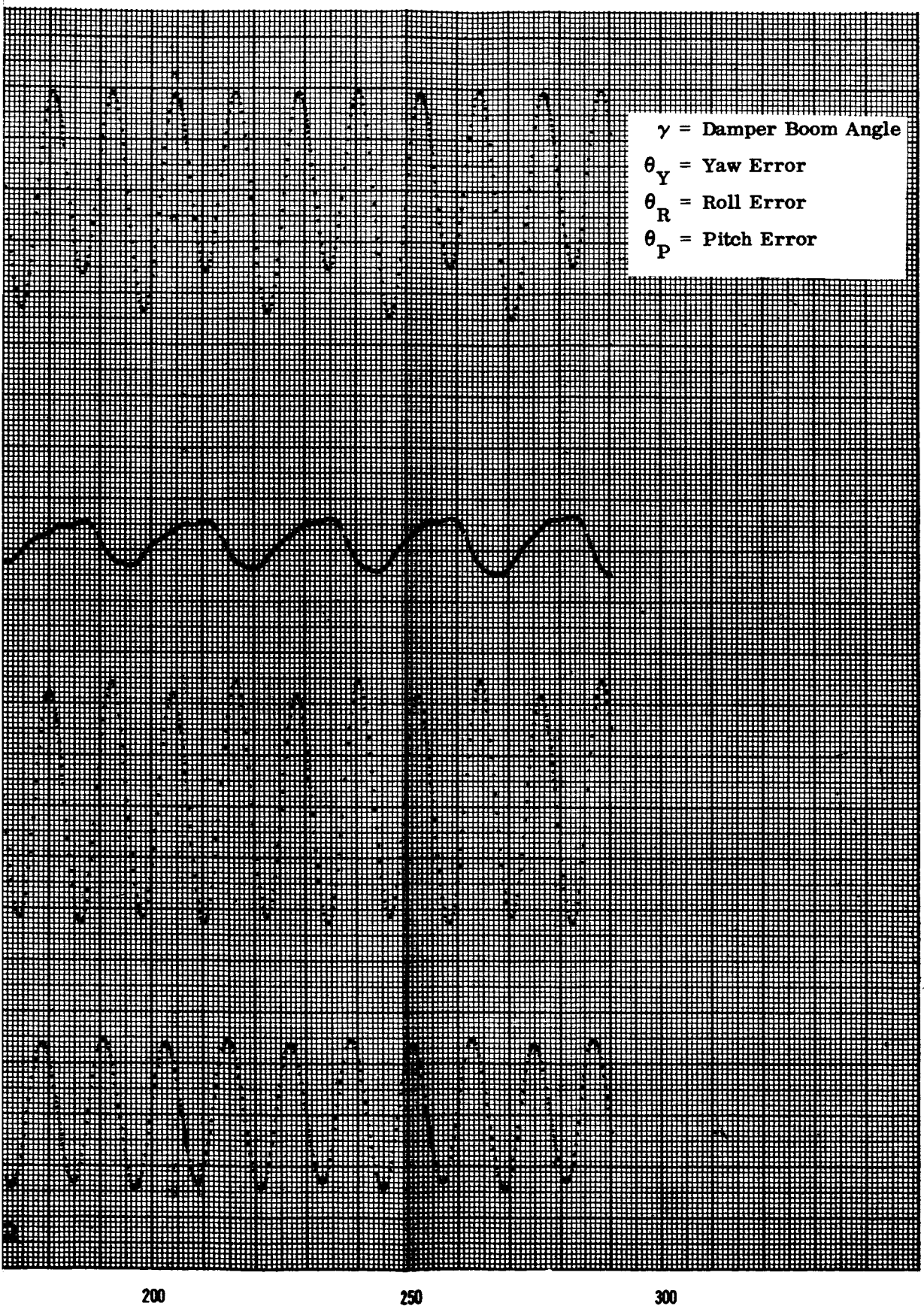


Figure 2.1.5.1-2. Effect on Thermal Bending, SAGEE

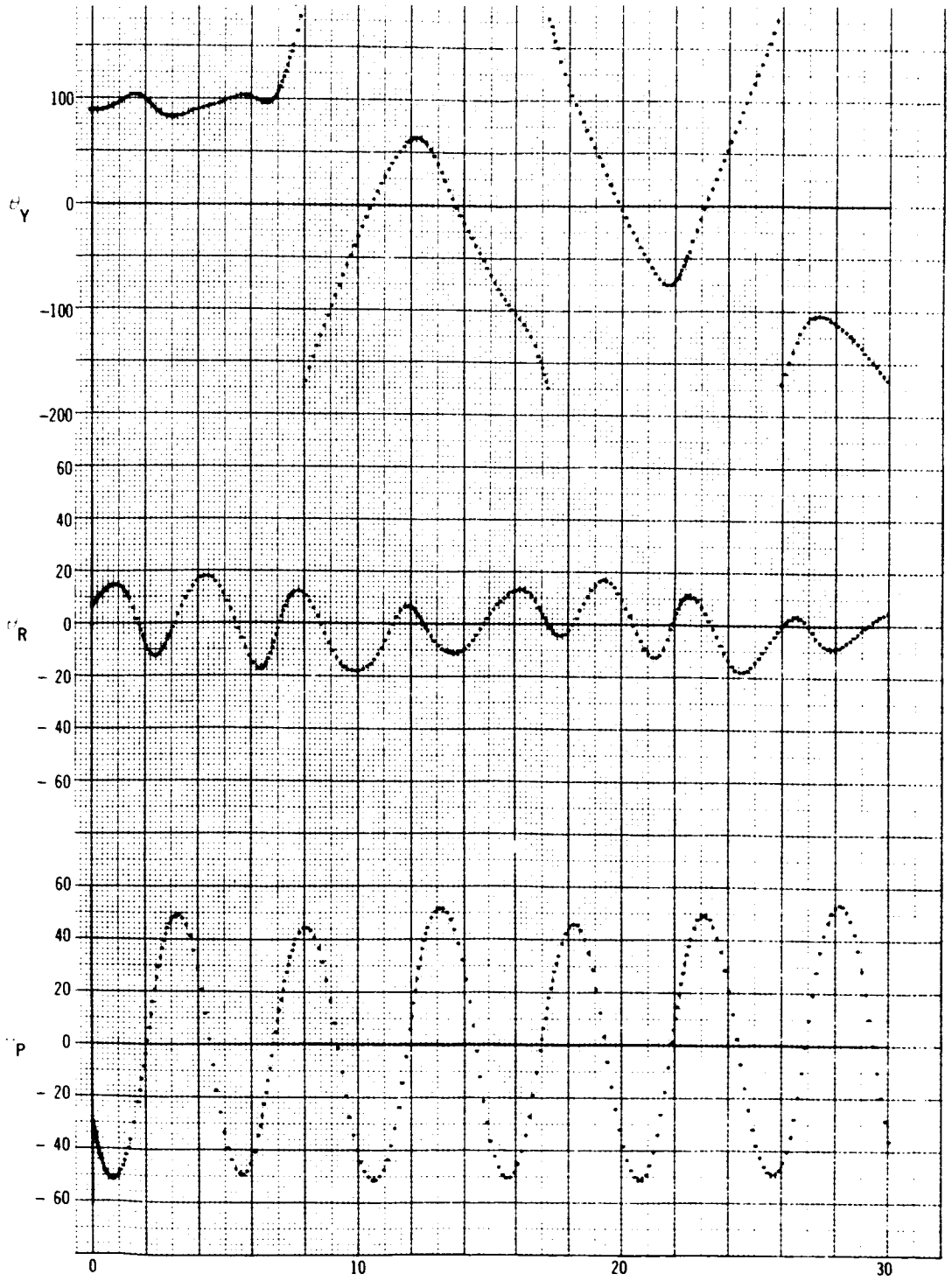


Figure 2.1.5.2-1. Capture of Magge

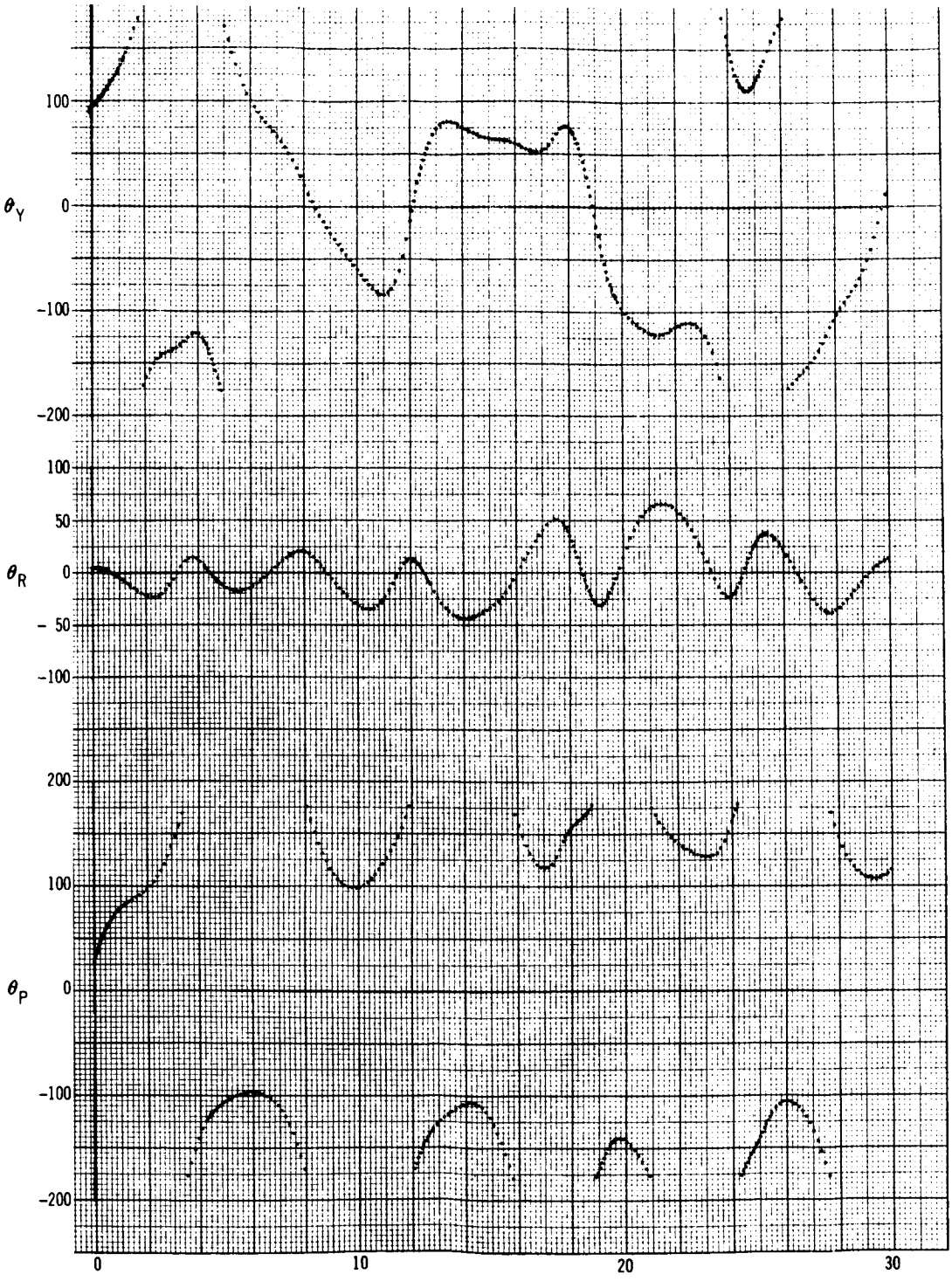


Figure 2.1.5.2-2. Capture of Magge

for completing the maneuver within a station pass was recognized. In addition, information on thrust uncertainty, rise time, and decay time characteristics for the proposed thrusters was obtained from HAC. To accomplish the maneuver in 2.50 hours or less, it is necessary to select a new value of nominal thrust for the thrusters, and specify a corresponding timing sequence. Since potential subcontractors for the engine have indicated that the previously specified thrust tolerance of 10 per cent was very difficult to meet, it became necessary to evaluate the effects of thrust error and establish realistic tolerance requirements. Results of the studies to date are presented and gives information sufficient for determining a nominal thrust, timing sequence and permissible thrust tolerance.

The total time for the maneuver should be limited to between 2.50 and 2.00 hours; the two hour minimum is required in order to keep the boom oscillations from becoming too large. To allow for the uncertainties in thrust rise time, thrust misalignments, etc., the maximum overshoot contributed by thrust level tolerance should be limited to about 30 degrees. This permits a maximum thrust tolerance of between 12 and 16 percent of the nominal thrust. The nominal thrust must be selected based on the consideration of both thrust tolerance and timing response. Higher thrust levels permit slightly larger thrust tolerances. A thrust of 4.2×10^{-4} pounds with an allowable tolerance of ± 15 percent is recommended. This will permit the maneuver to be completed in about 2.3 hours.

For this study, it has been assumed that the inversion maneuver will be performed in an open loop manner, entirely by the use of preset timers which cannot be altered from the ground after flight. This appears to be the only feasible way of performing the operation since attitude information would probably not be available to a satellite monitoring station in time to permit an operator to control the maneuver from the ground. Thruster misalignments, rise and decay times, and variations between the accelerating and retarding thrusters have not been evaluated in this part of the study. The torques are assumed to be essentially "square waves" (one positive, one negative) placed "back to back" with no coast phase, Item 13 of

Section 4 covered studies including thruster misalignments. Analysis of the turn-over maneuver is continuing, and a subsequent PIR will discuss the effects of thrust rise and decay transients.

Figure 2.1.5.3-1 shows the maximum overshoot the vehicle experiences after the inversion maneuver as a function of thrust level. The overshoot is taken as the amplitude of the first oscillation after the retarding thruster has been turned off and is the angle the vehicle exceeds (in a + or - direction) 180 degrees. Three timing sequences have been studied, corresponding to 2.50 hours, 2.30 hours, and 2.00 hours total maneuver time.

Figure 2.1.5.3-2 shows the allowable variation in the torque level for overshoots up to approximately 40 degrees (for the three maneuver times considered). The tolerance has been made symmetrical (assuming that plus and minus errors in thrust are equally likely) by adjusting the nominal torque (Figure 2.1.5.3-3). The allowable tolerance increases as the total maneuver time is reduced. In evaluating the overshoot, effects from thruster misalignments, center of mass wander due to thermal bending, rise and decay times, and unequal thrusters (+ and - direction) must ultimately be considered. All of these factors will serve to reduce the margin on a successful maneuver, hence the allowable overshoot contributed by thrust level error has been tentatively selected to be 30 degrees.

The motion of the satellite in pitch during the inversion maneuver is shown in Figures 2.1.5.3-4 through -6, for the three timing sequences. Note that at the

high torque levels, the vehicle has overshot, and is returning towards 180 degrees before the thrust is terminated. These plots were used to obtain the cross plots of Figure 2.1.5.3-1 through -3. Using Figure 2.1.5.3-7, the thrust level corresponding to the given torque levels can be determined.

2.1.5.4 Orbital Equations for Eccentricity Maneuvers

Prior to the removal of the requirement for a MAGGE orbit eccentricity change using pulsed solid rocket thrusters, orbit equations incorporating the effects of these thrusters were generated for use in the ATS Math Model. Three sets of orbital equations are required.

The first set is for the initial satellite orbit prior to the application of thrust. The precession of the line of nodes and the line of apsides is included.

The second set is for the satellite orbit during the application of thrust. It is assumed that the motion of the satellite is confined to a plane. This plane is the orbital plane at the instant immediately prior to the application of thrust. At the end of the thrust period, the satellite is in a new orbit which is described by the first set of equations, but with new orbital parameters.

The third set is for the earth's orbit. This is needed to determine the direction of the sun.

2.1.5.4.1 Satellite Orbit Equations with no Applied Thrust

The right ascension of the ascending node is:

$$\Omega = \Omega_i + \dot{\Omega} (t - t_i), \tag{1}$$

where Ω_i is the initial value, $\dot{\Omega}$ is the average nodal procession rate, t is the instantaneous time, and t_i is the initial time at injection into orbit.

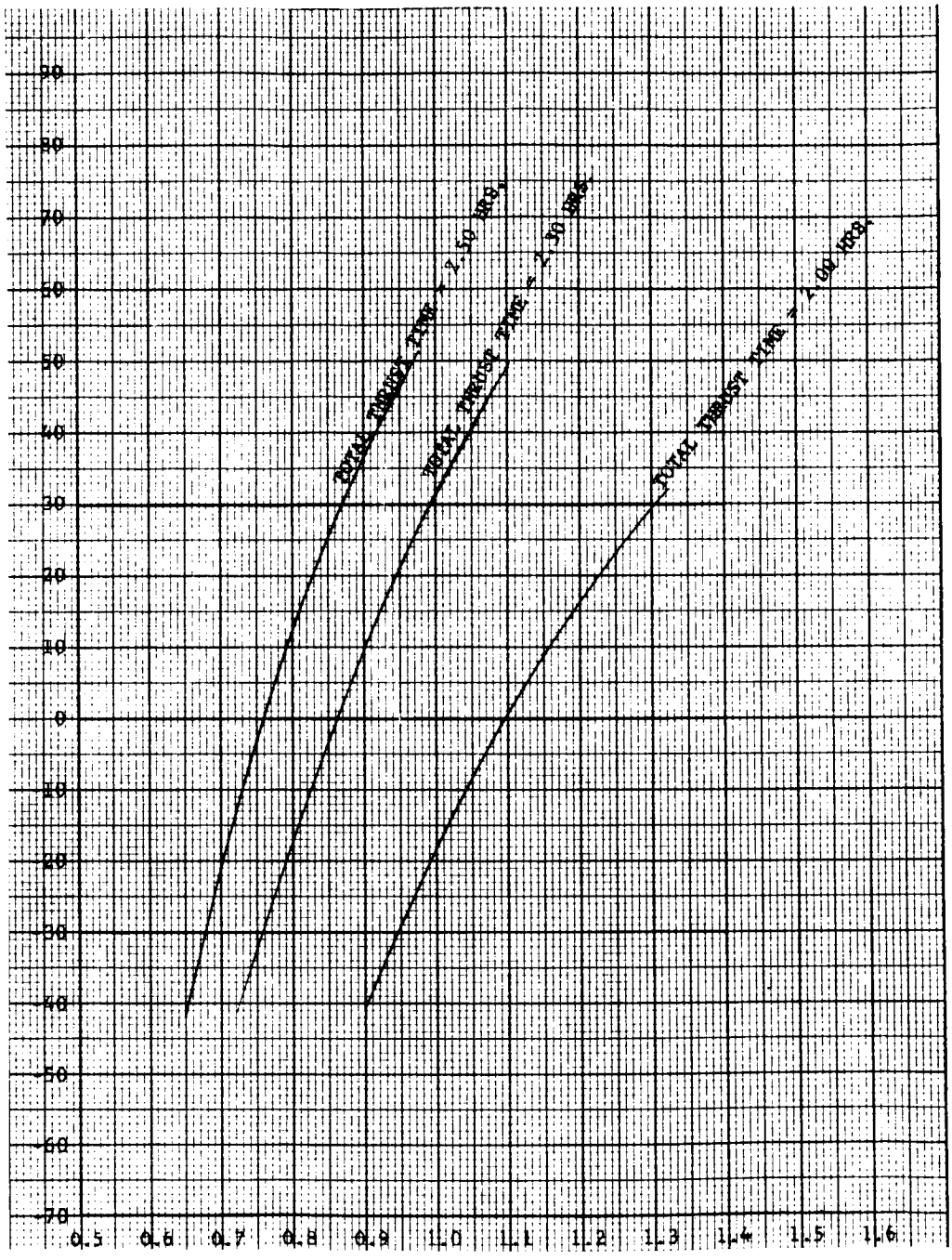


Figure 2.1.5.3-.1 Variation of Angular Overshoot with Thrust Level

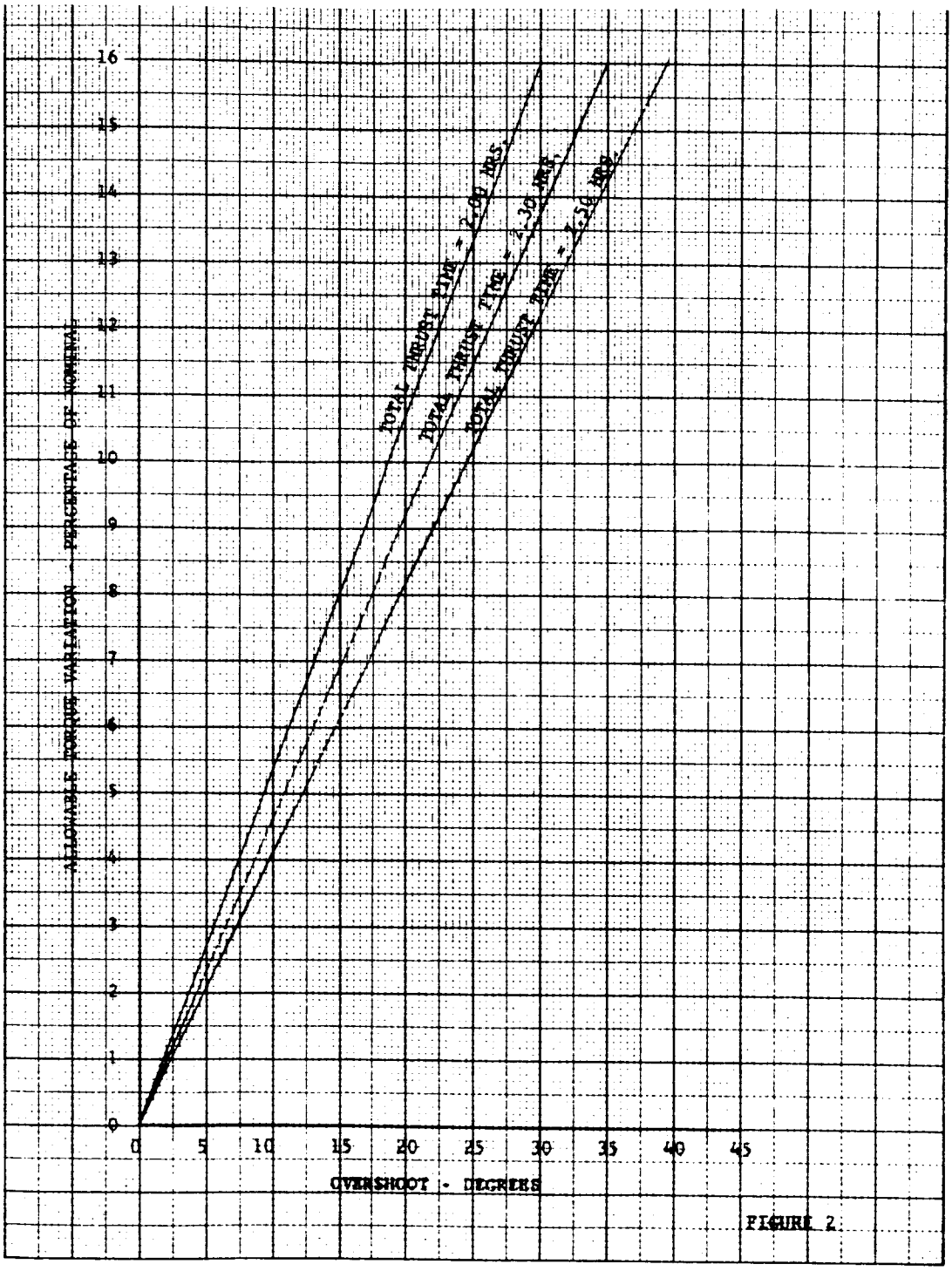


Figure 2.1.5.3-2. Allowable Variation in Torque Level

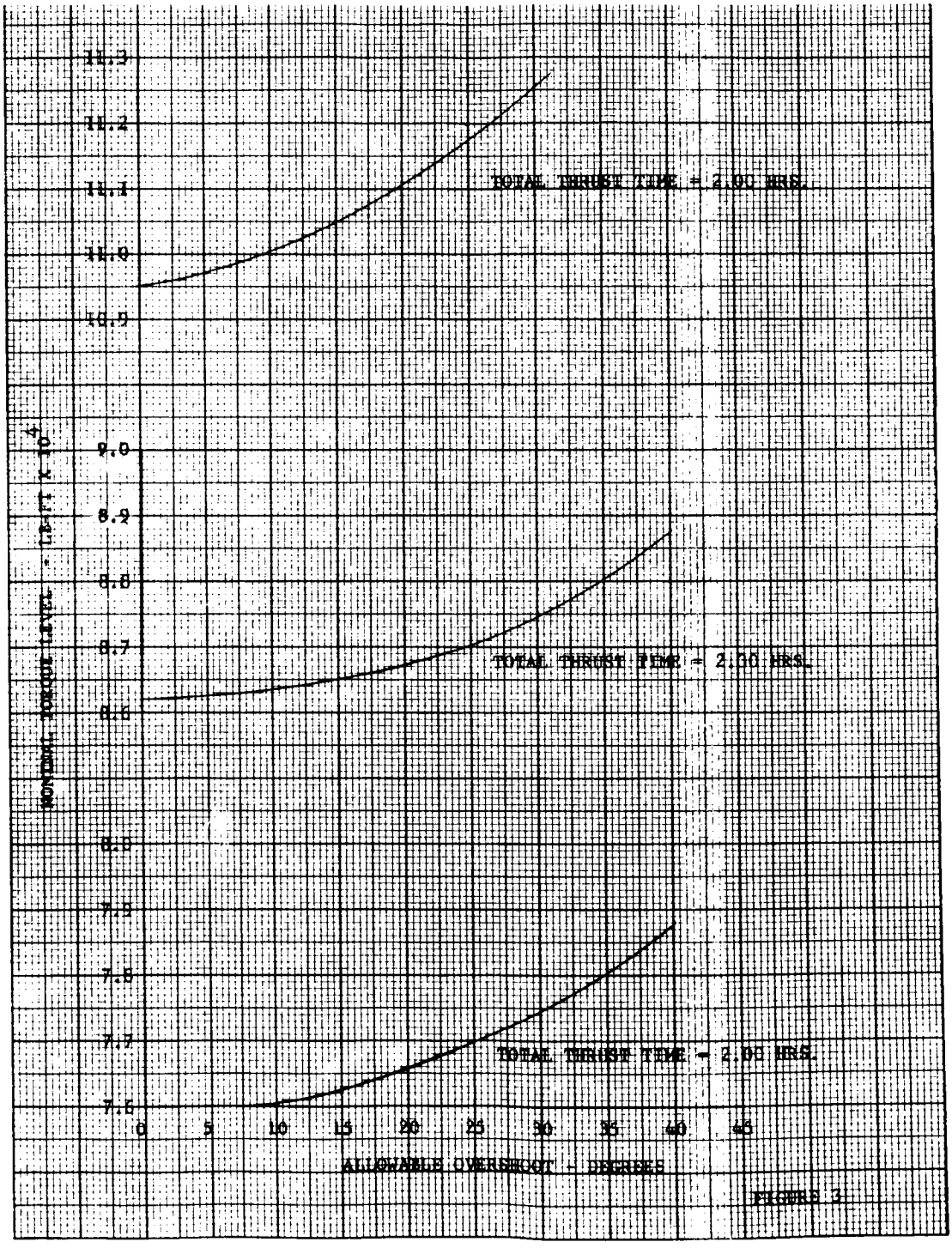


Figure 2.1.5.3-3. Nominal Torque Level as a Function of Allowable Overshoot

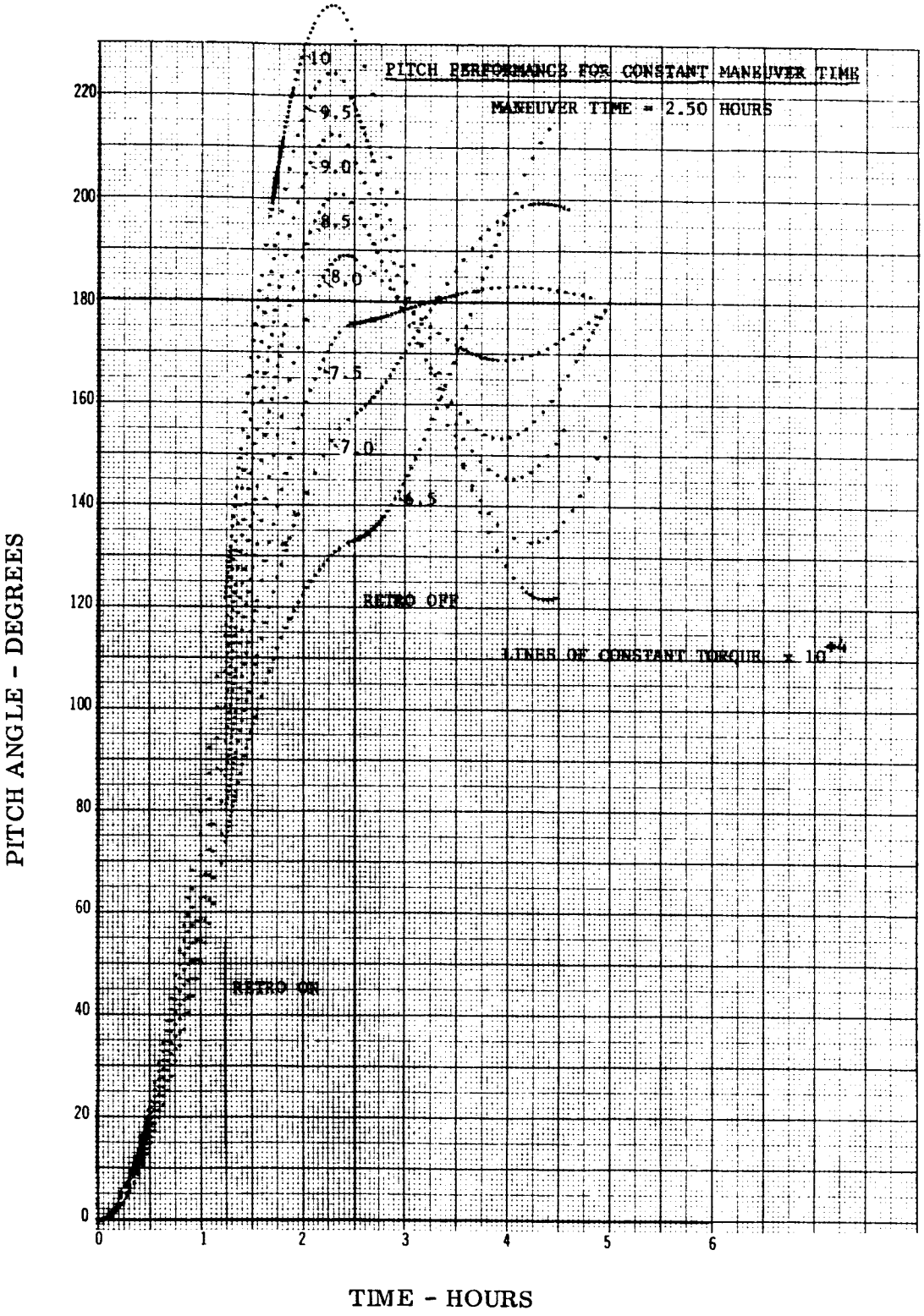


Figure 2.1.5.3-4. Pitch Performance for Constant Maneuver Time

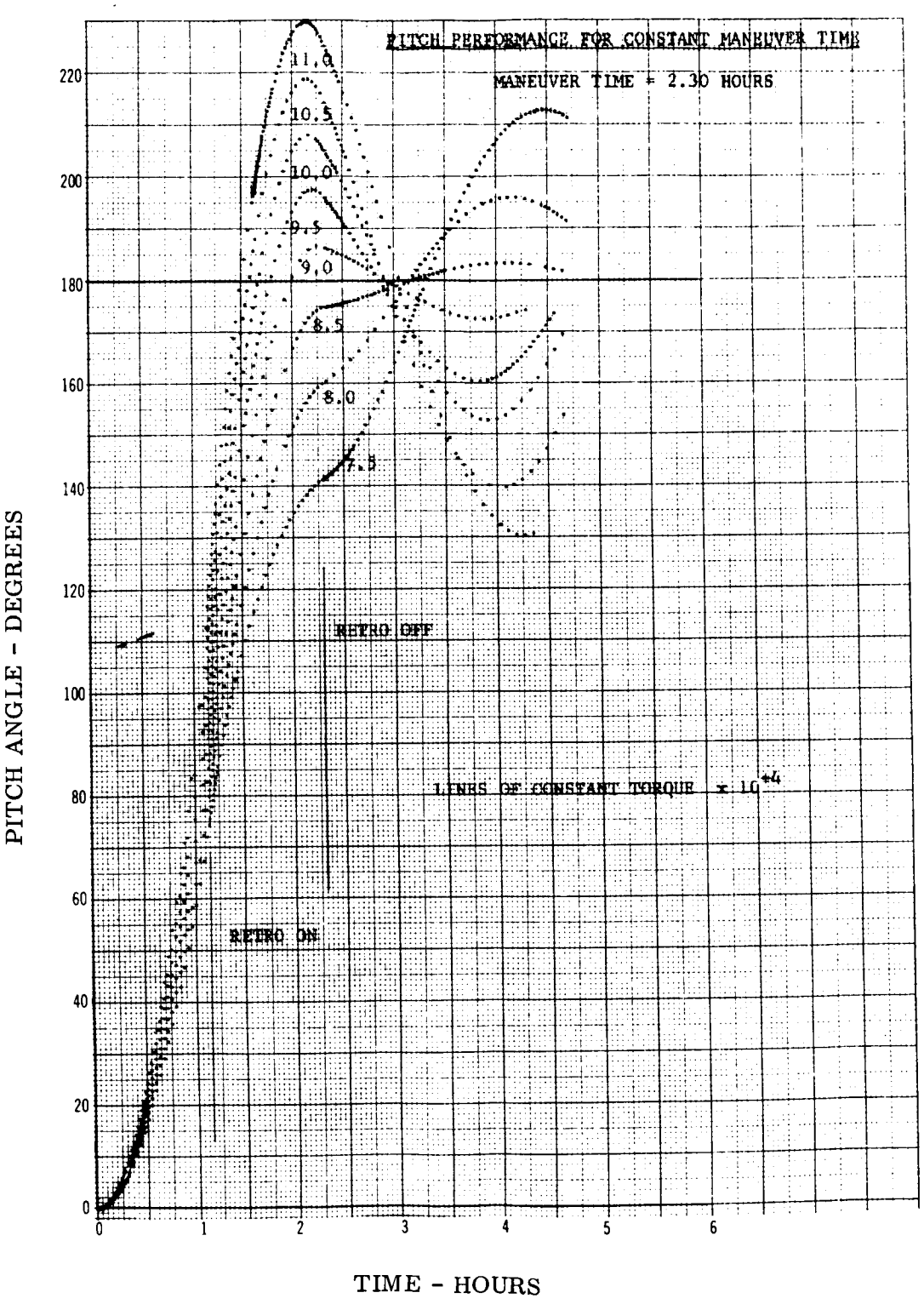


Figure 2.1.5.3-5. Pitch Performance for Constant Maneuver Time

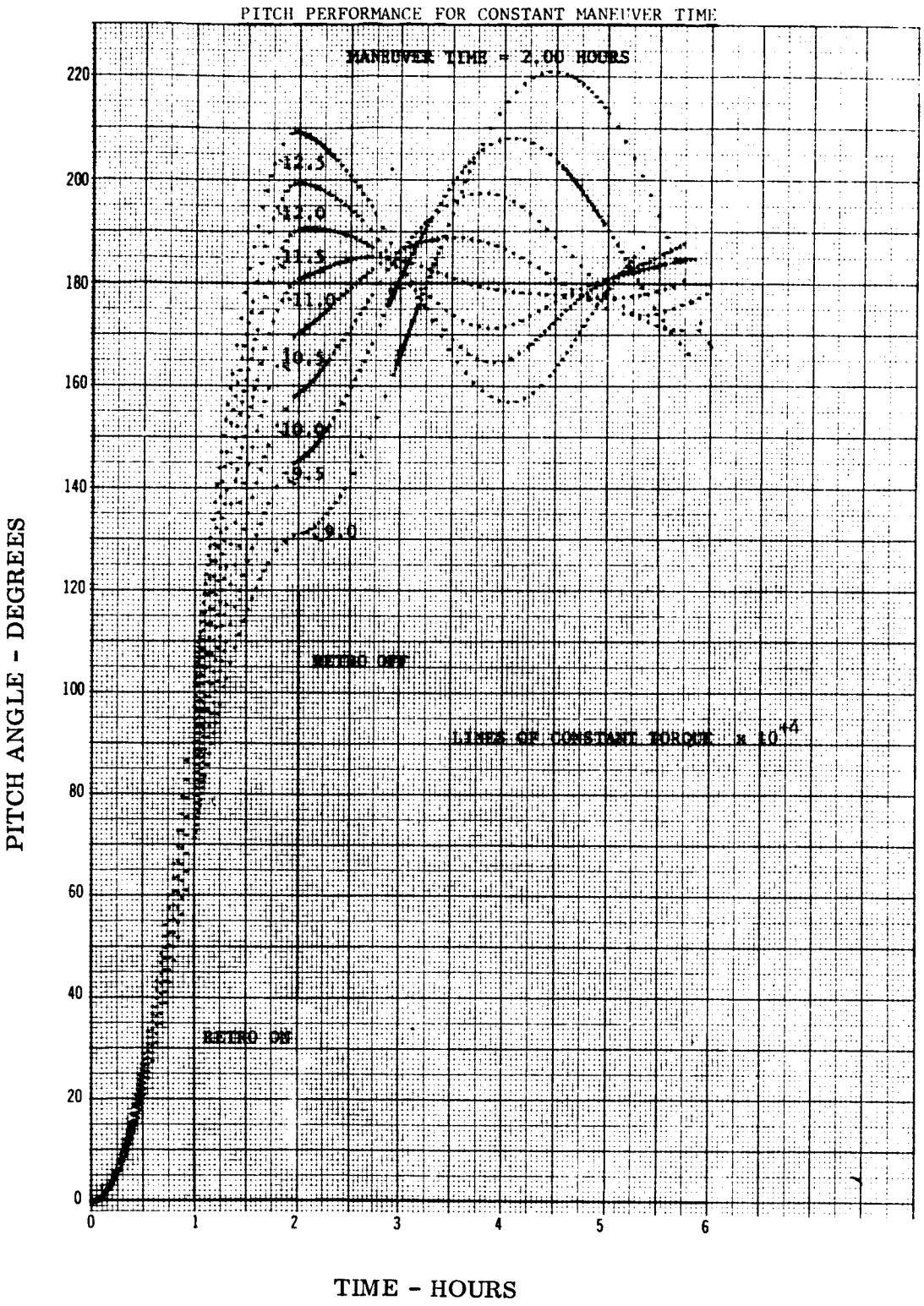


Figure 2.1.5.3-6. Pitch Performance for Constant Maneuver Time

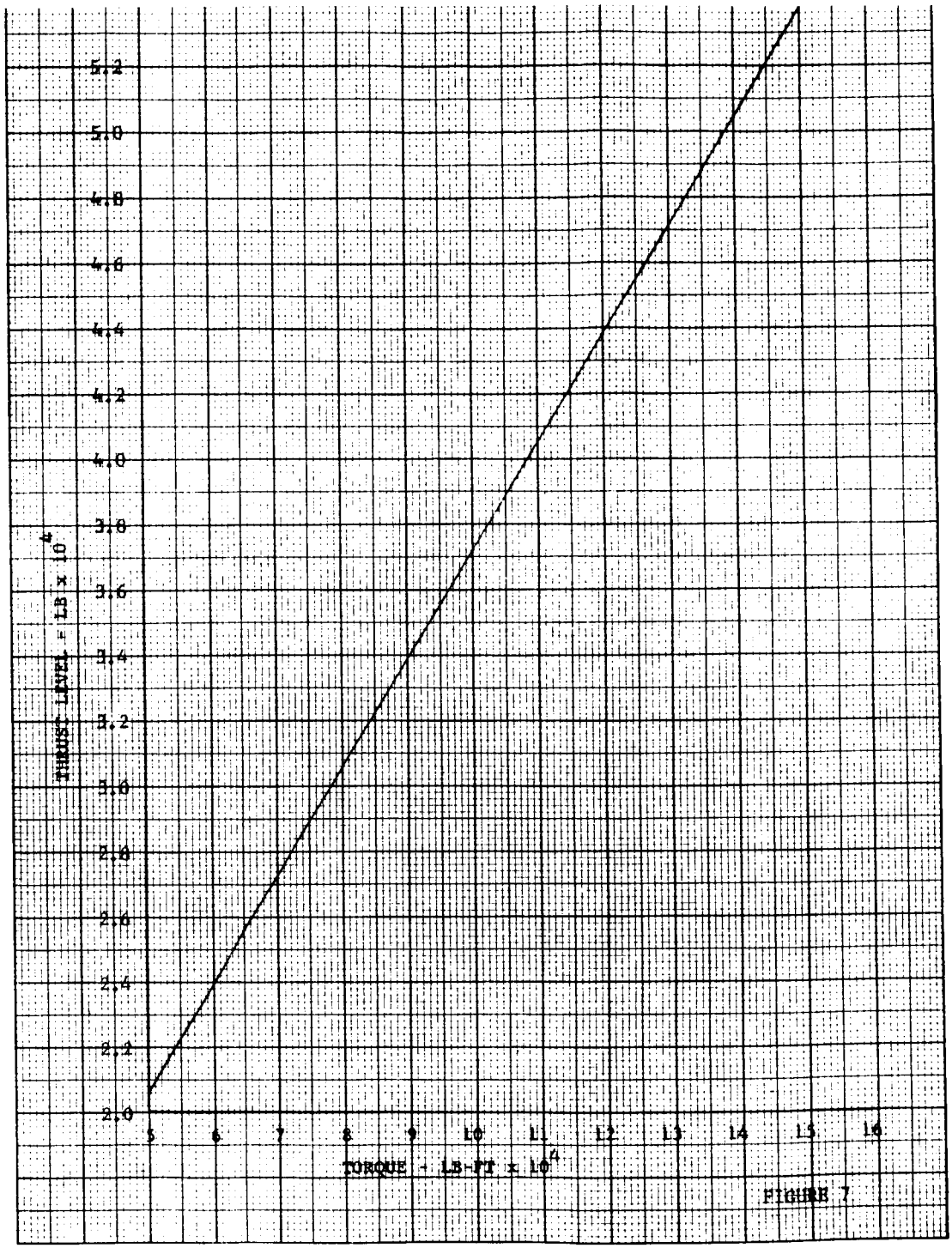


Figure 2.1.5.3-7. Thrust Level as a Function of Required Torque

The argument of perigee is:

$$\Upsilon_p = \Upsilon_{pi} + \dot{\Upsilon}_p (t - t_i), \tag{2}$$

where the symbols have the same or similar meanings as the above, and $\dot{\Upsilon}_p$ is the rate of precession of the line of apsides.

The orbital angle measured from the ascending node is Υ. The orbital angle measured from perigee is $(\Upsilon - \Upsilon_p)$.

If the apogee, A, and perigee, P, are given, the semimajor axis, a, is computed from:

$$a = \frac{1}{2} (A + P) \tag{3}$$

The eccentricity, e, of the orbit is:

$$e = \frac{A - P}{A + P} \tag{4}$$

If the semimajor axis and the eccentricity are given, the apogee is computed from:

$$A = a (1 + e) \tag{5}$$

and the perigee is computed from:

$$P = a (1 - e). \tag{6}$$

The angular momentum per unit mass is:

$$h = \sqrt{K a (1 - e^2)}, \tag{7}$$

where K is the universal gravitational constant multiplied by the mass of the earth.

The orbital period, τ, is

$$\tau = 2\pi a \sqrt{\frac{a}{k}} = \frac{2\pi a^2}{h} \sqrt{1 - e^2} \tag{8}$$

If t_p is the time of perigee passage, the elapsed time since perigee is $(t-t_p)$, where t has been reduced modulo τ. Kepler's equation is:

$$E - e \sin E = \frac{2\pi}{\tau} (t-t_p), \tag{9}$$

where K is the eccentric anomaly, in radians. An iterative procedure for solving this equation is presented. Assume that E_o is the value of E at the previous time interval, t_o. For

$$t = t_o + \Delta t, \tag{10}$$

then,

$$E = E_o + \Delta E, \tag{11}$$

is to be found. The first trial value of ΔE is

$$\Delta E_1 = \frac{2\pi \Delta t}{\tau (1 - e \cos E_o)} . \tag{12}$$

The first trial value of E is

$$E_1 = E_o + \Delta E_1. \tag{13}$$

The second trial value of ΔE is

$$\Delta E_2 = \frac{2\pi \Delta t}{\tau (1 - e \cos E_1)} . \tag{14}$$

The second trial value of E is,

$$E_2 = E_o + \Delta E_2. \tag{15}$$

This procedure is repeated until the change in two consecutive trial values of E is less than a prescribed amount.

The orbital angle Υ', relative to perigee, is

$$\Upsilon' = \Upsilon - \Upsilon_p \tag{16}$$

This is computed from

$$\text{Tan}\left(\frac{\Upsilon'}{2}\right) = \sqrt{\frac{1+e}{1-e}}\ \tan\left(\frac{E}{2}\right) \tag{17}$$

where $(\Upsilon'/2)$ is in the same quadrant as $(E/2)$. If Υ' and E are equal to or greater than 2π, then 2π should be subtracted from each, and the orbit count should be increased by one. Υ is computed from,

$$\Upsilon = \Upsilon' + \Upsilon_p. \tag{18}$$

The geocentric altitude is

$$R_A = a\,(1-e\cos E). \tag{19}$$

The orbital angular velocity is

$$\dot{\Upsilon} = \frac{h}{R_A^2}\,. \tag{20}$$

The radial velocity is

$$\dot{R}_A = \frac{e\,h\sin\Upsilon'}{a\,(1-e^2)} = \frac{e\,h\sin E}{R_A\sqrt{1-e^2}}\,. \tag{21}$$

The orbital angular acceleration is

$$\ddot{\Upsilon} = \frac{-2h}{R_A^3}\ \dot{R}_A\,. \tag{22}$$

The radial acceleration is

$$\ddot{R}_A = \frac{e\,h\,(\dot{\Upsilon}-\dot{\Upsilon}_p)}{a\,(1-e^2)}\ \cos\Upsilon'. \tag{23}$$

If $\dot{\tau}_p$ is zero, the radial acceleration is

$$\ddot{R}_{AO} = \frac{-K}{R_A^2} \tag{24}$$

2.1.5.4.2 Satellite Orbit Equations with Applied Thrust

The reference frames used are explained in section 2.1.5 of the ATS First Quarterly Report, Document No. 64SD4361, 16 October 1964.

Thrust for changing the eccentricity of the orbit or for station-keeping will be applied nominally along specified directions with respect to the main body reference frame, $X_1\ Y_1\ Z_1$. For the sake of generality, and to provide for studies of the effects of misalignments, the thrust will be assumed to have a component along each of the three reference axes. These components are F_{X1}, F_{Y1}, and F_{Z1}. The consequent accelerations are:

$$A_{X1} = \frac{F_{X1}}{M_m + M_s}\ , \tag{25}$$

$$A_{Y1} = \frac{F_{Y1}}{M_m + M_s}\ , \tag{26}$$

$$A_{Z1} = \frac{F_{Z1}}{M_m + M_s}\ , \tag{27}$$

where M_m is the mass of the main body, and M_s is that of the secondary body. The components in the orbital frame, RPQ, are,

$$\begin{bmatrix} A_R \\ A_P \\ A_Q \end{bmatrix} = \left[E_1\right]^t \begin{bmatrix} A_{X1} \\ A_{Y1} \\ A_{Z1} \end{bmatrix}. \tag{28}$$

It is assumed that A_Q and $\dot{\Omega}$ are so small that their effects can be neglected during the thrusting period. The problem is then a two-dimensional one in the orbit plane,

and can be solved as described below. If the assumption that the out-of-plane components are negligible is not justified, then the three-dimensional problem must be solved.

The values of the geocentric altitude, R_A, its velocity, $\dot{R}_A$, designated u, the orbit angle, Υ, and its rate, $\dot{\Upsilon}$, designated v, are known at the beginning of the thrust period, from the orbital equations.

During application of thrust, the radical acceleration is,

$$\ddot{R}_A - R_A \dot{\Upsilon}^2 = A_R - \frac{K}{R_A^2} . \tag{29}$$

The acceleration along the perpendicular direction in the orbit plane is,

$$R_A \ddot{\Upsilon} + 2\dot{R}_A \dot{\Upsilon} = A_P. \tag{30}$$

These equations may be rearranged,

$$\dot{\mu} = R_A v^2 + A_R - \frac{K}{R_A^2} , \tag{31}$$

$$\dot{v} = \frac{A_p - 2\mu v}{R_A} . \tag{32}$$

These may be integrated with respect to time to obtain the instantaneous values of μ (or $\dot{R}_A$) and of v (or $\dot{\Upsilon}$). Then $\dot{R}_A$ and $\dot{\Upsilon}$ may be integrated with respect to time to obtain instantaneous values of R_A and Υ.

The out-of-plane component, A_Q, may be integrated with respect to time, to find the corresponding velocity increment due to thrusting,

$$v_Q = \int_0^t A_Q \, dt. \tag{33}$$

At the end of the thrust period, the instantaneous values of the variables are respectively designated R_{AO}, $\dot{R}_{AO}$, Υ_O, and $\dot{\Upsilon}_O$. These values are used to find the new orbit parameters.

The angular momentum per unit mass is,

$$h = R_{AO}^2 \dot{\Upsilon}_O. \tag{34}$$

The semiparameter of the orbit is,

$$S_P = a(1-e^2) = \frac{h^2}{K}: \tag{35}$$

The eccentricity is computed from

$$e_c = e \cos(\Upsilon_O - \Upsilon_P) = \frac{S_P}{R_A} - 1, \tag{36}$$

$$e_s = e \sin(\Upsilon_O - \Upsilon_P) = \frac{\dot{R}_{AO} S_p}{h}, \tag{37}$$

$$e^2 = e_c^2 + e_s^2, \tag{38}$$

and e is the positive square root of e^2. The quantity $(\Upsilon_O - \Upsilon_p)$ is computed from,

$$\sin(\Upsilon_O - \Upsilon_p) = \frac{e_s}{e}, \tag{39}$$

$$\cos(\Upsilon_O - \Upsilon_p) = \frac{e_c}{e}. \tag{40}$$

Then the argument of perigee, Υ_p, is computed by using the known value of Υ_O.

The semimajor axis is,

$$a = \frac{S_p}{1-e^2}. \tag{41}$$

The orbital period is,

$$\tau = 2\pi a \sqrt{\frac{a}{K}} \quad . \tag{42}$$

During the ensuing no-thrust period, the equations of Section I are used. The initial conditions for this period are the instantaneous values at the end of the thrust period.

2.1.5.4.3 Earth Orbit Equations

These equations are given in Section 2.1.5 of the ATS First Quarterly Report, Document No. 64SD4361, 16 October 1964.

Also given are the components S_{XI}, S_{YI}, and S_{ZI}, of the solar unit vector S, in the inertial frame. The components in the orbital frame are:

$$\begin{bmatrix} S_R \\ S_P \\ S_Q \end{bmatrix} = [A] \begin{bmatrix} S_{XI} \\ S_{YI} \\ S_{ZI} \end{bmatrix} . \tag{43}$$

The components in the satellite main body frame are,

$$\begin{bmatrix} S_{XI} \\ S_{YI} \\ S_{ZI} \end{bmatrix} = [E_1] \begin{bmatrix} S_R \\ S_P \\ S_Q \end{bmatrix} . \tag{44}$$

2.1.5.5 Variations in Damping Time Due to Off-Nominal Angles Between the Plane of the Damping Boom and the Plane of the X-Booms

Tinling and Merrick in their paper "The Exploration of Inertial Coupling in Passive Gravity Gradient Stabilized Satellites"* discussed the effect on damping of changing the angle between the secondary boom and the plane of the X-rods. A

*Item 14 of Section 4.

plot showing the effect of this angle was included in their paper. This plot indicated that for a change of ±4 degrees about the nominal angle (62.5 degrees), the damping time increased by ten percent. The increase is not linear for angle changes less than 4 degrees, but the scale of the plot does not permit accurate determination of the correct values. The change in damping can be assumed linear with angle change, however, as a slightly pessimistic approach.

2.1.5.6 Effect of Spring Constant on Damping Performance of MAGGE

An investigation of tolerances on the spring constant of the ATS Gravity Gradient configuration was prompted by statements of Tinling and Merrick in their AIAA paper (see item 14 of Section 4) regarding the sensitivity of damping of ATS type systems to variations in spring constants. Specific mention was made of the poor performance exhibited by a system which has a spring constant lower than the recommended nominal value. Figure 7 of Tinling and Merrick's paper shows a sudden drop-off in system damping capability for a spring constant which is approximately 18 percent lower than nominal.

The loss of damping capability is more apparent than real, however, and appears because of the technique Tinling and Merrick used to evaluate the system. In this technique, the equations of motion are linearized about a specific operating point, and the minimum damping time constant determined by a computer solution to the linearized equations. One characteristic of the operating point is that the secondary boom must be stable about a null point in the horizontal plane. To achieve this stability, a minimum spring constant is required. If the spring constant is lower than this minimum, the analysis will indicate instability with no damping. This fact was pointed out by Tinling and Merrick in their paper. In actuality, the system as a whole is stable and will re-orient itself about a new static position.

Studies performed by GE with "sub-minimum" spring constants (using both root locus techniques and computer runs) show that the damping about the new position

is of the same order of magnitude as that achieved for the "nominal" operating point. To demonstrate this, a computer run was made on the GAPS III computer program with a spring constant 20% lower than nominal. The results are shown in Figure 2.1.5.6-1. Note that the damping is approximately the same as with the nominal spring constant (Figure 2.1.5.6-2) but the secondary boom stabilizes about a new position approximately ten degrees below the null spring point. This causes a rotation of the principal moments of inertia of the system which results in a 0.6 degree pitch bias and a 0.5 degree roll bias (which, because of the scale of Figure 2.1.5.6-1, are not evident).

Successful operation of the system with a low spring provides a "safety margin" making the tolerances on the spring constant less critical, but the presence of the biases on the axes makes it undesirable to have low spring constants. The tolerance on the spring constant for the ATS damper was, therefore, set at -0, +20% specifically to avoid this difficulty. The performance of a system which has a spring constant 20% high and a computer run was made for this system (Figure 2.1.5.6-3). Comparison of Figure 2.1.5.6-3 with Figure 2.1.5.6-2 shows an increase in damping time (particularly in yaw) as expected. However, the damping time is still good and should cause no difficulty. The steady state performance of the high spring constant system will be evaluated in the future.

2.1.6 SYSTEM REQUIREMENTS FOR TV

2.1.6.1 Requirements

The following paragraphs describe the basic system requirements for the TV camera to be flown as an integral part of the ATS gravity gradient experiments. Current plans call for two cameras on MAGGE and one camera on each SAGGE flight. The primary objectives of the TV system are as follows (in order of descending priority):

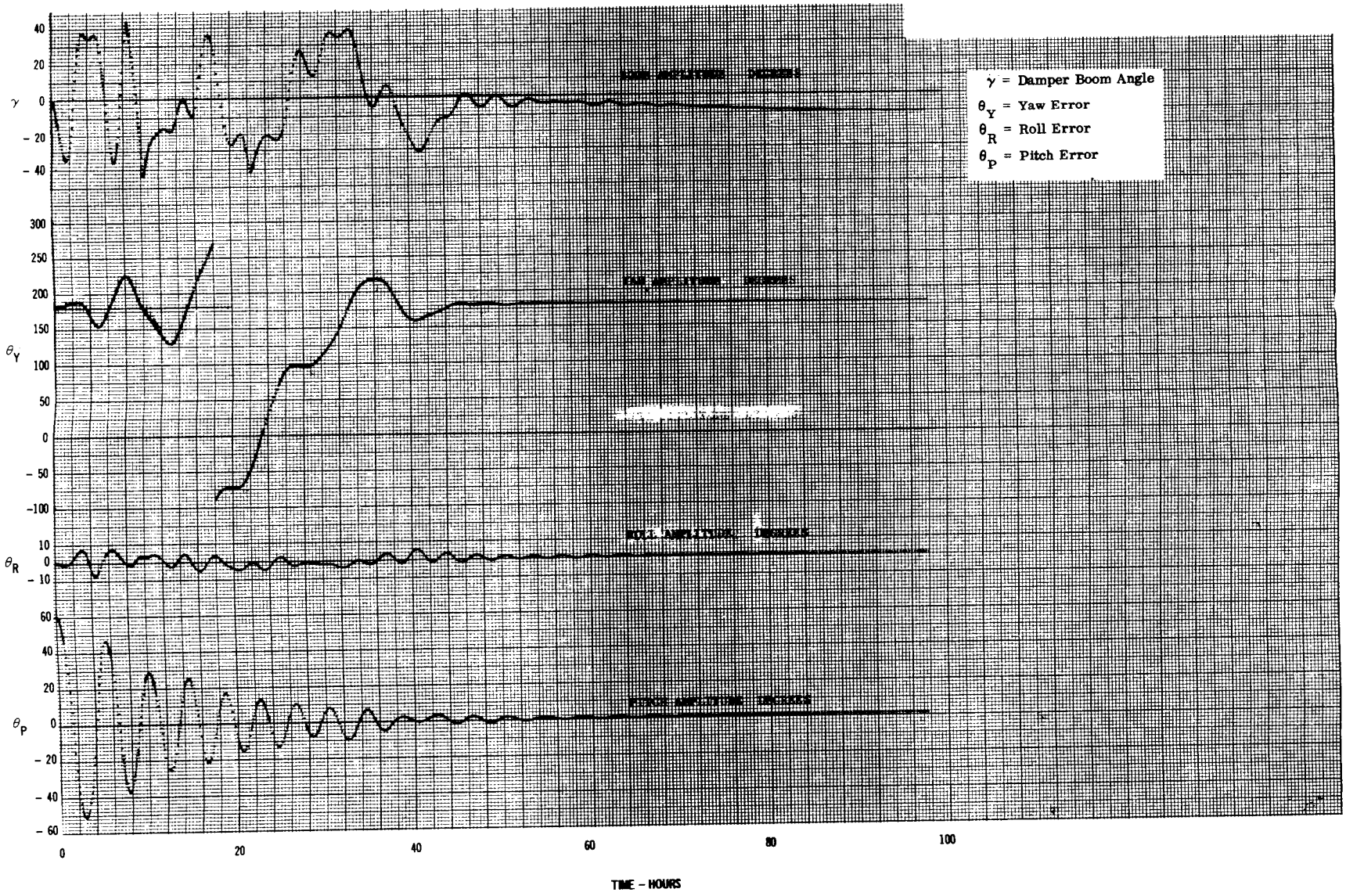


Figure 2.1.5.6-1. Transient Performance of MAGGE Spring Constant 20% Low — 7.38×10^4 lb/ft/rad

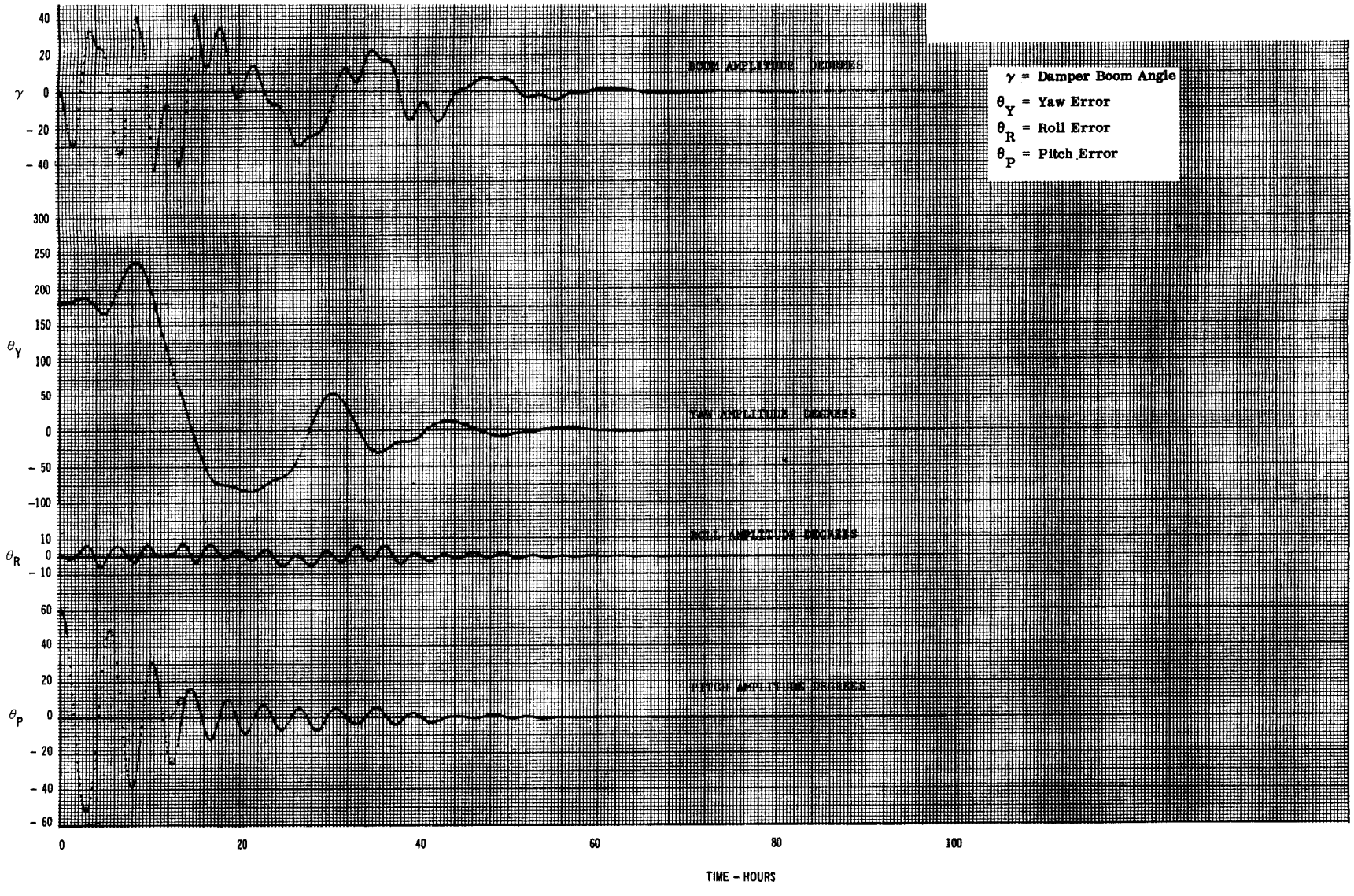


Figure 2.1.5.6.2. Transient Performance of MAGGE Spring Constant Normal — 9.22×10^4 lb-ft/rad

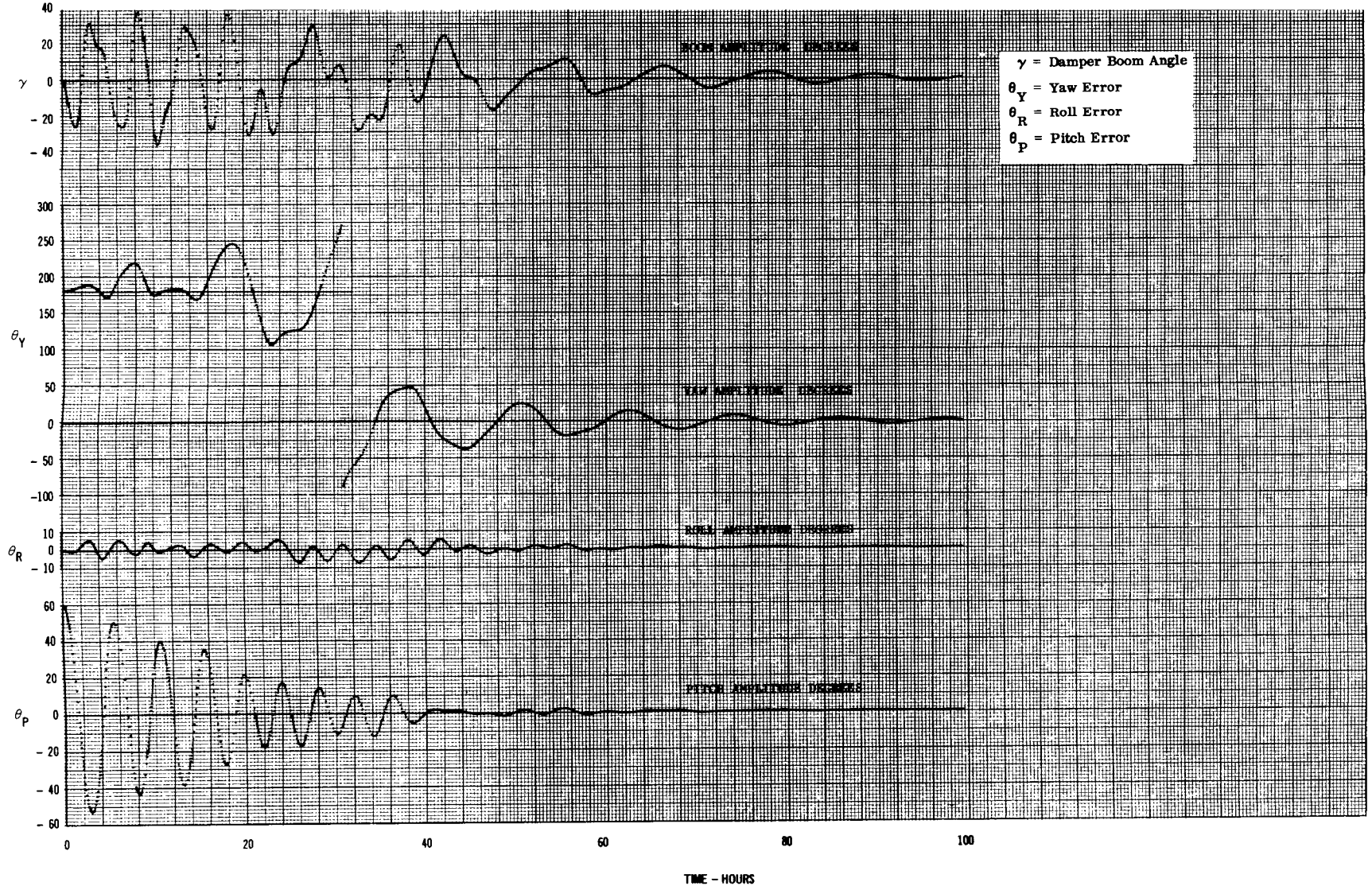


Figure 2.1.5.6-3. Transient Performance of MAGGE Spring Constant 20% High — 11.06×10^{-3} lb-ft/rad

1. Provide sufficient data for the verification of the boom thermal bending model employed as an integral part of the ATS Mathematical Model. The equation for thermal bending will employ empirical coefficients; these coefficients will be adjustable so that the model can be empirically modified to fit observed test data.

2. Provide sufficient data for the verification of mathematical procedures used to estimate the magnitude and nature of boom dynamic excitation phenomena.

3. Provide the capability for real time gross attitude determination at each of the ATS ground stations. Real time data is of critical importance in making real time procedural decisions at the ground stations. Only a minimum computer capability will be present at the ground stations and there is a strong probability that the only real time attitude data that can be made available at the ground stations is a presentation of direct output from ATS sensors. Calibration charts and curves, used in conjunction with sensor output raw data, may provide a gross indication of attitude. The outputs of the earth sensor and the TV camera seem to offer the most distinct possibilities.

4. Provide backup data for ATS attitude determination. Since the earth will appear in the field of view of the TV camera (during near steady state operation) the use of the cameras as a backup source of attitude information seems a distinct possibility. Identifiable land masses would provide yaw information and the location of the earth sphere in the field of view of the cameras will provide pitch and roll information. Attitude determination will be a relatively slow process, however, unless automated procedures are utilized.

In addition, to the above, the TV cameras will monitor boom deployment during the initial capture phase. The objective here is primarily diagnostic in nature — the cameras will present visual evidence of the success, or the mode of failure, of the critical boom deployment sequence. In addition, if sufficient TV picture resolution can be obtained, it would be highly desirable to determine the time history of tip mass twist as the booms are deployed. This will be the only opportunity to determine absolute twist of the rods; twist measurements after deployment will only be relative in nature. Twist measurements may be the most critical piece of information required to diagnose reasons for possible disagreement between predicted boom phenomena and observed boom phenomena (Objectives 1 and 2 above).

All four boom targets on MAGGE should be monitored during the deployment sequence. Time-sharing of the two cameras is permissible for power conservation but each camera should provide pictures at a rate of at least one frame every two seconds for the duration of deployment. Power to the attitude sensors can await completion of deployment. The booms will be deployed at a rate of 2 (+1, -1/2) ft/sec. A flat, circular target (currently six inches in diameter) is attached to the tip of each boom. Target diameter, by redesign, may be increased slightly; a 12-inch diameter, however, should be regarded as maximum with the six-inch diameter a strong preference. For 100-foot booms, the total time for deployment is nominally 50 seconds, but may be as slow as 67 seconds or as fast as 33 seconds. The booms will be deployed in the 19-degree half-angle configuration; each TV camera is required to observe total deployment of two tip masses (targets) so that all four targets are monitored during initial deployment. The cameras should begin transmission approximately 20 seconds before deployment and continue for another 30 seconds after completion of deployment; the slower deployment rate of 67 seconds therefore sets an upper limit of about two minutes transmission time to cover the deployment sequence. At a transmission rate of one frame/second (one frame every two seconds from each of two cameras), 120 frames will be provided for data analysis and reduction.

The following types of information should be available from the final picture format provided GE's data processing group:

(a) Relative change in tip mass (target) location as a function of time — Magnitude and angular direction are required — one frame each two seconds, over the total period of observation, is assumed adequate for time history. Changes in tip mass displacement of two inches should be detectable; changes in angular direction of displacement of five-degrees should be detectable.

(b) Absolute location of tip mass, relative to boresight of TV camera, as a function of time — Accuracy of absolute measurements need not be as fine as accuracy of relative measurements. Typically, a magnitude accuracy of four-inches (±2-inches) and an angular accuracy of 10 degrees (±5-degrees) should be acceptable.

(c) Relative twist of boom over the period of observation — This requires a detectable pattern on the boom-tip target which will reveal orientation of the target about an axis normal to the target. (Changes of five degrees should be detectable.)

(d) Absolute twist of boom relative to fixed root of boom — This, probably, will depend on an analysis of the boom deployment pictures; nominal twist after completion of deployment, plus the relative twist of (c), will give an indication of absolute twist.

(e) Boom curvature — If the criteria of (a) through (d) are satisfied, there should be sufficient resolution to observe at least a portion of the boom itself. Complete boom curvature will then be approximated by extrapolating the observable curvature out to the observed target location.

The following tables summarize requirements of the TV system. The first table (Table 2.1.6-1) summarizes parametric requirements; the second table (Table 2.1.6-2) summarizes tests designed to accomplish the stated objectives, the estimated number of data frames and the time phasing of TV camera usage. Stated objective numbers refer to the four enumerated objectives at the beginning of this memo. To Table 2.1.6-2 should be added a requirement for observing the booms during scissoring maneuvers.

2.1.6.2 Compromises

It is evident from the previous discussion that a TV scan rate of 30 frames per minute is adequate to meet all of the required objectives. The advantages of reducing scan rate of TV subsystems as presently conceived have been discussed with representatives of NASA/GSFC many times and are reported in Section 2.4.2.1 of the Fifth Monthly Progress Report. Further discussion of a slow scan version of the TV camera subsystem follows in Section 2.4.4 of this report. However, recognizing that the economic considerations of the ground station equipment may be a determining factor, General Electric is proceeding with the recent NASA/GSFC directive to employ the standard-scan system. Taking into account that all of the parameters of the TV system are still not defined, e.g., overall video bandwidth and method of data reduction, those areas of the design objectives in which performance is lagging are discussed in the following paragraphs.

TABLE 2.1.6-1. TV SYSTEM PARAMETRIC REQUIREMENTS

1. Target Parameters:

   (a) Diameter: 6 in.-12 in. (current design is 6 in.; the 12 in. diameter should be avoided, if possible, due to installation problems).

   (b) Target pattern: pattern must be detectable with a resolution satisfying the twist measurement requirements; if possible, the target should consist of patterns of opaque and transparent materials to provide proper illumination during all phases of desired measurements.

   (c) Assume target to be 100 feet from lens of TV camera; for SAGGE this distance may increase to 150 feet. (Use 100 feet for design; if 150 feet used, degraded performance will be accepted.)

2. Frame Rate:

   One frame every two seconds (30 frames per minute) seems adequate for all requirements.

3. Measurement Accuracies:

(a)	Relative tip displacement:	2 in. detection threshold
(b)	Absolute tip displacement:	±2 in. relative to boresight
(c)	Relative angular displacement:	5^{o} detection threshold
(d)	Absolute angular displacement:	$\pm 5^{o}$
(e)	Relative twist of target:	5^{o} detection threshold

In reference to the time history of tip mass twist, the TV camera must be able to see a reference mark on the boom target in order to indicate twist. If we assume a 2-inch wide stripe on a 6-inch diameter target, it is estimated that the TV camera can provide an indication of twist as the boom is reeled out in deployment from the vehicle up to a deployed distance of almost 27 feet. Moreover, at this maximum distance of 27 feet, it appears that the least angle of rotation determinable will be almost 6 degrees. Beyond 27 feet, the camera cannot resolve the 6-inch long stripe distinctly enough to indicate twist. This limitation could be overcome by increasing camera resolution (greater video bandwidth or slower scan rate) or by using a larger boom target.

TABLE 2.1.6-2. TV SYSTEM MEASUREMENTS SEQUENCE

Frames recorded for data reduction — frames for real time display at ground stations not included.

Cumulative Days in Orbit	Measurement No.	Measurement	Objective Number	Time in Orbit	Number Frames	Duty Cycle
0+	(1)	Boom deployment during initial capture phase — permanent record made at ground station	Diagnostic plus (1)	2 min.	120	30 frames/minute, each camera, for 120 seconds beginning 20 seconds prior to boom deployment; frames from alternate cameras interlaced time-wise for a transmission rate of one frame/second.
2	(2)	(Cameras on for one minute per orbit to monitor boom dynamics during capture phase)	(2)	2 days	480	30 frames/minute, each camera, for one minute each orbit, for two days = 60 x 8 = 480 frames.
4	(3)	Structural damping test-cameras on periodically to observe decay in boom tip displacement per cycle of oscillation (tip displacement history to be interpolated between sample observations)	(2)	2 days	8640	30 frames/minute, each camera, for one minute every ten minutes while in view of ground station: three ground stations (assume view-time of one hour/orbit) = 18 minutes per orbit; 8 orbits = 144 minutes = 8640 frames.
4+	(4)	(Cameras on for one minute each 10 minutes for first hour of first large angle displacement maneuver — to observe boom dynamic reaction to displacement torque application)	(2)	1 hour	360	30 frames/minute, each camera, for one minute every ten minutes for one hour = 360 frames.
23	(5)	Cameras off during orbit tests 2-4 except as required for real time attitude display at ground stations	(3) and (4)	19 days	—	Real time attitude display assumed to require only one minute per orbit each ground station using only the camera nearest the earth; if earth not in field of view, steady state has not been achieved.
27	(6)	Measurement of thermal "twang" and effect of variable solar incidence angle	(1)	4 days	8640	Start camera away from earth one minute prior to eclipse exit; observe booms for five minutes continuously after eclipse exit and at one minute intervals each 10 minutes thereafter for the next two hours — repeat test eight times with each of two dampers (two hours on, 4.4 hours off, 4 days)
140	(7)	Cameras off during orbit tests 6-8 except as required for real time attitude display at ground stations — 60 days of no gravity gradient tests included in this interval	(3) and (4)	113 days	—	(Same duty cycle as measurement no. (5) — prior to transmittal of commands, ground station operators should have visual real time indication that spacecraft is in steady state attitude).

TABLE 2.1.6-2. TV SYSTEM MEASUREMENTS SEQUENCE (Continued)

Frames recorded for data reduction — frames for real time display at ground stations not included.

Cumulative Days in Orbit	Measurement No.	Measurement	Objective Number		Number Frames	Duty Cycle
200	(8)	Eccentricity change*	(2)	60 days	1800	30 frames/minute, one camera, 10 minutes, once every ten days = 180 frames.
336	(9)	Cameras off except for real time attitude* display	(3) and (4)	136 days	—	(Repeat of tests 2-8, orbit test plan, in eccentric orbit)
342	(10)	Inversion maneuver; invert, allow to settle to steady state; re-invert	(2)	6 days	2160	30 frames/minute, each camera, for one minute every ten minutes for three hours = 30 x 2 x 18 = 1080 — Repeat during reinversion — cameras off during remainder.
356	(11)	Rod retraction and evaluation of thermal bending for shorter rods	(1) (2)	14 days	12,240	30 frames/minute, one camera — similar test to measurement #6 after rods retracted; 30 frames/minute, three minutes every orbit for remainder of time = 8640 frames plus ten days x 4 orbits/day x 3 minutes/orbit x 30 frames per minute = 8640 + 3600 = 12,240 frames.
				356 days	34,460	Days for data reduction = 7/5 (356) 497
						34,460 / 497 70 frames/day based on a five-day work week.

*Requirement deleted after publication of this table.

The second area of lagging performance is in indicating the angular direction of displacement as little as 5 degrees. The TV camera constructs the picture from horizontal lines, in an x-direction and vertically stacked lines in a y-direction. The angular displacement is therefore determined as the angle whose tangent is the ratio of y to x. Since we can determine y or x to about 2 1/4 inches at 100 feet, the quadrature direction for a 5-degree angle is readily computed to be almost 26 inches. This is the obviously worst case, in which one of the variables is assumed to have moved only one resolution element in its direction. More commonly, each variable will change more than one resolution element, in which case the angle will be greater. Nevertheless, the worst case does represent a datum of valid interest. Considerable improvement in resolution would be necessary to reduce the 26-inch dimension above to only a few inches.

The other system requirements will be largely satisfied. Much of the performance of the TV camera depends upon lighting conditions at the boom target. The lighting condition will be optimum only a short time each orbit. At these times the TV camera will perform best. The major part of the present design effort is being directed to maintain performance under as wide a range of illumination conditions as possible by both camera and target design.

If improvement in the areas of lagging performance is necessary from a systems standpoint, some greater latitude in TV camera parameters must be granted. This greater latitude has thus far not been approved. Finally, the accuracy and resolution described above hold for a 5 mc bandwidth and grow worse as bandwidth is reduced.

Such a reduced bandwidth would not allow the other system performance values to be met, since these are consistent with the 5 m bandwidth capabilities.

2.1.7 BOOM THERMAL BENDING STUDIES

Thermal bending of the boom is produced by a temperature gradient across the boom bending section. Boom curvature can be determined from the temperature gradient and the physical properties of the boom as:

$$C = \Delta T\, a/2r$$

where

C = curvature (1/in)

ΔT = temperature gradient (^{o}F)

a = coefficient of thermal expansion (in/in - ^{o}F)

r = rod radius (in.).

Under the condition that the boom is considered as a hollow-rod, the temperature distribution in the rod is symmetrical about the sun-rod centerline plane; the rod high temperature point will be toward the sun and the low temperature point directly away from the sun. In Document No. 63SD725 (see item 2, Section 4) the determination of the temperature gradient for this condition is given as:

$$\Delta T = \frac{\alpha S r^{2}}{kt}$$

where

α = coefficient of absorptivity

S = flux density (BTU/Hr-Ft^2)

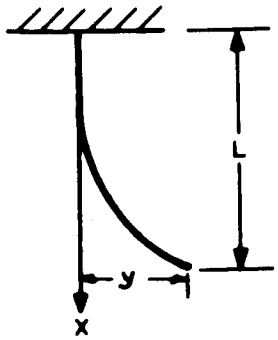
r = radius of rod (Ft.)

k = thermal conductivity (BTU/Hr-Ft-^{o}F)

t = material thickness (Ft.).

The deflection of the boom can be obtained from the curvature as:

$$y = \int_{0}^{L} \int_{0}^{L} C\,dx\,dx.$$



In the event that the curvature can be considered as constant the deflection at X = L is:

$$y_L = \frac{1}{2}CL^2.$$

In reference Document No. 63SD725 (Item 2, Section 4) it was shown that this approach predicted deflections of an overlapped rod which were in essential agreement, in magnitude, with deflections measured during test.

The tests showed, however, that the rod did not deflect only in the sun-rod plane but also deflected to the side. In some instances, dependent on sun position relative to the overlap, the deflections were as much as 45^o relative to the sun-rod plane.

Analytic temperature distributions, Reference Document No. 64SD4368, (Item 3 of Section 4), revealed the not unexpected fact that the rod circumferential temperature distributions were unsymmetrical. The distributions generally showing a strong discontinuity at the overlap. Two analytic approaches were undertaken in order to better understand the bending of an overlapped rod under a temperature distribution of this kind. The shell equations for an overlapped rod were written and prepared for solution by digital computer. A second approach decomposed the temperature distribution into components which reveal the position and magnitude of the symmetrical temperature gradient.

These two approaches are presented in Reference Document No. 64SD4368. (Item 3 of Section 4)

The above reference also presents results of a series of tests in which predicted deflection magnitudes and measured deflection magnitudes generally disagree by a factor of about two. Effort spent in attempting to resolve this discrepancy has been hampered by the lack of reliable measurements of rod temperatures during test. Current efforts are being directed toward the definition of an additional test which will produce the required temperature and deflection measurements to an

accuracy compatible with requirements for correlation with analytical predictions. Effort is also being devoted to the programming and solution of the shell equations for comparison with results predicted by beam theory. The determination of a stiffness matrix for gravity gradient rod elements is discussed in Appendix E. Section 2. 1. 8 covers a discussion of gravity gradient corrections to thermal bending tests and indicates the effect is negligible.

2. 1. 8 GRAVITY CORRECTION FOR THERMAL BENDING TESTS

The rod is fixed at the upper support and held in a vertical orientation. Due to the thermal gradient the rod assumes a curvature, C(x) = 1/R. Due to the effect of gravity there is a moment set up which reduces the curvature.

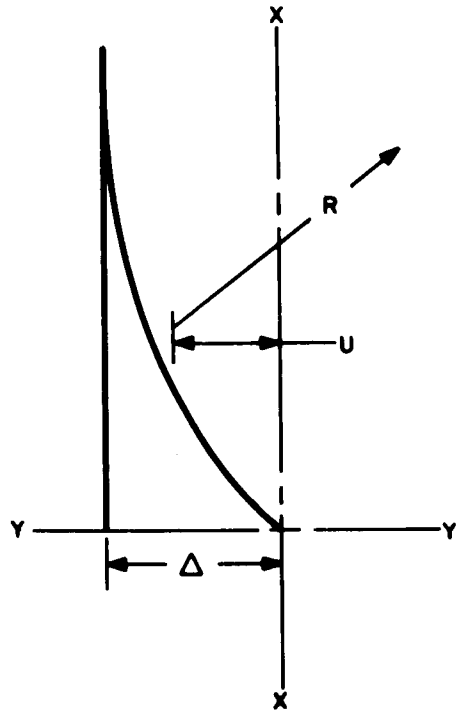
$$\frac{1}{R} = C(x) - \frac{M}{EI}$$

Referring to figure (1) the deflection of the rod is $\Delta - u$

The slope is $\theta = \int \frac{1}{R}\, dx$

and the deflection is

$$\Delta - u = \iint \frac{1}{R} dx dx$$



For convenience the origin is chosen at the free end of the rod with an X-X axis selected parallel to the undeflected rod. This choice of coordinates simplifies the handling of the equation for moments.

The moment due to gravity is

$$m = \int_0^x mg\, u\, dx$$

where

mg = the weight of the rod per unit length

u = the deflection of the rod as defined in the figure

x = the distance from the free end.

Then

$$\frac{d^2u}{dx^2} = \frac{1}{R} = C(x) - \int_0^x \frac{mg}{EI}\, u\, dx$$

Differentiating this expression gives

$$\frac{d^3u}{dx^3} + \frac{mg}{EI}\, u = \frac{d\,C(x)}{dx}$$

This expression is general in that to this point no assumption has been made regarding variation of mg/EI with length. For the case of the thermal bending test mg/EI was constant so this will be the case considered here. The solution to this equation is composed of two parts:

$$u = u_c + u_p$$

where u_c is the solution for the case

$$\frac{d\,C(x)}{dx} = 0$$

and u_p is the particular solution for

$$\frac{d\,C(x)}{dx} \neq 0$$

Although it was not an accomplished fact, the intent in the thermal bending test was to provide a thermal distributor which did not vary along the length of the rod. For this case d C(x)/dx = 0.

The behavior of the rod then is described by

$$\frac{d^3u}{dx} + \phi^3 u = 0$$

where

$$\phi = \sqrt[3]{\frac{mg}{EI}}$$

The solution to this equation is

$$u = C_1 e^{-\phi x} + e^{\frac{\phi}{2}x}\left[C_2 \cos\left(\frac{\sqrt{3}}{2}\phi X\right) + C_3 \sin\left(\frac{\sqrt{3}}{2}\phi X\right)\right] + \frac{C(x)X^2}{2}$$

Further

$$\theta = -\phi C_1 e^{-\phi x} + \frac{\phi}{2} e^{\frac{\phi}{2}x}\left[\left(C_2 + \sqrt{3}\, C_3 \cos\left(\frac{\sqrt{3}}{2}\phi X\right)\right.\right.$$
$$\left.\left. + C_3 - \sqrt{3}\, C_2 \sin\left(\frac{\sqrt{3}}{2}\phi x\right)\right)\right] + C(x)X$$

$$\frac{1}{R} = \phi^2 C_1 e^{-\phi x} + \frac{\phi^2}{2} e^{\frac{\phi}{2}x}\left[\left(-C_2 + \sqrt{3}\, C_3 \cos\left(\frac{\sqrt{3}}{2}\phi X\right)\right.\right.$$
$$\left.\left. + (-C_3 - \sqrt{3}\, C_2) \sin\left(\frac{\sqrt{3}}{2}\phi x\right)\right)\right] + C(x)$$

$$\frac{d\left(\frac{1}{R}\right)}{dx} = -\phi^3\left[C_1 e^{-\phi x} + e^{\frac{\phi}{2}x}\left\{C_2 \cos\left(\frac{\sqrt{3}}{2}\phi x\right) + C_3 \sin\left(\frac{\sqrt{3}}{2}\phi x\right)\right\}\right]$$

The boundary conditions are when X = 0, u = 0

$$\frac{1}{R} = C(x)$$

and when X = ℓ, θ = 0

From these boundary conditions the constants of integration are

$$C_1 = \frac{C(x)\,\ell}{\phi\left[e^{-\phi\ell} + 2\,e^{\phi/2\,\ell}\cos\left(\frac{\sqrt{3}}{2}\phi\ell\right)\right]}$$

$$C_2 = -\frac{C(x)\,\ell}{\phi\left[e^{-\phi\ell} + 2\,e^{\phi/2\,\ell}\cos\left(\frac{\sqrt{3}}{2}\phi\ell\right)\right]}$$

$$C_3 = -\frac{\sqrt{3}\,C(x)\,\ell}{\phi\left[e^{-\phi\ell} + 2\,e^{\phi/2\,\ell}\cos\left(\frac{\sqrt{3}}{2}\phi\ell\right)\right]}$$

Then

$$u = C(x)\left\{\frac{X^2}{2} + \frac{\ell}{\phi\left[e^{-\phi\ell} + 2\,e^{\phi/2\,\ell}\cos\left(\frac{\sqrt{3}}{2}\phi\ell\right)\right]}\left[e^{-\phi x} - e^{\frac{\phi}{2}x}\left(\cos\left(\frac{\sqrt{3}}{2}\phi x\right) + \sqrt{3}\sin\left(\frac{\sqrt{3}}{2}\phi x\right)\right)\right]\right\}$$

For the conditions of the thermal bending test

ℓ = 96 inches

mg = 1/4 oz per foot = 1/768 lbs/inch

EI $\approx$ 2000 lb-in^2

ϕ = .008667 in^{-1}

Δ = u when X = ℓ

Δ = C(x) (4608 - 86) = 4522 C(x)

Of this total deflection 4608 C(x) is due to the curvature due to the thermal loading and 86C(x) is the effect of the weight of the rod under a one g gravity field.

Thus the deflections measured are 98% of the expected deflection in a zero g field and the correction for the effect of gravity is negligible.

2.1.9 BOOM DYNAMICS STUDIES

Progress has been made in the development of a stiffness representation of the gravity gradient and damper rods for use in dynamic analysis. Since the rod has an open seam along its length, it is incapable of supporting shear and the stiffness may be seriously reduced from that expected from beam theory for some loadings. Development of an analysis of the rod stiffness from shell theory has been undertaken. This analysis is shown in Appendix E.

Programming for a digital computer to perform a numerical evaluation of the results is presently under way.

2.1.9.1 Dynamic Response Due to Relief of Thermal Gradients When Passing Into Eclipse

The dynamic effect of relief of thermal bending when the vehicle passes into eclipse may become significant for both boom design and for vehicle behavior if the time rate of relief of bending tunes poorly with relation to boom natural frequencies.

If the thermal gradient at each lengthwise station of the rod can be expressed as a linear function of time, i.e.,

$$\text{gradient} = C_1 f(t)$$

the deflections due to temperature can also be expressed as a function of time

$$u_T = C f(x) f(t) \qquad (1)$$

where

- u_T is any deflection parameter such as displacement, or rotation.
- C is a constant relating the temperature gradient to deflection
- $f(x)$ is the function which relates the deflection to the position of the rod, i.e., for a circular arc the deflection is $C x^2/2$ and the rotation is CX.
- $f(t)$ is the temperature function of time.

Now the force in the system is a product of the stiffness and the difference between the absolute value of the coordinate and its steady state temperature equilibrium value at the coordinate. This force is balanced by the inertia and damping of the system since there are no externally applied forces

$$K(u_a - u_T) + M\ddot{u}_a = 0$$

or

$$M\ddot{u}_a + K u_a = K u_T$$

$$= K C f(x) f(t) \qquad (2)$$

where

- M is the mass matrix
- K is the stiffness matrix
- $\ddot{u}_a$ and u_a are the absolute acceleration and displacement vectors
- f(x) is the vector defining the displacements as in equation (1).

This equation can be solved for the response due to the change in thermal gradient, passing in or out of eclipse, by methods similar to those used for response to orbit eccentricity pulse beginning on page 2-84 of the First Quarterly Report. The solution is straightforward and will be performed when the time function of the temperature gradient is defined.

2.1.10 TESTING

General Electric test requirements for the Hugh Aircraft system thermal and vibration test for the ATS program are given in the following paragraphs.

2.1.10.1 Thermal Test Requirements

In the first quarter of 1965 HAC is planning a System Thermal Test in which approximately 150 separate thermocouples will be installed throughout the spacecraft. The following requirements apply to the components to be used for the HAC system thermal test.

All hardware to be supplied for the T-2 thermal tests must simulate the flight equipment in both external geometry and mode of mechanical/thermal attachment. In addition, external surface treatment and internal power dissipation must be simulated where applicable. In general, the simulation of heat capacity is also required since transient as well as steady state test operation is anticipated.

The individual heat dissipators should be sized for twice the expected power at 30 volts dc. The recommended type of heating element to be used for the simulation of package internal power is: Dale Resistor type RH-Mil-R-18546C available from Newark Electronics Corporation, Catalog No. 75, 1964.

General Electric will be responsible for the installation of all thermocouples on the gravity gradient components. These installations must meet the following requirements:

1. Thermocouples shall be AWG No. 30 Copper-Constantan
2. External lead length shall be approximately five feet.

Thermocouples, installed in the following locations, will be needed for the HAC System Thermal Test.

Combination Passive Damper — 1 Thermocouple

a. Thermocouple on flat exposed surface of damper.

TV Cameras — 5 Thermocouples

Camera 1

1. Thermocouple on lens
2. Thermocouple on vidicon face plate
3. Thermocouple on external surface of electronics housing
4. Thermocouple on camera housing

Camera 2

Thermocouple on vidicon face plate

Solar Aspect Sensor — 6 Thermocouples

1. Thermocouple on each detector surface that is exposed (5).
2. Thermocouple on electronics package

IR Earth Sensor — 4 Thermocouples

Sensor 1

1. Thermocouple on filter
2. Thermocouple on lens
3. Thermocouple on cavity wall

Sensor 2

Thermocouple on lens

Power Control Unit — 1 Thermocouple

Thermocouple on external surface of housing.

Damper Boom — 3 Thermocouples

1. Thermocouple installed on external surface of tip mass of the boom mechanisms (2).
2. Thermocouple installed on erection unit.

Primary Boom — 2 Thermocouples

Thermocouple installed on external surface of each housing (2).

2.1.10.2 Vibration Test Requirements

Mechanical components of the Gravity Gradient subsystem will be delivered to HAC in the second quarter of 1965. The following requirements apply to these components:

Each component will approximate the flight hardware in mass, c.g., dimensional envelope, and material.

No functional tests are required for these components.

HAC will be responsible for the installation, calibration, sensitivity checks, and recording instrumentation of all vibration monitors.

A total of 75 accelerometers and four strain gages are required for instrumenting the Gravity Gradient components in the following locations;

Damper/HAC Structure — 6 Accelerometers

1. 1 triaxial accelerometer at the bottom of Damper close to attachment point.
2. 1 triaxial accelerometer at the upper end of Damper close to attachment point. (Opposite side to bottom triaxial accelerometer)

Damper/Damper Boom — 9 Accelerometers, 4 Strain Gages

1. 1 triaxial accelerometer at GE/DeHavilland interface.
2. 1 triaxial accelerometer on Damper boom center structure.
3. 1 triaxial accelerometer on one of the tip masses.
4. 4 strain gages on the bottom cover in the vicinity of the uncage pins.

Primary Boom Housing/HAC Structure — 12 Accelerometers

2 triaxial accelerometers near two opposite attachment points of boom housing to HAC structure. 2 Components

One triaxial accelerometer should be installed near attachment of each of the following components. (Exact location later)

TV Camera/HAC Structure — 6 Accelerometers

2 Components

TV Electronics/HAC Structure — 6 Accelerometers

2 Components

SAS Detector/HAC Structure — 15 Accelerometers

5 Components

SAS Electronics/HAC Structure — 3 Accelerometers

1 Component

IR Earth Sensor/HAC Structure — 6 Accelerometers

2 Components

Power Control Unit/HAC Structure — 3 Accelerometers

1 Component

2.1.10.2.1 Data Requirements

1. All GE data channels should be grouped so efficient data transmission can be made at the conclusion of the test.
2. The original tape or a copy is requested of all GE channel information including a record of the system input occurring at that time.
3. In order that analysis can be performed at GE the data should be on one-inch tape and be compatible with GE Tape System.

2.2 BOOM SUBSYSTEM

The boom subsystem of the ATS Spacecraft consists of the four primary gravity-gradient booms, the mechanism required for extending and scissoring the primary booms, and the two damper booms including the canister for storage and ejection of the damper booms.

The basic requirements for the boom subsystem are as follows:

1. Provide a set of four erectable booms which can be stowed within the confines of the ATS Spacecraft during launch and be deployed at separation to form an "X" configuration about the spacecraft. Weights are installed at the boom tips to achieve a prescribed set of inertias about the three principal axes of the spacecraft.
2. Provide a means of retracting these rods on command to desired lengths.
3. Provide a means of changing the angles included between the booms in a manner that maintains a symmetrical configuration about the satellite yaw axis. This action, which is limited to a total of 20 degrees on each boom, is generally referred to as scissoring.
4. Provide a set of two damper borne booms which will each extend to a length of 45 feet along the same straight line in opposite directions. These booms are to carry tip masses to their ends which will provide the proper interia for the operation of the damper. After initial deployment, no mechanical connection or wiring is to extend from the damper boom platform to the spacecraft body. The damper booms are not required to retract.
5. Accomplish the above within the tolerance/disturbance constraints of the gravity-gradient stabilization system performance requirements.

The basic extendible boom selected for this mission is the Storable Tubular Extendible Member (STEM) developed by the deHavilland Aircraft of Canada, Limited. This technique involves the formation of a tubular section from a flat metal strip which is formed and heat-tested in the tubular form then flattened under stress and wound onto a storage drum. Subsequent erection in orbit is accomplished by paying out the stowed strip through a set of guides which allow the boom to form into its natural tubular shape. The edges of the metal strip overlap each other to render stiffness to the operating section.

Storage/erection units for the STEM tubing are of both motorized and self-erecting type. The motorized type employs a motor to drive the storage drum and thereby provide a means of retracting the extended booms. The self-erecting type units use the strain energy in the stowed metal strip to rotate the storage drum and erect the boom.

Motorized units were selected for the primary booms due to the requirement to retract. Self-erecting units were selected for the secondary (damper) booms.

Initial considerations for the scissoring mechanism included several which provided mechanical coordination of the motion of all four primary booms. Design studies included versions using bull gears, pulley systems, bellcrank linkages, and jackscrews. However, the constraints imposed by spacecraft size and other equipment in the boom mounting area proved the mechanical connection of all booms to be impractical. An evaluation of the coordination required between booms for both extension and scissoring showed that a system which depended on electrical synchronization was not impractical. Accordingly, the following system was devised:

1. The four boom units are divided into two pairs.
2. The two units making-up each pair are mounted as close as possible to one another and are coupled by a bell-crank linkage to transmit scissoring motion and a gear train to coordinate extension drum drive.
3. Each pair of units is provided with one motor for extension and one motor for scissoring. The motors are encased in a hermetically sealed container to preserve their useful life in space, torque being delivered through a flexible membrain.
4. The two units of each pair, their drive train, motor, and scissoring linkage are all mounted with a single framework. Extension units are provoted to this framework.
5. Motion between the two pairs of units is coordinated electrically.

The technical aspects of the Boom Subsystems are fully described in paragraph 2.2 of the "First Quarterly Report," Document No. 64SD4361, published by GE

on October 16, 1964. General Electric Specification SVS 7316 delineates the requirements for the Boom Subsystem.

2.2.1 150-FOOT ROD CONSIDERATIONS

One of the initial requirements for the primary booms was that the rods for MAGGE and SAGGE be 100 feet long. The different inertial levels for the medium and synchronous vehicles were achieved by different weighted tip masses; the heaver tip mass would be used on the SAGGE. The use of 150-foot rods was investigated to establish the weight saving that could be effected by the longer rods for the same inertial levels as the shorter rods. Better than 70 percent saving is possible in the weight of the tip masses when the longer rods are used. A comparison of the tip mass weights is shown in Table 2.2-1 for the 100-foot and 150-foot rods for MAGGE and SAGGE.

TABLE 2.2-1. TIP MASS WEIGHT PER ROD

Rod Length	Tip Mass Weight (Approx. pounds)	
(feet)	MAGGE	SAGGE
100	2.5	10
150	.56	2.25

The 150-foot rod would weight 0.75 pounds more than the 100-foot rod due to the additional weight.

The investigation also included a consideration of results when the tip mass weight was held to the original requirement (2.5 and 10 pounds respectively) while increasing the rod lengths to 150 feet. This ratio of rod length to tip mass weight would increase the inertia levels by a factor of 2-1/4 relative to the 100-foot rods, and would have the added advantage of increasing the gravity gradient torques.

Disadvantages include added cost for the maintenance of straightness tolerance and more sophisticated test equipment required during manufacture of the longer rods. One-third more silver plating would be required to coat the longer rods, and a

greater rate of material would be scrapped during manufacture to keep the longer rods within specified straightness tolerances.

2.2.2 LUBRICATION REQUIREMENTS

Lubrication is required in the boom mechanism to protect the equipment from the phenomenon of cold welding when exposed to spacial vacuum. Lubrication techniques was the subject of a joint meeting with NASA, deHavilland and General Electric during the reporting period. Three types of lubricants were proposed for consideration; these include liquid lubrication, the use of self-lubricating materials, and dry film lubricants.

2.2.2.1 Liquid Lubrication

The hermetically sealed drive system (a deHavilland bellows drive unit) will be filled with argon or helium at 5 psia. The drive motor utilizes carbon brushes which require some absorbed water or organic vapor for effective operation. The absence of such vapor results in increased contact noise and rapid brush wear. deHavilland has proposed adding water vapor to the sealing medium. Perhaps some organic vapor will be provided by the bearing lubricant or motor winding insulation materials.

The erection and scissoring mechanism is, by necessity, open to the space environment. The aperture size will be such that a labyrinth, molecular type seal is effected. Preliminary calculations based on F-50 fluid vapor pressure and molecular weight, the mean free path of the fluid molecules in the vapor phase, and a sticking coefficient of 1, and piece part geometry have indicated a total leak rate of 2.235×10^{-2} gm/year. Lubricant replenishment would be provided by a lubricant reservoir leaking through a Veeco molecular seive. Bearings would be of the standard precision type lubricated by F-50 oil or G-300 grease. All outboard shaft bearings would be shielded to limit lubricant loss by creepage and evaporation. Teflon or other forms of anti-wetting agents will not be used since Teflon would reduce the sticking coefficient of the molecules striking the labyrinth seal; therefore the evaporation rate would increase and may become excessive.

2.2.2.2 Self-Lubricating Materials

Self-lubricating materials (Teflon, MoS_2 or Teflon filled plastic material) are prime material candidates for journal bushings and gears. The main disadvantages of such materials are lack of dimensional stability, lack of radiation resistance, and low thermal conductivity for heat rejection. Main emphasis will be placed on a filled polycarbonate material which consists of polycarbonate, 40% glass and 12% Teflon filled. The material is injection molded and exhibits good dimensional stability. Mating gear material will be of the same material (filled polycarbonate) or hard anodized (dense aluminum oxide coated aluminum).

2.2.2.3 Dry Film Lubricants

deHavilland had proposed the use of tungsten disulphide as the major constituent of any dry film lubrication system. In this proposed system the coating will be the Teleflex material, a Teflon and tungsten disulphide material using a low fired ceramic binder.

Fischer Bearing Company, manufacturer of precision instrument bearings, has indicated a willingness to develop a soft metal plating consisting of Teflon and tin to be applied to standard bearings.

2.2.2.4 Other Approaches

2.2.2.4.1 Soft Metal Plating

Soft metal platings, such as gold and silver, have been used with some degree of success as lubricants for bearings. The relatively high coefficient of friction of such materials and the difficulty in obtaining a reliable plated bearing assembly have virtually eliminated soft metal platings as lubricant materials.

2.2.2.4.2 Cemented Carbides

Cemented carbides display many favorable attributes with respect to bearing applications. One of the drawbacks on these materials is the relatively high friction

occurring when sliding is in the boundary friction region. Various researchers have investigated the possibilities of incorporating a solid film lubricant into the surface of the cemented carbides. Major emphasis has been placed on high temperature applications.

2.2.2.5 Recommended Lubricants

As a result of meetings with the subcontractor and study, a design philosophy was established revelant to the use of lubricants with recommendations for the optimum lubricant for use in the boom subsystem mechanism. The two guidelines used in the selection are:

1. Lubrication of the open unit by liquid lubricants is prevented by the possibility of forming polymerized films on the booms, thereby drastically changing its thermal radiative properties.
2. Slow speed and/or intermittent operation bearing applications generally require some dry film or boundary lubricant to be applied to all surfaces in relative contact. Therefore, the bearing races and balls should be coated with MoS_2, either as a burnished film or bonded as in the Molykote X-15 coating. Bearing elements should be finished by precision grinding techniques (4 to 6 microinch surface finish) followed by a thorough cleaning before the dry film lubricants are applied.

Materials chosen as promising lubricant selection are summarized in Table 2.2-2.

The recommendations made in the GE investigation include lubricants for sealed units and open units. These are:

1. Sealed Unit
   a. Erection Motor Bearings - 440C CRS, lubricated by F-50 or MIL-L-6085 diester fluid.
2. Open Unit
   a. Bearings - 440C, Duroid 5813 separator, dry film lubricated by Alpha Molykote X-15
   b. Gears - Teflon and glass filled polycarbonates idler gears.
   c. Tape Guide - Teflon coated fiberglass laminate or electroformed material.

TABLE 2.2-2. PROMISING LUBRICANT SELECTION

Application	Basic Material	Lubrication	
		Liquid	Dry Film
Sealed Unit Bearings		F-50, MIL-L-6085 Depending on Design Requirements	
Races	440 C (Corrosion Resistant Stainless Steel-CRS)		
Separator	Duroid 5813		
Balls	440C (CRS)		
Open Unit Bearing			
Races	440C (CRS), Cobalt alloy Star J or Haynes 6B[1]		Alpha Moly Kote X-15[2]
Separator	Duroid 5813[3]		
Balls	440 (CRS) Cobalt alloy Star J or Haynes 6B		
Gears	Polycarbonates, Epoxy Teflon, Polymides		Idler gears of the self-lubricating mtl driver of 2024 aluminum
Spring			Burnished film of MoS_2
Tape Guide	1. Fiberglass Laminated 2. Electroformal Material		Teflon coatings (fused or epoxy bonded)

1. Due to the short delivery time of engineering hardware, bearing races made of Star J or 6B Cobalt alloys may be unobtainable therefore 440C races should be used. If the cobalt alloys are obtainable they should be heat treated at 800-850°F for 48 hours to stabilize the hexagonal structure necessary to prevent mass material transfer during boundary friction operation.
2. Alpha Molykote X-15 is a MoS_2 dry film which uses a sodium silicate binder.
3. Duroid 5813 - The material is an extruded composite consisting of Teflon filled with 15% glass and 10% MoS_2.

These recommendations were presented at the latest design review held at deHavilland late in November. They will form the basis for the lubrication techniques for the ATS boom system mechanics.

2.2.3 MOTOR SELECTION

The boom system employs four DC motors per satellite, two for primary boom extension and retraction and two for primary boom scissoring.

The types of DC motors considered for this application were:

1. Permanent magnet type.
2. Split series wound type.
3. Shunt wound type.

The shunt wound motor was selected for this application because the shunt wound motor offers a much finer speed control over the range of possible variations in applied voltage and ambient temperature. Figures 2.2-1 and 2.2-2 show a comparison of speed variations between shunt wound and series wound motors of the size and type suitable for this application. Curves are presented for speed versus torque over the full ranges of temperature and applied torque anticipated. The cross-hatched areas delineate the range of required torques. Examination of the curves in the expected loading areas readily shows that the shunt wound motor speed will vary much less with variations in loading, temperature, and voltages. It is necessary to limit the variations in motor speed in order to preclude deleterious effects on boom structural integrity and capture performances.

The use of shunt wound motors requires a slightly more complex power switching system than does the split series motor, but this is offset by the attendant advantages in speed control.

The use of the permanent magnet type is precluded by the residual magnetic dipole remaining after power is removed.

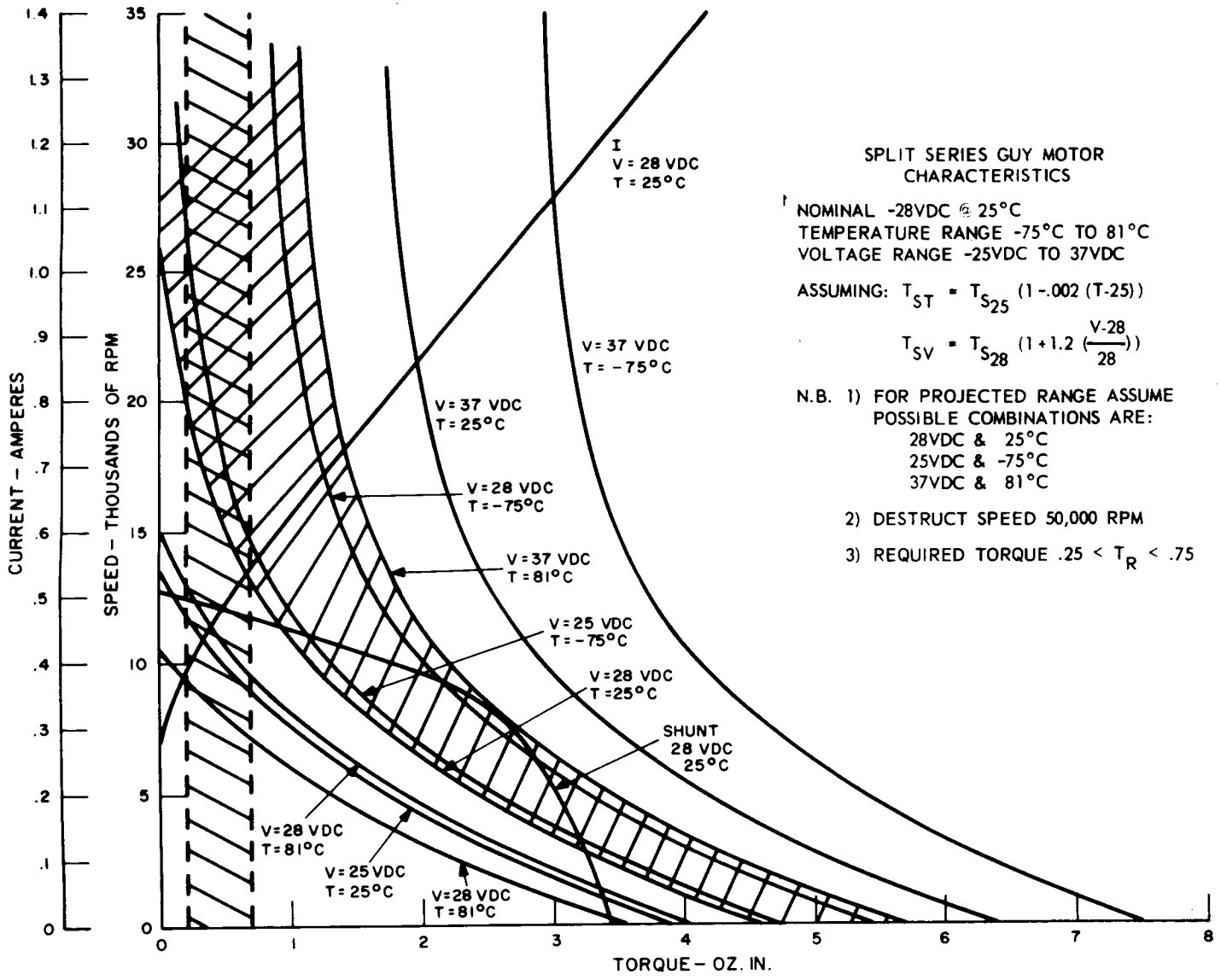


Figure 2.2-1. Split Series GJY Motor Characteristics

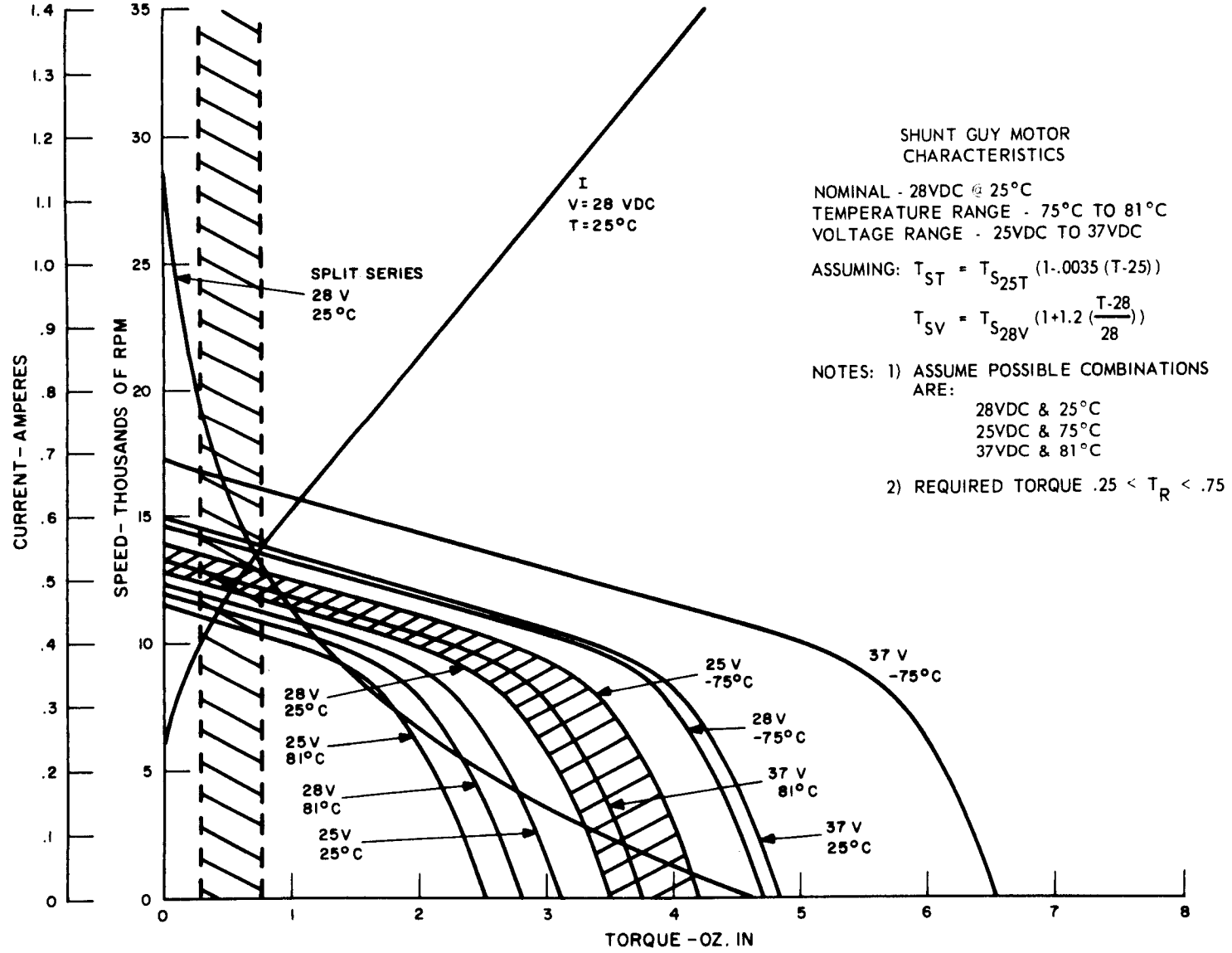


Figure 2.2-2. Shunt GJ

2.2.4 POTENTIOMETER BOOM LENGTH INDICATOR

The original design concept employed a magnetic reed switch to monitor primary boom erection. This system, although simple in sensor concept, easy to calibrate, and not susceptible to boom erection jeopardization, had the disadvantage of requiring a counter circuit in the telemetry set to measure boom length. In the event of power interruption, the count would be lost. In order to have up-to-date boom length information readily available at the ground station at all times, it would be necessary to design a memory circuit into the telemetry set. The complexity that this requirement introduced into the telemetry set was not considered offset by the advantages associated with the reed switch. Accordingly, a rotary potentiometer was included in the extension drive transmission box to monitor boom length in orbit. Calibration of this potentiometer on the ground will use the output of the reed switches mounted directly on the erection units, but the reed switches will not be used for in-orbit telemetry.

2.2.5 100-FOOT STOP

When using a 150-ft primary boom, it becomes necessary to provide a "positive" extension stop at 100 feet to insure the capability of accurately evaluating the performance of 100-ft booms during orbit tests. The use of a micro-switch stop (as is used at the fully extended length) is precluded since this would require slots in the boom material which might adversely affect strength. Accordingly, it was decided that a threshold detector would be included in the PCU. The detector would sense the output of the extension potentiometer and would be preset to trigger at 100 feet during initial boom extension and thereby cutoff motor power. All other boom length adjustments would be accomplished by proportional command.

2.2.6 MICROSWITCH FUNCTIONS

Table 2.2-3 lists the microswitches used in the boom system and their functions.

TABLE 2.2-3. MICROSWITCH FUNCTIONS

Function	Type	No. Req'd./Sys.
Full Retraction Power Limit for Ground Test	S.P.S.T. (Removable)	4
Full Extension Power Limit	D.P.3.T.	4 (Note: The 2 switches for each 1/2 system will be wired in series.)
Full Extension Telemetry Monitor	S.P.D.T.	4 Independent
Clutch Solenoid Power Limit	S.P.S.T.	4
Clutch Solenoid Telemetry Monitor	S.P.D.T.	8
Scissors Power Limit	S.P.S.T.	4

2.2.7 BOOM ELECTRICAL ISOLATION

During this reporting period, GE was requested to provide DC electrical isolation of the primary booms from the spacecraft and to reduce the capacitance between the boom and the spacecraft to a minimum.

The resistance between each primary boom and the spacecraft structure is to be a minimum of 10^8 ohms when measured at laboratory ambient conditions. The design goal for capacitance between the boom assemblies and the spacecraft is to be 50 picofarads with a maximum allowable capacitance of 200 picofarads.

The design is proceeding toward accomplishing these electrical isolation requirements. It appears that the resistance requirement will be readily realized, but realization of the capacitance requirement will be marginal.

2.2.8 TIP TARGET CONFIGURATION

A change in the tip target configuration from an articulated 6-inch diameter disc to a 9-inch diameter disc fixed at a 50^o angle to each primary boom is currently

under consideration. This configuration would simplify the tip target design in that the targets could be stowed tangent to the spacecraft solar array during launch without the use of an articulated joint. This design is being evaluated for T/V camera visability.

2.2.9 CLUTCH DESIGN

Prior to the design review meeting held at the subcontractor's facility in late November, the clutch design embodied two solenoids which drove the clutch to each of the two required clutch positions. A bistable spring held the clutch in the desired position when solenoid power was removed. Concern was expressed over the reliability of the spring and the amount of power required by the solenoids (current drain was 10 amps for 30 milliseconds).

Accordingly, the following design change is being considered. Both solenoids and the bistable spring would be replaced by a single rotary solenoid which would be stable in either position. The new rotary solenoid would draw 2.54 amps at the nominal 28 VDC supplied by the power supply and would draw 3.36 amps at the maximum expected voltage of 37 VDC.

2.2.10 DAMPER BOOM RELEASE MONITOR

In order to provide a telemetry event monitor of damper boom release, a design improvement is being undertaken to add two microswitches to the upper damper surface. These microswitches would be triggered by motion of the tip assemblies of the damper booms as they move away from the CPD. These switches would be mounted so that they would not interfere with the motion of the damper booms after deployment. This design would require no wiring between the damper booms and the CPD.

2.3 COMBINATION PASSIVE DAMPER

2.3.1 INTRODUCTION

Two dampers, one a hysteresis damper and the other an eddy-current damper, are combined with a clutching mechanism into a single package referred to as the Combination Passive Damper (CPD). These dampers (coupled to a damping boom) are alternately operated during the Applications Technology Satellite (ATS) mission to damp the vibrations of those vehicles that utilize gravity gradient stabilization techniques. In addition to providing damping torques, the CPD also must meet a requirement to restore the damper boom to a "null" position with respect to the satellite. This restoring torque is provided by a magnetic torsional restraint device incorporated in the eddy current damper system, and by the torsion wire suspension (tendency to "untwist") in the hysteresis damper system.

2.3.1.1 Basic CPD Functional Description

Basic functions currently incorporated in the CPD design and the associated hardware to perform these functions are listed below:

Function	Associated Component(s)
Damping	Hysteresis disc and magnets Eddy Current Disc and Magnets
Torsional Restraint	Torsion Wire (Hysteresis Damper) Magnetic T.R. (EC Damper)
Suspension	Torsion Wire (Hysteresis Damper) Diamagnetic Cones and Magnets (EC Damper)
Clutching Mechanism	Solenoid actuator and Diaphragm Clutch
Boom Angle Indicator	Optical Device
Mode Indicator	Microswitches
Caging for Launch	Pyrotechnic Devices

Function	Associated Component(s)
Stops at ± 45° rotation extremes	Spring stop
Minimum Dipole	"Bucking" magnets properly oriented

2.3.1.2 Chronological Summary of Major Events During Reporting Period

A chronological summary of events is presented below to review the perturbations that occurred in the CPD effort during the reporting period. Several of these events resulted in a major re-direction of the CPD design effort.

15 Oct. 1964 — Presentation of CPD design concept (2 lever) to NASA representative at GE. As a result of this meeting an all-out effort was made to simplify the design by deleting the boom/damper alignment feature and working on the assumption that clutching could occur only at the boom null position.

15-30 Oct. 1964 — Intensive redesign activity investigating various methods of clutching at null only, plus overall simplification of the entire concept. Reviewed resulting designs with NASA on 30 October at GE but no single concept was satisfactory.

6 Nov. 1964 — Presented working model of 2-lever concept of the CPD at a meeting at NASA Goddard. Model demonstrated smooth operation and stability of 2-lever concept; however, it still was considered too complex.

13 Nov. 1964 — Presented the "Diaphragm Clutch" concept at NASA meeting. This concept contained only one moving part plus the actuator, and agreement to proceed with this design concept was reached.

17 Nov. 1964 — The CPD to Spacecraft mounting arrangement concept was agreed upon during the NASA/Hughes/GE Interface Meeting at GE.

2 Dec. 1964 — GE was requested by NASA to obtain a proposal from Space Technology Labs (STL) for the development and delivery of the Hysteresis Damper portion of the CPD. GE would continue to be responsible for the entire CPD package including the eddy-current damper.

9 Dec. 1964 — STL personnel visited GE to receive the RFQ (including GE Specification SVS 7331 and associated Work Statement) on which to base their proposal for the Hysteresis Damper.

30 Dec. 1964 — GE Specification SVS 7315 for the CPD Boom Angle Indicator was issued.

30 Dec. 1964 — STL completed their Hysteresis Damper Proposal and forwarded it to GE on this date.

2.3.2 DESIGN EFFORT

2.3.2.1 General

During this report period, there has been a continuing design effort in the form of conceptual layouts and development engineering activities (discussed below) to meet the general requirements specified for the CPD.

At the end of the last quarterly report period, the volume in the spacecraft available for the CPD package had been reduced and in that report, a preliminary layout was presented and discussed that would fit in the designated envelope and which provided all of the required functions. A "rough" working model of the essential elements of the design was built which demonstrated that the concept of switchover and damper centering, as shown in SK56130-808-12 (included in the last quarterly progress report), was feasible. A picture of this model is shown in Figure 2.3-1. On 6 Nov. 1964, the model and layout were shown to and discussed with NASA representatives. The relatively large number of parts, including several friction type rotating joints, raised a question as to the reliability of the design. The requirement to include a device which aligned the damper index or null point with boom null position at the time of clutching or switchover was the dominant cause of the relatively large number of parts.

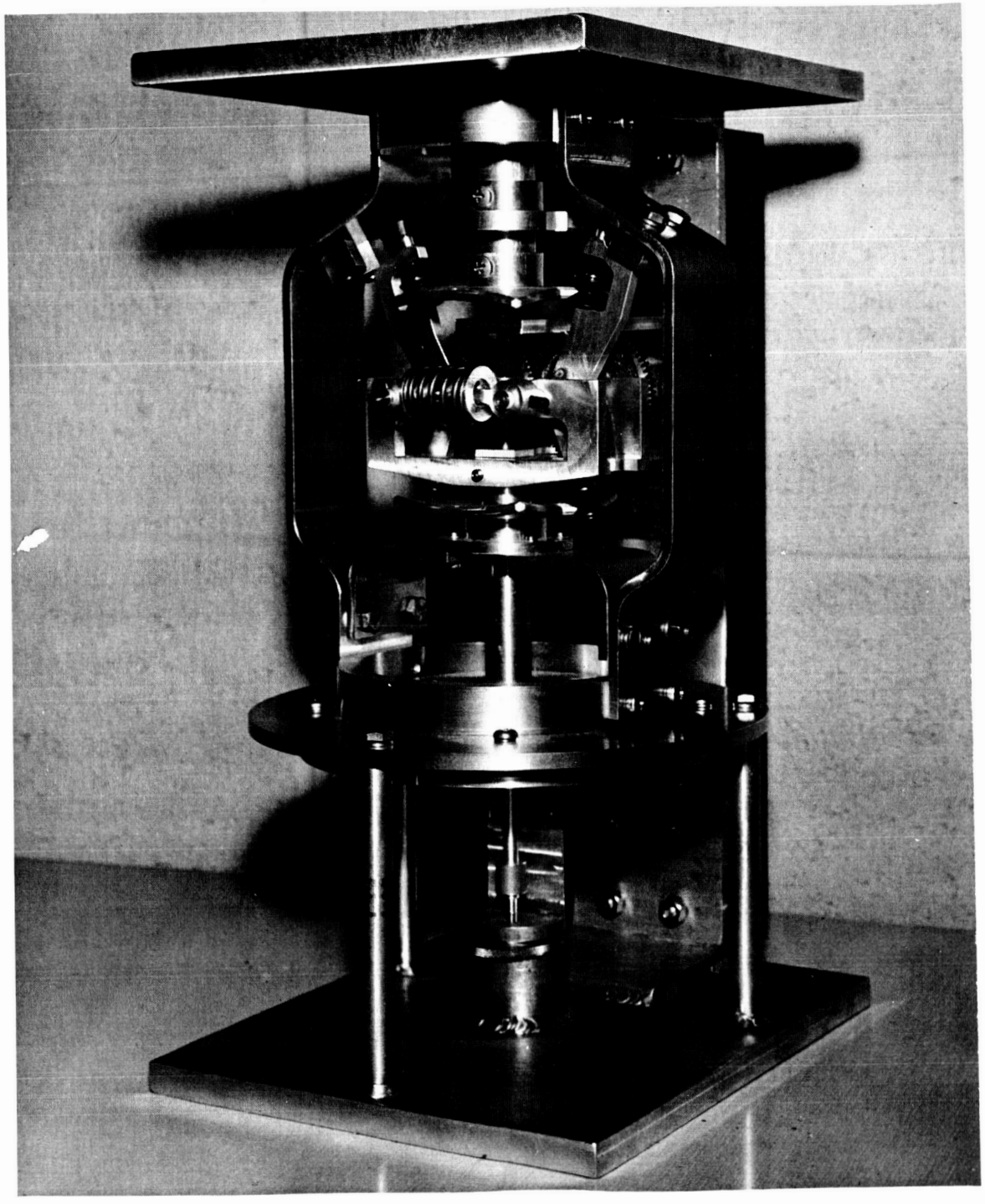


Figure 2.3-1. "Rough" Working Model

Because of the complexity of the design, it was agreed that a design which would not include the aforementioned alignment feature would be used. GE then conceived and laid-out a CPD design, utilizing a so-called "Diaphragm Clutch" switchover mechanism, which had no aligning capability. This design was less complex than previous designs, not only because of the single moving part (plus the actuator member), but also because with this concept, it was possible to use a two-way solenoid in place of a rotary motor as the actuation device. The reliability of the rotary motor actuation had been questioned because it utilized several rotating bearings and a sliding member. The problems engendered by direct current electrical motors were also a major concern with the motor actuator. While in concept the diaphragm clutch, similar to a pleated Belleville washer, is virtually the ultimate in simplicity, in practice it has proved to be very difficult to analyze and predict its performance with any accuracy. Therefore, considerable time was spent in contacting various vendors to determine what experience they might have had in similar diaphragm applications. However, it was learned that none of the vendors had any assistance to offer nor could they recommend any method for analyzing the performance of this type of diaphragm.

While efforts were under way to obtain either test data or vendor information on these diaphragms, GE was verbally requested by NASA (on 2 Dec. 1964) to investigate the practicality of incorporating a separable passive hysteresis damper (PHD), such as might be developed by Space Technology Laboratories (STL), into the CPD package in place of the hysteresis damper developed by GE. In response to this request by the customer, a specification was prepared, preliminary engineering discussions were held and STL has completed a proposal to GE to supply such a self-contained damper package. Inclusion of a separable damper package caused a marked change in the design philosophy of the CPD package. With an integrated, GE designed damper, the components of the hysteresis damper were incorporated into the CPD package structure. With the separable concept, more space was required within the CPD package to accept a vendor-furnished PHD. Distinct, and space consuming mounting

and output interfaces were also required both on the damper and in the CPD package, resulting in less efficient weight and space utilization.

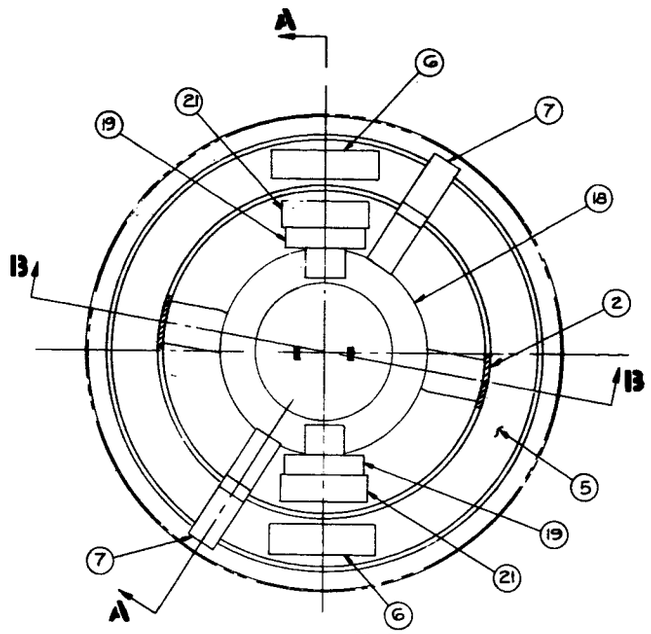
The conceptual layout shown in Figure 2.3-2 shows the CPD configuration with the GE-designed hysteresis damper. Also shown on this drawing are the required modifications to the package to accept the proposed STL hysteresis damper. This layout includes the diaphragm clutch and a solenoid-actuation adapter.

While the foregoing general design effort discussions have been chiefly concerned with the activity associated with the overall package design, a considerable amount of engineering development effort has been applied to the hysteresis damper, the magnetic suspension, magentic torsional restraint and eddy current damping. These activities are discussed in some detail in the following sections.

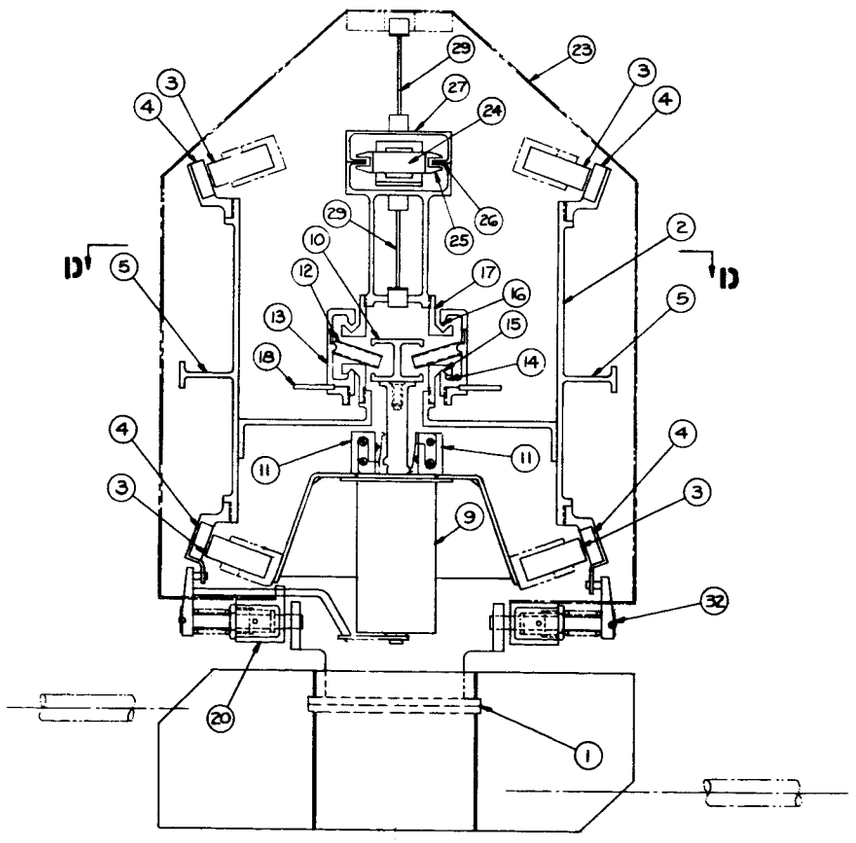
2.3.2.2 Damper Configuration Currently Proposed

The current concept of the damper package (as shown in Figure 2.3-2), is a cylinder approximately 9 inches in diameter by 12 inches long with the two corners on the end adjoining the spacecraft being tapered for clearance.

STL DAMPER AS

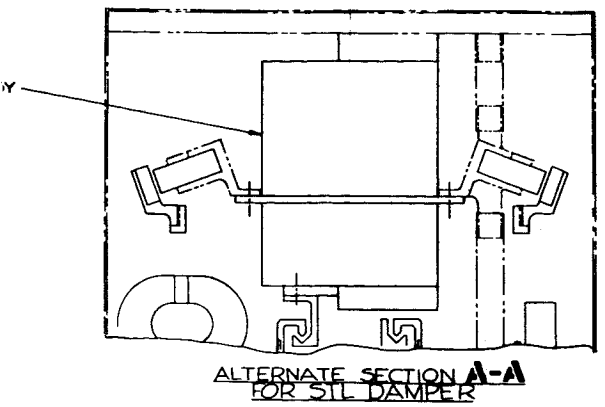


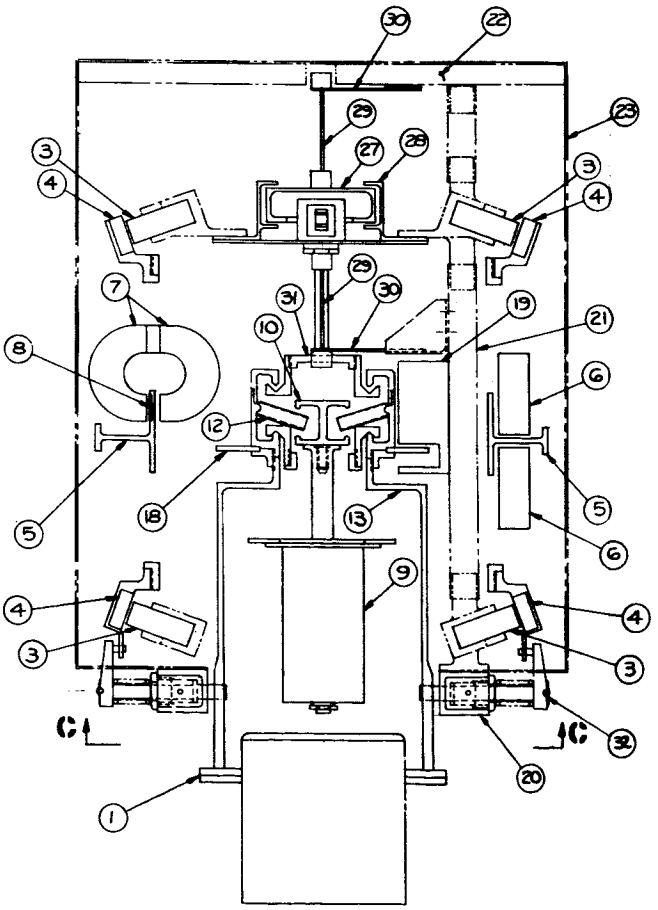
SECTION D-D



SECTION B-B

1190





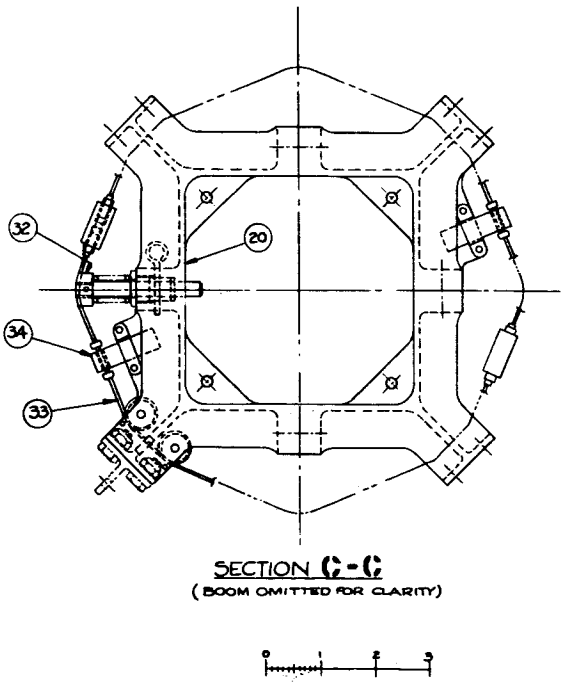


Figure 2.3-2. Damper Configuration

The damper is supported at two points at the spacecraft end and at four points at the outer or boom end. Struts from the spacecraft support the outer end with the mounting configuration to be determined in subsequent interface meetings. The DeHavilland damper boom assembly attaches to a suitable interface ①* located at the outer end and in operation rotates plus and minus 45° from a null position and about the axis of the CPD package.

During launch, the loads from the booms and the connected part in the damper package are carried through four caging pins into the end plate of the damper and to the strut connections. The pins are held in engagement by a cable as discussed in Section 2.3.3.5. Provisions will also be provided for individual manual caging of the eddy-current rotor during handling and during testing of the hysteresis damper. This feature is required since the diamagnetic suspension will not support the eddy-current damper in earth's gravitational field.

The eddy current damper structure② will be supported by 12 magnets③ located at each end of the package. Each set of suspension magnets will be mounted, poles facing out, in a flat cone of total included angle of about 140° apex. The magnets support the rotor by the diamagnetic repulsion of the pyrolytic graphite④ mounted on the rotor. The angular arrangement of the magnets is such that the largest force is supplied in the radial direction, which is the direction of greatest loads, while there is axial component resulting from the angle of the cone which produces sufficient axial force to support the imposed loads in that direction. There is a nominal clearance of 0.050 inch between the graphite and the magnet face. Stops will be provided to prevent the magnets and the pyrolytic graphite rings from contacting in the event that transient forces experienced are greater than the design operating loads. No physical damage will occur when such stops are engaged.

*The circled numbers throughout this section refer to the numbered callouts on Figure 2.3-2.

The structure (2) of the eddy current rotor connects the two pyrolytic graphite rings (4) with the damping ring (5).

The eddy-current damping is created by the magnetic flux of the two sets of two magnets (6) each causing electrical currents to flow in the aluminum ring. The interaction of the flux resulting from the current flow in the aluminum and the flux of the magnets produces the damping force and consequently the torque. The faces of the magnets are spaced approximately 0.050 inch away from the aluminum surface.

Torsional restraint for the eddy-current damper is provided by an arrangement of magnets (7) and a thin crescent of magnetic material (8) mounted on an extension of the eddy-current damper disc. The wider portion of the thin crescent is attracted by the magnets creating a torque. The principle utilized in this torsional restraint device was discussed in the report on the result of the first six weeks effort (Document No. 64SD4326). There are two sets of torsional restraint magnets arranged symmetrically about the centerline of the damper to produce balanced loads on the diamagnetic suspension.

The solenoid (9) is used to shift the damper boom between the eddy current and hysteresis dampers. It is fitted with a spool shaped part (10) at the end of its plunger. The plunger has a half-inch stroke and is provided with a magnetic or other detent to hold in either extreme of stroke with about 1 lb force, a capability of about 2 lb to overcome the detent, and 10 lb force at the point where the switchover is initiated. The solenoid is double acting to allow shifting in either direction. It is actuated by a timed pulse of current, but is equipped with limit switches (11) used to indicate which damper (eddy-current or hysteresis) is connected to the damper boom.

The spool of the solenoid engages the inside diameter of a coned diaphragm (12) which has two stable positions and is used as an over-center toggle joint. The outside diameter of the diaphragm is mounted in the structure (13) attached to the damper booms. In one operating position, the diaphragm is coned such that it forces a

circular vee clutch groove ⑮, connected to one damper, into a matching surface ⑭ in the boom structure. When the solenoid is operated it pushes the diaphragm flat and then overcenter so that it assumes a conical shape in the opposite direction. It then forces the opposite vee clutch plate ⑯, into the corresponding groove ⑰ on the boom structure. In the operating position the solenoid spool has a nominal clearance to the diaphragm of about 0.1 inch in any direction, and the inoperative clutch vee and groove has a nominal clearance of about 0.1 inch. Because of this clearance, the axial position of the damper booms is displaced a nominal 0.1 inch (relative to the spacecraft) in the eddy-current mode as compared to its position in the hysteresis mode. The vee shape of the engaging surfaces of the clutch plates insures that the mating parts will be properly aligned (axially and radially) after switchover occurs. The diaphragm is sized to give much larger engaging forces than are required during operation to facilitate alignment and testing in a gravity field.

The disk of the angle indicator ⑱, which is attached to the boom structure, is of glass of varying opaqueness, and is symmetrical about a diametral line such that two opposite sensors of the indicator ⑲ will yield a net electrical signal indicating the angle of rotation of the booms from the null position. One purpose for using two sensors is to minimize the effect of motion in the plane of the disk on the angle indication. The indicator sensor ⑲, in essence, consists of a light source which directs a beam through the glass disc ⑱ to a light-sensitive indicator. The electronic package needed for the sensors will be mounted in or on the damper package as determined by the size of the package.

In Figure 2.3-2, details relative to the incorporation of the STL damper into the CDP package are shown. The STL and GE damper would occupy the same general location at the inboard end of the package. In the GE hysteresis damper design the magnet ㉔ is stationary and connected to the stationary part of the structure. The bar magnet ㉔ is used with pole pieces ㉕ that fork over the damper disk ㉖ and are so arranged to allow clearance of about 0.050 inch. The disk ㉖ in which the hysteresis energy loss takes place, is mounted on the rotor ㉗ which rotates through an angle of $\pm$ 45^{o}

during operation. There are also axial and lateral stops (28) to prevent contact between magnet poles and the disc, or other excessively large motion. The rotor is mounted on torsion wires (29) which in turn are supported at their outboard ends by leaf springs (30) which are anchored to the structure. The spring is used to tension the torsion wire thereby producing axial and lateral support without any other contact with the rotor. The spring is sufficiently flexible to permit movement of the rotor within its stop limits without overstressing the torsion wire. The outboard end of the rotor has an extension (31) that connects to the vee ring clutch plate (17), used to connect the hysteresis damper to the booms. Adjustment will be built into the torsion wire attachments which will allow alignment between the damper, the clutch and the boom attachment structure. This adjustment will be carefully made to insure friction free operation under all specified loads in gravity free space.

If the hysteresis damper developed by STL is used, it will be positioned as shown in the layout designated as "Alternate Section A-A for STL Damper" on Figure 2.3-2. The STL package will be mounted in such a manner as to permit all adjustments necessary to align the rotor and stator of the damper to the CPD package.

Angular stops will be provided for both dampers and the boom structure allowing a range of rotation of $\pm$ 45^{o} from the null position. Simple cantilever springs will be used in conjunction with the boom structure to give torsional restraint in addition to the specified 21 dyne cm per degree for MAGGE and 5 dyne cm per degree for SAGGE. The added torsional restraint will be 1000 dyne cm per degree for MAGGE and 250 dyne cm per degree for SAGGE in the range of 40^{o} to 45^{o} for both directions of rotation. No contact will exist between the cantilever springs and the rotatable member of the damper in the range of $\pm$ 40^{o} rotation.

The main structure of the damper package will consist of the outer end plate (20), two diametrically opposite structural members (21) attached to the end plate running parallel to the damper axis, and a member (22) perpendicular to the axis running across the

ends of longitudinal members at the inner end of the package. They will carry all launch and operating loads and give the necessary stiffness without the help of the outer cover (23). The arrangement of these load carrying members will permit easy assembly of components and adjustment and testing after assembly. The outer cover will be primarily a dirt, light and handling damage shield.

Two limit switches (not shown) will be mounted on the end plate of the damper package contacting the end masses of the damper booms. When the booms extend, the switches will indicate this action.

The interface with the deHavilland Boom Package is at two flanges (1) in a common plane perpendicular to the damper axis with bolts in each flange to carry the loads.

2.3.2.3 Diaphragm Analysis

2.3.2.3.1 Background

As a result of studies which yielded a large number of concepts for the bi-stable clutch, it was decided to use an axial shift arrangement which utilizes an over-center toggle mechanism in the form of an annular Belleville washer or diaphragm (Figure 2.3-3). The toggle mechanism allows either of the two sets of clutch plates to be held in engagement without contact between the solenoid actuator and the diaphragm (which would interfere with proper damper performance) after the diaphragm is pushed over center. The diaphragm appears simpler than a more conventional spring and linkage toggle arrangement.

A number of spring manufacturers were contacted in an unsuccessful attempt to find an already developed diaphragm to meet the requirements. The desired size-deflection-force requirements are 2.4 inches O.D., 0.5 inch I.D., with a 0.3 inch working height and a force of approximately 8 lb at the working height.

A design analysis and experimental program was initiated to develop a diaphragm to meet these requirements. An approximate analysis for a number of different diaphragm concepts was made to determine their potential. Four designs were deemed worthy of experimental evaluation and/or further analysis. These designs are discussed in the following sections.

2.3.2.3.2 Corrugated Diaphragm (Figure 2.3-3)

This diaphragm is shown on the drawing, in blank and after forming. Its holding fixture is shown in the upper right-hand corner of the drawing. In the totally free condition this diaphragm or corrugated disk lies flat. When it is constricted circumferentially in the holding fixture it will cone-up in the center. The force required at the calculated point where toggling action occurs is about 9 lbs which will result in a maximum stress of about 100,000 psi. A sample diaphragm is being fabricated and will be tested for its force-deflection characteristics.

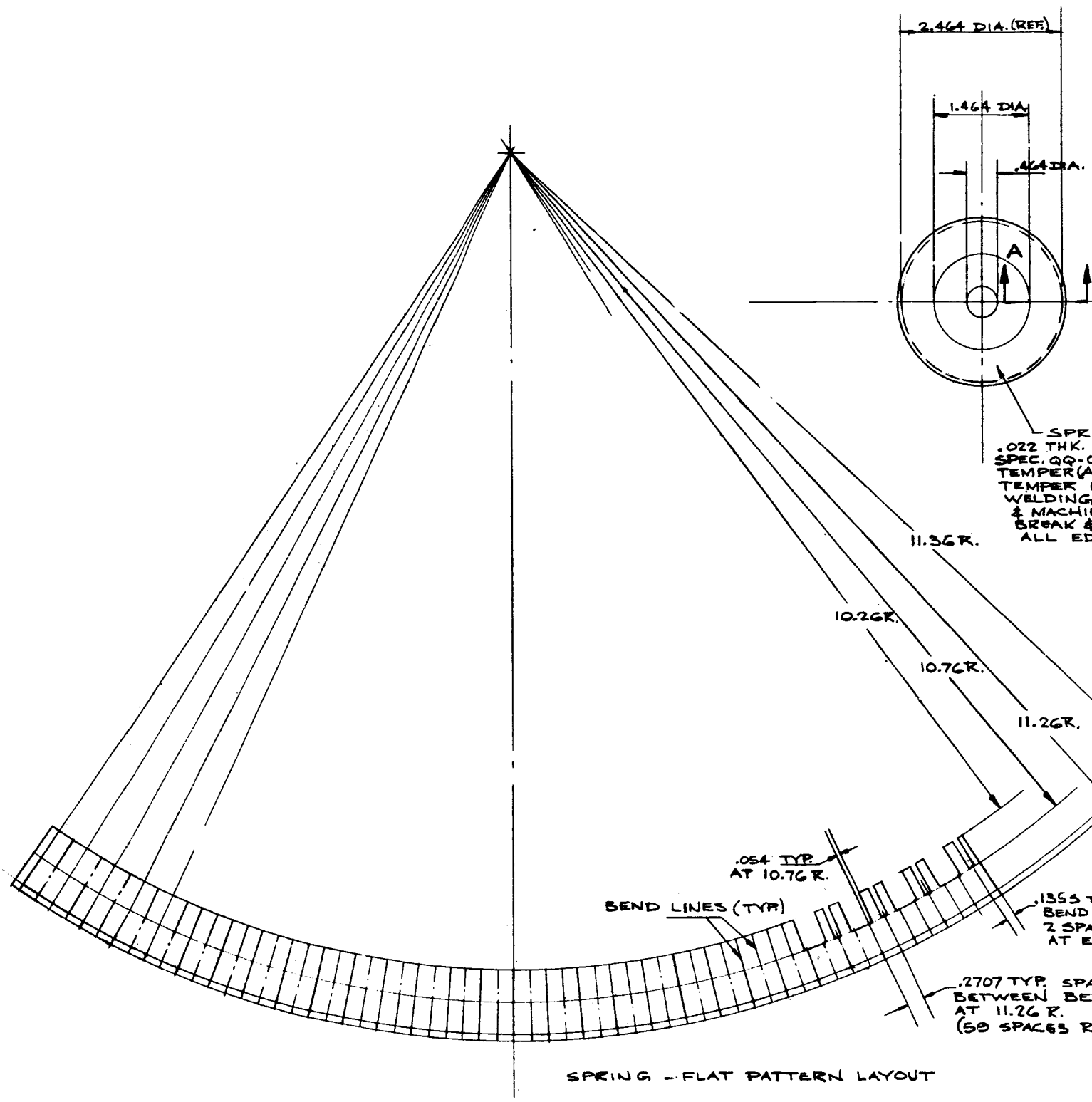
2.3.2.3.3 "Flip-Through" Diaphragm (Fluted)

General equations expressing the load deflection characteristics and maximum stresses were developed for the type washer shown in Figure 2.3-4. The results are shown graphically in Figures 2.3-5 and 2.3-6 for four different diaphragm geometries.

A diaphragm of this type 0.012 inch thick and to fit in the holding fixture shown in drawing Figure 2.3-3 is also to be fabricated and tested.

2.3.2.3.4 Back-to-Back Fluted Diaphragm

The Flip-Through Diaphragm (Fluted) discussed in the preceding paragraph showed some tendency toward tangential motion (scuffing) along its outer periphery. With the hope of eliminating this action the more symmetrical shape shown in Figure 2.3-7 was conceived. Preliminary analytical work is underway to



SPRING - FLAT PATTERN LAYOUT

197
1

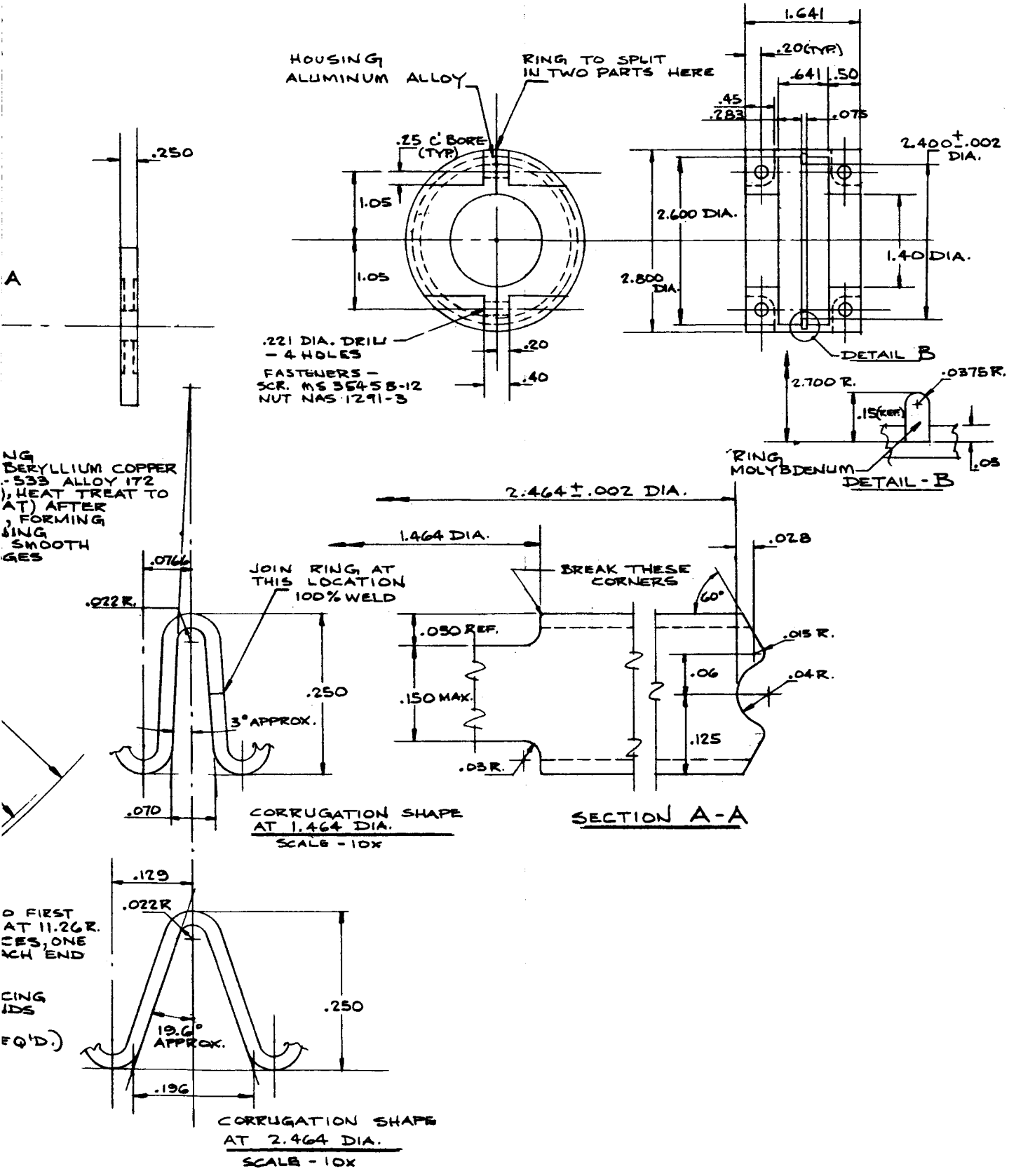


Figure 2.3-3. Corrugated Belleville Washer

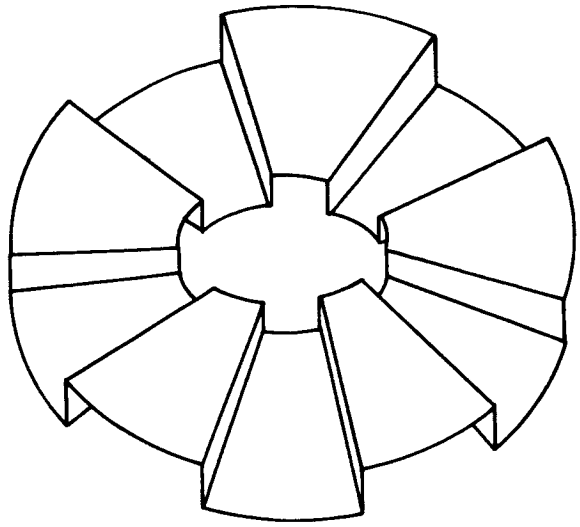


Figure 2.3-4. Clutch Washer

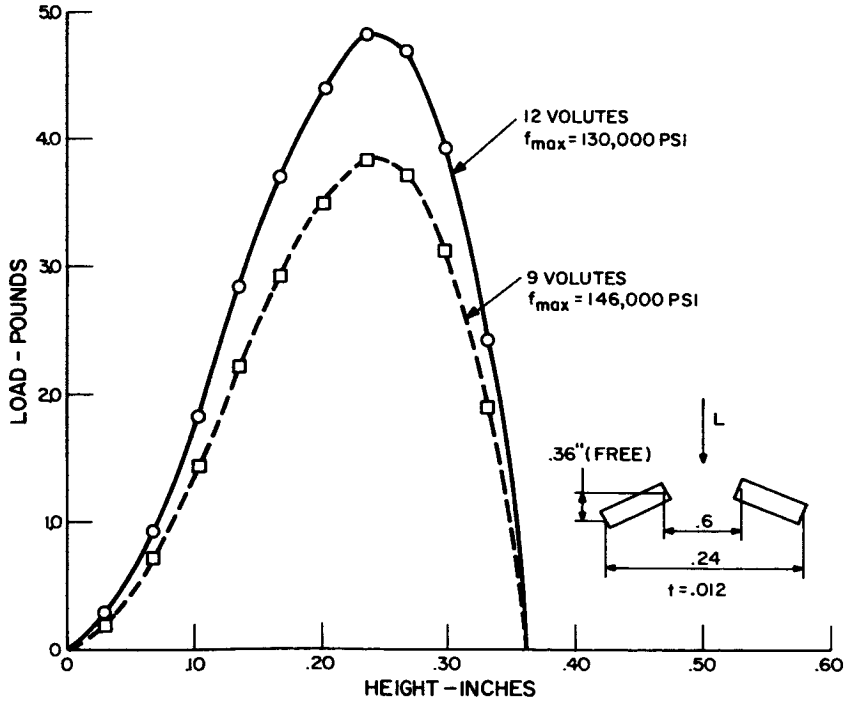


Figure 2.3-5. Load Deflection Characteristics and Maximum Stresses (Cases 1, 2)

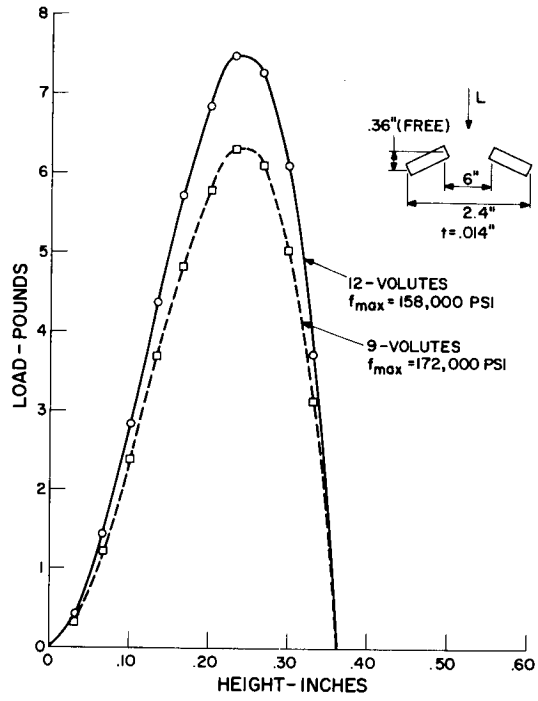


Figure 2.3-6. Load Deflection Characteristics and Maximum Stresses (Cases 3, 4)

determine a configuration to suit the requirements. A sample will then be built and its force-deflection characteristics measured. This diaphragm configuration consists of two rings placed back-to-back with radial corrugations about 1/8 inch high. Slotted "fingers" are arranged so as to clamp the rings together and also to form members by which the solenoid force is transmitted to the diaphragm. The number of corrugations and fingers, the width, thickness, diameter and material can be varied to best meet the design requirements. The fingers could be made of a plastic material with good anti-galling characteristics when working against the metallic boom structure, clutch plates and solenoid spool.

Two conditions that are difficult to determine analytically, but can be evaluated during developmental testing, are buckling and the torque required to twist the diaphragm about its circumferential axis. This latter torque subtracts from the torque producing the snap-through action.

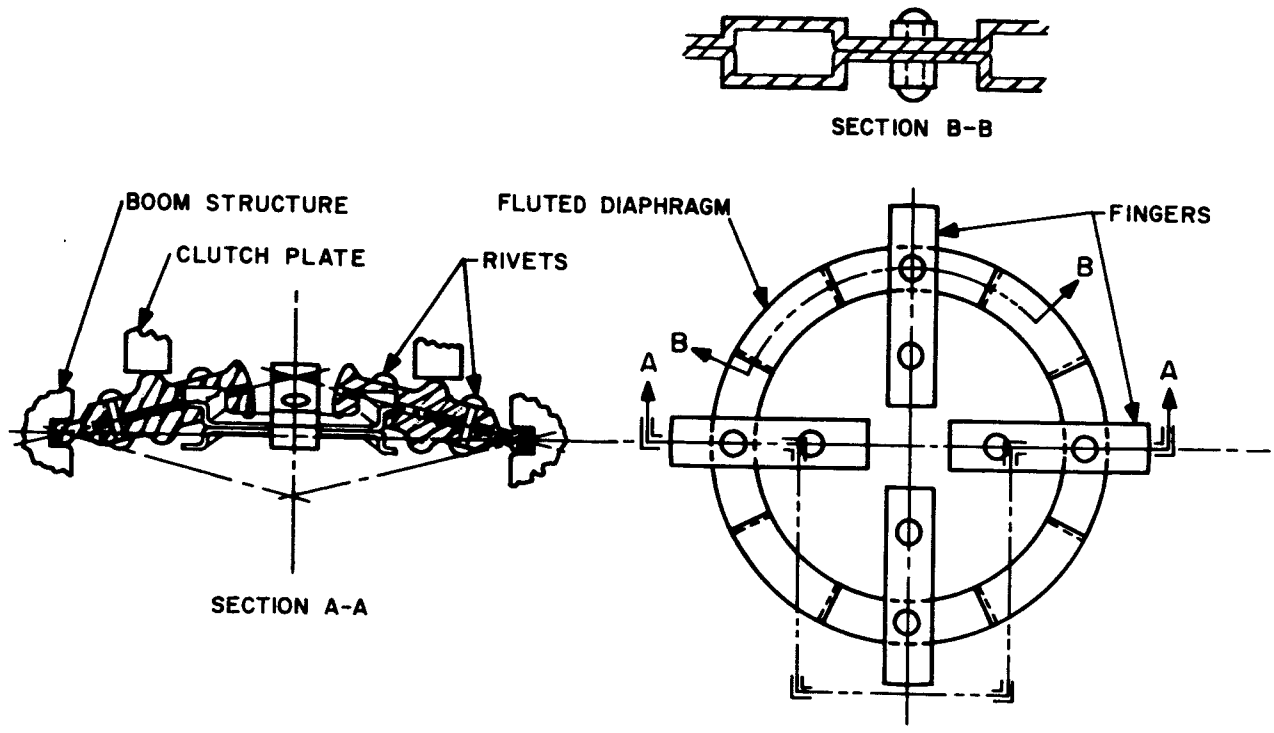


Figure 2.3-7. Back-to-Back Fluted Diaphragm

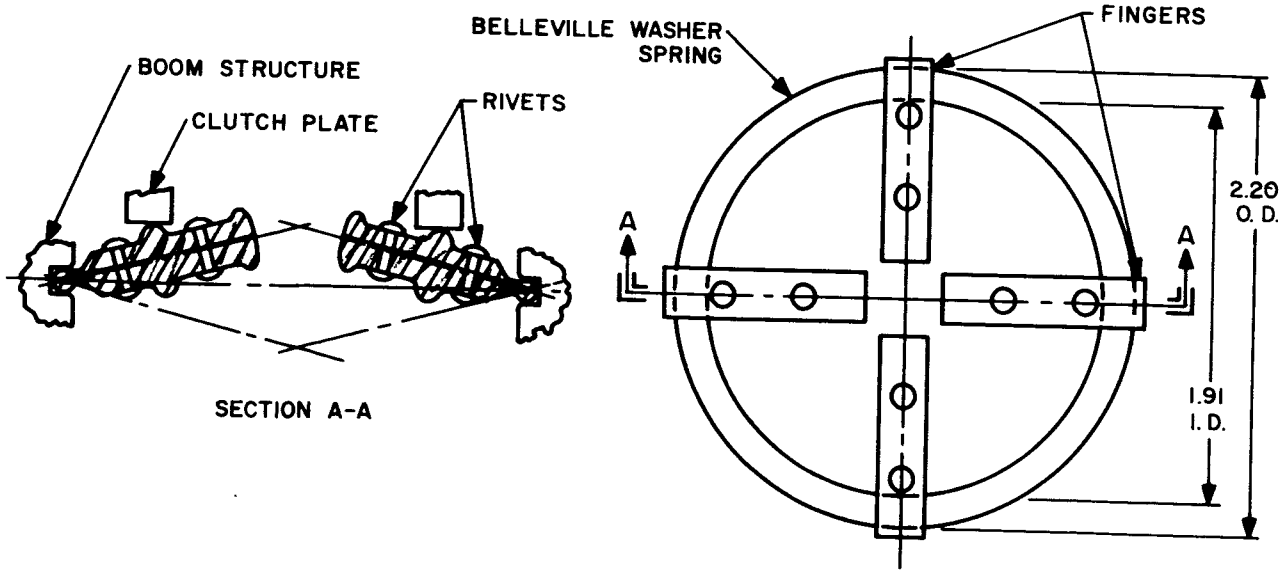


Figure 2.3-8. Belleville Washer with Fingers

2.3.2.3.5 Belleville Washer with Fingers

This concept is illustrated in Figure 2.3-8 and consists of a Belleville washer with fingers clamped to it by riveting. The number of fingers used would be determined by the buckling characteristics of the washer. A washer of the diameters shown and a free height of 0.069 inch made from 0.010 inch thick beryllium copper, is calculated to provide 7.2 lbs force at 0.3 inch working height at the solenoid spool. The stress when the washer is flat is calculated to be 234,000 psi. A washer has been obtained of 0.010 inch beryllium copper which is: 1.5 inch O.D., 1.07 inch I.D., .060 inch free height of cone. This washer will not satisfy the design requirements, but it will be tested with varying numbers of fingers to obtain an evaluation of the force-deflection characteristics with buckling and the location of the over-center toggling point. Any washer of the simple Belleville type will always yield less force for a given displacement off center in one direction than in the other. This is not true of the three other configurations described, and thereby gives them an advantage.

2.3.3 DEVELOPMENT ENGINEERING ACTIVITIES

2.3.3.1 Diamagnetic Torsional Restraint

An unsuccessful attempt was made to prove the feasibility of a diamagnetic torsional restraint device for the eddy-current damper. The primary justification for such a device, in lieu of a magnetic torsional restraint, would be the elimination of the magnetic torsional restraint's lateral attraction force, which exerts a large load on the diamagnetic suspension. The effect (as determined by a preliminary analysis) on the diamagnetic suspension of using diamagnetic torsional restraint would be the possible reduction of suspension magnets from 24 to 10 or 12 magnets. This would reduce the CPD weight by about 2.5 pounds.

Two different approaches were tried. The first would make use of the anisotropic character of the negative magnetic susceptibility of pyrolytic graphite; i.e., this

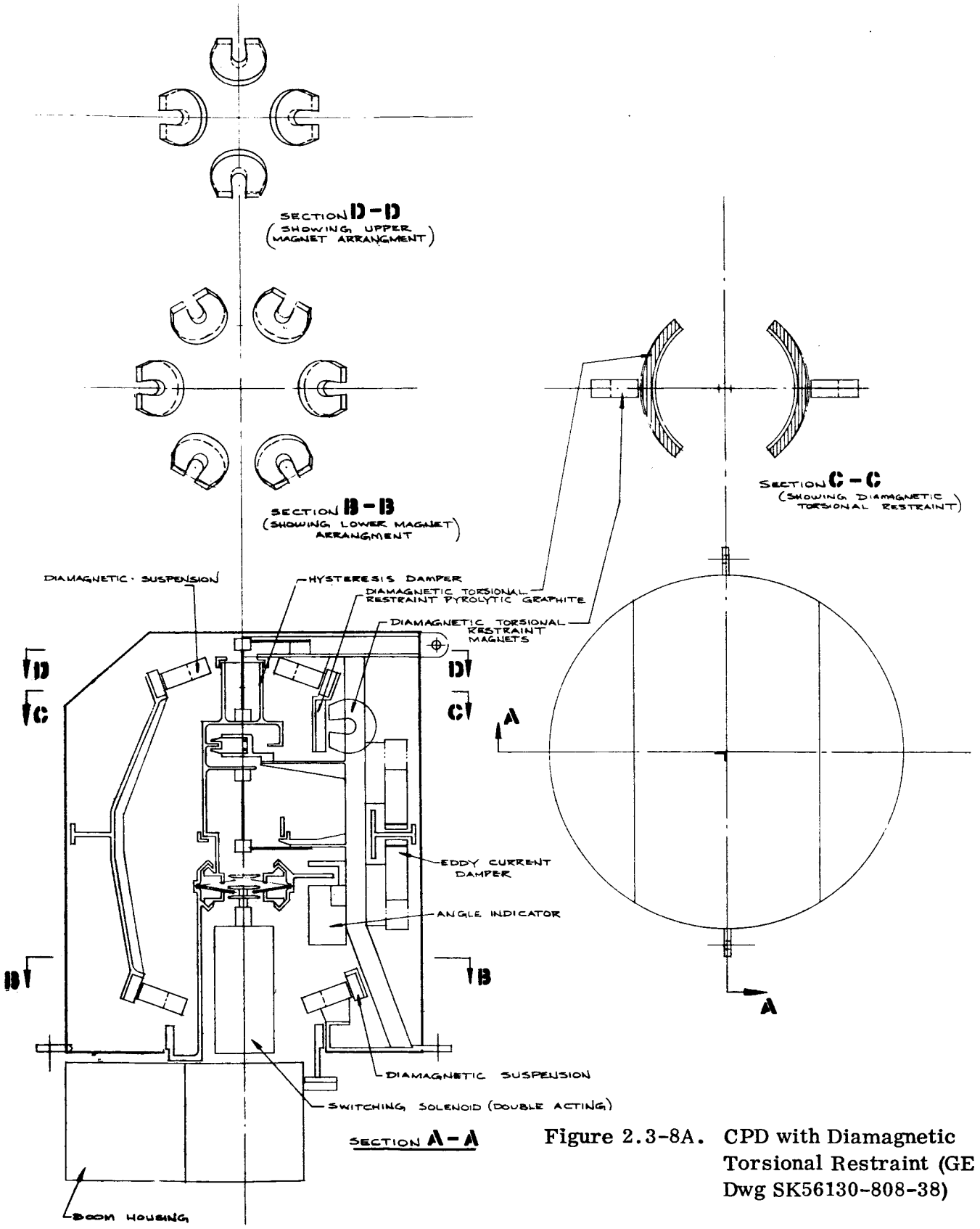


Figure 2.3-8A. CPD with Diamagnetic Torsional Restraint (GE Dwg SK56130-808-38)

material would experience a much stronger repulsion force in the direction perpendicular to its laminations than in a direction parallel to its laminations. The second concept utilizes a varying volume of diamagnetic material placed in a magnetic field to generate the necessary forces.

The magnetic susceptibility of pyrolytic graphite has been reported to be about 10 times greater in one direction than the other (i.e., the susceptibility in the direction of "growth" of graphite is 10 times that in a direction perpendicular to the growth).

A torsional restraint element using this property (as in the first approach) would contain two or more ring segments of pyrolytic graphite mounted on the rotor, and an equal number of magnets, mounted on the stator, located as shown in Figure 2.3-8A. In the null position the repulsion force would be directed through the axis, and produce no torque. When the rotor is rotated away from null, the direction of the repulsion force would also rotate and produce a torque tending to restore the null position. By design control over the magnitude of this force a linear restoring torque versus angle would be achieved.

Pyrolytic graphite elements shaped as shown in Figure 2.3-8A were obtained and initial tests were conducted using a test fixture as shown in Figure 2.3-9. In this photograph, the segments for this first concept are shown in the background while the crescents used in the second approach are mounted on the disc under the magnet poles. The test results were very disappointing, the system being unstable at the null position. The repulsion force in the direction in which the graphite was grown (i.e., perpendicular to the laminations in the graphite) was less than twice as great as the force parallel to the laminations, instead of being ten times as great, as reported in the literature.

Although the pyrolytic graphite used in the rings were suspect, and although a different arrangement of the magnets would tend to produce slightly better results, it was decided for schedule reasons not to conduct any further tests and to discontinue the investigation.

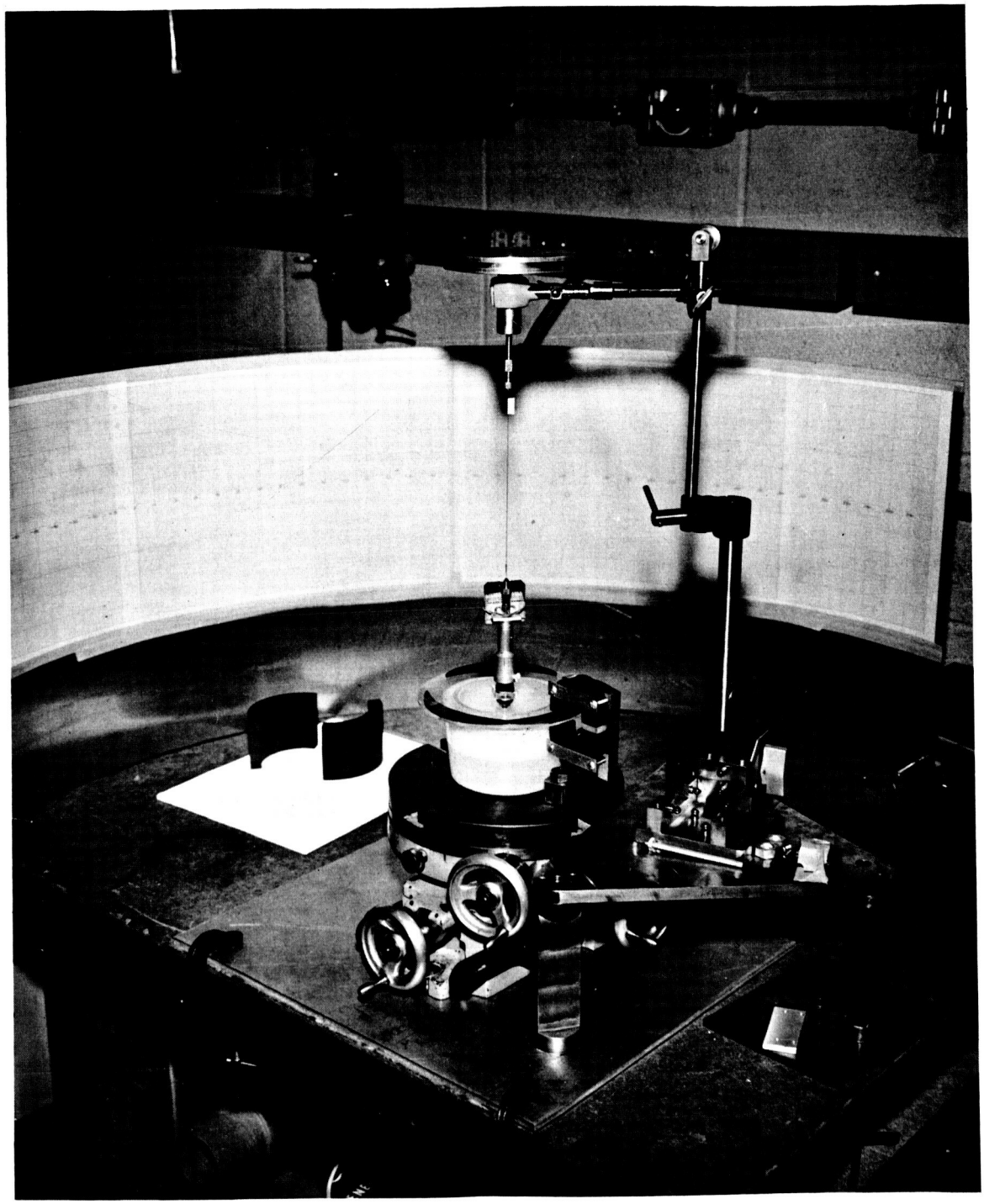


Figure 2.3-9. Test Fixture

The elements used for the second concept are shown mounted on the disk in Figure 2.3-9. The elements are crescent shaped with the laminations of the graphite being perpendicular to a chord drawn between the two "horns" of crescent. In this concept, the crescents are placed end-to-end as shown and the null point is located where the "horns" touch. This is because the least volume of diamagnetic material is located in the magnetic field at this point. As the magnets are rotated so that a larger volume of diamagnetic material is present in the air gap of the magnets, there is a force generated which attempts to rotate the disc in a direction back towards the null point.

The test was conducted using the largest magnet which could be feasibly included in the CPD and with a near optimum thickness of graphite. The forces obtained in the test did not meet those which would be required for the MAGGE torsional restraint element although they did exceed by a more than adequate margin the requirements for a SAGGE mission. The success of this concept had been predicated on tests run some time ago with a similar configuration which utilizes Bismuth as the diamagnetic element. So again, there is reason to suspect the pyrolytic graphite. However, to be assured of success, it was felt that it would be necessary to embark on a development program requiring more time than ATS schedule would permit.

Thus, the disparity between obtained and desired results dictated that the effort to produce a workable diamagnetic torsional restraint for a MAGGE version of ATS be discontinued. Because of the decision that there be only minor differences between MAGGE and SAGGE versions for the ATS CPD package, it will not be considered for use on the SAGGE version. It is felt that a suitable diamagnetic torsional restraint element with its attendant advantages could be readily developed for CPD to be used only for a synchronous application.

2.3.3.2 Diamagnetic Suspension

Many aspects of diamagnetic suspensions were investigated experimentally in order to obtain information needed for the design of the CPD. A series of 65

tests were conducted during this reporting period, in which measurement was made of the repulsion force versus air gap for various permanent magnets in combination with flat samples of pyrolytic graphite of various thicknesses. The results of these investigations are summarized below.

2.3.3.2.1 Selection of Permanent Magnet

The force characteristics were determined for five different type permanent magnets (all Alnico V). The GE Catalog No. 5U41B magnet was found to be superior to all others tested, in force per unit weight of magnet. All subsequent tests were conducted using this type magnet.

2.3.3.2.2 Selection of Pyrolytic Graphite Thickness

Force characteristics were obtained using 5U41B magnets with pyrolytic graphite samples of 1/8 inch, 1/4 inch, and 3/8 inch thicknesses. A large improvement in suspension capability (about 40 percent) is obtained by increasing thickness from 1/8 inch to 1/4 inch, but the improvement in going from 1/4 inch to 3/8 inch is less than 5 percent. Therefore, the thickness of the pyrolytic graphite cones for the CPD was specified as 1/4 inch.

2.3.3.2.3 Effect of Pyrolytic Graphite Layers

The manufacturing process for the pyrolytic graphite cones requires the use of more than one cone, nested together to give the required 1/4 inch thickness. Tests were run with two 1/8 inch flat samples, and the results did not differ significantly from tests using one 1/4 inch flat sample. No harmful result is expected from use of nested cones in the CPD.

2.3.3.2.4 Consistency of Pyrolytic Graphite Samples

A significant difference was noted between pyrolytic graphite samples of the same thickness. Two 1/8 inch samples produced forces about 15 percent

different, and two 1/4 inch samples produced forces about 10 percent different. This variation must be considered in the design.

2.3.3.2.5 Consistency of 5U41B Magnets

Various 5U41B magnets produced the same forces when used in combination with a given pyrolytic graphite sample, and when charged to the same magnetic strength. To obtain the desired suspension characteristics, all magnets used in the suspension will be charged to the same strength and checked prior to assembly.

2.3.3.2.6 Effect of Magnet Grouping

A series of tests were conducted with magnets in groups of two and three magnets, spaced about 0.4 inch apart, as in the CPD preliminary design. Force levels in these tests were found to be just two and three times the force measured for a single magnet. The tests were repeated for smaller spacings. Only when the spacing was reduced to 0.1 inch did a significant effect appear; at 0.1 inch the decrease in force was about 10 percent.

2.3.3.2.7 Effect of Magnet Polarity

The tests described immediately above were repeated with the relative polarities of the magnets reversed. The test results were approximately the same. The magnet polarity is immaterial for magnet spacings greater than 0.1 inch.

2.3.3.2.8 Effect of Mounting Surfaces

It is planned to grind two flats on the curved parts of the horseshoe magnets to facilitate mounting. This was done to three of the magnets used in the series of tests. The depths of cut were 0.030 inch, 0.050 inch, and 0.070 inch, respectively. The magnets were recharged. Force characteristics were then measured and found to be identical with those measured prior to machining.

2.3.3.2.9 Useful Region of Pyrolytic Graphite

A series of tests were conducted to determine which portion of the pyrolytic graphite was useful in producing force. In these tests the magnet was located at various positions relative to the edge of the pyrolytic graphite. From these tests it was determined that the pyrolytic graphite surface should overlap the projected pole face by 0.1 inch on each "side", where "side" of the magnet is defined as shown in Figure 2.3-10. No "overlap" is necessary on each end, again as shown in Figure 2.3-10. That is, the magnet side leakage flux contributes force, but the end leakage flux does not.

2.3.3.2.10 Selection of Magnet Gap Setting

It was pointed out in the first Quarterly Progress Report (p 2-135) that the radial force gradient is as follows:

$$K_r = \frac{1}{2} F_o \, m \, e^{-m \, g_o} \, n \, \cos^2 \beta$$

where $F = a + F_o \, e^{-mg}$ represents the force between a single magnet and a diamagnetic specimen as a function of air gap, g. Values for the parameters F_o and, m, may be determined experimentally. The suspension capability, P_r, is found by multiplying K_r by the maximum radial displacement, r,

$$\text{where } r = g_o / \cos \beta$$

Therefore

$$P_r = \frac{1}{2} F_o \, n \, \cos \beta \left[m \, g_o \, e^{-m \, g_o} \right]$$

The function in the brackets has been normalized and plotted as Figure 2.3-11. This curve shows that the maximum load capacity is obtained when the initial air gap is set at 1/m where m is the decay rate of the single magnet force characteristic. This decay rate has been found experimentally to be $m = 15 \text{ inches}^{-1}$ for the 5U41B magnet. The optimum air gap setting then would be 0.067 inches. A value 25 percent above or below this figure would result in a decrease in capacity

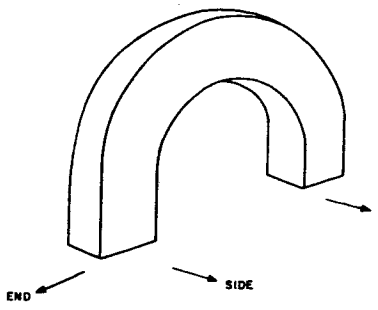


Figure 2.3-10. Definition of Magnet Side

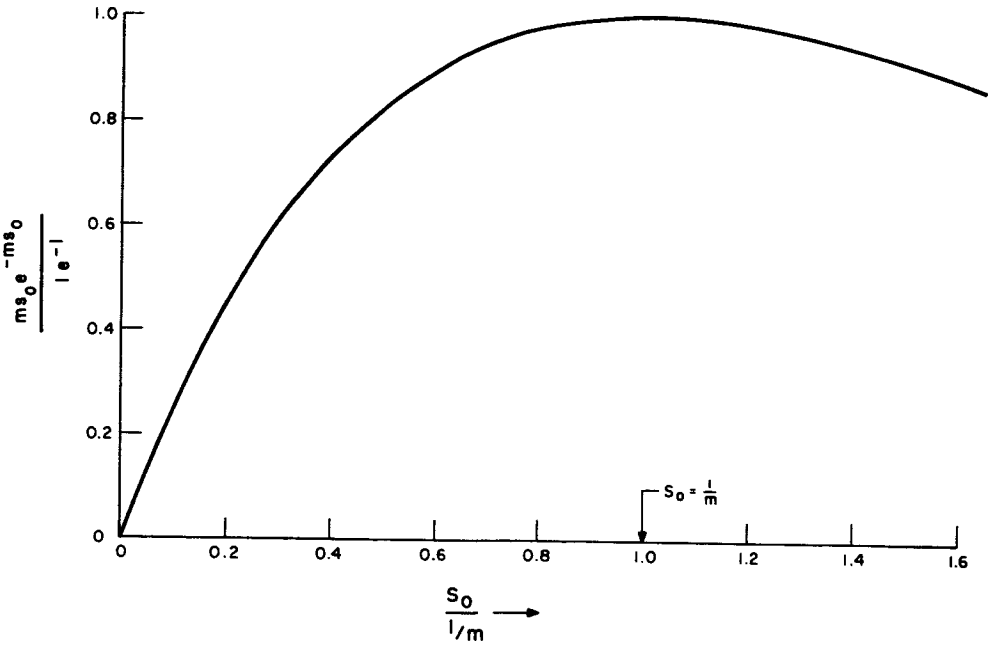


Figure 2.3-11. Suspension Load Capacity vs. Initial Air Gap Setting

of only about 3 percent, so the initial gap setting for the CPD is specified to be in the range from 0.050 to 0.083 inch in order to satisfy the suspension capacity requirements. Other factors must determine the actual setting. The actual setting should be kept as small as possible within the specified range, in order to maximize the radial force gradient, or stiffness, K_r. Mechanical tolerances and launch environmental stresses also must be considered in finalizing the initial gap setting.

2.3.3.3 Eddy-Current Damper

An eddy-current damper disc for the CPD was designed and fabricated, based on the test data reported in the First Quarterly Report (p 2-144). The aluminum damper disc has an outside diameter of 8.60 inches and a thickness of 0.100 inch. This damper is presently undergoing functional testing in the test set-up shown in Figure 2.3-12. Initial test results for this damper indicate a damping coefficient of 1,200,000 dyne-cm/radian/second, which is 20 percent below the specified value. The present series of tests will evaluate the effect of increasing disc thickness, and indicate what disc thickness is required to produce a damping coefficient of 1,500,000 dyne-cm/radian/second. Other techniques, involving increases in the magnetic flux developed, will be evaluated if necessary. As a backup, a copper damper disc has also been prepared for test. Because of its greater electrical conductivity, the copper disc is expected to produce up to 130 percent of the required damping, but will weigh about 1.0 pound, as compared to 0.3 pound for aluminum.

2.3.3.4 Hysteresis Damper

2.3.3.4.1 Introduction

In order to verify the reported performance of BTL* Hysteresis Damper, the magnetic portion of the damper was fabricated to BTL drawings and tested. The applicable parts of the damper were made exactly as specified in the BTL drawings plus some supplementary information received from BTL in a meeting with them on 24 September 1964.

* Bell Telephone Laboratories

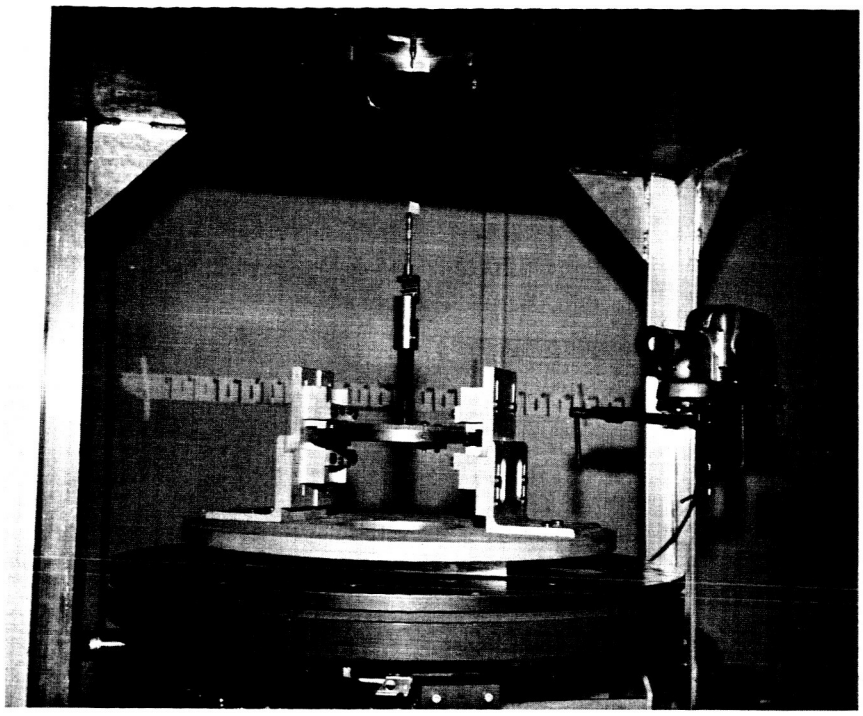


Figure 2.3-12. Test Setup for Eddy-Current Damper

Basically, the BTL Hysteresis Damper consists of a disc of low carbon steel having the dimensions of approximately 1.75 inch O.D., 1.12 inch I.D., and thickness varying from 0.003 to 0.010 inch. An Alnico V bar magnet with pole pieces on the ends is placed internal to the disc. The flux from the magnets travels circumferentially around the disc, varying from a region of zero flux, adjacent to the ends of magnets to a maximum value 90° away. Actually, the disc is saturated much before the 90° position. As the magnet rotates, every elemental volume of disc between the zero flux and the saturated level undergoes a change in flux density which results in a hysteresis loss. The magnitude of the hysteresis loss is independent of rate.

2.3.3.4.2 Damper Test Techniques

Two basic tests were run: hysteresis damping and minor loop characteristics. These tests give the basic performance characteristics of the damper. The test

procedure for measuring the hysteresis damping was as follows: the disc was hung from a calibrated torsion wire and the magnet was mounted on the sidereal rate table. The magnet was rotated at a constant rate and the deflection of the disc measured optically in a calibrated scale. The standard rate for these tests was 750°/hr.

The minor loop characteristics were run in a similar manner except that instead of running the magnet continuously in one direction, it was reversed in an oscillating mode for various amplitudes of travel. In order to determine dynamic effects during the oscillating mode, the inertia of the disc was changed and its effects on the minor loop characteristics studied. From the minor loop characteristics, the so-called $\Delta\theta$ angle can be determined. This angle represents the angle required for the damping torque to build up to steady state after reversal.

The characteristics of a number of different materials and heat treatments were tested. Generally, only one sample of each material was tested. Although this was not an ideal situation, it was done to limit the scope of investigation. The following materials were tested:

0.003 inch 1010 CRS (Shim Stock) -- Annealed and Unannealed

0.010 inch 1010 CRS (Shim Stock) -- Annealed and Unannealed

0.010 inch 1010 CRS (Bar Stock) -- Unannealed

0.0014 inch Pure Iron -- Unannealed.

It should be noted that the damper was not tested in an identical manner to the method used by BTL. BTL used a double torsion wire holding the damping disc, one from the top and the other from the bottom. This prevented axial or radial movement of the disc relative to the magnet.

The tests at GE were based on a single torsion wire suspension because:

1. It was desired to test through 360°.
2. Test equipment available (rate table) was not adaptable to attaching a bottom torsion wire without an elaborate test jig.

There was no apparent evidence that this single wire suspension method contributed in any way to the "ripple" problem discussed below.

2.3.3.4.3 Damper Test Results

These tests have demonstrated several interesting and important performance parameters, which may be critical from the systems aspect. These performance problems are listed and discussed below:

2.3.3.4.3.1 Variation of Damping Torque (See Table 2.3-1 for Referenced Tests)

As the magnet rotates relative to the damping disc, the hysteresis damping torque was found to vary with magnet position. This variation (ripple) is reproducible and was found to exist for all samples tested and is independent of rate. This can be attributed to the magnetic anisotropy. BTL reported less than 10 percent ripple for cold rolled steel (CRS) whereas our values were much higher, only two tests giving less than 10 percent with "typical" values between 20 percent and 40 percent. Considerable investigations were made into the nature of this discrepancy with no positive answers. Among the possible causes are:

1. Test equipment. BTL used double torsion wire and GE used a single wire.
2. Test method. GE rotated magnets continuously. BTL may have used a static method.
3. Data. GE took data over 360^{o} of disc; BTL only over $\pm 20^{o}$ to $\pm 30^{o}$ range. GE can read disc deflection to $.1^{o}$ giving torques to 10 dyne cm.
4. Materials. GE used standard shim stock at BTL's suggestion. BTL did not provide information on the source of their materials.

Composite discs made of two or more discs stacked up so that their anisotropic torques subtract from each other were tested. The magnitude of ripple was reduced substantially (Tests 46, 47 and 48). The limiting condition for using composite discs is the magnitude of damping torque and the thinnest disc which can be rolled.

TABLE 2.3-1 SUMMARY OF RESULTS

Material	Test No.	Damping Torque T_d - Dyne Cm	Ripple - T_R Dyne Cm (Peak-Peak)	$\frac{T_R}{T_D}$	Remarks
Unannealed .003" 1010 CRS	3	790	176	.223	302 stainless steel holders
Annealed .003" 1010 CRS	1	316	110	.348	302 stainless steel holders
Annealed .003" 1010 CRS	8	298	112	.376	302 stainless steel holders 3000°/hr rate
Annealed .003" 1010 CRS	9	303	112	.369	302 stainless steel holders
Annealed .003" 1010 CRS	18	272	95	.350	302 stainless steel holders
Annealed .003" 1010 CRS	19	285	132	.463	302 stainless steel holders magnet cocked
Annealed .003" 1010 CRS	20	316	116	.367	302 stainless steel holders new magnet
Annealed .003" 1010 CRS	29	162	44	.271	Plastic holders
Annealed .003" 1010 CRS	34	162	40	.247	Plastic holders
Annealed .003" 1010 CRS	37	162	53	.327	Plastic holders
Annealed .003" 1010 CRS	41	154	-	-	Plastic holders
Unannealed .010" 1010 CRS	5	2240	285	.127	302 stainless steel holders
Unannealed .010" 1010 CRS	27	2260	197	.087	302 stainless steel holders
Unannealed .010" 1010 CRS	33	2190	215	.0982	Plastic holders
Unannealed .010" 1010 CRS	31	1100	143	.13	Disc fabricated from bar stock/plastic holders
Unannealed .010" 1010 CRS	32	1130	167	.148	Disc fabricated from bar stock disc rotated 90°/plastic holders
Annealed .010" 1010 CRS	4	395	285	.722	302 stainless steel holders 3000°/hr rate
Annealed .010" 1010 CRS	26	438	158	.361	302 stainless steel holders
Annealed .010" 1010 CRS	30	342	182	.532	Plastic holders
Annealed .010" 1010 CRS	45	351	141	.402	Plastic holders/Data over 180°

TABLE 2.3-1. SUMMARY OF RESULTS (Continued)

Material	Test No.	Damping Torque T_d - Dyne Cm	Ripple - T_R Dyne Cm (Peak-Peak)	$\frac{T_R}{T_D}$	Remarks
Stainless steel holders	24	238	83	.349	
	25	217	88	.402	Demagnetized
	28	246	92	.375	After 700°C stress relief
Unannealed .0014" Pure Iron	46	263	285	1.08	Sample 1/Plastic holders
Unannealed .0014" Pure Iron	47	263	176	.67	Sample 2/Plastic holders
Unannealed .0014" Pure Iron	48	594	176	.275	Composite of samples 1 and 2 aligned to reduce ripple.

Magnetic anisotropy is a function of the metallurgical processing of a material. The material composition, amount of cold work, intermediate anneals, etc., greatly affects the magnetic characteristics.

The magnitude of the ripple is independent of rotational rate. It was also present when the damping disc was tilted, being approximately the same magnitude as untilted. The substitution of a "good" magnet for one which was thought to be "poor" had no effect on ripple. Typical test data is given by tests 37, 30, 31, 33 and 46.

2.3.3.4.3.2 302 Stainless Steel Holders

BTL specified 302 SS Holders to position the damping disc. It was found that the hysteresis damping torque in 0.010 inch holders was approximately 238 dyne cm. (See test 28). BTL drawings specified 0.004 inch holders which, if used, would produce approximately 94 dyne cm. BTL reported that they experienced no loss in these holders, but did not know if they had been annealed during fabrication. The hysteresis loss appears excessive, especially for SAGGE which requires 41 dyne cm damping torque. Annealing may solve this problem, provided that the effects of the radiation environment is not significant.

2.3.3.4.3.3 Eddy-Current Damping

The magnitude of the eddy-current damping torque in the hysteresis damper was measured and is less than 10 percent -- probably in the magnitude of 10 dyne cm for 0.003 inch annealed CES at a rotational rate of 750 to 3000°/hour.

2.3.3.4.3.4 Minor Loops

Two rules can be established regarding the formation of minor hysteresis loops:

(1) If steady state conditions prevail and the direction of rotation of the magnet is reversed, a certain angle, $\Delta\theta$, is required for the damping to reach steady state value. This angle is a function of the magnitude of hysteresis damping, inertia, and the magnetic angle due to material characteristics and flux distribution.

(2) If the $\Delta\theta$ angle is greater than the angle of oscillation, steady state damping will be reached when the position of reversal is reached. Typical tests are 11 and 16. (See Table 2.3-2.)

TABLE 2.3-2. "$\Delta\theta$" TEST SUMMARY

Material	Inertia	Oscillation	Test No.	"$\Delta\theta$" Direction		Holders
				CW to CCW	CCW to CW	
.003 Annealed	Minimum	$\pm 90^{o}$	38	35^{o}	35^{o}	Plastic
		$\pm 45^{o}$	39	35^{o}	35^{o}	Plastic
	Medium	$\pm 50^{o}$	16	100^{o}	$>100^{o}$	SS
.010 inch Annealed	Medium	$\pm 90^{o}$	43	20^{o}	30^{o}	Plastic
	Maximum	$\pm 90^{o}$	44	20^{o}	25^{o}	Plastic

2.3.3.4.3.5 "Hang-Off" Angle

With hysteresis damping there is an inherent hang-off angle which is defined by the ratio of damping torque to wire spring constant. This angle represents the limits of a dead band.

2.3.3.4.4 Analysis of Related BTL Test Data

The above discussion summarizes the test results on a BTL damper which was fabricated and tested at GE. One of the unexplained characteristics was the large magnitude of ripple which was measured at GE but which BTL did not observe. BTL forwarded to GE test data and the discs, which were used for the tests, for GE to run comparative tests. An analysis of the BTL test data that was sent was made to determine the magnitude of ripple. Since the BTL data was taken over $\pm 20^{o}$ rather than 360^{o}, a simple statistical analysis of the GE data for $\pm 20^{o}$ was made to obtain a common basis for comparison and to determine if any substantial difference in ripple exists.

2.3.3.4.4.1 Results of Analysis

1. BTL Data

Material	$\frac{\text{Damping Torque}}{T_D \text{ - dyne cm}}$	$\frac{T_{Ripple}}{T_D}$
0.004 inch 1010 CRS Unannealed	593	.11
Annealed	339	.20
0.006 inch 1010 CRS Unannealed	1242	.06
Annealed	480	.14
0.008 inch 1010 CRS Unannealed	1385	.06
0.0204 inch Vanadium Permandur (Field Aligned)	905	.07

2. G. E. Data

a. Material -0.003" 1010 CRS (Shim Stock)
Test #37
T_D = 162 dyne cm.

	T_R	$\frac{T_R}{T_D}$	$\frac{\%T_R}{T_D}$
Maximum T_R over 360°	53	.327	100%
Over 40° Band			
Mean of 18 readings	22	.136	41.6
Mode of 18 readings	22	.136	41.6
Median of 18 readings	26	.161	49.2
Minimum of 18 readings	4.4	.027	8.3
Over Selected 90° Band (±45°) Minimum T_R	13.2	.082	

b. Material - .010" 1010 CRS (Shim Stock)
Test #30
T_D = 342 dyne cm.

Maximum T_R over 360°	182	.532	100%
Over 40° Band			
Mean of 36 readings	66	.193	36.3
Mode of 36 readings	66	.193	36.3
Median of 36 readings	77	.225	42.2
Minimum of 36 readings	22	.0642	12.1
Over Selected 90° Band (±45°) Minimum T_R	44	.128	

2.3.3.4.4.2 Discussion of Results

1. BTL Data

   On the basis of six tests on four different materials and heat treatments run over only $\pm 20^{o}$ (40^{o} total), BTL reported three as having more than 10 percent ripple. This gives further credance to the concept that magnetic anisotropy does exist in the dampers and there is a significant amount of ripple.

2. GE Data

   By a random selection of the operating point of the disc and for a $\pm 20^{o}$ travel, the magnitude of ripple can be substantially reduced. On the two tests selected, the magnitude of ripple can be reduced from 32.7 percent to about 15 percent for 0.003 inch annealed and 53.2 percent to about 20 percent for 0.010 inch annealed. However, by operating over a selected area, the ripple can be reduced to approximately 3 percent and 6.4 percent, respectively, for $\pm 20^{o}$ of travel. For the ATS application which has $\pm 45^{o}$ of travel a selection of operating area would give ripples of 8.2 percent and 12.8 percent, respectively.

   A 0.010 inch CRS annealed (at 840^{o} C) disc was sent to the GE Research Laboratory for a metallurgical analysis. They reported that the grain size was somewhat larger than optimum but not large enough to be serious. No other "peculiarities" of the disc were observed by them. They recommended a lower temperature anneal, 600^{o}C, for smaller grain size and reduced magnetic anisotropy.

3. Additional Work

   It is planned to test several of the samples of material that BTL sent to GE in order to provide additional correlation in the hysteresis investigation. Further tests will substantiate the results that have been thus far attained as well as to check GE's test technique against BTL'S.

2.3.3.4.5 Torsion Wire Suspension Investigation

A test fixture (Figure 2.3-13) was designed and manufactured for the purpose of investigating the wire suspension system for the hysteresis damper. The fixture was designed to nearly simulate the suspension which will be used on the hysteresis damper system of the final CPD Configuration. Tests are planned to check various materials and configurations for both functional and environmental performance. Included in the test plans are the measurement of wire suspension spring

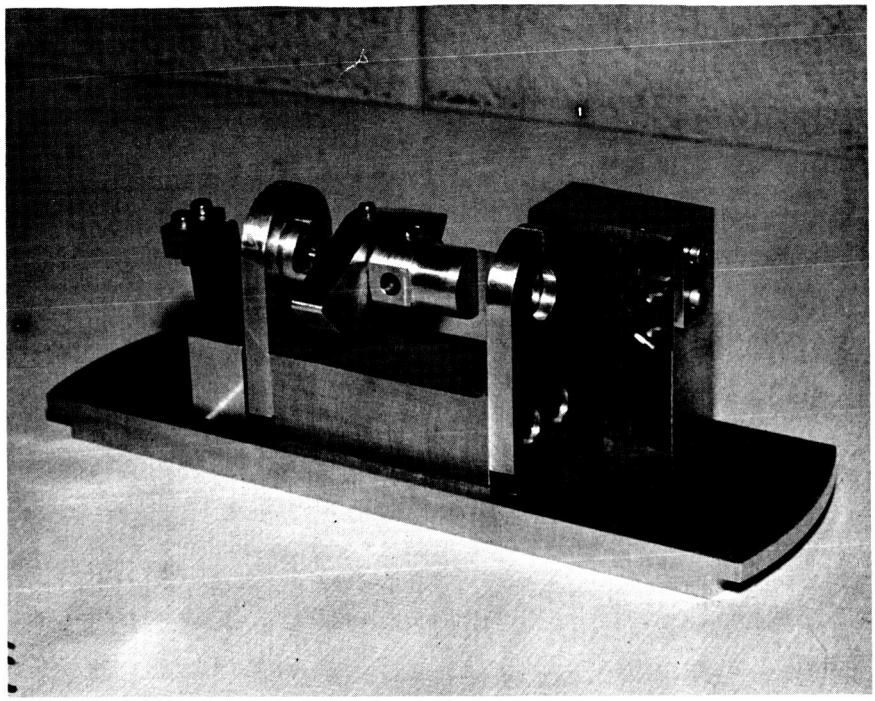


Figure 2.3-13. Torsion Wire Suspension Test Fixture

characteristics, wire torsional restraint characteristic, wire to spring attachment methods, spring and wire fatigue limits and/or characteristics, vibration tests, life tests, and repeatability tests.

The fixture has been assembled and preliminary adjustments made on the suspension springs.

2.3.3.5 Caging

A damper boom caging device is included on Fig. 2.3.2. It utilizes four spring-loaded pins (32) that are extendable from the base of the CPD case (20) into the damper boom shaft. The pins are released by the cutting of a cable (33) by pyrotechnic cable cutters (34). At present, design effort is being directed to incorporate the caging device for the eddy-current damper with the damper boom caging device. If this combination of caging devices is practical it offers a weight saving, a command channel saving and should be more reliable. Caging of the hysteresis damper will probably be a separate device.

2.3.3.6 Instrumentation

Instrumentation in the CPD has been reduced to the angle detector discussed in Section 2.3.4.2 and the mode indicators used to verify that the shift from one damper to the other damper has taken place. The mode indicators are SPDT hermetically sealed switches which are available from commercial sources as qualified components.

2.3.3.7 Magnetic Dipole

It is specified that the magnetic dipole of the CPD not exceed 100 pole-centimeters; i.e., the torque on the CPD due to interaction with an ambient magnetic field should not exceed 100 dyne-centimeters per oersted of ambient field.

In order to evaluate the magnetic dipole characteristics of the CPD, a magnetic mock-up was constructed in accordance with the CPD preliminary design as is pictured in Figure 2.3-14. This mock-up contained all 24 suspension magnets, the damping magnets and the torsional restraint magnets. A magnetic shield was not used in this test. This mock-up was suspended from a torsion wire in a known magnetic field and its magnetic dipole was measured for all three axes. The net magnetic dipole vector for the entire unshielded CPD was determined from these data to be 1170 pole-cm, nearly twelve times the specified value of 100 pole-centimeters.

An auxiliary magnet weighing less than 10 grams was added to the assembly in an effort to cancel the magnetic dipole vector of the CPD. This approach was successful in reducing the dipole from approximately 1015 pole-centimeters in the axis measured to approximately 180 pole-centimeters. As this was a simplified initial attempt at cancelling the dipole, it was felt that even better results could be attained. It was decided to continue these investigations after the magnetic configuration of the CPD had become more firm. At that time other techniques for reducing magnetic dipole will be investigated; for example, the reversal of polarity of some selected magnets, and, if necessary, the addition of magnetic shielding to the assembly.

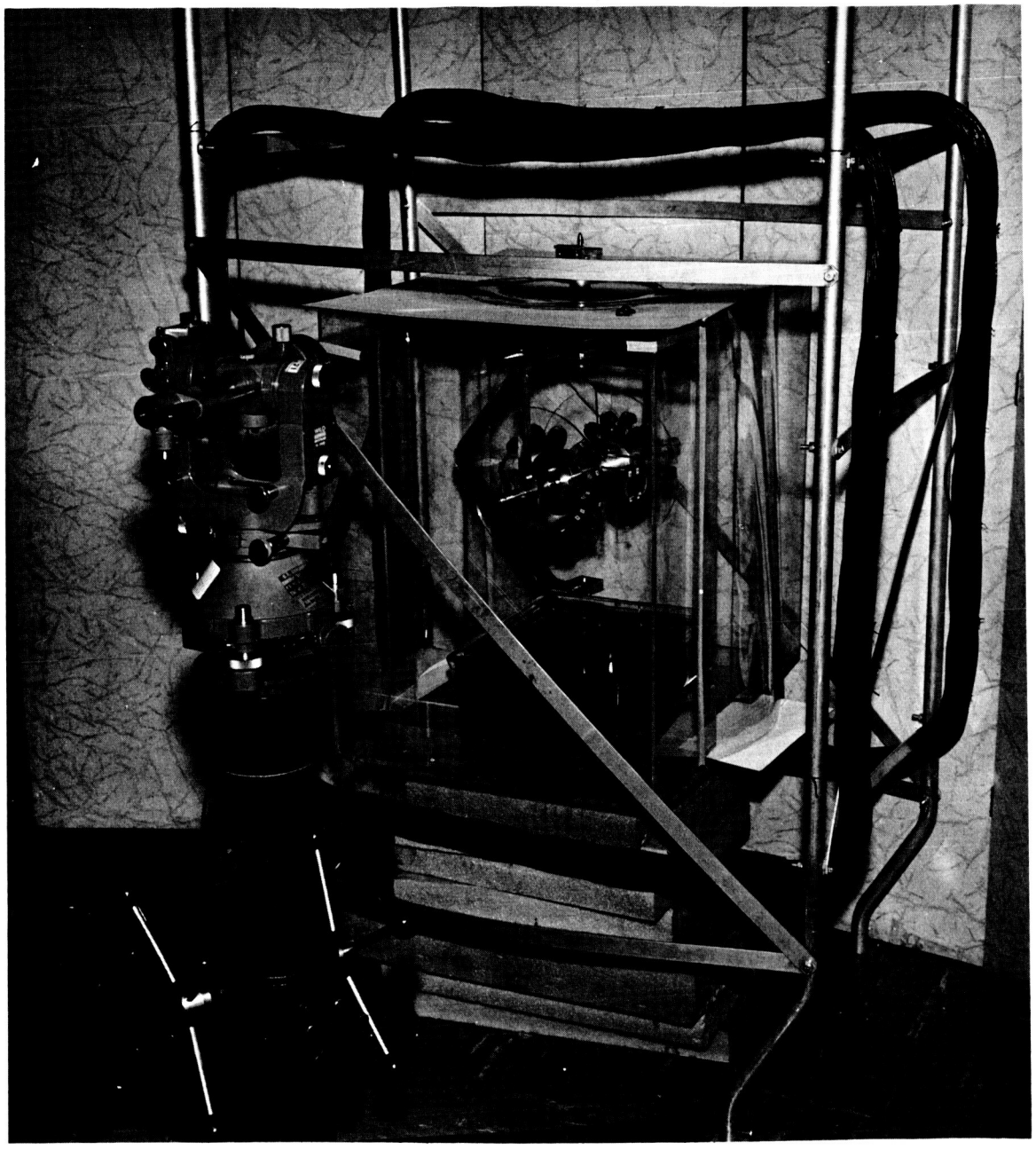


Figure 2.3-14. Magnetic Mock-up

2.3.4 SUB-CONTRACT ACTIVITIES

2.3.4.1 Hysteresis Damper (STL)

As stated previously, a proposal was requested from Space Technology Laboratory (STL) for a completely self-contained hysteresis damper which would have a mounting and an output interface to mount within the CPD package. STL visited General Electric on 9 December 1964 to review Specification SVS 7331 and associated Work Statement, 4176-WS-008. GE was informed by STL that their proposal had been completed and was being mailed on 30 December 1964.

2.3.4.2 Boom Angle Detector (DRC)

The angle detector specification (SV 7315) and work statement (4176-WS-005) have been issued and contract negotiations are in process. The final contract is expected to be signed in mid-January, with delivery of the first unit planned for the end of March, 1965.

The angle detector will be accurate to within $\pm 1^{o}$ through an angular displacement of the boom of ± 10 degrees about null and ± 10 percent for the angular range of +10 to +45 and -10 to -45 degrees about null. Electrical and mechanical interfaces will be finalized when final design of the CPD is nearer completion. Since the CPD thermal environment has not been defined, the operating temperature limits for the angle indicator have been established based on previous designs by the vendor. The radiation environment is still unresolved. The power consumption is estimated to be between 3 to 3.5 watts.

2.3.4.3 Solenoid

Eleven solenoid manufacturers were contacted to obtain design and manufacturing information on a "two-way" solenoid for changing the damping mode of the CPD.

Results of the search indicated that a solenoid, to perform this function would be approximately 3.5 inches long by 1.5 inches in diameter. The weight would be approximately 1.3 pounds.

The required performance of the solenoid would be as follows:

Stroke Length: 0.5 inches

Force vs Travel:	Force (lbs)	Travel (inches)
	2	0.50
	10	0.35
	20	0.10

Minimum Holding Force at End of Travel: 1.0 lb.

The specification (SVS 7333), specification control drawing (47-207087) and work statement (4176-WS-003) have been completed.

2.3.5 TEST EQUIPMENT PROGRESS

2.3.5.1 Low Order Force Fixture No. 1 (LOFF)

LOFF No. 1 has been in continuous use since the conception of the ATS program. It is being used to evaluate the eddy current damper suspension concepts.

The air bearing was repaired and made operative with in-house efforts and no operational difficulties have been encountered. The new vertical motion adjuster and the leveling device have been designed and manufactured and are ready to be incorporated into the setup when the need arises. Modifications will be made to the crossarm as soon as some downtime is acquired.

The fixtures to adapt the CPD to the LOFF, for suspension force and over-turning torque tests have not been designed. The detailed design of the adapting fixtures will begin when the CPD interface is firmly established.

2.3.5.2 LOFF No. 2

The design of LOFF No. 2 is complete with the exception of the CPD Adapting Fixtures. The LOFF is presently being assembled in the CPD test area. The air bearing for the LOFF will be delivered and installed at the end of January. The assembly of the bearing air control panel is in process and will be completed upon arrival of the air bearing.

All other components for LOFF No. 2 have been completed. It is anticipated that the LOFF will be checked out and ready for use by the middle of February.

2.3.5.3 Advanced Damping Test Fixture (ADTF)

All hardware for the ADTF has been designed with the exception of the CPD adapters pending final configuration drawings for the CPD. The vertical height adjuster and horizontal adjuster are in manufacturing and will be completed by mid-January.

The air bearing will be delivered in mid-January. Upon delivery of the air bearing, the torquer-pickoff will be installed and tests run to verify operation and to check calibration. All recording and control instrumentation has been checked for proper operation and no serious difficulties or problems have been encountered.

The room modifications have been completed and air currents are now at a minimum and will have little effect upon the performance of both damping and LOFF tests.

Portions of the damping test fixture have been utilized for the past 3 months for obtaining design information on both the eddy current and hysteresis damper.

2.3.5.4 Dipole Test Equipment

The Helmholtz Coil has been designed, built and preliminary tests run to verify field strength versus coil current and field consistency. The coil is presently being used for engineering dipole tests. The CPD adapting fixtures are to be designed again awaiting completion of final CPD envelope. The remaining hardware has been obtained and is presently in use. No difficulties have been encountered in operation of this equipment.

2.4 ATTITUDE SENSOR SUBSYSTEM

2.4.1 SUBSYSTEM DESCRIPTION

The original concept of the Attitude Sensor Subsystem of the Gravity Gradient Stabilization System for the Applications Technology Satellite is described in the Program Plan (Item 4 of Section 4), and is accompanied by a discussion of the operating characteristics of each sensor and electronics package. A further description of the subsystem and detailed discussion of each component is given in the First Quarterly Report (Item 1 of Section 4). Since a number of events have occurred which have changed the original concept, another brief description is presented here.

As shown in Figure 2.4-1, the Attitude Sensor Subsystem presently consists of two sensors that are procured by the General Electric Company, a three-axis Magnetic Torquing Coil, and the power control and telemetry circuits associated with the other components of the Gravity Gradient Stabilization System. One of the TV Camera systems and the 3-axis Torquing Coil may not be required on the synchronous flights. Although the present status of the two Infrared Earth Sensors, which were to be supplied by NASA/GSFC to the General Electric Company for incorporation into the GGSS Attitude Sensor Subsystem, is not clear, the power control circuits for these two components are included in the Power Control Unit (PCU).

In accordance with NASA/GSFC direction, all squibs will be redundant, as indicated by "A" and "B" in Figure 2.4-1, to perform the three primary squib functions. To further increase the reliability, each squib has its own firing circuit in the PCU, which in turn can be activated by a command from either of the redundant command decoders provided in the spacecraft. Therefore, each of the three Combination Passive Damper (CPD) mechanisms, Boom, Damper No. 1, and Damper No. 2, may be released by any one of four commands from the ground. In addition, consideration is being given to the automatic detonation of the Damper Boom Release squibs, depending on the separation sequence to be established. The initial deployment of the primary booms will be started automatically by the separation timer, although the exact time delay has not yet been finalized.

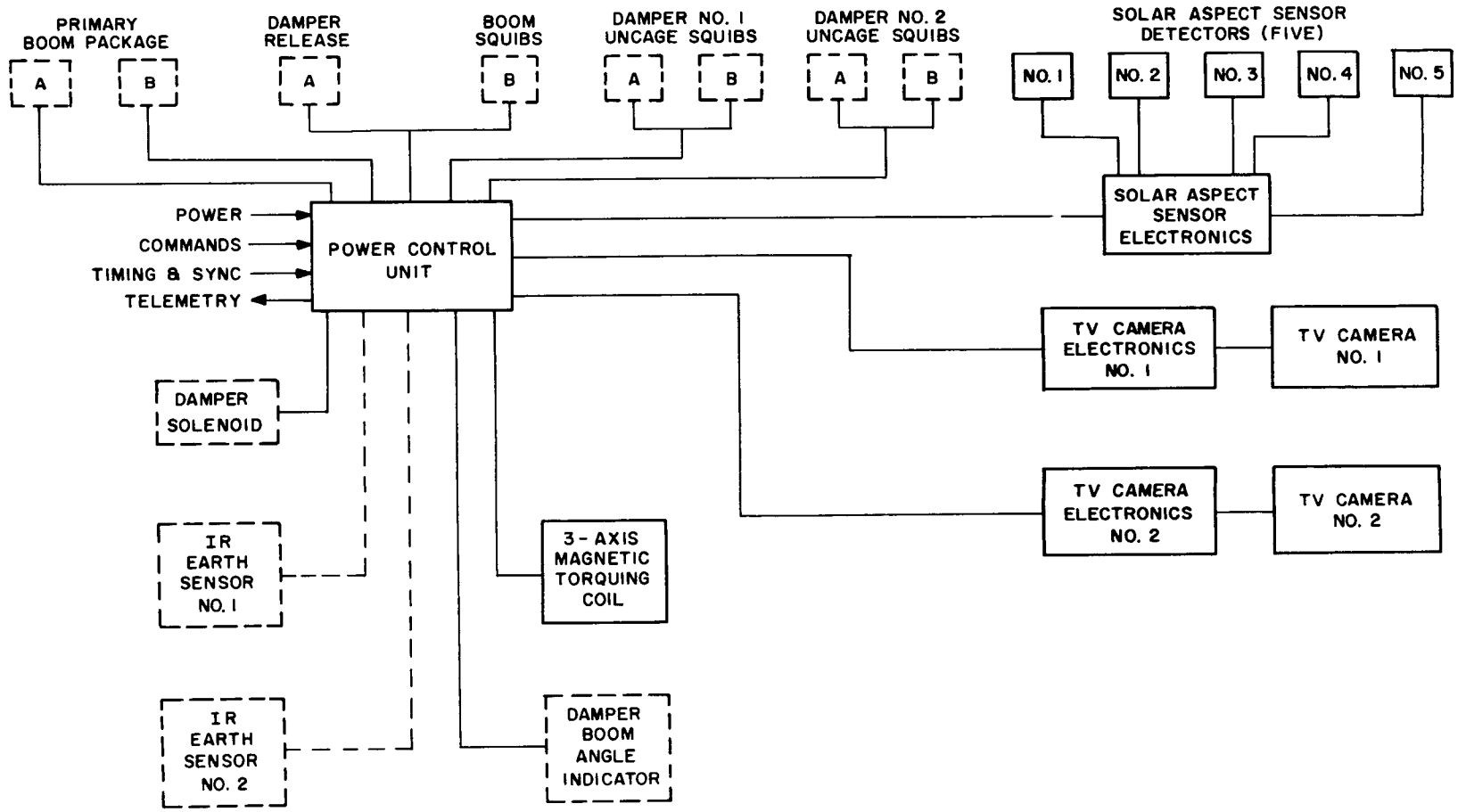


Figure 2.4-1 GGSS Attitude Sensor Subsystem

2.4.2 POWER CONTROL UNIT

2.4.2.1 Summary

During the report period, preliminary circuit and packaging design was performed and updated to meet new requirements, on the command interface, power switching, and diagnostic measurement circuits in the Power Control Unit. Detailed design was performed in areas where the requirements were considered to be firm. Individual circuits have been constructed on breadboards and tested, and the assembly and testing of the composite breadboard should be completed during the next report period. Manufacturing of some of the modular assemblies for the Engineering Units has begun.

2.4.2.2 General Description

The Power Control Unit accepts power and command input lines from the ATS system and processes them so that individual control of power to the various attitude sensing equipment and control devices within the Gravity Gradient Stabilization System is obtained. The unit houses the electronic circuits necessary for making temperature, event, and other diagnostic measurements within the system and provides outputs to the spacecraft telemetry encoders for these measurements. The Power Control Unit also contains the Separation Timer circuits which accept and process inputs from the vehicle clock to provide the signals required for initial deployment of stabilization and damper booms. The design of the PCU centralizes the interface between the spacecraft and the Gravity Gradient Stabilization system, except where it is clearly more practical and more reliable to run telemetry leads directly from a monitor to the two vehicle telemetry encoders.

2.4.2.3 Electrical Design

Quite conservative design margins were used in the circuits of the main control functions of the units. For example, most transistors can experience degradations in common emitter current gain of 75% and still perform the desired switching functions. Since, in most cases, the output loads are not completely defined as yet, formalized detailed design to show the specific margin has not been made.

2.4.2.3.1 Command Interface Circuits

The design of these circuits was taken directly from the ATS Interface Document, Appendix A supplied by HAC. Only the resistor types have been changed to another qualified type so that General Electric's manufacturing operation can use their normal welded module construction. This change will actually give more design margin in the circuit.

These circuits are used as buffers for all interfaces with the spacecraft command decoders and the vehicle clock. They are used to drive latching type relays directly, or, with further amplification, to drive motor or solenoid type loads. In use, their drive capability is never required to supply more than 2/3 the load specified in the HAC design notes for this circuit and a preliminary calculation shows an adequate design margin.

2.4.2.3.2 Squib Driver

Initially, the preliminary design of the Power Control Unit used the command buffer circuits with some added stages of amplification that would drive a transistor switch to fire pyrotechnique devices. Subsequent investigation revealed that HAC uses a circuit for firing such devices which will not respond to false command pulses of less than 500 milliseconds duration. In order to protect the Gravity Gradient Stabilization System from such failure modes (though the probability of this occurrence is not known to General Electric), it was decided to use a similar circuit for this function, as shown in figure 2.4.2-1.

An oscilloscope photograph of one of the preliminary tests is shown in Figure 2.4.2-2, where the sweep rate was 200 milliseconds per centimeter. The top trace is the applied command execute pulse of approximately 1.9 seconds and the lower trace represents the squib firing pulse, about 50 milliseconds wide, and delayed by almost 800 milliseconds. The rise of the simulated execute pulse is not seen in the photograph since the oscilloscope was triggered from this signal.

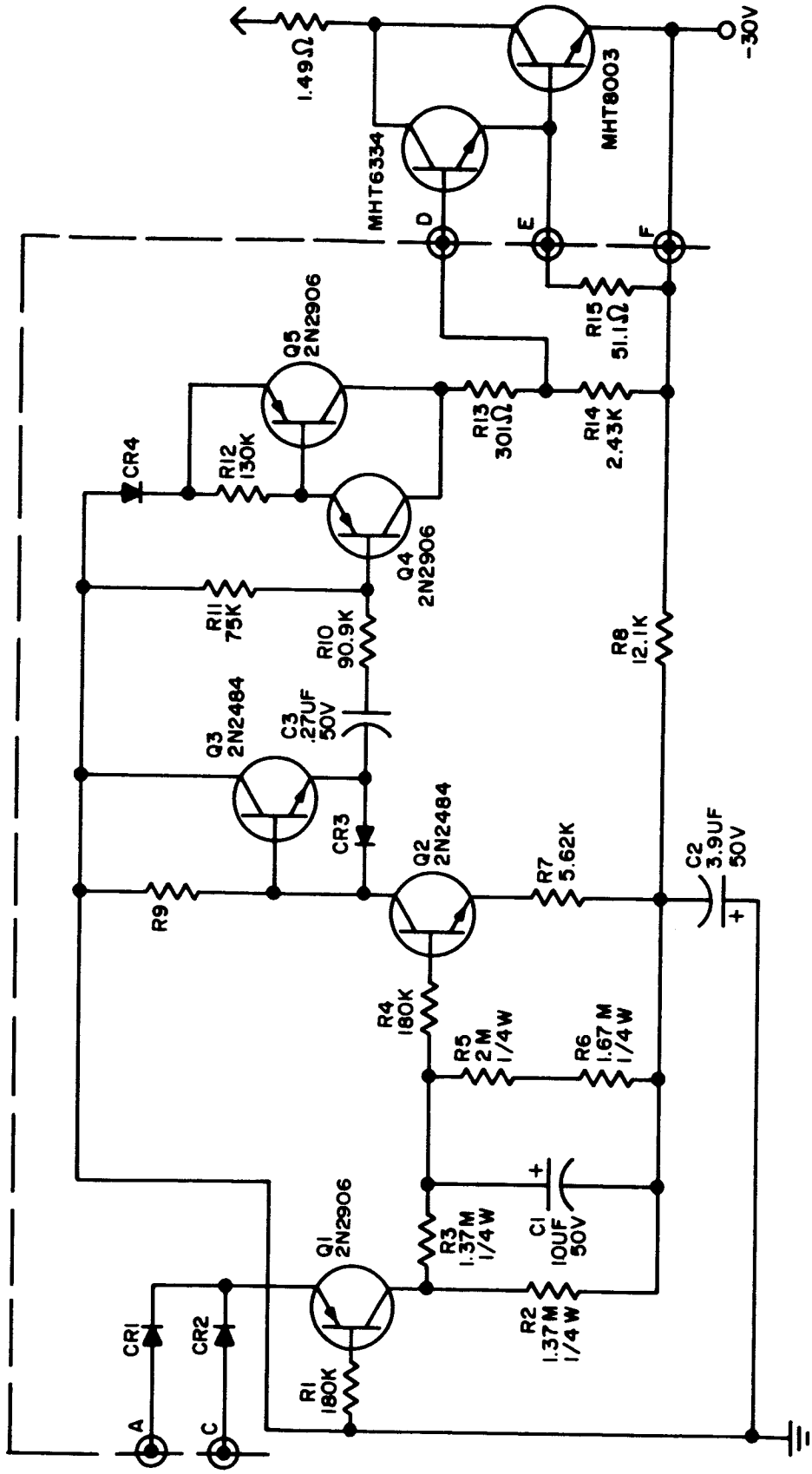


Figure 2.4.2-1. Squib Driver Schematic

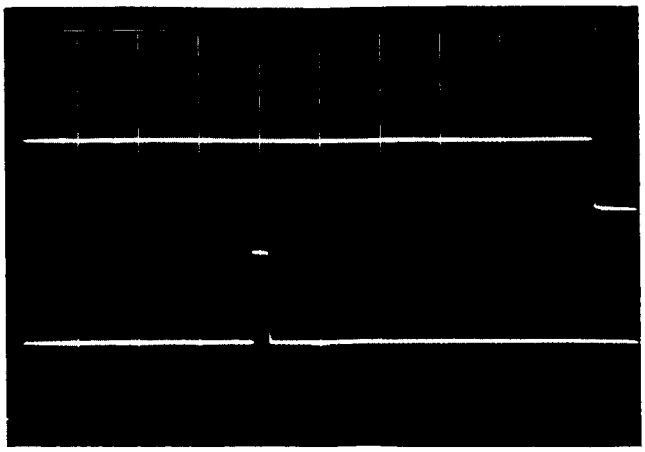


Figure 2.4.2-2. Oscilloscope of Preliminary Squib Driver Tests (Sweep Rate = 200 msec/cm)

2.4.2.3.3 Solenoid and Motor Armature Drivers

As can be seen from the schematics shown in Figures 2.4.2-3 and -4; these circuits are an extension of the command interface circuits with added stages of amplification. The output drive capability of the motor driver is about 1.5 amperes. Resistors R4 and R8 are used for current limiting and may be reduced to give some added design margin, if required, at a slight expense of pulsed power when the units are on. The output drive capability of the Solenoid Driver is about 10 amperes. Both circuits depend on the resistance of the load windings to limit the output currents. In both of these circuits, diodes are used at the outputs to quench the inductive stored energy of the load. The diodes were sized to take currents on the order of the peak load currents.

2.4.2.3.4 Motor (Field) Driver

Figure 2.4.2-5 shows the schematic of a bipolar transistor driver that will be used to drive 100ma through the field windings of a shunt motor with a reversible polarity, so that both directions of rotation can be obtained. There is a loss of 2 to 3 volts of the available 25 to 36 volt power supply in this type of driver circuit and the results of this loss with regard to motor performance must be established before the design can be finalized. The alternative to this transistorized driver, a DPDT latching relay, does not experience the additional voltage drop.

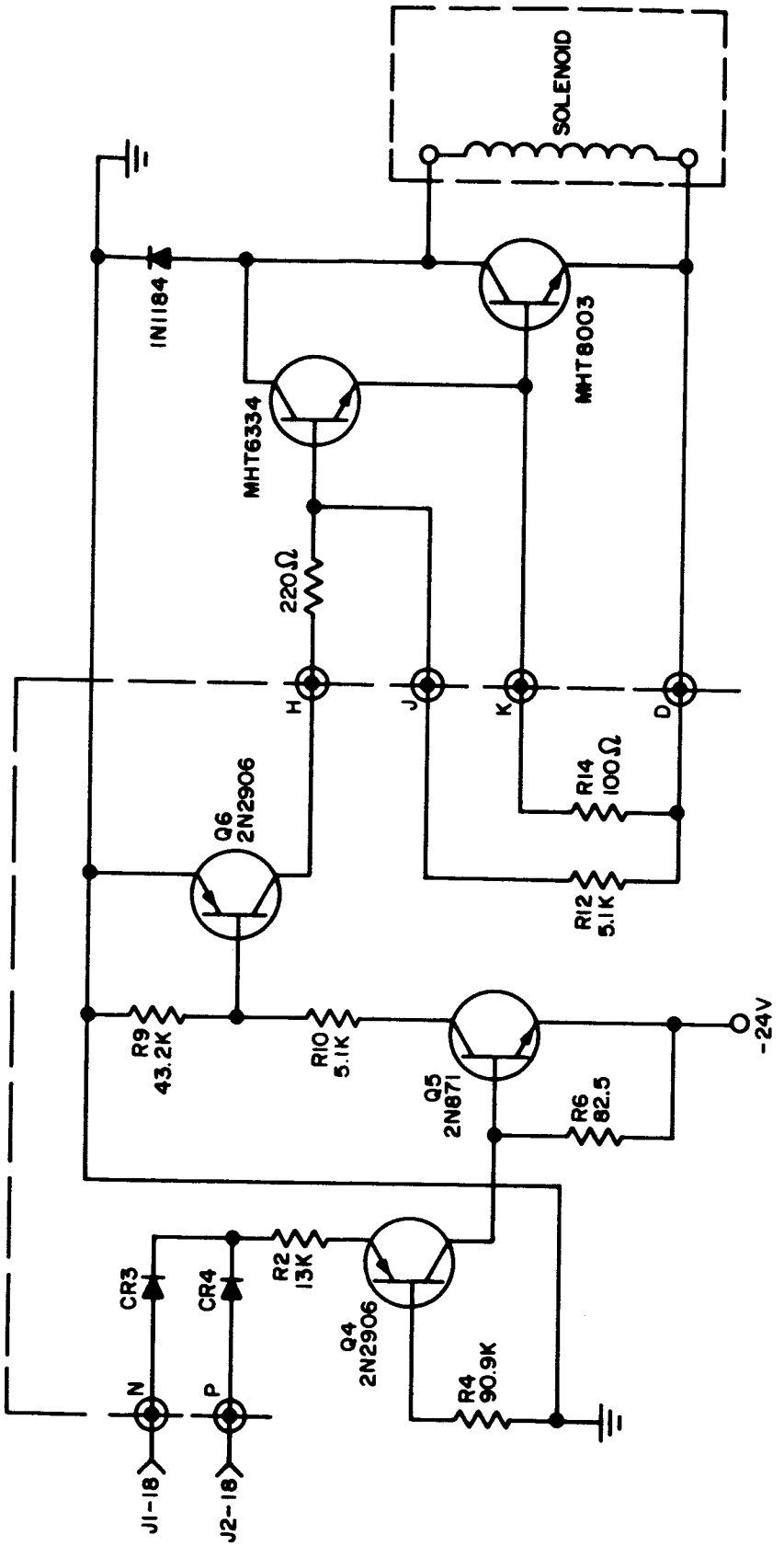


Figure 2.4.2-3. Solenoid Driver Schematic

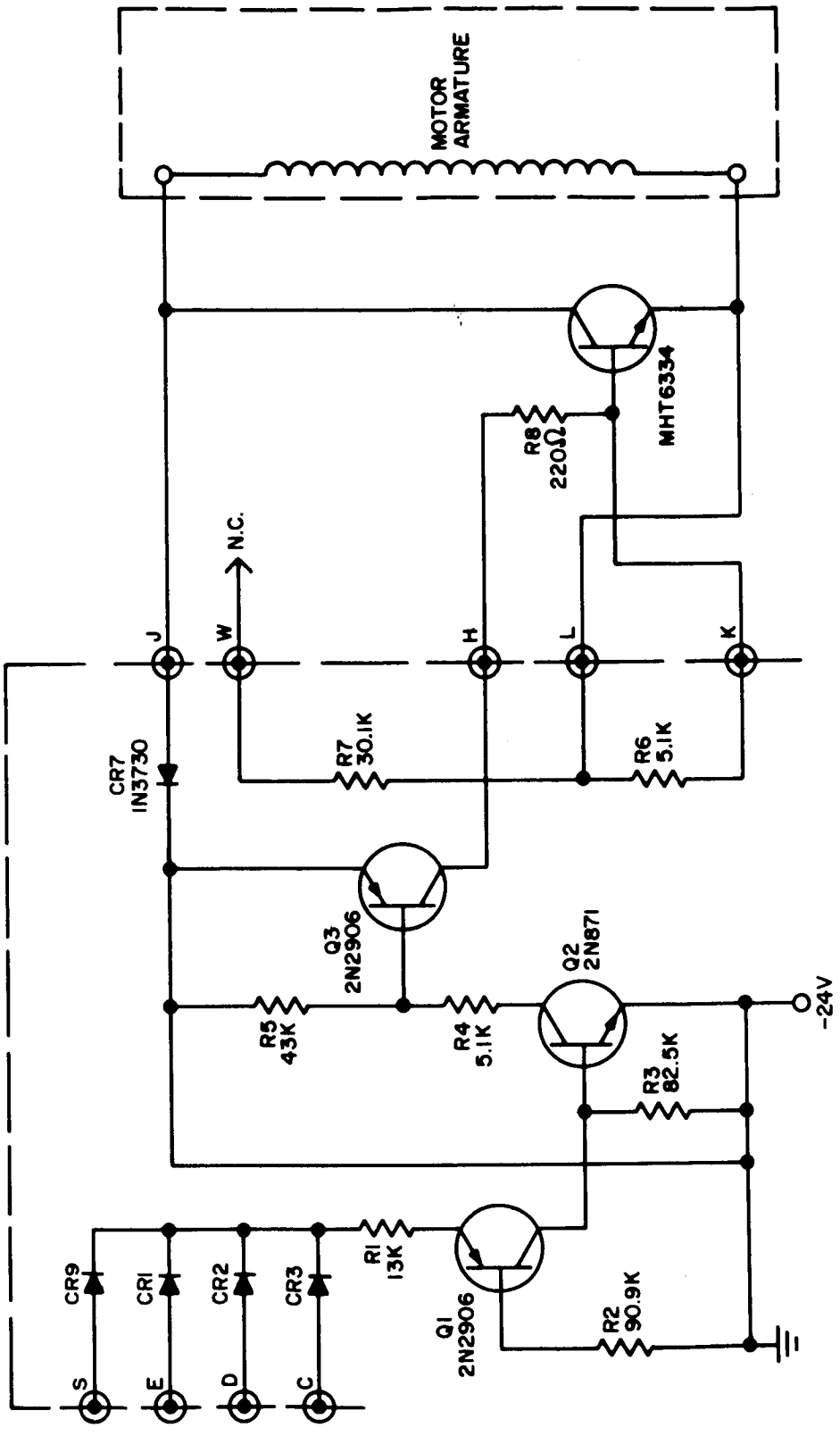


Figure 2.4.2-4. Motor Driver

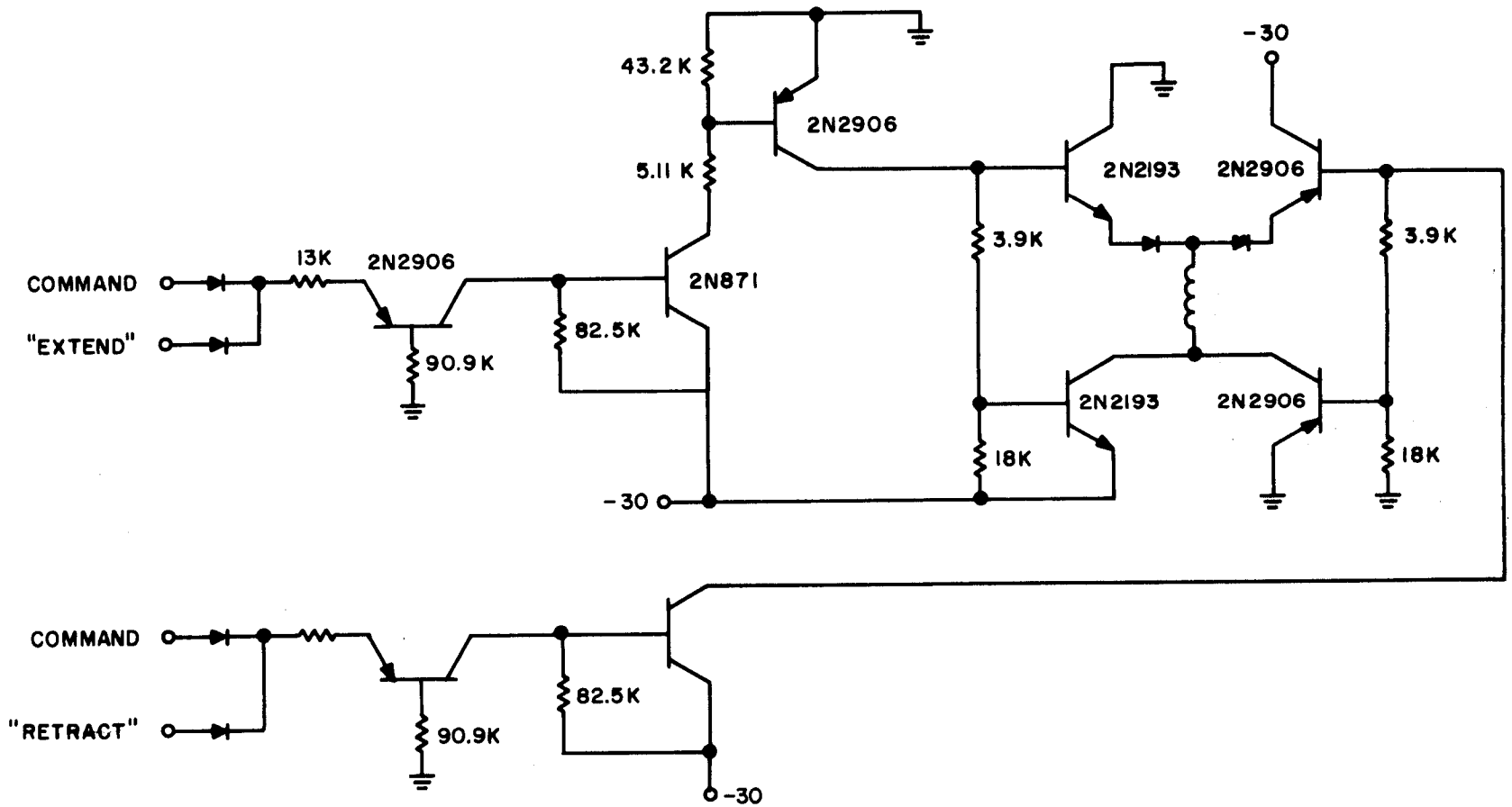


Figure 2.4.2-5. Motor Field Driver

2.4.2.3.5 Reference Power Supplies

The Power Control Unit generates a -5 volt reference power supply for certain telemetry functions and a -6 volt reference supply for thermistor temperature measurements. Both of these supplies make use of the -10 volt reference signals of the telemetry encoders to establish the diagnostic measurements relative to this source rather than to a separate, absolute voltage reference, e.g., a zener diode. Both supplies are identical except for the resistance divider networks establishing the reference voltage.

Refering to the schematic shown in Figure 2.4.2-6, it can be seen that two reference voltages inputs appear. The power supply output is designed to follow the most negative input, since either or both these input voltages may appear at the same time. Enough open loop gain is provided to reduce the closed loop output impedance to approximately one ohm. C1 was chosen to be a large enough value for open loop roll-off so as to prohibit closed loop oscillations. R18 in the output network is provided in the event analysis shows need for this resistor in designing against oscillations.

The inaccuracies inherent in the circuit are the temperature and lifetime tracking of the resistance divider networks, and the base-emitter junction drops of the differential transistor stages. Initial testing has shown performance accuracies of ±10 millivolts over the operating ranges of temperature and load conditions.

2.4.2.3.6 Video Switch

The Power Control Unit provides the mechanism to switch the output of the desired TV camera to the wide-band VCO in the satellite transponder. In order to accomplish this switching, a latching relay of the type used for power switching was tested for this application and determined to be completely satisfactory. Isolation between the inputs is 60 db or greater from d-c to 8 megacycles and insertion loss is less than 1 db from d-c to 8 megacycles. Tests were conducted at a signal level of approximately 0.25 volts rms across 75 ohms. As shown in Figure 2.4.2-1, this

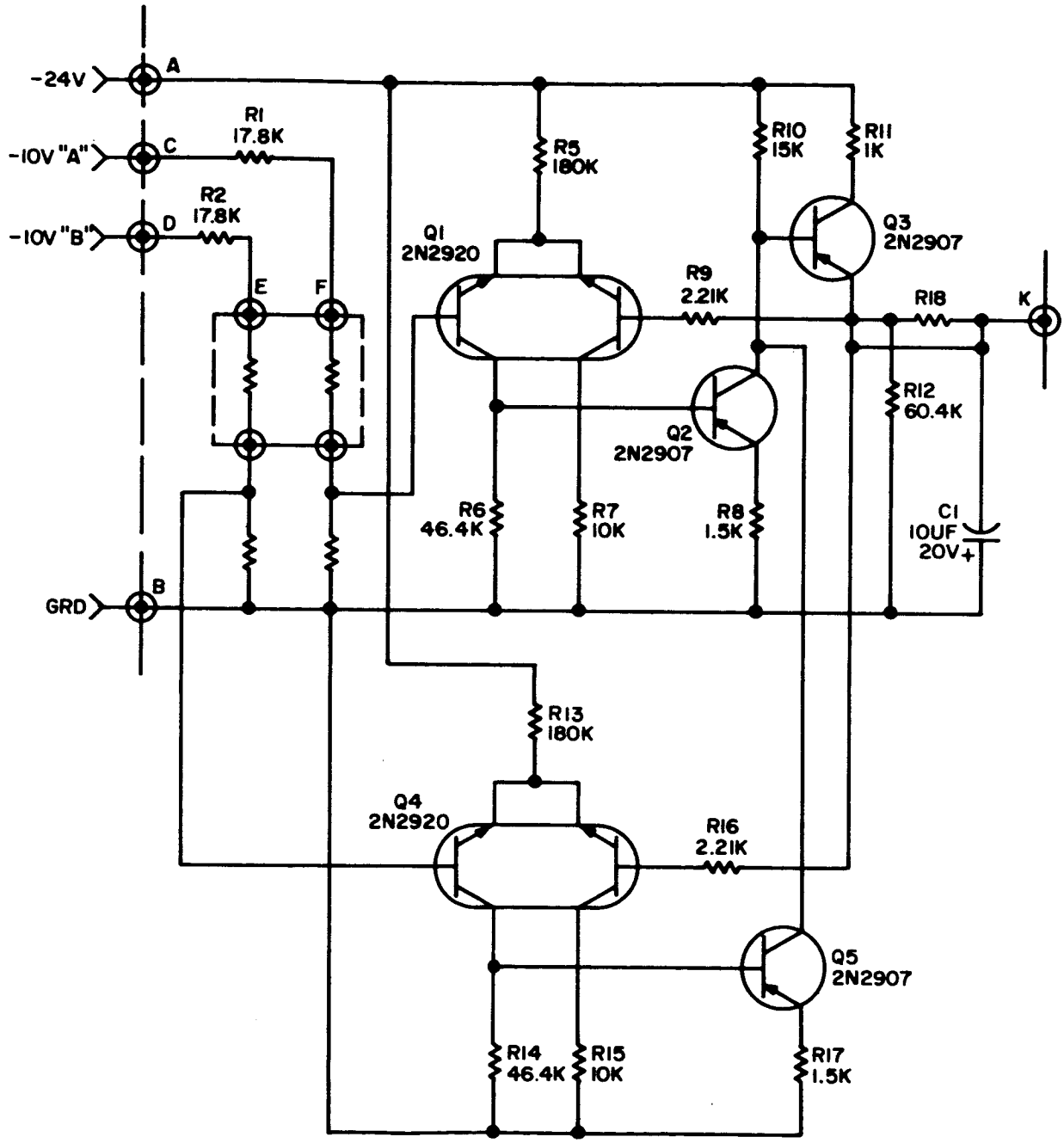


Figure 2.4.2-6. -5 Volt Power Supply

relay will be housed in a separate RF compartment of the PCU and have its power and control signal enter via feedthru type capacitors with the video signals coming in through miniature coaxial connectors.

2.4.2.3.7 D-C Current Sensors (See Figure 2.4.2-7)

These sensors are used for the diagnostic measurements of the motor currents. The sensor is a modification of a standard magnetic amplifier saturating core type sensor which has been used on other space programs at General Electric.

The average current in the secondary of T2 is theoretically equal to the current in the primary winding multiplied by the turns ratio. Errors from theory arise in the design due to:

1. Finite magnetizing current of core materials
2. Deviation from squareness of the cores
3. A-C input voltage and frequency variations.

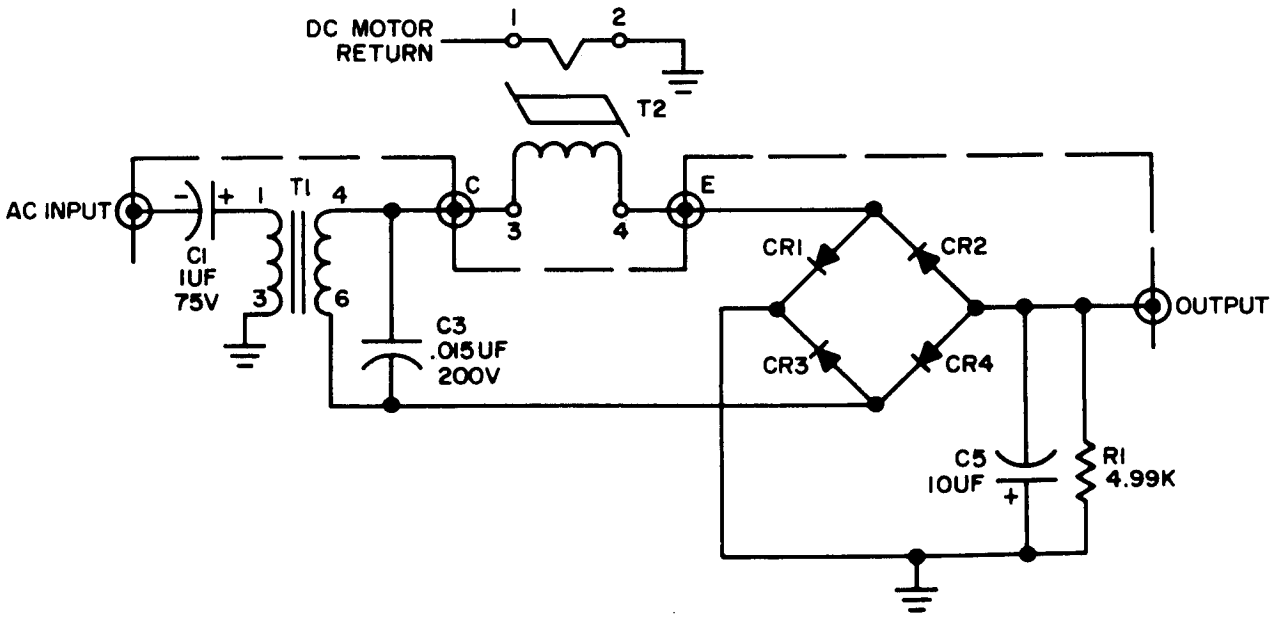


Figure 2.4.2-7. Current Sensor Schematic

Transformer T1 is used to couple the required a-c drive signal from an isolated source to T2. Empirical results with the breadboard show that the measurement inaccuracies should be less than ± 1% after initial calibration of the offset and linearity.

2.4.2.3.8 A-C Power Supply (See Figure 2.4.2-8)

The a-c power supply is required as a source to drive the d-c current sensor modules. In order to conserve power, it is gated to the on state only when one of the motors is being operated and the measurement is desired.

A positive signal (GND) will appear at the anode end of one of diodes CR1 thru CR10 when a motor drive command or timer input goes through one of the Motor Drive Modules. This signal turns on Q4 which supplies power to the free running multivibrator. Trickle current from -24 volts through R4 to keep Q1 turned on in standby assures starting of the multivibrator. Q3 is a buffer output which along with bypass CR15 present a low driving impedance for the two current sensor circuits.

2.4.2.3.9 Ladder Switch

The Ladder Switch shown in Figure 2.4.2-9 is a transistorized single-pole, double throw switch whose output is either -5 volts or ground. It is used for event monitoring where only a single-pole, single throw switch is available, to convert this type output to that which is necessary for driving a digital to analog combining network.

The input will accept either a signal which goes directly to ground in its closed position or through a limiting resistor to the -24 volt regulated or -30 volt unregulated bus. In the former case R6 is connected to the input point while in the latter it is left unused.

2.4.2.4 Mechanical Design

Conceptual layouts have been completed, based upon preliminary schematic information. The design approach utilizes standard GE-MSD cordwood modules, plugged into printed circuit boards. The boards will be foam encapsulated and compression packed.

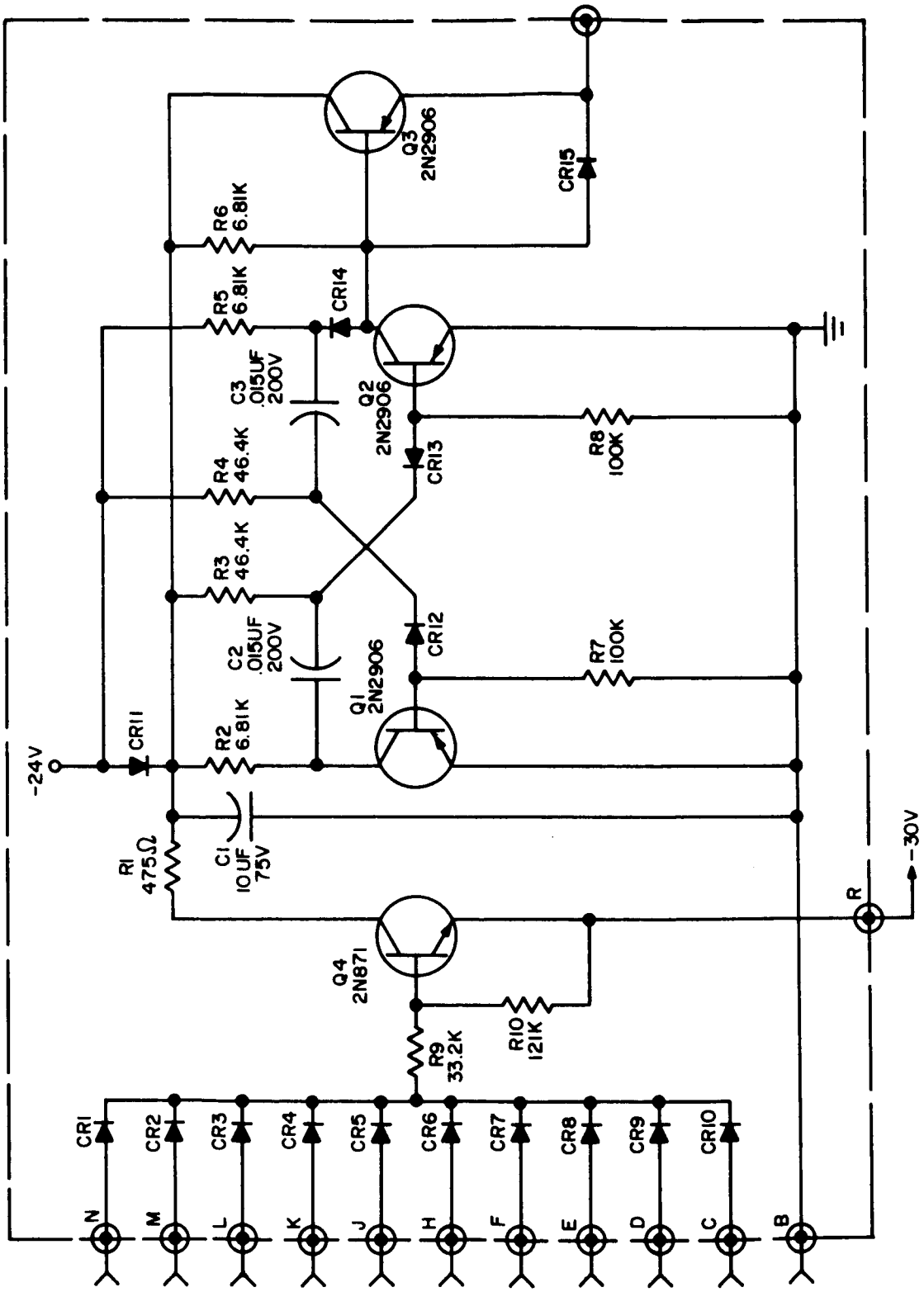


Figure 2.4.2-8. A-C Power Supply

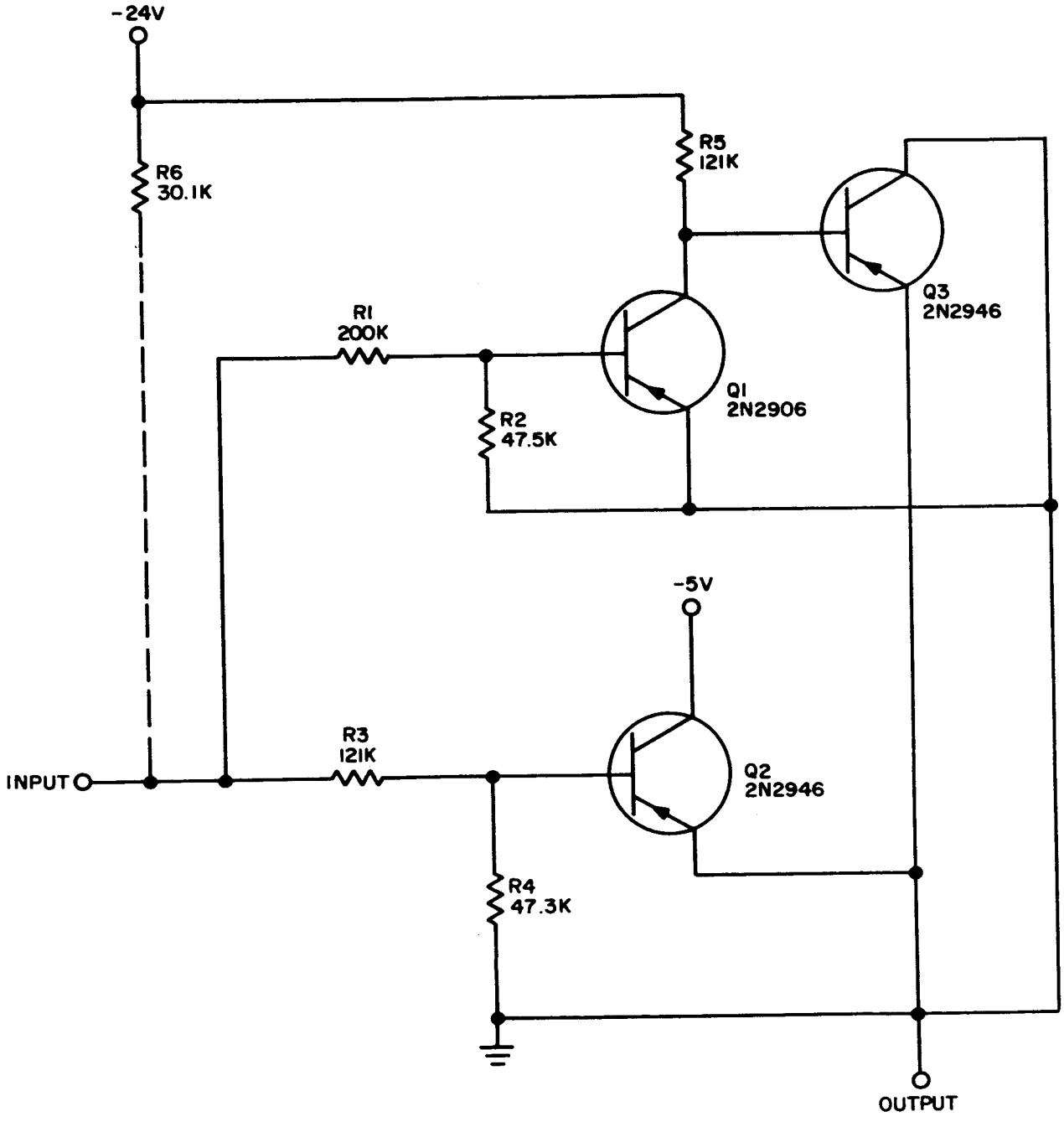


Figure 2.4.2-9. Ladder Switch

Two envelopes were developed, one conforming to an outline drawing received from Hughes.

Five module types have been detailed and released for production of engineering models. Six others have been designed to the layout stage. These eleven module types represent all of the circuits presently defined in the PCU.

2.4.2.4.1 Module Design

This method of packaging parts for spacecraft launch and orbit environment has been standard in General Electric — MSD for more than three years. Over one million failure free module hours of testing have been logged, providing a high level of confidence in the material and processes used. The module is designed to be a rugged, reliable, replaceable unit.

2.4.2.4.2 Interconnection

Due to the extremely high density of connections in the PCU as well as for lightweight and ruggedness, printed circuit boards are used to mount the modules, and to provide the intermodule connections. Six printed circuit boards are used. Parts which are too large to be conveniently located in modules, such as power transistors, and transformers, are wired and attached directly to the circuit board. Each of the circuit boards terminates in a connector, carrying 70 to 80 pins. The mating connectors are mounted in a harness raceway assembly which carries the outgoing wires to the eight 50-pin interface connectors on the box.

2.4.2.4.3 Mechanical Assembly

The harness is secured in the raceway by lightweight foam encapsulant, applied as a final assembly step. The printed circuit boards are riveted in "picture frame"

hangers which are secured to the box by floating anchor nuts. A visco-elastic damping foam is placed between the circuit boards to reduce the amplitude response of the assemblies during vibration.

The box itself is conceived as a brazed assembly of aluminum plates, accessible from two sides by means of removable covers. An R-F proof enclosure to provided for the video relay. Mounting flanges and connectors are located as shown in the Hughes outline drawing No. X-297593.

2.4.2.4.4 Potential Problems

Nearly 400 wires will be required to run in the harness raceway. The mass of wire which must be handled may create severe problems in assembly. Consideration will be given to the use of preformed flat cabling.

2.4.2.4.5 Breadboard Construction

The latest breadboard model is shown partially completed in Figure 2.4.2-10. The top shelf contains the power transistors for the motor, solenoid, and squib driver circuits, and the enclosed relay for switching the video outputs of the TV Cameras. Other shelves contain, in descending order, the current sensors and reference power supply; temperature detector resistors, event ladders and ladder switch circuits; motor and solenoid command circuits; relay driver command circuits; squib, torquing coil driver circuits and frame sync buffer amplifiers. Inputs to the separation timer are wired to the left side of the second shelf, but no logic circuits have been built up, since the requirements are not yet firm.

The Power Control Unit Component Test Rack for the breadboard and engineering models is shown in Figure 2.4.2-11.



Figure 2.4.2-10. Power Control Unit Breadboard

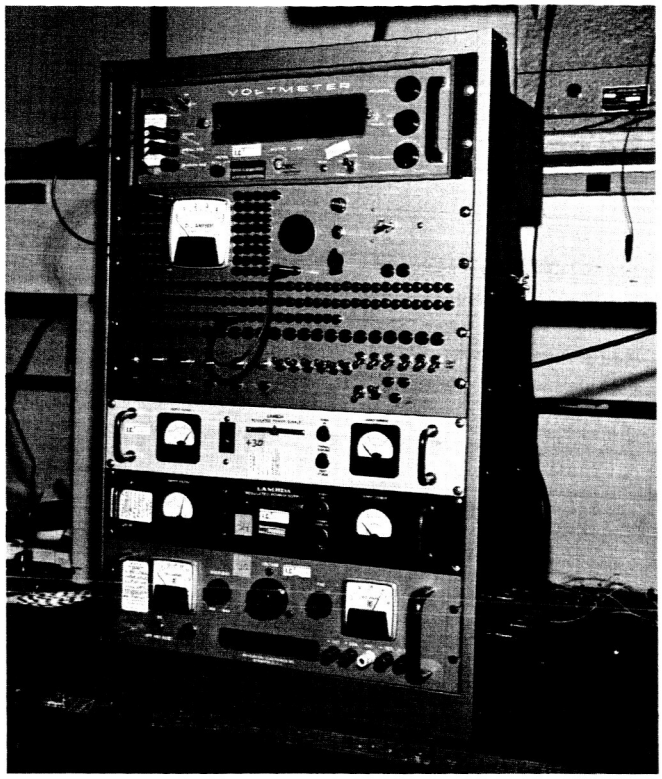


Figure 2.4.2-11. PCU Test Rack

2.4.3 SOLAR ASPECT SENSOR

During finalization of the Solar Aspect Sensor GE Component, Specification, SVS-7306, several questions arose regarding the performance of the sensor. The three most important questions were:

1. Degree and source of cross-coupling of the geometrically orthogonal detector eyes,
2. Maximum error to be expected in the sun direction measurement, and
3. Possible false triggering caused by sunlight reflected from the earth.

The first of these problems was investigated by analytical means and found to be quite strong for measurements of angles not in the plane of the detector eye slit and the normal to the eye. It was then calculated that the error in the measurements of the angles actually telemetered ranges from a minimum of 0.48 degree to a maximum of 1.3 degrees. The complete analysis of the first two questions is given in Appendix C of this report.

The influence of the earth-shine on the performance of the Solar Aspect Sensor has also been investigated analytically.

2.4.3.1 General Description of the Problem

A solar aspect system with full spherical coverage will have both the sun and the earth in its field of view at the same time. The system must, therefore, be able to distinguish between the two.

The proposed solar aspect system consists of five detector units with overlapping fields. One of these detectors is selected by the electronic unit and its readings are the only information processed. Detector selection is made by comparison of signals from "AGC" cells which are part of each detector. The detection sensitivity is at least 1 degree, which corresponds to 3.3% of the signal at 64 degrees.

Interference with sun sensor operation in this case would mean that the flux received from the earth is so nearly equal the flux received from the sun, in a worst case arrangement that the detector facing the earth would be selected. Erroneous information would then be presented to the telemetry.

Analysis of the problem, therefore, consists of establishing the magnitude of both the earth-shine flux and the solar flux at the AGC cells. The worst case exists in the lower (6000 nm) orbit and when one detector is oriented parallel to the earth terminator while the other detector is inclined 64 degrees to the sun.

The analysis shows that the solar flux received at the AGC cell is eight times the flux received due to earth shine. False detector selection can, therefore, be ruled out.

2.4.3.2 Analysis

A. Dennison (Item 5 of Section 4) formulates the problems as follows:

$$dF_c = \frac{B_E \cos \alpha'_E \cos \alpha'_c}{\rho'^2} dA_E \, dA_c \qquad (1)$$

where

F_c = the luminous flux at the cell due to the brightness B_E of an infinitesimal earth area dA_E

dA_c = the infinitesimal cell area being illuminated

ρ' = the distance from dA_E to dA_c

$\cos \alpha'_E = \vec{\eta}_E \cdot \vec{\rho}'$

$\cos \alpha'_c = \vec{\eta}_c \cdot \vec{\rho}'$

The geometry is shown in Figure 2.4.3-1. For a small, planar cell $\rho' = \rho$, $\alpha'_E = \alpha_E$, $\alpha'_c = \alpha_c$, where the unprimed quantities refer to the center of the cell.

Equation (1), therefore becomes

$$dF_c = \frac{B_E \cos \alpha_E \cos \alpha_c}{\rho^2} dA_E \, dA_c \qquad (2)$$

$$dF_c = \frac{B_E A_c \cos \alpha_E \cos \alpha_c}{\rho^2} dA_E$$

(The integral over the cell can be performed since α_E, α_c and ρ are independent of the coordinates of dA_c.)

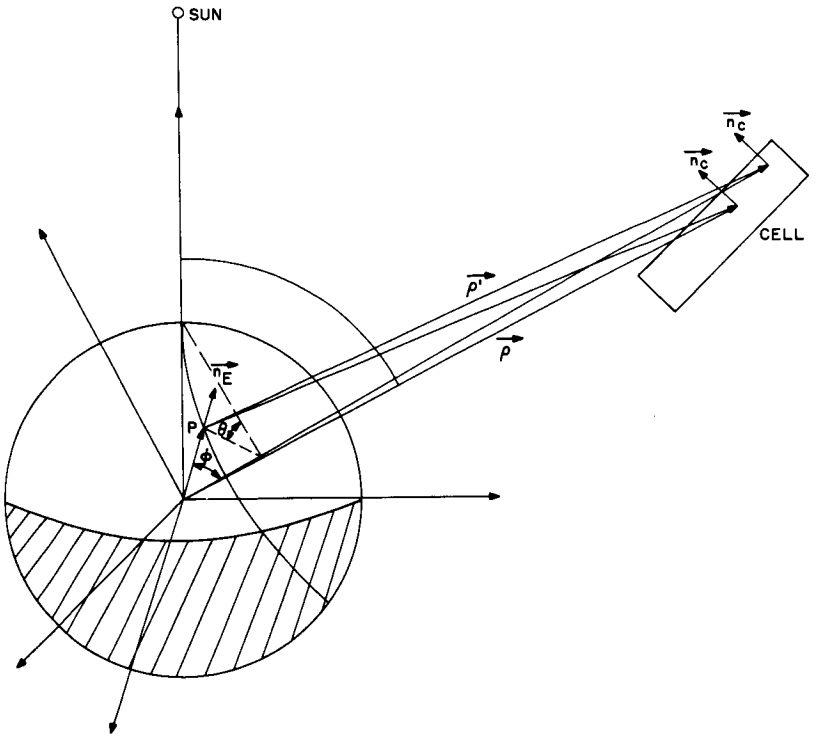


Figure 2.4.3-1. SAS Geometry

Rewriting (2) in terms of E_c, the illumination of the cell,

$$dE_c = \frac{B_E \cos \alpha \, E \cos \alpha_c}{\rho^2} \, dA_E \tag{3}$$

The brightness, B_E, of dA_E due to the sun is defined in terms of E_E, the illumination, as

$$B_E = \frac{a}{\pi} E_E \quad (a = \text{earth's albedo}) \tag{4}$$

From Figure 2.4.3-2 and the definition of E_E,

$$E_E = \frac{\pi B_s}{R'^2} \cos \sigma'_E \tag{5}$$

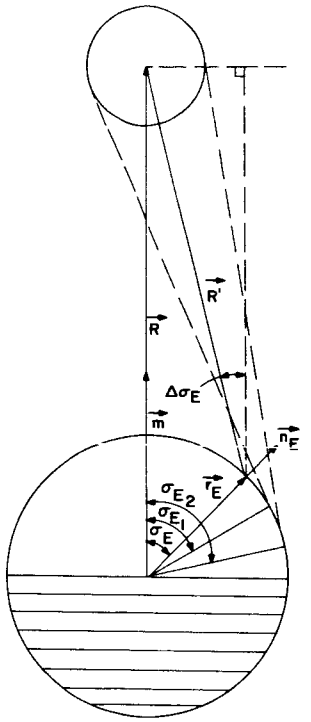


Figure 2.4.3-2. Brightness Definition

where

B_s = brightness of the sun (assumed uniform over the surface of the sun)

R' = distance to the sun

$\cos \sigma'_E = \vec{\eta}_E \cdot \vec{R}'$

Equation (5) holds only when dA_E is illuminated by the entire sun. This condition is satisfied for $\sigma_E \leq \sigma_{E_1}$ (see Figure 2.4.3-3). However, $E_E = 0$ for $\sigma_E \geq \sigma_{E_2}$, such that the area of concern is $\sigma_{E_1} < \sigma_E < \sigma_{E_2}$. $\sigma_{E_2} - \sigma_{E_1} < 0.6^o$ because of the dimensions involved, so that it can be assumed with little error that $\sigma_E \leq \sigma_{E_1}$.

From Figure 2.4.3-2 is is evident that $\sigma'_E = \sigma_E + \Delta\sigma_E$. But $\Delta\sigma_E$ is at most the half-angle the earth subtends as seen from the sun, $\Delta\sigma_E < 8''$. If the sun is not considered a point sounce, $\Delta\sigma_E \approx 1/4^o$. In either case we, therefore, assume $\sigma'_E \approx \sigma_E$.

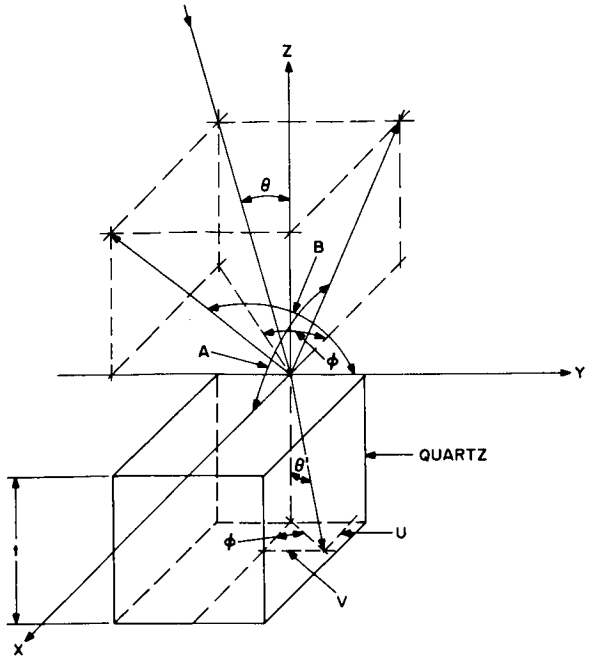


Figure 2.4.3-3. Infinitesimal Earth Area (dA_C) Illuminated by Entire Sun

Finally, $(R-r_E) \leq R' < R$, but $r_E < 10^{-4}$ R, and we can safely say that

$$R' \approx (R-r_E)$$

Then

$$E_E = S \cos \sigma_E$$

S = illumination due to the sun at the earth's surface (zero air mass)

$$B_E = \frac{a \cdot S}{\pi} \cos \sigma_E \tag{6}$$

Equation (3) becomes then

$$dE_c = \frac{a\,S}{\pi} \frac{\cos \alpha_E \cos \alpha_c \cos \sigma_E}{\rho^2} dA_E \tag{7}$$

where

$$\cos \sigma_E = \vec{n}_E \cdot \vec{m}$$

$$dA_E = r_E^2 \sin \phi \, d\theta \, d\phi$$

or

$$E_c = \alpha S F$$

$$F = \frac{r_E^2}{\pi} \int_{\theta} \int_{\phi} \frac{\sin\phi \cos\sigma_E \cos\alpha_E \cos\alpha_c}{\rho^2} d\phi \, d\theta \tag{8}$$

The functions under the integral in F can be expressed as follows:

$$\cos\alpha_E = \frac{r\cos\phi - r_E}{\sqrt{r^2 + r_E^2 - 2rr_E\cos\phi}}$$

$$\cos\alpha_c = \frac{r\cos\beta_c + r_E\left[\sin\phi \sin\beta_c \cos(\theta - r_c) - \cos\phi \cos\beta_c\right]}{\sqrt{r^2 + r_E^2 - 2rr_E\cos\phi}} \tag{9}$$

$$\cos\sigma_E = \cos\phi \cos\sigma_c + \sin\phi \cos\theta \sin\sigma_c$$

Reference 5 proceeds with the numerical integration of Equation (8) for various cases. However, the interest is in the maximum value of F only.

For this case $\beta_c = 0$, $r_c = 0$, $\sigma_c = 0$, $\frac{r_E}{r} \le \cos\phi \le 1$, $0 \le \theta \le 2\pi$ and substituting these into equations (9).

$$F_{MAX} = \frac{r_E^2}{\pi} \int_0^{2\pi} \int_0^{\cos^{-1} r_E/r} \frac{\sin\phi \cos\phi \left(r - r_E\cos\phi\right)\left(r\cos\phi - r_E\right) d\phi \, d\theta}{\left(r^2 + r_E^2 - 2rr_E\cos\phi\right)^2} \tag{10}$$

Reference 6 gives the value of the integral (10) as

$$F_{MAX} = 2r_E^2 \left[\frac{\cos\phi}{4rr_E} - \frac{\left(r^2 - r_E^2\right)^2}{8r^2r_E^2\left(r^2 + r_E^2 - 2rr_E\cos\phi\right)}\right]_{\cos\phi = 1}^{\cos\phi = r/r_E}$$

$$F_{MAX} = \frac{r_E^2}{r^2} = .13 \quad \text{For } r - r_E = 6000 \text{ n.m.} \tag{11}$$

Using a = .40 and substituting into equation (8).

$$E_c = .05\ S \tag{12}$$

The illumination due to the sun inclined at 64^o,

$$E_s \approx S\tau \cos 64^o \tag{13}$$

τ = added reflection losses at the surface due to the inclination.

$\tau \cos 64^o \approx .40$

$$E_s = .40\ S \tag{14}$$

The flux incident on the two cells is then,

$$F_s = E_s A_s$$

$$F_E = E_c A_E$$

where A_s is the effective area of the sun oriented cell and A_E the effective area of the earth oriented cell.

It is apparent from the physical situation that

$$A_s = A_E = WL,$$

for W = slit width,

L = width of the cell,

since the earth subtends only an angle of 42^o as seen from 6000 n. m.

The flux on the sun oriented cell is then

$$F_s \approx .40\ S\ A_s$$

$$\approx .40\ \frac{E_c\ A_E}{.05}$$

$$\approx 8\ F_E$$

2.4.4 TV CAMERA SUBSYSTEM

2.4.4.1 Summary

Investigation of the TV Camera Subsystem and boom target characteristics continued throughout the reporting period. Extensive consideration and analysis was devoted to trade offs associated with slow scan. Despite the distinct advantages of better resolution and signal-to-noise ratio of a slow-scan system, the modifications required to existing ground station receiving and recording equipment have dictated that the TVCS design remain with the standard television scan rates and format.

The selected vendor, Lear Siegler, revised his cost quotation based on the use of Hughes Aircraft Company high reliability approved parts. However, a recent decision to use commercially available parts with selection after a shortened burn-in period is presently being incorporated into the TVCS component specification and work statement, prior to obtaining a new quotation.

Tests were made in the laboratory of several sample target materials to determine the reflection properties of scaled targets against various backgrounds. Other tests included the insertion of wideband noise into the video information to determine the effects of a reduced signal-to-noise ratio caused by the communications link.

A more detailed discussion of these and other studies is contained in the following sections.

2.4.4.2 Standby Filament Power

In response to a customer inquiry, consideration has been given to the advantages of keeping on the filament heater power in the vidicon tube of the TV camera. Three advantages can be ascribed to this procedure:

1. The TVCS is available immediately on demand without an approximate 30 second delay for vidicon tube warm-up.
2. Heat dissipated in the vidicon would tend to keep its temperature closer to optimum during cold ambient environment.
3. Less power is switched when TV camera is activated.

On the other hand, four disadvantages accrue:

1. Continuous sensor power is increased.
2. Heat dissipated in the vidicon would tend to cause the vidicon to exceed its optimum temperature during hot ambient environment.
3. Life of the heater is expended without actual use of the TV camera.
4. The extra power consumed provides no increase in performance.

Considering the advantages in order: (1) there is no known need to provide for TV camera operation quicker than the 30-second warm-up specified in SVS-7310, provided that the heater power can be turned on at least 30 seconds prior to separation, (2) the heater is remote from the critical temperature area of the faceplate and its power is not very effective in warming the faceplate over the whole cold temperature range, (3) the extra power switched is a minor percentage of the total power.

On the other hand, the power wasted in keeping the filaments energized compares to the total power inversely as the duty cycle (16%). At times when one TVCS is facing the sun and cannot be used, a greater risk of overheating the vidicon ensues if the filament power is maintained on. While there is ample life in the heaters to perform during the required mission life, there are still, according to reliability theory, only a finite number of hours of operation obtainable. Lastly, according to the TVCS vendor the performance of the TV camera is neither enhanced nor degraded by maintaining continuous filament power on the vidicon.

It is concluded that unless operation of the TVCS is required immediately on demand, the application of continuous filament power on the vidicon is unnecessary and not recommended.

2.4.4.3 A Slow Scan Version of the TV Camera Subsystem

Optimization of the TVCS requires some reduction in overall video bandwidth without a corresponding reduction in realizable resolution after data reduction. The several variables that are affected by the equipments in the communications link from the TV camera to final ground-based data reduction have been given much consideration and the range of slow scan parameters can now be defined. This range of parameters is based upon the following objectives:

1. Readout of boom angular position to within ±2 inches at 100 feet after final data reduction.
2. Utilization of a video bandwidth of not less than 2.5 mc to modulate the HAC transponder.
3. A received down link signal-to-noise ratio at the receiver output of at least 38 db.
4. Not more than 10% degradation of resolution in recording a permanent copy of a TV frame.

In order to meet these objectives, characteristics of the system must be specified. At present, the following characteristics are either calculated or estimated to be necessary, based upon discussions with vendors and experts in data reduction.

The required number of vertical lines is based upon the relation

$$V = \frac{Rv\,(1+1/Kv)}{\eta}$$

η = Recording resolution efficiency - 90%

Kv = vertical flyback velocity ratio - 12

V = total scan lines

Rv = required vertical resolution - 450

With Rv, η and Kv as listed, total lines must be 542 to obtain 450 line resolution in the vertical direction. This value is higher than that mentioned in Section 2.4.5.2 of the First Quarterly Report due to η and assumes that the boom position point can be identified with one vertical line, as was done previously.

To obtain 450 line resolution in the horizontal direction, the video bandwidth can be specified. It is noted that the 450 line horizontal resolution which is being specified is equal to the vertical resolution. The bandwidth is,

$$f_{max} = \frac{\frac{w}{h}\, mk\, f\, n^2}{2K} \times \frac{1+\frac{1}{kh}}{1+\frac{1}{kv}}$$

where:

f_{max} = video bandwidth

w/h = ratio of raster width to height - 4/3

m = ratio of horizontal to vertical resolution - 1.0

k = utilization ratio - 0.9

f = frame rate (fps)

n = total number of lines - 542

kh = horizontal velocity factor - 7

kv = vertical velocity factor - 13

K = data reduction efficiency - 0.9

Leaving frame rate (f) unspecified, it is seen that

$$f_{max} = 0.2065\, f \quad (mc).$$

Required bandwidth is plotted in Figure 2.4.4-1 as a function of frame rate. This graph shows that a 30 frame per second rate means a required video bandwidth of 6.1 mc. Furthermore, since present NASA ground equipment is limited to 4 mc, a frame rate below 20 fps is needed.

Before selecting a frame rate and video bandwidth, the received signal-to-noise ratio as a function of video bandwidth must be examined to be sure it is adequate. Figure 2.4.4-2 is a graph of signal-to-noise ratio at the output of the ground station receiver versus video bandwidth based on the parameters and calculations given in Appendix F. Signal-to-noise is defined there as peak signal-to-rms noise. The graph of Figure 2.4.4-2 is based on a 40-foot dish, 90^{o}K noise temperature, 5^{o} elevation angle and clear weather. It is noted that 5^{o} elevation is not usable in bad weather and the loss at 5^{o} compared to zenith is 3.1 db.

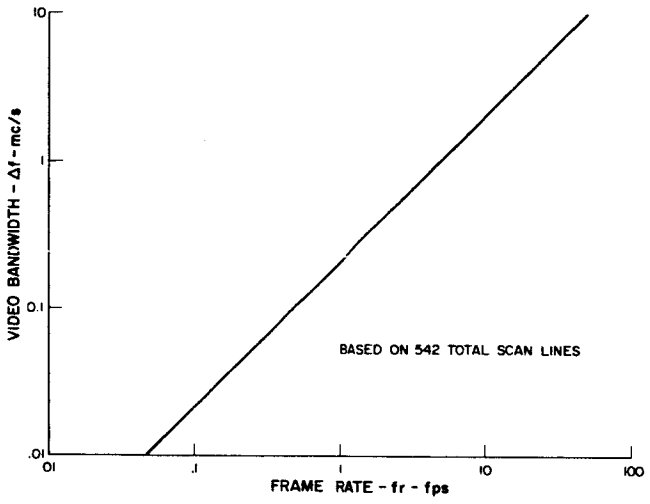


Figure 2.4.4-1. TVCS Video Bandwidth (mc) versus Frame Rate (fps)

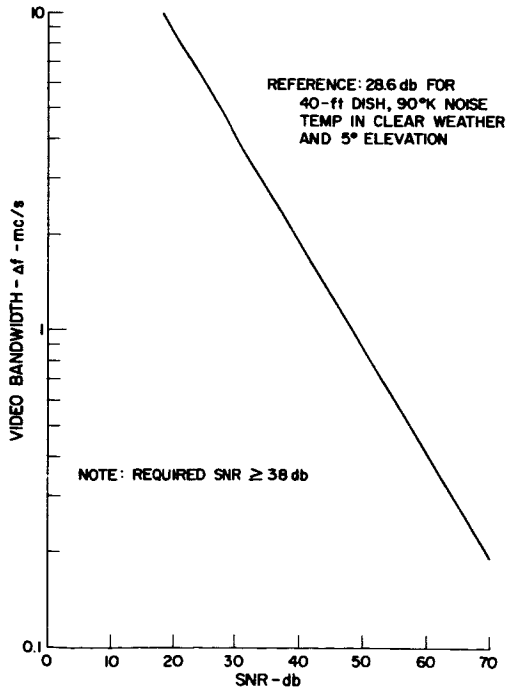


Figure 2.4.4-2. TVCS Received Signal/Noise

The required signal-to-noise ratio is now stated as 38 db or greater. This is considered a minimum needed so as not to allow a further degradation in resolution due to a noisy signal. It would also be a reasonable engineering approach to allow a degradation due to noise and then require a correspondingly wider bandwidth to recover the anticipated loss. One further comment is that the CCIR recommendation here would be for a minimum of 45 db (unweighted) signal-to-noise ratio. In summary, the required minimum SNR is approximately 4 db below CCIR recommendations at zenith and 7 db below them at 5^{o} elevation.

From Figure 2.4.4-2 the maximum bandwidth allowed to obtain 38 db signal-to-noise is 2.2 mc. Referring to Figure 2.4.4-2, a bandwidth of 2.2 mc is available with the proposed slow scan raster of 542 lines if the frame rate is slightly less than 11 frames per second.

The exact number of lines and the exact frame rate cannot be as arbitrarily implemented as could be inferred from the analysis above without considerable complication to the circuits. However, with these as a basis, the exact values can be determined. The standard scan of the camera presently considered for use has a 31.5 kc master oscillator. This frequency is divided down by frequency dividers in the ratios 7, 5, 5 and 3 to generate 525 lines interlaced at 60 fields per second and 30 frames per second. In selecting the slow scan parameters it can be shown that by using a 5.4 kc master oscillator and by dividing in the ratios 6, 6, 5, 3 there will be 540 lines, non-interlaced generated and the frame rate of 10 frames per second is also realized. The changes in the sync generators of the camera are then simply a change of counting ratio from 7 to 6 and from 5 to 6 in the first two frequency dividers. In addition, the slight resolution improvement of non-interlace is provided.

The possible choices of the number of scan lines that are applicable to give the required resolution and which at the same time do not require extensive redesign by the TVCS vendor are examined according to the following reasoning. Frequency dividers for standard 525 scan lines are in the ratios 3, 5, 5, 7. Other possibilities for an odd number of scan lines are:

Ratios	Scan Lines
3, 3, 5, 5	225
3, 5, 5, 5	375
5, 5, 5, 5	625
3, 5, 7, 7	735

and for an even number of scan lines are:

3, 5, 5, 6	450
3, 4, 6, 7	504
3, 5, 6, 6	540
4, 4, 5, 7	560
4, 4, 6, 6	576
3, 4, 7, 7	588
3, 5, 6, 7	630

It is noted that for interlace, an odd number of lines is a practical requirement. For non-interlaced scan any number of lines can be used. It has been established that a greater number of lines than 525 is desirable to allow for degradation due to data reduction. Since the current design divides the frequency between 3 and 7 times per divider stage, and since it uses only four stages, these become the conditions for minimal circuitry changes. As the table shows, the choice of 540 lines requires a change in two dividers: i.e., one of the x5 dividers must increase its count to x6, and the x7 divider must decrease its count to x6. Changing two dividers by one count each represents a least change to the frequency divider system and may require only circuit adjustment. The only other changes anticipated are a reduction of master oscillator frequency from 31.5 kc to 5.4 kc, and correction of coupling time constants throughout, both of which are inevitable when frame time is reduced.

The use of a slower scan has been discussed with representatives of the proposed vendor of the TV Camera Subsystem, and it was determined that a frame rate of 10 fps does not require use of the shuttering technique and is not a major change to the component as quoted.

In conclusion, the parameters affecting the ultimate performance of the TVCS have been analyzed and it has been determined that the optimum raster should contain 540 lines and have a frame rate of 10 frames per second. The General Electric Company therefore recommends to NASA/GSFC that the TV Camera Subsystem operate at a frame rate of 10 frames per second, to take advantage of the increased resolution and reduced video bandwidth without a concomitant increase in size, weight or power.

2.4.4.4 Available Readout Accuracy of TV Camera Subsystem

The readout accuracy of boom position after data recording at the ground station has been estimated based upon the concept of equivalent video bandwidth. The principal effect is upon the horizontal readout accuracy since the vertical readout accuracy is largely determined by the number of active scan lines.

The vertical readout accuracy at the camera was previously determined to be 2.1 inches at 100 feet. Allowing a 10% deterioration during data recording the vertical readout accuracy becomes 2.3 inches.

The horizontal readout accuracy is a function of the overall effective video bandwidth. An adequate (30 db) signal-to-noise ratio is tacitly assumed. For a 5-mc overall bandwidth, the horizontal readout accuracy would be 3.75 inches. However, the overall bandwidth is a function of the bandwidth of the separate band-limiting stages through the system. These are approximately identified as follows:

TV Camera	5.6 to 8 mc
HAC Transponder	2.5 to 5 mc
Ground Tape Recorder	4 to 4.3 mc

In addition, an estimated 10% deterioration in recorded data reproduction should be provided for. Certain comments are pertinent about these video bandwidths. The TVCS component specification calls for 8 mc bandwidth. However, if HAC parts

must be used it is likely that a good trade in performance will require a reduction in video bandwidth at the camera. The vendor has already indicated 5.6 mc as a minimum consistent with other requirements. There remains no written input as to the bandwidth of the HAC transponder. 2.5 and 5 mc are the extremes reportedly suggested by Hughes. Ground tape recorders are rated between 4.0 and 4.3 mc according to NASA/GSFC.

The two extreme cases will be considered. For the optimistic case the video bandwidths are 8, 5 and 4.3 mc respectively. Assuming the individual responses are down 3 db at these frequencies, the overall response is 3.85 mc, and 3.46 mc with a 10% deterioration for reproduced data.

Considering the pessimistic case, the video bandwidths are 5.6, 2.5 and 4 mc respectively and the corresponding overall response is 2.5 mc, and 2.25 mc with the 10% deterioration.

These overall responses were determined graphically based upon a realizable ratio of 1.8 of frequency at 3 db point with compensated complifiers to that without compensation. A rigorous analysis of the overall response of the 6 to 9 individual video amplifier stages is extemely complex and unwarranted. The graphical method used is described below.

It can be seen from the graph of Figure 2.4.4-3 that the obtainable horizontal readout accuracy will be between 4.8 and 6.7 inches at 100 feet.

2.4.4.4.1 Graphical Method

The usual video amplifier consists of one or more stages of amplification in which the amplitude response is compensated so as to obtain a moderate gain over a wide bandwidth. The approximate voltage transfer characteristic of a simple video stage has the following La Place transform —

$$\frac{e_o}{e_i} = K \times \frac{S^3 + as + b}{S^4 + CS^2 + b}$$

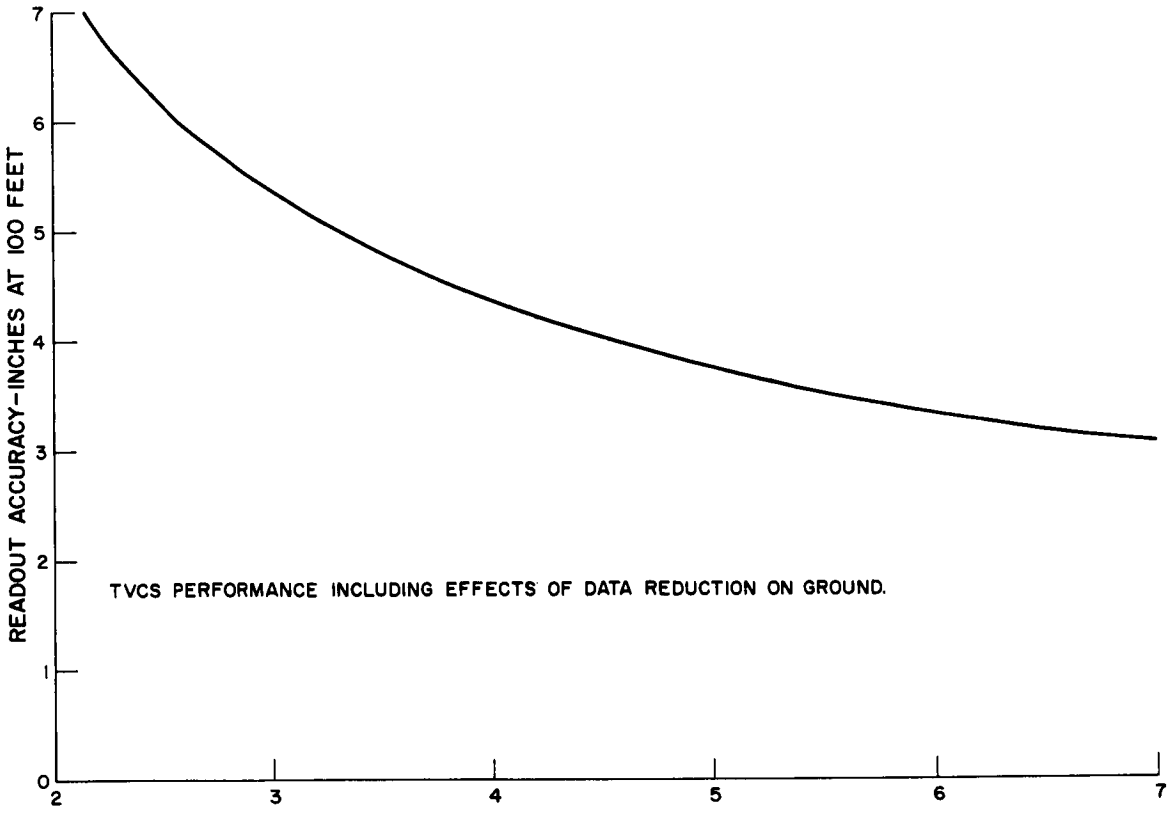


Figure 2.4.4-3. Horizontal Readout Accuracy versus Overall Equivalent Video Bandwidth

where

$a = (n-1)/n^2$

$b = 1/n^2$

$c = (2n-1)/n^2$

K = voltage gain

n = modified damping ratio

This is seen to reduce to a simple lag for a value of n equal to zero. A moderate extension of high frequency response occurs if n is given a value of 1/2 in that the 3-db point occurs at 1.8 f_o where f_o is the frequency for 3-db loss of amplitude when n is zero. As a rough approximation it is assumed that each contributing component of the system has this type of amplitude response with its own particular value of the -3 db frequency. By letting all K's be unity and plotting

each response around the normalized frequency of $1.8f_o$ the graphs of Figure 2.4.4-4 and 2.4.4-5 were obtained. These figures contain three curves of amplitude versus frequency corresponding to the three elements of the system plus a fourth curve which is constructed by summing algebraically the ordinates of the other three at each frequency. The overall system bandwidth is then described by the frequency of the resultant curve at which 3db loss occurs. This frequency is 3.85 mc/s for Figure 2.4.4-4 and 2.5 for Figure 2.4.4-5.

2.4.4.5 Testing, TV Camera

Figures 2.4.4-6, 2.4.4-7, and 2.4.4-8 summarize the results to date of the sample target materials that have been used to determine the reflection properties of scaled targets against bright (to simulate cloud cover) and dark (to simulate the sky) backgrounds. The optimum reflection surface was found to consist of a specular aluminum coating on the back of Lucite disc with a very thin coating of a "frosting" material on the front. This represents the best of eleven samples tested to date.

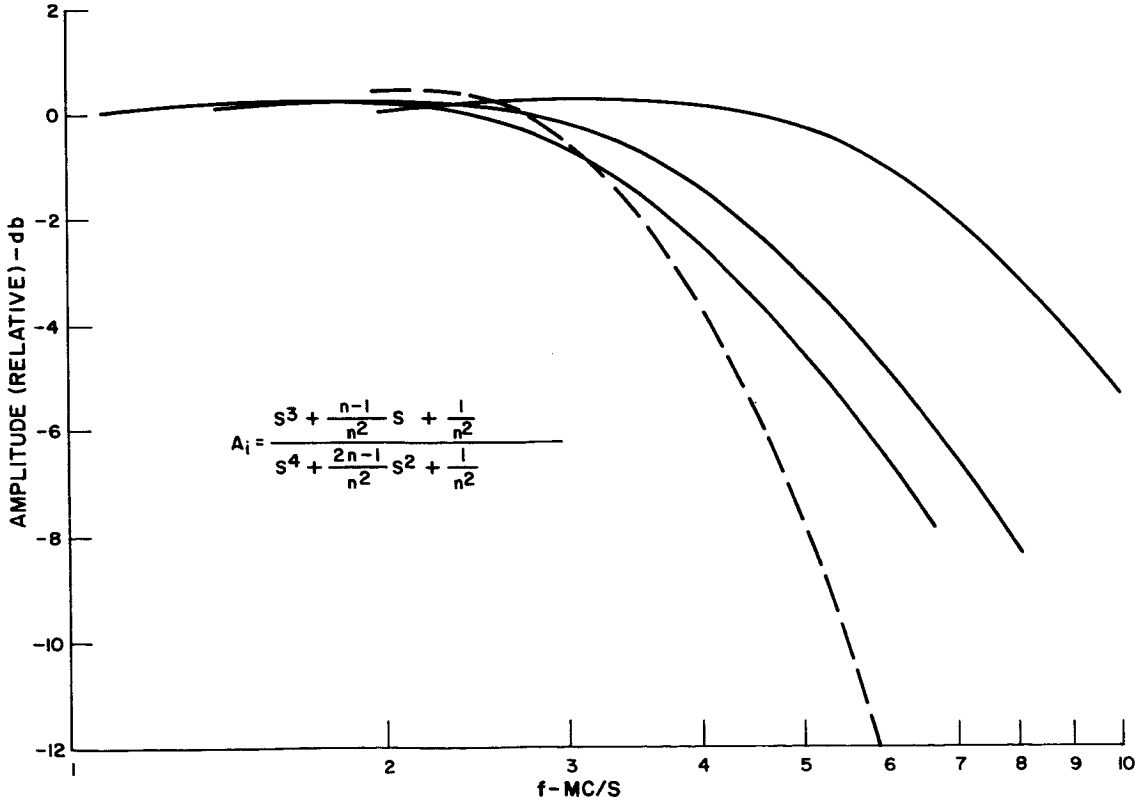


Figure 2.4.4-4. Composite Response of 3 Video Responses Having -3db Points at 8, 5, & 4.3 mc/s

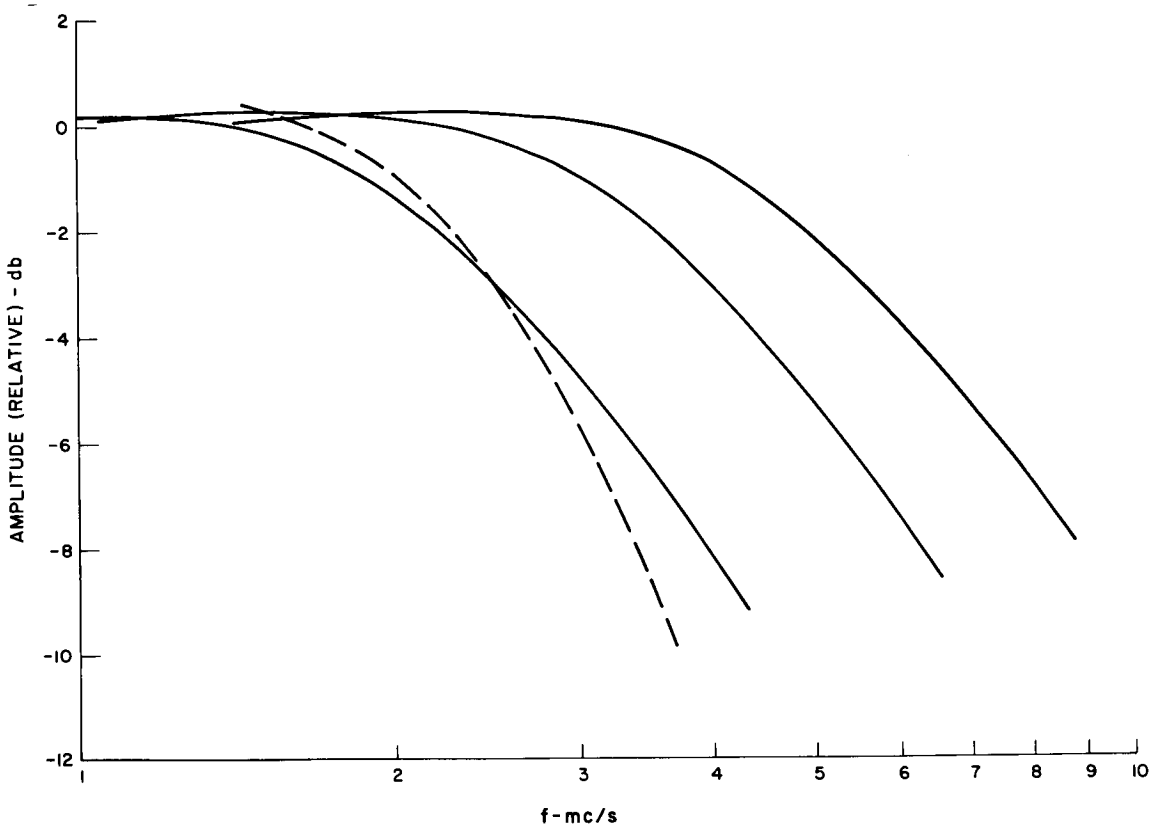


Figure 2.4.4-5. Composite Response of 3 Video Responses Having -3 db Points at 5.6, 4 & 25 mc/s

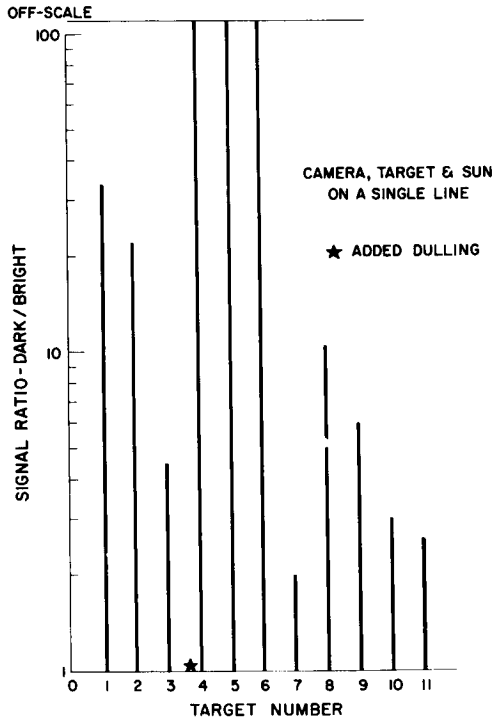


Figure 2.4.4-6. Signal Ratio vs Target Type

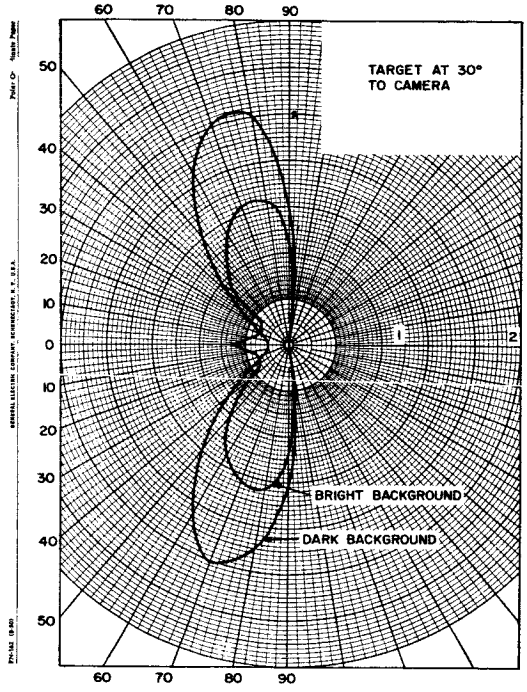


Figure 2.4.4-7. Relative Signal vs Sun Angle

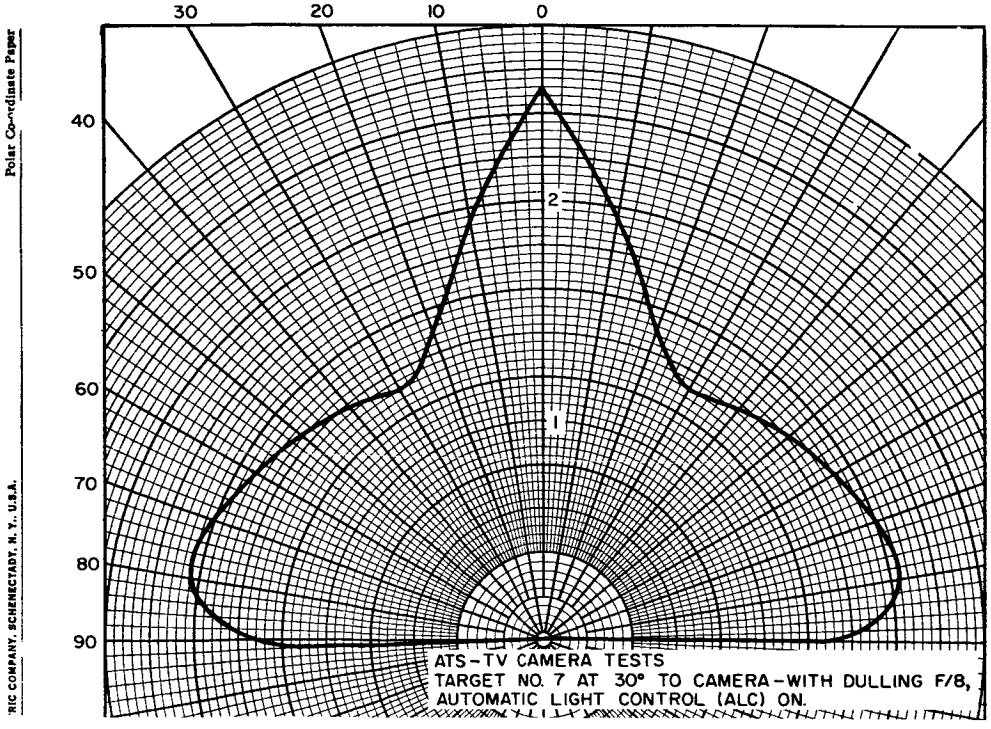


Figure 2.4.4-8. Signal Ratio vs Sun Angle

The most recent approach is an attempt to obtain a relatively improved contrast against the backgrounds, from black sky to very white clouds, by a color discrimination. Sample targets for this approach have been prepared but not yet tested.

Other tests have been made to determine the effects of the communications link by inserting wideband white noise into the video information. While noise that represents the actually expected noise has not yet been used in these tests, results using a somewhat wider noise bandwidth indicate that the threshold of target discernibility is about 22 db and that minimum acceptable results can be expected only if the signal-to-noise ratio is 27 db or greater.

Tests have also been made of the least observable signal. This condition was obtained by changing the angle of "sun" illumination against a white (cloud) background.

It was observed that even though the target "pip" could be detected on the single scan line displayed on an oscilloscope, extremely careful adjustment of the monitor controls was required to observe the target on the TV monitor after a change in apparent target brightness due to a change of sun angle.

2.4.5 INFRARED EARTH SENSOR

Since the status of the IR Earth Sensor has not been clearly defined, no significant effort has been expended on this component during this reporting period. However, the electrical interface of temperature monitoring circuits was defined and is documented here for future reference.

The Power Control Unit will develop a -6 volt ±0.5% reference voltage for use by other temperature detectors in the Attitude Sensor Subsystem, covering the range of $-10^{o}C$ to $+50^{o}C$. In series with the return path of these sensors are 4990 ohm ±1% resistors across which the telemetry voltage is developed, as shown in Figure 2.4.5-1.

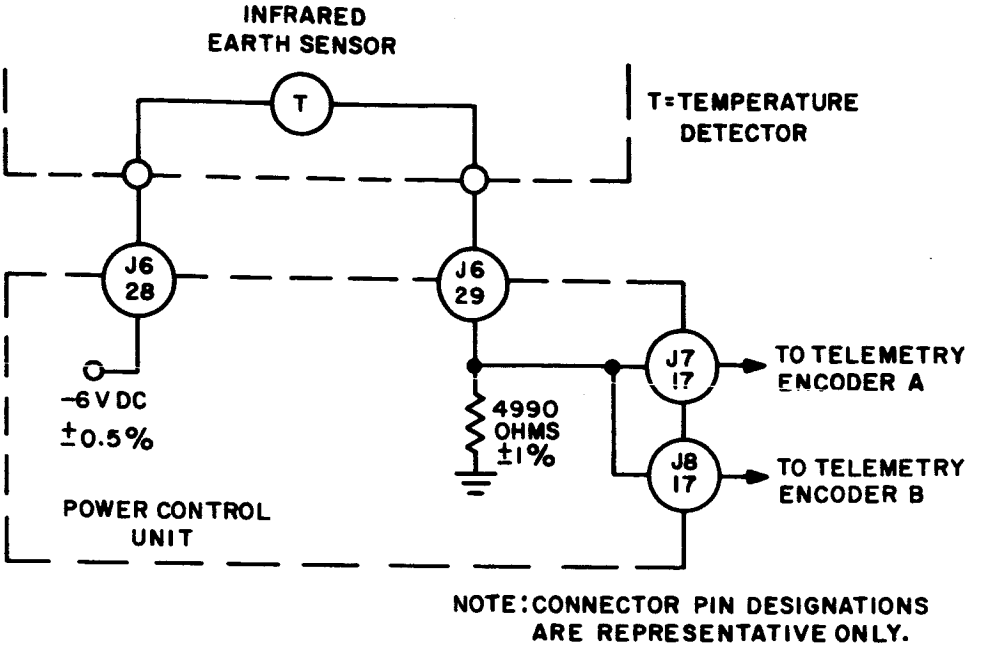


Figure 2.4.5-1. Temperature Measuring Circuit for Infrared Earth Sensor

2.4.6 RF ATTITUDE SENSOR

2.4.6.1 Introduction

This report describes the work performed toward the development of a Radio Frequency Attitude Sensor for the Applications Technological Satellite. Had the work been pursued to completion, the program would have resulted in an RF Attitude Sensor designed and produced to meet the environmental conditions of a satellite, in orbits out to synchronous.

The sensor would have received a signal at 6212.094 mc and measured its angle of arrival to within one degree. This attitude data would have been presented to an on-board telemetry system in digital form with eight bits of data for each of the measured (pitch and roll) channels.

The design goal for the equipment reliability over a three-year operating life was to be 80 percent, with a 50 percent operating duty cycle. This goal was to be met through the use of high reliability components and extensive component derating.

The RF Attitude Sensor was to have consumed five watts maximum from the spacecraft power supply and weighed no more than eight pounds. The physical size of the equipment (Figure 2.4.6-1) was to be six inches by six inches by six inches excluding connectors and mounting feet. The antenna face of the unit included a boresight mirror for alignment with the spacecraft structure.

2.4.6.2 Electrical Design

The RF Attitude Sensor is based upon three receiver channels and a data processor as shown in Figure 2.4.6-2. The central receiver is used to feed phase detectors, referenced by a locally generated 10-kc signal. The output of the quadrature phase detector is used, via a dc amplifier and stabilizing filter, to control a voltage tuned crystal oscillator. The 18.94 mc output of the crystal oscillator is multiplied by 324 and 328 to generate two signals at 6136.4 Mc and 6212.1 mc. The 6136.4 mc signal serves as a LO signal to mix with the received signal to produce a 75.76 mc IF signal. When the loop is locked the 6212.1 mc signal (pilot tone) will be 10-kc away from the received signal and mix with it in the detector to produce a 10 kc video output from the receiver. This output 10 kc carries the phase angle information of the received signal. Both the received signal and the pilot tone signal are processed through many common stages; as a result the phase delays of these stages affect both signals. Due to the common effect of these phase delays they are removed as errors from the system.

The in-phase phase detector output is used as a "lock on" signal for telemetry purposes and as a sweep inhibit to assure lock on of the pilot tone on the proper side of the received signal. A video signal proportional to received amplitude (minimum expected signal) is taken from the limiter and used as a sweep stop signal.

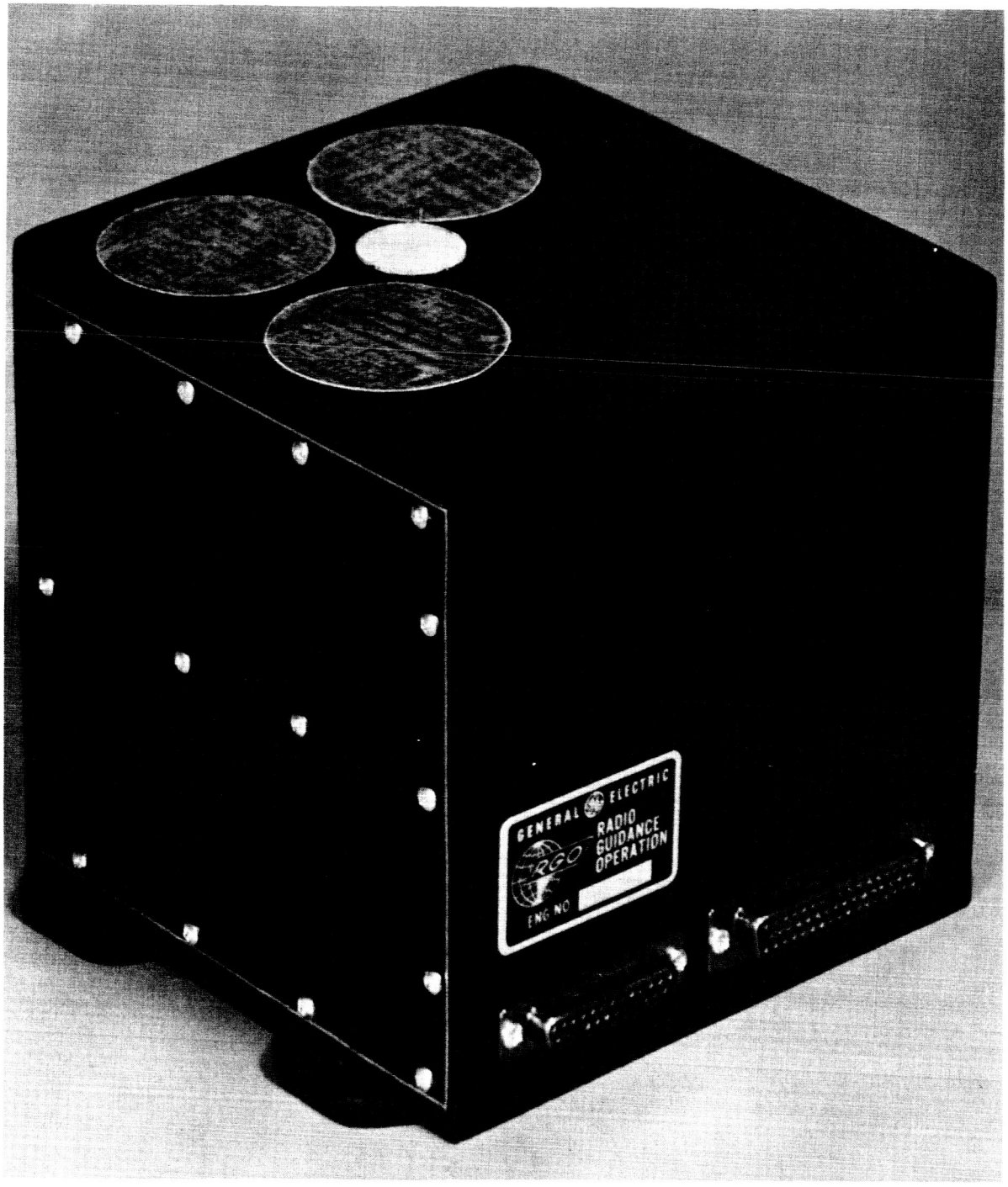


Figure 2.4.6-1. RF Attitude Sensor Mockup

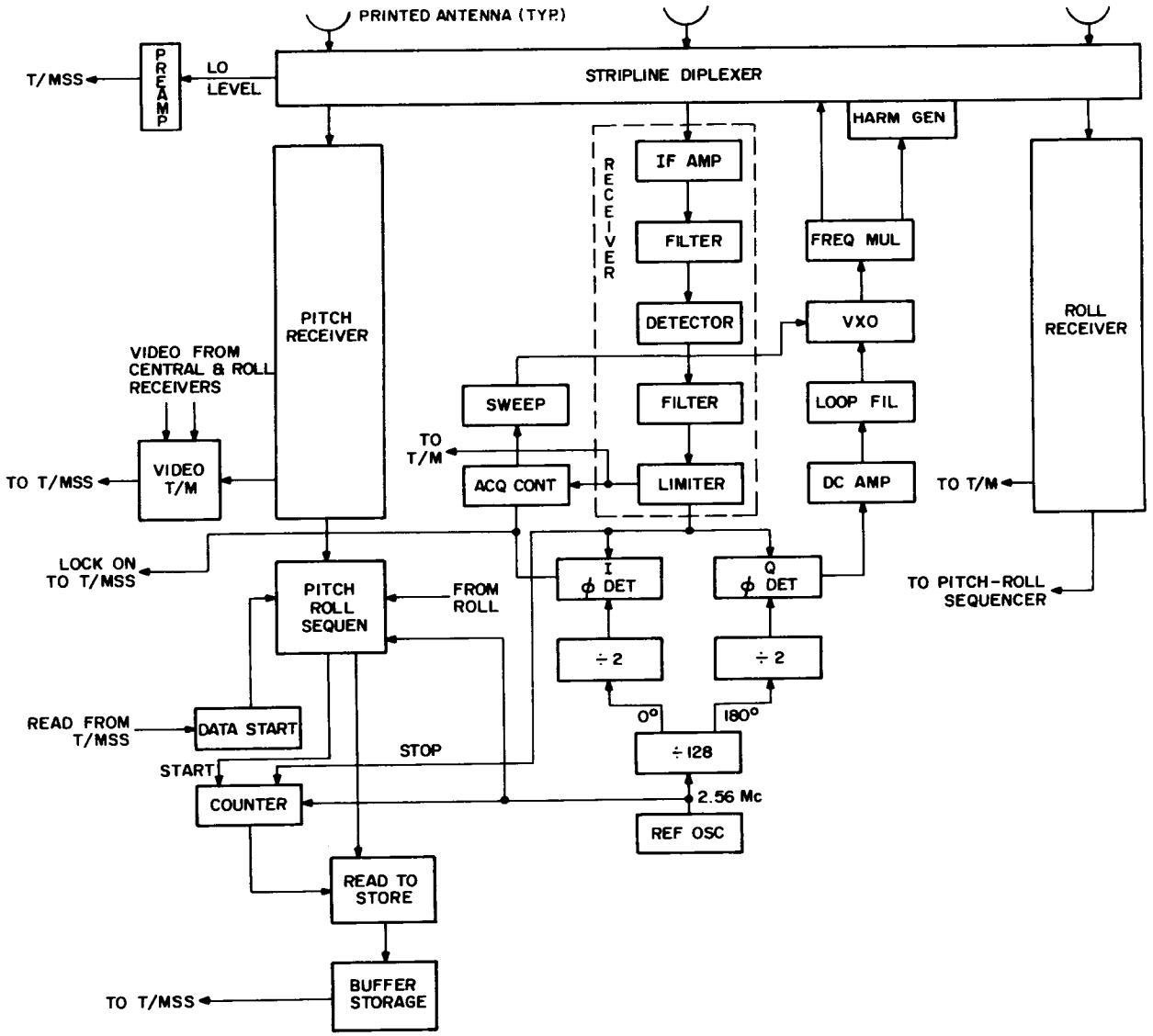


Figure 2.4.6-2. RF Attitude Sensor Block Diagram

Thus advantage is taken of the good received signal-to-noise-ratio to allow a relatively fast acquisition search rate. This same video is sent, from each of the three receivers, to a summer where they are combined to telemeter receiver video level to the ground.

Upon receipt of a read pulse from the vehicle telemetry subsystem (TMSS) a data collection process in the attitude sensor is started. Power is applied to the digital circuits and the next positive going zero crossing of the pitch video starts an eight bit counter counting the 2.56 mc signal from which the 10 kc reference signal is derived. The first positive going zero crossing of the central video stops the counting process. The resultant count accumulated is a digital representation of the spacecraft pitch axis attitude with respect to the received phase front. This signal is then read to buffer storage where it is presented to the telemetry subsystem.

This process is then repeated for the roll channel after which power is removed from all digital processing circuits (except the buffer storage) until the next read pulse. In the data collection area there are two approaches under consideration. If the noise generated by the ground and sensor oscillator-multipliers proves to be such as to degrade the data seriously the data sample will be taken over 128 cycles (of the 10 kc) in each channel. This will reduce the noise errors by more than ten. This area is discussed in more detail in Appendix G.

2.4.6.2.1 75.76 MC IF Amplifier

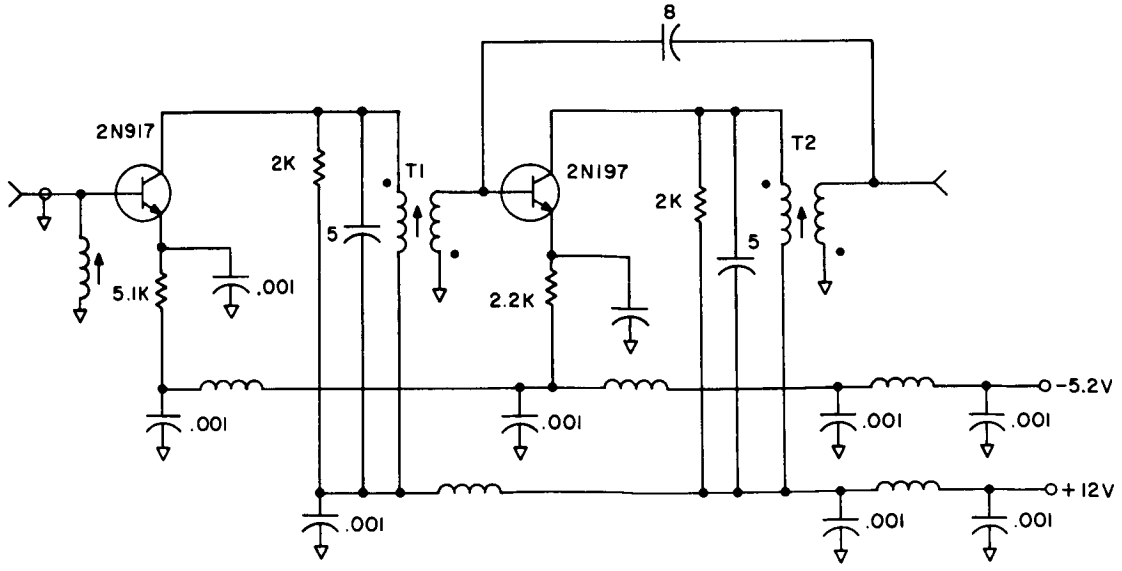
In an effort to reduce design time to a minimum, and use proven circuitry, the 75 mc IF was obtained by redesigning an existing 68 mc low noise preamplifier. Since the 68 mc pre-amplifier had sufficient gain and bandwidth it was only necessary to retune the tank circuits to 75.76 mc, and adjust the emitter biasing resistors to accommodate the change in emitter voltage from -12 volts to -5.2 volts.

Figure 2.4.6-3 is a complete schematic of the 75 mc IF amplifier. The IF consists of two stages of amplification, which for stability are loaded with 2K ohm resistors in the collector circuits. Neutralization is also used in the output stage.

The 75 mc IF was also constructed in its final configuration using Modular Weldment. Table 2.4.6-1 is a comparison of the breadboard IF with the final package in several stages of completion.

TABLE 2.4.6-1. 75 MC IF MEASUREMENTS

Breadboard		Final Configuration		Cover
		Pre Potting	Post Potting	
Gain	30 db	29 db	28 db	30 db
Bandwidth	10 mc	11 mc	10.3 mc	10.3 mc
Input Saturation Level	-37 dbm	-35 dbm	-35 dbm	-35 dbm



ALL CAPS EXPRESSED IN WHOLE NO. ARE IN PF
ALL OTHERS IN μ F
L1 7T # 32 WIRE SPACEWOUND WITH 1 WIRE DIA BETWEEN EACH TURN CORE 0.21" OD
T1, T2 PRI 7 1/2T SEC 1 1/2T # 34 WIRE CORE 0.16" OD

Figure 2.4.6-3. 75.76 Mc IF Schematic

As can be seen from Table 2.4.6-1 there is very little difference between the breadboard, and the final module with cover. However, comparing the breadboard with the pre and post potting stage, there are slight differences in both gain and bandwidth.

No temperature testing was done on either the breadboard or the final module before the project was halted. No difficulty is expected in temperature since the 68 mc pre-amplifier was designed and tested to operate over the temperature range of $-35^{o}C$ to $+125^{o}C$.

2.4.6.2.2 IF Filter

The signal to noise ratio for the minimum expected signal must be positive prior to the detector to avoid signal suppression by the noise. With the expected overall noise figure of 10 db and a minimum expected signal of -84 dbm the signal-to-noise ratio in a 10 mc bandwidth should be +10 db. Thus, to provide a safe design that guards against signal suppression, it appears that an IF bandwidth of 10 mc is a convenient upper bound.

To achieve a better signal-to-noise ratio a filter for the IF was designed. This filter (Figure 2.4.6-4) was a direct adaptation of one used on another program. The bandwidth (3 db) of the filter was 1.5 megacycles and the filter had an insertion loss of approximately six db.

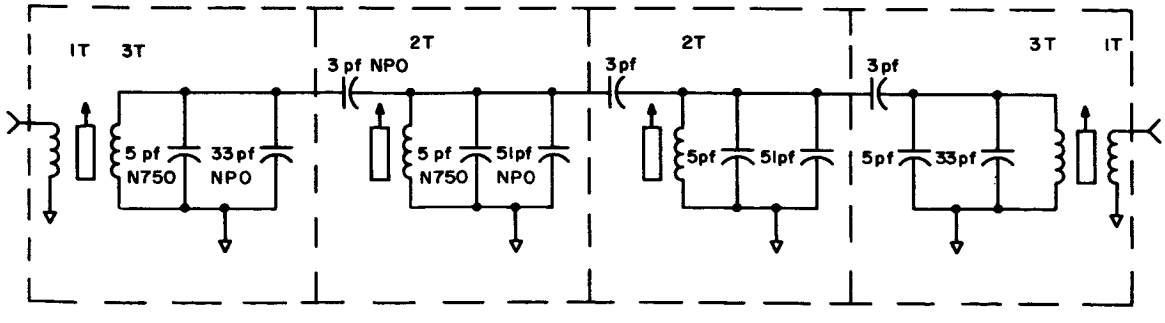


Figure 2.4.6-4. Receiver IF Filter

The breadboard filters were built in final module configuration. The resultant size was 1/2 by 1/2 by 2-1/2 inches. The construction of filters in a form factor such as this, has shown to have large effects upon operation. It was for this reason that the first breadboard module was made in the final module form factor.

2.4.6.2.3 IF Amplifier - Detector

The last IF amplifier and detector circuit is shown in Figure 2.4.6-5. The amplifier is a simple tuned stage incorporating a 2N917. The transistor is biased to allow the amplifier to remain linear up to and including the largest signal level encountered. With this system of signal processing this maximum "signal" is the pilot tone which remains constant. The amplifier is coupled to a simple diode detector which is in turn ac coupled to an emitter follower. The 10 kc tone being the signal of interest in the system, the dc level of the detector is unimportant. Over the entire range of circuit and signal dynamics the output level of this detector ranges between 10 and 300 millivolts peak to peak. Considerable care must be taken with stray signals - especially the 10 kc - to prevent spurious modulation in the system. The chokes and capacitors shown on the +12 volt supply line are to assure good filtering over the frequency range of 10 kc to 76 mc.

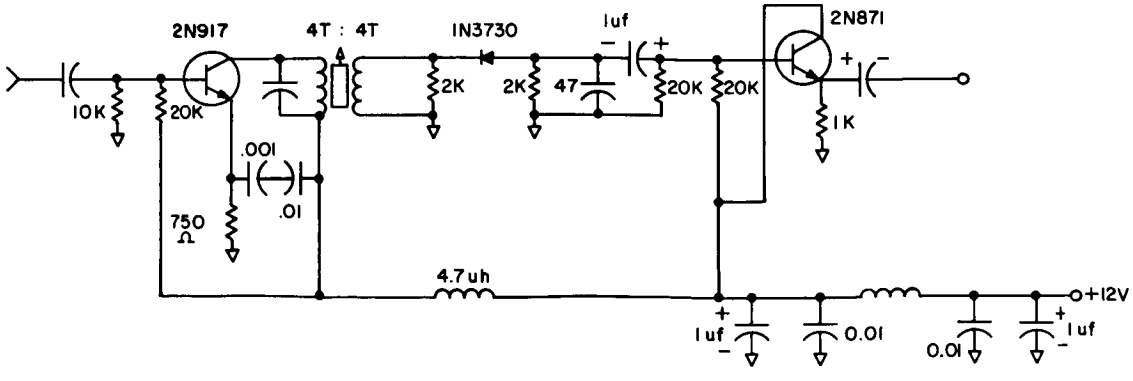


Figure 2.4.6-5. Last IF Amplifier-Detector

2.4.6.2.4 Video Filter

The video filter following the detector in the receiver should meet an interesting set of conditions. In order to preserve the phase angle of the signal received by the antennas, the filters in all three channels should be nearly identical. A reasonable tolerance to allow for phase differential between the three filters is one degree. The easiest way to assure meeting such a specification would be to keep the bandwidth wide. If a wide-band filter is used, however, the signal-to-noise ratio at the input of the limiter-phase measuring system may not be high enough to get accurate data. Another drawback to a wide filter is the harmonic distortion arising from the detection process on the single sideband type of signal from the IF amplifier. To hold harmonic distortion errors down in the system it is desirable to have all harmonics 50 db or more below the carrier.

From the phase-angle viewpoint it would be simple and desirable to use a low pass filter to get rid of thermal noise. Indeed if thermal noise of the receiver front end were the predominant noise in the system, from a noise viewpoint this would be sufficient. For the breadboard evaluation of the IF and the data processing concept this is the type of filter that was used. For the final system however, the second harmonic distortion begins to dominate the filter picture. To achieve 20 db filtering of the second harmonic relative to the 10 kc fundamental it is necessary to utilize a bandpass type of filter. Thus, phase tracking and control of this filter must be handled with care.

If a 10 kc filter with a bandpass of two kc were used it would be expected to exhibit a phase slope on the order of 0.15 degree per cycle per second change in frequency. With a one percent drift in filter frequency due to temperature, a phase error in the order of 0.75 degree would be expected per channel, or worst case 1.5 degrees error per measurement. With ten percent tracking, filter-to-filter, the error should be held to 0.15 degree per measurement. Thus while care is required, the requirements are within the state of the art.

A type of filter that appeared attractive for this application was the twin tee feedback amplifier. Figure 2.4.6-6 shows a schematic diagram of the circuit tried. The feedback resistor (R_f) controls the bandwidth of this amplifier and for the values shown the bandwidth was 2 kc at the three db points. Two units were built utilizing one percent resistors and five percent capacitors. The center frequency of the two units differed by five percent. A group of capacitors were then matched to one percent or less on a bridge and all circuit capacitors were replaced. The frequency difference, filter-to-filter, was now less than one percent.

An unfortunate characteristic of this type of filter was discovered, however. The output terminal of the micrologic amplifier looks at a point that is essentially wideband. As a result there is no filtering of internally generated noise by the overall circuit. For weak signal case then, the noise generated in the filter amplifier becomes limiting. Enough work was not done to determine if this could be cured by a following low pass filter. If this type of filter should prove to be unusable

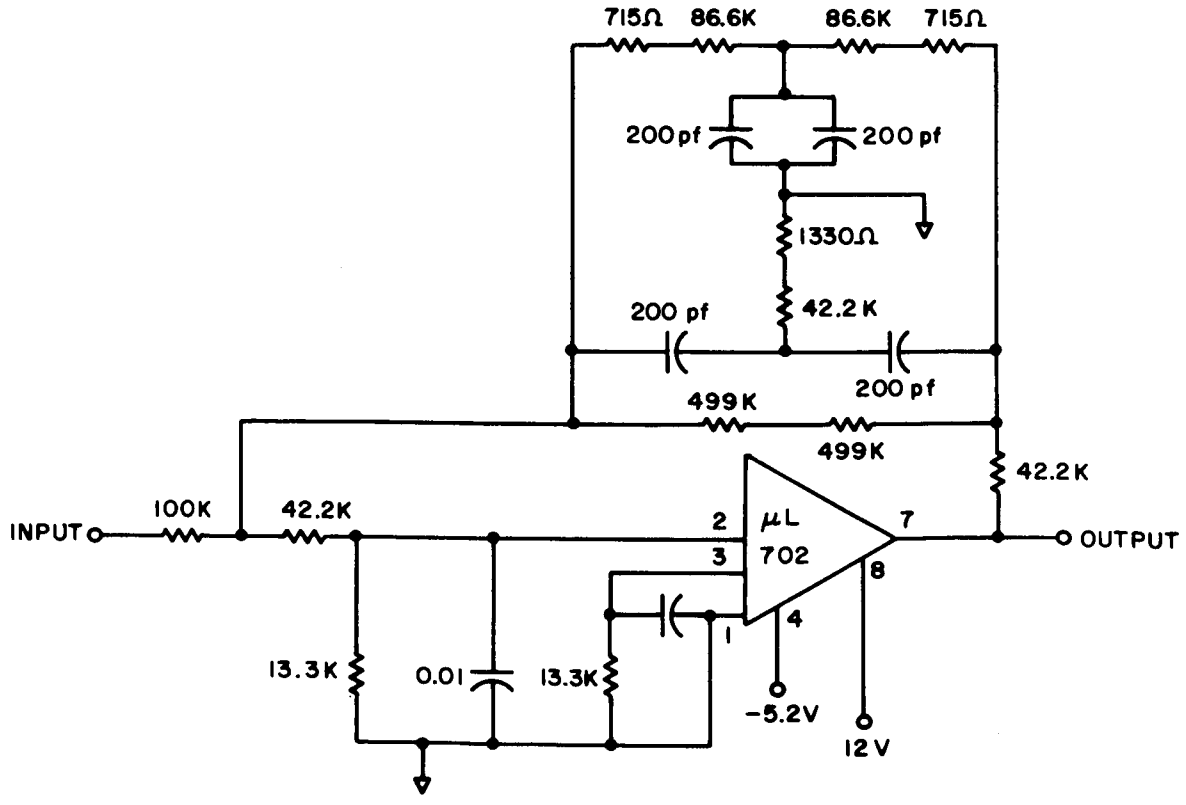


Figure 2.4.6-6. 10 Kc Filter

an L-C tuned circuit could be used with some increase in size. Vendor data indicates frequency drifts with temperature of 0.1 percent can be achieved over the entire temperature range of interest.

2.4.6.2.5 Limiters

Since the received signal amplitude varies over a dynamic range of 30 db, some form of amplitude control is necessary. With a good signal-to-noise ratio existing prior to detection the simplest form of control is one of video limiting. The circuit of Figure 2.4.6-7 is currently used in the breadboard. This circuit is designed to carefully control clipping levels throughout the dynamic range so as to minimize zero crossing phase shifts. The gain of the amplifiers up to the point where the telemetry video output is taken, is controlled so as to remain linear up to minimum expected signal. At the minimum expected signal level the limiting action is just beginning. Therefore this point is a valid signal for the telemetry verification of received signal and for acquisition sweep-stop purposes.

By selecting diodes as matched pairs it is found that the symmetry of clipping can be achieved by the circuit at the output end of the limiter as well as the circuit at the input end. To simplify the design (as well as to eliminate the same noise problem discussed in the video filter section) the final equipment would not incorporate the micrologic amplifier approach to the limiter.

2.4.6.2.6 Acquisition Control

The acquisition control circuit (Figure 2.4.6-8) for the attitude sensor has two inputs. A 10 kc signal from the limiter is fed to an emitter follower detector. This detector is designed to give a single pulse to a Schmitt trigger circuit as the received signal is swept into the bandpass of the loop. The Schmitt trigger (utilizing a Fairchild μL 702 amplifier) is used to stop the sweep circuit. The 10 kc signal input will only stop the sweep momentarily as the signal approaches. If the VXO frequency is

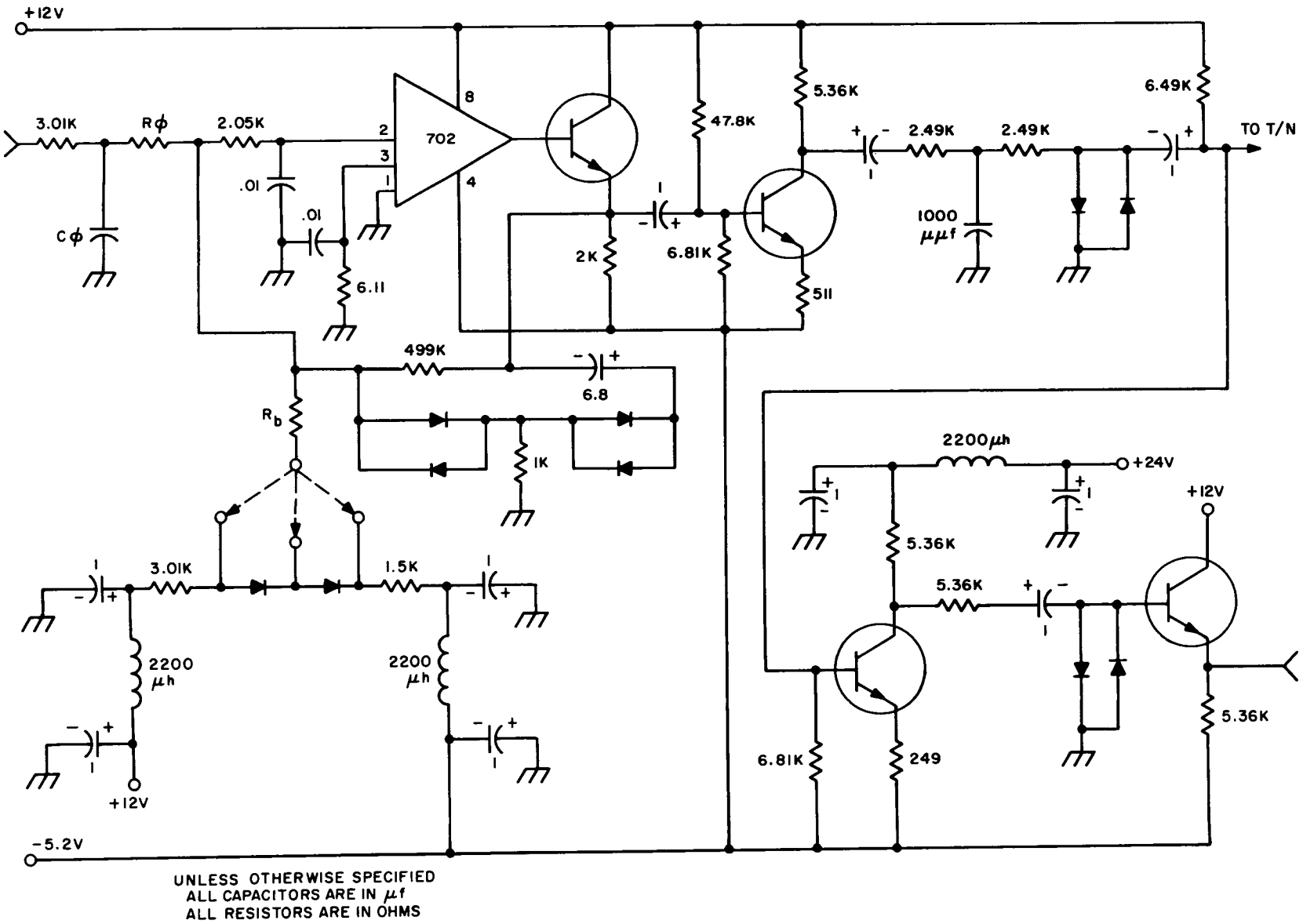


Figure 2.4.6-7. Limeters Schematic

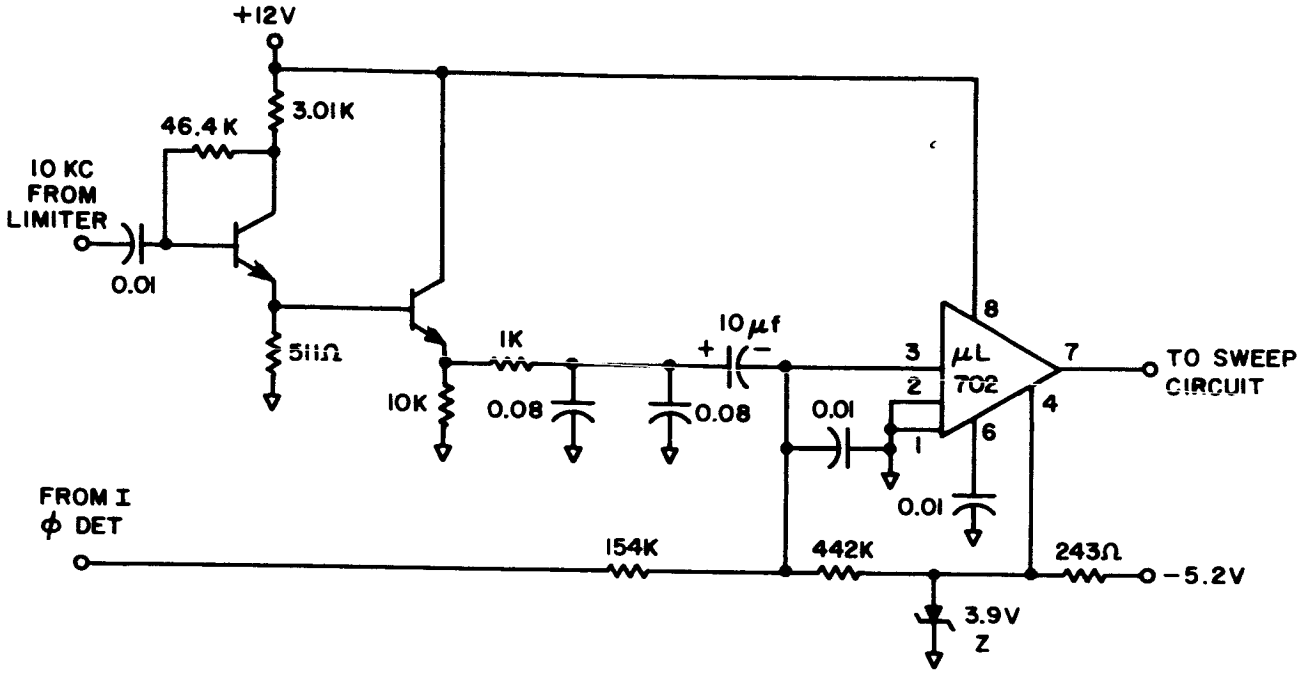


Figure 2.4.6-8. Acquisition Control

such that the pilot tone is on the proper side of the received signal the input from the "I" phase detector rises as lock occurs. This then permanently triggers the Schmitt trigger to keep the sweep stopped.

2.4.6.2.7 Sweep Circuit

To meet the specification for acquisition time for the attitude sensor a sawtooth type of sweep circuit was designed. This waveform will "waste" the least time in searching at an acquirable rate. A requirement of the sweep is to stop-and-hold when the received signal is in the bandpass of the phase-locked loop. A perfect stop-and-hold is not possible so the sweep rate under the "stopped" condition must be low enough to allow the phase locked loop to respond and acquire the signal. Due to the maximum acquirable rate of the loop, the search rate must be in the order of one search every two seconds. A rate as low as this dictates dc coupling as the only practical approach. With the sweep directly coupled to the VXO it was

decided to have the sweep circuit provide the bias for the varicap in the oscillator circuit. In addition, provision was made for a temperature compensation (T/C) network in the VXO to be coupled to the sweep, to control the varicap bias level. Temperature compensation of the entire circuitry involved in frequency control is therefore accomplished through a bias voltage. The circuit for this bias control can be seen at the lower left of the sweep circuit schematic Figure 2.4.6-9.

The acquisition control circuit gives out a positive level whenever the received signal is in the bandpass of the phase locked loop. This signal is applied to two cascaded inverter circuits to provide the proper control levels to "stop" the sweep circuit, control the rate after "stop" and prevent flyback under lock conditions.

The sweep voltage proper is generated by an integrating amplifier utilizing a μL 702 micrologic operational amplifier. A second μL 702 is used as a Schmitt trigger to sense when the sweep has reached a preset value and generate a flyback pulse. This pulse is coupled through a diode and R_a to reset the integrating capacitor (6 μf non polar). Selecting the value of R_a controls the amplitude of the sweep by determining reset or flyback excursion. The diode between pins one and two on the integrating μL 702 prevents overdrive and "hang-up" from the reset pulse. Adjustment of the values of R_1 and R_2 controls the sweep rate of the circuit. The circuit will operate over a range of rates from 0.07 to 10 cps. The amplitude can be adjusted from four to eight volts peak-to-peak. Operation is satisfactory over a temperature range of -35^{o}C to $+85^{o}$C.

2.4.6.2.8 Frequency Multiplier

The frequency multiplier is required to provide sufficient power at eight and 12 times the oscillator's frequency to drive the harmonic generator and varactor chain, with a minimum of side band interaction.

Table 2.4.6-2 shows the specification to which the multiplier was designed.

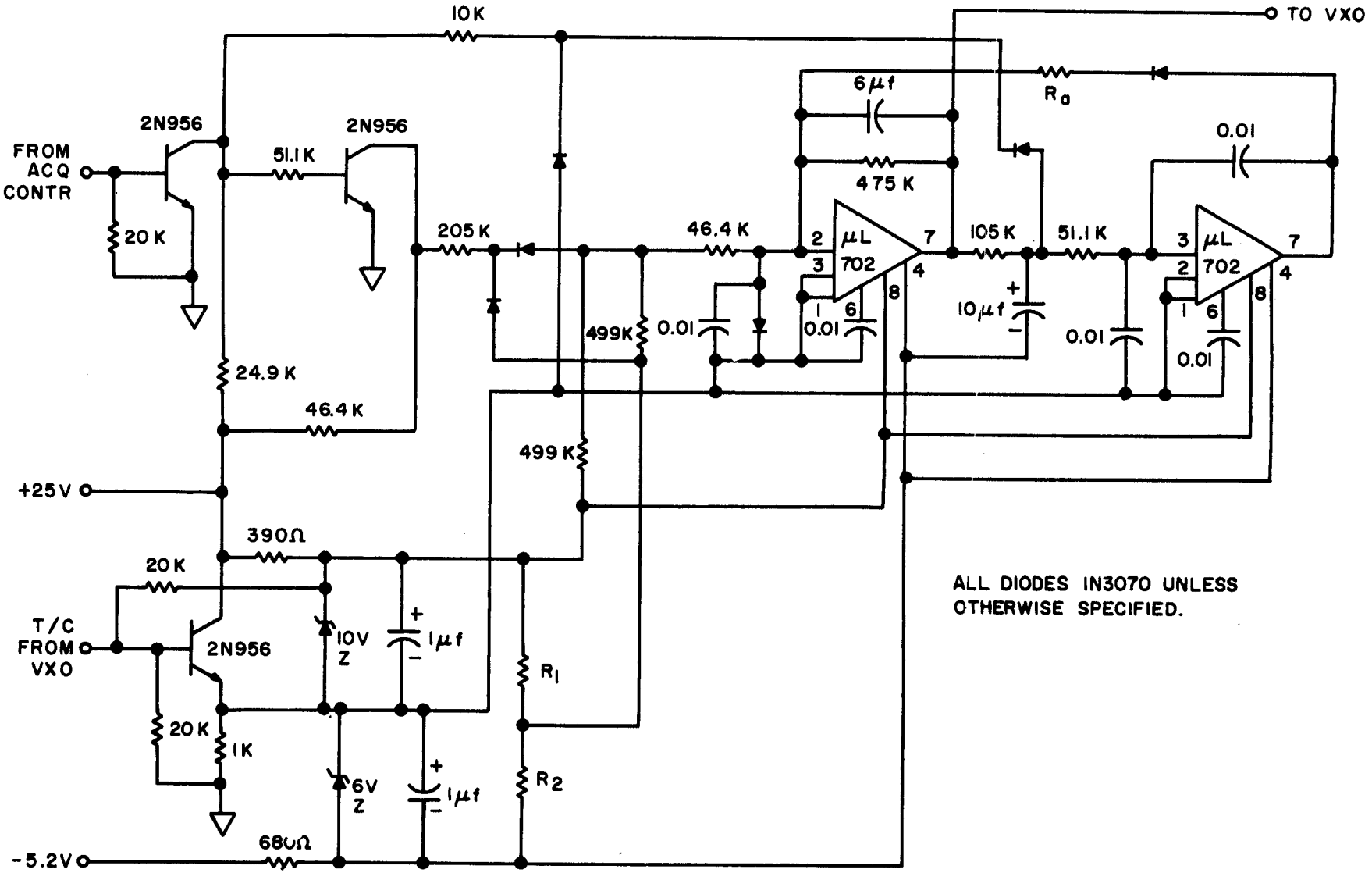


Figure 2.4.6-9. Sweep Circuit

TABLE 2.4.6-2. FREQUENCY MULTIPLIER SPECIFICATION

fo	18.94 mc
Input level	-10 dbm
Output frequencies	8 f_o and 12 f_o
Output levels	8 f_o at + 13 ± 1-1/2 dbm
	12 f_o at + 16 ± 1-1/2 dbm
Side Band Suppression	-70 db min. below output
Input, Output Impedance	50 ohms
Temperature Range	-35°C to + 85°C
Line Voltage Variation	V_c ± 3%

Other conditions imposed on the design of the frequency multiplier were: 1) the use of approved types of components, 2) component derating to 25% of maximum rating value, and 3) designing the circuit such that it could be split into modules whose length would not exceed 5 inches.

Figure 2.4.6-10 is a block diagram of the multiplier showing each block as a module and the function of each block.

Figure 2.4.6-11 is a schematic of the X2 module. It consists of a transistor doubler followed by a double tuned bandpass filter and finally a 37.88 mc amplifier. The output of the X2 circuit is split and fed to the X4 and X6 modules.

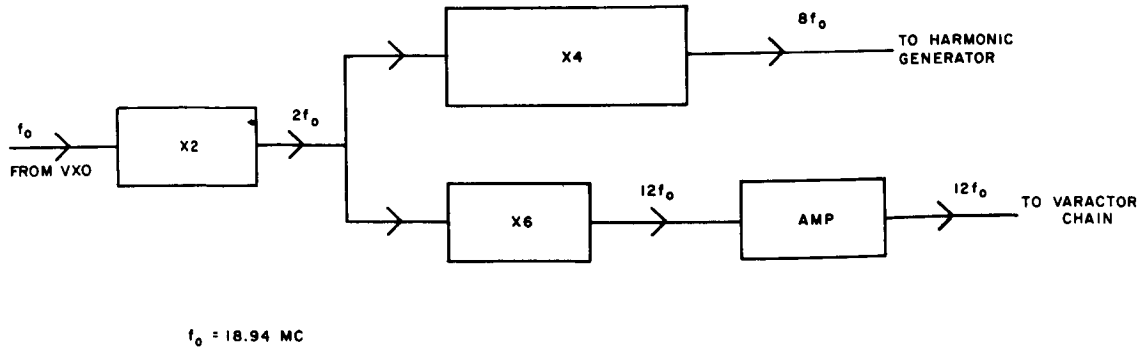
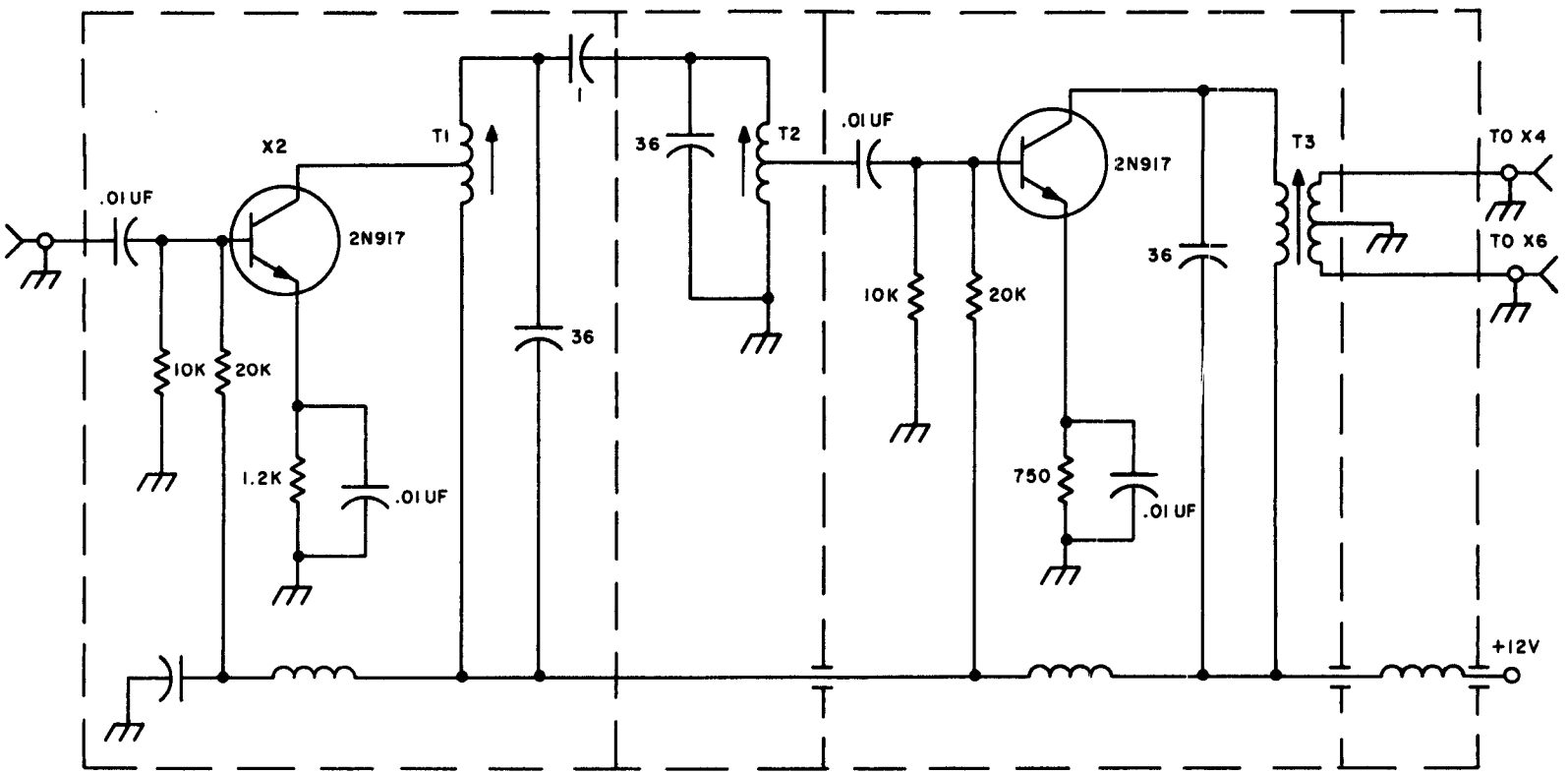


Figure 2.4.6-10. Multiplier Block Diagram



UNLESS OTHERWISE SPECIFIED
ALL CAPACITORS ARE IN UUF
ALL RESISTORS ARE IN OHMS

T1 & T2 - 8 TURNS TAPPED AT 2 TURNS
NO. 32 WIRE, CORE 0.16 INCH O.D.
T3 - PRIMARY 7 TURNS NO. 32 WIRE
SECONDARY 1 TURN NO. 32 BIFILAR WIRE
CORE 0.16 INCH O.D.

Figure 2.4.6-11. X2 Circuit Schematic

Table 2.4.6.3 lists the measured parameters of the X2 module.

TABLE 2.4.6-3. SPECIFICATION OF X2 MODULE

Gain		16 db
Bandwidth		1.12 Mc
Side Band Suppression	f_o	84 db below output
	$3f_o$	84 db below output
	$4f_o$	24 db below output

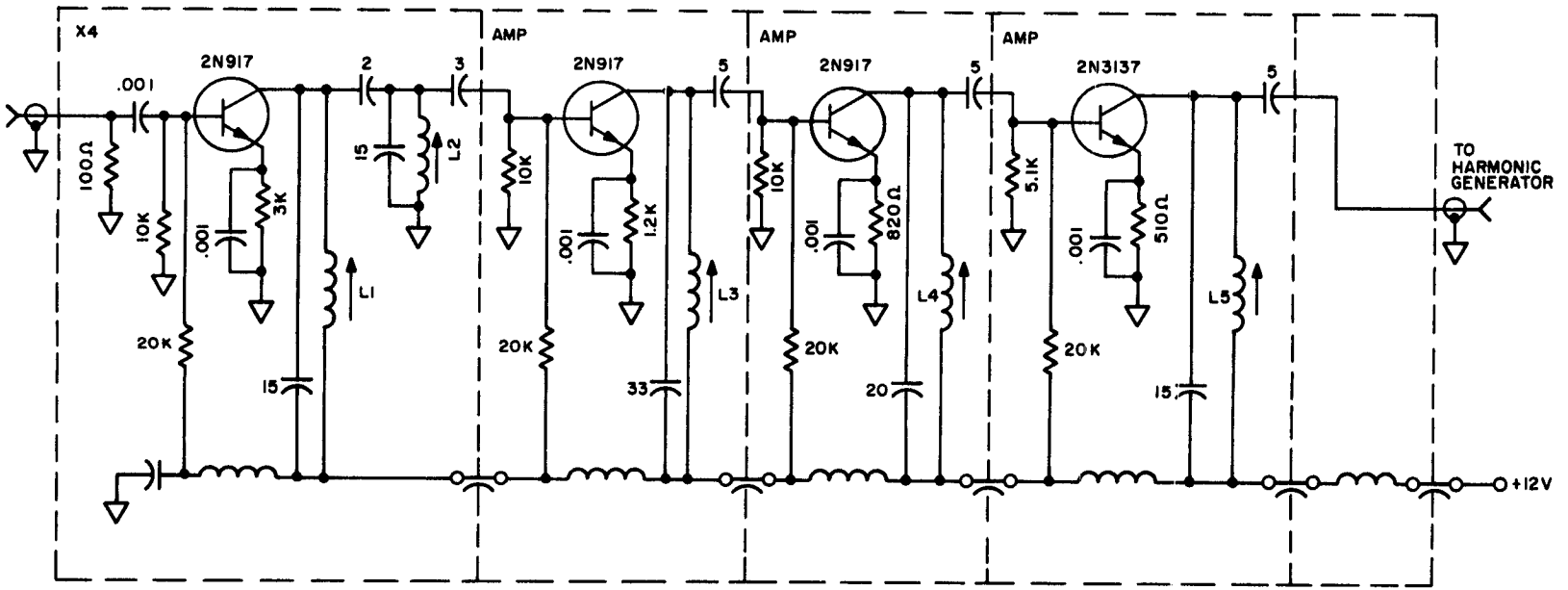
The X4 schematic is shown in Figure 2.4.6-12. In this circuit the first stage is a quadrupler and the following stages are used to provide filtering and amplification. L-type coupling is used at the higher frequencies in preference to transformer coupling due to better control in matching and higher Q's in the L-type. Due to the limitation that no variable capacitors were available, matching is limited by the range of inductance tuning, which is limited due to the number of turns used. To obtain the required sideband suppression, a sacrifice was made in gain.

Table 2.4.6-4 lists the measured parameters of the X4 circuit.

TABLE 2.4.6-4. X4 CIRCUIT SPECIFICATION

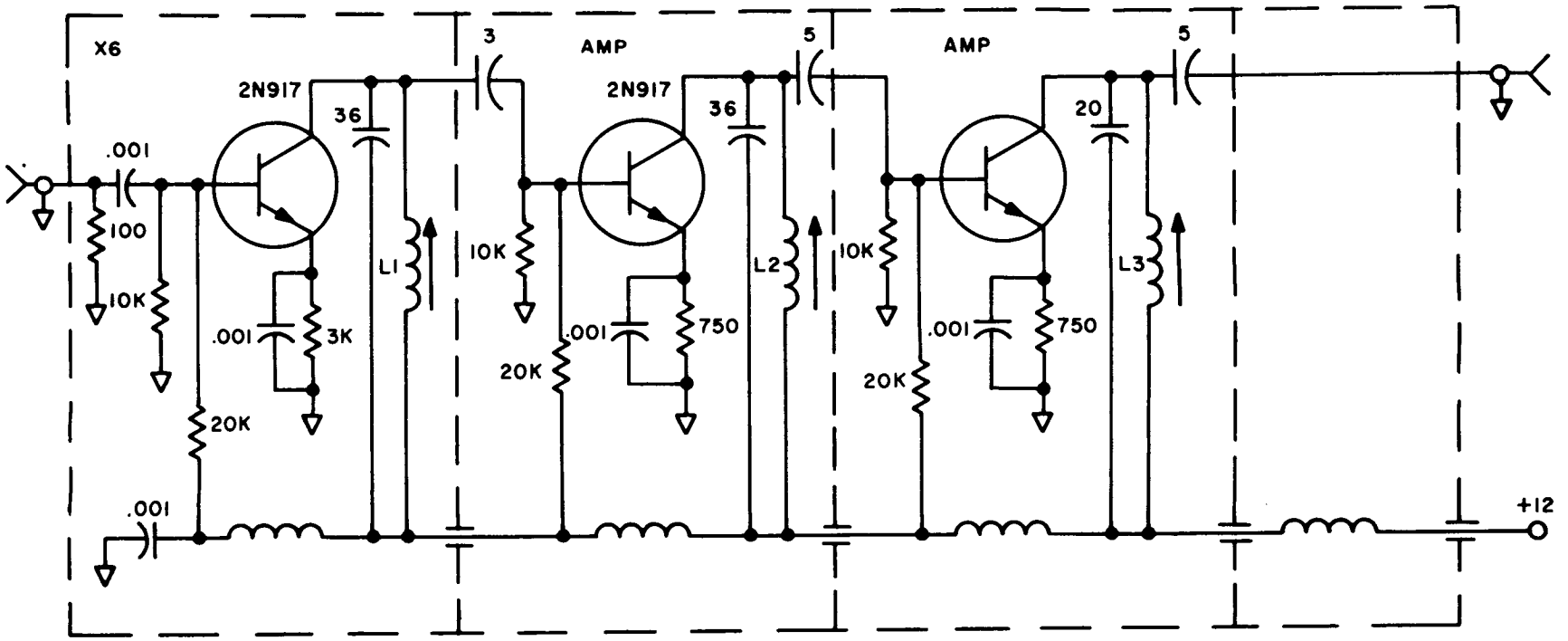
Gain	13 db
Bandwidth	3.2 Mc
Sideband Suppression	All sideband 80 db or more below output.

Figure 2.4.6-13 shows the schematic of the X6 circuit. The multiplying is done in the first stage with the remaining stages providing gain and filtering. In Figure 2.4.6-14 the circuit of the 227.28 mc amplifier is shown. It was necessary to match the input of the amplifier to the 500 ohm coaxial cable used, since the mismatch produced too much loss of gain. Variable capacitors would have been particularily helpful in this circuit to obtain better matching conditions at the output.



ALL CAPS EXPRESSED IN WHOLE NUMBERS ARE IN pf
ALL OTHERS IN μf
L1 AND L3 1 1/2 T NO. 22 WIRE CORE 0.16" O.D.
L2, L4, AND L5 2T NO. 22 WIRE CORE 0.16" O.D.

Figure 2.4.6-12. X4 Circuit Schematic



ALL CAPS EXPRESSED IN WHOLE NO. ARE IN PF
ALL OTHERS IN μF

L1, L2 2T NO. 14 WIRE CORE 0.21" O.D.
L3 1T NO. 14 WIRE CORE 0.21" O.D.

Figure 2.4.6-13. X6 Circuit Schematic

Difficulty is anticipated when the transition from breadboard to final package of the X6 and X6 amplifier circuit is made, since at 227 mc lead lengths and grounding can become significant problem areas. Trouble was encounted in the breadboard in both these areas.

Table 2.4.6-5 shows the measured parameters of the breadboard X6 and X6 amplifier.

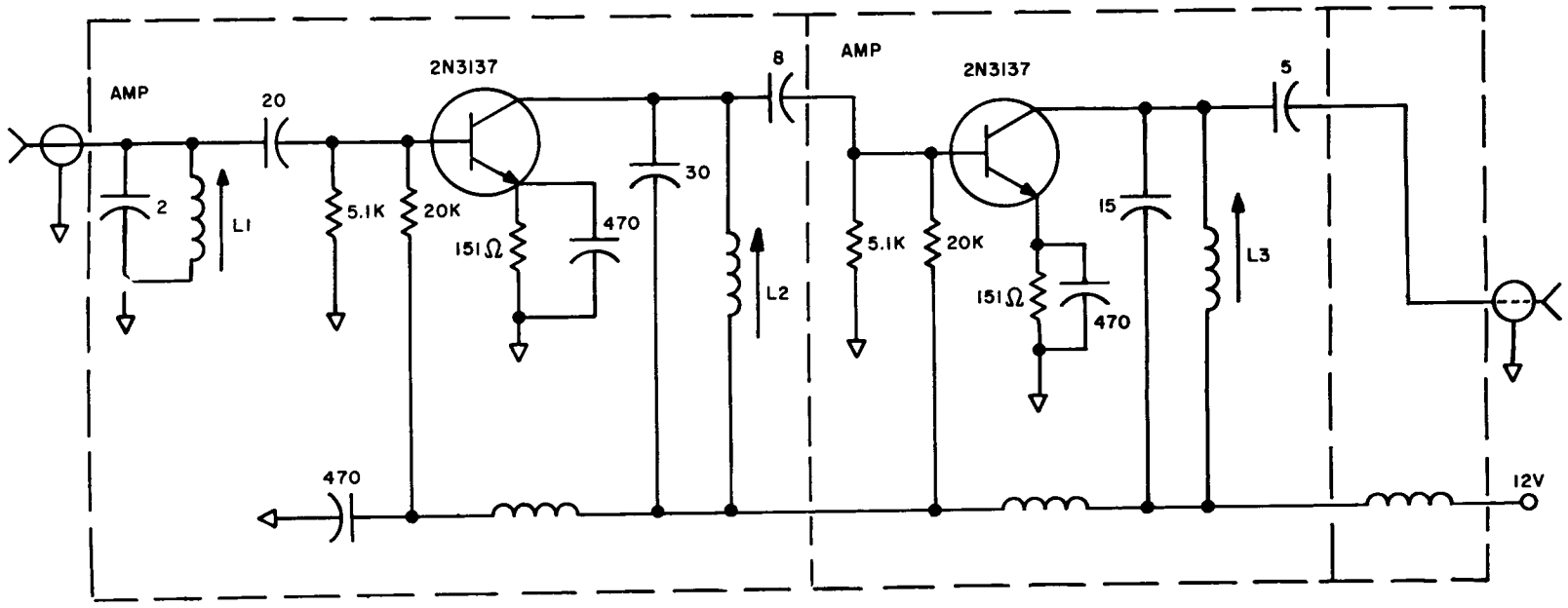
TABLE 2.4.6-5. X6 and X6 AMPLIFIER SPECIFICATIONS

Gain	13 db
Bandwidth	7.8 mc
Sideband Suppression	All side bands down 75 db below output

With all modules interconnected with coaxial cable not exceeding 4 inches, and all outputs measured into 50 ohms the parameters of interest of the complete multiplier were measured and the results are shown in Table 2.4.6-6.

TABLE 2.4.6-6. MULTIPLIER SPECIFICATION

Input (at 18.94 mc)	-10 dbm
Output	
at 151.52 mc	22 mw (+13.4 dbm)
at 227.28 mc	42 mw (+16.2 dbm)
Bandwidth	
at 151.52 mc	3.2 mc
at 227.28 mc	7.8 mc
DC Dissipation	624 mw
Sideband Rejection	
at 151.52 mc output	All sidebands are 77 db or more below output
at 227.28 mc output	All sidebands are 72 db or more below output



ALL CAPS IN Pf
L1 1½T NO. 14 WIRE CORE 0.21 IN. OD
L2 ½T NO. 14 WIRE CORE 0.21 IN. OD
L3 1T NO. 14 WIRE CORE 0.21 IN. OD

Figure 2.4.6-14. 227.8 Mc Amplifier Circuit Schematic

A comparison of Table 2.4.6-2 with Table 2.4.6-6 shows that with the exception of line variation and temperature the multiplier meets the initial requirements.

With a constant input of -10 dbm at 18.94 mc the output power variation for ±3% line variation was from 22 to 27.5 mw for the X8 output and from 37 to 44 mw for the X12 output, which is within the specification. If the input is also allowed to vary ± 3 db along with the line voltage then the extremes in output power variation becomes 20 to 29 mw for the X8 output, while the X12 output remained unchanged at 37 to 44 mw.

Over the temperature range of 25°C to 85°C the output power of the X8 output decreased over 3 db, from 24 mw to 10.5 mw, while with line voltage variation the X8 output drops further to 8.5 mw at 85°C. The X12 output power remained a constant 40 mw to 85°C and decreased 5 mw with the line voltage variation.

The main reason for the X8 output dropping with temperature is that the X8 portion of the multiplier is operated as a linear device for minimum noise output, and no temperature compensation is included. In the X12 circuitry a portion is operated in saturation thus providing some temperature compensation. No further work was done on improving the temperature responses of the multiplier since the program was halted.

To finish the design of the frequency multiplier there are two major areas which require further work. One is to temperature compensate the X8 circuitry while still maintaining a low noise output. The other area is in going from breadboard to final package configuration of the X6 and X6 amplifier.

2.4.6.2.9 2.56 Mc Oscillator

The 2.56 mc signal for the 10 kc reference divider is generated by a crystal oscillator as shown in Figure 2.4.6-15. The series resonant mode for the crystal is used in the feedback loop of the oscillator to assure crystal-controlled

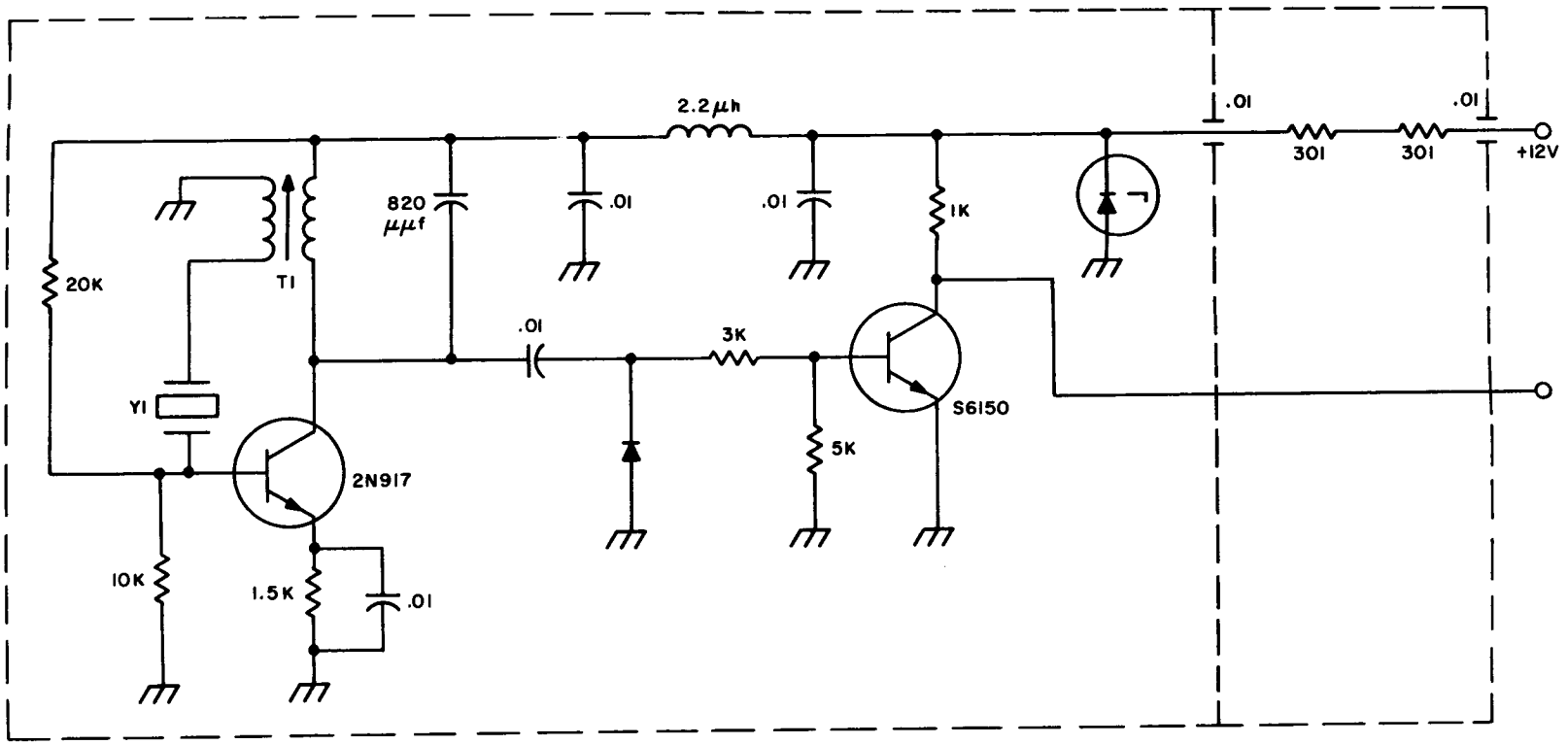


Figure 2.4.6-15. 2.56 Mc Oscillator and Buffer

oscillation. The output of the oscillator is capacitively coupled to a video buffer which amplifies the signal and shapes it into a series of pulses for use in the eight bit divider.

2.4.6.2.10 Digital Processing

The following describes pertinent characteristics and design considerations of the digital circuitry contained in RF Attitude Sensor. About 75% of the circuits discussed in this report were breadboarded and tested at room temperature; therefore, the details contained in the enclosed schematic diagrams can be considered quite firm. While size restrictions dictated the use of integrated circuits to perform all logic functions, due to input power limitations, conventional circuits had to be used in some cases.

The digital portion in this unit can be divided in two major sub-groups:

1. The pitch/roll counter and associated storage
2. The divider (by 256) and phase detector.

The pitch/roll counter subassembly, the block diagram of which is shown in Figure 2.4.6-16, is by far the larger of the two and it consists of:

1. One 8-bit counter time-shared by the roll and pitch channels
2. Sixteen buffer storage stages, eight for each channel
3. Miscellaneous switching and steering circuits.

In order to keep the power consumption to a bare minimum, the DC voltage necessary to energize this subassembly, except the storage stages, is turned on for two milliseconds out of every three seconds by a pulse generated by the leading edge of the "READ" command. These two milliseconds are used as shown in Figure 2.4.6-17.

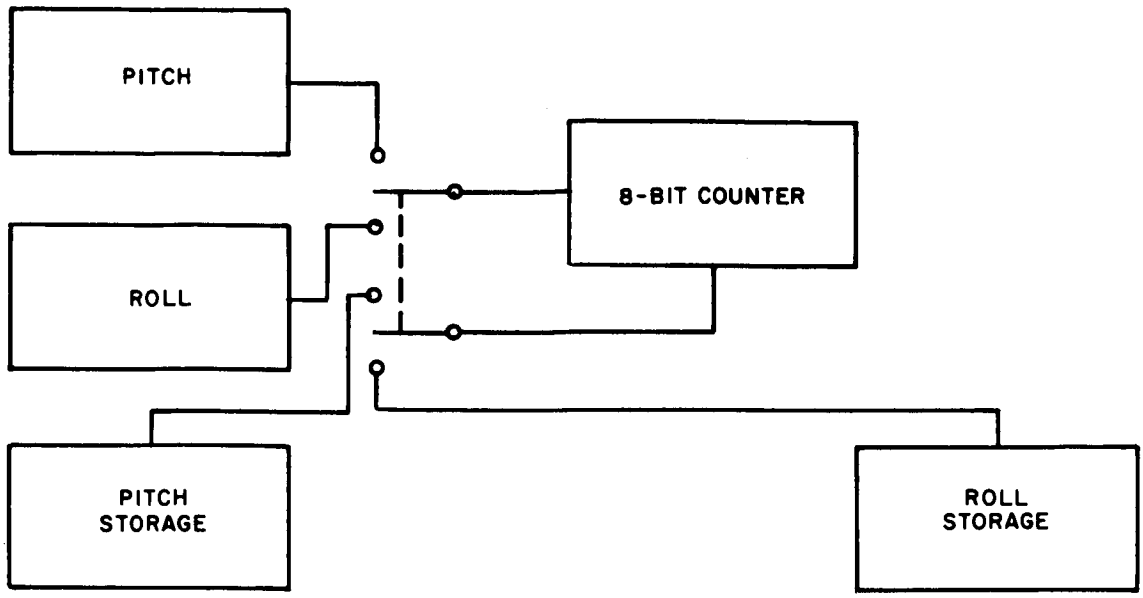


Figure 2.4.6-16. Digital Data Collection

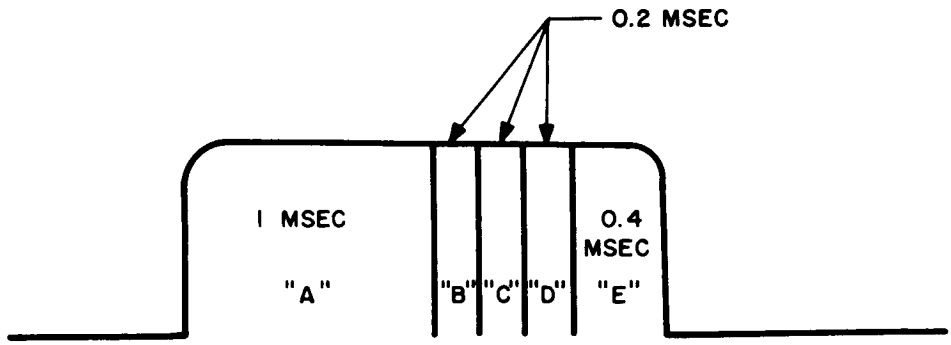


Figure 2.4.6-17. Data Timing Diagram

Where:

"A" and "E" - time allowed for the rise and fall respectively of the power supply

"B" - time utilized to count and store the quantized phase of the pitch channel

"C" - inoperative time between pitch and roll counts

"D" - time utilized to count and store the quantized phase of the roll channel.

Figures 2.4.6-18 and 2.4.6-19 show the complete logic diagrams for the data collection circuits of the attitude sensor. During time "B" the pitch and the central signals are allowed to set and reset respectively, the flip-flop A-5, thus opening the gate A-6 and letting through a burst of 2.56 mc pulses for a period equal to the time difference between the two signals. This burst of pulses is counted and then stored in binary form in the "pitch" buffer storage stages. Flip-flop A-11 ensures that one and only one burst of pulses is allowed through, while the one shot A-14 allows for the counter's trickle time before generating the "STORE PITCH" pulse. A reset pulse of very small duration (.25 μsec or less) is generated at the beginning of time "B" and "D" to empty out the counter just prior to the arrival of the burst of pulses to be counted.

Nothing happens during time "C", and at time "D" the Roll information goes through the same sequence as the pitch information did at time "B". The information stored in both the pitch and roll registers is available for almost three full seconds before being erased by the clear pulse which occurs when the next "READ" command is received.

2.4.6.2-11 256 Divider and Phase Detector

This subassembly (Figure 2.4.6-20) consists of an eight stage straight divider and a quadrature phase detector using half adders.

The 2.56 mc signal is divided by 256 and then it is compared with the signal coming from the central channel. The 90 degrees phase shift is obtained by paralleling the eighth stage of the divider with an additional flip-flop which is triggered by the "FUNCTION" output of the seventh stage rather than the $\overline{\text{"FUNCTION"}}$.

Differential amplifier level translators are used in all cases for the transition from integrated to conventional circuitry in order to minimize temperature effects.

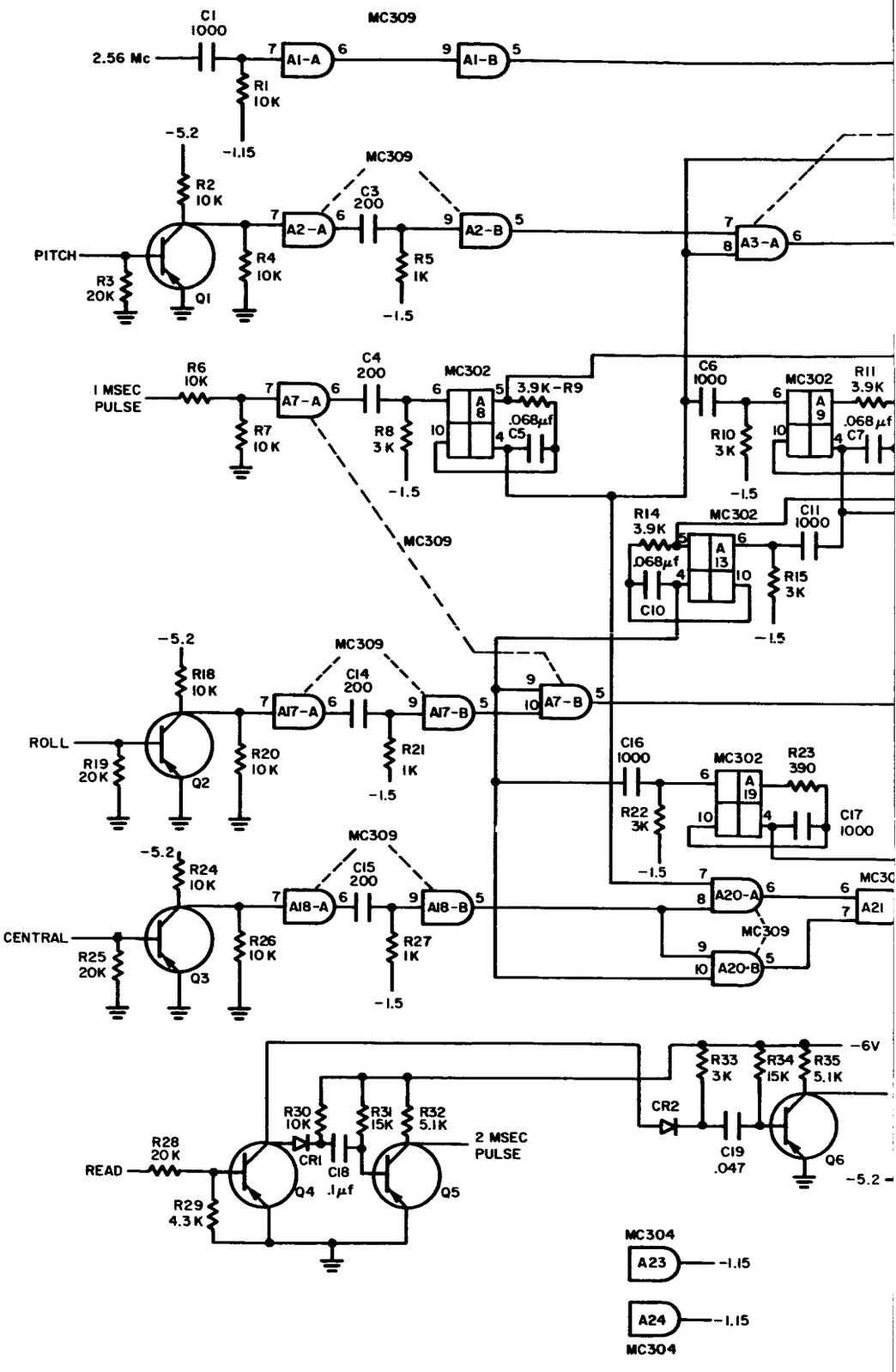
2.4.6.2.12 Video Telemetry Circuit

The purpose of the video telemetry circuit was two fold. It was desired to have a summer circuit which would have three discrete output levels as a function of three discrete inputs, and it was necessary to convert these to outputs having a separate ground from the Attitude Sensor circuits.

The pitch, roll, and central signals are fed to emitter followers of the 3-channel summer (See Figure 2.4.6-21) Q_1, Q_3, and Q_5. The signals are then coupled to amplifiers Q_2, Q_4, and Q_6. The signals are half wave rectified and summed across the 2.05K resistor. The summer output is fed to D_1 of the chopper amplifier. The input, feeding the base of Q_1 of the chopper amplifier, (see Figure 2.4.6-22) is a square wave proportional to the summer output signal. The output of Q_1 is then fed to the Q_2, Q_2 combination which is a Darlington circuit phase-splitter.

The square wave outputs on the emitter and collector of Q_3 are coupled to the full wave bridge network. The full wave bridge converts its inputs to D-C voltages and the output is applied to the 2 μf 10K filter combination which is terminated to the second ground plane.

The output levels of the video telemetry circuit remained distinct as a function of the temperature as indicated in Table 2.4.6-7. As the temperature was varied between the extremes (-35°C to +85°C) the output voltage varied linearly.


C1
1000
MC309
2.56 Mc
A1-A
A1-B
R1
10K
-5.2
-1.15
R2
10K
MC309
C3
200
PITCH
A2-A
A2-B
A3-A
R3
20K
Q1
R4
10K
R5
1K
-1.5
R6
10K
C4
200
MC302
1 MSEC
PULSE
A7-A
3.9K-R9
C6
1000
MC302
R11
3.9K
R7
10K
R8
3K
.068μf
C5
R10
3K
.068μf
C7
R14
3.9K
MC302
C11
1000
MC309
.068μf
C10
R15
3K
-5.2
R18
10K
MC309
C14
200
A7-B
ROLL
A17-A
A17-B
R19
20K
Q2
R20
10K
R21
1K
C16
1000
MC302
R23
390
R22
3K
C17
1000
-5.2
R24
10K
MC309
C15
200
A18-A
A18-B
A20-A
MC30
CENTRAL
R25
20K
Q3
R26
10K
R27
1K
MC309
A20-B
A21
-6V
R33
3K
R34
15K
R35
5.1K
R30
10K
R31
15K
R32
5.1K
CR2
2 MSEC
PULSE
R28
20K
CR1
C18
.1μf
C19
.047
Q6
READ
Q4
Q5
R29
4.3K
-5.2
MC304
A23
-1.15
A24
-1.15
MC304

2270

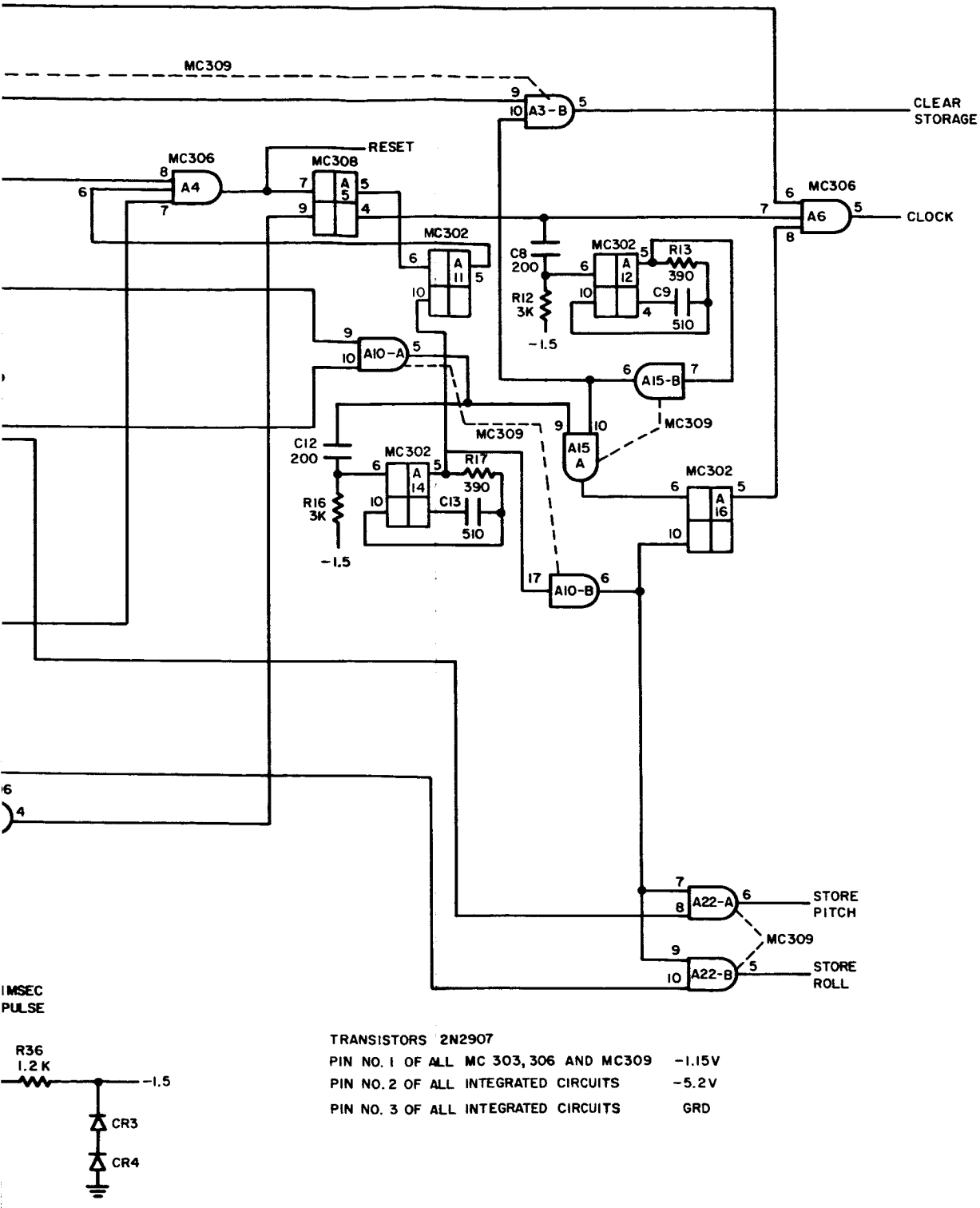
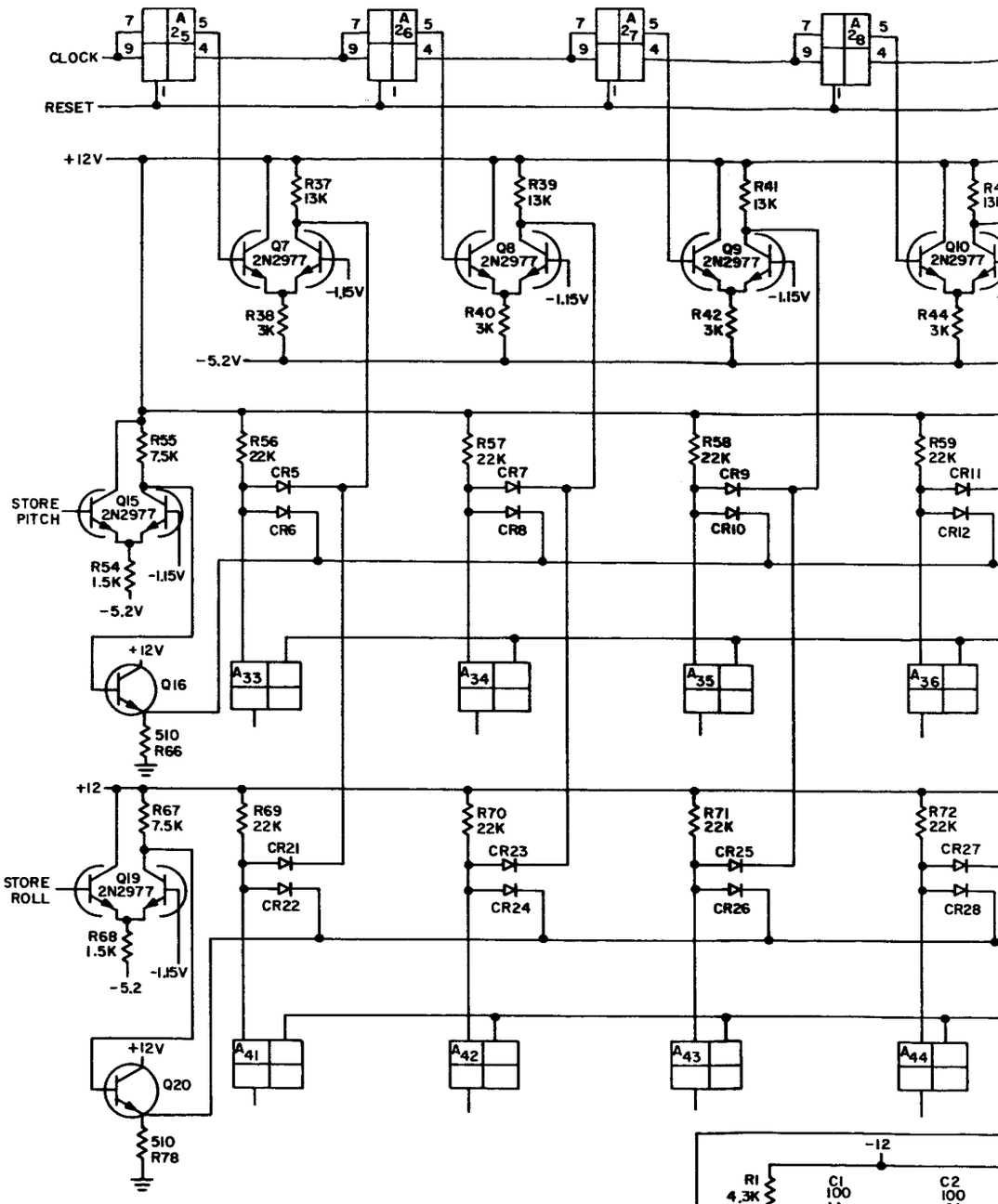
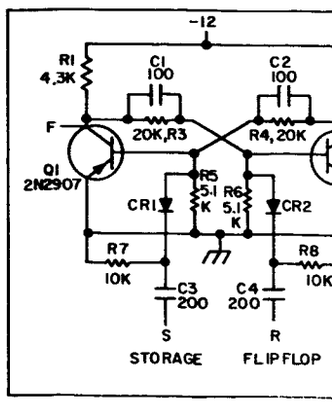


Figure 2.4.6-18. 8-Bid Counter



ALL DIODES IN3730



9290

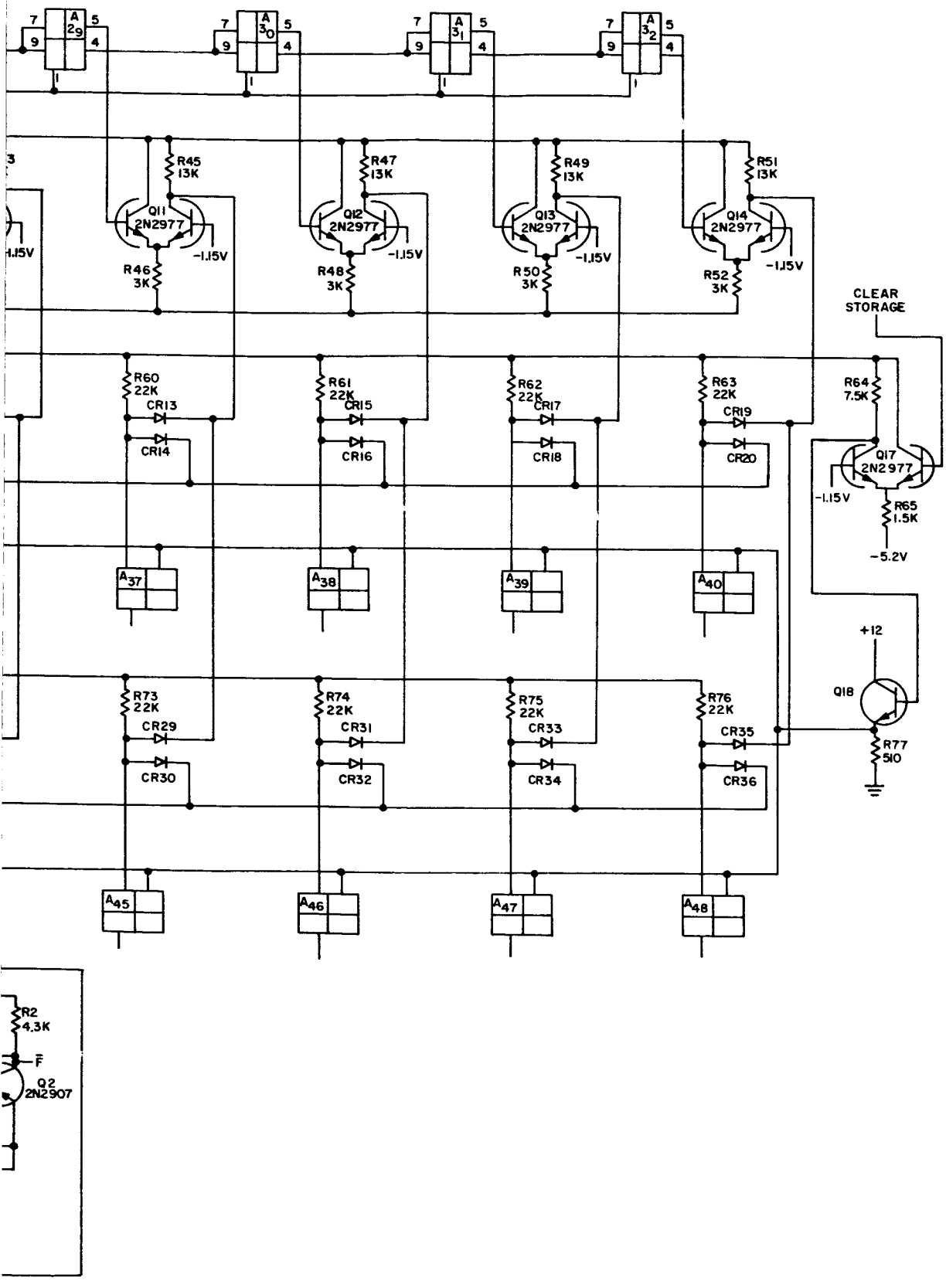


Figure 2.4.6-19. 8-Bit Counter

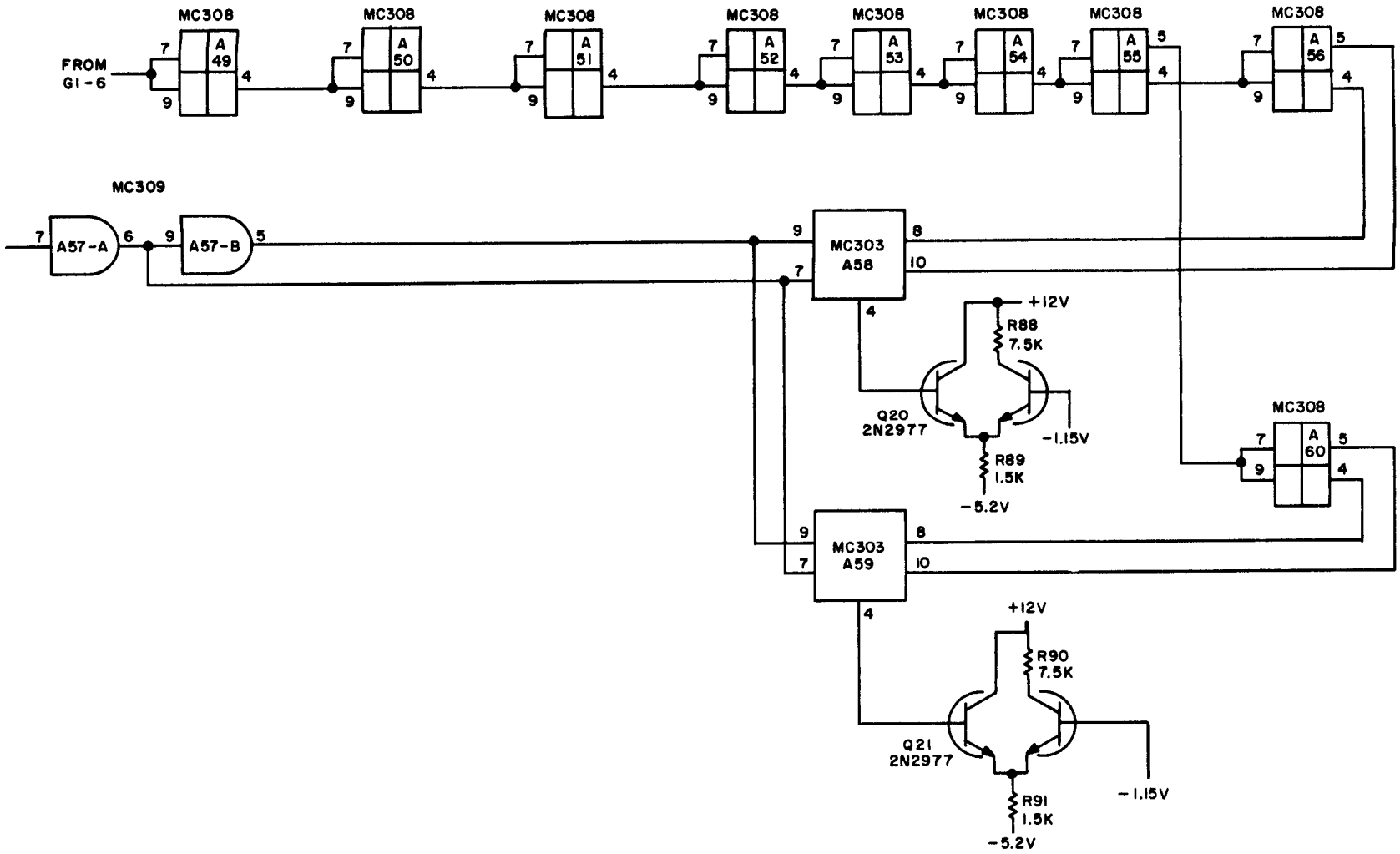


Figure 2.4.6-20. 256 Divider and Phase Detectors

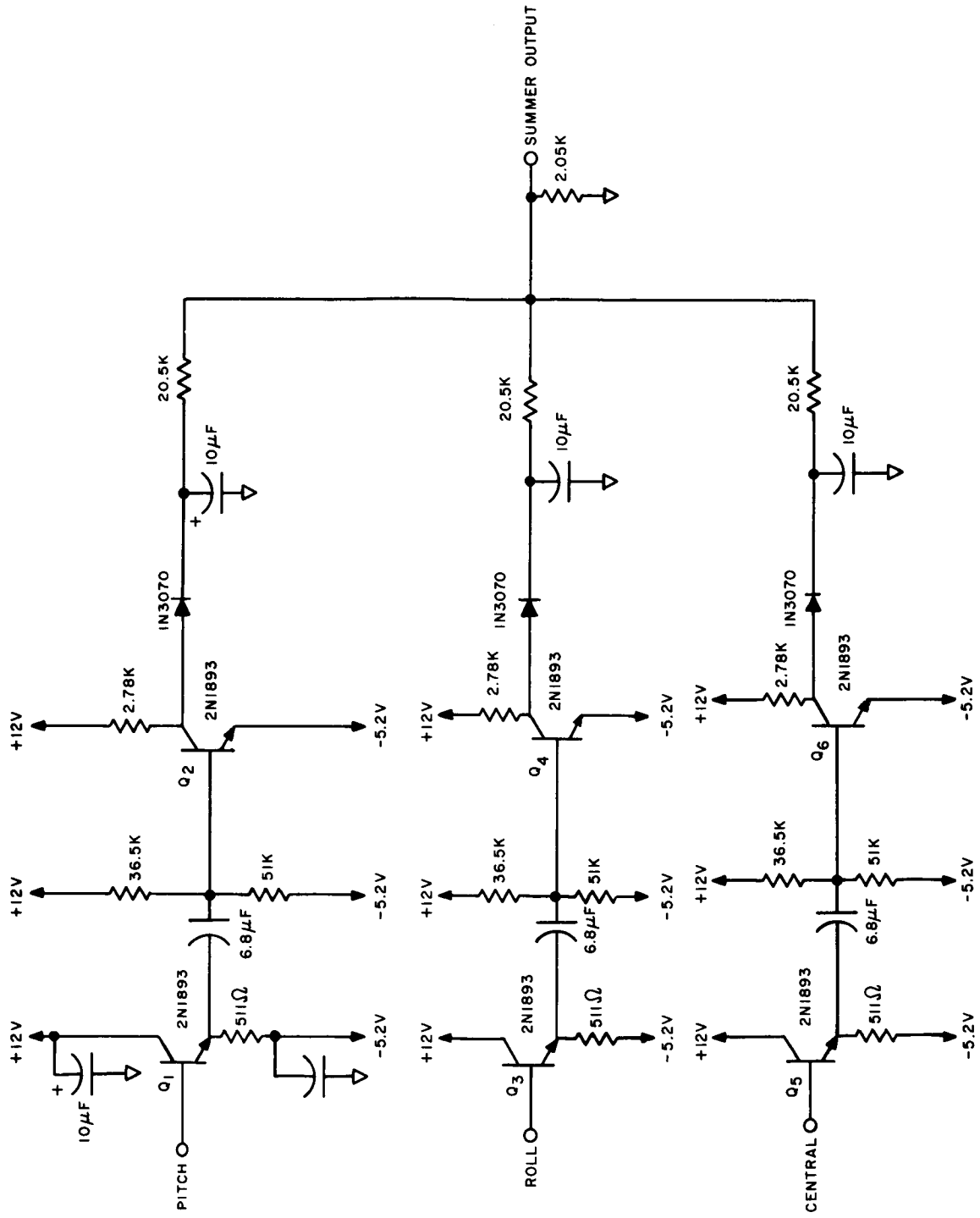


Figure 2.4.6-21. 3-Channel Summer

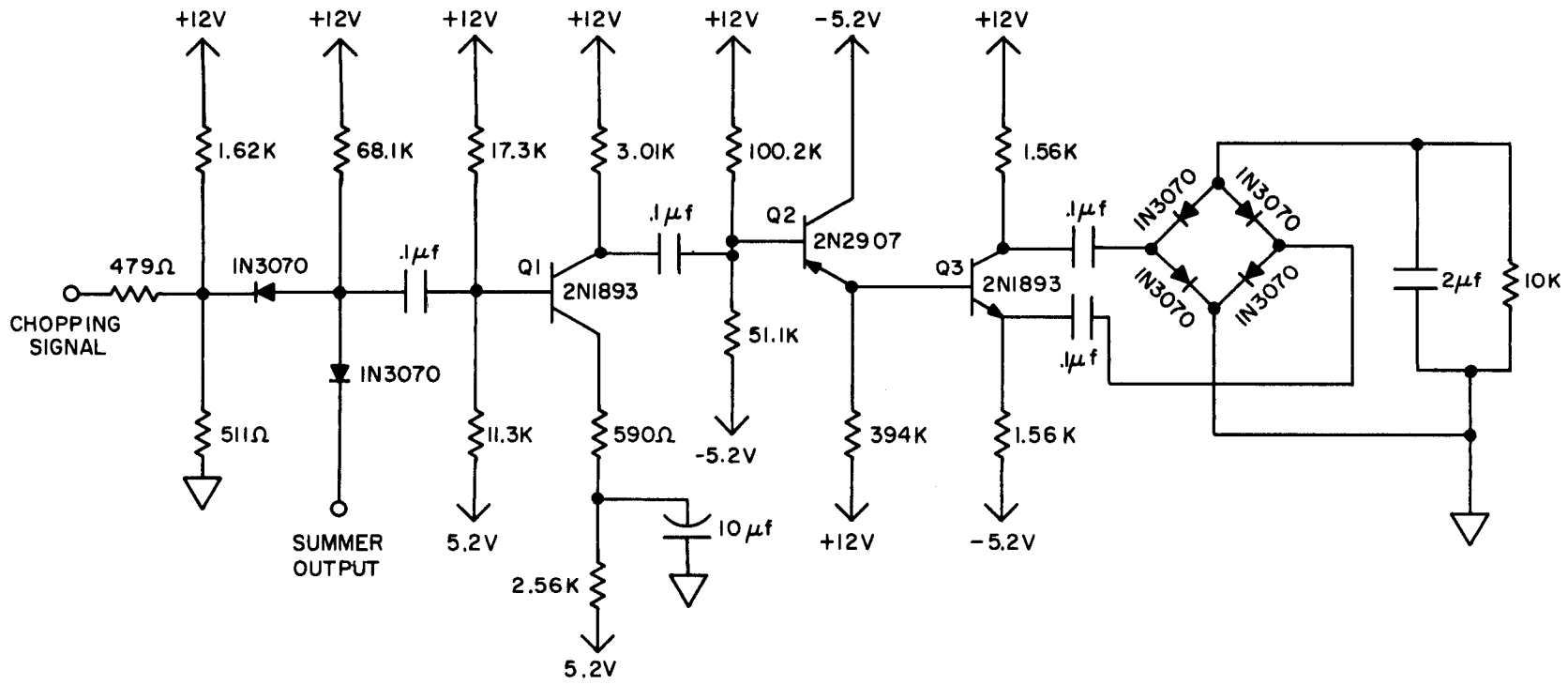


Figure 2.4.6-22. Chopper Amplifier

TABLE 2.4.6-7. OUTPUT VOLTAGE VS NUMBER OF CHANNELS ON AS A FUNCTION OF TEMPERATURE

Channels On	Temperature		
	$-35^{o}C$	$25^{o}C$	$+85^{o}C$
1	-0.75V	-0.9V	-1.3V
1&2	-2.9V	-3.2V	-3.8V
1&2&3	-4.5V	-4.8V	-5.1V

2.4.6.2.13 Power Supply

The requirements for low power consumption and very efficient voltage conversion are recognized as a strong requirement for satellites. Just as important are the requirements for small size and weight. With these in mind it was decided that a square wave DC to DC converter was the most acceptable. An attempt was made to do without a regulator, since the spacecraft power source nominal voltage is reasonably constant except for occasional voltage transients. These transients are to be filtered with input and output filters to within tolerable limits.

It was estimated that the following voltage and power levels would be required:

Voltage	Current (milliamperes)	Power (watts)
+25.0	20	.500
+12.0	150	1.800
-5.2	1,170	6.100
-12.0	50	.600

In order to obtain a small and efficient power supply it was necessary to employ a conversion frequency in the neighborhood of 20 kc. This frequency allows the use of small filters as well as the use of Permalloy tape-wound cores for the transformer instead of Orthonol which is normally used at lower frequencies. In addition, Permalloy power loss is an order of magnitude less than the Orthonol material.

The design is a basic square wave converter which employs a saturating, current limited drive transformer to provide base drive for power transistors which switch a nonsaturating power transformer. The drive transformer is a tape wound bobin core which is current limited by a resistor when the core goes into saturation. The power transistor has a very low saturation resistance, high current gain, high voltage breakdown, and a reasonably fast switching speed. The wire size for the power transformer was chosen as large as possible to minimize the IR drops. Since no regulating scheme was anticipated, it was extremely important to minimize voltage drops in the transistor switches, transformer and lead wire. Thus with temperature and load fluctuations the output voltage change can be minimized. The greatest anticipated effect on output voltage is due to the output rectifiers which have a temperature coefficient of about 1.8 millivolts per degree and thus a maximum change over temperature environment of about 216 millivolts. This effect can partially be compensated by the change due to the copper conductor IR drop.

A scheme for reduction of power consumption in the logic circuitry has been devised. This scheme switches power to the logic circuitry for two milliseconds and then the logic circuit is turned off for three seconds. Thus the instantaneous logic power of about 5 watts, averages out to about 10 to 20 milliwatts. However, the switching transistors, diodes, etc., must still be capable of the peak current demand. Switching the logic load was tried on the breadboarded power supply. This produced transients of several tenths of volts on the other output voltages as was expected. Additionally this limits the input source impedance to a very low value. This then limits the amount of input filtering which can take place.

Since the duty cycle of this load is very low, the final design would incorporate a separate converter for the logic circuitry. This will eliminate the transient problems, and if necessary a voltage regulator can be used because of the low duty cycle involved. Time did not permit the design of this circuitry.

A schematic of the power supply which supplies all but the logic circuitry is shown in Figure 2.4.6-23. The efficiency obtained for a power input of 5.0 watts was 78%. Thus the power loss was about 1.1 watts. Approximately 400 mw is attributed to rectification. The transformer magnetizing current of 20 ma accounts for another 560 mw. The remaining 160 mw is attributed to transistor, copper, drive, and stray losses.

The input filter will be a combination RLC filter. This will account for an additional 3 to 5 percent loss in efficiency. The power supply for the logic circuitry can be as inefficient as 50 percent and still not affect the overall efficiency because of the low duty cycle. Thus an overall efficiency of 72 percent is expected, requiring about 5.25 watts of input power.

2.4.6.3 Mechanical Design

Specifications for the RF Attitude Sensor package included dimensions of 6 by 6 by 6 inches and a design-goal weight of 8 pounds. The mechanical design approach to accomplish the packaging of the equipment shown in Figure 2.4.6-24 is described in detail in the sections that follow. Basically, all items utilized in the package are necessary to the design, and where possible are required to share functions.

No primary structure is provided. The circuit modules are mounted to equipment plates, and these in turn serve as the structural link between the RF assembly and the package base (or mounting) plate.

The RF assembly, equipment plates, and base plate are tied together with thin rigid covers. The covers are forced to take stress loading and are in reality a strong link in the package structure.

The equipment plates provide mounting for the circuit modules, house the DC and signal inter-module cabling (thus eliminating haywire) provide functional circuit

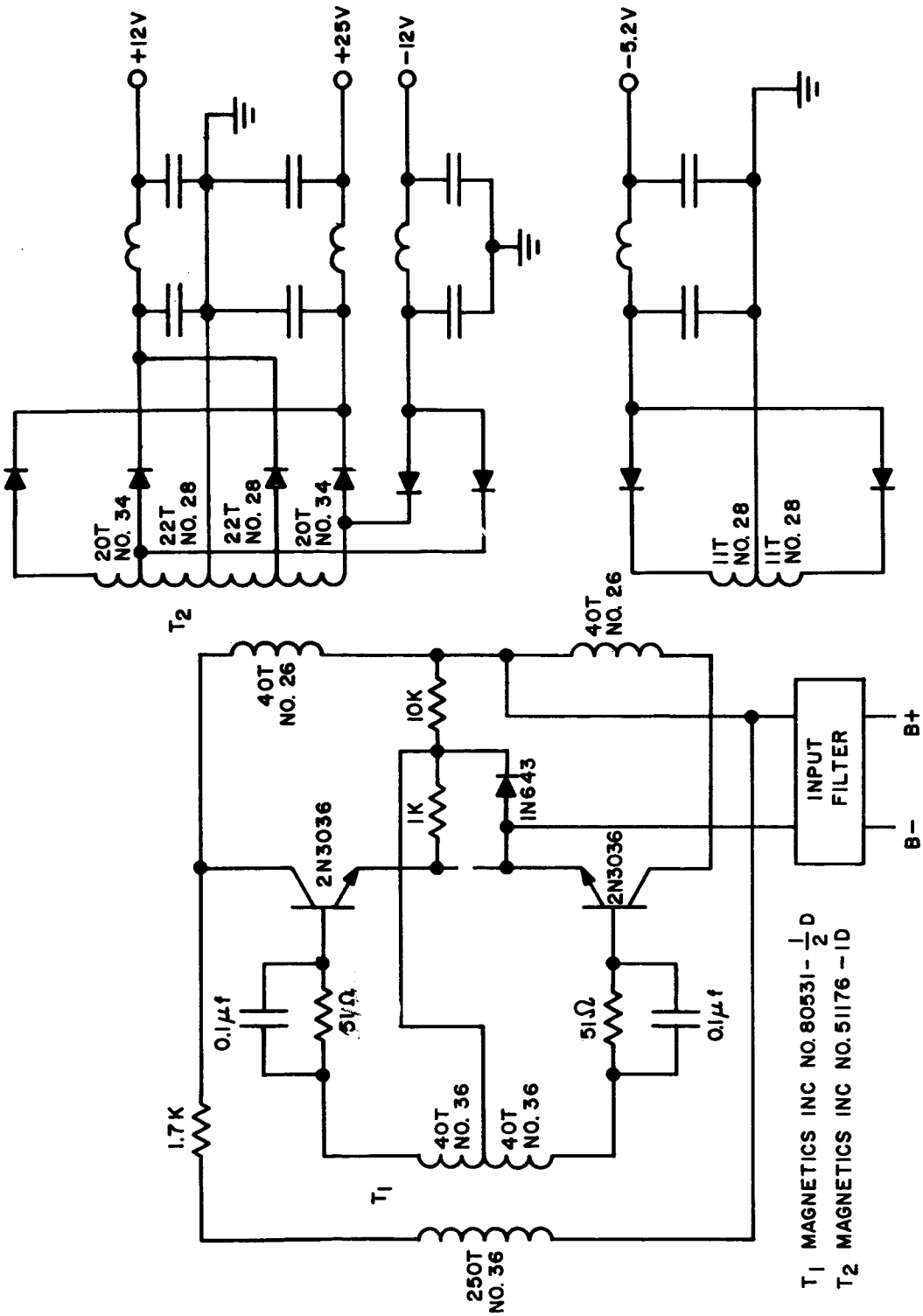


Figure 2.4.6-23. Power Supply

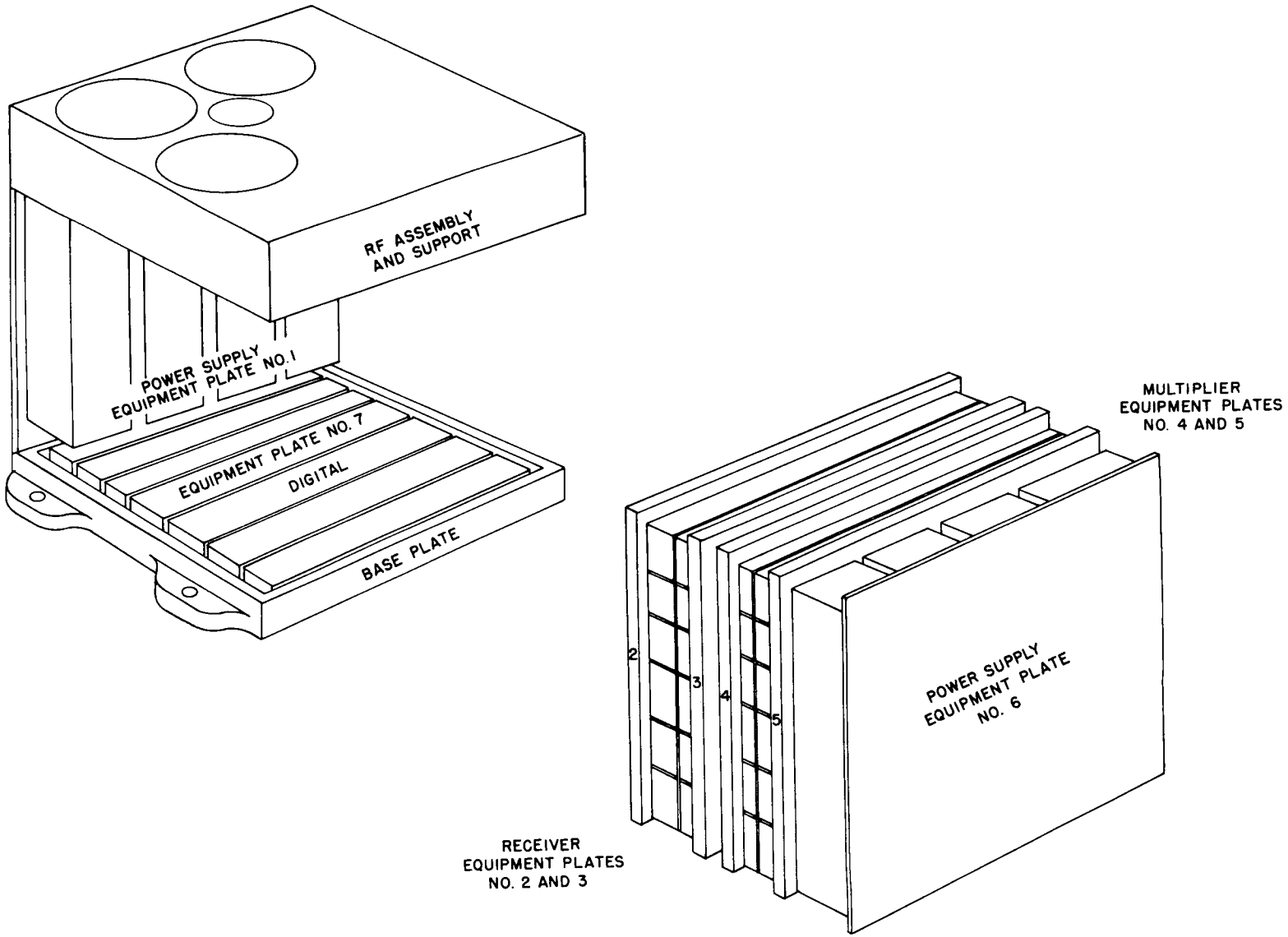


Figure 2.4.6-24. RF Attitude Sensor Packaging

grouping to reduce interconnection, provide structural integrity for both package and modules, and provide heat transfer paths for both modules and other package elements.

The package was divided into the following functional areas:

1. RF assembly
2. RF support
3. Equipment Plates
   a. No. 1-Power Supply
      - Filters
      - Power Transformer
   b. No. 2-Receiver
      - Modules for IF loops
   c. No. 3-Receiver
      - Modules for IF loops
   d. No. 4-Multiplier
      - Modules for Multiplier Chain
   e. No. 5-Multiplier
      - Modules for Multiplier Chain
      - Varactor Chain Assembly
   f. No. 6-Power Supply
      - Filters
      - Power Transformer
   g. No. 7-Digital
      - Modules for Data Processing and Readout
4. Base Plate
5. Covers

For purposes of this report the work will be itemized under the following headings:

1. RF Assembly
2. RF Support
3. Varactor Chain
4. Base Plate
5. Covers
6. Modules
7. Equipment Plates

2.4.6.3.1 RF Assembly

The RF assembly was to be purchased as a tested unit with co-axial IF outputs, LO output, varactor chain input, and test points for each antenna.

The unit was designed to bolt directly into the RF support element.

RFI shielding was provided at the interface between the RF unit and package mating parts.

2.4.6.3.2 RF Support

The RF support was designed as a welded and machined part. The upper section mated directly with the RF unit, while the lower section mated with the equipment plate sub-assemblies.

Vibration and thermal loading was distributed by the section design. Two sides of the support accepted removable covers, the other two sides accepted the cover plates for power supply equipment plates (No. 1 and No. 6). All four cover surfaces were grooved to accept rectangular RFI mesh. Stress load was directed through the equipment plate subassemblies (No. 1 through No. 6) to the base plate. Thermal paths from the RF unit were provided by the RF support into the equipment plate subassemblies, and then into the base plate.

2.4.6.3.3 Varactor Chain

The varactor chain was to be purchased as a tested unit with co-axial output and input connectors.

The unit was to be mounted to equipment plate No. 5, which also contained the multipliers required to drive the unit.

Equipment plate No. 5 provided a solid heat sink into which the varactor chain unit was mounted. Thermal paths were provided through the equipment plate frame and into the base plate.

2.4.6.3.4 Base Plate

The base plate was designed as a welded, machined part to accept the equipment plate subassemblies, package covers, and house equipment plate No. 7.

The base plate section contained four package mounting lugs. Grooves for RFI shielding at the cover junctions and equipment plate No. 7 periphery were also provided in the section.

2.4.6.3.5 Covers

Two removable package covers were provided to allow for connection of the IF outputs of the RF assembly to equipment plates No. 2 and No. 3. The covers also facilitated connections from the various equipment plates to the power supply equipment plates and telemetry connectors.

Both power supply equipment plates were designed such that the outer plates of each assembly acted as package covers. Thus it was possible to remove four covers, making the receiver and multiplier equipment plates more accessible. Equipment plate No. 6 contained the access port for connection of RF co-axial cables for external RF test.

2.4.6.3.6 Modules

Module design for RF Attitude Sensor utilized plug-in functional modules. The system is called MODULAR WELDMENT and has been described fully in TECHNICAL PROPOSAL for the SENSOR, ATTITUDE, RADIO FREQUENCY.

During the initial stages of design effort the modules were defined functionally as follows:

1. IF
2. Detector
3. Filter-Limiter
4. Digital #1
5. Digital #2
6. Digital #3
7. Digital #4
8. Digital #5
9. Digital #6
10. Digital #7
11. Digital #8
12. Digital #9
13. Digital #10
14. Digital #11
15. Telemetry Amplifier
16. DC amplifier
17. Sweep
18. Power amplifier #1
19. Power amplifier #2
20. X6 multiplier #1
21. X6 multiplier #2
22. X4 multiplier
23. X2 multiplier
24. VCO
25. VXO
26. Input/RFI filter
27. Chopper
28. +24 filter
29. +12 filter
30. -12 filter #1
31. -12 filter #2
32. -5.2 filter

Preliminary layouts for modules Nos. 1, 2, 22, and 23 were essentially completed. Preliminary layouts for modules Nos. 4 through 14 were in process but involved considerable interconnection to complete.

Enough general information about module function and complexity was available to allow for preliminary equipment plate assignment.

All module tooling was in place and ready for implementation in the building phase.

2.4.6.3.7 Equipment Plates

Module assignments are as indicated in the introduction. Equipment plate design is as follows:

1. Provision is made on the top cover plate for mounting DC plugs, passage of co-axial and DC cabling, and connectors where applicable.
2. DC wiring is accomplished from an edge-connector to the various DC plugs.
3. Co-axial cables are run to interconnect modules and provide intra-equipment plate connections.
4. An edge frame is provided to space the top and bottom cover plates and rigidize the assembly. As described previously, the frame also distributes stress and thermal loads.
5. After mechanical and electrical tests the unit is assembled, placed in a retaining fixture, and the space between the cover plates filled with hard foam potting compound.
6. Modules are assembled to the DC plugs and the RF cables are attached.
7. The equipment plate can now be checked electrically for proper operation within limits of its modules' functions.

2.4.6.3.8 Equipment Plate Subassemblies

Modules are mounted to the power supply equipment plates with screws. These modules are one inch by one inch cross section and are quite heavy. The individual screw mounting is required for electrical and mechanical integrity.

Digital modules are one half inch by one half inch cross section and are plugged directly into a receptacle to distribute their many interconnecting wires. The modules are mounted through the receptacle with mounting screws.

Receiver and multiplier modules are one half inch by one half inch cross section and are installed on DC plugs mounted in the equipment plate. Both receiver equipment plates are bolted together as an assembly and both multiplier equipment plates are bolted together as an assembly. Both assemblies require co-axial connection to the RF assembly and must be connected to power supply equipment Plate No. 1 and digital Plate No. 7. Signal interconnection must also be provided between these assemblies but most co-axial runs remain within the equipment plates.

2.5 RELIABILITY

2.5.1 PARTS, MATERIALS AND STANDARDS

The emphasis during this quarter in the reliability program for ATS was in the parts, materials and standards area. Selection and qualification of parts for all GE equipment were mutually discussed at three presentation meetings between representatives of NASA/GSFC and GE on October 23 and November 6 and 19, 1964.

At the meeting on October 23rd held at NASA/GSFC, the following parts and standards topics were discussed:

1. Part Status in respect to HAC Specifications
2. Part Qualification Program
3. Compatibility of the ATS Schedule with the Parts Program
4. Standards activity on ATS
5. Effect of radiation on spacecraft electronics.

The second meeting at NASA on November 6th consisted of a review of the requirements contained in NPC-250-1 and its relation to the ATS Program. On November 19th, a presentation was given to NASA representatives at VFSTC concerning General Electric's compliance to NPC-250-1 on the ATS Program. Manpower estimates, tasks and exceptions were included as part of the presentation.

2.5.1.1 Documentation

Major documentation prepared and distributed during this quarter was:

490L106 - Approved Parts List (ATS)

490L107 - Approved Materials List (ATS)

SVS7325 - Use of Standard Parts, Materials and Processes (Rev. A, B & C)

All component specifications and work statements were reviewed for inclusion of reliability requirements and tasks. An analysis of the radiation spectrum for

MAGGE and SAGGE flights, especially, the solar flare activity was made for its effect on the semiconductors and other susceptible parts in the ATS equipment. As a result of this analysis, the expected degradation in various part parameters was incorporated into SVS7325 Revision B. By NASA direction on December 30, 1964, these analyses were held in abeyance pending further study of this area. GE was instructed to restrict the allowance of radiation effects on semiconductors to the much lower figure described in Revision C of Specification SVS-7325.

2.5.1.2 Part Tasks

1. Cover drawings for all HAC Specifications were prepared for issue and designated R45XX.
2. 490L106 was revised and updated twice to include the revisions to 53 HAC drawings received November 18th as well as to change the format.
3. Advanced order lists were prepared for all subcontractors and designated as 490L108 through -113. These were prepared to provide documentation and control of advance ordering consolidation requested by NASA for overall program cost improvement. A study of the cost reductions attainable by this consolidation was presented in detail to NASA on November 18th and subsequent revisions of this indicated that these savings were not sufficient to cover the extra costs of integrating and rescheduling the subcontractors' orders. Integration, including Hughes and GE, was also evaluated with the same conclusion.
4. Material Substantiation Forms were prepared for qualification tests of the non-qualified parts. (This is applicable only to parts not already qualified under HAC specifications).
5. Technical support was provided to Receiving Inspection, Production Control, Manufacturing, Purchasing, Engineering and subcontractors in the reliability, part and standards areas.
6. Reviewed subcontractors' requests for 103 exceptions to the approved Parts List.
7. Provided specific recommendation to Lear-Seigler to use five semiconductors appearing on the approved Parts List in lieu of their selection, as well as nine selected connectors in preference to those requested.
8. Reviewed four Lear-Seigler transformer drawings for conformance to ATS program requirements.

9. Prepared a semiconductor drawing for Adcole, which is in the revision process to incorporate data submittal requirements.

10. Four semiconductor specifications are in process for Adcole to incorporate additional electrical requirements to cover the anticipated degradation due to the radiation environment.

11. Similar tasks have also been undertaken for the Power Control Unit and Albedo Sensor.

12. The question of what component testing should be undertaken to supplement the high reliability parts program and provide an assurance of a 3-year performance capability under space environments and operational mission profiles was studied. This question is of particular importance in those instances in which program costs or schedules preclude the use of high reliability parts (e.g., the decision to use the same design with the same part types as the subcontractor has previously used in the television camera).

    Test requirements for this latter type of situation was issued as section 3.10 of SVS-7325, Revision B and called for a minimum of 1000 hours of testing under launch and space environments with a terminal period of 700 hours of failure-free operation as a requirement prior to shipment. This type of test would not only supplement the high reliability parts program but would provide reasonable assurance at practicable costs that not only were the parts themselves suitable for the ATS application, but also that their design application and their manufacture and test at component (black box) level was thoroughly developed, de-bugged and failure free.

    Since such tests had not been included in the program cost structure, the specific requirements of section 3.10 were deleted from SVS-7325, Revision C. These can be added at such time as such programs are resolved.

2.5.2 PARTS PROGRAM

The GE parts program is built around the Approved Parts List 490L106, the Application Standards SVS-7325.

This Parts List is at present chiefly comprised of Hughes Aircraft Company 988,000 series parts.

The GE plan as agreed upon with NASA on October 23, 1964 to utilize parts which have the highest probability of failure-free operation during the mission life of the satellite. The program will be implemented as follows:

1. Select the most reliable part types
2. Select the best suppliers as determined by past performance and vendor survey per NASA 200-3
3. Perform sound electrical and environmental screening tests
4. Power age the devices
5. Select the parts which exhibit the most stability during power aging.

   Data cards will be submitted by parts vendors by part serial number, machine compiled; and this data evaluated by parts specialists.

Parts Procurement Documents will detail the test particulars including the applicability of:

1. Pre-screening environmental tests (100% basis)
2. Group A Electrical (functional) tests (100% basis)
3. Type B Environmental Tests (sampling basis)
4. X-Ray Examination (100% basis)
5. Burn-in Tests ($\simeq$240 hrs, 100% basis)
6. Power-Aging Tests ($\simeq$1250 hrs, 100% basis)
7. Qualification requirements (sampling or one-shot basis)

Additions and changes to the Approved Parts List is to be processed as follows:

1. Sub-contractors shall submit requests for approval for use of all parts (semi-conductors, valves, connectors, etc.) in ATS hardware that do not appear on Approved List 490L106 and de-rated per Application Standard SVS-7325. This request shall contain, as a minimum, the following information:
   a. Part Type (e.g., IN914, RN65, etc.)
   b. Manufacturing name and code
   c. Maximum application ranges which part is subjected to in the design (environmental and electrical derating factors)
   d. Procurement Specification if available.
   e. Data or documentation that satisfies at <u>least one</u> of the following:
      (1) Test results to demonstrate the part meets the important tests (vibration, shock, temperature, life) of the nearest applicable MIL specification.

(2) For common usage parts (those parts used by several ATS contractors and subcontractors), the following shall be included:

(a) A statement that qualification of the part was (or is being) conducted on the ATS Program and by whom.

(b) The applicable part specification or the Quality Assurance section of the parts specification.

(c) Qualification test data available.

(3) Evidence that the part is covered by an acceptable vendor high reliability program and specification.

(4) Details of previous successful application in spacecraft similar to ATS.

(5) Data in accordance with (1) through (4) for an existing similar part. Acceptance will be considered if the part is of the same construction, material, processing and quality level and possesses similar environmental tolerance and failure modes.

2. The subcontractor is obligated to apply similar disciplines to his sub-tier vendor. The subcontractor shall submit sub-tier vendor requests to GE for review in accordance with Para. 1 above.

3. The subcontractor shall submit a parts specification (unless a specific Federal specification is used). This specification shall, as a minimum, include the following:

a. Performance and environmental requirements for the application including tolerances and parameter changes with life and environments.

b. Complete acceptance criteria including specific ACCEPT/REJECT definitions and parameter limits. The acceptance test section may be patterned after the nearest applicable MIL Specification.

c. Reliability Assurance provisions such as screening, burn-in, etc.

d. Identification and data provisions

e. Complete qualification requirements

4. The subcontractor is obligated to review and approve their sub-tier Vendors' Part Procurement Specifications. The subcontractor will submit their sub-tier vendor documents and their evaluation and action to GE for review.

5. GE will prepare the Missile and Space Quality Purchase Part Specification (MSQ) and spell out the necessary additional screening, power aging and special environmental tests required on subcontractors Parts Procurement Specification. See Figure 2.5-1.

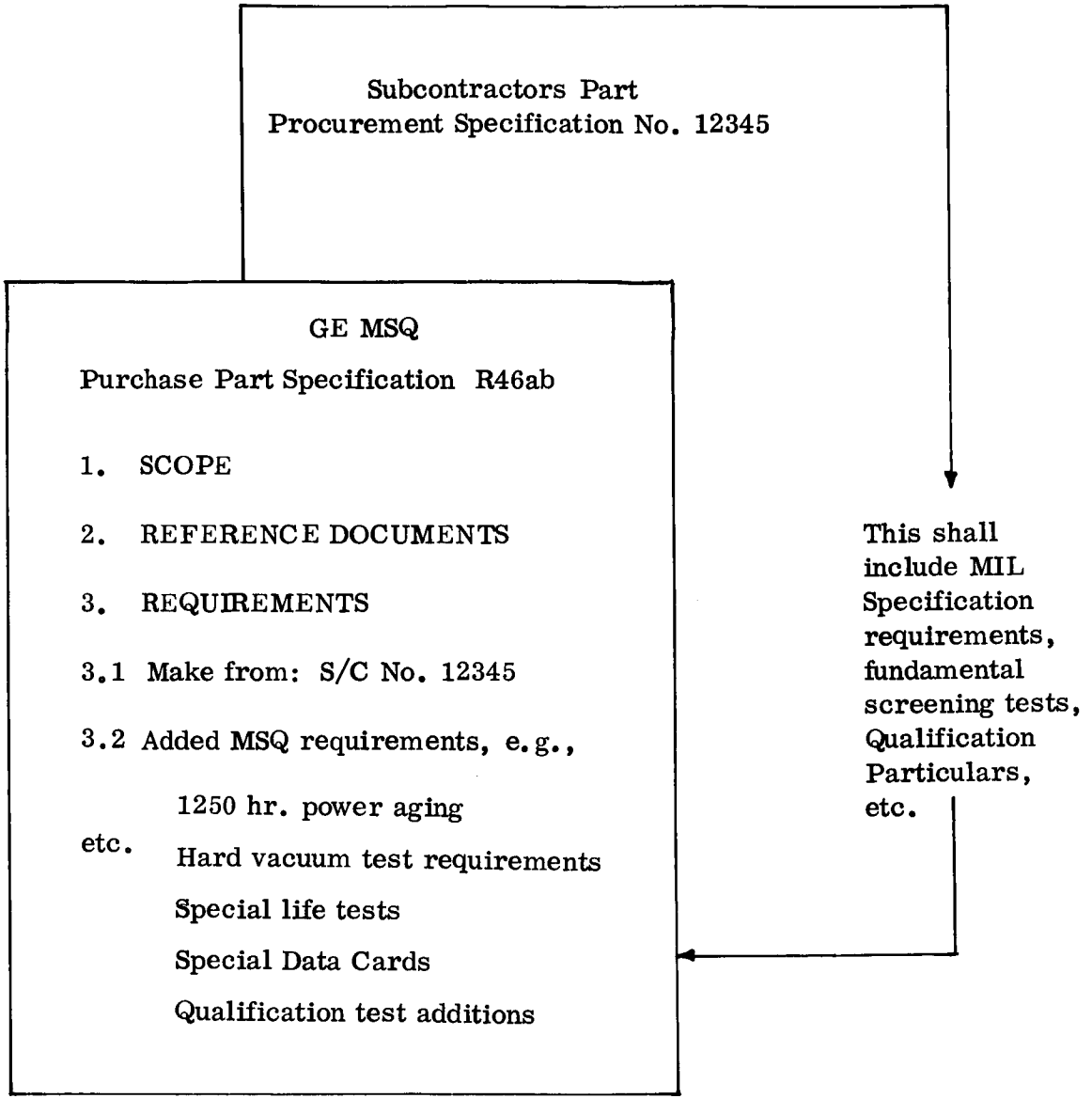


Figure 2.5-1. GE Missile and Space Quality Purchase Part Specification (Typical MSQ)

GE will reconcile data and respond formally. In general, the part(s) will be entered on the Approved Parts List 490L106.

Parts Qualification Testing will be conducted by GE (or GE authorized agency) in accordance with the parts qualification test section of the Approved Parts Procurement Specification.

1. Prior to conducting full-scale parts qualification consideration shall be given to the following elements:
   a. Conduct the qual test on parts and parts application as a portion of higher levels of assembly testing, e.g., module tests, subsystems tests, etc.
   b. Review other sources of qualification information, e.g., IDEP, ECRC, PRINCE, other ATS subcontractors, etc. The results of this review will be documented and entered into the Qualification Matrix Record.
   c. Part criticality in its application shall be given priority in the decisions for qualification testing.
   d. Failure modes shall be utilized as a prime tool in determining critical environments that are used in the Test Plan for parts qualification testing.
2. GE will submit full qualification test reports. A Qualification Matrix Record will be maintained in addition.

Power Aging Test Data and Degradation Analysis data cards for GE procured parts and for subcontractor procured parts will be analyzed at GE; parts will be selected by individual serial number for use in flight hardware. It is estimated 1/2 of the total procured parts will be selected for use in delivered hardware.

Several elements of the parts business and current assumptions in the GE parts program are outlined as follows:

1. Disposition of rejected parts as a result of degradation analysis. Nearly half of all purchased parts will be affected.
2. Parts prices (including power aging, data cards, data reduction and degradation analysis and resultant decisions) will be an order of magnitude more costly than a MIL + 250 hour Screened Part.

Historical data on parts included on Approved List 490L106 is to be maintained in the parts portion of the ATS Project Data Book. This handbook will include:

1. Parts test results
2. Source of information
3. Established failure rate for specific part (or for the generic part)
4. Stress and de-rating curves
5. Application notes and recommended areas of use
6. Precautions.

Some of this information, developed on the Advent Program will be directly applicable to ATS Program due to certain similarities in mission requirements.

A flow chart which is typical of part qualification procedures is shown in Figure 2.5-2. The procedure by which parts are screened is shown in Figure 2.5-3, and the process by which additional parts are added to the Approved Parts list is given in Figure 2.5-4.

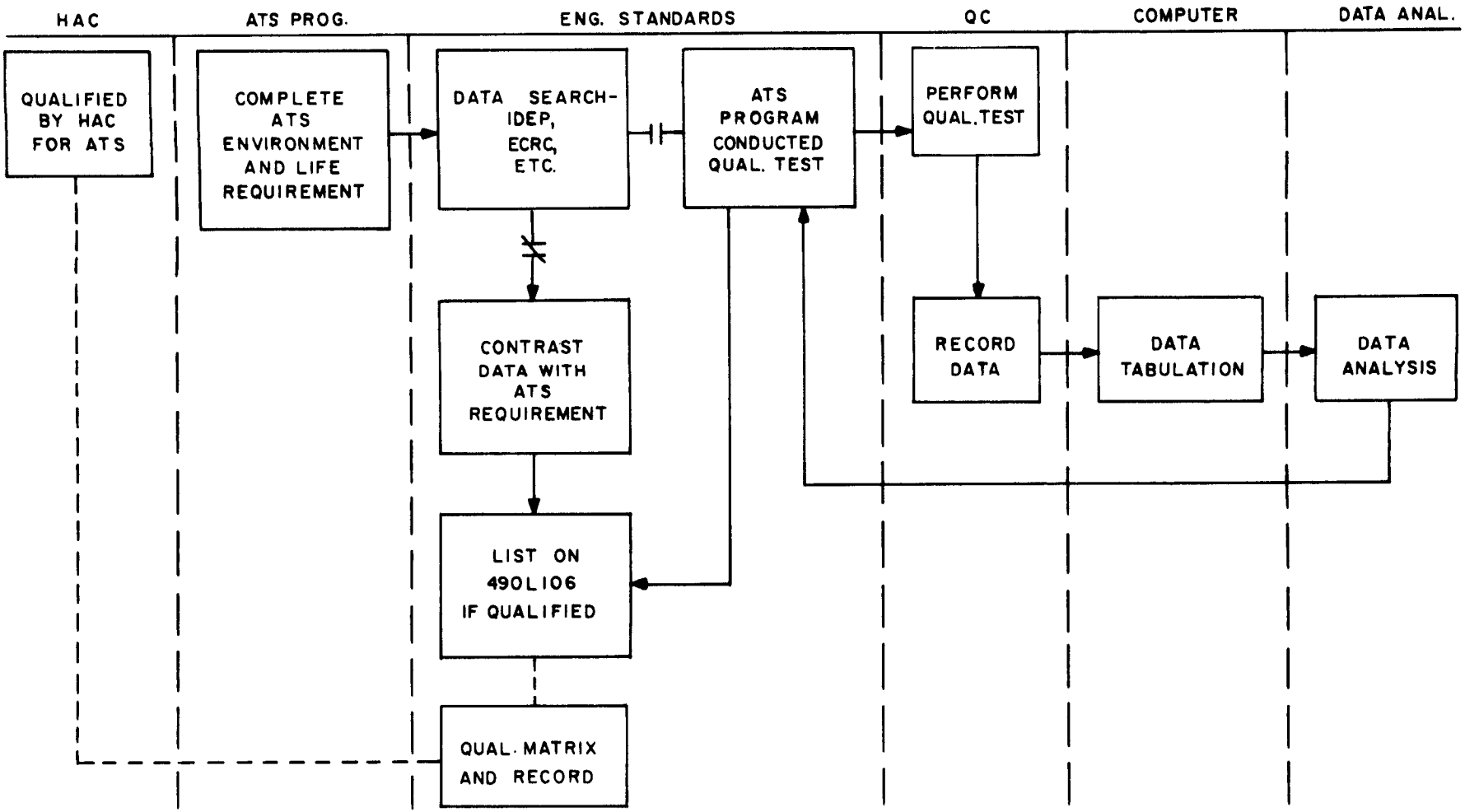


Figure 2.5-2. Flow Chart - Part Type Qualification

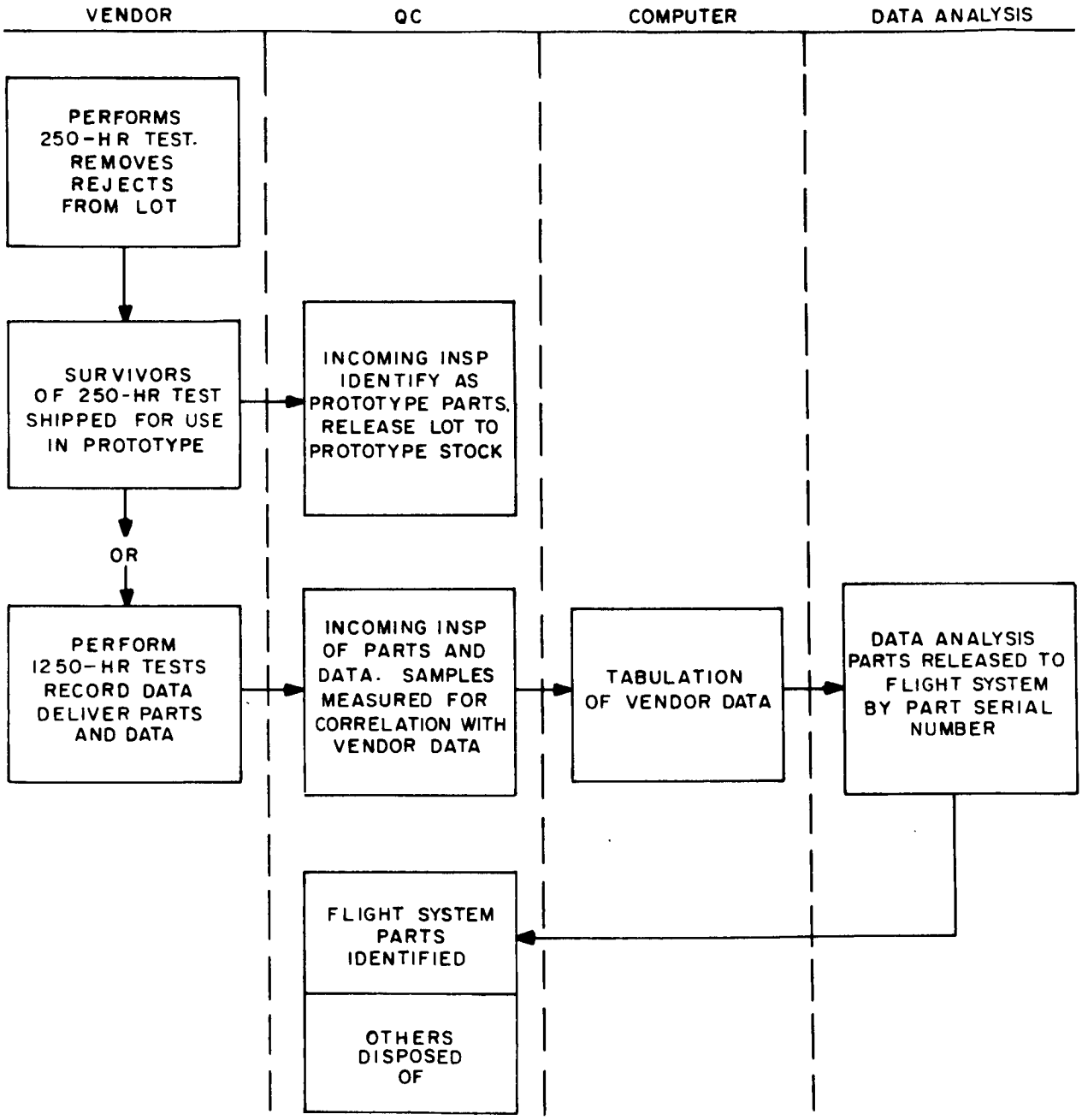


Figure 2.5-3. Flow for Screening Parts

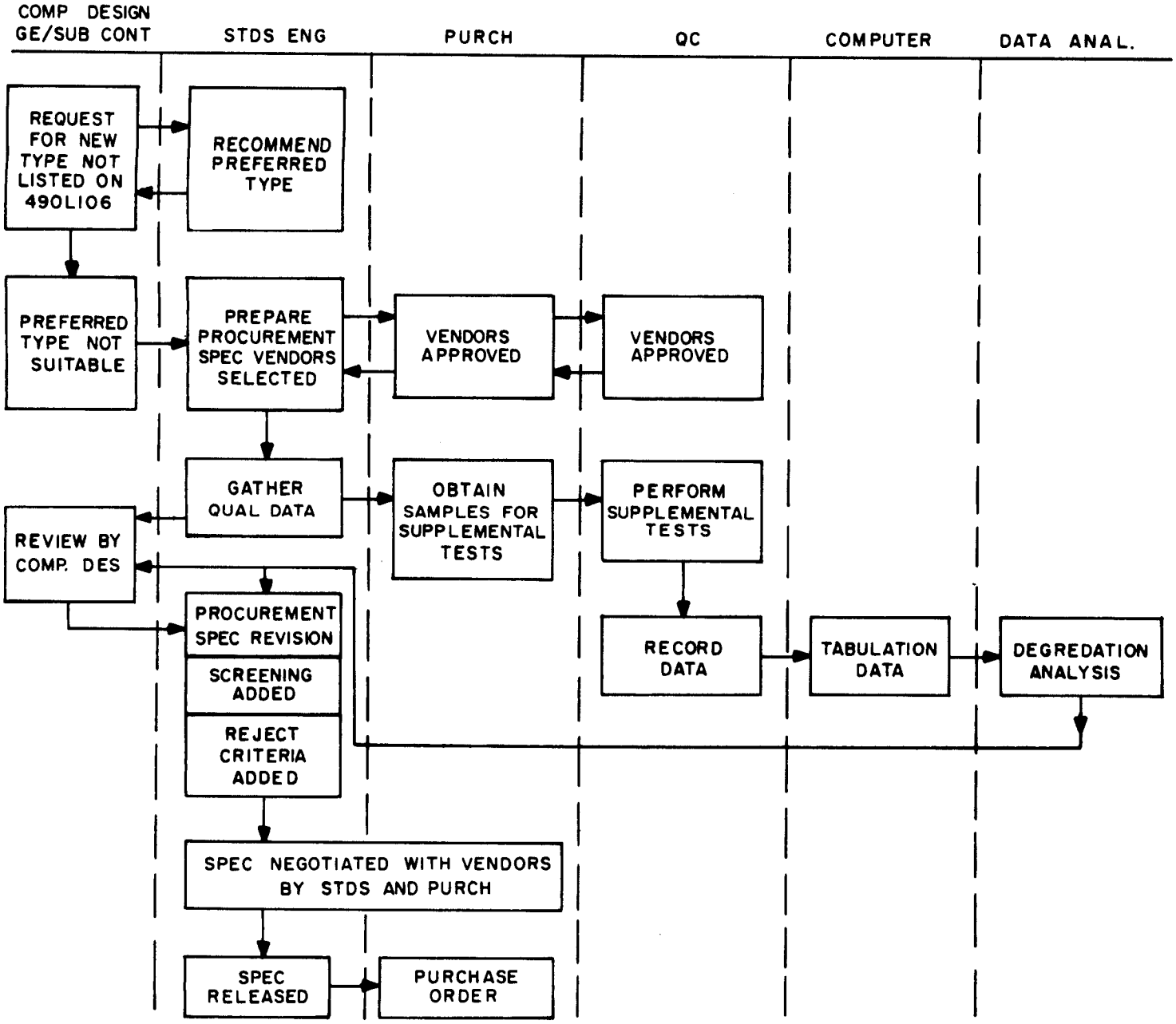


Figure 2.5-4. Flow for Adding Parts to Approved Parts List, 490L106

2.6 QUALITY CONTROL

Testing procedures were defined and facilities implemented in support of design engineering evaluation for the components and subsystems that comprise the ATS Gravity Gradient Stabilization System. Quality Control activities for this effort are described in the following paragraphs.

2.6.1 PRIMARY AND SECONDARY BOOM SUBSYSTEMS

Contact was made with deHavilland to discuss test methods and test equipment. Tentative agreement was reached on the testing of several critical items such as rod thickness, rod straightness, and the requirements of a test track. A test track was designed to accept the deploying rods. Particular concern is the determination of deployment rate. Processes were incorporated into the design to measure boom length. A facility was located in the Spacecraft Department Complex to house the test equipment.

2.6.2 COMBINATION PASSIVE DAMPER

Quality Control requirements were determined and incorporated into the following Specifications and Work Statements:

Component	SVS	Work Statement
Angle Detector	7315	9744-WS-005
Passive Hysteresis Damper	7331	4176-WS-008
Two-Way Solenoid	7333	4176-WS-003

A vendor facility survey to determine the capability of Dynamics Research Co. to produce an Angle Detector of highest quality was accomplished. It is felt that this vendor can meet the quality requirements of this component.

Initial quality requirements for the Passive Hysteresis Damper were discussed with Space Technology Laboratories.

Quality requirements pertaining to the manufacture of Air Bearings, which form part of the Low Order Force Fixture (LOFF) and Advanced Damping Test Fixture (ADTF), were incorporated into Work Statement 9744-WS-004. These Air Bearings are being manufactured by GE Ordnance Dept. and are subject to Surveillance Inspection by our QC representative at that Plant.

QC inspection is being accomplished on both the LOFF and ADTF test fixtures. Each of these units is under construction.

2.6.3 RF ATTITUDE SENSOR

A survey of RGO's facility and quality system for conformance with NASA NPC 200-3 was conducted by Spacecraft Department's Vendor Quality Assurance group. The survey indicated that RGO conformed to 200-3.

Quality Control Engineering participated in the determination of the component specification and the RGO work scope. In addition, the component spec (SVS 7506) and the Work Statement (WS-9744-003) were reviewed and signed off by the responsible QC Engineer.

Based on the Component Spec and the Work Statement, a Quality Control Plan was developed by QC Engineering and issued which, in detail, spells out the specific responsibilities of each Quality Control Functional Group and informs ATS Program Management at Spacecraft Department of the detailed QC activity that will be required to achieve the high reliability objectives of the Program.

The test requirements associated with the Spacecraft Department's Development, Qualification, and Acceptance tests were determined after numerous discussions with representatives of Design and Test Equipment Engineering.

All QC effort was stopped during F/W 49 when the RF Attitude Sensor was dropped from the ATS Program.

2.6.4 SOLAR ASPECT SENSOR

Effort during the past quarter on the Solar Aspect Sensor test program has been principally directed toward the following areas:

1. Defining the basic tests to be performed at General Electric and specifying the needed test equipment
2. Designing the 6-inch xenon solar simulator and securing vendor quotation for its fabrication
3. Reviewing Adcole test plans and test equipment
4. Providing support to the program office and component engineer in the preparation of the component specification and in the estimation of costs.

The basic test in the Solar Aspect Sensor test program will be the ambient temperature functional test where a complete evaluation of the component's accuracy, field of view, output impedance, power consumption, and other important electrical and mechanical characteristics will be made. The component will be mounted on a 2-axis calibrated table and stimulated with the 6-inch solar simulator during these tests.

The operation of the sensor over the full temperature range predicted for the orbit environment will be checked by placing the sensor in a temperature chamber with an optical window to allow stimulation with the 6-inch solar simulator. It will be possible to introduce small variations in the angle of incidence of the simulated solar beam of about 20^{o} to fully evaluate bit transition accuracy, eye selection capability, and otherwise check the proper functioning of the component under extreme temperature conditions.

The operating requirements for the thermal vacuum, and humidity tests will be met by applying power to the SAS and stimulating one of the five detectors with a non-collimated tungsten light source in such a manner as to produce an all "ones" gray coded output. It will be the purpose of these tests to demonstrate simply that all of the electronic bit channels are operative and will not demonstrate the accuracy of the SAS under these conditions.

The schedule limiting item in the test equipment program is the 6-inch solar simulator and it is thus the only equipment item which has received extensive attention to

date. The solar simulator will be designed to produce a 6-inch diameter beam of light whose collimation duplicates the $1/2^{o}$ collimation of the sun and whose intensity is equal to that of the sun in the vicinity of the earth. Measurements have been made at GE as a part of the program which indicate that the 5 KW xenon bulb produces an average effective brightness of about 3.7 times that of the sun in a 1/2 mm square region near the cathode of the lamp. These measurements, plus calculations made with the aid of published GE lamp data, have shown that an optical system designed to collect energy from the brightest 1.5 mm square region of the 5 KW xenon arc with a collection half angle of about 27^{o}, will make it possible to produce a full solar constant of illumination with $1/2^{o}$ collimation if the transmission efficiency of the optics is above 45%.

An optical system was tentatively laid out which utilizes a pair of condensing lenses to image the arc on a field stop which is sized to select only the brightest 1.5 mm square region of the arc to serve as the object image for a parabolic reflecting objective mirror. Detailed calculations have been made to predict the characteristics of this and other similar systems with regard to transmission efficiency, chrommatic aberation, commatic aberation, and image quality. A Work Statement was written and vendor quotations secured for the detailed design and fabrication of the simulator.

2.7 MANUFACTURING

During the reporting period close liaison has been maintained between Design Engineering and Manufacturing Engineering. All design drawings have been reviewed and signed off by Manufacturing prior to release, which to date includes primarily engineering test equipment for the combination passive damper.

In addition a working model of a previously proposed clutch mechanism for the damper was produced, and work is in process to produce component parts for the latest solenoid actuated clutch mechanism design concept. This part is a corrugated Belleville washer made of beryllium copper.

2.7.1 POWER CONTROL UNITS

Five module drawings have been received for fabrication.

Coordinated tooling is being built to control the location of outgoing leads to match the potting molds and the printed circuit boards.

2.7.2 PROCESS DEVELOPMENT

The cleaning procedure for control against magnetic particle contamination of critical component parts in the combination passive damper during the manufacturing cycle is not yet finalized. The present plan, however, is to utilize as much as possible the cleaning procedures used on other in-house passive damper programs requiring similar cleaning requirements, and which have been proven effective based upon test results.

2.7.3 MAKE OR BUY STRUCTURE

In accordance with recent program changes the following is the up-to-date make or buy structure.

Item	Make	Buy
Combination Passive Damper	X	
TV Camera System		X
Power Conditioning Unit	X	
Sun Sensor		X
Angle Detector		X
Magnetic Torquing Coil	X	
Damper Rods/Mechanisms		X
Gravity Gradient Rods/Mechanisms		X

2.8 MATERIALS RESEARCH AND DEVELOPMENT

Materials effort centered on the Combination Passive Damper and the boom erection mechanism. In addition a thermal control coating development has started to encompass the entire system requirement. Specific design information is included in the respective component sections of this report.

Internal reports issued covering materials support of the system are listed below.

PIR	Title
PIR 9381-0326	Short Abstracts Concerning the Properties of Teflon, July 21, 1964
PIR 9381-0328	Gradient Rad Micrometeorite Damage Study, July 22, 1964
PIR 9381-0346	Lubricants and Mechanical Components of Lubrication Systems for the GGEP System, September 3, 1964
PIR 9381-0356	Preliminary Thermal Control Data on Metallic Films and Surfaces, October 23, 1964
PIR 9382-0089	Adhesive Bonding of Mirrors Aligned to Component Surfaces, October 16, 1964
PIR 4371-0001	Torsional Damper Spring, October 26, 1964
PIR 4371-0002	Joint GE-NASA-deHavilland Meeting Concerning Lubricants for the Boom Erection and Scissoring Mechanism, October 27, 1964
PIR 4371-0009	ATS Lubrication Discussions Held at Goddard Space Flight Center, November 9, 1964
PIR 4371-0023	Non-Magnetic Mating Material for the BcCu Belleville Spring, December 21, 1964
PIR 490L107	Approved Materials and Processes for ATS
PIR 4371-0003	Proposed SMR&D Program to Support the Thermal Control Development Effort, October 28, 1964
PIR 4371-0032	Mechanical Strengths of Plastics and Coefficients of Frictions of Metals for Application in the Bi-Stable Clutch, December 29, 1964

PIR	Title
PIR 9381-0337	Torsion Wire Spring Candidate Materials, August 19, 1964
PIR 9381-0347	Thermal Control Coatings for the GGEP System, September 8, 1964

3. NEW TECHNOLOGIES

There are no new technologies to be reported this quarter. Efforts to monitor the analytical and developmental areas will continue and new technologies will be reported as they are developed.

4. BIBLIOGRAPHY

1. "ATS Gravity Gradient Stabilization Systems, First Quarterly Report," GE Document No. 64SD4361, dated 16 October 1964
2. "Gravity Gradient Thermal Bending Test Report," GE Document No. 63SD725, dated July 10, 1963
3. "Gravity Gradient Thermal Bending Test Report," GE Document No. 64SD368, dated October 23, 1964
4. ATS Program Plan
5. Dennison, A.J., "The Illumination of a Cell Surface in Space Due to the Sunlight Reflected from Earth," GE TIS No. 61SD101
6. von Shelling, H., et al, "Preliminary Report, Infrared Horizon Sensor Study, Phase I," GE General Engineering Laboratory, March 1960
7. Documents of the 10th Plenary Assembly, CCIR, Vol IV, Report 205
8. Giger, A.J., et al, "The Ground Transmitter and Receiver," pp 1099-1100, "The Telstar Experiment Part 1, BSTJ, July 1963
9. Documents of the 9th Plenary Assembly, CCIR, Vol I, Rec. 277 (Replaced by REC. 405 of 10th Plenary Assembly)
10. Report of the Television Allocations Study Organization, Special Issue, Proc. IRE, June 1960
11. Reference No. 1 Rec. 354
12. Document of the 10th Plenary Assembly, Vol V, Rec 421
13. Inversion Maneuvers of the MAGGE Configuration, GE PIR 9750-035, dated September 18, 1964
14. Tinling, B., and Merrick, V., "The Application of Inertial Coupling in Passive Gravity Gradient Stabilized Satellites," AIAA Paper No. 63-342, August 12, 1963

5. GLOSSARY

The following is a list of abbreviations and definitions for terms used throughout this report.

CPD	Combination Passive Damper
Crab Angle	Out-of-orbit angle flight caused by changes in X-rod angle
GE-MSD	General Electric Company Missile and Space Division
G^2S/ATS	Gravity Gradient System/ATS
HAC	Hughes Aircraft Company
Local Vertical	Imaginary line extending from the satellite center of mass to the center of mass of the earth
LOFF	Low Order Force Fixture
MAGGE	Medium Altitude Gravity Gradient Experiment (6000-nautical mile orbit flight)
MTBF	Mean Time Before Failure
MTTF	Mean Time To Failure
PIR	Program Information Request/Release, GE documentation
RGO	Radio Guidance Operation of the General Electric Company at Utica, New York
SAGGE	Synchronous Altitude Gravity Gradient Experiment (24-hour orbit flight)
SAS	Solar Aspect Sensor
Scissoring	Changing the angle included between the primary booms in a manner that maintains a symmetrical configuration about the satellite yaw axis
STEM	Storable Tubular Extendable Member
SVA Fixture	Shock and Vibration Attachment Fixture
Thermal Twang	Sudden thermal bending which the booms will experience in passing from a region of total eclipse into a region of continuous sunlight or vice versa
TR	Torsional Restraint
TVCS	TV Camera Subsystem
PCU	Power Control Unit

APPENDICIES

APPENDIX A

SATELLITE ATTITUDE DETERMINATION VIA ON-BOARD EARTH DETECTOR & RADIO SENSOR INFORMATION

I. Introduction & Summary

This memorandum is the first of a series of analytical studies of possible attitude determination systems (or schemes) utilizing received radio signals from Earth-based radar stations in conjunction with vehicle on-board sensor information. The systems studied thus far are:

1) Line-of-sight from one radio station, and Earth sensor information
2) Line-of-sight from one radio station, and Sun sensor information
3) Line-of-sight from two stations, and Sun sensor information
4) Lines-of-sight from two stations, received simultaneously

Equations for attitude determination and for the evaluation of the accuracy of this determination, for the first system, are developed in this initial memorandum. The treatment is expansive, but material is included which is basic to the study of all the aforementioned systems. In particular, the various coordinate transformation matrices, and the equations for radio line-of-sight direction cosines, presented in detail here, will not be repeated in the subsequent memoranda. The fundamental difference in the studies of the various systems lies in the attitude determination equations and in the concomitant error equations.

Two kinds of orbits are considered herein. The pitch and roll errors are essentially the same as that of the Earth sensor, $3\sigma\,(\Delta\alpha_E) = 3^\circ$. Graphs of yaw error are presented, encompassing all possible relative geometries of radio station site and satellite position, within the purview of line-of-sight horizon and sensor field-of-view constraints. For the specified Earth sensor accuracy, and radio sensor accuracy, $3\sigma\,(\Delta\alpha_I) = 1^\circ$, the 3σ yaw error can vary from 16° to 32° for the synchronous orbit, and from 3° to 44° for the inclined orbit, within the constraint of the expected attitude angle excursions. The excessive yaw error would militate against use of the Earth sensor-radio sensor system; or the system could find limited use in conjunction with another system.

II. Line-of-sight Orientation in Body System

In Fig. 1, let the vehicle body reference system (usually, principal axes) be denoted $\bar{\imath}_X$, $\bar{\imath}_Y$, $\bar{\imath}_Z$. The unit vector from body center of mass to Earth center is designated $\bar{\imath}_E$. Its orientation is given by the direction angle triad α_E, β_E, θ_E, where each of these angles, by definition, lies between 0° and 180°. Alternatively, the orientation of $\bar{\imath}_E$ can be given by the pair ϕ_E, θ_E, where $0 \le \phi_E \le 360^\circ$. In similar fashion, the orientation of a line-of-sight to a radio transmitting station is given by α_{S_1}, β_{S_1}, θ_{S_1}. Thus

$$\bar{\imath}_E = \cos\alpha_E\,\bar{\imath}_X + \cos\beta_E\,\bar{\imath}_Y + \cos\theta_E\,\bar{\imath}_Z$$

$$= \cos\phi_E \sin\theta_E\,\bar{\imath}_X + \sin\phi_E \sin\theta_E\,\bar{\imath}_Y + \cos\theta_E\,\bar{\imath}_Z$$

$$= l_E\,\bar{\imath}_X + m_E\,\bar{\imath}_Y + n_E\,\bar{\imath}_Z \qquad (1)$$

$$\bar{\imath}_{S_1} = \cos\alpha_{S_1}\,\bar{\imath}_X + \cos\beta_{S_1}\,\bar{\imath}_Y + \cos\theta_{S_1}\,\bar{\imath}_Z$$

$$= l_1\,\bar{\imath}_X + m_1\,\bar{\imath}_Y + n_1\,\bar{\imath}_Z \qquad (2)$$

Note that

$$l_E^2 + m_E^2 + n_E^2 = 1$$

$$l_1^2 + m_1^2 + n_1^2 = 1$$

The radio sensor measures direction angles directly, as follows. From Fig. 2, in the $\bar{\imath}_S - \bar{\imath}_X$ plane, a radio plane wave transmitted from S_1 is received at the two antennas at different times. The phase difference is

$$\phi = \frac{2\pi d}{\lambda}\cos\alpha_S$$

where λ is wave length of the radio signal. α_S is greater or less than 90° according to whether the center antenna receives its signal sooner or later than the X-axis antenna. It should be noted that the field-of-view of the radio sensor is limited to 25°, that is

$$0 \leq \theta_{S_1} \leq 25^\circ$$

It will be shown in the sequel that α_E, β_E can be computed from certain measurements made by an Earth (disc) sensor. The angle θ_E is deduced from the orthonormality condition; unambiguously, because of field-of-view restrictions.

It is demonstrated in the Appendix, that measurements of the orientation angles of at least two (and preferably three) non-collinear lines-of-sight must be made, in order to establish completely, the attitude of the vehicle. For the combination of sensors under consideration here, namely, an Earth sensor and a radio sensor, a method exists for ascertaining the signs of $\cos\alpha_E$ and $\cos\beta_E$; thus, simultaneous measurement of the orientations of $\bar{\imath}_E$ and $\bar{\imath}_S$, is sufficient to establish the vehicle attitude unambiguously.

III. Coordinate Systems

The attitude of the vehicle body axis system is described by the orientation of this system with respect to a local vertical system, centered at the body, and rotating with respect to inertial space, at the vehicle orbital rate. One of six possible descriptions exists, depending upon the order of rotations ascribed to the body system in obtaining its orientation. Two such descriptions are given herewith. The first description is more efficient for attitude computations; the second description is the one, however, mutually agreed upon for evaluation of the efficacy of the A.T.S. stabilization system. The relations between the two descriptions will be presented.

Let the local vertical system be denoted $\bar{\imath}_V$, $\bar{\jmath}_V$, $\bar{k}_V$, where $\bar{k}_V$ is in the direction of (downward) vertical, $\bar{\jmath}_V$ is directed opposite to orbital rate vector, and $\bar{\imath}_V$ forms a right-handed system (see Fig. 3). Consider that the body system obtains its orientation with respect to the vertical system by means of a succession of three rotations - yaw, pitch, and finally, roll. These attitude, or Euler, angles, are denoted ψ_B , θ_B , ϕ_B . The transformation from vertical to body system is given by the following:

$$\begin{pmatrix} \bar{\imath}_X \\ \bar{\imath}_Y \\ \bar{\imath}_Z \end{pmatrix} = \begin{bmatrix} \cos\theta_B \cos\psi_B & \cos\theta_B \sin\psi_B & -\sin\theta_B \\ \begin{pmatrix} \sin\phi_B \sin\theta_B \cos\psi_B \\ -\cos\phi_B \sin\psi_B \end{pmatrix} & \begin{pmatrix} \sin\phi_B \sin\theta_B \sin\psi_B \\ +\cos\phi_B \cos\psi_B \end{pmatrix} & \sin\phi_B \cos\theta_B \\ \begin{pmatrix} \sin\theta_B \cos\phi_B \cos\psi_B \\ +\sin\phi_B \sin\psi_B \end{pmatrix} & \begin{pmatrix} \cos\phi_B \sin\theta_B \sin\psi_B \\ -\sin\phi_B \cos\psi_B \end{pmatrix} & \cos\phi_B \cos\theta_B \end{bmatrix} \begin{pmatrix} \bar{\imath}_V \\ \bar{\jmath}_V \\ \bar{k}_V \end{pmatrix}$$

or

$$\begin{pmatrix} \bar{\imath}_X \\ \bar{\imath}_Y \\ \bar{\imath}_Z \end{pmatrix} = \widetilde{V_1} \begin{pmatrix} \bar{\imath}_V \\ \bar{\jmath}_V \\ \bar{k}_V \end{pmatrix} \tag{3}$$

Consider a re-labeling of the vertical system:

$$\begin{pmatrix} \bar{\imath}_p \\ \bar{\imath}_q \\ \bar{\imath}_r \end{pmatrix} = \begin{pmatrix} \bar{\imath}_V \\ -\bar{\jmath}_V \\ -\bar{k}_V \end{pmatrix} \tag{4}$$

With respect to the $\bar{p}, \bar{q}, \bar{r}$ system, consider the series of rotations pitch θ_p, roll θ_R, yaw θ_y. The transformation from vertical system to a (re-labeled) body system (see Fig. 4) is given by:

$$\begin{pmatrix} \bar{\imath}_{X_1} \\ \bar{\imath}_{Y_1} \\ \bar{\imath}_{Z_1} \end{pmatrix} = \begin{bmatrix} \cos\theta_R \sin\theta_p & -\sin\theta_R & \cos\theta_R \cos\theta_p \\ \begin{pmatrix} \cos\theta_y \cos\theta_p \\ +\sin\theta_y \sin\theta_R \sin\theta_p \end{pmatrix} & \sin\theta_y \cos\theta_R & \begin{pmatrix} -\cos\theta_y \sin\theta_p \\ +\sin\theta_y \sin\theta_R \cos\theta_p \end{pmatrix} \\ \begin{pmatrix} -\sin\theta_y \cos\theta_p \\ +\cos\theta_y \sin\theta_R \sin\theta_p \end{pmatrix} & \cos\theta_y \cos\theta_R & \begin{pmatrix} \sin\theta_y \sin\theta_p \\ +\cos\theta_y \sin\theta_R \cos\theta_p \end{pmatrix} \end{bmatrix} \begin{pmatrix} \bar{\imath}_p \\ \bar{\imath}_q \\ \bar{\imath}_r \end{pmatrix}$$

or

$$\begin{pmatrix} \bar{\imath}_{X_1} \\ \bar{\imath}_{Y_1} \\ \bar{\imath}_{Z_1} \end{pmatrix} = \hat{V}_{\varrho} \begin{pmatrix} \bar{\imath}_{P} \\ \bar{\imath}_{Q} \\ \bar{\imath}_{R} \end{pmatrix} \tag{5}$$

Note the following relation:

$$\begin{pmatrix} \bar{\imath}_{X} \\ \bar{\imath}_{Y} \\ \bar{\imath}_{Z} \end{pmatrix} = \begin{pmatrix} \bar{\imath}_{Y_1} \\ -\bar{\imath}_{Z_1} \\ -\bar{\imath}_{X_1} \end{pmatrix} \tag{6}$$

Since $\bar{\imath}_E = \bar{k}_V$, we have

$$l_E = \bar{k}_V \cdot \bar{\imath}_X = -\bar{\imath}_R \cdot \bar{\imath}_{Y_1} = \cos \mathcal{L}_E = -\sin \theta_B$$
$$= \cos \theta_Y \sin \theta_P - \sin \theta_Y \sin \theta_R \cos \theta_P \tag{7}$$

$$m_E = \bar{k}_V \cdot \bar{\imath}_Y = \bar{\imath}_N \cdot \bar{\imath}_{Z_1} = \cos \beta_E = \sin \phi_B \cos \theta_B$$
$$= \sin \theta_Y \sin \theta_P + \cos \theta_Y \sin \theta_R \cos \theta_P \tag{8}$$

$$n_E = \bar{k}_V \cdot \bar{\imath}_Z = \bar{\imath}_R \cdot \bar{\imath}_{X_1} = \cos \theta_E = \cos \phi_B \cos \theta_B$$
$$= \cos \theta_R \cos \theta_P \tag{9}$$

If $\mathcal{L}_E$ and β_E are measured, we have directly,

$$\theta_B = \sin^{-1}(-l_E) \; ; \quad 0 \leq |\theta_B| \leq 90^\circ \tag{10}$$
$$= \mathcal{L}_E - 90^\circ$$

$$\phi_B = \tan^{-1}\left(\frac{m_E}{n_E}\right) ; \tag{11}$$

quadrant from signs of m_E and n_E

(Note that $n_E = \pm\sqrt{1 - l_E^2 - m_E^2}$; the positive sign is ascribed if Earth signal comes from the detector emplaced along the $+\bar{\imath}_Z$ direction, the negative sign if signal comes from detector emplaced along the $-\bar{\imath}_Z$ direction). The yaw angle will be shown, later, to be computable from the Earth and radio sensor measurements and knowledge of the orientation of the radio line-of-sight in the vertical (orbit) system.

Evidently, if θ_Y could be computed from ℓ_E, m_E and radio sight measurements, the angle θ_ρ, θ_R, would, from eq's. 7, 8, and 9 be given by

$$\theta_\rho = \sin^{-1}\left[\ell_E \cos\theta_Y + m_E \sin\theta_Y\right];\ 0 \le |\theta_\rho| \le 90^\circ \tag{12}$$

$$\theta_R = \tan^{-1}\left[\frac{m_E \cos\theta_Y - \ell_E \sin\theta_Y}{m_E}\right] \tag{13}$$

It is more efficient to compute ψ_B, θ_B, ϕ_B; the alternative set of attitude angles is then readily found, if desired, from

$$\tan\theta_\rho = \frac{-\bar{\imath}_Z \cdot \bar{\imath}_V}{\bar{\imath}_Z \cdot \bar{k}_V} = -\tan\theta_B \cos\psi_B - \frac{\tan\phi_B \sin\psi_B}{\cos\theta_B} \tag{14}$$

$$\tan\theta_R = \frac{-\bar{\imath}_Z \cdot \bar{\jmath}_V \sin\theta_\rho}{-\bar{\imath}_Z \cdot \bar{\imath}_V}$$

$$= \frac{(\sin\phi_B \cos\psi_B - \cos\phi_B \sin\theta_B \sin\psi_B)\sin\theta_\rho}{(-\sin\theta_B \cos\phi_B \cos\psi_B - \sin\phi_B \sin\psi_B)} \tag{15}$$

$$\tan\theta_Y = \frac{-\bar{\imath}_X \cdot \bar{\jmath}_V}{\bar{\imath}_Y \cdot \bar{\jmath}_V} = \frac{-\cos\theta_B \sin\psi_B}{\sin\phi_B \sin\theta_B \sin\psi_B + \cos\phi_B \cos\psi_B} \tag{16}$$

It is to be observed that for small attitude angles, $\theta_\rho \approx -\theta_B$, $\theta_R \approx \phi_B$, $\theta_Y \approx -\psi_B$.

In order to specify the orientation of the radio line-of-sight in the vehicle-centered local vertical system, it will be necessary to use the transformation between a geocentric, equatorial, inertial system and the vertical system. In Fig. 5, $\bar{\imath}_I$, $\bar{\jmath}_I$, $\bar{k}_I$ is the geocentric equatorial system. Let

λ_ρ = rt. ascension of satellite

δ_ρ = declination of satellite

Ω_ρ = rt. ascension of ascending node of satellite orbit

ι_ρ = inclination of satellite orbit

u_ρ = central angle of satellite position, measured from ascending node

e transformation is

$$\begin{pmatrix} \bar{\imath}_V \\ \bar{\jmath}_V \\ \bar{k}_V \end{pmatrix} = \begin{bmatrix} \begin{pmatrix} -\sin u_\rho \cos \Omega_\rho \\ -\cos u_\rho \cos i_\rho \sin \Omega_\rho \end{pmatrix} & \begin{pmatrix} -\sin u_\rho \sin \Omega_\rho \\ +\cos u_\rho \cos i_\rho \cos \Omega_\rho \end{pmatrix} & \cos u_\rho \sin i_\rho \\ -\sin i_\rho \sin \Omega_\rho & \sin i_\rho \cos \Omega_\rho & -\cos i_\rho \\ \begin{pmatrix} -\cos u_\rho \cos \Omega_\rho \\ +\sin u_\rho \cos i_\rho \sin \Omega_\rho \end{pmatrix} & \begin{pmatrix} -\cos u_\rho \sin \Omega_\rho \\ -\sin u_\rho \cos i_\rho \cos \Omega_\rho \end{pmatrix} & -\sin u_\rho \sin i_\rho \end{bmatrix} \begin{pmatrix} \bar{\imath}_I \\ \bar{\jmath}_I \\ \bar{k}_I \end{pmatrix}$$

or

$$\begin{pmatrix} \bar{\imath}_V \\ \bar{\jmath}_V \\ \bar{k}_V \end{pmatrix} = \bar{\bar{I}} \begin{pmatrix} \bar{\imath}_I \\ \bar{\jmath}_I \\ \bar{k}_I \end{pmatrix} \tag{17}$$

Note that $\bar{k}_V$ can also be written

$$\bar{k}_V = -\left[\cos\delta_\rho \cos\lambda_\rho \, \bar{\imath}_I + \cos\delta_\rho \sin\lambda_\rho \, \bar{\jmath}_I + \sin\delta_\rho \, \bar{k}_I\right] \tag{18}$$

Certain trigonometric relations are useful, and are indicated in the inset of Fig. 5. Note that for given i_ρ the angular position of the satellite can be specified by either the pair Ω_ρ, u_ρ or by the pair $\lambda_\rho, \delta_\rho$.

IV. Line-of-Sight Orientation in Vertical System

In Fig. 6, a radio station S_1 is located at a geocentric latitude δ_1 and a longitude (measured east from Greenwich Meridian) L_1. At a given time, the right ascension (or sidereal angle) of the site, measured from vernal equinox, is λ_1. The Earth radius at S_1 is ρ_1. At this time, the satellite is at a distance from Earth center of r_ρ, and has angular coordinates $\lambda_\rho, \delta_\rho$. The site-satellite distance is R_1. Then

$$\bar{r}_\rho = \bar{\rho}_1 + \bar{R}_1 \tag{19}$$

$$\bar{\imath}_{s1} = -\frac{\bar{R}_1}{R_1} = -\left[\frac{\bar{\rho}_p - \bar{\rho}_1}{R_1}\right] = \frac{\rho_p \bar{k}_V + \bar{\rho}_1}{R_1} \tag{20}$$

where, from Fig. 7,

$$R_1 = \sqrt{\rho_1^2 + \rho_p^2 - 2\rho_p \rho_1 \cos\gamma_1} \tag{21}$$

and, from Fig. 8,

$$\begin{aligned}\cos\gamma_1 &= \sin\delta_1 \sin\delta_p + \cos\delta_1 \cos\delta_p \cos(\lambda_p - \lambda_1) \\ &= \cos\delta_1 \cos(\lambda_1 - \Omega_p)\cos u_p \\ &\quad + \sin u_p \left[\cos\delta_1 \cos i_p \sin(\lambda_1 - \Omega_p) + \sin\delta_1 \sin i_p\right]\end{aligned} \tag{22}$$

Taking the Earth as locally spherical at the site, we have the condition of visibility of the satellite from the station:

$$0 \le \gamma_1 \le \cos^{-1}\left(\frac{\rho_1}{\rho_p}\right) < 90^\circ \tag{23}$$

Let

$$\bar{\imath}_{s1} = l_1' \bar{\imath}_V + m_1' \bar{\jmath}_V + n_1' \bar{k}_V \tag{24}$$

Note that

$$\frac{\bar{\rho}_1}{\rho} = \cos\delta_1 \cos\lambda_1 \bar{\imath}_I + \cos\delta_1 \sin\lambda_1 \bar{\jmath}_I + \sin\delta_1 \bar{k}_I \tag{25}$$

Then utilizing eq's. 20, 25 and matrix I from Eq. 17, we obtain

$$l_1' = \bar{\imath}_{s1} \cdot \bar{\imath}_V = \frac{\bar{\rho}_1}{R_1} \cdot \bar{\imath}_V$$

or

$$\begin{aligned}\left(\frac{R_1}{\rho_1}\right) l_1' &= \cos u_p \left[\sin\delta_1 \sin i_p + \cos\delta_1 \cos i_p \sin(\lambda_1 - \Omega_p)\right] \\ &\quad - \sin u_p \cos\delta_1 \cos(\lambda_1 - \Omega_p)\end{aligned} \tag{26}$$

$$m_1' = \bar{\imath}_{s1} \cdot \bar{\jmath}_V = \frac{\bar{\rho}_1}{R_1} \cdot \bar{\jmath}_V$$

or

$$\left(\frac{R_1}{\rho_1}\right) m_1' = \cos\delta_1 \sin i_\rho \sin(\lambda_1 - \Omega_\rho) - \sin\delta_1 \cos i_\rho \qquad (27)$$

$$m_1' = \cos\psi_1 = \bar{\imath}_{s_1} \cdot \bar{k}_V = \frac{\bar{r}_\rho}{R_1} + \frac{\bar{\rho}_1}{R_1} \cdot \bar{k}_V$$

or

$$\left(\frac{R_1}{\rho_1}\right) m_1' = \frac{r_\rho}{\rho_1} - \cos\gamma_1 \qquad (28)$$

Note the orthornormality condition

$$(l_1')^2 + (m_1')^2 + (n_1')^2 = 1$$

Note also that

$$0 \leq \psi_1 \leq \sin^{-1}\left(\frac{\rho_1}{r_\rho}\right) < 90^\circ$$

From Fig. 7, it is seen that the elevation angle of the radio line-of-sight is

$$\mathcal{E}_1 = 90 - (\gamma_1 + \psi_1) \qquad (29)$$

and an alternative to condition 23 for visibility is

$$0 \leq \mathcal{E}_1 \leq 90^\circ$$

that is, positive elevation angle.

(It should be observed that range from radio site to satellite may be directly measured, or it may be computed, via eq's. 21 and 22, if orbit determination is accomplished from measurements made from other stations. In any event, errors in l_1', m_1', n_1' will be due to errors in orbit determination, as well as errors in station coordinate determination. The latter, are primarily due to errors in one latitude determination and impreciseness in knowledge of the figure of the Earth).

For given $i_\rho, r_\rho, \delta_\rho$, the independent parameters in eq's 26, 27, and 28 are $(\lambda_1 - \Omega_\rho), u_\rho$. Actually, for a specified orbit, $\lambda_1, u_\rho, r_\rho$ are functions of time. Thus,

$$\lambda_1 = GHA_\gamma(t) + L_1 \qquad (30)$$

where $GHA_\gamma(t)$ = Greenwich hour angle (in degrees) at Universal time t, measured from 0 hours of the day.

For a circular satellite orbit, r_ρ is constant and

$$u_\rho = (u_\rho)_0 + \omega_0 t \qquad (31)$$

where

$(u_\rho)_o$ = satellite central angle at $t = 0$

For an eccentric orbit, r_ρ and u_ρ are deduced from orbit determination measurements.

For the special case of a circular equatorial orbit, we have

$$i_\rho = 0 \ , \ \Omega_\rho = 0 \ , \ \delta_\rho = 0, \ \lambda_\rho = u_\rho = GHA_\gamma + L_\rho$$

Then eq's. 26, 27, and 28 reduce to

$$\left(\frac{R_1}{\rho_1}\right) l_1' = -\cos\delta_1 \sin(L_\rho - L_1) \tag{32}$$

$$\left(\frac{R_1}{\rho_1}\right) m_1' = -\sin\delta_1 \tag{33}$$

$$\left(\frac{R_1}{\rho_1}\right) n_1' = \left(\frac{r_\rho}{\rho_1}\right) - \cos\delta_1 \cos(L_\rho - L_1) \tag{34}$$

The independent parameter is seen to be $(L_\rho - L_1)$. If the satellite is at synchronous altitude, $(L_\rho - L_1)$ is constant. Also,

$$r_\rho = \left[\left(\frac{T}{2\pi}\right)^2 \mu_E\right]^{\frac{1}{3}} \tag{35}$$

where

T = 86164 = no. of seconds in sidereal day

μ_E = 62747 n. miles^3/sec^2

whence r_ρ = 22,766 n. miles.

The Earth radius, at site geocentric latitude δ_1, is given by

$$\rho_1 = \frac{\rho_E\sqrt{1 - l_E^2}}{\sqrt{1 - l_E^2 \cos^2\delta_1}} \tag{36}$$

where

ρ_E = Earth's equatorial radius = 3440 n.miles

l_E^2 = square of eccentricity of Earth shape, taken as oblate spheroid

= .006723

For $\theta_1 = 35.33^\circ$, we obtain $\rho_1 = 3436$ n. miles.

V. Determination of Pitch and Roll Angles from Earth Sensor (Disc) Measurements

Earth sensors are to be emplaced, one each, at the intersection of the vehicle yaw axis with the cylindrical surface of the vehicle (see Fig. 9). Now, in the vertical plane through $\bar{\imath}_z$, that is, the $\bar{\imath}_z - \bar{\jmath}_V$ plane, the unit vector along line-of-sight from the sensor optical center to Earth center is designated $\bar{\imath}_E$ (see Fig. 10). The radius of Earth (considered spherical) is ρ; the distance from Earth center to vehicle center of mass is r; the distance from vehicle center to optical center is c; the sensor focal length is f. The projection of the Earth disc, at the detector grid center, and in the plane normal to $\bar{\imath}_E$, is a circle whose radius is d, where

$$d = \left(\frac{f}{\cos\theta_E'}\right) \tan\psi \tag{37}$$

$$\psi = \sin^{-1}\left(\frac{\rho}{r_\rho'}\right) \tag{38}$$

Note: $r_\rho' \approx r_\rho$, since $c \ll r$

$\theta_E' \approx \theta_E$, since $q \approx 0$

The intercept of this circle by the detector grid, is, however, an **ellipse** the center of the ellipse is displaced laterally from the circle center by an amount (see Fig. 11).

$$\rho' - \rho = \frac{a_2 - a_1}{2} \tag{39}$$

and the semi-major axis of the ellipse is

$$a = \frac{a_1 + a_2}{2} \tag{40}$$

From Fig. 11,

$$a_1 \cos\theta_E' = \frac{f}{\cos(\theta_E' - \psi)} \sin\psi \tag{41}$$

$$a_2 \cos\theta_E' = \frac{f}{\cos(\theta_E' + \psi)} \sin\psi \tag{42}$$

$$\rho = f \tan\theta_E' \tag{43}$$

From eq's. 41 and 42, taking $\theta_E' \approx \theta_E$,

$$a = \frac{f \sin\psi \cos\psi}{(\cos^2\theta_E - \sin^2\psi)} \tag{44}$$

$$\rho' - \rho = \frac{f \sin^2\psi \tan\theta_E}{(\cos^2\theta_E - \sin^2\psi)} \tag{45}$$

$$\rho' = \frac{f \sin\theta_E \cos\theta_E}{(\cos^2\theta_E - \sin^2\psi)} \tag{46}$$

The base circle through the ellipse center (see Fig. 12) enables determination of the semi-major axis of the ellipse. Thus, utilizing eq. 45, we obtain

$$b = \frac{f \sin\psi}{\sqrt{\cos^2\theta_E - \sin^2\psi}} \tag{47}$$

In the focal plane, consider now a grid system of axes erected parallel to $\bar{i}_x, \bar{i}_y$ at 0". The ellipse center is off-set from grid-center and the ellipse axes are rotated by the angle ϕ_E measured from $\bar{i}_x$ (see Fig. 13). The coordinates of a point in the primed system are

$$\left.\begin{aligned} x' &= X\cos\phi_E + Y\sin\phi_E + \rho' \\ Y &= Y\cos\phi_E - X\sin\phi_E \end{aligned}\right\} \tag{48}$$

The equation of the ellipse is

$$\frac{(x')^2}{a^2} + \frac{(y')^2}{b^2} = 1$$

Inserting the set 48 into the ellipse equation, and setting X equal to zero gives an equation from which the intercepts Y_1 & Y_2 can be obtained. Substituting the expressions for a, ρ', and b from eq's 44, 46, and 47 the sum and difference of these intercepts are found to be given by

$$\frac{(Y_1 + Y_2)}{2f} = \frac{-\cos\theta_E \cos\beta_E}{(\cos^2\psi - \cos^2\beta_E)} \tag{49}$$

$$\frac{(Y_1 - Y_2)}{2f\cos\psi} = \frac{\sqrt{\sin^2\psi - \cos^2\lambda_E}}{(\cos^2\psi - \cos\beta_E)} \tag{50}$$

wherein use has been made of the relations

$$\cos\lambda_E = \cos\phi_E \sin\theta_E \tag{51}$$

$$\cos\beta_E = \sin\phi_E \sin\theta_E \tag{52}$$

In like fashion, setting γ equal to zero in the ellipse equation yields the following results:

$$\frac{(X_1 + X_2)}{2f} = \frac{-\cos\Theta_E \cos\alpha_E}{(\cos^2\psi - \cos^2\alpha_E)} \tag{53}$$

$$\frac{X_1 - X_2}{2f\cos\psi} = \frac{\sqrt{\sin^2\psi - \cos^2\beta_E}}{(\cos^2\psi - \cos^2\alpha_E)} \tag{54}$$

Equations 50 and 54 can be solved simultaneously to obtain $\cos\alpha_E$, $\cos\beta_E$. It has been shown therefore, that ℓ_E, m_E can be obtained from the Earth sensor measurements only, whence pitch and roll angles can be computed, as indicated in Section II.

Of course, solutions for $\cos\alpha_E$, $\cos\beta_E$ must be verified in eq's. 50 and 54, since extraneous solutions may be introduced by squaring processes. Since solutions will actually yield $\cos^2\alpha_E$, $\cos^2\beta_E$ signs may be ascribed by consideration of the signs of the intercept sums, as follows, for positive .

$Y_1 + Y_2$	$\cos\beta_E$	β_E
+	−	$90° \le \beta_E \le 180°$
−	+	$0° \le \beta_E \le 90°$

$X_1 + X_2$	$\cos\alpha_E$	α_E
+	−	$90° \le \alpha_E \le 180°$
−	+	$0° \le \alpha_E \le 90°$

The reverse situation holds for negative $\cos\Theta_E$.

Errors in measurement of the grid intercepts arise from quantization and resolution effects, optical errors, assumption of Earth sphericity, and variable cloud cover or mountains.

For a synchronous, circular, equatorial orbit, using a mean Earth radius ρ = 3436 n. miles, eq. 38 gives $\psi = 8.68°$. For an inclined circular orbit altitude 6000 n.mi., $\psi = 21.3°$. For a field of view limited detector, we must have, from Fig. 111,

$$0 \le \Theta'_E + \psi \le \Theta_{LIMIT}$$

For $\Theta_{LIMIT} = 30°$ then,

$$0 \le \Theta'_E \le 30° - \psi$$

or

$$0 \leq \theta_E \leq 21.3^\circ \qquad \text{for synch. orbit}$$

$$0 \leq \theta_E \leq 8.68^\circ \qquad \text{for 6000 n.mi. orbit}$$

Suppose the expected limits of pitch and roll angles are

$$-10^\circ \leq \theta_B \leq +10^\circ$$

$$-10^\circ \leq \phi_B \leq 10^\circ$$

Then, from eq's. 7, 8, and 9, the expected limits corresponding on are

$$80^\circ \leq \alpha_E \leq 100^\circ$$

$$80^\circ \leq \beta_E \leq 100^\circ$$

$$0^\circ \leq \theta_E \leq 14.5^\circ$$

Evidently, the Earth will be "seen" by the detector, at the extreme pitch and roll attitude, on the synchronous orbit, but not on the 6000 n.mile orbit, if the half field of view is limited to 30°; for visibility of the Earth from the latter orbit, θ_{Limit} would need to be about 36°.

VI. Determination of Yaw Angle from Earth Sensor and Radio Sensor Measurements

From the matrix relation 3,

$$\bar{i}_x \cdot \bar{j}_v = \cos\theta_B \sin\psi_B \qquad (55)$$

$$\bar{i}_x \cdot \bar{i}_v = \cos\theta_B \cos\psi_B \qquad (56)$$

But, from eq's. 2 and 24,

$$\bar{i}_x = \frac{l_1' \bar{i}_v + m_1' \bar{j}_v + n_1' \bar{k}_v - m_1 \bar{i}_y - n_1 \bar{i}_z}{l_1} \qquad (57)$$

Sitting eq. 57 into eq's. 55 and 56, and making use of dot product relations in matrix $\widetilde{V_1}$, two simultaneous equations in $\sin\psi_B$ and $\cos\psi_B$ are obtained.

$$\left.\begin{aligned} A\sin\psi_B + B\cos\psi_B &= m_1' \\ -B\sin\psi_B + A\cos\psi_B &= l_1' \end{aligned}\right\} \qquad (58)$$

where

$$A = l_1\cos\theta_B + m_1\sin\phi_B\sin\theta_B + n_1\cos\phi_B\sin\theta_B \qquad (59)$$

$$B = m_1\cos\phi_B - n_1\sin\phi_B \qquad (60)$$

Note that ϕ_s, Θ_s are computed, eq's. 10 and 11, from the deduced measurements α_s, β_s of the Earth sensor; ℓ_1 and m_1 are measured directly by the radio sensor (see Section II) and n_1 is given by

$$n_1 = \sqrt{1 - \cos^2\alpha_{s_1} - \cos^2\beta_{s_1}}$$

$$= \sqrt{1 - \ell_1^2 - m_1^2}$$

Solving set 58 gives

$$\tan \psi_B = \frac{m_1' A - \ell_1' B}{\ell_1' A + m_1' B} \tag{61}$$

the quadrant of ψ_B determined by signs of numerator and denominator .

VII. Line-of-sight Limitations

It was previously stated that Earth detector and radio sensor signals will not be simultaneously received unless the field of view requirements of both sensors are simultaneously met, viz.:

$$0 \leq \Theta_{s_1} \leq 25^\circ$$

$$0 \leq \Theta_E \leq 21.3^\circ \quad \text{sync. equatorial orbit}$$

or $$0 \leq \Theta_E \leq 8.68^\circ \quad \text{6000 n.mile orbit}$$

It behooves us now to investigate the conditions under which the radio station will not "see" the satellite, so that a radio signal cannot be transmitted to the on-board radio sensor.

Considering first the equatorial orbit, the line-of-sight to the satellite will lie in the horizon plane if (see Fig. 14)

$$\cos\gamma_1 = \cos\delta_1 \cos(L_p - L_1) = \frac{\rho_1}{r_p} \tag{62}$$

For synchronous altitude,

$$\gamma_1\Big]_{\text{LIMIT}} = 81.32^\circ$$

For $\delta_1 = 35.33^\circ$, then the satellite is seen only if

$$-79.3^\circ \leq (L_p - L_1) \leq 79.3^\circ$$

For the inclined orbit, setting $\cos\gamma_1 = \frac{\rho}{r_p}$ in eq. 22 yields limiting values of u_p as function of $(\lambda_1 - \Omega_p)$:

$$\cos u_p = \frac{ad \pm b\sqrt{a^2+b^2-d^2}}{(a^2+b^2)} \tag{63}$$

where

$$a = \cos\delta_1 \cos(\lambda_1 - \Omega_p)$$

$$b = \cos\delta_1 \cos i_p \sin(\lambda_1 - \Omega_p) + \sin\delta_1 \sin i_p$$

$$c = \frac{\rho_1}{r_p}$$

In particular, for the 6000 n.mile altitude inclined orbit, $i_p = 28°$, and for station latitude of 35.33°. the limit contour, Fig. 15, is obtained.

VIII. Error Analysis

A Errors in Direction Angles of Earth Line-of-sight

We will concern ourselves only with errors in the determination of as a result of detector grid intercept measurement errors. At the outset, since

$$\cos^2\alpha_E + \cos^2\beta_E + \cos^2\theta_E = 1$$

then

$$d\theta_E = \frac{-\sin\alpha_E \cos\alpha_E}{\sin\theta_E \cos\theta_E} d\alpha_E - \frac{\sin\beta_E \cos\beta_E}{\sin\theta_E \cos\theta_E} d\beta_E \tag{64}$$

Differentiating eq's. 49 and 53 with respect to X_1, X_2, Y_1, Y_2, and making use of eq. 64, two equations in $d\alpha_E$ and $d\beta_E$ are obtained. These are solved simultaneously to obtain

$$d\alpha_E = \frac{A_1 C_2 - A_2 C_1}{A_1 B_2 - A_2 B} \; ; \; d\beta_E = \frac{C_1 B_2 - C_2 B_1}{A_1 B_2 - A_2 B_1}$$

where

$$A_1 = \sin\beta_E \left[\frac{\cos^2\beta_E}{\cos\theta_E} - \frac{\cos\theta_E (\cos^2\psi + \cos^2\beta_E)}{(\cos^2\psi - \cos^2\beta_E)}\right]$$

$$B_1 = \sin\alpha_E \cos\alpha_E \frac{\cos\beta_E}{\cos\theta_E}$$

$$A_2 = \sin\beta_E \cos\beta_E \frac{\cos\alpha_E}{\cos\theta_E}$$

$$B_2 = \sin\alpha_E \left[\frac{\cos^2\alpha_E}{\cos\theta_E} - \cos\theta_E \frac{(\cos^2\psi + \cos^2\alpha_E)}{(\cos^2\psi - \cos^2\alpha_E)}\right]$$

$$C_1 = \frac{1}{2f}\left(\cos^2\beta_E - \cos^2\psi\right)\left(\ell Y_1 + \ell Y_2\right)$$

$$C_2 = \frac{1}{2f}\left(\cos^2\alpha_E - \cos^2\psi\right)\left(\ell X_1 + \ell X_2\right)$$

Assume that the errors $\Delta X_1, \Delta X_2, \Delta Y_1, \Delta Y_2$ are independent random errors with zero means, but with the same variance $\sigma^2(\Delta Y)$. Taking expectations,

$$\sigma^2(\Delta\beta_E) = \left(\frac{B_2}{D}\right)^2 \sigma^2(C_1) + \left(\frac{B_1}{D}\right)\sigma^2(C_2) \quad (65)$$

$$\sigma^2(\Delta\alpha_E) = \left(\frac{A_1}{D}\right)^2 \sigma^2(C_2) + \left(\frac{A_2}{D}\right)^2 \sigma^2(C_1) \quad (66)$$

$$E(\Delta\alpha_E \Delta\beta_E) = -\frac{1}{D^2}\left[B_2 A_2 \sigma^2(C_1) + B_1 A_1 \sigma^2(C_2)\right] \quad (67)$$

where

$$\sigma^2(C_1) = E(C_1)^2 = \frac{1}{2f^2}\left(\cos^2\beta_E - \cos^2\psi\right)^2 \sigma^2(\Delta Y)$$

$$\sigma^2(C_2) = E(C_2)^2 = \frac{1}{2f^2}\left(\cos^2\alpha_E - \cos^2\psi\right)^2 \sigma^2(\Delta Y)$$

$$D = \left(A_1 B_2 - A_2 B_1\right)$$

In general then, $\Delta\alpha_E$ and $\Delta\beta_E$ are not uncorrelated, their variances are equal and non-stationary (i.e., not constant). However, for zero pitch and roll, eq.'s 7, 8, and 9 show that $\theta_E = 0$, $\alpha_E = \beta_E = 90^\circ$. Under these conditions,

$$A_1 = B_2 = -1\,; \quad B_1 = A_2 = 0\,; \quad D = 1$$

$$\sigma^2(C_1) = \sigma^2(C_2) = \frac{\cos^4\psi}{2f^2}\,\sigma^2(\Delta Y)$$

$$\sigma^2(\Delta\beta_E) = \sigma^2(\Delta\alpha_E) = \sigma^2(c_1)$$

$$E(\Delta\alpha_E \Delta\beta_E) = 0$$

For the A.T.S. experiment, it is expected that pitch and roll will not exceed $\pm 10^0$. Hence, with good validity $\Delta\alpha_E$, $\Delta\beta_E$ can be treated as independent, with equal and constant variances.

B. Errors in Attitude Determination

From eq. 10, immediately, $\delta\theta_B = \delta\alpha_E$, whence $\sigma(\Delta\theta_B) = \sigma(\Delta\alpha_E)$. Differentiation of eq. 8 yields

$$\sigma^2(\Delta\phi_B) = \left(\frac{\partial\phi_B}{\partial\beta_E}\right)^2 \sigma^2(\Delta\beta_E) + \left(\frac{\partial\phi_B}{\partial\alpha_E}\right)^2 \sigma^2(\Delta\alpha_E) \quad (68)$$

where

$$\frac{\partial\phi_B}{\partial\beta_E} = -\sqrt{1 + \left(\frac{\tan\theta_B}{\cos\phi_B}\right)^2} \quad (69)$$

$$\frac{\partial\phi_B}{\partial\alpha_E} = \tan\phi_B \tan\theta_B \quad (70)$$

In particular, if $\phi_B = \theta_B = 0$, then $\sigma(\Delta\phi_B) = \sigma(\Delta\beta_E)$. Differentiations of eq. 61 leads to the following:

$$\sigma^2(\Delta\psi_B) = \left[\left(\frac{\partial\psi_B}{\partial\alpha_E}\right)^2 \sigma^2(\Delta\alpha_E) + \left(\frac{\partial\psi_B}{\partial\beta_E}\right)^2 \sigma^2(\Delta\beta_E)\right] + \left[\left(\frac{\partial\psi_B}{\partial\alpha_{S_1}}\right)^2 \sigma^2(\Delta\alpha_1) + \left(\frac{\partial\psi_B}{\partial\beta_{S_1}}\right)^2 \sigma^2(\Delta\beta_1)\right] \quad (71)$$

$$= \sigma^2(\Delta\psi_B)_{EARTH} + \sigma^2(\Delta\psi_B)_{RADIO}$$

where

$$(A^2+B^2)\cos\theta_B\cos\phi_B\left(\frac{\partial\psi_B}{\partial\alpha_E}\right) = (m_1'\cos\psi_B - l_1'\sin\psi_B)\left[m_1\cos(\phi_B+\theta_B)\cos(\phi_B-\theta_B\right.$$

$$\left.+(m_1\sin\phi_B - l_1\sin\theta_B\cos\theta_B)\cos\phi_B\right] + \left[l_1'\cos\psi_B + m_1'\sin\psi_B\right]\left[m_1\sin\phi_B + m_1\cos\phi_B\right]\sin\phi_B\sin\theta_B$$

$$\frac{n_1\left(A^2+B^2\right)}{\sin\alpha_{s_1}}\left(\frac{\partial\psi_B}{\partial\alpha_1}\right) = \left[m_1'\cos\psi_B - l_1'\sin\psi_B\right]\left[l_1\sin\theta_B\cos\phi_B - n_1\cos\theta_B\right] + l_1\left[l_1'\cos\psi_B + m_1'\sin\psi_B\right]\sin$$

$$\frac{\left(A^2+B^2\right)}{\left(\frac{\partial\phi_B}{\partial\beta_E}\right)}\left(\frac{\partial\psi_B}{\partial\beta_E}\right) = \left[m_1'\cos\psi_B - l_1'\sin\psi_B\right]\left[m_1\cos\phi_B - n_1\sin\phi_B\sin\theta_B\right] + \left[l_1'\cos\psi_B + m_1'\sin\psi_B\right]\left[m_1\sin\phi_B + n_1\cos\right.$$

$$\left(\frac{\partial\psi_B}{\partial\beta_1}\right) = \frac{\left(\frac{\partial\psi_B}{\partial\beta_E}\right)}{\left(\frac{\partial\phi_B}{\partial\beta_E}\right)}\,\frac{\sin\beta_{s_1}}{n_1}$$

and where A and B are given respectively by eq's. 59 and 60.

In particular, if $\psi_B = \phi_B = \theta_B = 0$, then $l_1' = l_1$, $m_1' = m_1$, $n_1' = n_1$. Taking $\sigma(\Delta\alpha_E) = \sigma(\Delta\beta_E)$ and $\sigma(\Delta\alpha_1) = \sigma(\Delta\beta_1)$, eq. 71 reduces to

$$\sigma^2(\Delta\psi_B) = \frac{1}{\sin^4\psi_1}\left[\sin^2\psi_1\cos^2\psi_1\,\sigma^2(\Delta\alpha_E) + \left(\sin^2\psi_1 - 2l_1^2m_1^2\right)\sigma^2(\Delta\alpha_1)\right]$$

For $\sigma^2(\Delta\alpha_E)$ substantially greater than $\sigma^2(\Delta\alpha_1)$

$$\sigma^2(\Delta\psi_B) \approx \operatorname{ctn}^2\psi_1\,\sigma^2(\Delta\alpha_E)$$

so that the error is largest when ψ_1 is smallest.

For the equatorial orbit,

$$\cos\gamma_1 = \cos\delta_1\cos\left(L_p - L_1\right) \tag{72}$$

In general, (See Fig. 7),

$$\tan\psi_1 = \frac{\rho_1\sin\gamma_1}{r_p - \rho_1\cos\gamma_1} \tag{73}$$

Substituting eq. 72 into eq. 73 and differentiating ψ_1, with respect to $(L_p - L_1)$, the conditions are obtained for maximum or minimum ψ_1:

$$(L_p - L_1) = 0; \text{ gives } \psi_{1(\text{minimum})}$$

$$\cos(L_p - L_1) = \frac{1}{\cos\delta}\left(\frac{\rho_1}{r_p}\right); \text{ gives } \psi_{1(\text{maximum})}$$

From these conditions, for synchronous altitude orbit, $\psi_{1(MAX)} = 8.68^\circ$, $\psi_{1(MIN)} = 5.74^\circ$. Thus, $\sigma(\Delta\psi_B)_{MAX}$ occurs for a zero longitude difference.

Substitution of eq. 22 into eq. 73 and subsequent differentiation with respect to μ_p, for given $(\lambda_1 - \Omega_p)$, yields conditions for minimum and maximum ψ_1. Maximum ψ_1 occurs if the satellite is sighted at the horizon; for the 6000 n.mile altitude, 28° inclined orbit, $\psi_{1(MAX)} = 21.3^\circ$. The minimum ψ_1, occurs at such μ_p satisfying the following equation:

$$\tan\mu_p = \cos i_p \tan(\lambda_1 - \Omega_p) + \frac{\tan\delta_1 \sin i_p}{\cos(\lambda_1 - \Omega_p)} \tag{74}$$

The value of μ_p for minimum ψ_1 (angle between radio line-of-sight and satellite local vertical) is shown in Fig. 16. The physical picture for the situation is shown in Fig. 17. Minimum γ_1 (and minimum ψ_1) occurs when the Earth-station-satellite plane is normal to the orbit plane. This value of γ_1 is given by

$$\cos(\gamma_1)_{MIN.} = \frac{\cos(\lambda_1 - \Omega_p)\cos\delta_1}{\cos\mu_p} \tag{75}$$

where μ_p is the value satisfying eq. 74. Minimum ψ_1 is then given by eq. 73. $\psi_{1(MIN)}$ and $\varepsilon_{1(MAX)}$ are shown, Fig. 16.

It is thus evident that the error in ψ_B increases as ψ_1 decreases, i.e., as satellite-Earth line and radio line-of-sight approach closest to a collinear situation. Note that approximately, $\sigma(\Delta\psi_B)$ max. occurs for $\mu_p = \lambda_1 = \Omega_p$.

As a final observation, the errors in the attitude angles defined by matrix $(\overline{V_2})$ (see Section II) are most expeditiously found by matrix methods. Let $\overline{\Delta\alpha\,\Delta\alpha^T}$ be the moment matrix of the measurement errors:

$$\overline{\Delta\alpha\,\Delta\alpha^T} = \begin{bmatrix} \sigma^2(\Delta\alpha_2) & & & 0 \\ & \sigma^2(\Delta\beta_2) & & \\ & & \sigma^2(\Delta\alpha_1) & \\ 0 & & & \sigma^2(\Delta\beta_1) \end{bmatrix} \tag{76}$$

Then

$$\sigma^2(\Delta\Theta_P) = \widetilde{\Theta_{P-\alpha}}\ \overline{\widetilde{\Delta\alpha}\,\widetilde{\Delta\alpha}^T}\ \widetilde{\Theta_{P-\alpha}}^T \tag{77}$$

where

$$\widetilde{\Theta_{P-\alpha}} = \begin{bmatrix} \frac{\partial\Theta_P}{\partial\Psi_B} & \frac{\partial\Theta_P}{\partial\Theta_B} & \frac{\partial\Theta_P}{\partial\Phi_B} \end{bmatrix} \Theta_{B-\alpha} \tag{78}$$

$$\widetilde{\Theta_{B-\alpha}} = \begin{bmatrix} \frac{\partial\Psi_B}{\partial\alpha_E} & \frac{\partial\Psi_B}{\partial\beta_E} & \frac{\partial\Psi_B}{\partial\alpha_I} & \frac{\partial\Psi_B}{\partial\beta_I} \\ 1 & 0 & 0 & 0 \\ \frac{\partial\Phi_B}{\partial\alpha_E} & \frac{\partial\Phi_B}{\partial\beta_E} & 0 & 0 \end{bmatrix} \tag{79}$$

In like fashion, $\sigma^2(\Delta\Theta_R)$, $\sigma^2(\Delta\Theta_Y)$ may be obtained, P ⟶ R or P ⟶ Y. The required partials which are elements of the matrices $\widetilde{\Theta_{P-\alpha}}$, $\widetilde{\Theta_{R-\alpha}}$, $\widetilde{\Theta_{Y-\alpha}}$ are listed herewith:

$$\frac{\partial\Theta_P}{\partial\Psi_B} = -\tan\Theta_R\cos\Theta_P$$

$$\frac{\partial\Theta_P}{\partial\Theta_B} = -\frac{\cos\Theta_Y\cos\Theta_P}{\cos\Theta_R}$$

$$\frac{\partial\Theta_P}{\partial\Phi_B} = -\frac{\sin\Psi_B\cos\Theta_P}{\cos\Phi_B\cos\Theta_R}$$

$$\frac{\partial\Theta_R}{\partial\Psi_B} = \sin\Theta_P;\quad \frac{\partial\Theta_R}{\partial\Theta_B} = -\cos\Theta_P\sin\Psi_B;\quad \frac{\partial\Theta_R}{\partial\Phi_B} = \cos\Theta_Y$$

$$\frac{\partial\Theta_Y}{\partial\Psi_B} = \frac{\cos\Phi_B\sin\Theta_Y}{\sin\Phi_B\cos\Theta_R}$$

$$\frac{\partial\Theta_Y}{\partial\Theta_B} = \frac{\sin\Theta_P\sin\Theta_Y}{\cos\Theta_R}$$

$$\frac{\partial\Theta_Y}{\partial\Phi_B} = \sin\Theta_Y\tan\Theta_R$$

IX. Quantitative Evaluation of System Accuracy

Since the fundamental purpose of this evaluation is to enable a comparison of various possible attitude determination systems, consideration will be given only to the (noise) errors in sensor measurements. The effects of orbit determination errors (and possibly radar range error) and own site uncertainty will be assumed to be comparable for all the systems, and further, to be small compared to the measurement error effects. Once a system has been selected, the analysis can be expanded to evaluate effects of satellite and station coordinate uncertainties. The assumption made simply means, for the Earth and radio sensor combination, that the direction cosines of the radio line-of-sight, ℓ_1', m_1', n_1' in the local vertical (orbit) system, are taken errorless.

Within the expected limits, three possible orientations of body axes were considered:

$$\psi_B = \theta_B = \phi_B = 0$$

$$\psi_B = 20°, \; \theta_B = \phi_B = 10°$$

$$\psi_B = -20°, \; \theta_B = \phi_B = -10°$$

The corresponding orientation angles of Earth vertical (i_E) with respect to body axes system are as follows:

θ_B	ϕ_B	θ_E	ϕ_E	α_E	β_E
0	0	0.0	-	90.0	90.0
10	10	14.5	135.5	100.0	81.6
-10	-10	14.5	314.5	80.0	98.4

The station site was taken as majane ($\delta_1 = 35.33°$) ; results for Rosman ($\delta_1 = 36.133°$) are essentially the same, since these sites are essentially at the same latitude; furthermore, results are expressed as functions of longitude difference ($L_p - L_1$) or of site right ascension λ_1 .

Error coefficients runs were made for the synchronous equatorial orbit,

$$i_p = 0, \Omega_p = 0, r_p = 22,766 \quad \text{n. miles}$$

and for the circular, inclined orbit

$$i_p = 28°, \; r_p = 9440 \quad \text{n. miles}$$

The independent variable for synchronous orbit is $(L_P - L_1)$; the independent variables for inclined orbit are μ_P and $(\lambda_1 - \Omega_P)$. In order to perform the evaluation, it was necessary to simulate the (measured) direction cosines of the radio line-of-sight under non-zero conditions of body attitude angles. Equations for these are listed in the Appendix.

Runs were made as prescribed by the station visibility limits indicated in Section VII, (also, see Fig. 15). The EArth sensor field of view limit (30°half cone angle) is almost met for the pitch and roll limits. Whether the radio sensor field of view limit was met was ascertained by computing

$$\Theta_{S_1} = \cos^{-1} n_1$$

and comparing with 25°; if the computed angle was greater than the limit, error computations were not carried through. Θ_{S_1}, the angle between body yaw axis and radio line-of-sight, is shown for the synchronous orbit, Fig. 18. The elevation angle above Earth horizon ε_1, is also shown. It is seen that the field of view requirement is met for the synchronous orbit, for the attitude limits considered.

For the inclined orbit, with zero attitude angles, Θ_{S_1} is always less than 25° along the μ_P boundaries given in Fig. 15, since then $\Theta_{S_1} = \psi_1 = 21.3°$. However, going to the positive attitude angle limits, it is seen, comparing Figs. 15 and 19, that the Θ_{S_1} limit is reached before the upper horizon limit. For the negative attitude angle limits, the Θ_{S_1} limit is obtained at a μ_P value higher than the lower horizon limit, see Fig. 20. The result is a further curtailment of admissible values of μ_P, as shown, Fig. 21.

The values chosen for measurement errors were

$$\sigma(\Delta\alpha_E) = \sigma(\Delta\beta_E) = 1°$$

$$\sigma(\Delta\alpha_1) = \sigma(\Delta\beta_1) = 1/3°$$

The 3σ values of pitch and roll determination errors are then as follows, independent of orbit parameters:

ψ_B	Θ_B	ϕ_B	$3\sigma(\Delta\Theta_B)$	$3\sigma(\Delta\phi_B)$
0	0	0	3°	3°
20	10	10	3°	3.06°
-20	-10	-10	3°	3.06°

The 3σ limits of yaw determination error are shown, Fig. 22, for the synchronous orbit. Fig. 23 shows the yaw error for the inclined orbit, for zero attitude angles only; the curves for the non-zero attitude cases are virtually coincident with those shown. Evidently, the smallest yaw error occurs when the satellite is at the horizon, but even this value can be significable. Fig. 24 shows peak yaw error. The largest error occurs for $(\lambda_1 - \Omega_P) = -\mu_P = 90°$.

Under the condition that $\sigma(\Delta\alpha_E) = \sigma(\Delta\beta_E)$ and $\sigma(\Delta\alpha_1) = \sigma(\Delta\beta_1)$ Eq. 71 can be re-written,

$$\sigma^2(\Delta\gamma_B)_T = \sigma^2(\Delta\gamma_B)_E + \sigma^2(\Delta\gamma_B)_R = K^2_{\gamma_E}\sigma^2(\Delta\alpha_E) + K^2_{\gamma_R}\sigma^2(\Delta\alpha_1) \qquad (80)$$

where

$$K_{\psi_E} = \sqrt{\left(\frac{\partial \psi_B}{\partial \alpha_E}\right)^2 + \left(\frac{\partial \psi_B}{\partial \beta_E}\right)^2}$$

$$K_{\psi_R} = \sqrt{\left(\frac{\partial \psi_B}{\partial \alpha_1}\right)^2 + \left(\frac{\partial \psi_B}{\partial \beta_1}\right)^2}$$

Let

$$\eta = \frac{K_{\psi_E}}{K_{\psi_R}} \; ; \quad k = \frac{\sigma(\Delta \alpha_E)}{\sigma(\Delta \alpha_1)}$$

Then

$$\sigma(\Delta \psi_B)_T = \sqrt{\eta^2 k^2 + 1}\ \ \sigma(\Delta \psi_B)_R \qquad (81)$$

The 3σ values of $(\Delta \psi_B)_R$ are shown, Figs. 24 and 25. η is essentially 1. Thus, if $k = 3$

$$\sigma(\Delta \psi_B)_E = 3\sigma(\Delta \psi_B)_R$$

$$\sigma(\Delta \psi_B)_T = \sqrt{10}\,\sigma(\Delta \psi_B)_R$$

and the contribution of the Earth sensor errors is 96% as large as the total error. If Earth sensor and radio sensor contributions are made equal, that is $k = 1$, then

$$\sigma(\Delta \psi_B)_E = \sigma(\Delta \psi_B)_R$$

$$\sigma(\Delta \psi_B)_T = \sqrt{2}\,\sigma(\Delta \psi_B)_R$$

This would then effect about a 55% decrease in the total errors shown in Figs. 22 and 24. A comparison of a spread of peak values, for the two orbits considered and for zero attitude angles, is given in the table below.

$\sigma(\Delta\alpha_E)$	$\sigma(\Delta\alpha_1)$	Sync. Orbit $3\sigma(\Delta\psi_B)_T$		Incl. Orbit $3\sigma(\Delta\psi_B)_T$	
		Max.	Min.	Max.	Min.
1°	1/3°	31.8	18.7	43.6	8.0
1/3°	1/3°	14.3	8.3	19.5	3.7

Evidently, the difficulty in obtaining suitable yaw determination accuracy lies in the size of the magnification factor K_{ψ_R} which can vary from about 6 to 10 for the synchronous orbit, and from about 3 to 14 for the inclined orbit. A criterion for a satisfactory attitude determination system might therefore be that system which gives a magnification factor, at most, no greater than 1.

APPENDIX I - MINIMUM SENSING INFORMATION REQUIRED FOR ATTITUDE DETERMINATION

It will be shown here that measurement of the direction cosines of a line-of-sight in the vehicle body coordinate system, and a priori knowledge of the direction cosines of this line in the vehicle local vertical (orbit) system, does not alone provide sufficient information for complete attitude determination. From eq's. 2 and 24, and matrix eq. 3,

$$\begin{vmatrix} \ell_1 \\ m_1 \\ n_1 \end{vmatrix} = \widehat{V_1} \begin{vmatrix} \ell_1' \\ m_1' \\ n_1' \end{vmatrix} \tag{A-1}$$

or in short hand notation

$$\widehat{S_B} = \widehat{V_1}\,\widehat{S_V} \tag{A-2}$$

The elements of $\widehat{V_1}$ are functions of the attitude angles which we wish to determine. Solving for $\widehat{V_1}$ we have

$$\widehat{S_B}\,\widehat{S_V}^T = \widehat{V_1}\left[\widehat{S_V}\,\widehat{S_V}^T\right]$$

$$\widehat{S_B}\,\widehat{S_V}^T\left[S_V S_V^T\right]^{-1} = \widehat{V_1} \tag{A-3}$$

However, it is readily shown that $\left[S_V\ S_V^T\right]$ is a singular matrix and the inverse is undefined. Eq. A-3 has no solution; there is an insufficient number of constain equations. Alternatively, taking the transpose of both sides of Eq. A-2,

$$\widehat{S_B}^T = \widehat{S_V}^T \widehat{V_1}^T$$

or since $\widehat{V_1}$ is orthonormal and $\widehat{V_1}^T\widehat{V_1} = \widehat{V_1}^{-1}\widehat{V_1} = \widehat{I}$

$$\widehat{S_B}^T \widehat{V_1} = \widehat{S_V}^T$$

from which

$$\left[\widehat{S_B}\,\widehat{S_B}^T\right]\widehat{V_1} = \widehat{S_B}\,\widehat{S_V}^T$$

$$\widehat{V_1} = \left[\widehat{S_B}\,\widehat{S_B}^T\right]^{-1}\widehat{S_B}\,\widehat{S_V}^T \tag{A-4}$$

Similar to before, it can be shown that $\left[S_B S_B^T\right]$ is a singular matrix, so that Eq. A-4 has no solution.

From a different point of view, and more explicitly, let

$$\widehat{V_1} = \begin{vmatrix} a_1 & a_2 & a_3 \\ b_1 & b_2 & b_3 \\ c_1 & c_1 & c_3 \end{vmatrix}$$

Then Eq. A-1 can be written as a coelection of three simultaneous equations:

$$l_1 = a_1 l_1' + a_2 m_1' + a_3 n_1' \tag{A-5}$$

$$m_1 = b_1 l_1' + b_2 m_1' + b_3 n_1' \tag{A-6}$$

$$n_1 = c_1 l_1' + c_2 m_1' + c_3 n_1' \tag{A-7}$$

Now l_1', m_1', n_1' are known and l_1, m_1 are measured. Six equations due to orthonormality constraints can be written, viz.:

$$a_i^2 + b_i^2 + c_i^2 = 1, \text{ for } i = 1,2,3$$

$$a_i a_j + b_i b_j + c_i c_j = 0, \text{ for } \begin{matrix} i,j = 1,2,3 \\ i \neq j \end{matrix}$$

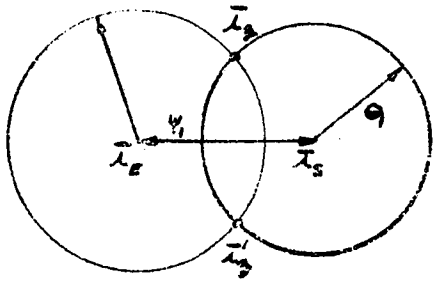
It can be readily shown that Eq. A-7 can be derived from Eq.s A-5, A-6, the orthonormality equations of constraint on the elements of $\widehat{V_1}$ and an orthonormality equation of constraint on the elements of $\widehat{S_B}$:

$$l_1^2 + m_1^2 + n_1^2 = 1$$

Thus, Eq. A-7 is not an independent equation. We have nine unknowns (the elements of $\widehat{V_1}$) and only eight independent equations. An additional piece of information is needed.

From the point of view of the physical situation, if the direction angles of a single line-of-sight with respect to body system are measured, the body axes can be rotated about the line-of-sight, forming three concentric cones. If the direction angles of an additional line-of-sight are measured (or in the present study, if the direction angles of satellite local vertical are measured) with respect to body system, the set of cones about this second line. The attitude of the vehicle is determined by the intersections of the two sets of cones. Considering, for example, theZ-axis cones (see Fig. 26), it is evident that a possible ambiguity arises due to intersection in two elements. This must be resolved by reason of field of view constraints or other means.

In the system analyzed in this study, the means is provided by the offset of the Earth detector from the satellite center, so that proper signs can be ascribed to $\cos\alpha_E$, $\cos\beta_E$; the sign of $\cos\Theta_E$ is obtained from knowledge of which Earth detector is activated. Then, Θ_S, Φ_S are uniquely determined; with radio line-of-sight information provided, ψ_A is uniquely determined.



Note; $\Theta_{S_1} + \Theta_E \geq \psi_1 \geq |\Theta_E - \Theta_1|$

Fig. 26

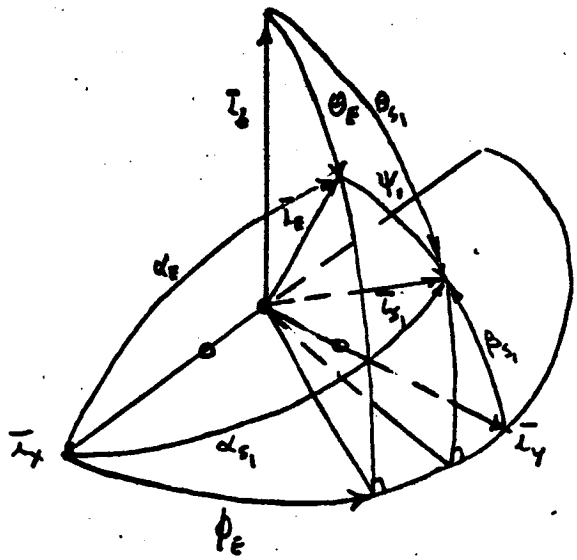
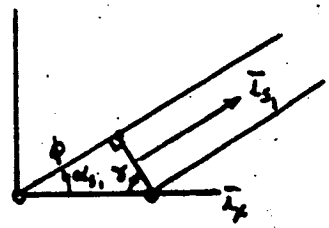
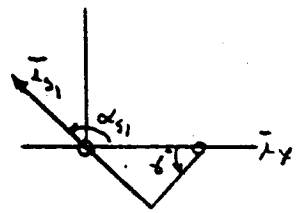


FIG. 1



$\phi \sim \sin\gamma = +$; $0 \leq \alpha_{s_1} \leq 90°$



$\phi \sim \sin\gamma = -$; $90 \leq \alpha_{s_1} \leq 180°$

FIG. 2

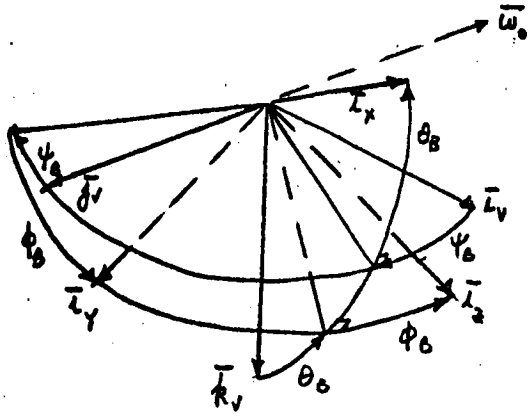


FIG. 3

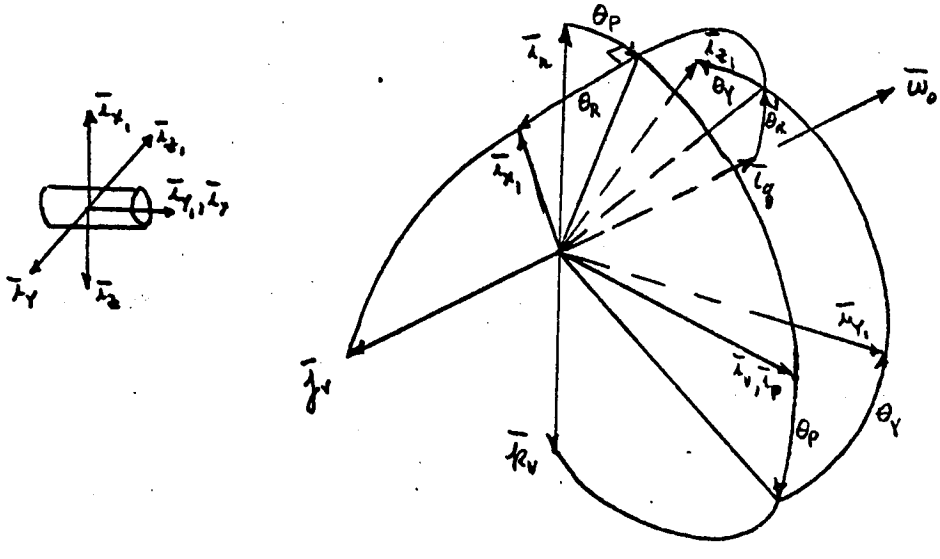
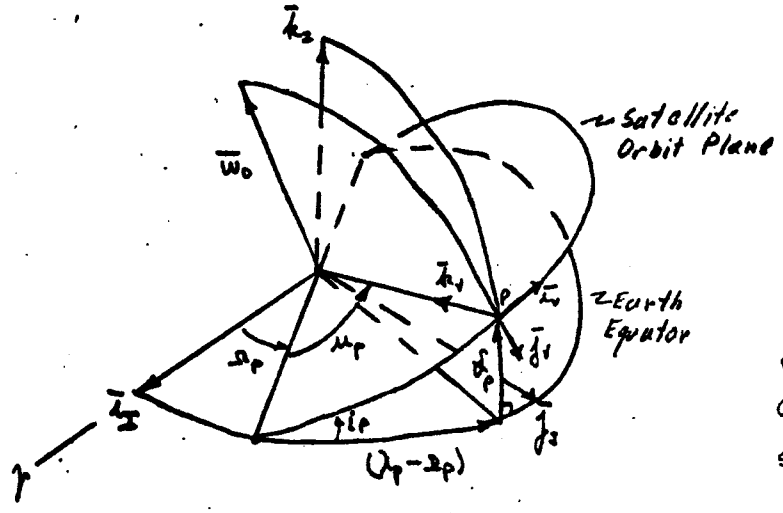
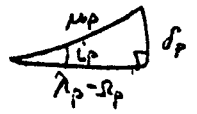


FIG. 4





$$\cos \mu_p = \cos(\lambda_p - \Omega_p) \cos \delta_p$$
$$\cos i_p = \operatorname{ctn} \mu_p \tan(\lambda_p - \Omega_p)$$
$$\sin(\lambda_p - \Omega_p) = \operatorname{ctn} i_p \tan \delta_p$$
$$\sin \delta_p = \sin i_p \sin u_p$$
$$\sin u_p \cos i_p = \cos \delta_p \sin(\lambda_p - \Omega_p)$$

FIG. 5

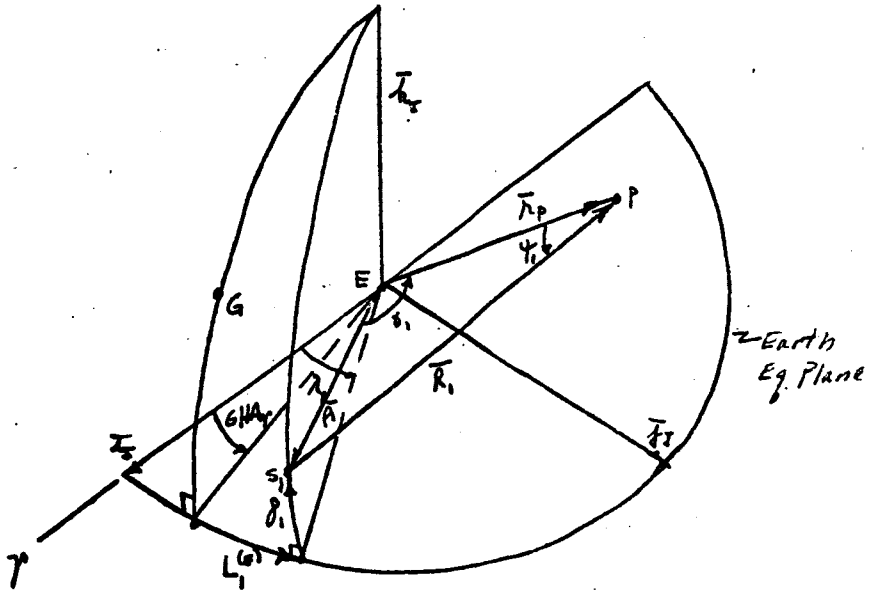


FIG. 6

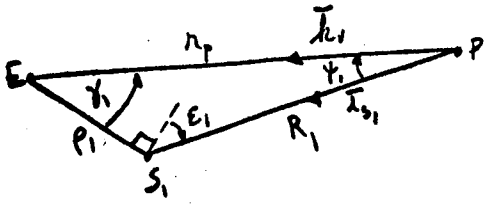


FIG. 7

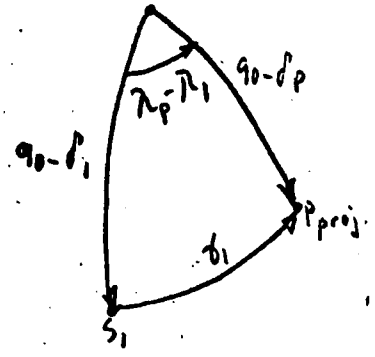


FIG. 8

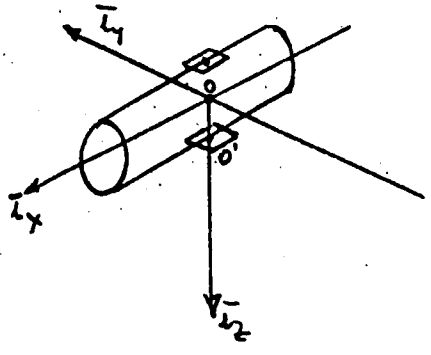


FIG. 9

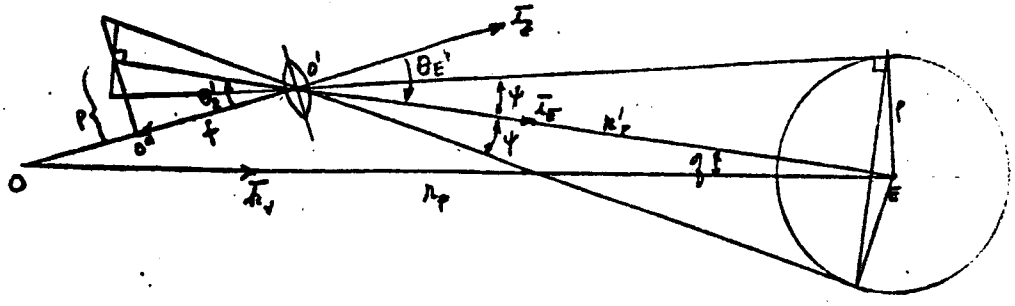


FIG. 10

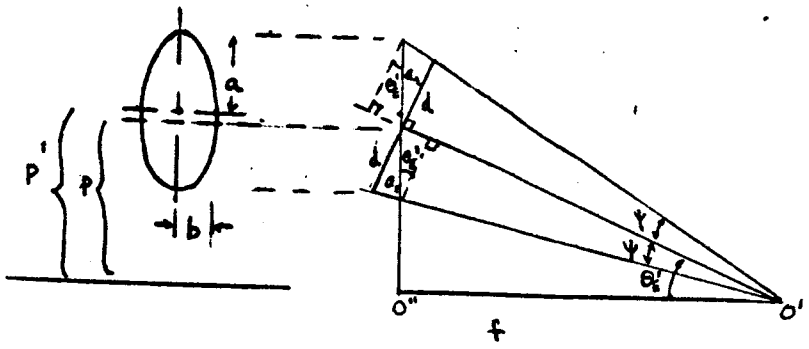


FIG. 11

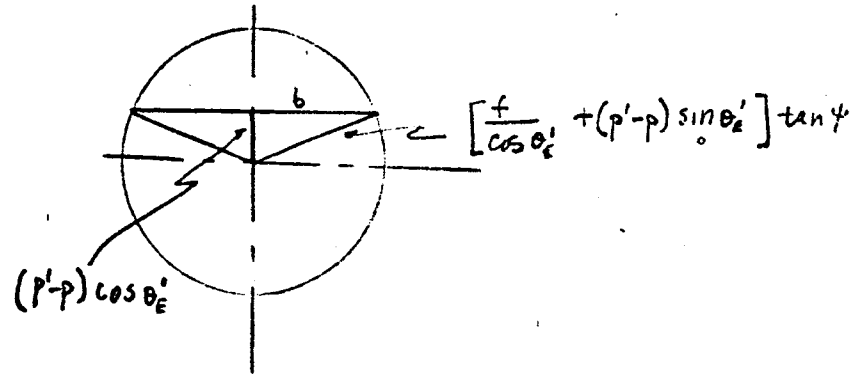


FIG. 12

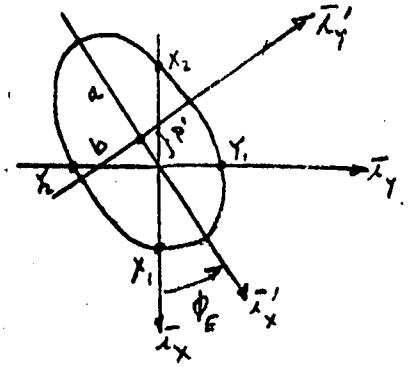


FIG. 13

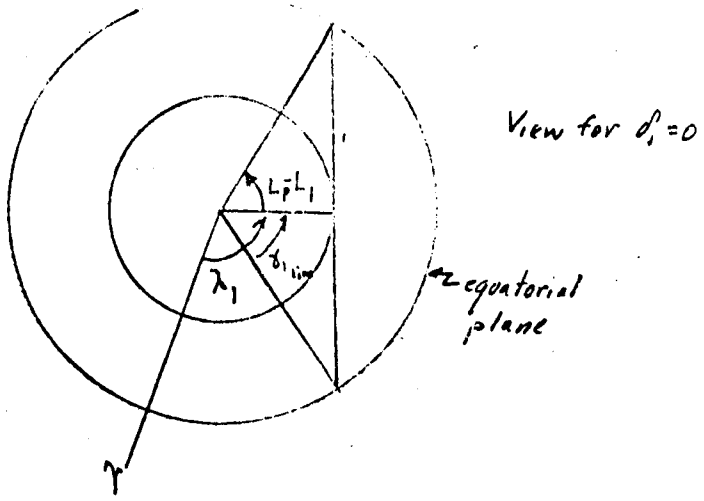


FIG. 14

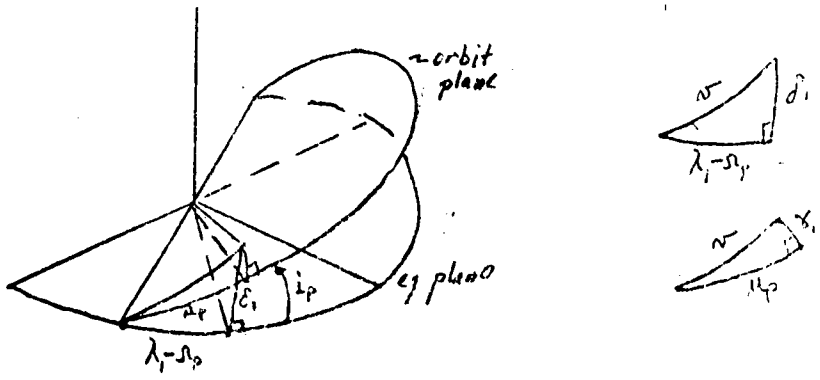


FIG. 17

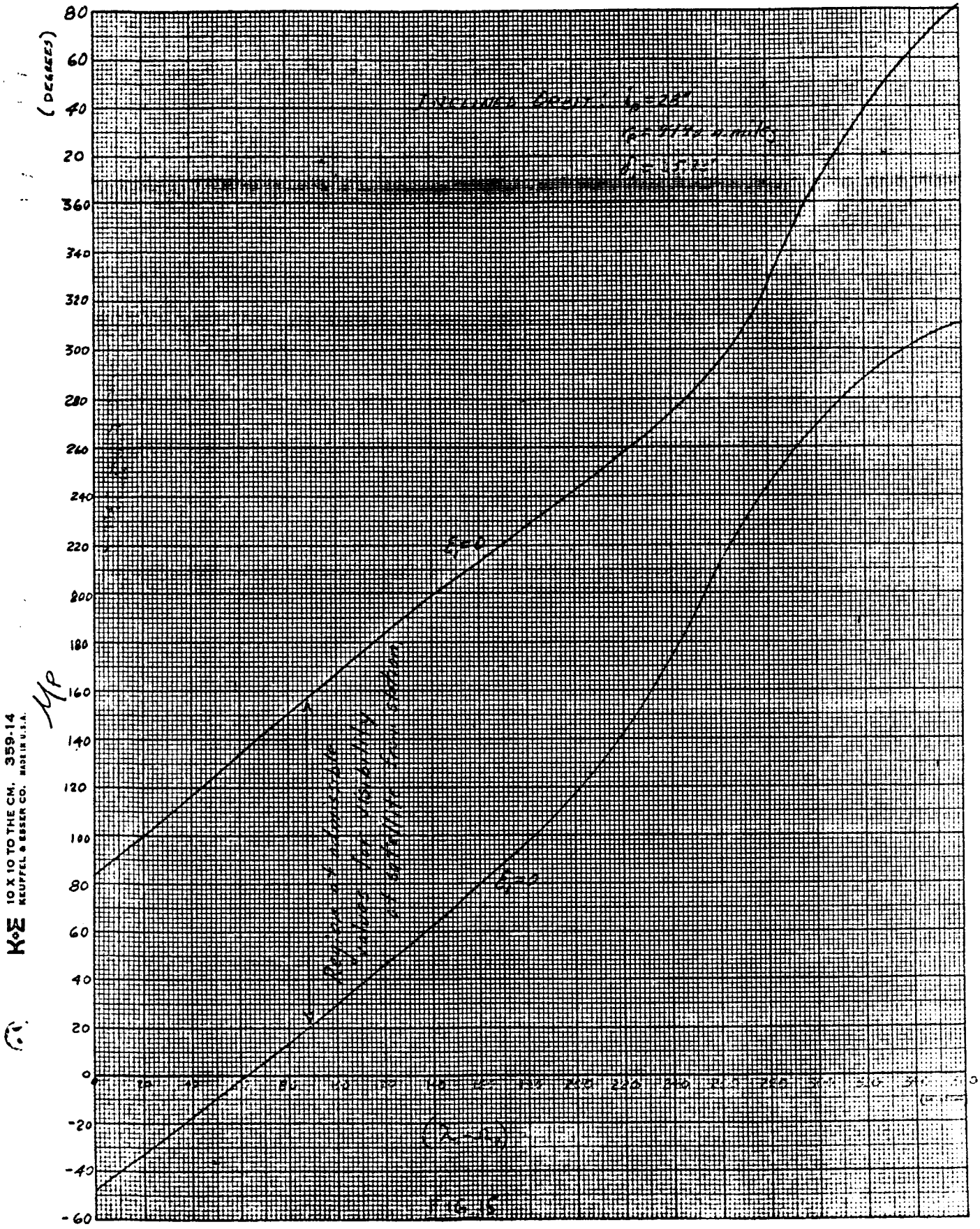

(DEGREES)
80
60
40
20
360
340
320
300
280
260
240
220
200
180
160
140
120
100
80
60
40
20
0
-20
-40
-60
ψ_p
$\zeta_f = 0$
$\zeta_f = 0$
$(\lambda - \psi_w)$
10 X 10 TO THE CM. 359-14
KEUFFEL & ESSER CO. MADE IN U.S.A.

FIG. 15

K·E 10 X 10 TO THE CM. 359-14
KEUFFEL & ESSER CO. MADE IN U.S.A.

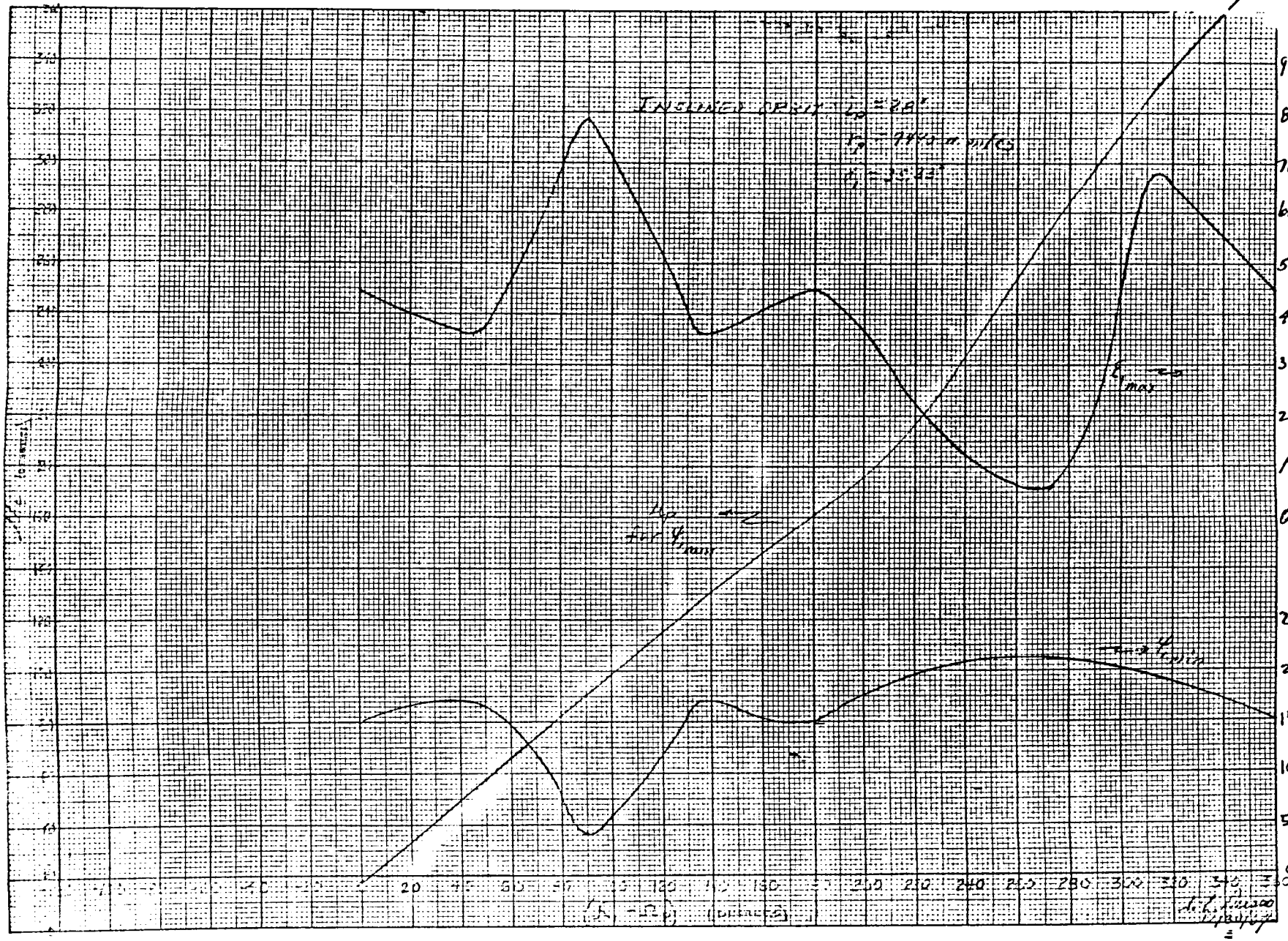


FIG 16

K•E 10 X 10 TO THE CM. 359-14
KEUFFEL & ESSER CO. MADE IN U.S.A.

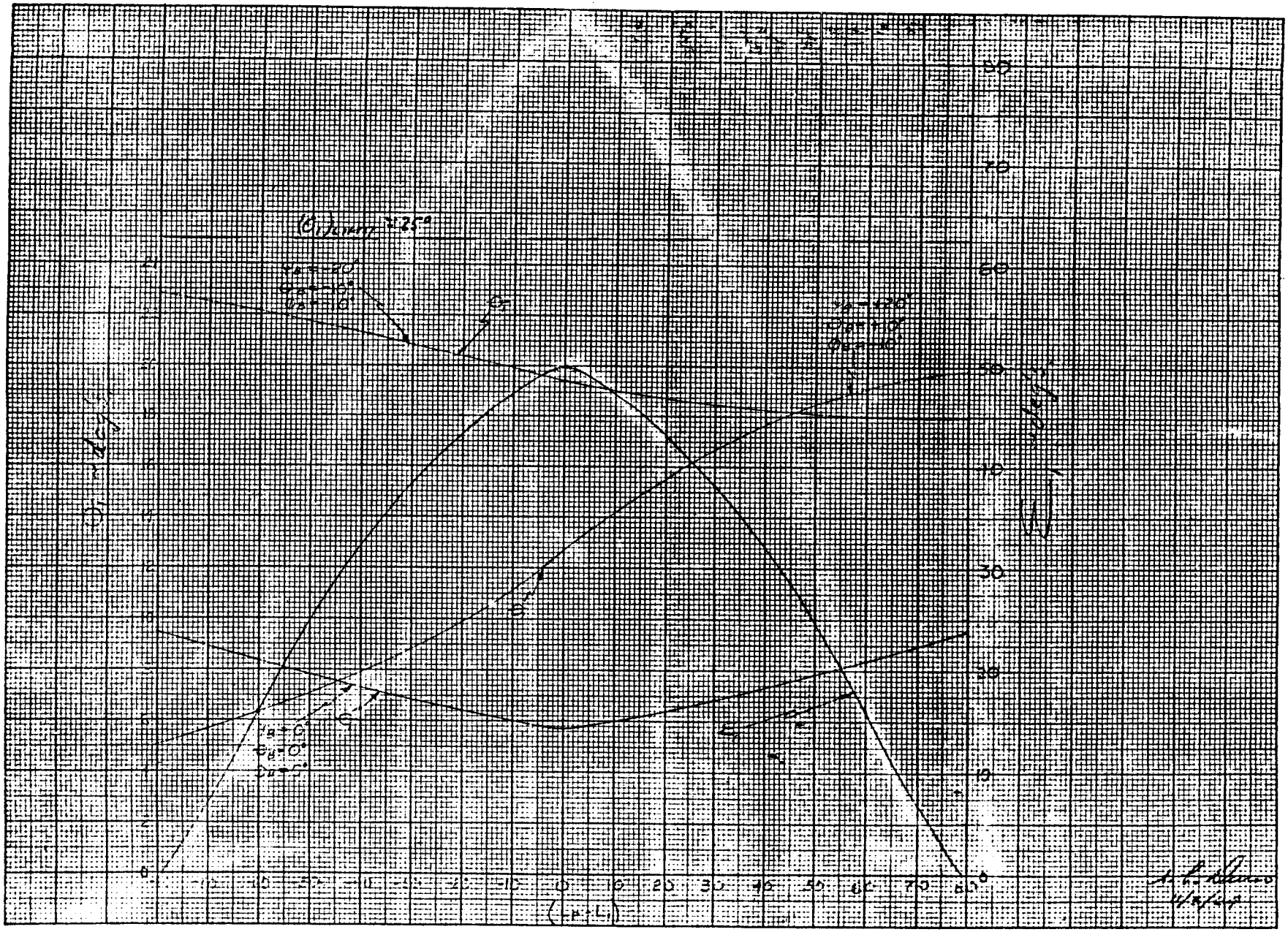


FIG. 18

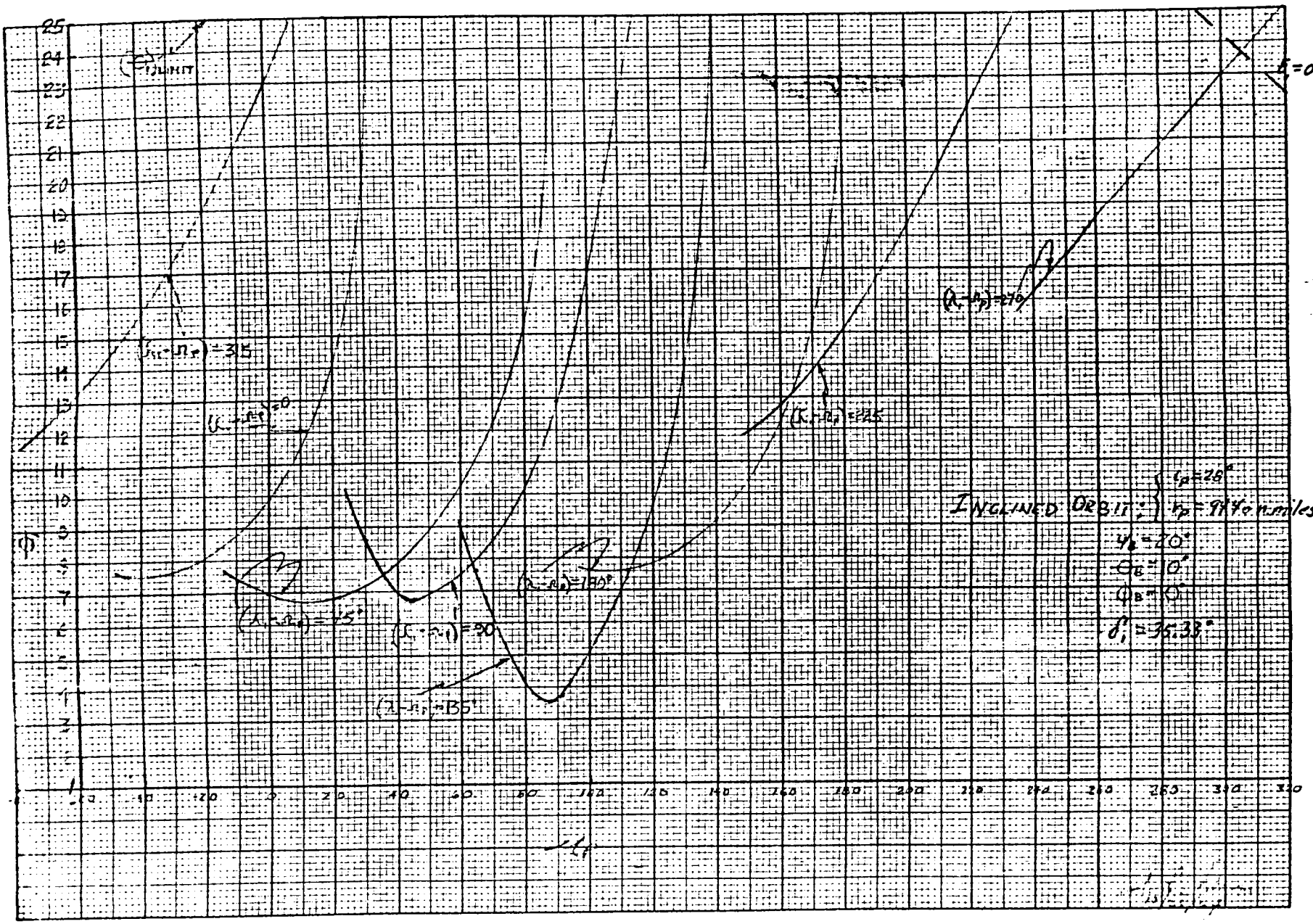

(Ω-Ω_P)=270°
(Ω-Ω_P)=180°
(Ω-Ω_P)=135°
(Ω-Ω_P)=90°
(Ω-Ω_P)=45°
(Ω-Ω_P)=0°
(Ω-Ω_P)=315°
(Ω-Ω_P)=225°
(Ω-Ω_P)=135°
(Ω-Ω_P)=45°
INCLINED ORBIT:
i_p=28°
h_p=9440 n.miles
γ_b=20°
σ_E=0°
Q_B=0
δ_1=35.38°
Φ
λ_f

FIG. 19

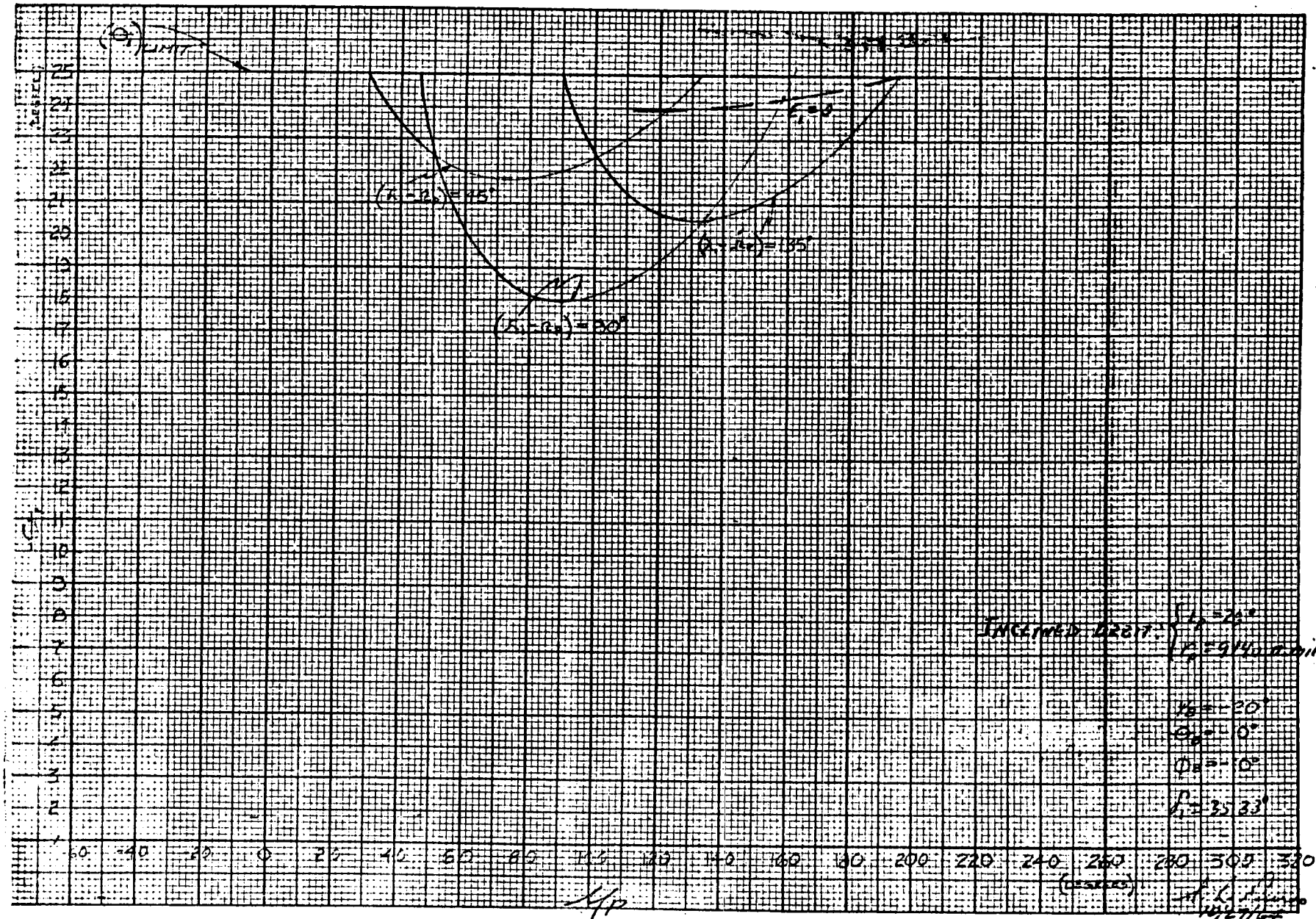

$(\theta_1)_{Limit}$
$\zeta_1 = 0$
$(\theta_1 - \theta_{1_0}) = 45°$
$(\theta_1 - \theta_{1_0}) = 135°$
$(\theta_1 - \theta_{1_0}) = 90°$
θ_1
γ_p
INCREMENTED AREA: $\begin{cases} \gamma_p = 2° \\ r_p = 9140 \text{ miles} \end{cases}$
$\gamma_{p_0} = -20°$
$\theta_{1_0} = 0°$
$\phi_B = -0°$
$\theta_{1_1} = 35.33°$
(DESIRED)
γ_p

FIG. 20

F1621

10 X 10 TO THE ½ INCH 359-11

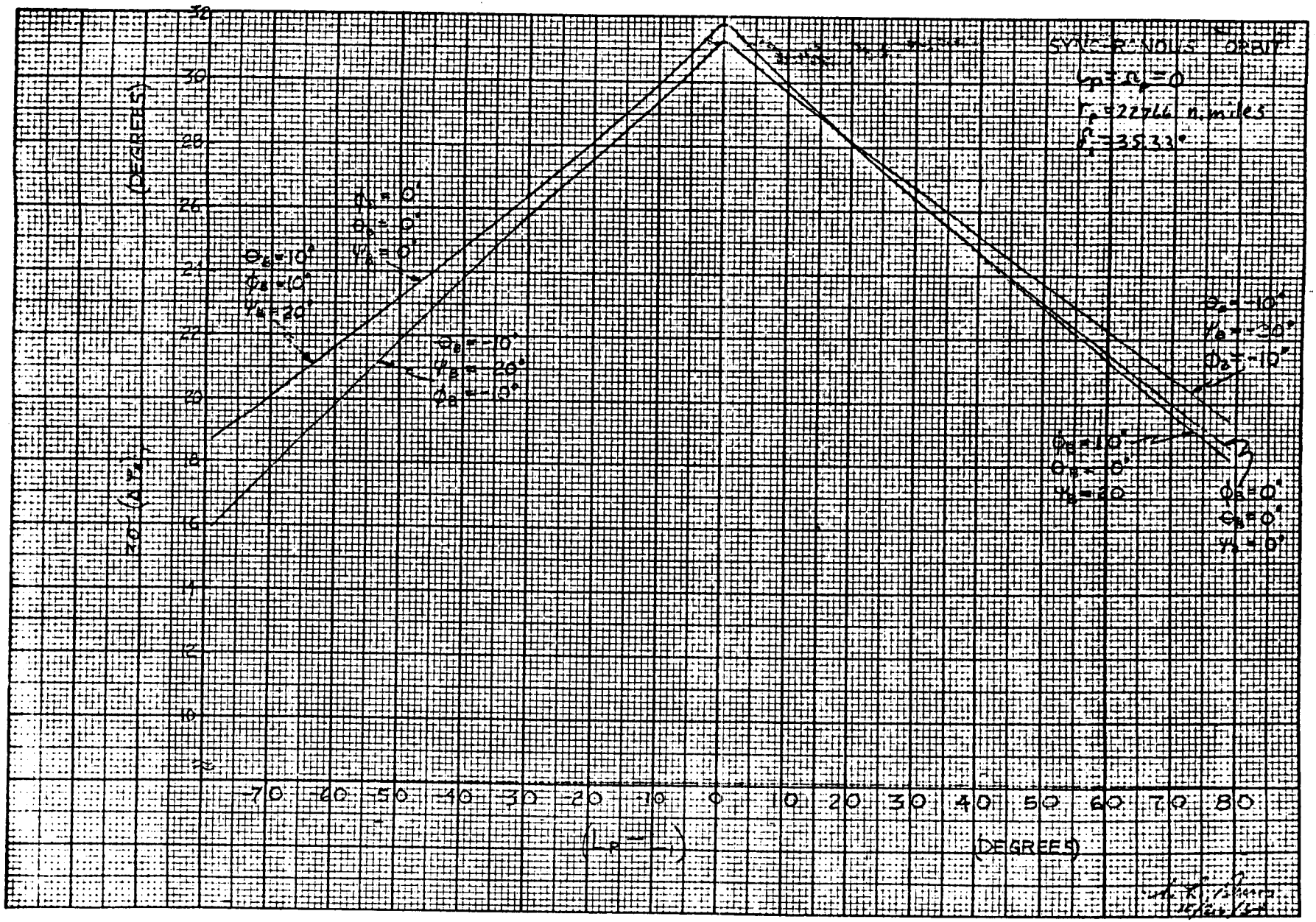
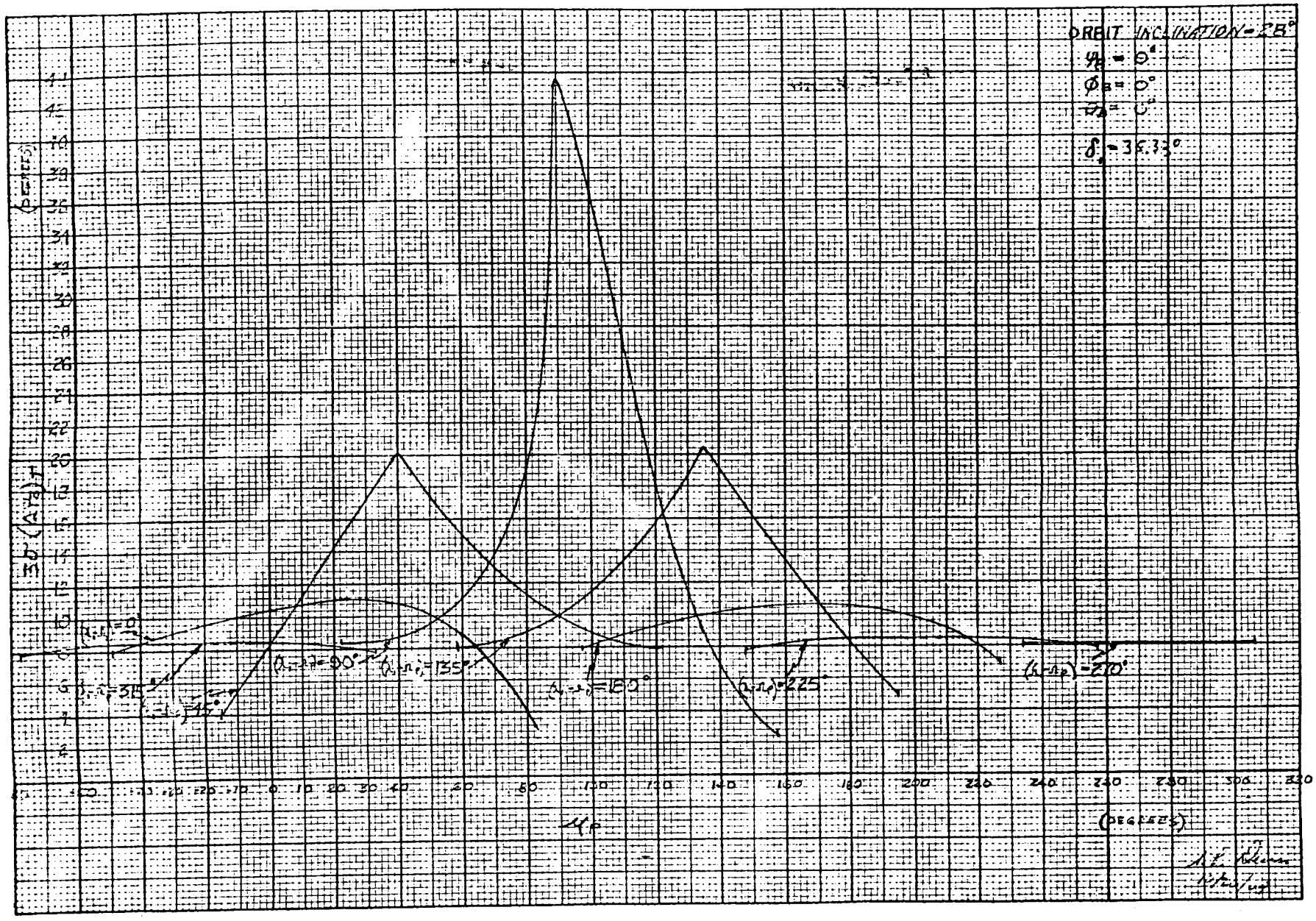

SYNCHRONOUS ORBIT
$\gamma_p = \Omega = 0$
$r_a = 22766$ n. miles
$i = 35.33°$
$\theta_B = 10°$
$\psi_B = 10°$
$\gamma_B = 20°$
$\theta_B = 0°$
$\psi_B = 0°$
$\gamma_B = 0°$
$\theta_B = -10°$
$\psi_B = -20°$
$\gamma_B = -10°$
$\theta_B = -10°$
$\psi_B = -30°$
$\gamma_B = -10°$
$\theta_B = 10°$
$\psi_B = 0°$
$\gamma_B = 20$
$\theta_B = 0°$
$\psi_B = 0°$
$\gamma_B = 0°$
$\left(\frac{1}{r_a} - \frac{1}{r_p}\right)$
(DEGREES)
(DEGREES)

FIG. 22


ORBIT INCLINATION = 28°
ψ_B = 0°
ϕ_B = 0°
ψ_A = 0°
δ_s = 35.33°
ΔV_{TD} (FT/SEC)
$(\Lambda - \Lambda_0) = 0°$
$(\Lambda - \Lambda_0) = 45°$
$(\Lambda - \Lambda_0) = 90°$
$(\Lambda - \Lambda_0) = 135°$
$(\Lambda - \Lambda_0) = 180°$
$(\Lambda - \Lambda_0) = 225°$
$(\Lambda - \Lambda_0) = 270°$
ψ_P
(DEGREES)

F16.23

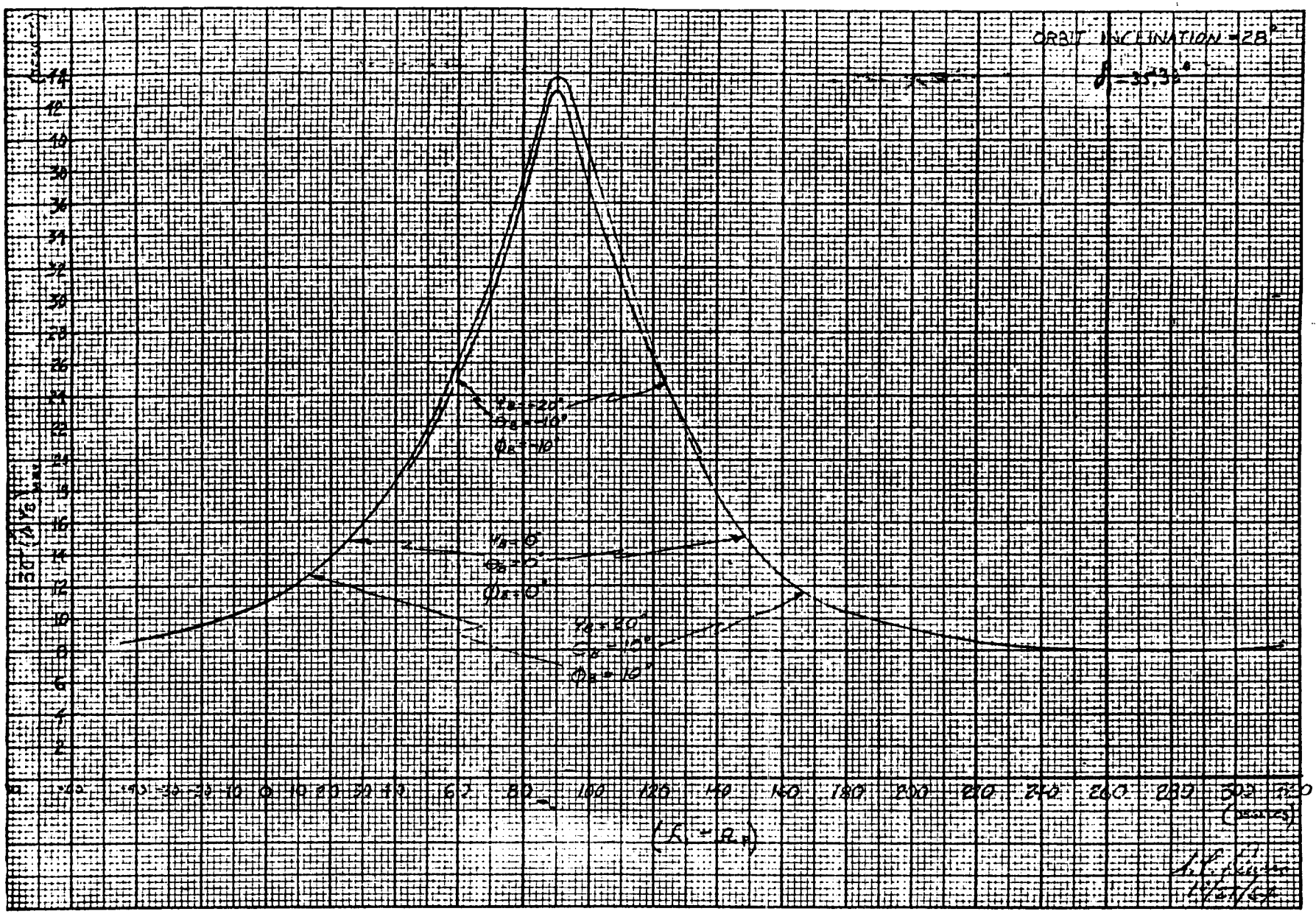
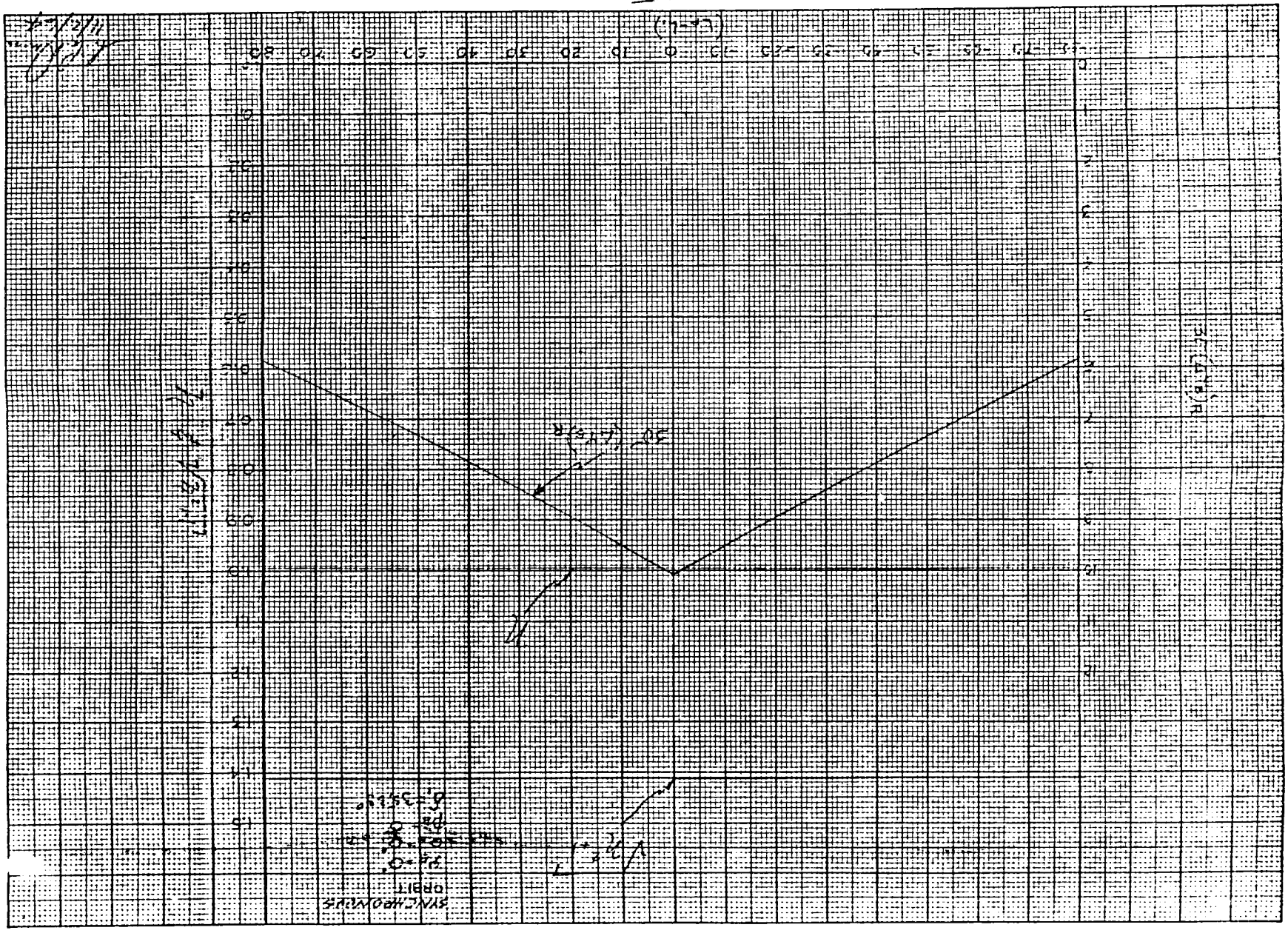
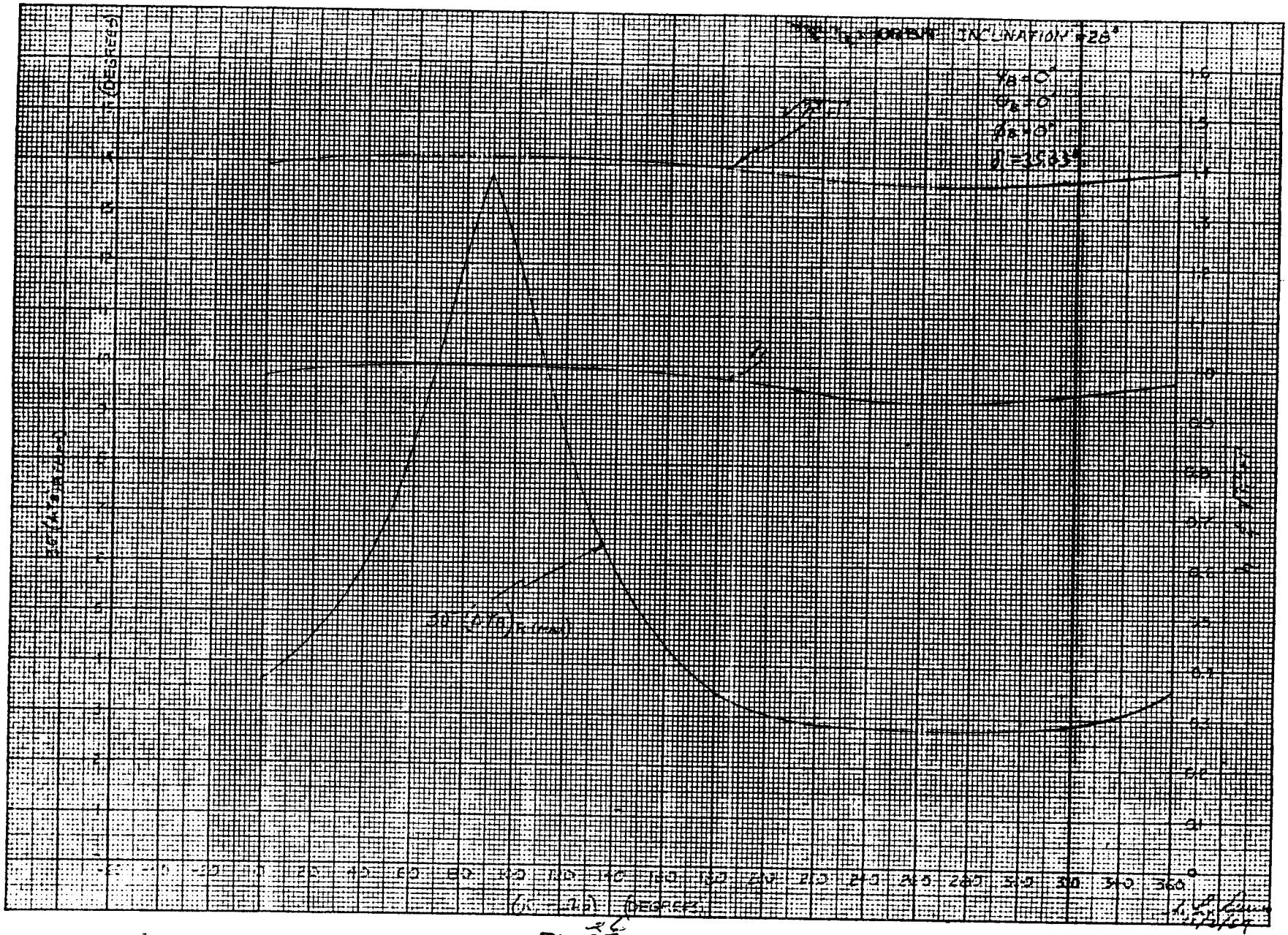

ORBIT INCLINATION = 28°
$\delta = 35.3°$
$\phi_R = 20°$
$\phi_R = 10°$
$\phi_R = 0°$
$\phi_R = 20°$
$\phi_R = 10°$
$\phi_R = 0°$
$\phi_R = -10°$
$\phi_R = -20°$
$(\zeta = R_E)$

FIG. 24

K&E 10 X 10 TO THE CM. 359-14
KEUFFEL & ESSER CO. MADE IN U.S.A.



K•E 10 X 10 TO THE CM. 359-14
KEUFFEL & ESSER CO. MADE IN U.S.A.


ANGLE OF INCLINATION = 28°
$\gamma_B = 0°$
$\theta_B = 0$
$\beta_B = 0°$
$\eta = 35.83°$
$\gamma_B = 28°$
$\theta_B = 0$
$\beta_B = 0°$
$\eta = 35.83°$
$30^{-1}\Sigma(\Phi_0)_{T-(rad)}$
$\Sigma(\Phi_0)_{T-(rad)}$
$\Sigma(\Phi_0)_{T-(rad)}$
$

APPENDIX II

$$\ell_1 = \bar{\imath}_{s_1} \cdot \bar{\imath}_X = \frac{(r_p \bar{k}_V + \bar{\rho}_1)}{R_1} \cdot \bar{\imath}_X \quad ; \alpha_1 = \cos^{-1} \ell_1 \, , \; 0 \le \alpha_1 \le 180^\circ$$

whence

$$\left(\frac{R_1}{\rho}\right) \ell_1 = -\left(\frac{r_p}{\rho}\right) \sin\theta_B + \sin\delta_1 \sin\theta_B \sin u_p \sin i_p$$

$$+ \sin\delta_1 \cos\theta_B \left[\cos\psi_B \cos u_p \sin i_p - \sin\psi_B \cos i_p\right]$$

$$+ \cos\delta_1 \sin\theta_B \left[\cos u_p \cos(\lambda_1 - \Omega_p) + \sin u_p \cos i_p \sin(\lambda_1 - \Omega_p)\right]$$

$$+ \cos\delta_1 \cos\theta_B \left[\begin{array}{l} \cos\psi_B \left\{\cos u_p \cos i_p \sin(\lambda_1 - \Omega_p) - \sin u_p \cos(\lambda_1 - \Omega_p)\right\} \\ \quad + \sin\psi_B \sin i_p \sin(\lambda_1 - \Omega_p) \end{array}\right]$$

$$m_1 = \bar{\imath}_{s_1} \cdot \bar{\imath}_Y = \frac{(r_p \bar{k}_V + \bar{\rho}_1)}{R_1} \cdot \bar{\imath}_Y \quad ; \beta_1 = \cos^{-1} m_1 \, , \; 0 \le \beta_1 \le 180^\circ$$

whence

$$\left(\frac{R_1}{\rho}\right) m_1 = \left(\frac{r_p}{\rho}\right) \sin\phi_B \cos\theta_B + \cos\delta_1 \sin\phi_B \sin\theta_B \cos\psi_B \left[\begin{array}{l} -\sin u_p \cos(\lambda_1 - \Omega_p) \\ +\cos u_p \cos i_p \sin(\lambda_1 - \Omega_p) \end{array}\right]$$

$$+ \cos\delta_1 \cos\phi_B \sin\psi_B \left[\sin u_p \cos(\lambda_1 - \Omega_p) - \cos u_p \cos i_p \sin(\lambda_1 - \Omega_p)\right]$$

$$+ \cos\delta_1 \sin i_p \sin\phi_B \sin\theta_B \sin\psi_B \sin(\lambda_1 - \Omega_p)$$

$$+ \cos\delta_1 \sin i_p \cos\phi_B \cos\psi_B \sin(\lambda_1 - \Omega_p)$$

$$+ \cos\delta_1 \sin\phi_B \cos\theta_B \left[-\sin u_p \cos i_p \sin(\lambda_1 - \Omega_p) - \cos u_p \cos(\lambda_1 - \Omega_p)\right]$$

$$+ \sin\delta_1 \sin\phi_B \sin\theta_B \left[\cos\psi_B \cos u_p \sin i_p - \sin\psi_B \cos i_p\right]$$

$$+ \sin\delta_1 \cos\phi_B \left[-\cos u_p \sin i_p \sin\psi_B - \cos i_p \cos\psi_B\right]$$

$$- \sin\delta_1 \sin\phi_B \cos\theta_B \sin u_p \sin i_p$$

$$n_1 = \bar{\imath}_{s_1} \cdot \bar{\lambda}_2 = \frac{(r_p \bar{R}_{V_1} + \bar{\rho}_1)}{R_1} \cdot \bar{\imath}_2 \quad ; \quad \theta_1 = \cos^{-1} n_1 \ , \ 0 \le \theta_1 \le 180^\circ$$

whence

$$\left(\frac{R_1}{\rho}\right) n_1 = \left(\frac{r_p}{\rho}\right) \cos\phi_B \cos\theta_B + \cos\delta_1 \sin\theta_B \cos\phi_B \cos\psi_B \left[\begin{array}{l} -\sin u_p \cos(\lambda_1 - \Omega_p) \\ +\cos u_p \cos i_p \sin(\lambda_1 - \Omega_p) \end{array}\right]$$

$$+ \cos\delta_1 \sin\phi_B \sin\psi_B \left[-\sin u_p \cos(\lambda_1 - \Omega_p) + \cos u_p \cos i_p \sin(\lambda_1 - \Omega_p)\right]$$

$$+ \cos\delta_1 \sin i_p \cos\phi_B \sin\theta_B \sin\psi_B \sin(\lambda_1 - \Omega_p)$$

$$- \cos\delta_1 \sin i_p \sin\phi_B \cos\psi_B \sin(\lambda_1 - \Omega_p)$$

$$+ \cos\delta_1 \cos\phi_B \cos\theta_B \left[-\cos u_p \cos(\lambda_1 - \Omega_p) - \sin u_p \cos i_p \sin(\lambda_1 - \Omega_p)\right]$$

$$+ \sin\delta_1 \sin\theta_B \cos\phi_B \left[\cos u_p \sin i_p \cos\psi_B - \cos i_p \sin\psi_B\right]$$

$$+ \sin\delta_1 \sin\phi_B \left[\cos u_p \sin i_p \sin\psi_B + \cos i_p \cos\psi_B\right]$$

$$- \sin\delta_1 \cos\phi_B \cos\theta_B \sin u_p \sin i_p$$

For the equatorial, circular orbit only: $(i_p = 0, \ \Omega_p = 0, \ \delta_p = 0, \ u_p = \lambda_p)$

$$\left(\frac{R_1}{\rho}\right) l_1 = \left[-\left(\frac{r_p}{\rho}\right) + \cos\delta_1 \cos(L_p - L_1)\right] \sin\theta_B - \left[\cos\delta_1 \cos\psi_B \sin(L_p - L_1) + \sin\delta_1 \sin\psi_B\right] \cos\theta_B$$

$$\left(\frac{R_1}{\rho}\right) m_1 = \left[\left(\frac{r_p}{\rho}\right) - \cos\delta_1 \cos(L_p - L_1)\right] \sin\phi_B \cos\theta_B$$

$$+ \cos\delta_1 \sin(L_p - L_1)\left[\cos\phi_B \sin\psi_B - \sin\phi_B \sin\theta_B \cos\psi_B\right]$$

$$- \sin\delta_1 \left[\cos\phi_B \cos\psi_B + \sin\phi_B \sin\theta_B \sin\psi_B\right]$$

$$\left(\frac{R_1}{\rho}\right) n_1 = \left[\left(\frac{r_p}{\rho}\right) - \cos\delta_1 \cos(L_p - L_1)\right] \cos\phi_B \cos\theta_B$$

$$- \cos\delta_1 \sin(L_p - L_1)\left[\sin\phi_B \sin\psi_B + \sin\theta_B \cos\phi_B \cos\psi_B\right]$$

$$+ \sin\delta_1 \left[\sin\phi_B \cos\psi_B - \sin\theta_B \cos\phi_B \sin\psi_B\right]$$

APPENDIX B

SATELLITE ATTITUDE DETERMINATION VIA ON-BOARD RADIO SENSOR MEASUREMENTS, TWO GROUND TRANSMITTER STATIONS

I. INTRODUCTION & SUMMARY

This memorandum presents the equations required for the computation of vehicle attitude utilizing the radio signals received, essentially simultaneously, from two separated earth-bound radio stations. The accuracy of this computation based on sensor measurement inaccuracy, is evaluated. It is found that the conditions for worst error are different for this system than for the previously studied system of earth-sensor, radio sensor combination. By properly selecting that system which yields the better accuracy, excessively high errors are avoided, although the yaw accuracy may still be considered inadequate.

Two types of orbits are considered: the equatorial synchronous orbit, and an inclined ($i_p = 28^\circ$) orbit with 6,000 n.m. altitude. By choosing the synchronous satellite longitude to lie midway between the longitude of the radio station sites, minimum errors are obtained (for zero attitude angles):

pitch error (3σ) = 1.9°
roll error (3σ) = $.7^\circ$
yaw error (3σ) = 17.2°

By exercising system selectivity, the maximum and minimum errors, for the inclined orbit are:

	max.	min.
pitch error (3σ)	3°	1°
roll error (3σ)	3°	$.6^\circ$
yaw error (3σ)	16.8°	2.2°

Errors may be further reduced by the judicious application of weighting techniques. An extensive numerical evaluation of the effect of these techniques on system errors has not been made; fundamentally, it would be necessary to investigate the degree of correlation between the two types of systems considered. Reference Memo, Flight Dynamics Data Memo 4143-FDDM-007, "Satellite Attitude Determination Via On-Board Earth Detector & Radio Sensor Information".

II. DETERMINATION OF LOCAL VERTICAL ORIENTATION

In Figure 1, consider the satellite at point , which is simultaneously in view of two radio stations on the surface of the earth, designated as S_1 and S_2. Further, the stations are within the field of view of a radio sensor on board the vehicle. Let the local vertical, directed from vehicle to earth center be denoted $\bar{r}_\varepsilon$. The angles ψ_1 and ψ_2 are readily determined from knowledge of the coordinates of sites and vehicle in the geocentric equatorial system. If the satellite orbit has been determined, the angular coordinates λ_p, δ_p and distance r_p are known as functions of time. Thus:

$$\bar{r}_p = r_p \left[\cos\delta_p \cos\lambda_p \bar{I}_I + \cos\delta_p \sin\lambda_p \bar{J}_I + \sin\delta_p \bar{k}_I \right] \quad (1)$$

The station vector is given by:

$$\bar{\rho}_1 = \rho_1 \left[\cos\delta_1 \cos\lambda_1 \bar{i}_I + \cos\delta_1 \sin\lambda_1 \bar{j}_I + \sin\delta_1 \bar{k}_I\right] \quad (2)$$

A like expression holds for $\bar{\rho}_2$. Note that δ_1 is constant, but λ_1 changes at earth rate:

$$\lambda_1 = GHA_\gamma(t) + L_1^{(E)} \quad (3)$$

where L_1 is longitude, measured positive eastward from Greenwich. The central angle γ_1 is given by:

$$\cos\gamma_1 = \frac{\bar{\rho}_1}{\rho} \cdot \frac{\bar{r}_p}{r_p} = \sin\delta_1 \sin\delta_p + \cos\delta_1 \cos\delta_p \cos(\lambda_p - \lambda_1) \quad (4)$$

$$0 \le \gamma_1 \le \cos^{-1}\left(\frac{\rho_1}{r_p}\right) < 90^\circ$$

and the line-of-sight distance is

$$R_1 = \sqrt{\rho_1^2 + r_p^2 - 2 r_p \rho_1 \cos\gamma_1} \quad (5)$$

where ρ_1 = earth radius at S_1. Angle ψ_1 is then obtained from

$$\eta_1' \triangleq \cos\psi_1 = \frac{r_p - \rho_1 \cos\gamma_1}{R_1} \quad (6)$$

$$0 \le \psi_1 \le \sin^{-1}\left(\frac{\rho_1}{r_p}\right) < 90^\circ$$

ψ_2 is found in similar fashion. It is to be noted that stations may determine ψ by direct measurement of range and elevation, but less accurately than from knowledge of orbit parameters and time, using the following relation (see Figure 2):

$$\tan\psi = \frac{\rho\cos\varepsilon}{R + \rho\sin\varepsilon} \quad (7)$$

Consider now the orientation of $\bar{i}_{s_1}$, and $\bar{i}_{s_2}$, the unit vectors along lines-of-sight from vehicle to radio stations, in a body coordinate system. If the stations transmit signals to the radio attitude sensor, the direction angles α_1, β_1, α_2, β_2 will be measured (see Figure 3). Thus

$$\bar{i}_{s_1} = \cos\alpha_1 \bar{i}_x + \cos\beta_1 \bar{i}_y + \cos\theta_1 \bar{i}_z \quad (8)$$

$$= l_1 \bar{i}_x + m_1 \bar{i}_y + n_1 \bar{i}_z$$

$$\bar{\iota}_{s_2} = \cos\alpha_2 \bar{\iota}_x + \cos\beta_2 \bar{\iota}_y + \cos\theta_2 \bar{\iota}_z \qquad (9)$$
$$= l_2 \bar{\iota}_x + m_2 \bar{\iota}_y + n_2 \bar{\iota}_z$$

where

$$n_1 = \sqrt{1 - l_1^2 - m_1^2}$$
$$n_2 = \sqrt{1 - l_2^2 - m_2^2}$$

(n_1 and n_2 must be positive because the radio sensor coverage is less than hemispherical). But $\bar{\iota}_E$ can be written

$$\bar{\iota}_E = \cos\phi_E \sin\theta_E \bar{\iota}_x + \sin\theta_E \sin\phi_E \bar{\iota}_y + \cos\theta_E \bar{\iota}_z \qquad (10)$$
$$= \cos\alpha_E \bar{\iota}_x + \cos\beta_E \bar{\iota}_y + \cos\theta_E \bar{\iota}_z$$
$$= l_E \bar{\iota}_x + m_E \bar{\iota}_y + n_E \bar{\iota}_z$$

The angles ϕ_E, θ_E are immediately given if α_E, β_E are determined.

$$\tan\phi_E = \frac{\cos\beta_E}{\cos\alpha_E} = \frac{m_E}{l_E} \qquad (11)$$

$$n_E \triangleq \cos\theta_E = \sqrt{1 - l_E^2 - m_E^2} \qquad (12)$$
$$0 \le \theta_E \le 90^\circ$$

(The positive root for n_E is taken since the radio sensor is along the positive $\bar{\iota}_z$ axis (defined to be coincident with $\bar{\iota}_E$ when $\theta_E = 0$; see reference memorandum for body coordinate system definition). Pitch and roll angles of the $i_x - i_y - i_z$ system with respect to localv vertical system are given by (see reference memo for derivation):

$$\theta_B = \sin^{-1}(-l_E) = \alpha_E - 90^\circ \qquad (13)$$
$$0 \le |\theta_B| \le 90^\circ$$

$$\phi_B = \tan^{-1}\left(\frac{m_E}{n_E}\right) \qquad (14)$$

The problem resolves into finding m_E, l_E.

(The body system and attitude set defined by the order of rotation yaw-pitch-roll is redrawn, from the reference memo, in Figure 4. An alternative set defined by the order pitch-roll-yaw id described in the reference memo; the functional relation between the two sets of angles is given therein and will not be repeated here. Note that determination of l_E, m_E, that is, the orientation of local vertical with respect to

body axes, does not alone suffice to provide information on yaw angle ψ_B constraints afforded by knowledge of $\bar{\iota}_{s_1}, \bar{\iota}_{s_2}$ orientations in the local vertical (orbit) system are required, but more this in the next section).

Now, from knowledge of ψ_1, and ψ_2, it is possible to determine ℓ_E and m_E, albeit with ambiguities, which can, however, be resolved by means of other sensor information. Taking the dot products of equations 8 and 9 with equation 10, we obtain:

$$\bar{\iota}_{s_1} \cdot \bar{\iota}_E \triangleq \cos\psi_1 = \ell_1 \ell_E + m_1 m_E + n_1 n_E \quad (15)$$

$$\bar{\iota}_{s_2} \cdot \bar{\iota}_E \triangleq \cos\psi_2 = \ell_2 \ell_E + m_1 m_E + n_1 n_E \quad (16)$$

But, the orthonormality condition must be met:

$$\ell_E^2 + m_E^2 + n_E^2 = 1 \quad (17)$$

Equations 15, 16, 17 constitute a set in the unknowns ℓ_E, m_E, n_E. Elimination of ℓ_E and n_E yields a quartic equation in m_E of the following form:

$$aX^4 + bX^3 + cX^2 + hX + \ell = 0 \quad (18)$$
$$X \triangleq m_E$$

The coefficients are functions of the measured angles $\alpha_1, \beta_1, \alpha_2, \beta_2$ and the orbit-site specified orientations of lines-of-sight with respect to vertical, ψ_1, ψ_2. The functional relations are set forth in the appendix. After equation 18 is solved, ℓ_E is given by:

$$\ell_E = A - BX \pm C\sqrt{-X^2 + DX + E} \quad (19)$$

The coefficient functions are tabulated in the appendix. n_E is then given, of course, by equation 12.

The physical reason for ambigiuties is seen in Figure 5. At a given instant of time, corresponding to when measurements are made, the body axis tread can be conceived to be capable of being rotated about the $\bar{\iota}_{s_1}$, vector, with $\bar{\iota}_E$ at the half-cone angle θ_1, and α_1, β_1, remaining unchanged. Likewise, there can be a conical rotation about $\bar{\iota}_{s_2}$. The position of $\bar{\iota}_E$ is found at one of two possible intersections of the cones; θ_E has, therefore, one of two possible values. After ambiguities due to squaring processes are eliminated by verification of solutions in the original set, equations 15, 16 17, further ambiguity can be resolved by comparing α_E, β_E with the values directly measured by an earth sensor,

which values are measured with fair precision, as indicated in the reference memo. Note that some false values can also be eliminated by consideration of intersection constraints:

$$|\theta_1 - \theta_E| \leq \psi_1 \leq \theta_1 + \theta_E$$

$$|\theta_2 - \theta_E| \leq \psi_2 \leq \theta_2 + \theta_E$$

It is to be noted that a unique solution to θ_E is obtained if $\bar{\iota}_E$, $\bar{\iota}_{s_1}$, $\bar{\iota}_{s_2}$ are co-planar or if the base circle (figure 5) are tangent; that is, if

$$\nu = \theta_1 + \theta_2, \text{ or } \nu = |\theta_1 - \theta_2|$$

$$\text{or } \nu = \psi_1 + \psi_2, \text{ or } \nu = |\psi_1 - \psi_2|$$

However, the co-planarity situation results in indeterminacy of yaw angle, ψ_B.

III DETERMINATION OF YAW ANGLE

Equations 8, 9 and 10 may be solved for $\bar{\iota}_X$.

$$Q\bar{\iota}_X = \bar{\iota}_{s_1}\left[\cos\beta_2\cos\theta_E - \cos\beta_E\cos\theta_2\right] \tag{20}$$

$$+\bar{\iota}_{s_2}\left[\cos\beta_E\cos\theta_1 - \cos\beta_1\cos\theta_E\right] + \bar{\iota}_E\left[\cos\beta_1\cos\theta_2 - \cos\beta_2\cos\theta_1\right]$$

where

$$Q = \bar{\iota}_E \cdot (\bar{\iota}_{s_1} \times \bar{\iota}_{s_2}) \tag{21}$$

$$= \ell_1(m_2 n_E - m_E n_2) + \ell_2(m_E n_1 - m_1 n_E) + \ell_E(m_1 n_2 - m_2 n_1)$$

In the above, the direction cosines of $\bar{\iota}_{s_1}$ and $\bar{\iota}_{s_2}$ (in the body system) are measured, and the direction cosines of $\bar{\iota}_E$ are presumed computed as indicated in the previous section. Now from the $\hat{V}_1$ matrix relating body axes to local vertical system (see reference memo, equation 3),

$$\tan\psi_B = \frac{\bar{\iota}_X \cdot \bar{\jmath}_V}{\bar{\iota}_X \cdot \bar{\iota}_V} \tag{22}$$

quadrant from signs of numerator & denominator

If the orbit has been determined, the direction cosines of $\bar{\iota}_{s_1}$, and $\bar{\iota}_{s_2}$ are known in the local vertical (orbit) system; that is,

$$\bar{\iota}_{s_1} = \ell_1'\bar{\iota}_V + m_1'\bar{\jmath}_V + n_1'\bar{k}_V \tag{23}$$

$$\bar{\iota}_{s_2} = \ell_2'\bar{\iota}_V + m_2'\bar{\jmath}_V + n_2'\bar{k}_V \tag{24}$$

(Expressions for these direction cosines are given in the reference memo, section IV). Inserting equations 23 and 24 into equation 20 and thence into equation 22, an equation is obtained for yaw angle in terms of measured and orbit determined quantities:

$$\tan \psi_B = \frac{(m_2 m_1' - m_1 m_2') n_E + (n_1 m_2' - n_2 m_1') m_E}{(m_2 l_1' - m_1 l_2') n_E + (n_1 l_2' - n_2 l_1') m_E} \quad (25)$$

This equation is valid only if the determinant D is non-zero. If equation 25 is represented as

$$\tan \psi_B = \frac{P}{Q}$$

then the quadrant of ψ_B if obtained from the signs of P/Q and β/Q.

IV ERROR ANALYSIS

Effects on attitude determination accuracy due to errors in orbit determination and in site corrdinates will be neglected because:

1) These effects will presumably be small compared to attitude sensor measurement error effects and
2) The primary purpose of the present analysis is to provide a comparison of the relative accuracy of various techniques of utilizing vehicle on-board measurements with ground-based computation to obtain attitude information; orbit determination error effects should be of similar magnitude for all of the techniques studied.

Assume that the measurement errors are independent random variables with zero means and equal variances (noise power), that is

$$\sigma(\Delta\alpha_1) = \sigma(\Delta\beta_1) = \sigma(\Delta\alpha_2) = \sigma(\Delta\beta_2) = \sigma(\Delta\alpha)$$

Then the attitude error variances are given by

$$\sigma^2(\Delta\theta_B) = \frac{1}{\cos^2\theta_B} \hat{l}_\alpha \hat{l}_\alpha^T \sigma^2(\Delta\alpha) \quad (26)$$

$$\sigma^2(\Delta\phi_B) = \hat{\phi}_{B_\alpha} \hat{\phi}_{B_\alpha}^T \sigma^2(\Delta\alpha) \quad (27)$$

$$\sigma^2(\Delta\psi_B) = \hat{\psi}_{B_\alpha} \hat{\psi}_{B_\alpha}^T \sigma^2(\Delta\alpha) \quad (28)$$

In the above

$$\hat{l}_\alpha = \left[\frac{\partial l_E}{\partial \alpha_1} \quad \frac{\partial l_E}{\partial \beta_1} \quad \frac{\partial l_E}{\partial \alpha_2} \quad \frac{\partial l_E}{\partial \beta_2} \right]$$

$$\widehat{\Phi}_{B\alpha} = \begin{bmatrix} \frac{\partial \phi_B}{\partial m_E} & \frac{\partial \phi_B}{\partial l_E} \end{bmatrix} \begin{bmatrix} \frac{\partial m_E}{\partial \alpha_1} & \frac{\partial m_E}{\partial \beta_1} & \frac{\partial m_E}{\partial \alpha_2} & \frac{\partial m_E}{\partial \beta_2} \\ \frac{\partial l_E}{\partial \alpha_1} & \frac{\partial l_E}{\partial \beta_1} & \frac{\partial l_E}{\partial \alpha_2} & \frac{\partial l_E}{\partial \beta_2} \end{bmatrix}$$

$$\widehat{\Psi}_{B\alpha} = \begin{bmatrix} \frac{\partial \psi_B}{\partial p} & \frac{\partial \psi_B}{\partial \varrho} \end{bmatrix} \begin{bmatrix} \frac{\partial p}{\partial \alpha_1} & \frac{\partial p}{\partial \beta_1} & \frac{\partial p}{\partial \alpha_2} & \frac{\partial p}{\partial \beta_2} \\ \frac{\partial \varrho}{\partial \alpha_1} & \frac{\partial \varrho}{\partial \beta_1} & \frac{\partial \varrho}{\partial \alpha_2} & \frac{\partial \varrho}{\partial \beta_2} \end{bmatrix}$$

Expressions for the elements of these matrices are tabulated in the appendix. Note that $l_1', m_1', n_1', = g_1$, $l_2', m_2', n_2', = g_2$ are considered errorless.

Conversion from the errors in attitude angles with respect to the X - Y - Z system to errors in attitude angles with respect to the X_1-Y_1-Z_1 system are readily found as follows:

$$\sigma^2(\Delta\Theta_P) = \widehat{\Theta}_{P-\alpha}\,\widehat{\Theta}_{P-\alpha}^T\,\sigma^2(\Delta\alpha) \qquad (29)$$

$$\sigma^2(\Delta\Theta_R) = \widehat{\Theta}_{R-\alpha}\,\widehat{\Theta}_{R-\alpha}^T\,\sigma^2(\Delta\alpha) \qquad (30)$$

$$\sigma^2(\Delta\Theta_Y) = \widehat{\Theta}_{Y-\alpha}\,\widehat{\Theta}_{Y-\alpha}^T\,\sigma^2(\Delta\alpha) \qquad (31)$$

where

$$\widehat{\Theta}_{P-\alpha} = \begin{bmatrix} \frac{\partial \Theta_P}{\partial \psi_B} & \frac{\partial \Theta_P}{\partial \Theta_B} & \frac{\partial \Theta_P}{\partial \phi_B} \end{bmatrix} \widehat{\Theta}_{B-\alpha}$$

$$\widehat{\Theta}_{R-\alpha} = \begin{bmatrix} \frac{\partial \Theta_R}{\partial \psi_B} & \frac{\partial \Theta_R}{\partial \Theta_B} & \frac{\partial \Theta_R}{\partial \phi_B} \end{bmatrix}$$

$$\widehat{\Theta}_{Y-\alpha} = \begin{bmatrix} \frac{\partial \Theta_Y}{\partial \psi_B} & \frac{\partial \Theta_Y}{\partial \Theta_B} & \frac{\partial \Theta_Y}{\partial \phi_B} \end{bmatrix}$$

$$\widehat{\Theta}_{B-\alpha} = \begin{bmatrix} \frac{\partial \psi_B}{\partial \alpha_1} & \frac{\partial \psi_B}{\partial \beta_1} & \frac{\partial \psi_B}{\partial \alpha_2} & \frac{\partial \psi_B}{\partial \beta_2} \\ \frac{\partial \Theta_B}{\partial \alpha_1} & \frac{\partial \Theta_B}{\partial \beta_1} & \frac{\partial \Theta_B}{\partial \alpha_2} & \frac{\partial \Theta_B}{\partial \beta_2} \\ \frac{\partial \phi_B}{\partial \alpha_1} & \frac{\partial \phi_B}{\partial \beta_1} & \frac{\partial \phi_B}{\partial \alpha_2} & \frac{\partial \phi_B}{\partial \beta_2} \end{bmatrix} = \begin{bmatrix} \widehat{\Psi}_{IB-\alpha} \\ \frac{1}{\cos^2\Theta_B}\widehat{l}_\alpha \\ \widehat{\Phi}_{B-\alpha} \end{bmatrix}$$

Formulae for the partials $\frac{\partial \Theta_P}{\partial \psi_B}$, etc. are listed in the reference memo. The foregoing indicates the great amount of computation required for evaluation of the accuracy of field data.

For present purposes in view of the small excursion expected in attitude angles ($\psi_B = \pm 20^\circ$, $\theta_B = \pm 10^\circ$, $\phi_B = \pm 10^\circ$) and because of results obtained for the error analysis of the system discussed in the reference memo, it suffices to simulate and evaluate accuracy for the condition of zero attitude angles.

For this special case, the following is obtained:

$$(n_1 n_2)^2 (m_1 l_2 - m_2 l_1)^2 \frac{\sigma^2(\Delta\theta_B)}{\sigma^2(\Delta\alpha)} = (m_2 n_2)^2 \left[(m_1 \sin\beta_1)^2 + (l_1 \sin\alpha_1)^2\right] + (m_1 n_1)^2 \left[(m_2 \sin\beta_2)^2 + (l_2 \sin\alpha_2)^2\right] \quad (32)$$

$$(n_1 n_2)^2 (m_1 l_2 - m_2 l_1)^2 \frac{\sigma^2(\Delta\phi_B)}{\sigma^2(\Delta\alpha)} = (l_2 n_2)^2 \left[(m_1 \sin\beta_1)^2 + (l_1 \sin\alpha_1)^2\right] + (l_1 n_1)^2 \left[(m_2 \sin\beta_2)^2 + (l_2 \sin\alpha_2)^2\right] \quad (33)$$

$$(n_1 n_2)^2 (m_1 l_2 - m_2 l_1)^2 \frac{\sigma^2(\Delta\psi_B)}{\sigma^2(\Delta\alpha)} = (m_1^2 l_2 n_2 - m_2^2 l_1 n_1)^2 \left[(n_2 \sin\beta_1)^2 + (n_1 \sin\beta_2)^2\right] + (l_1 l_2)^2 (n_1 n_2 - m_2 n_1)^2 \left[(n_2 \sin\alpha_1)^2 + (n_1 \sin\alpha_2)^2\right] \quad (34)$$

For zero attitude angles, $l_E = m_E = 0, n_E = 1$. Then from equation 21,

$$\Omega = l_1 m_2 - m_1 l_2$$

for $\psi_B = \theta_B = \phi_B = 0$. Evidently, if $\Omega = 0$, the errors will be extremely large. It behooves us to determine under what situation the $\Omega = 0$ condition will be met. The sites to be considered are:

Rosman: 36.133°N latitude, 82.833°W longitude
Mojave: 35.333°N latitude, 116.90°W longitude

Taking the more westardly site as S_1 (satellite in direct orbit comes into view of this station first), we have

$$\delta_1 = 35.33^\circ \qquad L_1 = -116.9^\circ$$

$$\delta_2 = 36.133^\circ \qquad L_2 = -82.833^\circ$$

$$L_2 - L_1 = 34.07^\circ$$

Consider the synchronous equatorial orbit first (see Figure 6). We cannot have $m_1 = m_2 = 0$ since the sites are not on the equator. We cannot have $\ell_1 = \ell_2 = 0$ since this implies coincidence of $\bar{\iota}_{s_1}$ and $\bar{\iota}_{s_2}$. We cannot have $\ell_1 = m_1 = 0$ or $\ell_2 = m_2 = 0$ since these would imply θ_1 or θ_2 equal to zero which cannot be. Finally, in order for $\bar{\iota}_2$ to lie in the $\bar{\iota}_{s_1}$-$\bar{\iota}_{s_2}$ plane, making $\bar{\iota}_2 \cdot (\bar{\iota}_{s_1} \times \bar{\iota}_{s_2}) = 0$, we must have:

$$\sin\delta_2 \cos\delta_1 \sin(L_p - L_1) = \sin\delta_1 \cos\delta_2 \sin(L_p - L_1)$$

Solving for $L_p - L_1$, weobtain $(L - L) = -70.6°$. It will be shown in the next section that this value is outside the limit for simultaneous visibility from both stations. For the synchronous orbit, therefore, there are no discontinuities in the error evaluations. It is clear however, that errors increase as the two lines of sight approach collinearity, that is, as approaches zero, where

$$\cos\psi = \bar{\iota}_{s_1} \cdot \bar{\iota}_{s_2} = \ell_1\ell_2 + m_1 m_2 + n_1 n_2$$

As will be shown, ψ decreases at the horizon visibility limits, so that errors would be expected to be large near these limits.

Now for an inclined orbit, either ℓ_1 or ℓ_2 can be zero, but they cannot be zero simultaneously. (ℓ_1 is zero when $\psi_1 = \theta_1$ goes through a minimum; θ_1 and θ_2 cannot be minimal at the same time). Neither m_1 or m_2 can be zero if the inclination of the orbit is less than site latitude. From equation 27 of the reference memo, m_1 can be zero only if

$$\cos\delta_1 \sin i_p \sin(\lambda_1 - \Omega_p) = \sin\delta_1 \cos i_p$$

$$\text{or} \quad \sin(\lambda_1 - \Omega_p) = \frac{\tan\delta_1}{\tan i_p}$$

For $\delta_1 > i_p$ the condition cannot be met. Finally, examining the condition $\ell_1 m_2 = m_1 \ell_2$, using equations 26 and 27 of the reference memo, we obtain the value of the angular position of the satellite measured from ascending node, for which the condition is met:

$$\tan u_{p_{CRIT.}} = \frac{\sin\delta_1 \cos\delta_2 \sin(\lambda_2 - \Omega_p) - \sin\delta_2 \cos\delta_1 \sin(\lambda_1 - \Omega_p)}{\cos\delta_1 \cos\delta_2 \sin i_p \sin(\lambda_2 - \lambda_1)}$$

$$+ \cos i_p \left[\sin\delta_1 \cos\delta_2 \cos(\lambda_2 - \Omega_p) - \sin\delta_2 \cos\delta_1 \cos(\lambda_1 - \Omega_p)\right] \quad (35)$$

where $\lambda_2 - \lambda_1 = L_2 - L_1 = 34.07°$

$$(\lambda_2 - \Omega_p) = (\lambda_1 - \Omega_p) + 34.07°$$

The critical value of u_p (note double value) as function of $\lambda_1 - \Omega_p$ and for $i_p = 28$, is shown, Figure 7. As shown in the next section, however, this value falls outside of the limits of simultaneous visibility from the radio stations, for most values of $\lambda_1 - \Omega_p$. Where $u_{p_{CRIT.}}$ does fall within visibility bounds, attitude computation cannot be performed.

V. VISIBILITY LIMITS

For visibility of the satellite from the radio stations, the

elevation of both lines-of-sight must be positive simultaneously; i.e., lines-of-sight must both be above the horizons at the stations. This is equivalent to the conditions

$$0 \leq \gamma_1 \leq \cos^{-1}\left(\frac{\rho_1}{r_p}\right) < 90^\circ$$

$$0 \leq \gamma_2 \leq \cos^{-1}\left(\frac{\rho_2}{r_p}\right) < 90^\circ$$

simultaneously met. In addition, the stations must both be within the field of view of the on-board radio sensor, whence the simultaneous conditions

$$0 \leq \theta_1 \leq 25^\circ$$

$$0 \leq \theta_2 \leq 25^\circ$$

must be met. For zero attitude angles, $\psi_1 = \theta_1$, $\psi_2 = \theta_2$. The maximum possible value of ψ_1 (or of ψ_2) is

$$\psi_1]_{MAX} = \sin^{-1}\left(\frac{\rho}{r_p}\right)$$

For the synchronous equatorial orbit, $\psi_{1\,MAX} = 8.68^\circ$. For the 28° inclined orbit, 6,000 n.m. altitude, $\psi_{1\,MAX} = 21.3^\circ$. Hence our concern need be only with the station (simultaneous) visibility limits.

The situation may be represented as in Figure 8. Simultaneous visibility starts when λ_{s_2} just comes in; it ends when λ_{s_1} just goes out. For the equatorial orbit,

$$\cos\gamma_1 = \cos\delta_1 \cos(L_p - L_1) \qquad (36)$$

Setting in $\gamma_1]_{LIM} = 81.32^\circ$ for the synchronous orbit, with $\delta_1 = 35.33$, gives the limits on $(L_p - L_1)$ for one sight line only:

$$-79.3^\circ \leq L_p - L_1 \leq 79.3^\circ$$

But the satellite will not be in view of the more easterly station unless

$$(L_p - L_1)_L = -79.3 + (L_2 - L_1) = -45.2^\circ$$

Simultaneous visibility then extends only for

$$-45.2^\circ \leq (L_p - L_1) \leq 79.3^\circ$$

or $$-79.3^\circ \leq (L_p - L_2) \leq 45.2^\circ$$

The corresponding permissible values of μ_p are given by

$$\mu_p = (L_p - L_1) + \lambda_1$$

Figure 9 gives a graphical representation of the concepts.

For the inclined orbit, repeating equation 22 of the reference memo,

$$\cos\gamma_1 = \cos\delta_1 \cos(\lambda_1 - \Omega_p)\cos\mu_p + \sin\mu_p\left[\cos\delta_1\cos i_p \sin(\lambda_1 - \Omega_p) + \sin\delta_1 \sin i_p\right] \quad (37)$$

Setting $\gamma_1]_{min} = 68.7^\circ$, upper and lower limits for μ_p as function of $(\lambda_1 - \Omega_p)$ can be obtained. Since $\delta_2 \approx \delta_1$ the μ_p limits as function of $(\lambda_2 - \Omega_p)$ are simply given by the values, from equation 37, at

$$(\lambda_2 - \Omega_p) = (\lambda_1 - \Omega_p) + (L_2 - L_1)$$

Superposition of the two sets of curves, yields the region of simultaneous visibility, Figure 10. Note the constricted range of μ_p, occurring at $\lambda_1 - \Omega_p = 270^\circ$, of only 37°.

VI. QUANTITATIVE ACCURACY ASSESSMENT

Figure 11 shows the elevation angles ε_1, ε_2 as well as the angle between lines of sight, γ, for the synchronous equatorial orbit. Evidnetly, maximum γ occurs for the satellite position about midway between the station meridians, or for $L_p - L_1 \approx 18^\circ$. 3 σ errors were computed for $\sigma(\Delta) = \frac{1}{3}^\circ$, with results shown in Figure 12. It is seen that errors are minimum when γ is maximum; that is, for $L_p = 99^\circ$ west. (Note that this is in contrast to the earth sensor-radio sensor system accuracy, where errors are minimal at the limit of visibility; that is, near the horizon). The yaw error is still excessive, even at minimum.

Figures 13, 14, 15 show attitude determination accuracy for the inclined orbit, $i_p = 28^\circ$, 6,000 n.m. altitude, and for zero attitude angles. Evidently very large errors can prevail, some time in orbit, for the inclined orbit case.

Let the system described be denoted system D; let the earth sensor radio sensor system be denoted as system A. If attitude information is available from both systems, the results from one or the other of the systems can be selected on the basis of system accuracy. The choice of system, for the synchronous orbit, depends on the satellite longitude L_p ; this choice is shown graphically, Figure 16. On this basis, given the choise of either system, pitch and roll errors will not exceed 3 degrees for any L_p (within view of either one or both radio stations): however, the yaw error does not go below 17 degrees. Figures 17 through 23 show accuracy, for the inclined orbit, when that system is chosen which provides the smaller error; dashed lines indicate imposed viewing limitations. Peak and minimum yaw errors are shown, Figure 24,

for the inclined orbit, when system selectivity is exercised. The spread is from 2 to 16½ degrees. Note that λ_1 is the instantaneous right ascension of Mojave when transmitting for the satellite; or if only Rosman is in view of the satellite, then Rosman's instantaneous right ascension is $\lambda_1 + 34.07$ degrees.

Given that both systems A and D are available for attitude determination, then this determination may be made over a considerable portion of the inclined orbit. For r_p = 9440 n.m. we have as orbital rate

$$\omega_o = \sqrt{\frac{\mu_E}{r_p^3}} = .0164 \text{ RADIANS/MIN.}$$

and the orbital period is

$$\frac{2\pi}{\omega_o} = 384 \text{ MINUTES}$$

Earth's rate is W_E = .00437 radians/minute. Thus

$$\frac{\dot{\mu}_p}{\dot{\lambda}_1} = \frac{\omega_o}{\omega_E} = 3.74$$

$$\tan^{-1} 3.74 = 75^\circ$$

Starting at any point on the lowest curve in Figure 10 (where $\dot{\lambda}_s$ comes in), a straight line inclined 75 degrees to the abscissa may be drawn; intersection ofthis line with the various curves yield values of λ_1 at which the successive events occur. Dividing the change in λ_1 by W_E gives the time transpired between events. The result is shown Figure 25. On the average, attitude determination can be obtained over 60% of the orbit, from the time when Mojave first sights the satellite.

VII. WEIGHTING TECHNIQUES

When both systems A and D produce attitude determination results, it may appear desirable to average these results, in an effort to reduce the noise error. It will be assumed that all measurement error sources produce purely random errors only. Let the weighting coefficients be denoted f_A and f_D and let the restriction be imposed that

$$f_A + f_D = 1$$

In particular, we wish to reduce the yaw error. Let the computed yaw angle from the systems be denoted ψ_A and ψ_D respectively. The average, or estimate of true value, is

$$\bar{\psi} = f_A \psi_A + f_D \psi_D \tag{38}$$

and the variance in this estimate is

$$\sigma^2(\Delta\bar{\Psi}) = f_A^2\,\sigma^2(\Delta\Psi)_A + f_D\,\sigma^2(\Delta\Psi)_D + 2 f_A f_D E(\Delta\Psi_A \cdot \Delta\Psi_D) \qquad (39)$$

where E is expectation operator. Note that the covariance is not zero since system D uses a radio line-of-sight.

Three weighting techniques willbe considered, in order of increasing complexity. Let $\sigma(\Delta\Psi)_A = k\sigma(\Delta\Psi)_D$. If $\sigma(\Delta\Psi)_A > \sigma(\Delta\Psi)_D$ then $k > 1$. A choice exists whether to accept Ψ_D alone, or whether to average with Ψ_A. The latter choice is only worthwhile if $\sigma(\Delta\bar{\Psi})$ is significantly less than $\sigma(\Delta\Psi)_D$. Suppose straight arithmetic averaging, that is, $f_A = f_D = \frac{1}{2}$. From equation 39, then,

$$\frac{\sigma(\Delta\bar{\Psi})}{\sigma(\Delta\Psi)_D} = \frac{1}{2}\sqrt{k^2 + 2\rho k + 1} \qquad (40)$$

where the correlation coefficient ρ is defined by

$$\rho = \frac{E(\Delta\Psi_A \cdot \Delta\Psi_D)}{\sigma(\Delta\Psi)_A \cdot \sigma(\Delta\Psi)_D} \qquad (41)$$

Note, in particular, that equation 40 yields the familiar result

$$\sigma(\Delta\bar{\Psi}) = \frac{1}{\sqrt{2}}\,\sigma(\Delta\Psi)_D$$

if $\rho = 0$ and $k = 1$, that is, a 30% reduction in error. Figure 26 gives a plot of equation 40. It is evident that only for $k = 1$ is the straight averaging technique acceptable over all possible ρ. (Note that for $k < 1$, a choice exists between $\bar{\Psi}$ and Ψ_A only, since $\sigma(\Delta\Psi)_A$ is then less than $\sigma(\Delta\Psi)_D$).

To obtain an optimum weighting function we must minimize equation 39, subject to the normality constraint on the weighting coefficients. Suppose ρ were zero. We would then wish to minimize

$$f_A^2\,\sigma^2(\Delta\Psi)_A + f_B^2\,\sigma^2(\Delta\Psi)_D - 2\lambda\left[f_A + f_D\right]$$

where λ is an undetermined parameter. Differentiating this function with respect to f_A and f_D respectively and setting equal to zero, and using the constraint condition the following results are obtained:

$$f_A = \frac{1}{k^2+1}, \qquad f_D = \frac{k^2}{k^2+1}$$

Evidently, use of this technique requires that $\sigma(\Delta\Psi)_A$ and $\sigma(\Delta\Psi)_D$ be evaluated in order to obtain k. If $\rho = 0$,

$$\frac{\sigma(\Delta\Psi)}{\sigma(\Delta\Psi)_D} = \frac{k}{\sqrt{k^2+1}}$$

which is the minimum error for all k. If however, ρ is not zero, then

$$\frac{\sigma(\Delta\Psi)}{\sigma(\Delta\Psi)_D} = \frac{k}{(k^2+1)}\sqrt{k^2+2\rho k+1} \qquad (42)$$

Equation 42 is shown plotted, Figure 27. Only if ρ is zero or negative, is this technique suitable over all values of k.

Finally, considering that ρ will not likely be zero, we minimize

$$f_A^2\sigma^2(\Delta\Psi)_A + f_D\sigma^2(\Delta\Psi)_D + 2f_A f_D \rho\sigma(\Delta\Psi)_A\sigma(\Delta\Psi)_D - 2\lambda\left[f_A+f_D\right]$$

This yields

$$f_A = \frac{1-\rho k}{(k^2-2\rho k+1)} \; ; \qquad f_D = \frac{k(k-\rho)}{(k^2-2\rho k+1)}$$

$$\frac{\sigma(\Delta\Psi)}{\sigma(\Delta\Psi)_D} = \frac{k\sqrt{1-\rho^2}}{\sqrt{k^2-2\rho k+1}} \qquad (43)$$

Equation 43 is shown plotted, Figure 28. Note that the error ratio is less than 1 for all k and for all ρ ; in particular, full correlation produces zero error.

The computation of ρ is generally quite complex. As a simplified case, if $\Psi_B = \Theta_B = \Phi_B = 0$ and if $\sigma^2(\Delta\alpha_i) = \sigma^2(\Delta\beta_i) = \sigma^2(\Delta\alpha)$, the covariance (for system A connoting station and Earth sensor viewing) can be shown to be given by the following:

$$n_1(m_1\ell_2 - m_2\ell_1)^2(1-n_1)^2\frac{E(\Delta\Psi_A\cdot\Delta\Psi_D)}{\sigma^2(\Delta\alpha)}$$

$$= \ell_2\ell_1 m_1\left[m_1 n_2(m_1^2-\ell_1^2) - m_2 n_1(1-\ell_1^2)\right] \qquad (44)$$

$$+ m_2^2 n_1\ell_1^2(1-n_1^2)$$

VIII ERRORS DUE TO NON-SIMULTANEITY OF RADIO SIGNALS

In Figure 29, for illustrative purposes, consider a circular, equatorial orbit. At time t_1, when station 2 is at S_2, the direction cosines of $\bar{\iota}_{S_1}$, in the body system, are measured. At a time $t_2 = t_1 + \Delta t$, when the satellite has moved from P_1 to P_2, and station 2 has moved from S_2 to S_2', the direction cosines of $\bar{\iota}'_{S_2}$ are measured. The later measurements are used in computing the attitude of the satellite at time t_1, that is when the orientation of $\bar{\iota}_{S_1}$ only was measured. Evidently errors are committed due to earth's rotation, satellite vertical rotation, and body system rotation, during Δt.

Let unprimed quantities represent conditions at time t, primed quantities refer to conditions at time t_2'. Subscript 1 or 2 refers to measurements, with respect to body system, of $\bar{\iota}_{S_1}$ or $\bar{\iota}_{S_2}$ respectively; subscript V refers to measurements with respect to satellite local vertical system. Thus,

$$\bar{\iota}_{S_2} = l_2 \bar{\iota}_X + m_2 \bar{\iota}_Y + n_2 \bar{\iota}_Z = l_{2V} \bar{\iota}_V + m_{2V} \bar{\jmath}_V + n_{2V} \bar{k}_V \tag{45}$$

$$\bar{\iota}'_{S_2} = l_2' \bar{\iota}_X' + m_2' \bar{\iota}_Y' + n_2' \bar{\iota}_Z' = l_{2V}' \bar{\iota}_V' + m_{2V}' \bar{\jmath}_V' + n_{2V}' \bar{k}_V' \tag{46}$$

Let

$$l_2' = l_2 + \Delta l_2 \; ; \; m_2' = m_2 + \Delta m_2 \; ; \; n_2' = n_2 + \Delta n_2$$

The errors committed are due to using l_2' instead of the (unmeasured and unknown) l_2, m_2' instead of m_2, n_2' instead of n_2. We wish to find $\Delta l_2, \Delta m_2, \Delta n_2$.

Now

$$\left.\frac{d\bar{\iota}_{S_2}}{dt}\right|_I = \left.\frac{d\bar{\iota}_{S_2}}{dt}\right|_V + \bar{\omega}_{(I)_V} \times \bar{\iota}_{S_2} = \left.\frac{d\bar{\iota}_{S_2}}{dt}\right|_B + \left[\bar{\omega}_{(V)_B} + \bar{\omega}_{(I)_V}\right] \times \bar{\iota}_{S_2} \tag{47}$$

whence

$$\left.\frac{d\bar{\iota}_S}{dt}\right|_B = \left.\frac{d\bar{\iota}_{S_2}}{dt}\right|_V - \bar{\omega}_{(V)_B} \times \bar{\iota}_{S_2} \tag{48}$$

in equation 48,

$$\left.\frac{d\bar{r}_{s_2}}{dt}\right|_B = \dot{l}_2\,\bar{i}_X + \dot{m}_2\,\bar{i}_Y + \dot{n}_2\,\bar{i}_Z \qquad (49)$$

$$\left.\frac{d\bar{r}_{s_2}}{dt}\right|_V = \dot{l}_{2_V}\,\bar{i}_V + \dot{m}_{2V}\,\bar{j}_V + \dot{n}_{2_V}\,\bar{k}_V \qquad (50)$$

It can be shown that (subscript B on attitude angles, indicating order of rotation of Euler angles adhered to throughout this memo, is implied):

$$\begin{aligned}\omega_{(V)_B} = {} & \left[\dot{\phi}\cos\theta\cos\psi - \dot{\theta}\sin\psi\right]\bar{i}_V \\ & + \left[\dot{\phi}\cos\theta\sin\psi + \dot{\theta}\cos\psi\right]\bar{j}_V \\ & + \left[\dot{\psi} - \dot{\phi}\sin\theta\right]\bar{k}_V\end{aligned} \qquad (51)$$

Substitution of equations 51 and 45 into equation 48, using transformation matrix $\overline{V_i}$ (see reference memo), and assuming small attitude angles and rates, the coefficients in equation 49 are obtained:

$$\dot{l}_2 \approx \left[\dot{l}_{2_V} + \dot{m}_{2V}\psi - \dot{n}_{2V}\theta\right] + \left[m_{2V}\dot{\psi} - n_{2_V}\dot{\theta}\right] \qquad (52)$$

$$\dot{m}_2 \approx \left[-\dot{l}_{2_V}\psi + \dot{m}_{2_V} + \dot{n}_{2V}\phi\right] + \left[n_{2V}\dot{\phi} - l_{2_V}\dot{\psi}\right] \qquad (53)$$

$$\dot{n}_2 \approx \left[\dot{l}_{2V}\psi - \dot{m}_{2_V}\phi + \dot{n}_{2V}\right] + \left[l_{2_V}\dot{\theta} - m_{2V}\dot{\phi}\right] \qquad (54)$$

From these,

$$\Delta l_2 = (\Delta l)_V + (\Delta l)_B \approx \dot{l}_{2_V}\Delta t + \left[m_{2V}\dot{\psi} - n_{2_V}\dot{\theta}\right]\Delta t \qquad (55)$$

$$\Delta m_2 = (\Delta m)_V + (\Delta m)_B \approx \dot{m}_{2_V}\Delta t + \left[n_{2V}\dot{\phi} - l_{2_V}\dot{\psi}\right]\Delta t \qquad (56)$$

$$\Delta n_2 = (\Delta n)_V + (\Delta n)_B \approx \dot{n}_{2_V}\Delta t + \left[l_{2_V}\dot{\theta} - m_{2V}\dot{\phi}\right]\Delta t \qquad (57)$$

Since the desired l_2 is $l_2' - \Delta l_2$, we can compensate for earth rotation and satellite angular orbit rate by subtracting $(\Delta l)_V$ from the measured l_2'. This can be done because l_{2_V}, m_{2V}, n_{2_V} and their rates

are computable as functions of time. These rates may be obtained by computer differentiation, or from the explicity equations listed in the appendix. If $\frac{e_2}{R_2}$ is sufficiently small, we may use

$$(\Delta \ell)_V \approx \dot{\ell}_{2V} \Delta t$$

Otherwise, it is necessary to use

$$(\Delta \ell)_V \approx \left[\dot{\ell}_{2V} + \dot{m}_{2V}\psi - \dot{n}_{2V}\theta\right] \Delta t$$

where ψ and θ are the approximately computed values before compensation. Similar remarks pertain to $(\Delta m)_V$, $(\Delta n)_V$. Note that no such compensation is required for the synchronous orbit, since ℓ_{s_2} does not rotate then with respect to local (satellite) vertical systems.

The residual error in ℓ_2, after compensation, is

$$\ell_2' - (\Delta \ell)_V - \ell_2 = (\Delta \ell)_B$$

whence

$$\sin \alpha_2 (\Delta \alpha_2)_B = \left[n_{2V}\dot{\theta} - m_{2V}\dot{\psi}\right] \Delta t \quad (58)$$

Likewise,

$$\sin \beta_2 (\Delta \beta_2)_B = \left[\ell_{2V}\dot{\psi} - n_{2V}\dot{\phi}\right] \Delta t \quad (59)$$

For $\psi = \theta = \phi = 0$, the following expressions hold:

$$\frac{\partial \theta}{\partial \alpha_2} = \frac{m_1 \ell_2 \sin \alpha_2}{n_2 (m_1 \ell_2 - m_2 \ell_1)} \quad (60)$$

$$\frac{\partial \theta}{\partial \beta_2} = \frac{m_1 m_2 \sin \beta_2}{n_2 (m_1 \ell_2 - m_2 \ell_1)} \quad (61)$$

$$\frac{\partial \phi}{\partial \alpha_2} = \frac{\ell_1 \ell_2 \sin \alpha_2}{n_2 (m_1 \ell_2 - m_2 \ell_1)} \quad (62)$$

$$\frac{\partial \phi}{\partial \beta_2} = \frac{\ell_1 m_2 \sin \beta_2}{n_2 (m_1 \ell_2 - m_2 \ell_1)} \quad (63)$$

$$\frac{\partial \psi}{\partial \alpha_2} = \frac{\ell_1 \ell_2 (n_2 m_1 - n_1 m_2) \sin \alpha_2}{n_2 (m_1 \ell_2 - m_2 \ell_1)^2} \quad (64)$$

$$\frac{\partial \psi}{\partial \beta_2} = \frac{(m_1^2 l_2 m_2 - m_2^2 l_1 m_1)\sin\beta_2}{m_2 (m_1 l_2 - m_2 l_1)^2} \qquad (65)$$

Since we are evaluating errors anywhere in orbit, the attitude rates will be taken as random variables, having the same distributions and equal variances, that is, $\sigma(\dot{\psi}) = \sigma(\dot{\theta}) = \sigma(\dot{\phi})$. Then utilizing equations 58 through 65, we obtain (for zero attitude angles only):

$$\sigma^2(\Delta\theta)_B = Var.\left[\frac{\partial\theta}{\partial\alpha_2}(\Delta\alpha_2)_B + \frac{\partial\theta}{\partial\beta_2}(\Delta\beta_2)_B\right] \qquad (66)$$
$$= \frac{m_1^2(l_2^2 + m_2^2)}{(m_1 l_2 - m_2 l_1)^2}\sigma^2(\dot{\theta})(\Delta t)^2$$

$$\sigma^2(\Delta\phi)_B = Var.\left[\frac{\partial\phi}{\partial\alpha_2}(\Delta\alpha_2)_B + \frac{\partial\phi}{\partial\beta_2}(\Delta\beta_2)_B\right] \qquad (67)$$
$$= \frac{l_1^2(l_2^2 + m_2^2)}{(m_1 l_2 - m_2 l_1)^2}\sigma^2(\dot{\phi})(\Delta t)^2$$

$$\sigma^2(\Delta\psi)_B = Var.\ \frac{\partial\psi}{\partial\alpha_2}(\Delta\alpha_2)_B + \frac{\partial\psi}{\partial\beta_2}(\Delta\beta_2)_B$$
$$= \sigma^2(\dot{\psi})_B(\Delta t)^2\left[\frac{(m_1^2 l_2 m_2 - m_2^2 l_1 m_1) + l_1^2 l_2^2 (m_1 m_2 - m_2 m_1)^2 + \cdots}{(m_1 l_2 - m_2 l_1)^4}\right] \quad (6$$

Denote

$$\xi_\theta = \frac{\sigma^2(\Delta\theta)_B}{\sigma^2(\dot{\theta})\cdot(\Delta t)^2} \div \frac{\sigma^2(\Delta\theta_B)}{\sigma^2(\Delta\alpha)}$$

where the dividend is given by equation 66, the divisor by equation 32. Like definitions hold for ξ_ϕ, ξ_ψ (see appendix for explicit formulation). The radio of std. dev. of error, due to time difference, to the std. dev. of error, due to measurement errors, is

$$\eta_\theta = \frac{\sigma(\Delta\theta)_B}{\sigma(\Delta\theta_B)} = \sqrt{\xi_\theta}\left[\frac{\sigma(\dot{\theta})\cdot\Delta t}{\sigma(\Delta\alpha)}\right]$$

The std. dev. of total error is then

$$\sigma(\Delta\theta)_T = \left[\sigma^2(\Delta\theta)_B + \sigma^2(\Delta\theta_B)\right]^{1/2} = \sqrt{\eta_\theta^2 + 1}$$

whence the fractional argmentation due to time difference in measurements, is

Similar definitions apply for $\Delta\phi$, $\Delta\psi$.

It will be assumed that, over any orbit, it is equally probable for each of the attitude rates to have any value between maximum expected limits; that is, uniform (rectangular) distributions are assumed. Taking the maximum value as .03 degrees/sec., Δt=9 secs, and $\sigma(\Delta\alpha)=\frac{\epsilon}{3}$ we have

$$\sigma(\dot{\theta}) = \frac{\dot{\theta}_{UM}}{\sqrt{3}} = .0173^{\circ}/\text{sec.}$$

$$\frac{\sigma(\dot{\theta})\cdot\Delta t}{\sigma(\Delta\alpha)} = .468, \quad \eta_{\theta} = .468\sqrt{\xi_{\theta}}$$

Figure 30 shows percent error augmentation, for the synchronous orbit only, and for zero attitude angles. Evidently, for Δ t=9 secs the effect of measurement time difference is less than 8% of the std. deviation under condition of measurement simultaneity. Figure 31 shows the effect of increasing Δ t on maximum percentage augmentation. If the maximum $3\sigma(\Delta\theta_B)$ is 3 degrees, based on system selection, for any $(L_p - L_1)$ (see Figure 16), and the inaccuracy of this estimate is not to exceed ½ degree, then Δt cannot be permitted to exceed 14 secs.

10 X 10 TO THE ½ INCH 359-11G
KEUFFEL & ESSER CO

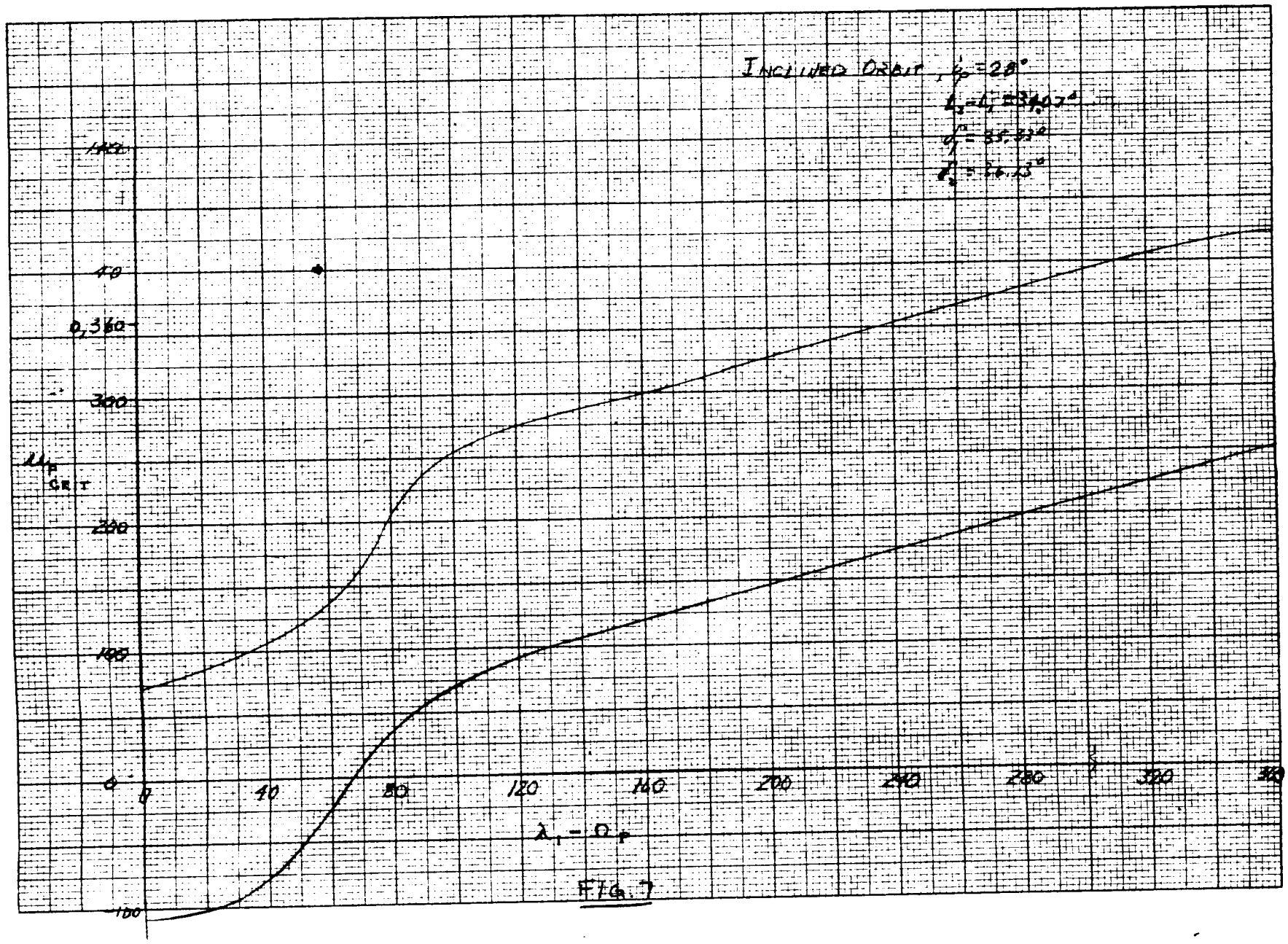


Fig. 7

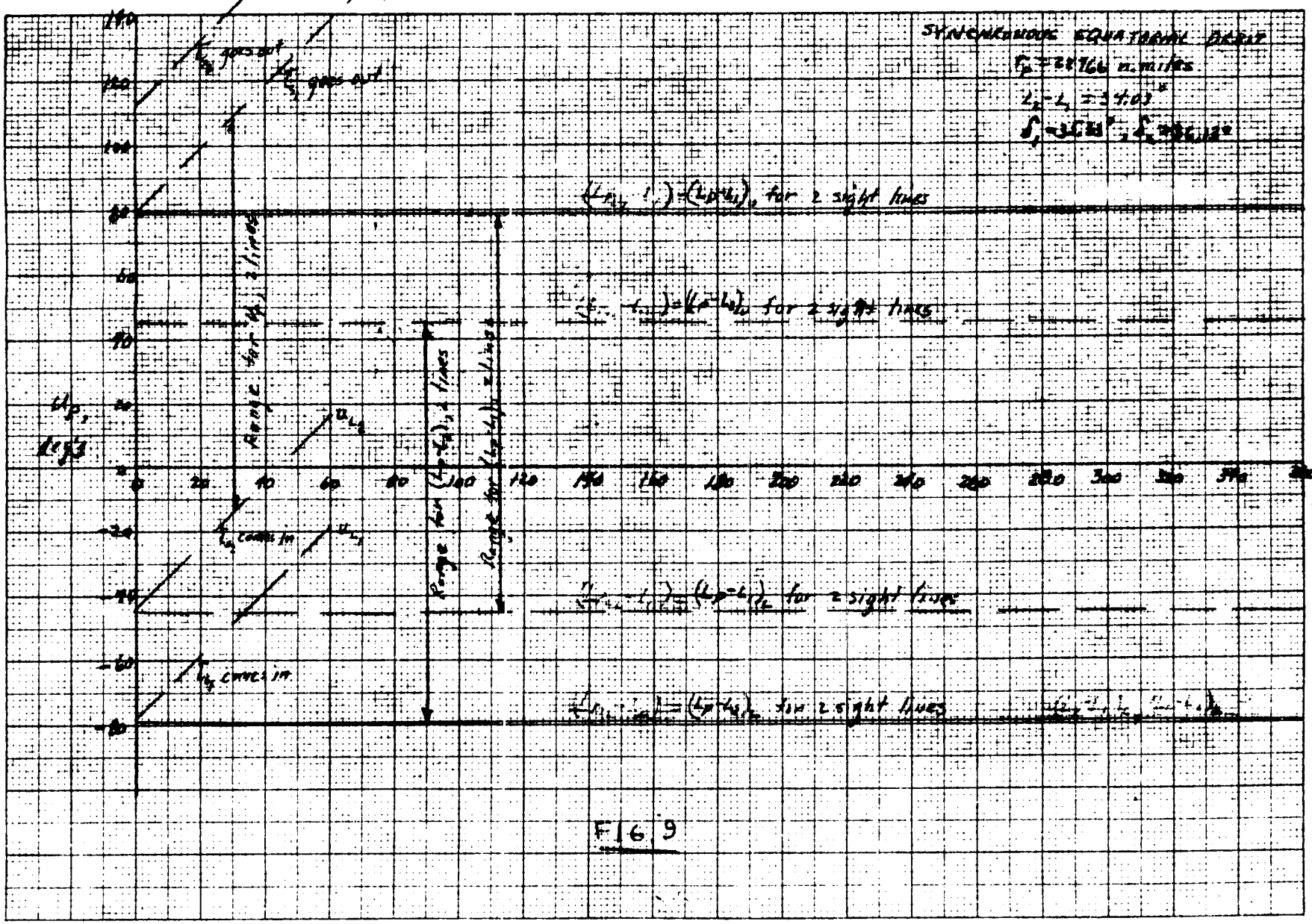

SYNCHRONOUS EQUATORIAL ORBIT
r_0 = 22,766 n. miles
$\lambda_2 - \lambda_1$ = 3°.03
δ_1 = -35.3°, δ_2 = +35.3°
$(L_{R_{12}})_1 = (L_R - L_{t_1})_1$ for 2 sight lines
$(L_{R_{12}})_2 = (L_R - L_{t_2})_2$ for 2 sight lines
$(L_{R_{12}})_{1,2} = (L_R - L_{t_1})_{1,2}$ for 2 sight lines
$(L_{R_{12}})_{1,2} = (L_R - L_{t_2})_{1,2}$ for 2 sight lines
$L_{R_{12}}$ degs
λ_1 degs
ω_{L_2}
ω_1
ω_{L_1}
L_{t_2} goes out
L_{t_1} goes out
Range for $(L_R - L_{t_1})_2$ 2 times
Range for $(L_R - L_{t_2})_1$ 2 times
L_{t_2} comes in
L_{t_1} comes in

FIG 9

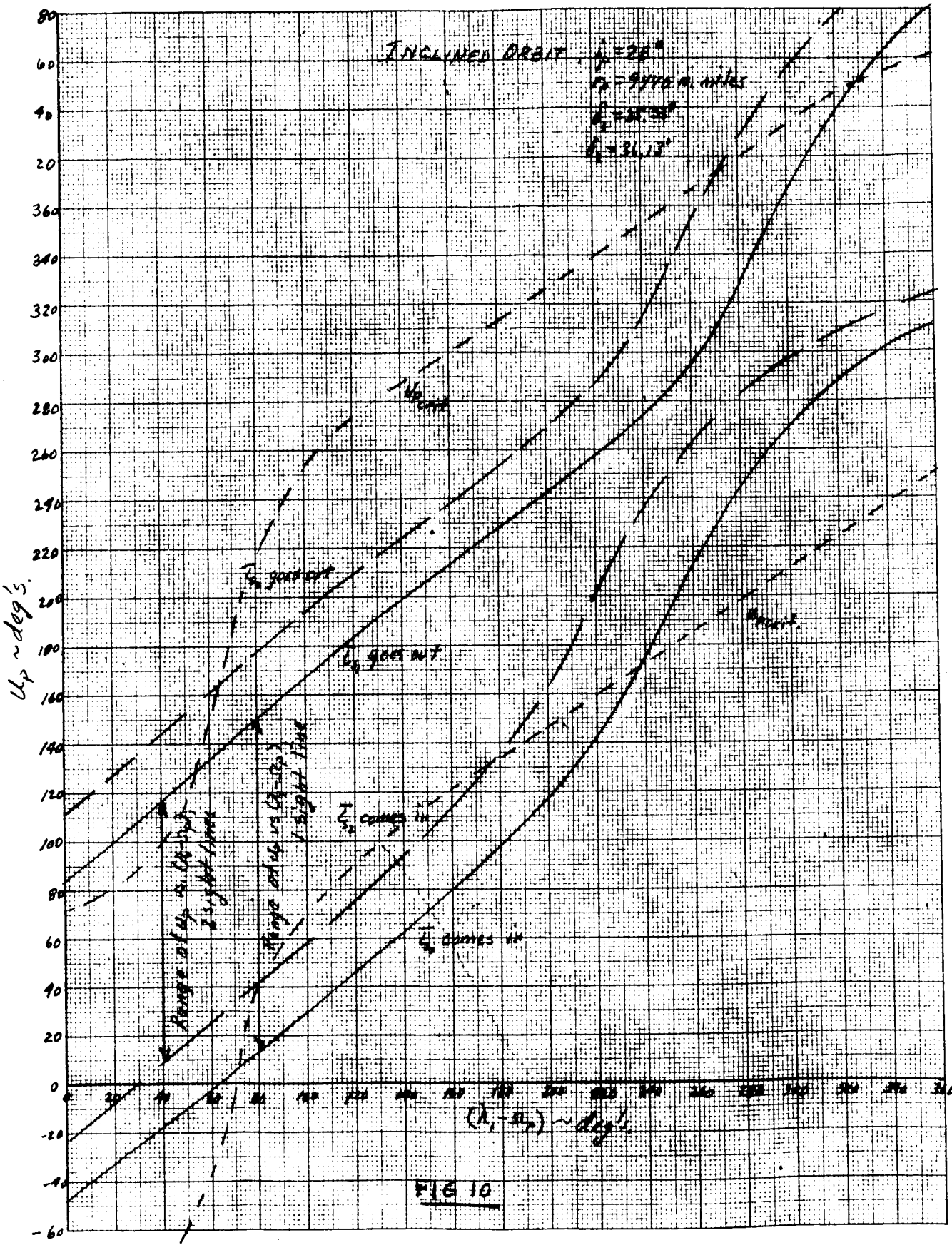
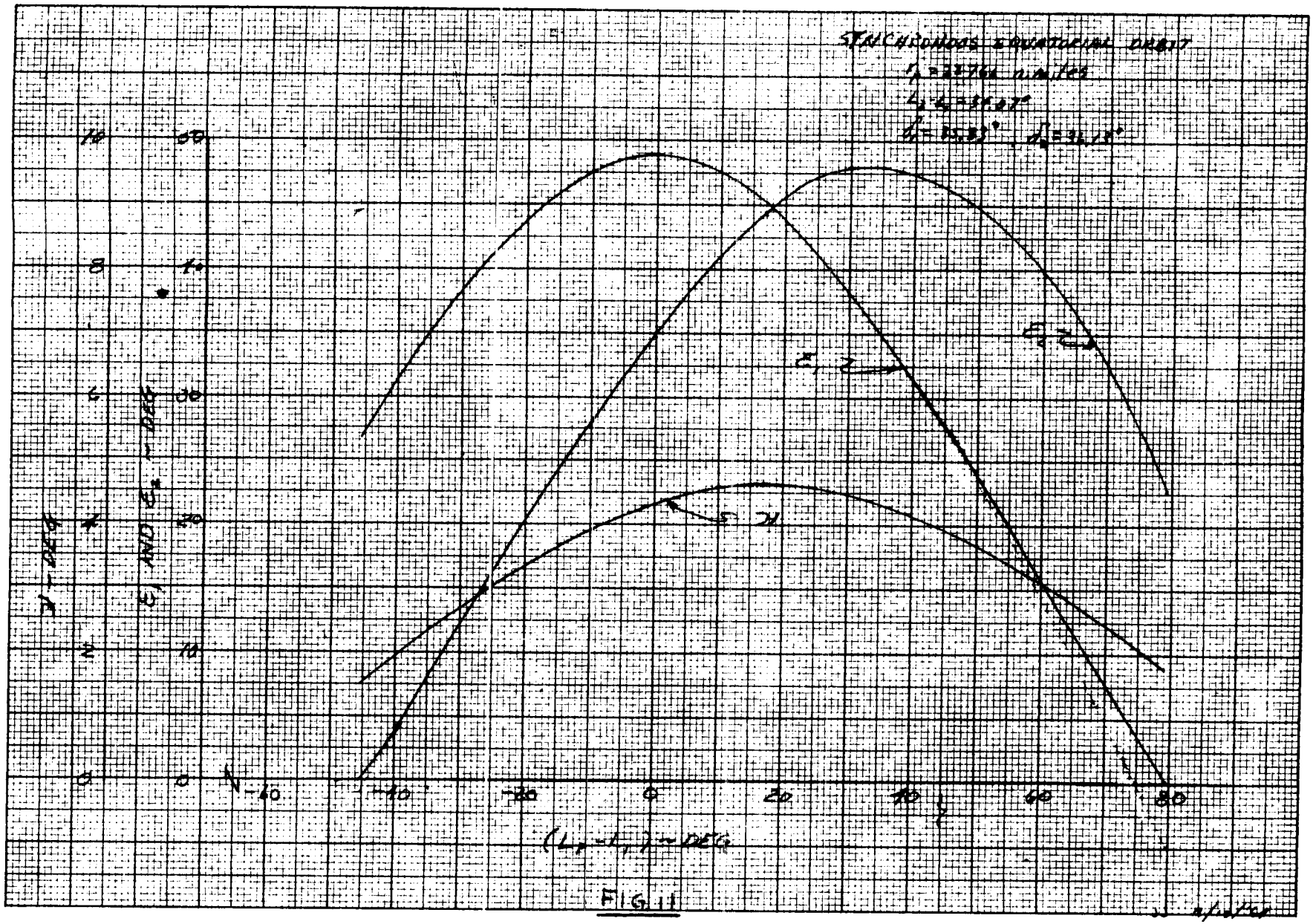


FIG 10

10 X 10 TO THE CM. 359-14
KEUFFEL & ESSER CO.

K&E 10 X 10 TO THE ½ INCH 359-11G
KEUFFEL & ESSER CO. MADE IN U.S.A.



K&E 10 X 10 TO THE ½ INCH 359-11G
KEUFFEL & ESSER CO.

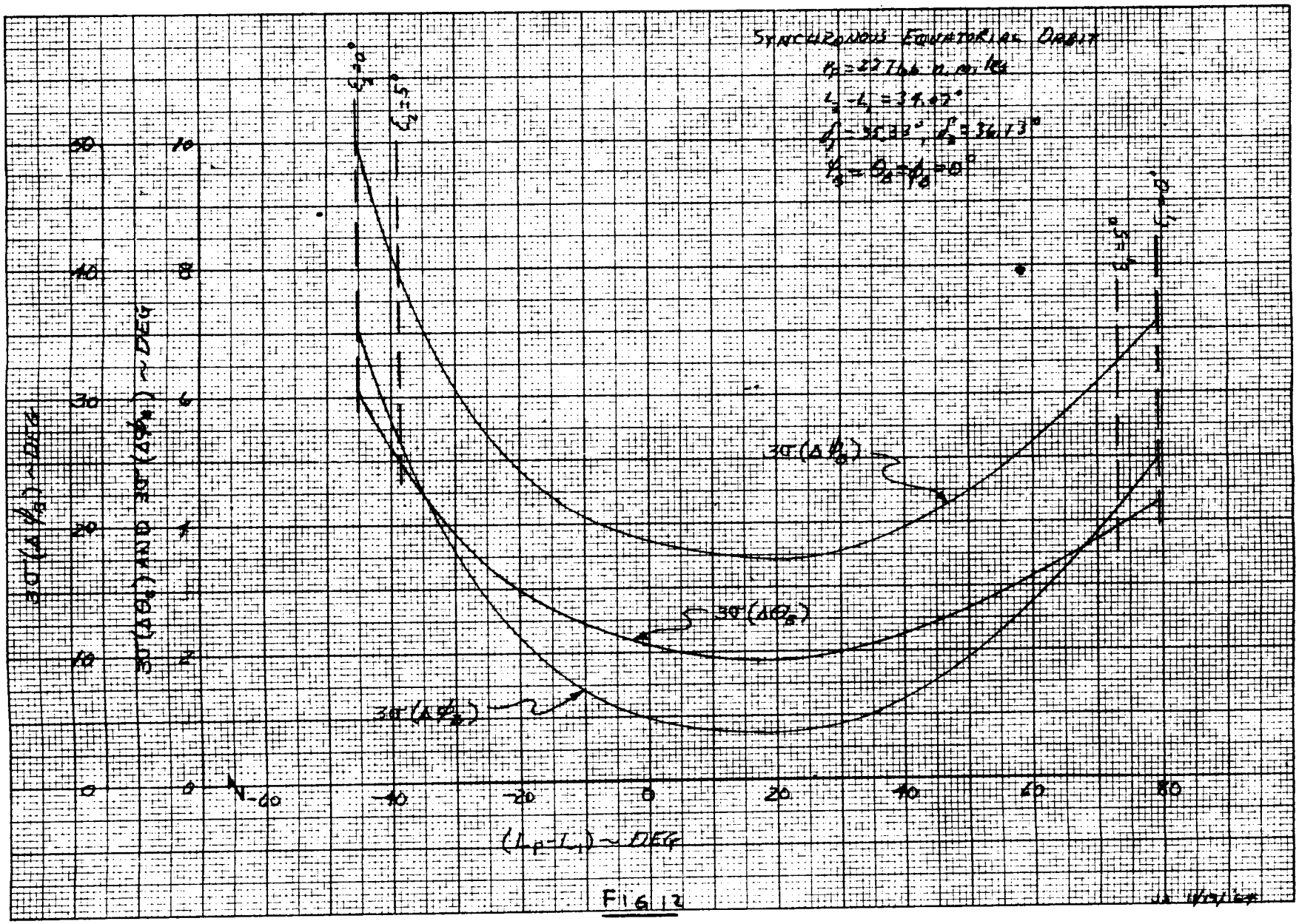


FIG 12

K&E 10 X 10 TO THE ½ INCH KEUFFEL & ESSER CO. 359-11G MADE IN U. S. A.

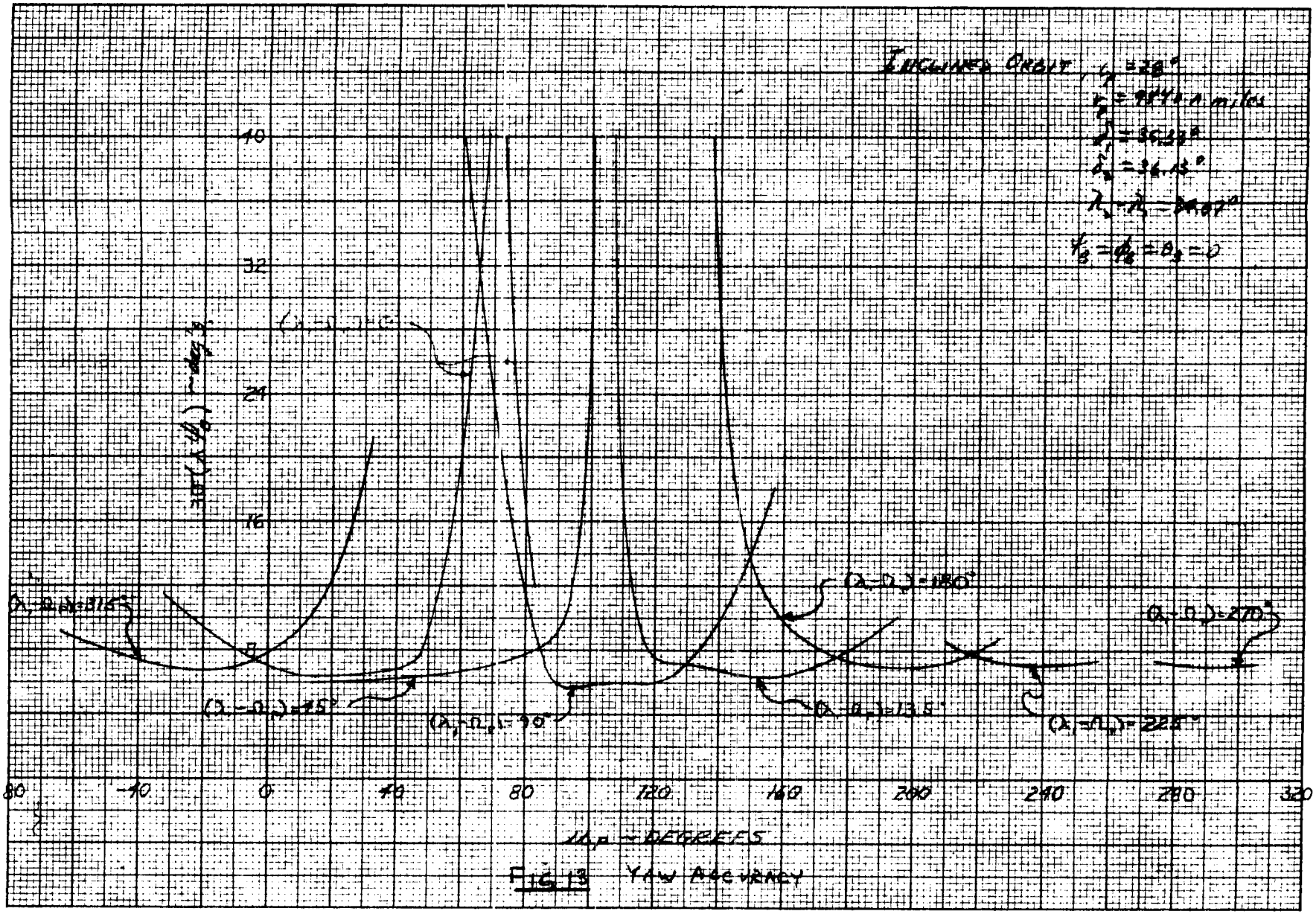


FIG. 13 YAW ACCURACY

K&E 10 X 10 TO THE ½ INCH 359-11G
KEUFFEL & ESSER CO. MADE IN U.S.A.

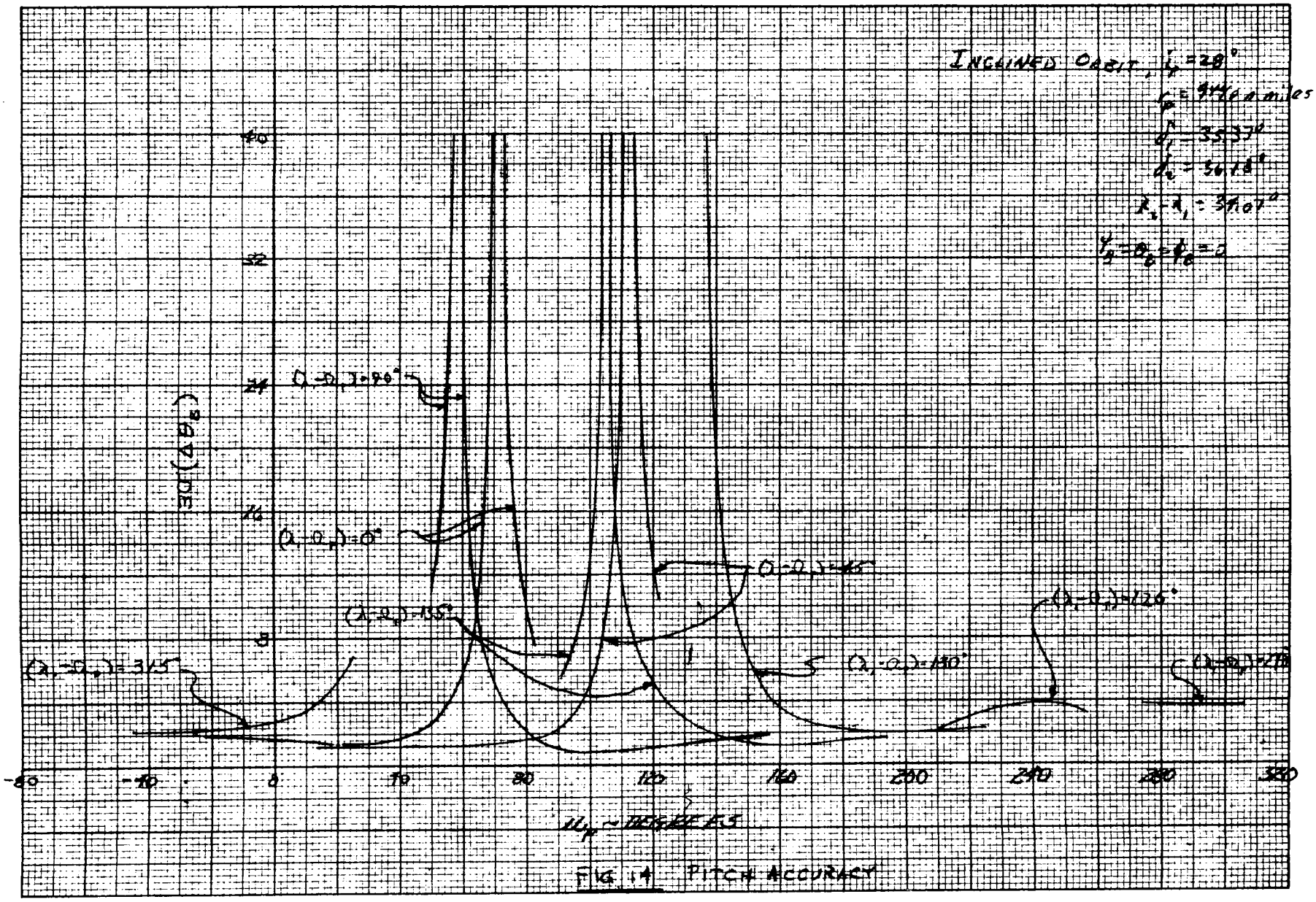


FIG. 14 PITCH ACCURACY

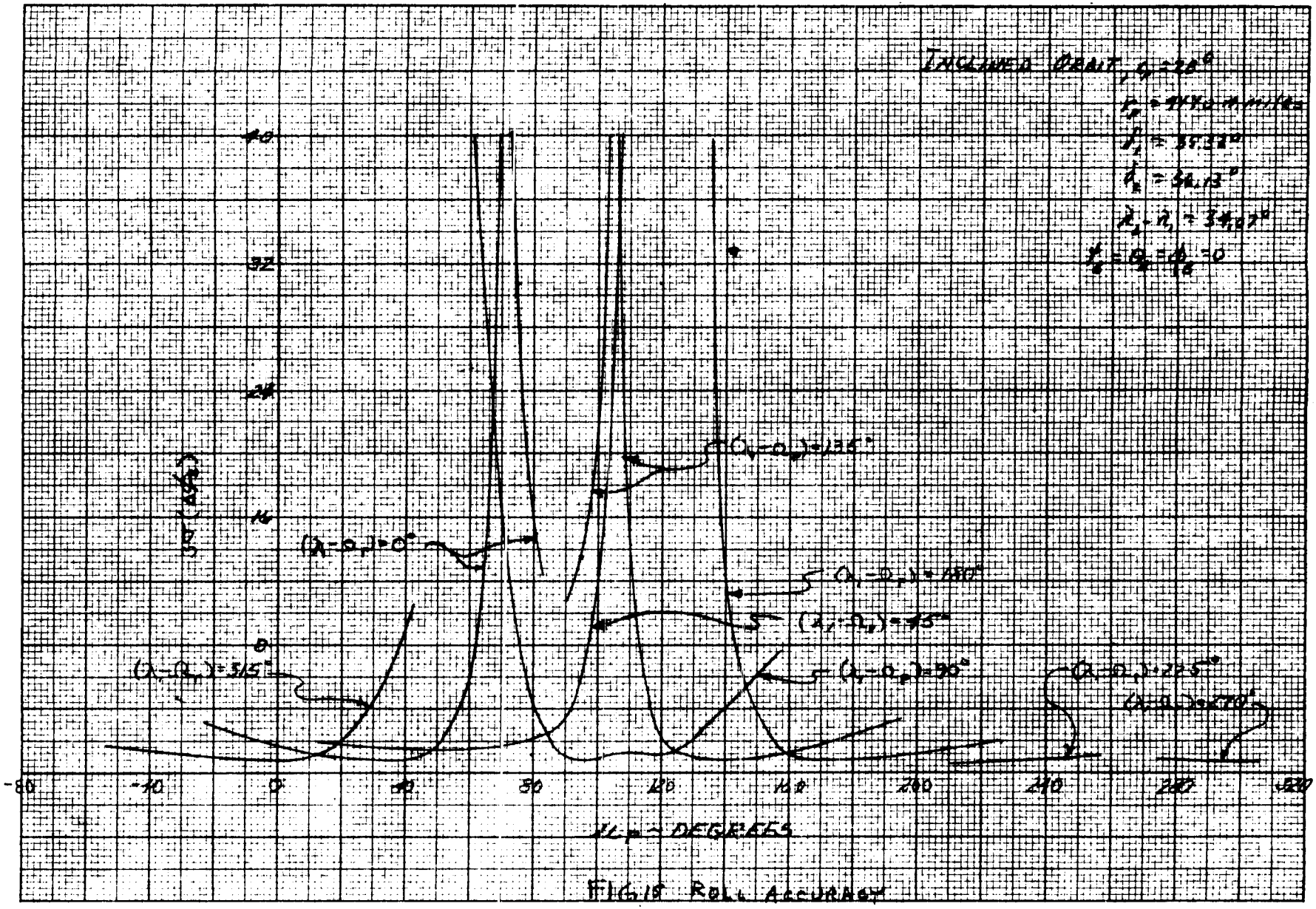
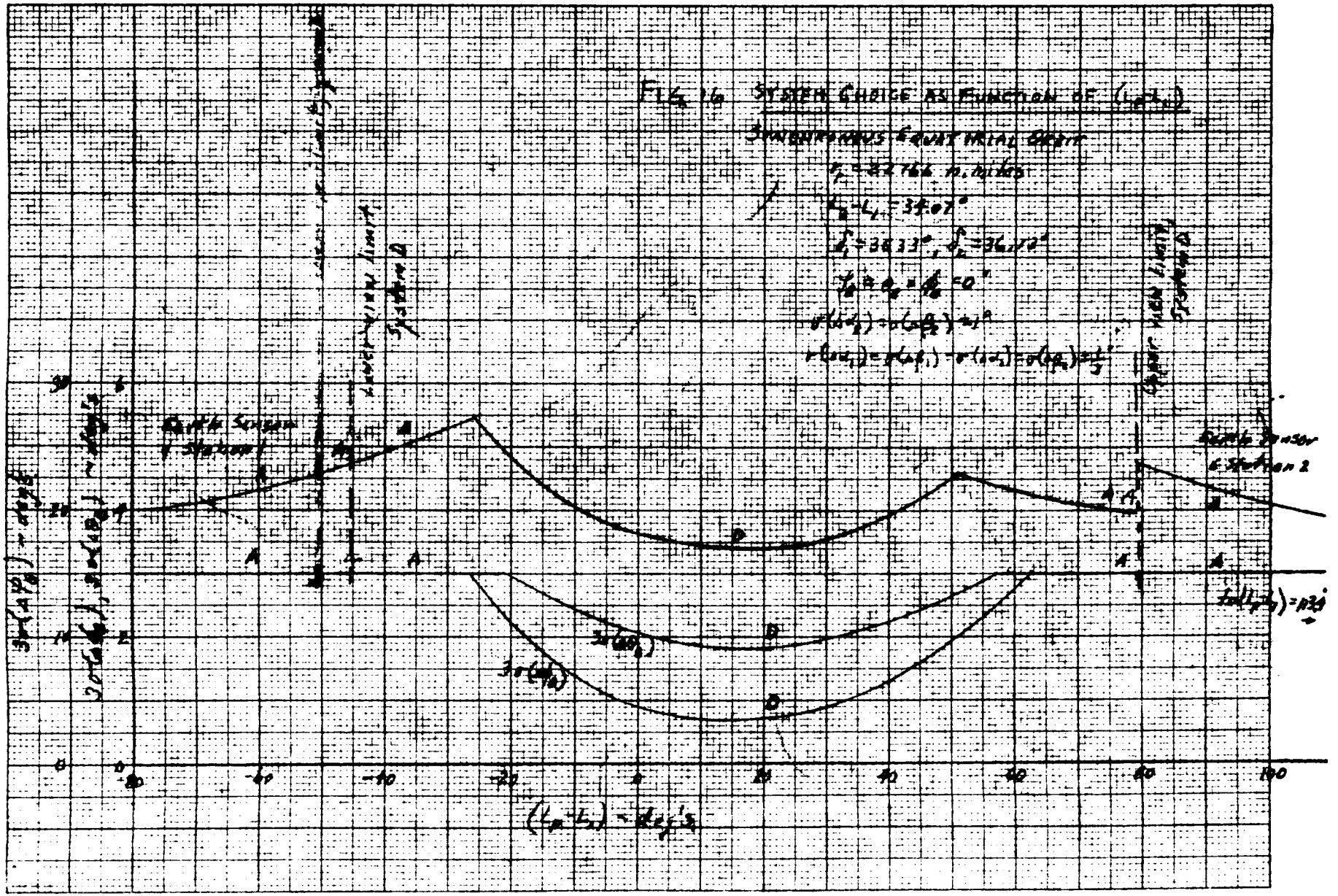
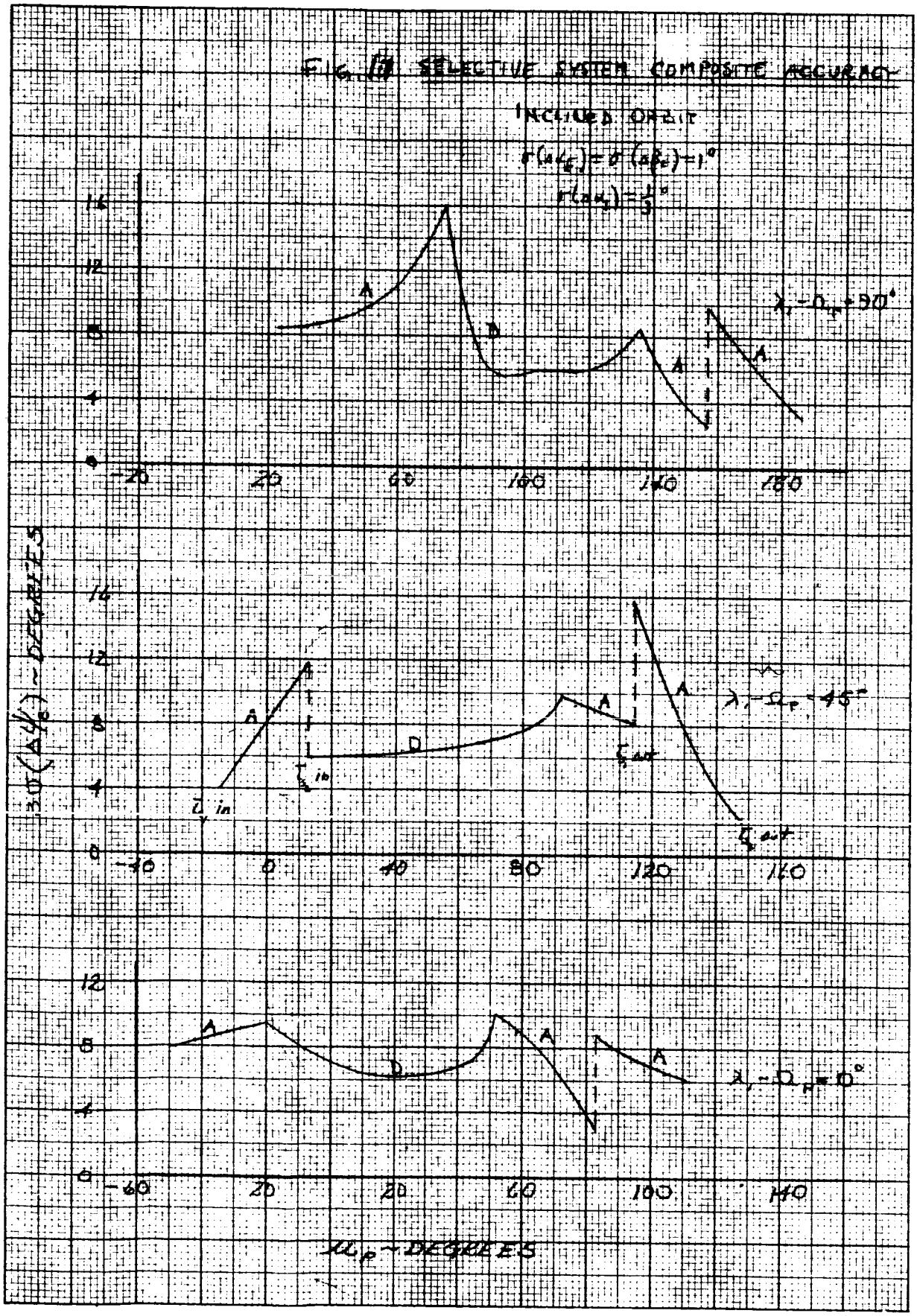


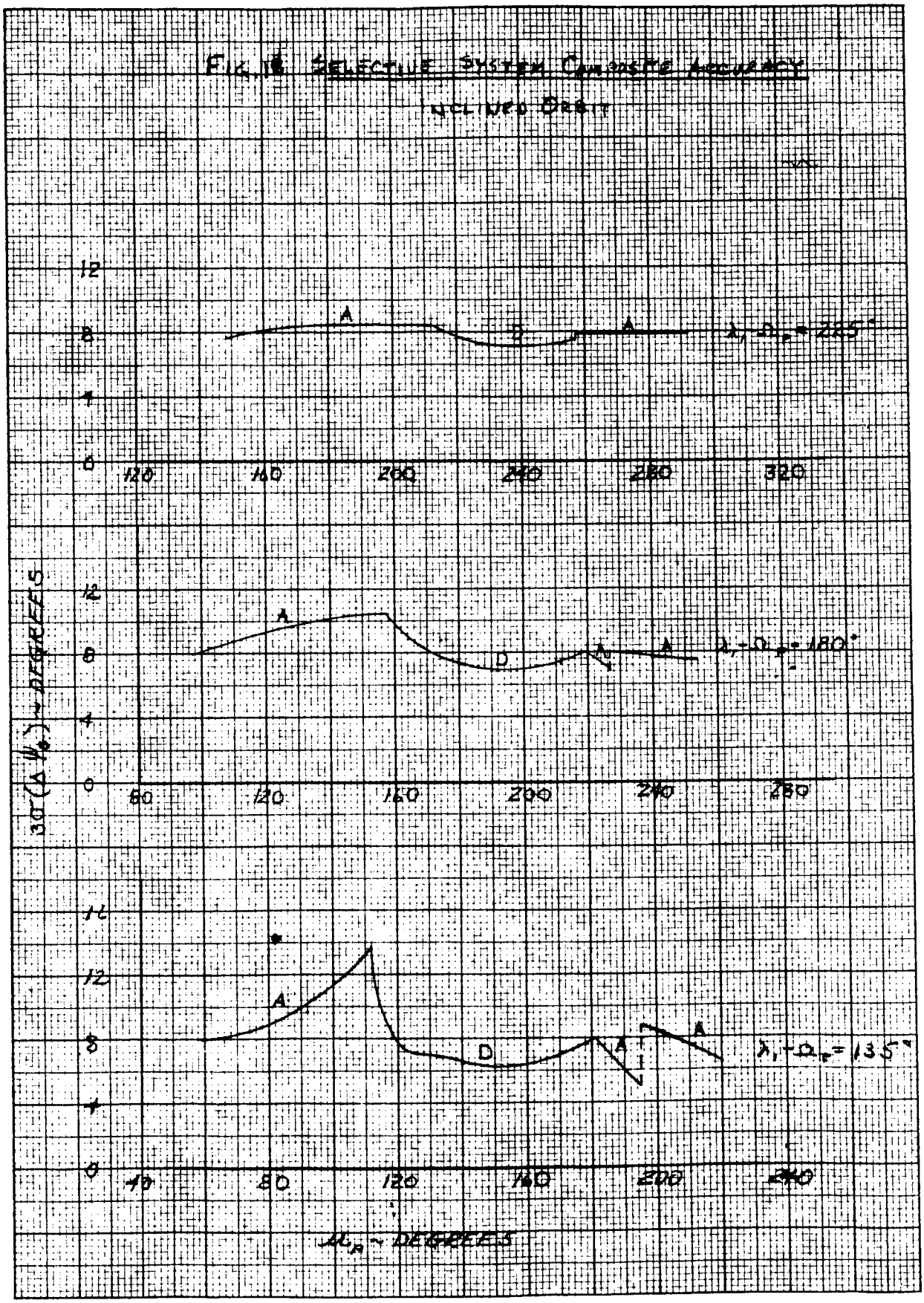
FIG. 18 ROLL ACCURACY

10 X 10 TO THE ½ INCH 359-11

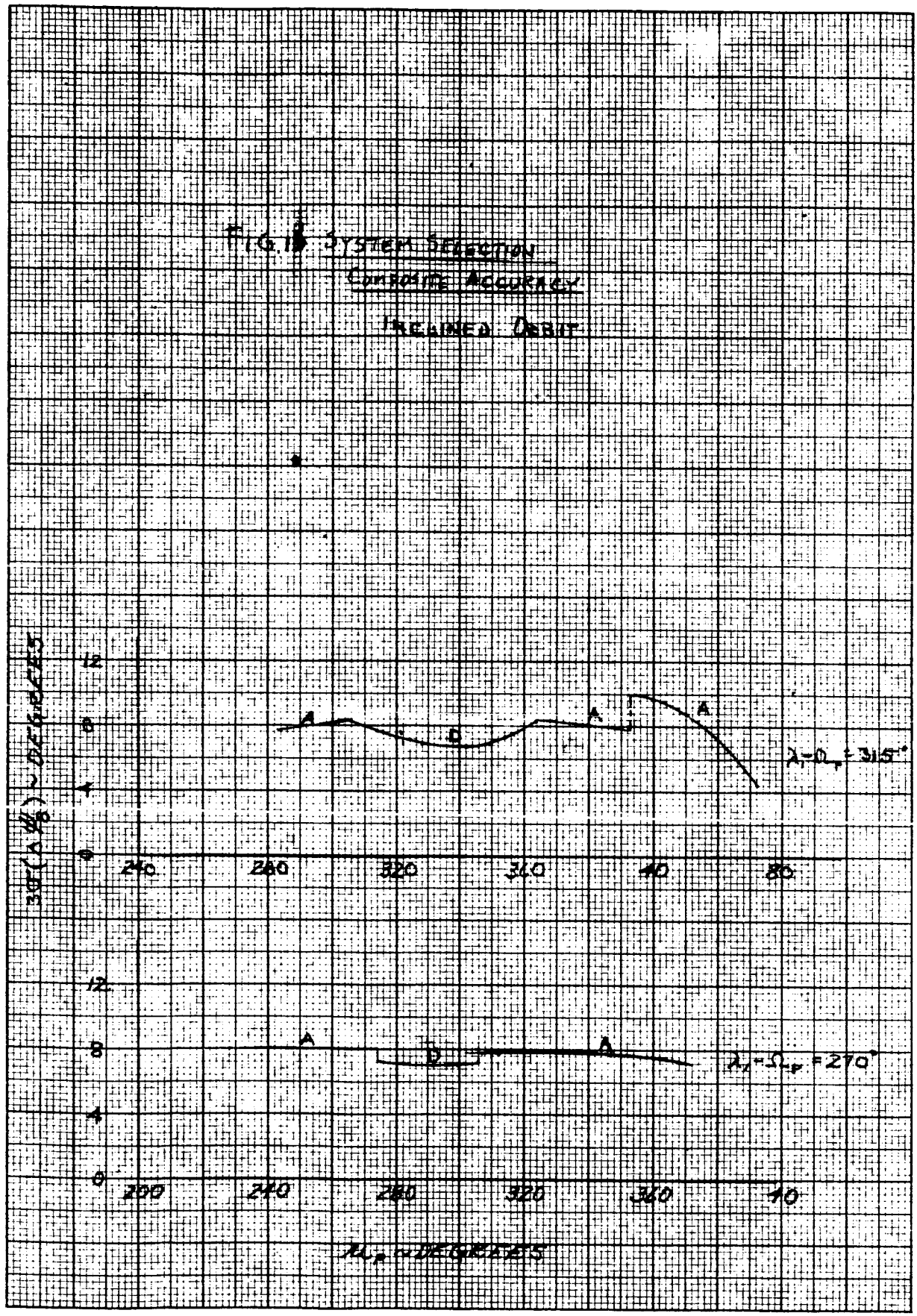

FIG. 16
SYSTEM CHOICE AS FUNCTION OF $(L_p - L_s)$
SYNCHRONOUS EQUATORIAL ORBIT
$r_s = 42,164$ n. miles
$L_p - L_s = 34.67°$
$\delta_s = 36.33°$, $\delta_p = 36.33°$
$i_s = \Omega_s = \Omega_p = 0°$
$\sigma(\omega_s, \omega_p) = \sigma(\omega_s, \beta_s) = \sigma(\omega_p, \beta_p) = 0°$
$\sigma(\omega_s, \omega_p) = \sigma(\omega_s, \beta_s) = \sigma(\omega_p, \beta_p) = 180°$
$\sigma(\omega_s, \omega_p) = \sigma(\omega_s, \beta_s) = \sigma(\omega_p, \beta_p) = 90°$
$\sigma(\omega_s, \omega_p) = \sigma(\omega_s, \beta_s) = \sigma(\omega_p, \beta_p) = 270



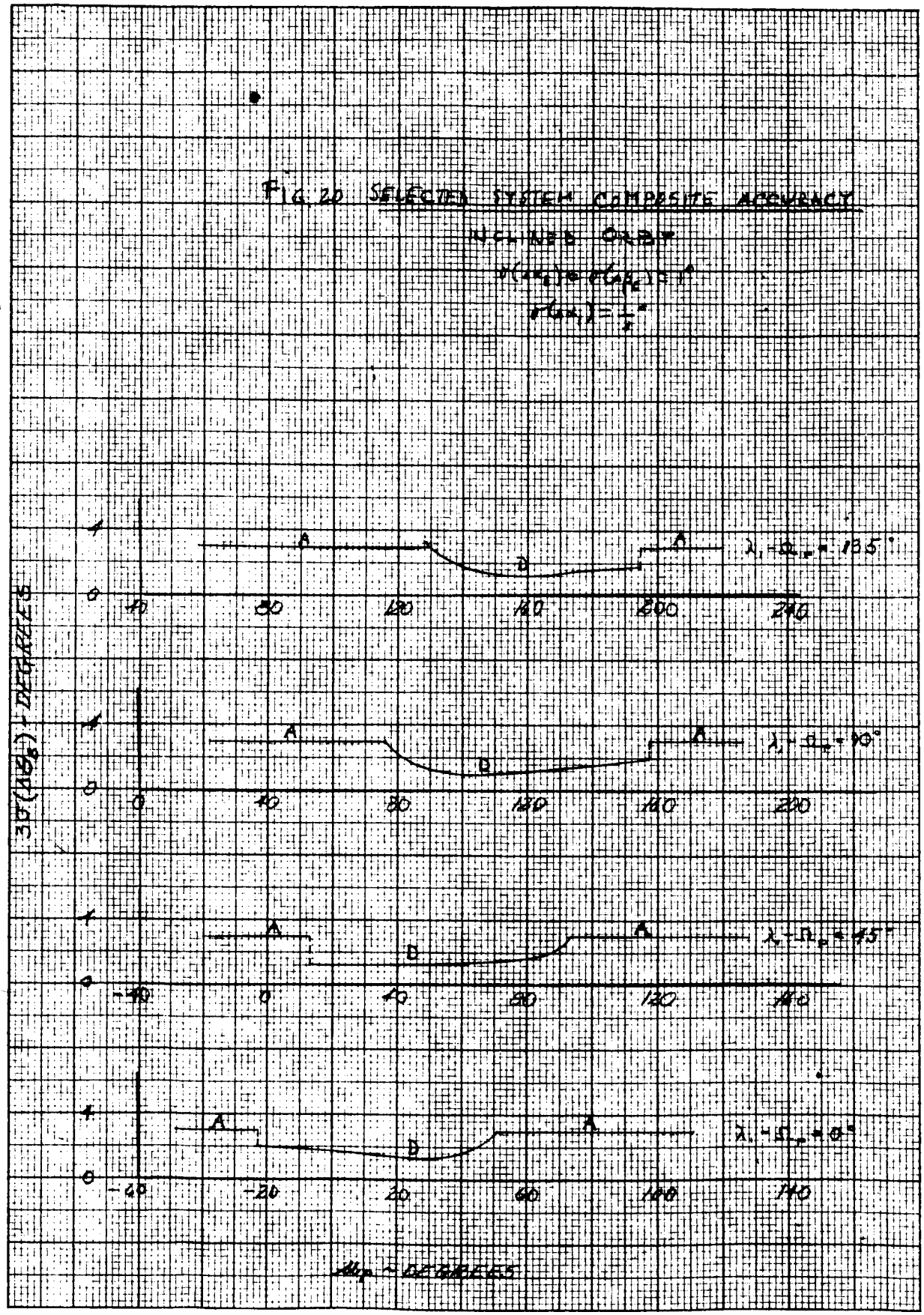
10 X 10 TO THE ½ INCH 359-11G
KEUFFEL & ESSER CO.



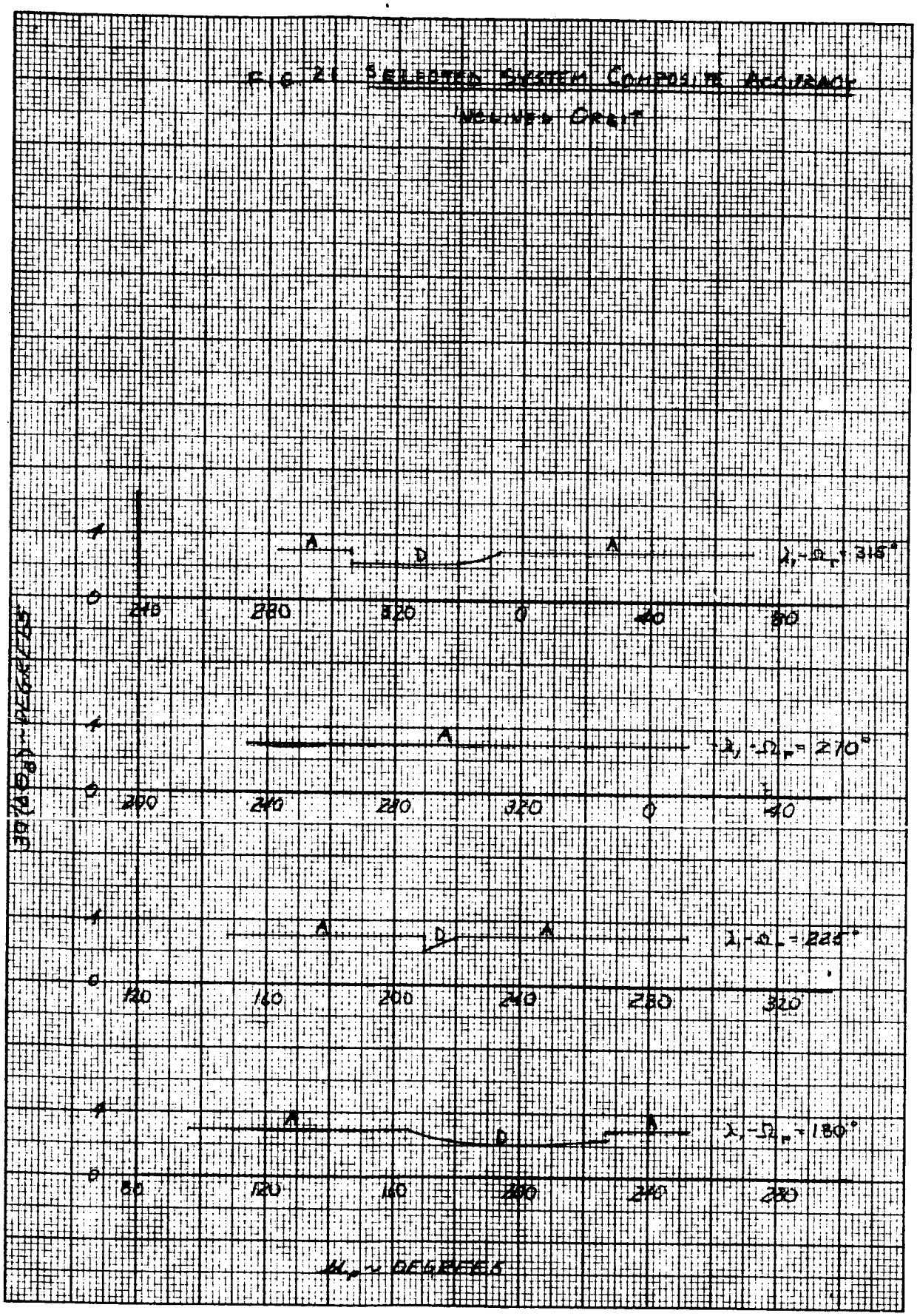
359-11G
10 X 10 TO THE ½ INCH
KEUFFEL & ESSER CO.



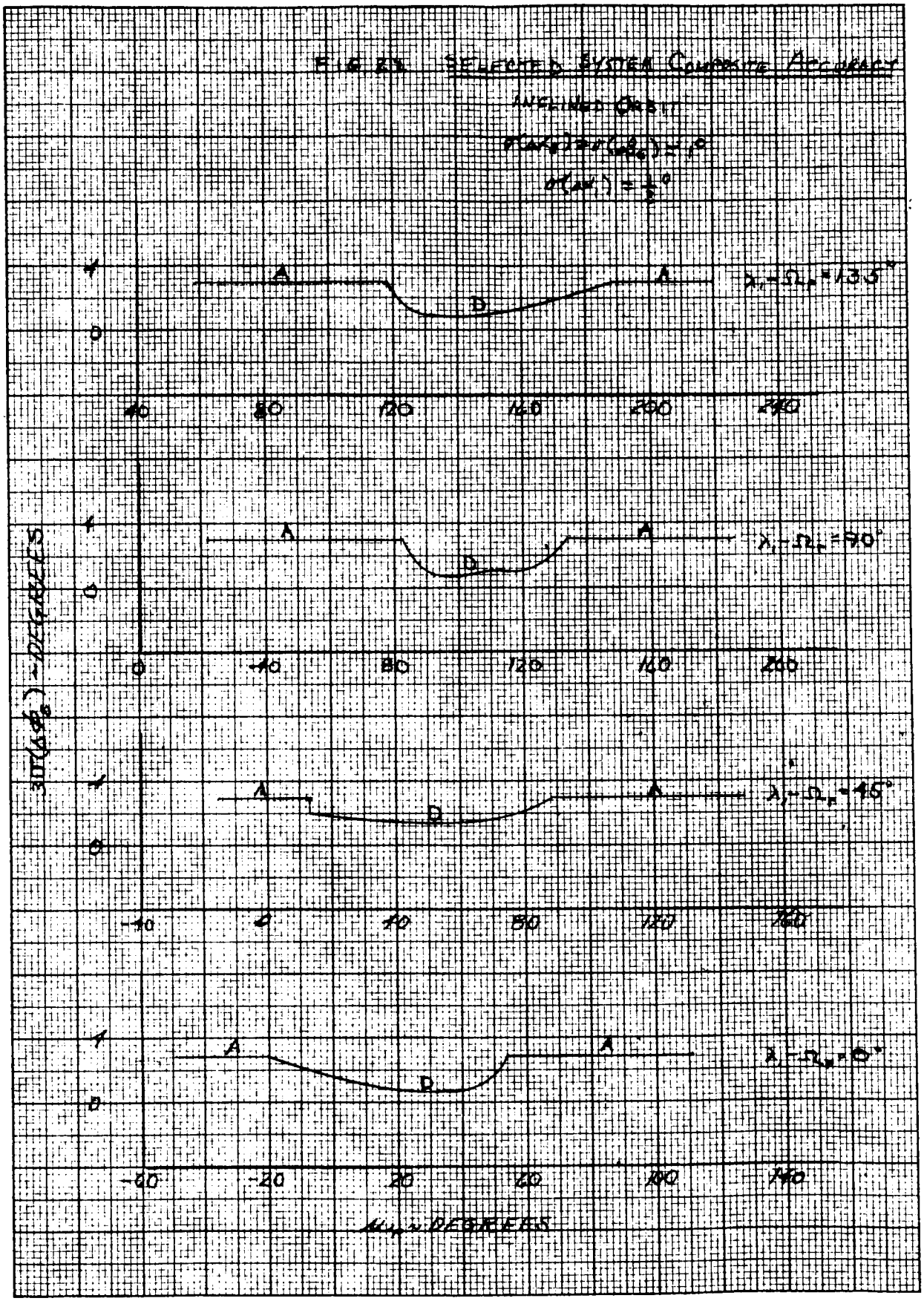
K&E 10 X 10 TO THE ½ INCH 359-11G
KEUFFEL & ESSER CO



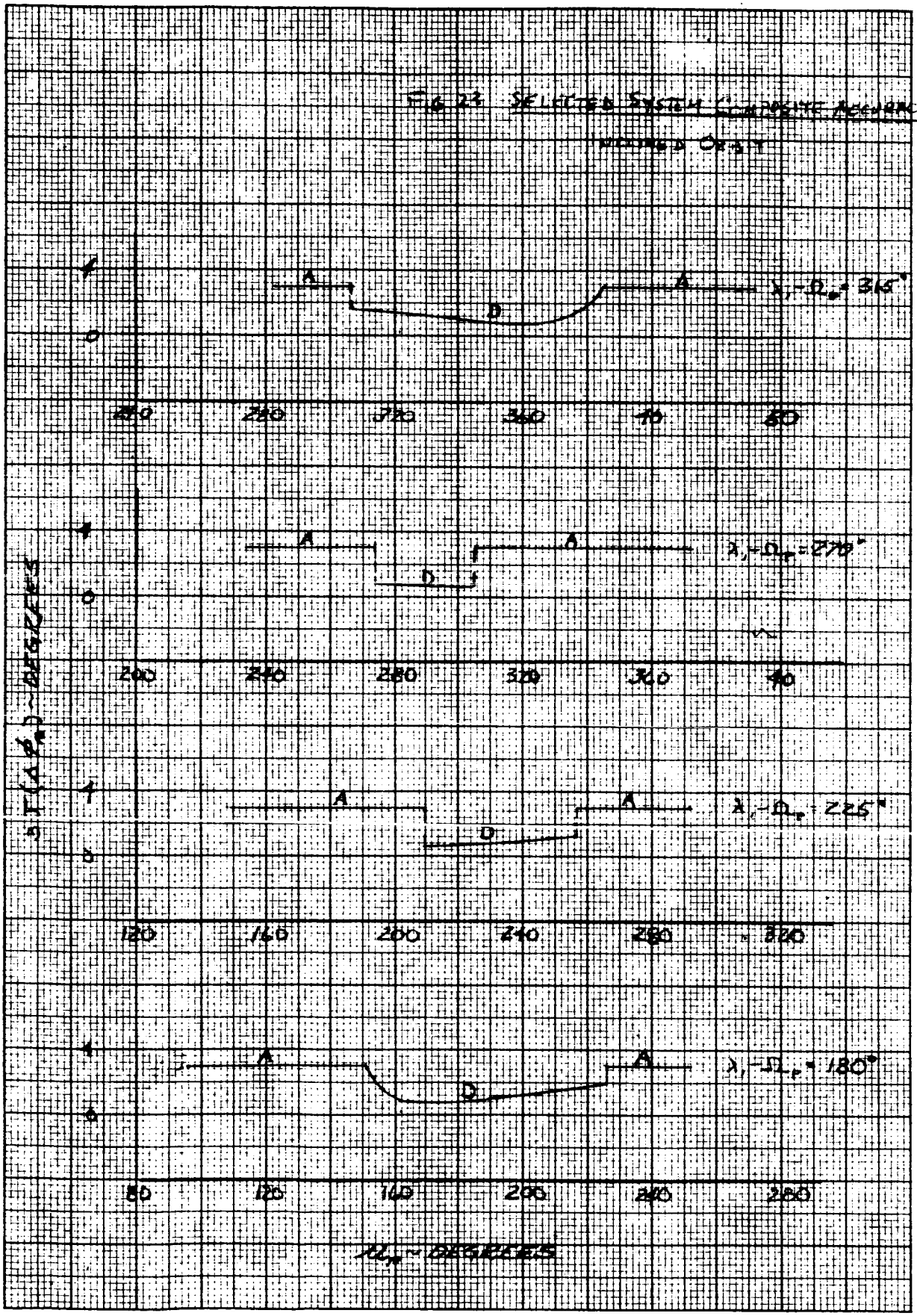
K&E 10 X 10 TO THE ½ INCH 359-11G
KEUFFEL & ESSER CO



10 X 10 TO THE ½ INCH 359-11G
KEUFFEL & ESSER CO.



10 X 10 TO THE ½ INCH 359-11G
KEUFFEL & ESSER CO.



K&E 10 X 10 TO THE ½ INCH 359-11G KEUFFEL & ESSER CO

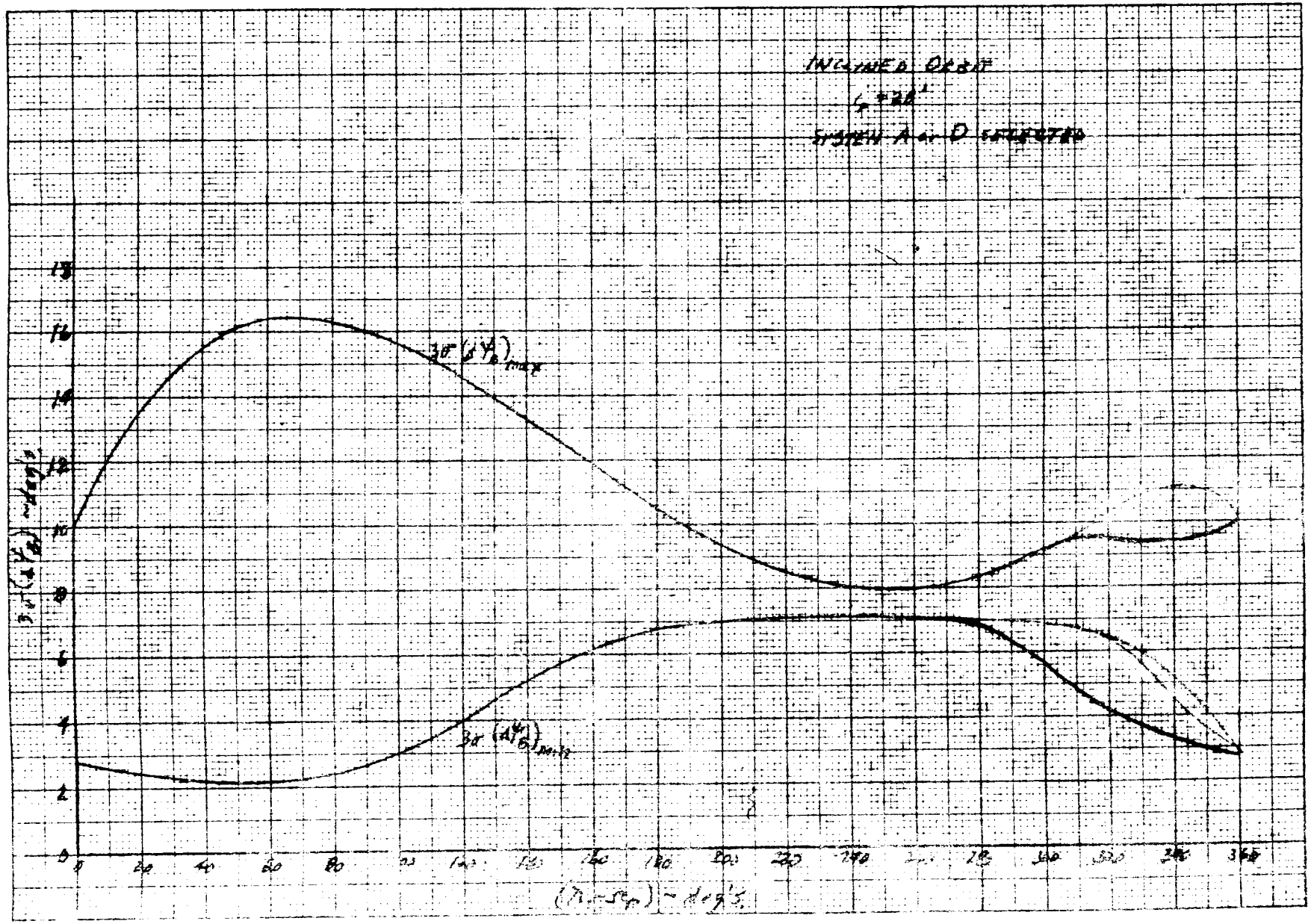
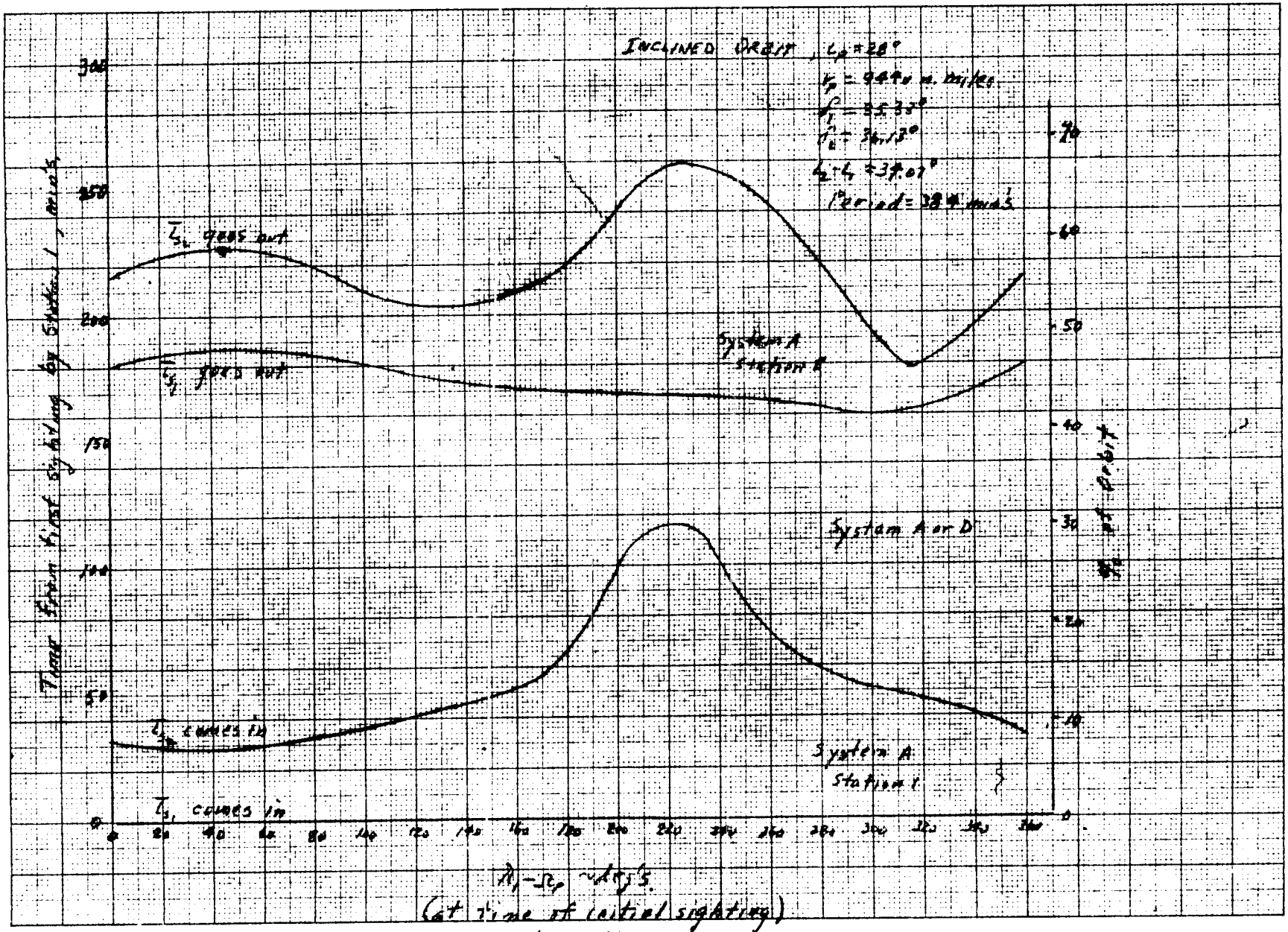

INCREASED DRAG
$\zeta = 2\zeta^*$
$\delta\theta\,(\Delta\gamma_b)_{max}$
$\delta\theta\,(\Delta\gamma_b)_{min}$
$(\gamma - \gamma_0)$ ~ deg's.

FIG. 6.24

K+E 10 X 10 TO THE CM. 359-14
KEUFFEL & ESSER CO. MADE IN U.S.A.



$\Delta\theta_1 - \Delta\theta_2$ vs θ_3
(at time of critical sighting)
by Station 1

FIG 25

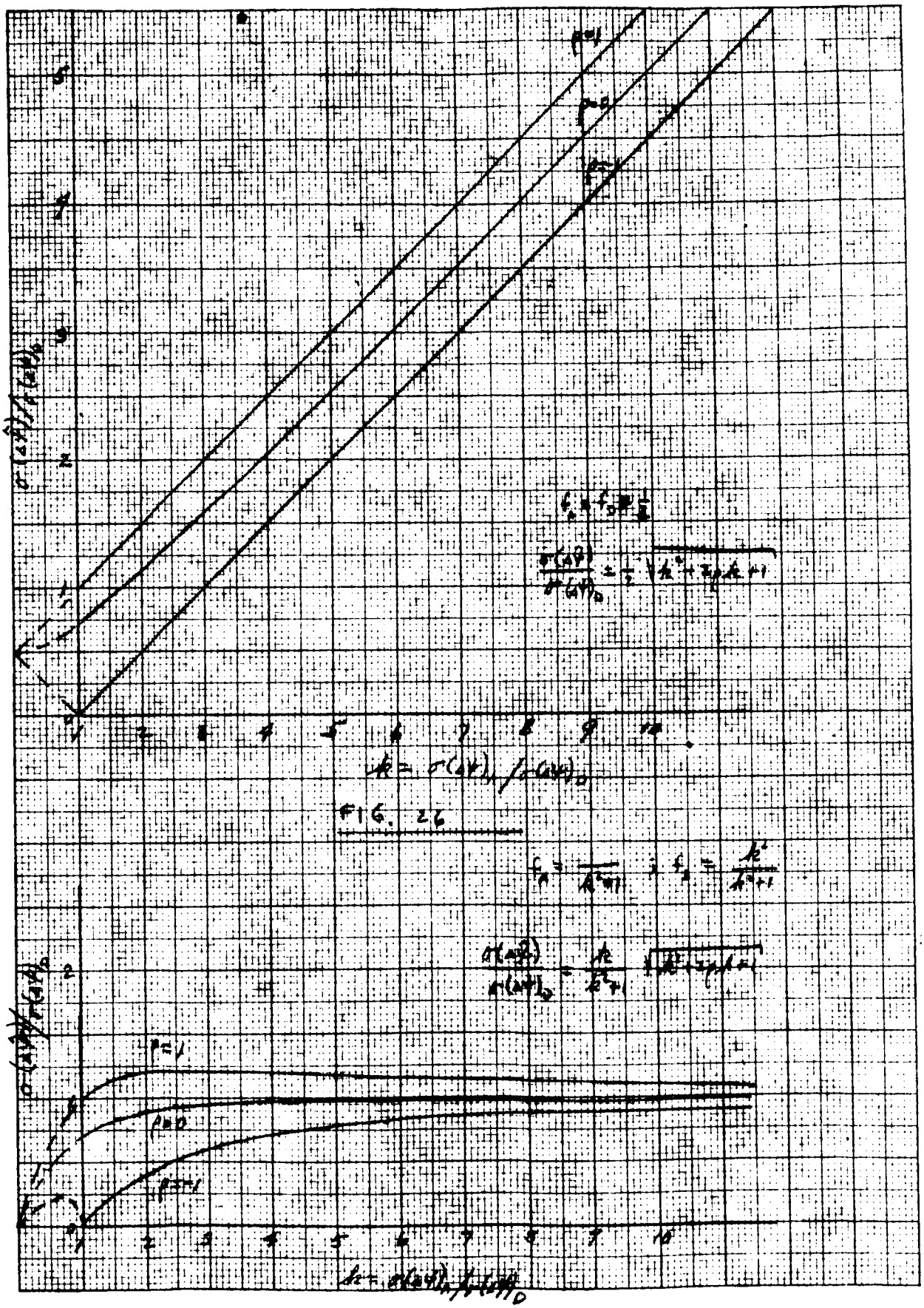
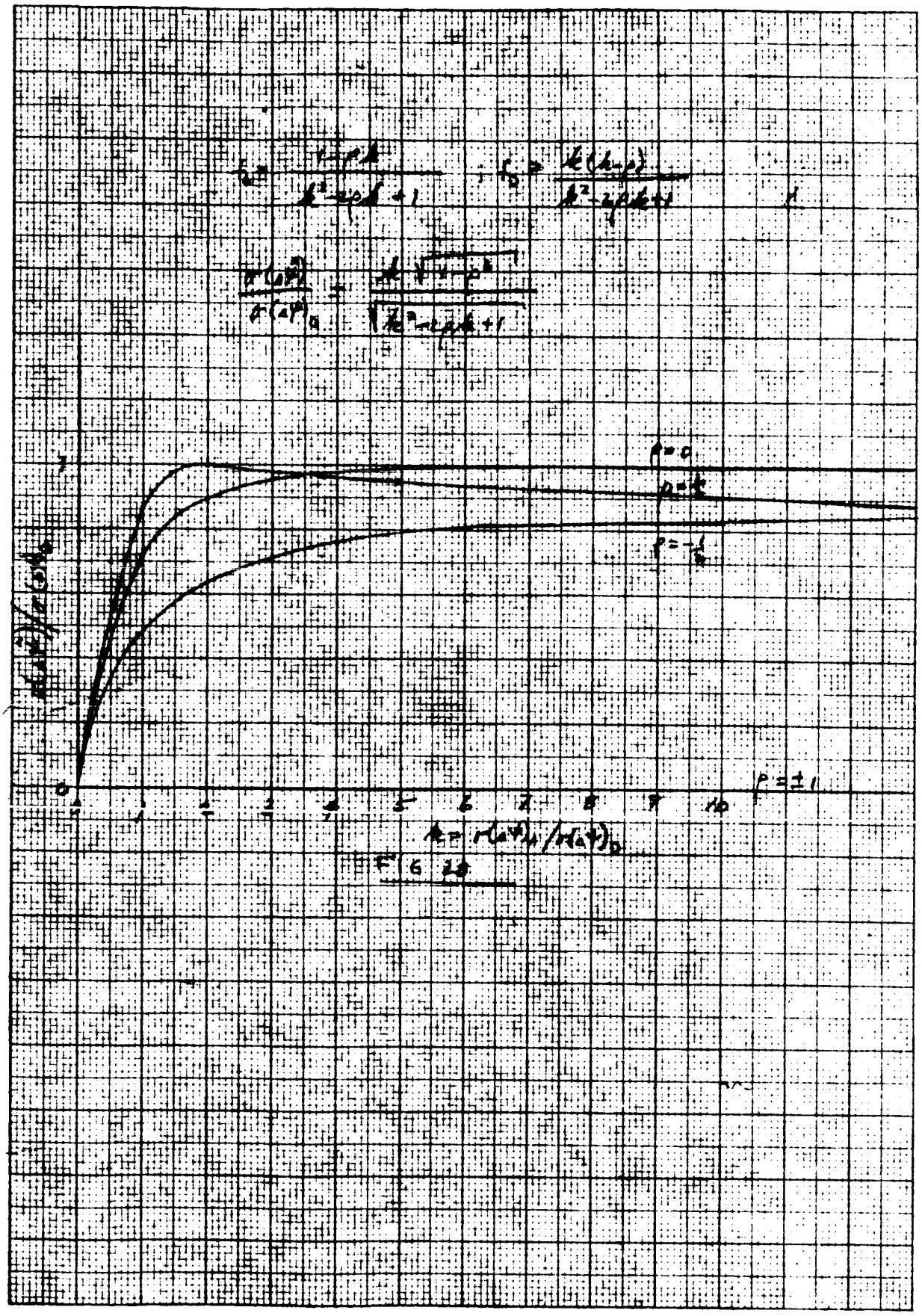


FIG. 26

FIG. 27



10 X 10 TO THE INCH 359-11

K+E 10 X 10 TO THE ½ INCH KEUFFEL & ESSER CO. 359-11G MADE IN U.S.A.

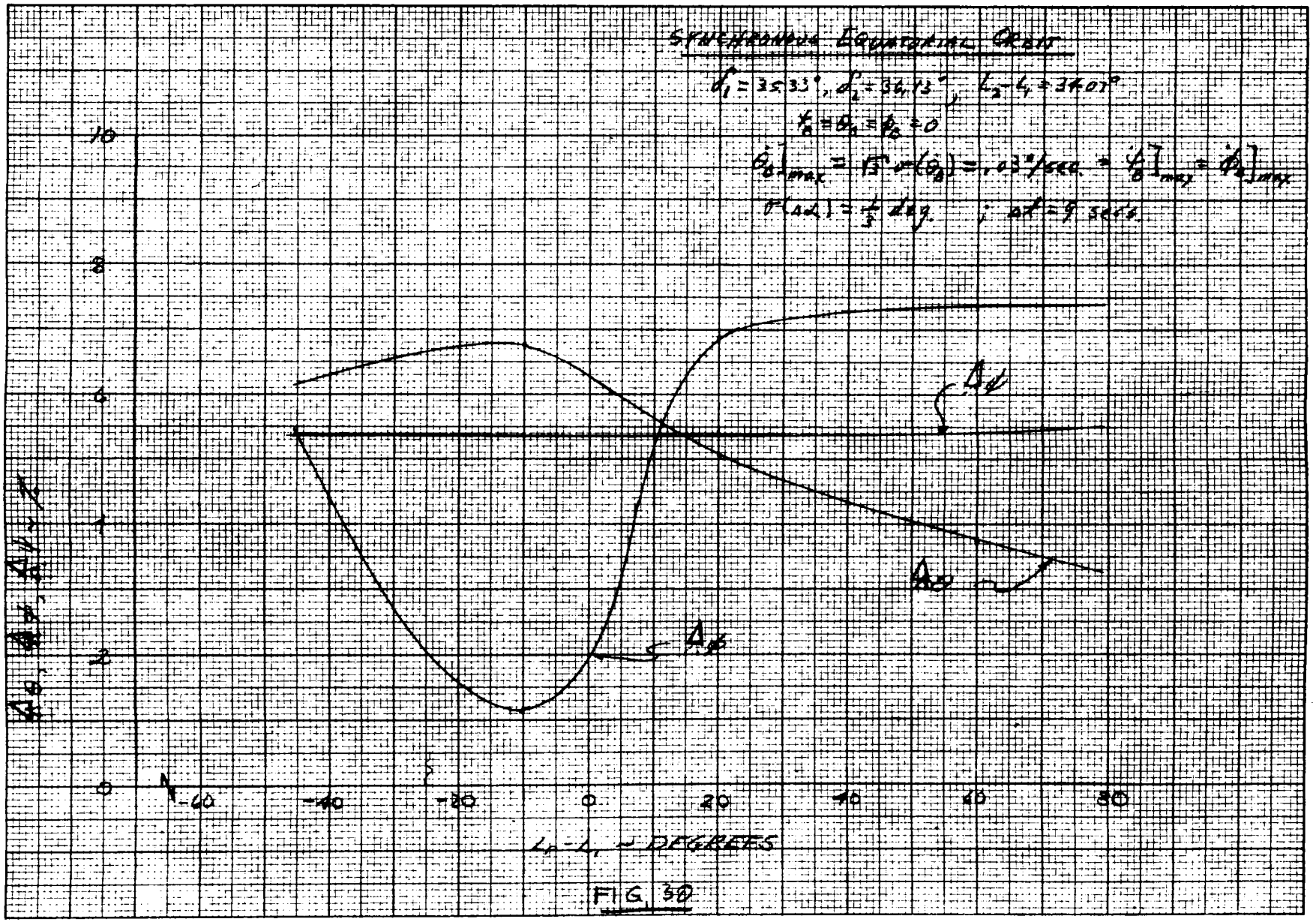


FIG. 30

K+E 10 X 10 TO THE ½ INCH 359-11G
KEUFFEL & ESSER CO. MADE IN U.S.A.

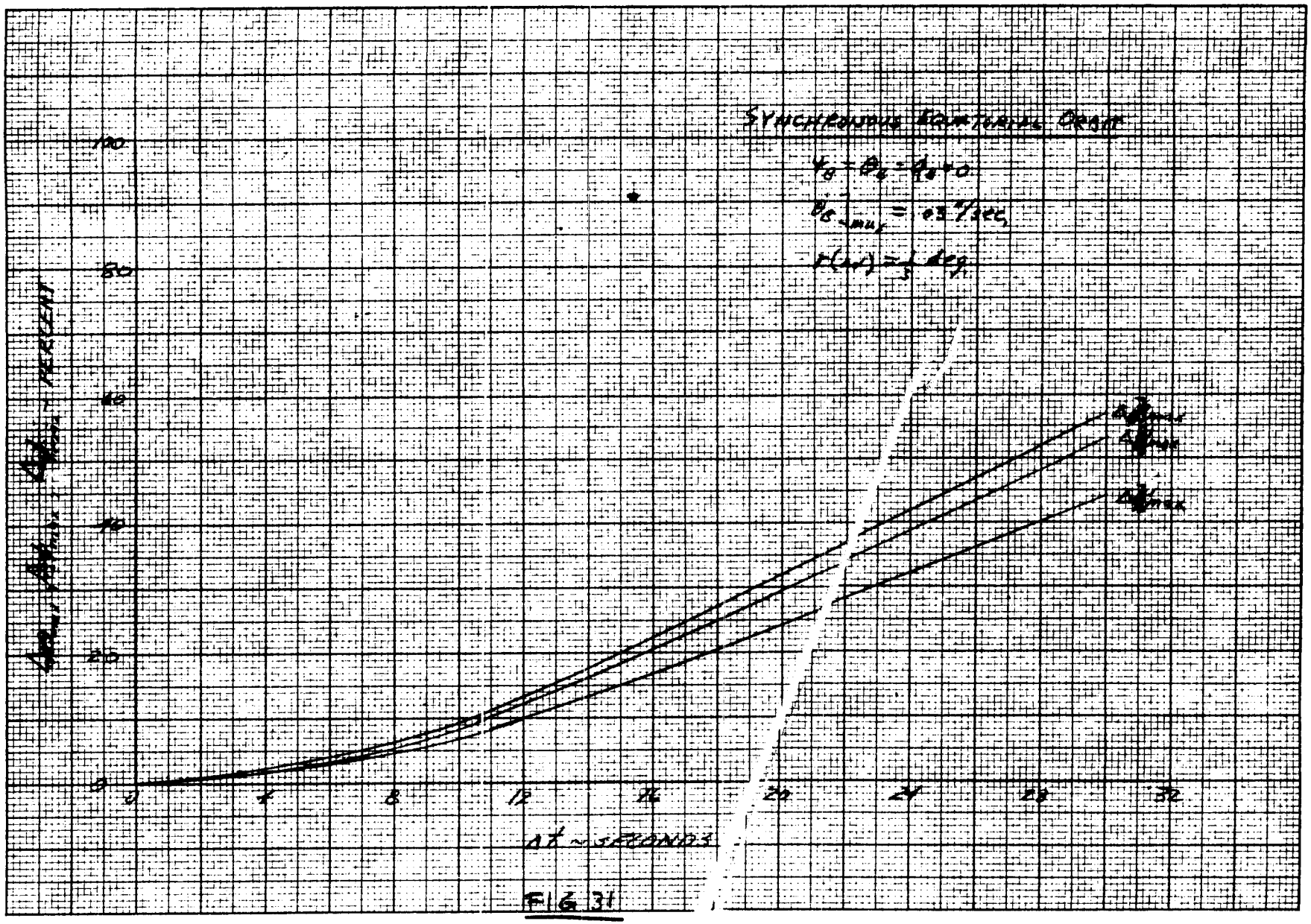


FIG 31

APPENDIX I - Coefficient Functions

m_E is given by solution of $aX^4 + bX^3 + cX^2 + hX + \ell = 0$,

$X \triangleq m_E$.

l_E is given by

$$l_E = A - BX \pm C\sqrt{-X^2 + DX + E}$$

whence

$$\alpha_E = \cos^{-1} l_E \; ; \quad 0 \le \alpha_E \le \pi$$

$$\beta_E = \cos^{-1} m_E \; ; \quad 0 \le \beta_E \le \pi$$

$$\theta_E = \sin^{-1}\sqrt{l_E^2 + m_E^2} \; ; \quad 0 \le \theta_E \le \pi/2$$

In the above:

$$a = (B'-B)^2\left[(B'-B)^2 + 2\{(C')^2 + C^2\}\right] + \left[(C')^2 - C^2\right]^2$$

$$b = 4(A-A')(B'-B)\left[(B'-B)^2 + (C')^2 + C^2\right]$$
$$- 2(B'-B)^2\left[C^2D + (C')^2D'\right] + 2\left[C^2 - (C')^2\right]\left[(C')^2D' - C^2D\right]$$

$$c = 2(B'-B)^2\left[3(A-A')^2 - EC^2 - E'(C')^2\right]$$
$$-4(B'-B)(A-A')\left[DC^2 + D'(C')^2\right] + \left[DC^2 - D'(C')^2\right]^2$$
$$+ 2(A-A')^2\left[C^2 + (C')^2\right] + 2\left[C^2 - (C')^2\right]\left[E'(C')^2 - EC^2\right]$$

$$h = 4(A-A')^3(B'-B) - 2(A-A')^2\left[C^2D + (C')^2D'\right]$$
$$-4(A-A')(B'-B)\left[C^2E + (C')^2E'\right] + 2\left[D'(C')^2 - DC^2\right]\left[E(C')^2 - EC^2\right]$$

$$\ell = (A-A')^4 - 2(A-A')^2\left[EC^2 + E'(C')^2\right] + \left[EC^2 - E'(C')^2\right]^2$$

Denote $\cos\psi_1 = \ell_1$, $\cos\psi_2 = \ell_2$

Then $A = \dfrac{\ell_1 l_1}{(l_1^2 + m_1^2)}$; $B = \dfrac{m_1 l_1}{(l_1^2 + m_1^2)}$; $C = \dfrac{n_1}{(l_1^2 + m_1^2)}$; $D = 2m_1\ell_1$; $E = n_1^2 + l_1^2 - \ell_1^2$

$A' = \dfrac{\ell_2 l_2}{(l_2^2 + m_2^2)}$; $B' = \dfrac{m_2 l_2}{(l_2^2 + m_2^2)}$; $C' = \dfrac{n_2}{(l_2^2 + m_2^2)}$; $D' = 2m_2\ell_2$; $E' = n_2^2 + l_2^2 - \ell_2^2$

APPENDIX II - Coefficient Partials

Elements of $\hat{l}_\alpha$:

$$\begin{bmatrix} \frac{\partial l_E}{\partial \alpha_1} & \frac{\partial l_E}{\partial \beta_1} \end{bmatrix} = \begin{bmatrix} \frac{\partial l_E}{\partial A} & \frac{\partial l_E}{\partial B} & \frac{\partial l_E}{\partial C} & \frac{\partial l_E}{\partial D} & \frac{\partial l_E}{\partial E} & \frac{\partial l_E}{\partial X} \end{bmatrix} \begin{bmatrix} \frac{\partial A}{\partial \alpha_1} & \frac{\partial A}{\partial \beta_1} \\ \frac{\partial B}{\partial \alpha_1} & \frac{\partial B}{\partial \beta_1} \\ \frac{\partial C}{\partial \alpha_1} & \frac{\partial C}{\partial \beta_1} \\ \frac{\partial D}{\partial \alpha_1} & \frac{\partial D}{\partial \beta_1} \\ \frac{\partial E}{\partial \alpha_1} & \frac{\partial E}{\partial \beta_1} \\ \frac{\partial m_E}{\partial \alpha_1} & \frac{\partial m_E}{\partial \beta_1} \end{bmatrix}$$

$$\begin{bmatrix} \frac{\partial l_E}{\partial \alpha_2} & \frac{\partial l_E}{\partial \beta_2} \end{bmatrix} = \frac{\partial l_E}{\partial X} \begin{bmatrix} \frac{\partial m_E}{\partial \alpha_2} & \frac{\partial m_E}{\partial \beta_2} \end{bmatrix}$$

Elements of $\hat{m}_\alpha$:

$$\begin{bmatrix} \frac{\partial m_E}{\partial \alpha_1} & \frac{\partial m_E}{\partial \beta_1} & \frac{\partial m_E}{\partial \alpha_2} & \frac{\partial m_E}{\partial \beta_2} \end{bmatrix} = \begin{bmatrix} \frac{\partial m_E}{\partial a} & \frac{\partial m_E}{\partial b} & \frac{\partial m_E}{\partial c} & \frac{\partial m_E}{\partial h} & \frac{\partial m_E}{\partial l} \end{bmatrix} \begin{bmatrix} \frac{\partial a}{\partial \alpha_1} & \frac{\partial a}{\partial \beta_1} & \frac{\partial a}{\partial \alpha_2} & \frac{\partial a}{\partial \beta_2} \\ \frac{\partial b}{\partial \alpha_1} & \frac{\partial b}{\partial \beta_1} & \frac{\partial b}{\partial \alpha_2} & \frac{\partial b}{\partial \beta_2} \\ \frac{\partial c}{\partial \alpha_1} & \frac{\partial c}{\partial \beta_1} & \frac{\partial c}{\partial \alpha_2} & \frac{\partial c}{\partial \beta_2} \\ \frac{\partial h}{\partial \alpha_1} & \frac{\partial h}{\partial \beta_1} & \frac{\partial h}{\partial \alpha_2} & \frac{\partial h}{\partial \beta_2} \\ \frac{\partial l}{\partial \alpha_1} & \frac{\partial l}{\partial \beta_1} & \frac{\partial l}{\partial \alpha_2} & \frac{\partial l}{\partial \beta_2} \end{bmatrix}$$

In the above the partials of coefficients appearing in the l_E and m_E equations are obtained by straightforward differentiation of the expressions in Appendix I.

Elements of $\hat{P}_\alpha$:

$$\left[\frac{\partial P}{\partial \alpha_1} \quad \frac{\partial P}{\partial \beta_1} \quad \frac{\partial P}{\partial \alpha_2} \quad \frac{\partial P}{\partial \beta_2}\right] = \left[\left(\frac{\partial P}{\partial \alpha_1}\right)' \left(\frac{\partial P}{\partial \beta_1}\right)' \left(\frac{\partial P}{\partial \alpha_2}\right)' \left(\frac{\partial P}{\partial \beta_2}\right)'\right]$$

$$+\left[\frac{\partial P}{\partial m_E} \quad \frac{\partial P}{\partial l_E}\right]\begin{bmatrix} \frac{\partial m_E}{\partial \alpha_1} & \frac{\partial m_E}{\partial \beta_1} & \frac{\partial m_E}{\partial \alpha_2} & \frac{\partial m_E}{\partial \beta_2} \\ \frac{\partial l_E}{\partial \alpha_1} & \frac{\partial l_E}{\partial \beta_1} & \frac{\partial l_E}{\partial \alpha_2} & \frac{\partial l_E}{\partial \beta_2} \end{bmatrix}$$

where $\left(\frac{\partial P}{\partial \alpha_1}\right)' = \frac{m_E m_2'}{n_1} \sin\alpha_1 \cos\alpha_1$

$$\left(\frac{\partial P}{\partial \beta_1}\right)' = \left(n_E m_2' + \frac{n_E' m_2' m_1}{n_1}\right) \sin\beta_1$$

$$\left(\frac{\partial P}{\partial \alpha_2}\right)' = -\frac{m_E m_1'}{n_2} \sin\alpha_2 \cos\alpha_2$$

$$\left(\frac{\partial P}{\partial \beta_2}\right)' = -\left(n_E m_1' + \frac{n_E' m_1' n_2}{n_2}\right) \sin\beta_2$$

$$\left(\frac{\partial P}{\partial m_E}\right) = -\frac{m_E}{n_E}\left(m_2 m_1' - m_1 m_2'\right) + \left(n_1 m_2' - n_2 m_1'\right)$$

$$\left(\frac{\partial P}{\partial l_E}\right) = -\frac{l_E}{n_E}\left(m_2 m_1' - m_1 m_2'\right)$$

Elements of $\hat{A}_\alpha$:

$$\left[\frac{\partial A}{\partial \alpha_1} \quad \frac{\partial A}{\partial \beta_1} \quad \frac{\partial A}{\partial \alpha_2} \quad \frac{\partial A}{\partial \beta_2}\right] = \left[\left(\frac{\partial A}{\partial \alpha_1}\right)' \left(\frac{\partial A}{\partial \beta_1}\right)' \left(\frac{\partial A}{\partial \alpha_2}\right)' \left(\frac{\partial A}{\partial \beta_2}\right)'\right]$$

$$+\left[\frac{\partial A}{\partial m_E} \quad \frac{\partial A}{\partial l_E}\right]\begin{bmatrix} \frac{\partial m_E}{\partial \alpha_1} & \frac{\partial m_E}{\partial \beta_1} & \frac{\partial m_E}{\partial \alpha_2} & \frac{\partial m_E}{\partial \beta_2} \\ \frac{\partial l_E}{\partial \alpha_1} & \frac{\partial l_E}{\partial \beta_1} & \frac{\partial l_E}{\partial \alpha_2} & \frac{\partial l_E}{\partial \beta_2} \end{bmatrix}$$

where

$$\left(\frac{\partial \rho}{\partial \alpha_1}\right)' = \frac{m_E l_2'}{n_1} \sin\alpha_1 \cos\alpha_1$$

$$\left(\frac{\partial \rho}{\partial \beta_1}\right)' = \left(n_E l_2' + \frac{m_E l_2' m_1}{n_1}\right) \sin\beta_1$$

$$\left(\frac{\partial \rho}{\partial \alpha_2}\right)' = -\frac{m_E l_1'}{n_2} \sin\alpha_2 \cos\alpha_2$$

$$\left(\frac{\partial \rho}{\partial \beta_2}\right)' = -\left(n_E l_1' + \frac{m_E l_1' m_2}{n_2}\right) \sin\beta_2$$

$$\left(\frac{\partial \rho}{\partial m_E}\right) = \frac{-m_E}{n_E}\left(m_2 l_1' - m_1 l_2'\right) + \left(n_1 l_2' - n_2 l_1'\right)$$

$$\left(\frac{\partial \rho}{\partial l_E}\right) = -\frac{l_E}{n_E}\left(m_2 l_1' - m_1 l_2'\right)$$

Elements of $\bar{\Phi}_m$:

$$\frac{\partial \phi_B}{\partial m_E} = \frac{1}{n_E} \quad ; \quad \frac{\partial \phi_B}{\partial l_E} = \frac{m_E l_E}{n_E (1 - l_E^2)}$$

Elements of $\bar{\Psi}_p$:

$$\frac{\partial \psi_B}{\partial \rho} = \frac{A}{(\rho^2 + A^2)} \quad ; \quad \frac{\partial \psi_B}{\partial \rho} = \frac{-\rho}{(\rho^2 + A^2)}$$

APPENDIX III - Formulas for $\dot{l}_{2_v}$, $\dot{m}_{2_v}$, $\dot{n}_{2_v}$

For the inclined orbit:

$$\left(\frac{R_2}{\rho_2}\right) = \sqrt{1 + \left(\frac{R_p}{\rho_2}\right) - 2\left(\frac{R_p}{\rho_2}\right)\cos\gamma_2}$$

$$\cos\gamma_2 = \cos\delta_2 \cos(\lambda_2 - \Omega_p)\cos u_p + \sin u_p \left[\cos\delta_2 \cos i_p \sin(\lambda_2 - \Omega_p) + \sin\delta_2 \sin i_p\right]$$

$$\left(\frac{R_2}{\rho_2}\right) l_{2_v} = \cos u_p \left[\sin\delta_2 \sin i_p + \cos\delta_2 \cos i_p \sin(\lambda_2 - \Omega_p)\right] - \sin u_p \cos\delta_2 \cos(\lambda_2 - \Omega_p)$$

$$\left(\frac{R_2}{\rho_2}\right) m_{2_v} = \cos\delta_2 \sin i_p \sin(\lambda_2 - \Omega_p) - \sin\delta_2 \cos i_p$$

$$\left(\frac{R_2}{\rho_2}\right) n_{2_v} = \left(\frac{R_p}{\rho_2}\right) - \cos\gamma_2$$

Then

$$\frac{R_2 \dot{l}_{2_v}}{\rho_2} = \omega_E \cos\delta_2 \left\{ \begin{array}{l} \left[\cos u_p + \frac{R_p}{R_2} l_{2_v} \sin u_p\right] \cos i_p \cos(\lambda_2 - \Omega_p) \\ + \left[\sin u_p + \frac{R_2}{R_2} l_{2_v} \cos u_p\right] \sin(\lambda_2 - \Omega_p) \end{array} \right\}$$

$$+ \omega_0 \left\{ \begin{array}{l} \left(\frac{R_p}{R_2}\right) l_{2_v} \left[\operatorname{ctn} u_p \cos\gamma_2 - \csc u_p \cos\delta_2 \cos(\lambda_2 - \Omega_p)\right] \\ - \left(\frac{R_2}{\rho_2}\right) l_{2_v} \tan u_p - \cos\delta_2 \cos(\lambda_2 - \Omega_p) \sec u_p \end{array} \right\}$$

$$\frac{R_2 \dot{\omega}_{2y}}{\rho_2} = \omega_e \cos\delta_2 \left\{ \cos(\lambda_2 - \Omega_p) \sin i_p \right.$$

$$\left. + \left(\frac{\omega_p}{\omega_e}\right) \omega_{2y} \left[\cos\mu_p \sin(\lambda_2 - \Omega_p) + \sin\mu_p \cos i_p \cos(\lambda_2 - \Omega_p) \right] \right\}$$

$$+ \omega_p \left(\frac{\omega_p}{\omega_e}\right) \omega_{2y} \left[\operatorname{ctn}\mu_p \cos\gamma_2 - \cos\delta_2 \cos(\lambda_2 - \Omega_p) \csc\mu_p \right]$$

$$\frac{R_2 \dot{\omega}_{2y}}{\rho_2} = \left[\left(\frac{\omega_p}{\omega_e}\right) \omega_{2y} - 1 \right] \left\{ \omega_e \left[\operatorname{ctn}\mu_p \cos\gamma_2 - \cos\delta_2 \cos(\lambda_2 - \Omega_p) \csc\mu_p \right] \right.$$

$$\left. + \omega_p \cos\delta_2 \left[\cos\mu_p \sin(\lambda_2 - \Omega_p) + \sin\mu_p \cos i_p \cos(\lambda_2 - \Omega_p) \right] \right\}$$

APPENDIX IV - Error Augmentation

For $\psi_3 = \theta_2 = \phi_1$ only:

$$\xi_\theta = \frac{\left[1 + \left(\frac{l_2}{m_2}\right)^2\right]}{2\left[\left(\frac{l_1}{m_1}\right)^2 + \left(\frac{l_2}{m_2}\right)^2\right] + \left[1 + \left(\frac{l_1}{m_1}\right)^2\right] + \left[1 + \left(\frac{l_2}{m_2}\right)^2\right]}$$

$$\xi_\psi = \frac{\left[1 + \left(\frac{m_2}{l_1}\right)^2\right]}{2\left[\left(\frac{m_1}{n_1}\right)^2 + \left(\frac{m_2}{n_2}\right)^2\right] + \left[1 + \left(\frac{m_1}{l_1}\right)^2\right] + \left[1 + \left(\frac{m_2}{l_2}\right)^2\right]}$$

$$\xi_\phi = \frac{\left[\left(\frac{m_1}{l_1}\right) - \left(\frac{m_1}{l_1}\right)\right]^2 + \left[\left(\frac{n_1}{l_1}\right) - \left(\frac{m_2}{l_2}\right)\left(\frac{n_1}{m_1}\right)\right]^2 + \left[\left(\frac{n_2}{l_2}\right)\left(\frac{m_1}{l_1}\right) - \left(\frac{m_2}{l_2}\right)\left(\frac{n_1}{m_1}\right)\right]^2}{\left[2 + \left(\frac{l_1}{l_1}\right) + \left(\frac{l_2}{n_2}\right)^2\right]\left[\left(\frac{n_1}{l_1}\right)\left(\frac{m_1}{l_1}\right) - \left(\frac{n_1}{l_1}\right)^2\left(\frac{n_1}{m_1}\right)\right]^2 + \left[2 + \left(\frac{m_2}{n_2}\right)^2 + \left(\frac{n_2}{n_1}\right)^2\right]\left[\left(\frac{n_2}{l_2}\right) - \left(\frac{m_2}{l_2}\right)\left(\frac{n_1}{m_1}\right)\right]^2}$$

In the above, for the symbols $\left(\frac{l_1}{m_1}\right)$, $\left(\frac{l_2}{m_2}\right)$, $\left(\frac{m_1}{n_1}\right)$ by replacing subscript 1 by 2 and 2 by 3 respectively.

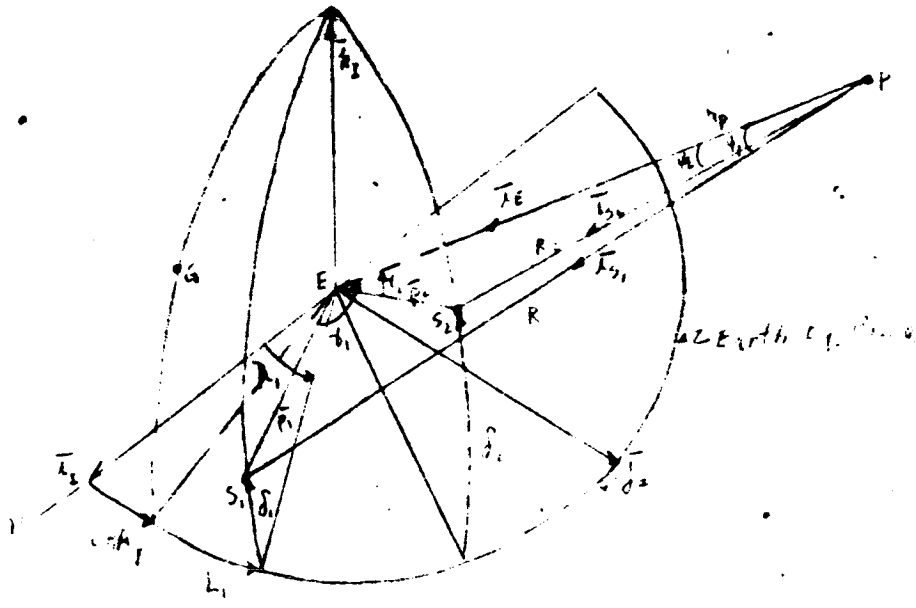


FIG 1

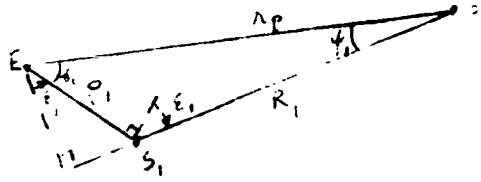


FIG 2

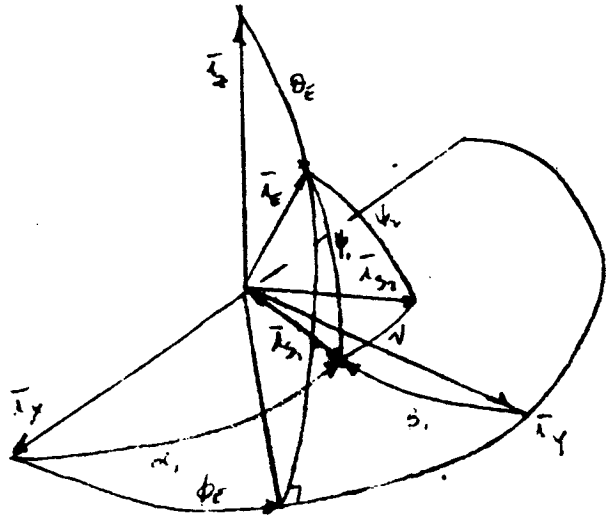


FIG 3

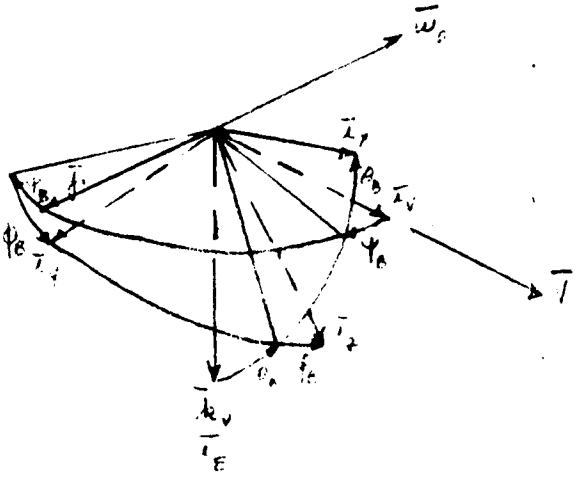
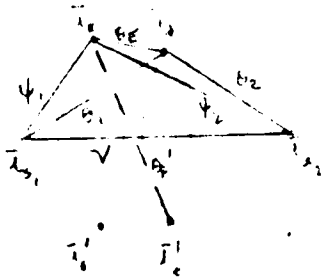


FIG 4



Note:

$0 < |\theta_2 - \theta_1| \leq V \leq \theta_1 + \theta_2 < 50°$

$0 < |\psi_2 - \psi_1| \leq V \leq \psi_1 + \psi_2$

FIG 5

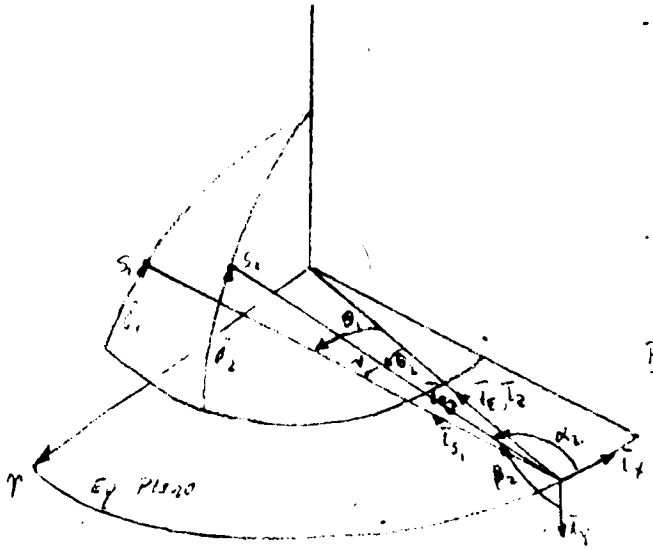


FIG 6

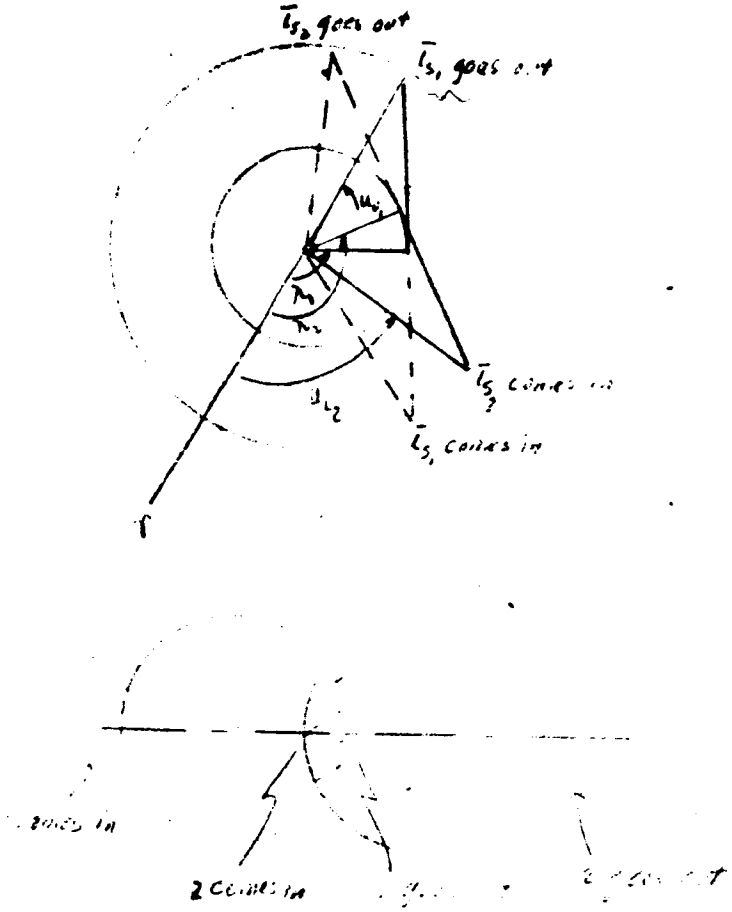

$\bar{l}_{s_2}$ goes out
$\bar{l}_{s_1}$ goes out
$\bar{l}_{s_2}$ comes in
$\bar{l}_{s_1}$ comes in
2 comes in

FIG 8

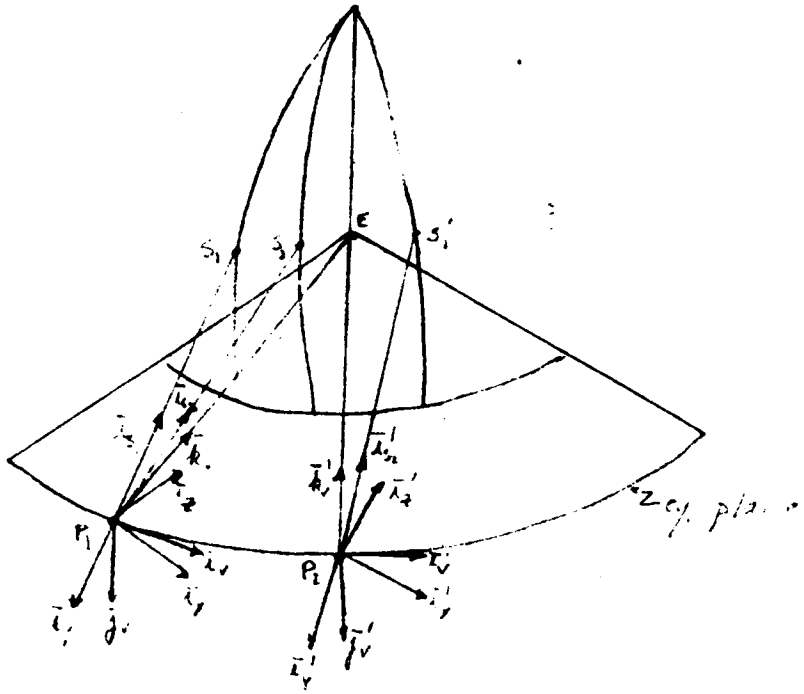

E
S_1
S_1'
P_1
P_2
Eq. plane

FIG. 29

APPENDIX C

ANALYSIS OF THE PROPOSED SOLAR ASPECT SYSTEM

1. Summary

The performance of the proposed Solar Aspect System was analysed and an exact transfer function was established.

By means of this transfer function quantitative answers were obtained in two areas of major interest as to the performance of the instrument:

1. The degree and source of cross-coupling of the two geometrically orthogonal detector eyes, and

2. The maximum error to be expected in the measurement of the sun direction.

The cross-coupling was found to be quite strong for measurement of angles not in the plane of the eye slit and the normal to the eye. That is, the output of the instrument would be gray code "128" for an angle of 64 degrees to the "0" direction and lying in the above plane, but the output would be gray code "98" if the angle is 64 degrees with respect to the "0" direction and 64 degrees with respect to the plane defined by the eye slit and the normal to the eye.

The error in the measurement of angles, A & B, in the two planes defined by the slits of the two eyes and the normal to the eyes is a function of the angles themselves. The maximum error ranges from 0.48 degrees at A = 50 degrees, B = 90 degrees to 1.3 degrees at A = 50 degrees, B = 26 degrees or B = 50 degrees, A = 26 degrees.

2. Derivation of the Transfer Function

The configuration of the Adcole sun sensor detector unit is shown in Figure 1. The coordinate system attached to the sensor will be used throughout this paper.

Figure 2 shows the construction of each eye of the detector. From this, it is evident that the angle which the incident light makes with the detector is determined once the light strikes particular solar cells behind the reticle. The instrument output, E, in gray code, is the number of digits the light beam is removed from the line directly below the slit when it strikes the bottom of the reticle. In general, for eye #1,

(1) $E_1 = n_1$ if $|n_1| \leq |F(A,B)| < |n_1+1|$
$|n_1| = 0, 1, 2, 3, \ldots, 128$

(2) $F(A,B) = U(A,B)/|K|$

for eye #2,

(3) $E_2 = n_2$ if $|n_2| \leq |g(A,B)| < |n_2+1|$
$|n_2| = 0, 1, 2, 3, \ldots, 128$

(4) $g(A,B) = V(A,B)/|K|$

The quantities in equation (1) through (4) are shown in Figure 3. Angles A and B are the angles the projection of the incident vectorsinto the X-Z-plane and Y-Z-plane, respectively, make with the X-Y-plane. U(A,B) and V(A,B) are the distances from the origin to the intercept of the light beam with a line parallel to the X-axis and Y-axis, respectively, on the bottom of the reticle. K is the width of the least significant bits shown in Figure 2.

The problem of finding the transfer function is, therefore, to find U(A,B), V(A,B) and K.

From the geometry shown in Figure 3 the following relations are evident:

(5) $$\cot\phi = U/V$$

(6) $$\cot\phi = \cot A \tan B$$

(7) $$\cot A = \tan\theta \cos\phi$$

(8) $$\cot B = \tan\theta \sin\phi$$

(9) $$t \tan\theta' = \sqrt{U^2 + V^2}$$

Also, using N = (index of refraction of quartz)$^{-1}$

(10) $$\sin\theta' = N \sin\theta$$

Combining (9), (5), and (6), we find

$$U^2 = \frac{t^2 \tan^2\theta'}{1 + \tan^2\phi}$$

(11) $$U^2 = \frac{t^2 \tan^2\theta'}{1 + \tan^2 A \cot^2 B}$$

Then $\tan^2\theta'$ can be found from (7), (10) and (6):

$$\cot\phi = \cot A \tan B$$

$$\cos^2\phi = \frac{\cot^2 A \tan^2 B}{1 + \cot^2 A \tan^2 B}$$

$$\tan^2\theta = \frac{\cot^2 A (1 + \cot^2 A \tan^2 B)}{\cot^2 A \tan^2 B}$$

$$\tan^2\theta = \cot^2 B + \cot^2 A$$

$$\sin^2\theta = \frac{\cot^2 A + \cot^2 B}{1 + \cot^2 A + \cot^2 B}$$

$$\sin^2\theta' = \frac{N^2(\cot^2 A + \cot^2 B)}{1 + \cot^2 A + \cot^2 B}$$

$$\cos^2\theta' = \frac{1 + (1-N^2)(\cot^2 A + \cot^2 B)}{1 + \cot^2 A + \cot^2 B}$$

(12) $$\tan^2\theta' = \frac{N^2(\cot^2 A + \cot^2 B)}{1 + (1-N^2)(\cot^2 A + \cot^2 B)}$$

Substituting (12) into (11),

$$U^2 = \frac{t^2 N^2 (\cot^2 A + \cot^2 B)}{(1 + \tan^2 A \cot^2 B)\left[1 + (1-N^2)(\cot^2 A + \cot^2 B)\right]}$$

$$U^2 = \frac{t^2 N^2 \cot^2 A}{1 + (1-N^2)(\cot^2 A + \cot^2 B)}$$

In a more recognizable form,

$$U^2 = \frac{t^2 N^2 \cos^2 A}{\sin^2 A + (1-N^2)(\cos^2 A + \cot^2 B \sin^2 A)}$$

$$U^2 = \frac{t^2 N^2 \cos^2 A}{1 - N^2\cos^2 A + (1-N^2)\cot^2 B \sin^2 A}$$

(13) $$U = \frac{-tN \cos A}{\sqrt{1 - N^2\cos^2 A + (1-N^2)\cot^2 B \sin^2 A}}$$

The minus sign is clear from the geometry.
The expression for V follows from (1), (2) and (8).

(14) $$V = \frac{-tN \cos B}{\sqrt{1 - N^2\cos^2 B + (1-N^2)\cot^2 A \sin^2 B}}$$

The digit width, K, can now be found from (13) or (14). The pattern is linear, each digit corresponds to 1/2 degree in the X-Z-plane (for eye #1), and the field-of-view of the instrument is 64 degrees. Therefore,

(15) $$K = U(90° - 64°, 90°)/128$$

Substituting (9) into (11),

$$K = \frac{-tN \cos 26°}{128\sqrt{1 - N^2\cos^2 26°}}$$

In summary, the transfer function for eye #1 is,

$$(16)\quad \begin{cases} E_1 = n_1 & |n_1| \le |F(A,B)| < |n_1+1| \\ & |n_1| = 0,1,2,\ldots,128 \\ F(A,B) = \dfrac{-L\cos A}{\sqrt{1-N^2\cos^2 A + (1-N^2)\cot^2 B \sin^2 A}} & \end{cases}$$

The transfer function for eye #2 is,

$$(17)\quad \begin{cases} E_2 = n_2 & |n_2| \le |g(A,B)| < |n_2+1| \\ & |n_2| = 0,1,2,\ldots,128 \\ g(A,B) = \dfrac{-L\cos B}{\sqrt{1-N^2\cos^2 B + (1-N^2)\cot^2 A \sin^2 B}} & \end{cases}$$

where

$$L = \frac{128\sqrt{1-N^2\cos 26^\circ}}{\cos 26^\circ}$$

When the instrument is in use, not equations (16) and (17) but their inverses A (E_1, E_2) and B (E_1, E_2) are needed.

A (E_1, E_2) and B (E_1, E_2) are more easily found from equations (5) through (10) than by simultaneous solution of (16) and (17). From (7) and (5) we have then,

$$\cot^2 A = \tan^2\theta \quad \frac{(U/V)^2}{1+(U/V)^2}$$

$$(18)\quad \cot^2 A = \frac{\tan^2\theta\, U^2}{U^2+V^2}$$

From equation (9) and (10),

$$\sin^2\theta' = \frac{\frac{1}{t^2}(U^2+V^2)}{1+\frac{1}{t^2}(U^2+V^2)}$$

$$\sin^2\theta = \frac{U^2+V^2}{N^2(t^2+U^2+V^2)}$$

$$\cos^2\theta = \frac{N^2t^2-(1-N^2)(U^2+V^2)}{N^2(t^2+U^2+V^2)}$$

(19) $$\tan^2\theta = \frac{U^2+V^2}{N^2t^2-(1-N^2)(U^2+V^2)}$$

Substituting (1), (2) and (19) into (18),

$$\cot^2 A = \frac{U^2}{N^2t^2-(1-N^2)(U^2+V^2)}$$

$$\cot^2 A = \frac{E_1^2}{L^2-(1-N^2)(E_1^2+E_2^2)}$$

(20) $$\cot A = \frac{E_1}{\sqrt{L^2-(1-N^2)(E_1^2+E_2^2)}}$$

Similarly,

(21) $$\cot B = \frac{E_2}{\sqrt{L^2-(1-N^2)(E_1^2+E_2^2)}}$$

3. Evaluation of Cross-Coupling Between the Detector Eyes

Examination of the transfer function, equation (16), shows that the quartz reticle is the source of the cross-coupling. "Cross-coupling" is to be understood as the dependence of E_1, the output of eye #1, on angle B which lies in an orthogonal plane to angle A.

Substitution of N = 1, i.e., the quartz block removed, into equation (16) yields:

(22)
$$\begin{cases} E_1 = n_1 & |n_1| \le |F(A,B)| < |n_1+1| \\ & |n_1| = 0, 1, 2, \ldots, 128 \\ F(A,B) = -L\cot A \\ L = 128\tan 26^\circ \end{cases}$$

Equation (22) is clearly a function of A only, no cross-coupling exists.

There is, however, also a real situation where f(A, B) is a function of A only. This occurs when B = 90°, then

(23) $$F(A,90) = \frac{-L\cos A}{\sqrt{1-N^2\cos^2 A}}$$

Equation (16) is plotted in Figure 4 with angle B as a parameter. From this the strong cross-coupling effect is evident; for instance, $E_1 = 128$ for $A = 26^\circ$, $B = 90^\circ$, while $E_1 = 98$ for $A = 26^\circ$, $B = 26^\circ$.

The points in the field-of-view where maximum cross-coupling occurs can be found by differentiating the term depending on the angle B in the denominator of (16), setting the result equal to zero and solving for A and B simultaneously.

$$\frac{\partial}{\partial A}\left(\cot^2 B \sin^2 A\right) = 2 \cot^2 B \sin A \cos B = 0$$

$$\frac{\partial}{\partial B}\left(\cot^2 B \sin^2 A\right) = -2 \cot B \csc^2 B \sin^2 A = 0$$

$$\cot B \cos A - \csc^2 B \sin A = 0$$

$$\cos B \sin B = \tan A \tag{24}$$

Portions of the left side and the right side of equation (24) are plotted in Figure 5. It is seen that the maximum cross-coupling occurs when A is between 26° and 26.6° and B is between 38.7° and 51.3° (only in these ranges have the curves the same values).

In summary, examination of the transfer function shows that:

1. Cross-coupling between the two geometrically orthogonal axes occurs because there are two different materials in the optical path of the light ray that is being measured, air and quartz.

2. No cross-coupling occurs at angles B, ($A = 90^\circ$, i.e., when the incident light lies in the X-Z-(Y-Z)-plane (see Figure 3).

3. The cross-coupling is a maximum when one angle, e.g. A, is at the edge of the field-of-view (26° to 26.6°) while the other angle, e.g., B, is between 38.7° and 51.3°.

4. Error Analysis

Two kinds of errors occur in the Adcole sun sensor, quantization errors and errors due to a shift of the edges of each digit (transition-edge errors).

The quantization error, ε_q, is due to the finite size of each quantum. Its maximum value is $\pm$ 1/2 digit from the center of the digit, its distribution is uniform.

The transition-edge error, ε_T, is due to manufacturing tolerances in the reticle, misalignment and drift in the electronics which establishes the edge by nulling the output of a "bit" cell with a control cell of 1/2 full output. The maximum transition-edge error is also $\pm$ 1/2 digit, its distribution can be assumed as normal.

The maximum error of the system measuring angles A and B is then, neglecting higher powers of D E,

$$DA = \frac{\partial A}{\partial E_1} DE_1 + \frac{\partial A}{\partial E_2} DE_2$$

$$(26) \quad \begin{cases} DA = DE \left(\frac{\partial A}{\partial E_1} + \frac{\partial A}{\partial E_2} \right) \\ DB = DE \left(\frac{\partial B}{\partial E_1} + \frac{\partial B}{\partial E_2} \right) \end{cases}$$

$DE = DE_1 = DE_2$ since the eyes are identical.

From the physical situation it is evident that the maximum error, DE , equals one digit, 1/2 digit due to quantization and 1/2 digit due to the shift of the transition edge in the worst case,

$$DE = 1 \text{ digit.}$$

To find the derivatives, $\frac{\partial A}{\partial E_1}$, $\frac{\partial A}{\partial E_2}$, $\frac{\partial B}{\partial E_1}$, $\frac{\partial B}{\partial E_2}$, the following procedure was used.

$$E_1 = f(A, B)$$

$$E_2 = g(A, B)$$

$$dE_1 = F_1 \, dA + F_2 \, dB$$

$$dE_2 = g_1 \, dA + g_2 \, dB$$

where $F_1 = \frac{\partial F_1}{\partial A}$, $F_2 = \frac{\partial F_2}{\partial B}$, $g_1 = \frac{\partial g_1}{\partial A}$, etc.

$$dA = \frac{\begin{vmatrix} dE_1 & F_2 \\ dE_2 & g_2 \end{vmatrix}}{\begin{vmatrix} F_1 & F_2 \\ g_1 & g_2 \end{vmatrix}}$$

$$dB = \frac{\begin{vmatrix} dE_1 & F_1 \\ dE_2 & g_1 \end{vmatrix}}{\begin{vmatrix} F_1 & F_2 \\ g_1 & g_2 \end{vmatrix}}$$

$$dA = \frac{g_2\, dE_1 - F_2\, dE_2}{D}$$

$$dA = \frac{\partial A}{\partial E_1} dE_1 + \frac{\partial A}{\partial E_2} dE_2$$

$$dB = \frac{g_1\, dE_1 - F_1\, dE_2}{D}$$

$$dB = \frac{\partial B}{\partial E_1} dE_1 + \frac{\partial B}{\partial E_2} dE_2$$

Therefore, equating coefficients,

$$(27) \quad \begin{cases} \dfrac{\partial A}{\partial E_1} = \dfrac{g_2}{D}, & \dfrac{\partial A}{\partial E_2} = \dfrac{-F_2}{D} \\ \dfrac{\partial B}{\partial E_1} = \dfrac{g_1}{D}, & \dfrac{\partial B}{\partial E_2} = \dfrac{-F_1}{D} \end{cases}$$

where $D = F_1 g_2 - F_2 g_1$

From equations (16) and (17),

$$F(A,B) = \frac{-L \cos A}{\sqrt{1 - N^2 \cos^2 A + (1-N^2) \cot^2 B \sin^2 A}}$$

$$g(A,B) = \frac{-L \cos B}{\sqrt{1 - N^2 \cos^2 B + (1-N^2) \cot^2 A \sin^2 B}}$$

Then,

$$
\text{(28)}\quad
\begin{cases}
F_1 = \dfrac{L \sin A \left[1 + (1-N^2)\cot^2 B\right]}{\left[1 - N^2\cos^2 A + (1-N^2)\cot^2 B \sin^2 A\right]^{3/2}} \\[2ex]
F_2 = \dfrac{-L (1-N^2)\cos A \sin^2 A \cot B \csc^2 B}{\left[1 - N^2\cos^2 A + (1-N^2)\cot^2 B \sin^2 A\right]^{3/2}} \\[2ex]
g_1 = \dfrac{-L (1-N^2)\cos B \sin^2 B \cot A \csc^2 A}{\left[1 - N^2\cos^2 B + (1-N^2)\cot^2 A \sin^2 B\right]^{3/2}} \\[2ex]
g_2 = \dfrac{L \sin B \left[1 + (1-N^2)\cot^2 A\right]}{\left[1 - N^2\cos^2 B + (1-N^2)\cot^2 A \sin^2 B\right]^{3/2}} \\[2ex]
D = \dfrac{L^2\left[1 - \cos^2 A\cos^2 B - N^2(\cos^2 A \sin^2 B + \sin^2 A \cos^2 B)\right]}{\sin A \sin B \left[1 - N^2\cos^2 A + (1-N^2)\cot^2 B \sin^2 A\right]^{3/2}\left[1 - N^2\cos^2 B + (1-N^2)\cot^2 A \sin^2 B\right]}
\end{cases}
$$

The derivatives are then, from (27) and (28),

$$
\text{(29)}\quad
\begin{cases}
\dfrac{\partial A}{\partial E_1} = \dfrac{\sin A \sin^2 B \left[1 + (1-N^2)\cot^2 A\right]\left[1 - N^2\cos^2 A + (1-N^2)\cot^2 B \sin^2 A\right]^{3/2}}{L\left[1 - \cos^2 A\cos^2 B - N^2(\cos^2 A \sin^2 B + \sin^2 A \cos^2 B)\right]} \\[2ex]
\dfrac{\partial A}{\partial E_2} = \dfrac{(1-N^2)\cos A \sin^3 A \cos B \csc^2 B \left[1 - N^2\cos^2 B + (1-N^2)\cot^2 A \sin^2 B\right]^{3/}}{L\left[1 - \cos^2 A\cos^2 B - N^2(\cos^2 A \sin^2 B + \sin^2 A \cos^2 B)\right]} \\[2ex]
\dfrac{\partial B}{\partial E_1} = \dfrac{(1-N^2)\cos B \sin^3 B \cos A \csc^2 A \left[1 - N^2\cos^2 A + (1-N^2)\cot^2 B \sin^2 A\right]^{3/}}{L\left[1 - \cos^2 A\cos^2 B - N^2(\cos^2 A \sin^2 B + \sin^2 A \cos^2 B)\right]} \\[2ex]
\dfrac{\partial B}{\partial E_2} = \dfrac{\sin^2 A \sin B \left[1 + (1-N^2)\cot^2 B\right]\left[1 - N^2\cos^2 B + (1-N^2)\cot^2 A \sin^2 B\right]^{3/2}}{L\left[1 - \cos^2 A\cos^2 B - N^2(\cos^2 A \sin^2 B + \sin^2 A \cos^2 B)\right]}
\end{cases}
$$

Evaluation of equations (29) and substitution into equation (26) then gives the maximum error to be expected at particular values of angles A and B.

Equations (29) and (26) were programmed for the IBM 7094 computer and the computer output is shown in Table I. The column headings have the following correspondence:

A	=	Angle A	in degrees
B	=	Angle B	" "
DA(1,1)	=	$\partial A/\partial E_1$	in radians per digit
DA(2,1)	=	$\partial B/\partial E_1$	" " " "
DA(1,2)	=	$\partial A/\partial E_2$	" " " "
DA(2,2)	=	$\partial B/\partial E_2$	" " " "
RMA	=	Maximum error in Angle A, in degrees	
EMB	=	Maximum error in Angle B, in degrees	

The maximum error in Angle A is 1.30 degrees when A = 50° and B = 26° which is consistent with the area of maximum cross-coupling of Figure 5.

The minimum error in Angle A occurs for A = 50°, B = 90° and is .48 degree. The error in A when it is measured in the X-Z-plane (see Fig. 3), however, is slightly larger than 1/2 degree. This occurs because, although $E_2 = 0$, there is a possible error of one digit in the reading of B.

The error calculations assume that the bias error which is present due to the antisymmetric placement of the pattern around zero is removed. That is, the pattern is placed such that the edge of the "0" digit is directly under the slit rather than its center. Therefore, 1/2 must be added to each reading E_1 or E_2 from the sensor before it is put into the inverse functions (20) or (21).

For example, outputs $E_1 = 0$, $E_2 = 0$ correspond to the following angles,

$$\cot A = \cot B = \frac{0.5}{\sqrt{112^2 - 0.531 \times 0.5}} \approx 4.46 \times 10^{-3}$$

$$A = B \approx 89.75^\circ$$

In summary, maximum errors for measurement of the angles A and B as a function of the angles themselves were obtained. The errors range from approximately 0.5 degrees to 1.3 degrees. There exists a bias error in the instrument due to the geometry of the pattern. This bias error must be removed before the readings are converted into angles.

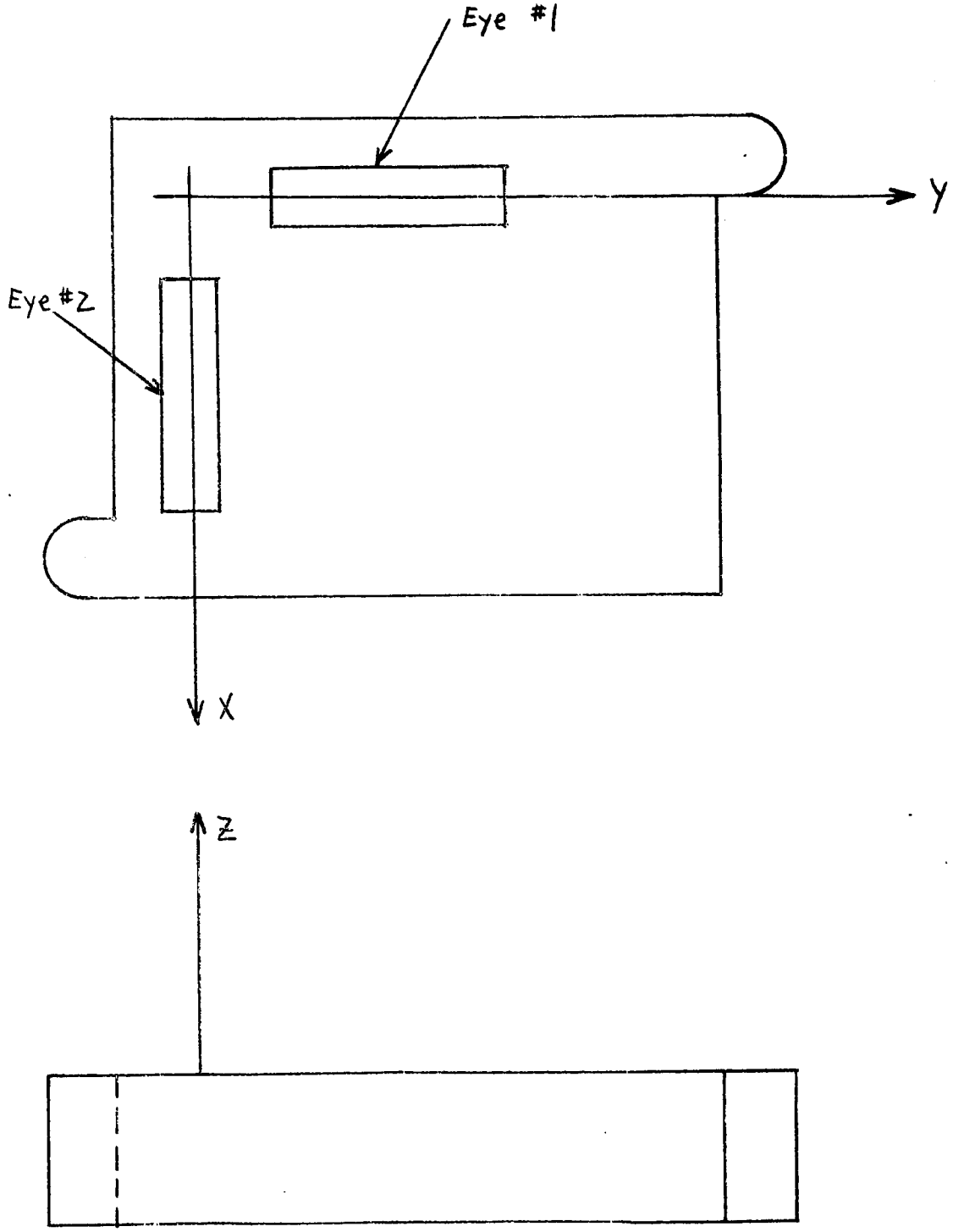
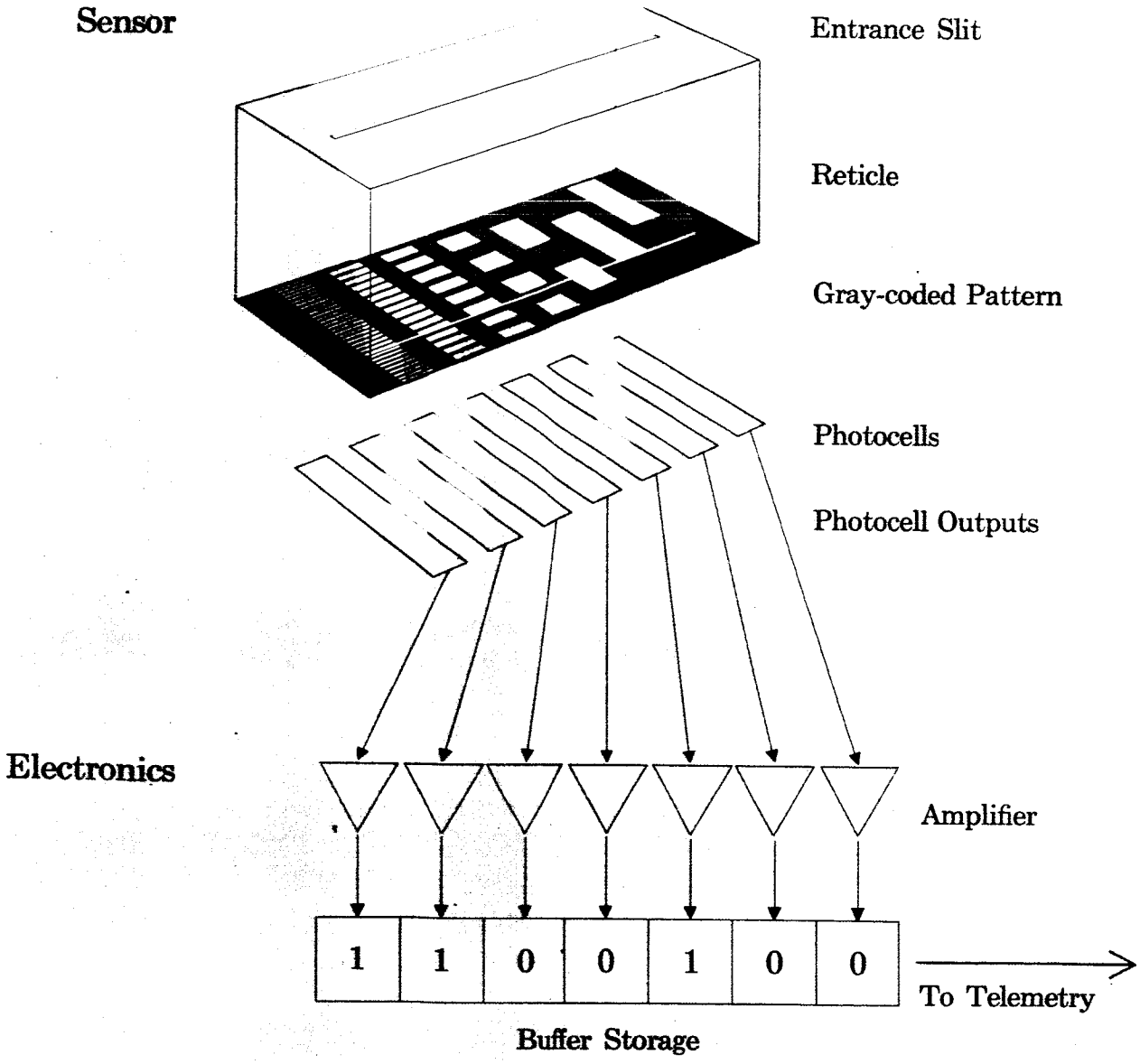


FIGURE 1

CONFIGURATION OF THE ADCOLE SUN SENSOR


Sensor
Entrance Slit
Reticle
Gray-coded Pattern
Photocells
Photocell Outputs
Electronics
Amplifier
1 1 0 0 1 0 0
To Telemetry
Buffer Storage

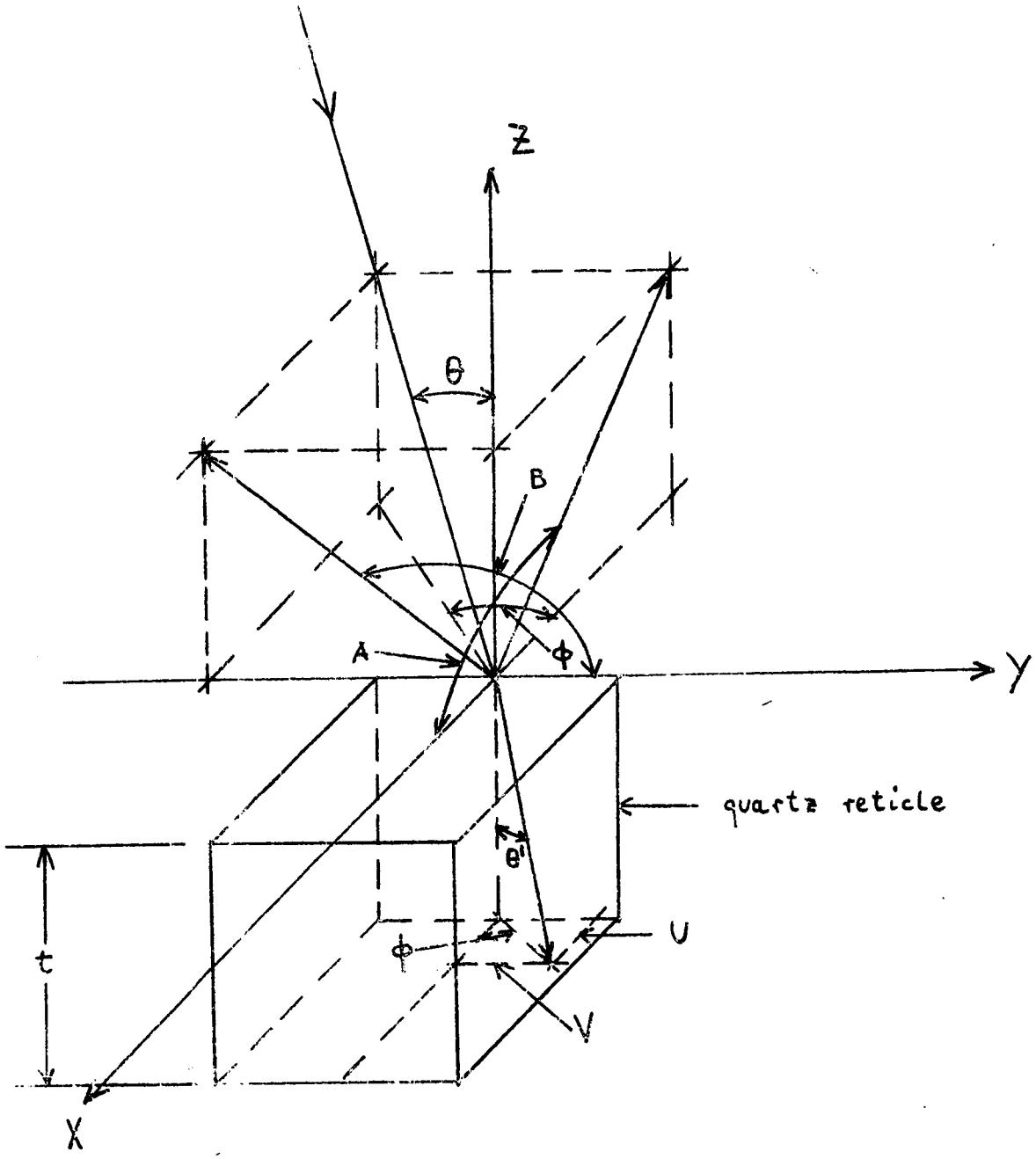


FIGURE 3

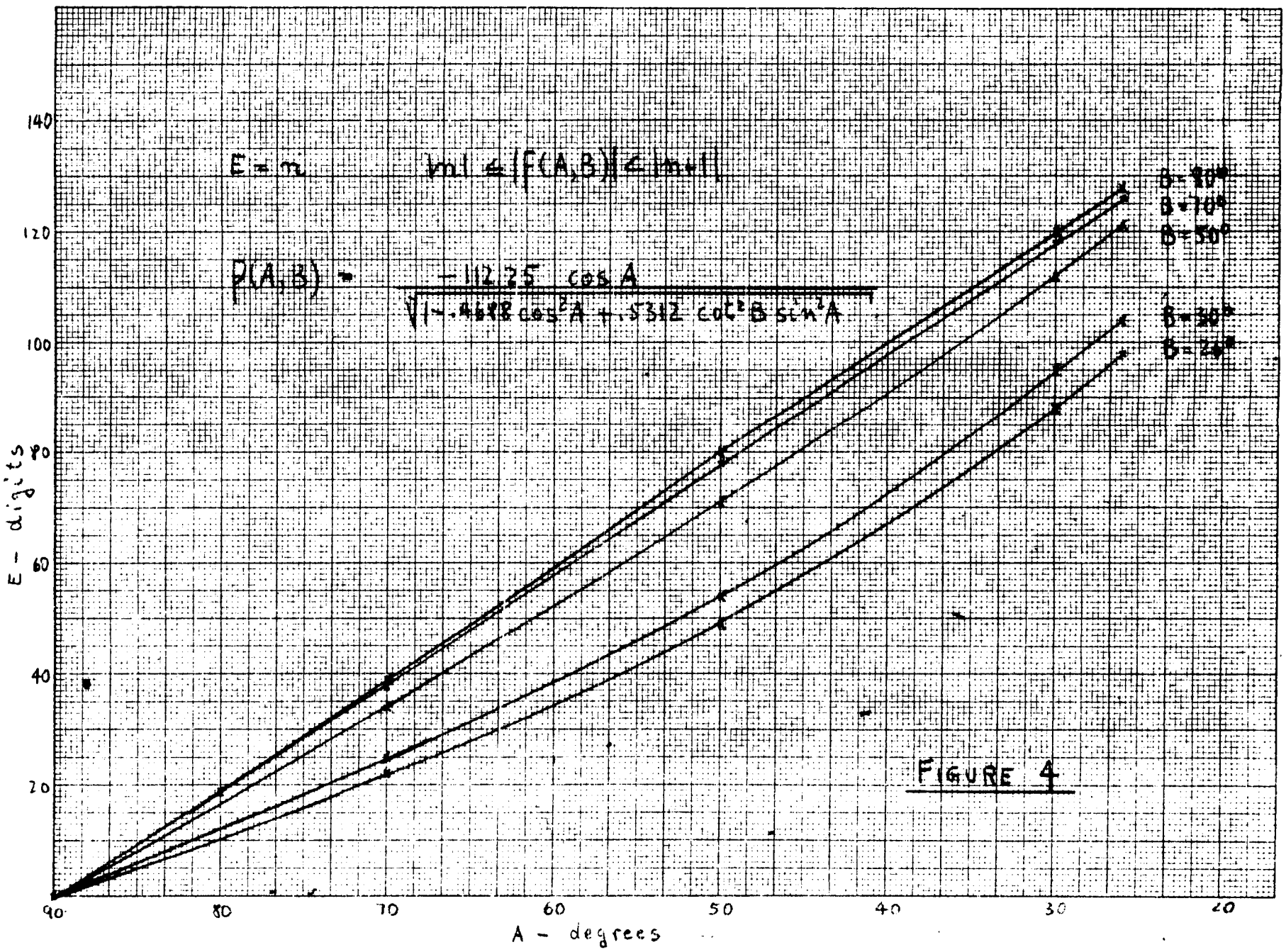

E = n m! ≤ |F(A,B)| < (m+1)!
F(A,B) = −11225 cos A / √(1−.4688 cos²A + .5312 cot²B sin²A)
B = 90°
B = 70°
B = 50°
B = 30°
B = 20°
E - digits
A - degrees
140
120
100
80
60
40
20
90
80
70
60
50
40
30
20

FIGURE 4

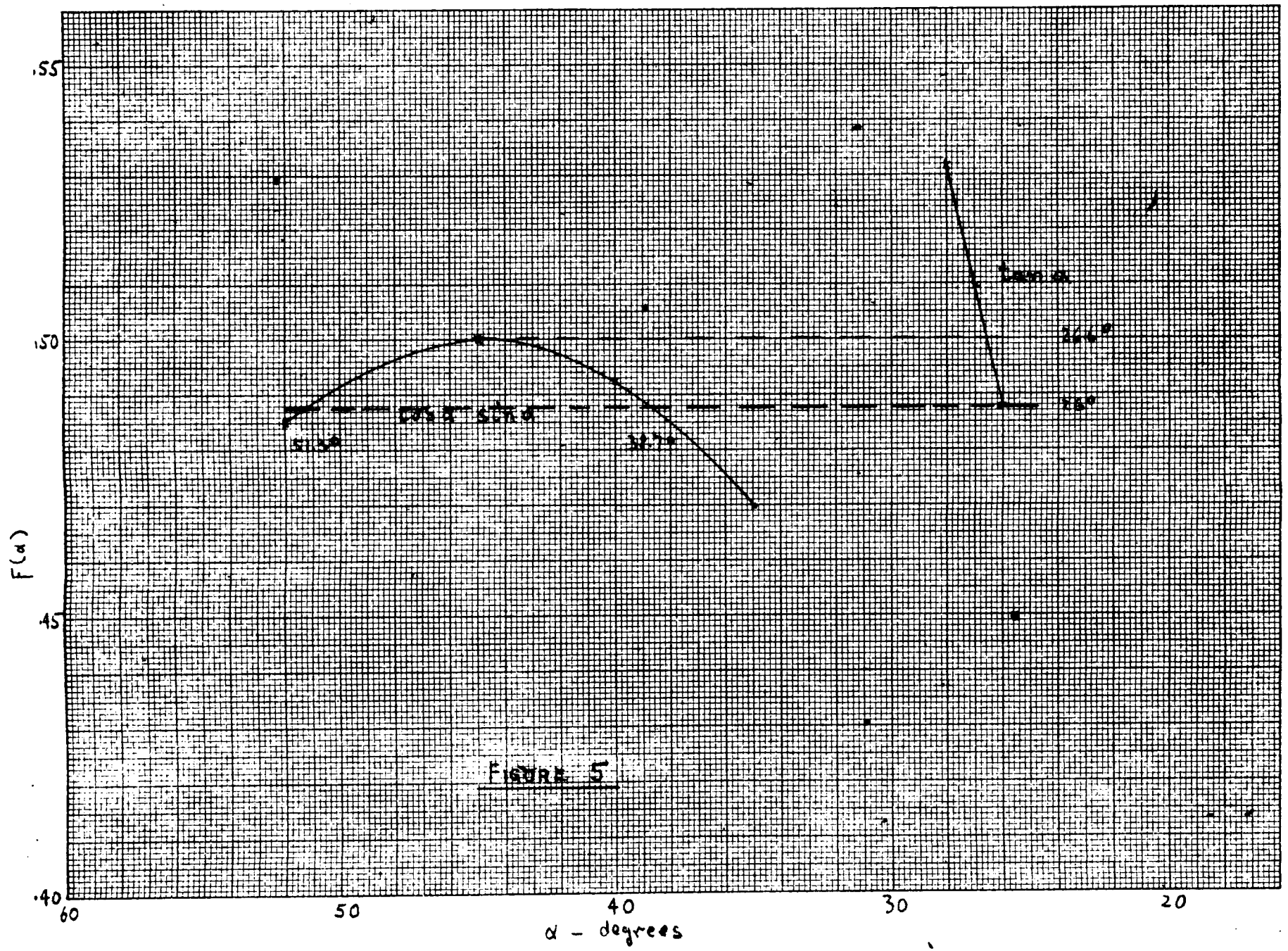


FIGURE 5

TABLE I

A	B	DA(1,1)	DA(2,1)	DA(1,2)	DA(2,2)	EMA	EMB
90.	90.	0.00891	0.00000	0.00000	0.00891	0.51044	0.51044
90.	85.	0.00893	0.	0.	0.00890	0.51148	0.50966
90.	80.	0.00898	0.	0.	0.00886	0.51464	0.50736
90.	75.	0.00908	0.	0.	0.00879	0.52008	0.50375
90.	70.	0.00922	0.	0.	0.00871	0.52809	0.49913
90.	65.	0.00941	0.	0.	0.00862	0.53911	0.49397
90.	60.	0.00967	0.	0.	0.00853	0.55379	0.48887
90.	55.	0.01000	0.	0.	0.00846	0.57306	0.48466
90.	50.	0.01044	0.	0.	0.00842	0.59832	0.48241
90.	45.	0.01102	0.	0.	0.00844	0.63161	0.48354
90.	40.	0.01180	0.	0.	0.00855	0.67609	0.49007
90.	35.	0.01286	0.	0.	0.00881	0.73675	0.50496
90.	30.	0.01435	0.	0.	0.00930	0.82202	0.53295
90.	26.	0.01602	0.	0.	0.00995	0.91776	0.57014
85.	90.	0.00890	0.00000	0.00000	0.00893	0.50966	0.51148
85.	85.	0.00891	0.00004	0.00004	0.00891	0.51276	0.51276
85.	80.	0.00897	0.00007	0.00007	0.00887	0.51802	0.51247
85.	75.	0.00906	0.00011	0.00011	0.00881	0.52568	0.51079
85.	70.	0.00920	0.00014	0.00015	0.00873	0.53609	0.50798
85.	65.	0.00939	0.00017	0.00020	0.00864	0.54978	0.50448
85.	60.	0.00965	0.00019	0.00026	0.00855	0.56754	0.50088
85.	55.	0.00998	0.00022	0.00032	0.00847	0.59048	0.49798
85.	50.	0.01042	0.00024	0.00040	0.00843	0.62026	0.49683
85.	45.	0.01100	0.00026	0.00051	0.00845	0.65937	0.49888
85.	40.	0.01177	0.00027	0.00065	0.00856	0.71166	0.50612
85.	35.	0.01283	0.00028	0.00085	0.00882	0.78341	0.52155
85.	30.	0.01431	0.00029	0.00115	0.00931	0.88544	0.54992
85.	26.	0.01597	0.00029	0.00152	0.00996	1.00190	0.58731
80.	90.	0.00886	0.00000	0.00000	0.00898	0.50736	0.51464
80.	85.	0.00887	0.00007	0.00007	0.00897	0.51247	0.51802
80.	80.	0.00893	0.00015	0.00015	0.00893	0.51978	0.51978
80.	75.	0.00902	0.00021	0.00022	0.00886	0.52955	0.52001
80.	70.	0.00916	0.00028	0.00031	0.00878	0.54222	0.51898
80.	65.	0.00934	0.00034	0.00040	0.00868	0.55841	0.51709
80.	60.	0.00960	0.00039	0.00051	0.00859	0.57902	0.51490
80.	55.	0.00992	0.00044	0.00064	0.00851	0.60533	0.51321
80.	50.	0.01036	0.00048	0.00080	0.00847	0.63927	0.51306
80.	45.	0.01093	0.00052	0.00101	0.00848	0.68371	0.51588
80.	40.	0.01169	0.00055	0.00128	0.00859	0.74319	0.52369
80.	35.	0.01273	0.00057	0.00167	0.00885	0.82516	0.53950
80.	30.	0.01419	0.00058	0.00226	0.00933	0.94270	0.56808
80.	26.	0.01583	0.00059	0.00299	0.00998	1.07844	0.60555

TABLE I (Cont'd.)

75.	90.	0.00879	0.00000	0.00000	0.00908	0.50375	0.52008
75.	85.	0.00881	0.00011	0.00011	0.00906	0.51079	0.52568
75.	80.	0.00886	0.00022	0.00021	0.00902	0.52001	0.52955
75.	75.	0.00895	0.00033	0.00033	0.00895	0.53176	0.53176
75.	70.	0.00909	0.00043	0.00045	0.00887	0.54651	0.53252
75.	65.	0.00927	0.00052	0.00059	0.00877	0.56498	0.53222
75.	60.	0.00951	0.00061	0.00075	0.00867	0.58815	0.53140
75.	55.	0.00983	0.00068	0.00094	0.00859	0.61748	0.53084
75.	50.	0.01025	0.00074	0.00118	0.00854	0.65510	0.53156
75.	45.	0.01081	0.00079	0.00148	0.00854	0.70425	0.53503
75.	40.	0.01155	0.00084	0.00189	0.00865	0.77008	0.54325
75.	35.	0.01257	0.00087	0.00246	0.00889	0.86110	0.55927
75.	30.	0.01400	0.00089	0.00332	0.00937	0.99247	0.58788
75.	26.	0.01561	0.00090	0.00439	0.01001	1.14549	0.62526
70.	90.	0.00871	0.00000	0.00000	0.00922	0.49913	0.52809
70.	85.	0.00873	0.00015	0.00014	0.00920	0.50798	0.53609
70.	80.	0.00878	0.00031	0.00028	0.00916	0.51898	0.54222
70.	75.	0.00887	0.00045	0.00043	0.00909	0.53252	0.54651
70.	70.	0.00899	0.00059	0.00059	0.00899	0.54915	0.54915
70.	65.	0.00917	0.00072	0.00077	0.00889	0.56961	0.55046
70.	60.	0.00940	0.00083	0.00098	0.00878	0.59502	0.55099
70.	55.	0.00971	0.00093	0.00123	0.00869	0.62693	0.55149
70.	50.	0.01012	0.00102	0.00153	0.00863	0.66767	0.55300
70.	45.	0.01066	0.00109	0.00192	0.00863	0.72080	0.55696
70.	40.	0.01137	0.00115	0.00245	0.00872	0.79197	0.56543
70.	35.	0.01236	0.00119	0.00319	0.00896	0.89062	0.58145
70.	30.	0.01374	0.00122	0.00430	0.00943	1.03371	0.60987
70.	26.	0.01530	0.00123	0.00567	0.01006	1.20150	0.64697
65.	90.	0.00862	0.00000	0.00000	0.00941	0.49397	0.53911
65.	85.	0.00864	0.00020	0.00017	0.00939	0.50448	0.54978
65.	80.	0.00868	0.00040	0.00034	0.00934	0.51709	0.55841
65.	75.	0.00877	0.00059	0.00052	0.00927	0.53222	0.56498
65.	70.	0.00889	0.00077	0.00072	0.00917	0.55046	0.56961
65.	65.	0.00906	0.00094	0.00094	0.00906	0.57263	0.57263
65.	60.	0.00928	0.00109	0.00119	0.00894	0.59988	0.57453
65.	55.	0.00957	0.00122	0.00149	0.00884	0.63389	0.57606
65.	50.	0.00996	0.00133	0.00186	0.00877	0.67713	0.57825
65.	45.	0.01047	0.00142	0.00233	0.00875	0.73340	0.58256
65.	40.	0.01116	0.00149	0.00295	0.00883	0.80876	0.59106
65.	35.	0.01210	0.00154	0.00384	0.00905	0.91342	0.60684
65.	30.	0.01343	0.00157	0.00517	0.00951	1.06579	0.63479
65.	26.	0.01494	0.00159	0.00680	0.01013	1.24538	0.67138

TABLE I (Cont'd.)

60.	90.	0.00853	0.00000	0.00000	0.00967	0.48887	0.55379
60.	85.	0.00855	0.00026	0.00019	0.00965	0.50088	0.56754
60.	80.	0.00859	0.00051	0.00039	0.00960	0.51490	0.57902
60.	75.	0.00867	0.00075	0.00061	0.00951	0.53140	0.58815
60.	70.	0.00878	0.00098	0.00083	0.00940	0.55099	0.59502
60.	65.	0.00894	0.00119	0.00109	0.00928	0.57453	0.59988
60.	60.	0.00915	0.00138	0.00138	0.00915	0.60322	0.60322
60.	55.	0.00943	0.00154	0.00172	0.00903	0.63880	0.60576
60.	50.	0.00979	0.00168	0.00214	0.00895	0.68386	0.60854
60.	45.	0.01028	0.00179	0.00268	0.00891	0.74236	0.61302
60.	40.	0.01093	0.00187	0.00339	0.00897	0.82066	0.62131
60.	35.	0.01182	0.00193	0.00440	0.00918	0.92953	0.63654
60.	30.	0.01309	0.00197	0.00591	0.00961	1.08846	0.66365
60.	26.	0.01452	0.00199	0.00776	0.01022	1.27653	0.69943
55.	90.	0.00846	0.00000	0.00000	0.01000	0.48466	0.57306
55.	85.	0.00847	0.00032	0.00022	0.00998	0.49798	0.59048
55.	80.	0.00851	0.00064	0.00044	0.00992	0.51321	0.60533
55.	75.	0.00859	0.00094	0.00068	0.00983	0.53084	0.61748
55.	70.	0.00869	0.00123	0.00093	0.00971	0.55149	0.62693
55.	65.	0.00884	0.00149	0.00122	0.00957	0.57606	0.63389
55.	60.	0.00903	0.00172	0.00154	0.00943	0.60576	0.63881
55.	55.	0.00929	0.00192	0.00192	0.00929	0.64238	0.64238
55.	50.	0.00963	0.00209	0.00238	0.00918	0.68854	0.64564
55.	45.	0.01009	0.00222	0.00298	0.00913	0.74832	0.65009
55.	40.	0.01069	0.00232	0.00376	0.00917	0.82825	0.65786
55.	35.	0.01153	0.00238	0.00486	0.00935	0.93940	0.67213
55.	30.	0.01273	0.00242	0.00651	0.00976	1.10200	0.69793
55.	26.	0.01408	0.00244	0.00852	0.01034	1.29497	0.73245
50.	90.	0.00842	0.00000	0.00000	0.01044	0.48241	0.59832
50.	85.	0.00843	0.00040	0.00024	0.01042	0.49683	0.62026
50.	80.	0.00847	0.00080	0.00048	0.01036	0.51306	0.63927
50.	75.	0.00854	0.00118	0.00074	0.01025	0.53156	0.65510
50.	70.	0.00863	0.00153	0.00102	0.01012	0.55300	0.66767
50.	65.	0.00877	0.00186	0.00133	0.00996	0.57825	0.67713
50.	60.	0.00895	0.00214	0.00168	0.00979	0.60854	0.68386
50.	55.	0.00918	0.00238	0.00209	0.00963	0.64564	0.68855
50.	50.	0.00950	0.00258	0.00258	0.00950	0.69221	0.69221
50.	45.	0.00991	0.00274	0.00322	0.00941	0.75231	0.69637
50.	40.	0.01048	0.00285	0.00405	0.00942	0.83251	0.70320
50.	35.	0.01126	0.00292	0.00522	0.00957	0.94400	0.71596
50.	30.	0.01237	0.00296	0.00695	0.00995	1.10725	0.73977
50.	26.	0.01364	0.00297	0.00907	0.01051	1.30140	0.77244

TABLE I (Cont'd.)

45.	90.	0.00844	0.00000	0.00000	0.01102	0.48354	0.63162
45.	85.	0.00845	0.00051	0.00026	0.01100	0.49888	0.65937
45.	80.	0.00848	0.00101	0.00052	0.01093	0.51588	0.68371
45.	75.	0.00854	0.00148	0.00079	0.01081	0.53503	0.70425
45.	70.	0.00863	0.00192	0.00109	0.01066	0.55696	0.72080
45.	65.	0.00875	0.00233	0.00142	0.01047	0.58256	0.73340
45.	60.	0.00891	0.00268	0.00179	0.01028	0.61302	0.74237
45.	55.	0.00913	0.00298	0.00222	0.01009	0.65009	0.74833
45.	50.	0.00941	0.00322	0.00274	0.00991	0.69636	0.75231
45.	45.	0.00979	0.00340	0.00340	0.00979	0.75584	0.75584
45.	40.	0.01031	0.00352	0.00426	0.00976	0.83499	0.76117
45.	35.	0.01103	0.00359	0.00546	0.00987	0.94488	0.77164
45.	30.	0.01206	0.00362	0.00724	0.01021	1.10577	0.79250
45.	26.	0.01323	0.00362	0.00941	0.01074	1.29733	0.82244
40.	90.	0.00855	0.00000	0.00000	0.01180	0.49007	0.67609
40.	85.	0.00856	0.00065	0.00027	0.01177	0.50612	0.71156
40.	80.	0.00859	0.00128	0.00055	0.01169	0.52369	0.74319
40.	75.	0.00865	0.00189	0.00084	0.01155	0.54325	0.77008
40.	70.	0.00872	0.00245	0.00115	0.01137	0.56543	0.79197
40.	65.	0.00883	0.00295	0.00149	0.01116	0.59106	0.80876
40.	60.	0.00897	0.00339	0.00187	0.01093	0.62131	0.82067
40.	55.	0.00917	0.00376	0.00232	0.01069	0.65786	0.82825
40.	50.	0.00942	0.00405	0.00285	0.01048	0.70319	0.83251
40.	45.	0.00976	0.00426	0.00352	0.01031	0.76117	0.83500
40.	40.	0.01023	0.00440	0.00440	0.01023	0.83802	0.83802
40.	35.	0.01088	0.00446	0.00561	0.01029	0.94443	0.84505
40.	30.	0.01182	0.00447	0.00738	0.01057	1.10034	0.86150
40.	26.	0.01289	0.00444	0.00954	0.01105	1.28532	0.88737
35.	90.	0.00881	0.00000	0.00000	0.01286	0.50496	0.73676
35.	85.	0.00882	0.00085	0.00028	0.01283	0.52155	0.78342
35.	80.	0.00885	0.00167	0.00057	0.01273	0.53950	0.82516
35.	75.	0.00889	0.00246	0.00087	0.01257	0.55927	0.86110
35.	70.	0.00896	0.00319	0.00119	0.01236	0.58145	0.89063
35.	65.	0.00905	0.00384	0.00154	0.01210	0.60684	0.91342
35.	60.	0.00918	0.00440	0.00193	0.01182	0.63654	0.92953
35.	55.	0.00935	0.00486	0.00238	0.01153	0.67213	0.93941
35.	50.	0.00957	0.00522	0.00292	0.01126	0.71596	0.94400
35.	45.	0.00987	0.00546	0.00359	0.01103	0.77164	0.94488
35.	40.	0.01029	0.00561	0.00446	0.01088	0.84505	0.94443
35.	35.	0.01087	0.00565	0.00565	0.01087	0.94627	0.94628
35.	30.	0.01171	0.00561	0.00738	0.01108	1.09387	0.95605
35.	26.	0.01269	0.00553	0.00947	0.01150	1.26939	0.97571

TABLE I (Cont'd.)

30.	90.	0.00930	0.00000	0.00000	0.01435	0.53295	0.82202
30.	85.	0.00931	0.00115	0.00029	0.01431	0.54992	0.88544
30.	80.	0.00933	0.00226	0.00058	0.01419	0.56809	0.94270
30.	75.	0.00937	0.00332	0.00089	0.01400	0.58788	0.99247
30.	70.	0.00943	0.00430	0.00122	0.01374	0.60987	1.03372
30.	65.	0.00951	0.00517	0.00157	0.01343	0.63479	1.06579
30.	60.	0.00961	0.00591	0.00197	0.01309	0.66366	1.08847
30.	55.	0.00976	0.00651	0.00242	0.01273	0.69793	1.10201
30.	50.	0.00995	0.00695	0.00296	0.01237	0.73977	1.10725
30.	45.	0.01021	0.00724	0.00362	0.01206	0.79249	1.10577
30.	40.	0.01057	0.00738	0.00447	0.01182	0.86150	1.10004
30.	35.	0.01108	0.00738	0.00561	0.01171	0.95605	1.09388
30.	30.	0.01182	0.00726	0.00726	0.01182	1.09321	1.09322
30.	26.	0.01269	0.00709	0.00923	0.01216	1.25579	1.10308
26.	90.	0.00995	0.00000	0.00000	0.01602	0.57015	0.91777
26.	85.	0.00996	0.00152	0.00029	0.01597	0.58732	1.00191
26.	80.	0.00998	0.00299	0.00059	0.01583	0.60555	1.07845
26.	75.	0.01001	0.00439	0.00090	0.01561	0.62526	1.14550
26.	70.	0.01006	0.00567	0.00123	0.01530	0.64698	1.20151
26.	65.	0.01013	0.00680	0.00159	0.01494	0.67138	1.24539
26.	60.	0.01022	0.00776	0.00199	0.01452	0.69943	1.27654
26.	55.	0.01034	0.00852	0.00244	0.01408	0.73246	1.29499
26.	50.	0.01051	0.00907	0.00297	0.01364	0.77244	1.30141
26.	45.	0.01074	0.00941	0.00362	0.01323	0.82244	1.29734
26.	40.	0.01105	0.00954	0.00444	0.01289	0.88737	1.28534
26.	35.	0.01150	0.00947	0.00553	0.01269	0.97571	1.26940
26.	30.	0.01216	0.00923	0.00709	0.01269	1.10307	1.25580
26.	26.	0.01294	0.00894	0.00894	0.01294	1.25334	1.25335

APPENDIX D

ATS SOLAR TORQUE

The solar torques on the main vehicle are derived for numerical integration where all shadowing and up to N-multiple specular reflections are considered on the main body with the effects due to the scallops, the rocket nozzle and recessed ends all considered. The diffuse reflections may be included for all convex external surfaces since no multiple reflections occur for this condition; however this analysis does not include the multiple diffuse reflections that occur in the ends. The system numerical integration was chosen due to the advantages: 1) Multiple reflections and shadowing produce quite complicated integrals; which, if all are integrable would yield some long computational equations, 2) A far more complex system may be analyzed than possible with the many assumptions needed to explicitly find the torque expressions, 3) The variation of the specular reflection with angle of incidence may also be considered without approximation. Although this is a numerical integration, it is doubtful that the computer time is greater than that needed for a comparable program of explicit torque expressions.

NOMENCLATURE

English

D_1, D_2 : The lengths of the main vehicle on each side of the x_s, y_s plane projected on the sun grid plane normal to s.

D_3 : Distance from the vehicle z_s axis to the midpoint of a scallop.

h_1 : Distance from the $y_s z_s$ plane to the $+z_s$ plane edge of the vehicle

h_2 : Length along z_s of scallops

h_3 : Distance along z_s from the $x_s y_s$ plane to the plane dividing the smaller and larger radii of the main vehicle.

h_4 : Distance from $x_s y_s$ plane to $-z_s$ end of the smaller cylinder of the main vehicle.

h_N : Distance the big end of the rocket nozzle is from the $x_s y_s$ plane measured along $-z_s$.

H : Distance the $+z_s$ cover end plane is from the $x_s y_s$ plane.

i_g, j_g: The number of squares along the $+x_{ss}$ and $+y_{ss}$ axes respectively from the $-x_{ss}$, $-y_{ss}$ corner of the sun grid. This is the area of integration

j: The number of the scallop in consideration

k: The number of the scallop closest to the sun physically.

k_s: The number of reflections (multiple)

k_z: The general quantity to tell the z_s coordinate of a disk (plane) parallel to the $x_s y_s$ plane to be reflected from.

m_1, m_2: The number of squares along the x_{ss} and y_{ss} sides of the sun grid which defines the grid division.

M_c: The slope of the rocket nozzle cone where $M_c < 0$. (If $M_c = 0$ the cone frustum would then be a cylinder).

n_o, n': The index of refraction of outer space and of the surface respectively.

r_1: Radius of the larger cylinder of the main vehicle on the $+z_s$ half.

r_2 : The maximum of r_m and r_1 thus defining the size of the sun grid.

r_3 : Radius of the smaller cylinder of the main vehicle

r_m : Radius of the cylinder that contains all scallops as defined by Equation (18).

r_{ms}: Distance from a general point on a scallop to the main vehicle axis.

r_N: Radius of the open end of the rocket nozzle.

r_{Nd}: Radius of the rocket nozzle where it intersects the plane of the shielding disk.

r_{Ndz}: Radius of the cross-section circle of the nozzle cone at an arbitrary point.

r_s: Radius of the scallop surfaces.

s_1, s_2, s_3: Light vector in $x_s y_s z_s$ components in general intersection equations.

s_{x1}, s_{y1}, s_{z1}: Unit vector away from the sun in x_1, y_1, z_1 components

U_1, U_2, U_3: Coordinates in x_s, y_s, z_s of the intersection of a reflected beam of light with the next surface it strikes.

x_1, y_1, z_1: Main body coordinates

x_s, y_s, z_s: Coordinate system with the sun $\bar{s}$ in the $x_s y_s$ plane

x_{ss}, y_{ss}, z_{ss}: Coordinate system used to find the sun grid

x_{cB}, y_{cB}, z_{cB}: Coordinates of the center of mass in $x_1, y_1 z_1$ components

Greek

α : Absorption coefficient subscripted to indicate the surface. The number of primes indicates the properties if the sun has been previously reflected this number of times. See $\rho_{si}^{[k]}$

δ : Ratio of diffuse to specular reflection

η : The angle of incidence of light on an incremental surface

η_c : The angle the cone nozzle incremental normal is from the $x_s y_s$ plane.

η' : The angle of refraction of an incremental area.

θ_1 : Angle measured at the vehicle axis including one full scallop and half the gap between on each side.

ξ : The angle between the $x_s z_s$ plane to the center of the k^{th} scallop.

α : The diffuse reflection coefficient subscripted and primed as for $\rho_{si}^{[k]}$

ρ_o : Solar flux pressure constant

$\rho_{si}^{[k]}$: ρ_s for each surface indicated by i subscript after k previous reflections.

ρ_s : Specular reflection coefficient (See $\rho_{si}^{[k]}$)

σ : General angle measured positively around $+z_s$ axis from $+x_s$ axis.

σ_a, σ_l : The angles the sun $\bar{s}$ makes with $-z_1$ axis and around $+z_1$ axis measuring from x_1 respectively.

ψ : Parameter used to find the light $\bar{S}_{ks}$ intersection vector $\vec{I}$ with a given surface of revolution.

Vectors

$\vec{c}$: Vector from the coordinate origin to the center of mass.

$\vec{dF}$: Incremental force vector due to photons striking an incremental area.

$\vec{I}$: The vector from the coordinate origin to the intersection of a reflected beam with its intercepting surface.

$\vec{\Delta L}$: Incremental torque vector of solar torque due to a small area used in the numerical integration.

$\vec{L}_T$: Instanteous torque vector in $x_1 y_1 z_1$ components in the process of numerical integration. At the end of the integration for a given attitude, $\vec{L}_T$ becomes the desired solar torque of the overall vehicle (less rods).

$\bar{n}$: Surface normal unit vector drawn such that $\bar{S}_{ks} \cdot \bar{n} > 0$ if the surface is illuminated by $\bar{S}_{ks}$.

Subscripts

Cl : Pertaining to the circular cylindrical surface of radius r_1 for light striking the outside surface only.

ClP : Same as Cl except for light striking the inside surface (at the end) only.

C3 : Pertaining to the circular cylindrical surface of radius r_3

d : Pertaining to the plane disk around the rocket nozzle covering that end (around the nozzle).

e : Pertaining to the disk recessed in the Cl cylinder

j : Pertaining to a general j^{th} scallop when light strikes its concave surface.

jp : Same as j except for light striking the convex scallop surface.

k_s : Indicating the number of previous reflections.

N : Pertaining to an imaginary absorbing disk over the open end of the nozzle.

Nd : Pertaining to the outer surface of the cone frustum of the rocket nozzle.

Si : A general subscript to denote any of the surface subscripts of the vehicle.

Figure 1 places the vehicle in its coordinate system. The sun is likewise defined in this coordinate system, by a unit vector away from the sun. The torques are drawn about a three axis off-set vector $\vec{c}$. In x_1y_1,z_1 coordinates these vectors are written*

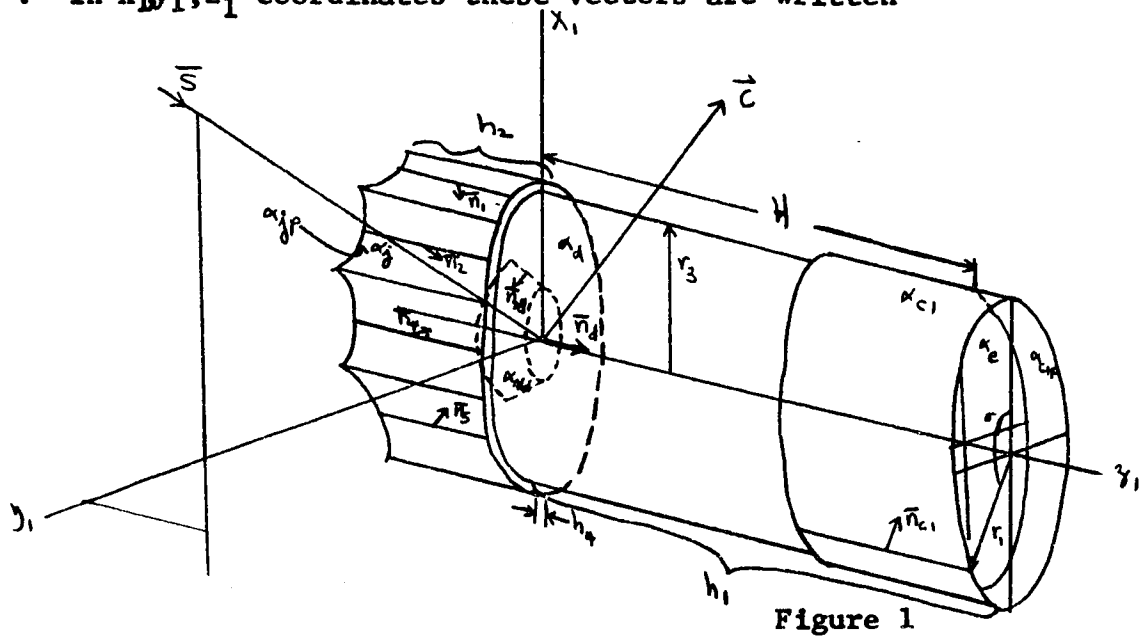


Figure 1

$$\bar{s} = \begin{pmatrix} s_{x_1} \\ s_{y_1} \\ s_{z_1} \end{pmatrix}_1 \qquad \vec{c} = \begin{bmatrix} x_{cB} \\ y_{cB} \\ z_{cB} \end{bmatrix}_1 \tag{1}$$

We assume the vehicle is composed of fourteen mathematically different surfaces but of these, there are nine (eight scallops and a cylinder extremedy) illuminated on the back. The unit normal vectors into the areas are respectively:

$\bar{n}_e$ for the thermal shield at the circular end, $\bar{n}_d$ for the ring disk around the conical nozzle, $\bar{n}_{c_1}$ for the larger cylindrical surface, $\bar{n}_{Nd}$ for the normal into the conical surface and $\bar{n}_N$ for an imaginary absorbing disk over the open end of the nozzle, and $\bar{n}_1$ to $\bar{n}_8$ for the individual scalloped surfaces starting numbering with the

* The sub 1 on the right side indicates the components are with respect to x_1, y_1, z_1 coordinates.

one on the positive x_1 axis and numbering counterclockwise as seen from $+z_1$ axis. The normals for the curved surfaces represent normals for arbitrary incremental areas. Note, the x_1y_1 plane lies in the plane of the extreme edge of all scallops and the other extreme of the $\bar{n}_{c3}$ smaller cylinder is h_4 from the x_1y_1 plane leaving the physical gap.

The force on an incremental area is

$$\vec{d^2F} \quad \rho_0 \prod_{i=S1}^{N_r} \rho_{Si}^{[N]} \, d^2A \, (\bar{S}\cdot\bar{n})\left[(\alpha_{S_{N_r}} \rho_{d_{S_{N_r}}})\bar{S} + (2\rho_{S_{S_{N_r}}} \bar{S}\cdot\bar{n} + \tfrac{2}{3}\rho_{d_{S_{N_r}}})\bar{n}\right] \qquad (2)$$

where $\rho_{S0} = 1$ for direct illumination (i = 0), and ρ_{Si} are the indirect illumination reflection coefficients determining the light of this force.

The lever arm for each incremental force on its area, denoted by $\vec{\ell}$, with an appropriate subscript, is drawn from the vehicle center of mass, $\vec{c}$, which the torques are about, to the incremental area. The torque is then

$$\vec{L} = \Sigma \iint \vec{\ell} \times d^2\vec{F} \qquad (3)$$

where integration is over each respective surface and the summation totals the components for all different surfaces. The approach to the integration is numerical due to the complicity of the geometry.

The two cylindrical outside surfaces are assumed to have no shadowing and of course have no multiple reflections. Integrations are simplified by converting to a coordinate system with the sun in a principal plane. We therefore write $\bar{S}$,

$$\left.\begin{aligned} \bar{S} &= \begin{pmatrix} S_{x1} \\ S_{y1} \\ S_{z1} \end{pmatrix} = \begin{pmatrix} -\sin\sigma_a \cos\sigma_\ell \\ -\sin\sigma_\ell \sin\sigma_a \\ -\cos\sigma_a \end{pmatrix}, \\ \sigma_a &= \cos^{-1}(-S_{z1}) \quad , \; 0 \le \sigma_a \le \pi \\ \sigma_\ell &= \tan^{-1}\frac{-S_{y1}}{-S_{x1}} \quad , \; 0 \le \sigma_\ell < 2\pi \end{aligned}\right\} \qquad (4)$$

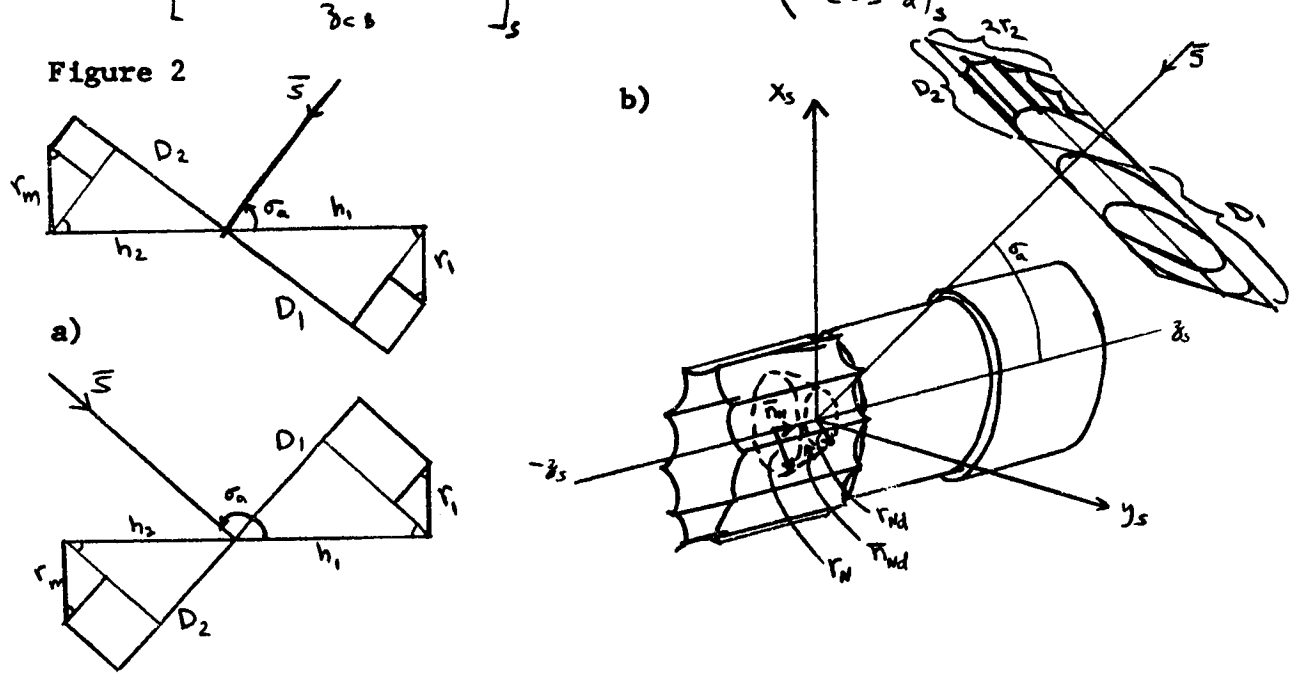
The new coordinate system is formed by rotating x_1 and y_1 about z_1 by σ_l so the new coordinate system, x_s, y_s, z_s has $\bar{S}$ in the $y_s z_s$ plane. Then

$$\begin{bmatrix} x_s \\ y_s \\ z_s \end{bmatrix}_s = \begin{pmatrix} \cos\sigma_l & \sin\sigma_l & 0 \\ -\sin\sigma_l & \cos\sigma_l & 0 \\ 0 & 0 & 1 \end{pmatrix} \begin{bmatrix} x_1 \\ y_1 \\ z_1 \end{bmatrix}_1 \tag{5}$$

Figure 2-b shows the vehicle in x_s, y_s, z_s with its torque center $\vec{c}$ and the sun, $\bar{S}$. From (1), (4) and (5), $\vec{c}$, and $\bar{S}$ in sun coordinates are

$$\vec{C} = \begin{bmatrix} x_{cB}\cos\sigma_l + y_{cB}\sin\sigma_l \\ -x_{cB}\sin\sigma_l + y_{cB}\cos\sigma_l \\ z_{cB} \end{bmatrix}_s \qquad \bar{S} = \begin{pmatrix} -\sin\sigma_a \\ 0 \\ -\cos\sigma_a \end{pmatrix}_s \tag{6}$$

Figure 2



All the light from the sun illuminating the entire cylindrical body passes through a rectangular segment of a plane normal to $\bar{S}$ as shown in Figure 2-b choose r_2 the maximum of r_1 and r_m,

$$r_2 = \max(r_1, r_m) \tag{7}$$

where r_1 is the radius of the cylinder at the $+\hat{z}_s$ end and r_m is the radius of a cylinder circumscribing the scallops whose radius is determined by the intersection of adjacent scallop surfaces circularly extended, (See Equation (18)). For the numerical integration, this plane normal to $\bar{S}$ is the surface to be integrated over. We section by dividing the one side by m_1, thus $\frac{D_1+D_2}{m_1}$ is an incremental length and dividing the other side $\frac{2r_2}{m_2}$ where now an incremental area on this plane is

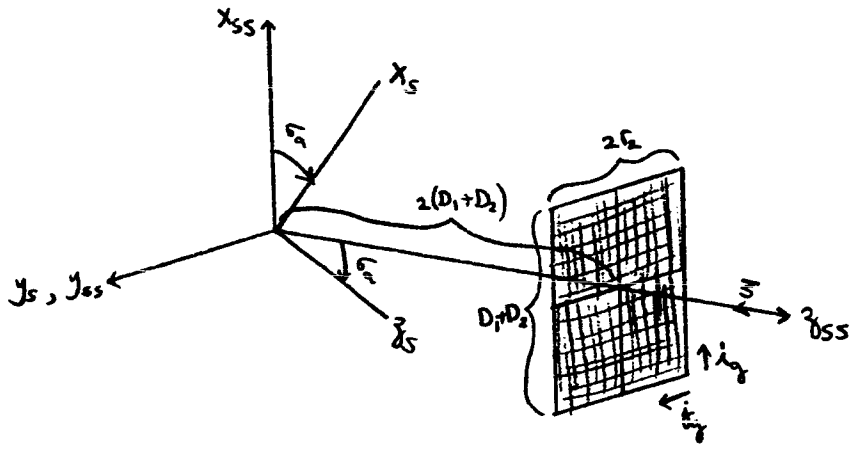
$$\Delta A = \frac{2r_2 (D_1+D_2)}{m_1 m_2} \tag{8}$$

Figure 2-a indicates the D_1 and D_2 functions are defined as

$$\left.\begin{aligned} D_1 &= h_1 \sin\sigma_a + r_1 |\cos\sigma_a| \\ D_2 &= h_2 \sin\sigma_a + r_m |\cos\sigma_a| \end{aligned}\right\} \tag{9}$$

The coordinates at the center of each ΔA are ound by writing $\bar{S}$ in a coordinate system such that $\bar{S}$ is along an axis, as in Figure 3.

Figure 3



This transformation is

$$\begin{bmatrix} x_s \\ y_s \\ z_s \end{bmatrix} = \begin{pmatrix} \cos\sigma_a & 0 & \sin\sigma_a \\ 0 & 1 & 0 \\ -\sin\sigma_a & 0 & \cos\sigma_a \end{pmatrix} \begin{bmatrix} x_{ss} \\ y_{ss} \\ z_{ss} \end{bmatrix} \tag{10}$$

Let the grid plane be labeled starting at the most negative x_{ss} and y_{ss} corner then the coordinates at the center of the i_g, j_g^{th} surface are

$$x_{ss} = -D_1 + \frac{D_1+D_2}{m_1}\left(i_g+\frac{1}{2}\right) \qquad y_{ss} = \frac{2r_2}{m_2}\left(j_g+\frac{1}{2}\right) - r_2 \qquad z_{ss} = 2(D_1+D_2) \tag{11}$$

thus we define a sun grid in coordinates x_{ss}, y_{ss}, z_{ss} defined by rotating x_s, y_s, z_s about y_s by $(+\sigma_a)$ thus putting the unit vector away from the sun, along $-z_{ss}$ axis, defined by Equation (10). The coordinates in (11) transformed by (10) are

$$\left.\begin{aligned} x_s &= \left[\frac{D_1+D_2}{m_1}\left(i_g+\frac{1}{2}\right)-D_1\right]\cos\sigma_a + 2(D_1+D_2)\sin\sigma_a \\ y_s &= \frac{2r_2}{m_2}\left(j_g+\frac{1}{2}\right) - r_2 \\ z_s &= -\left[\frac{D_1+D_2}{m_1}\left(i_g+\frac{1}{2}\right)-D_1\right]\sin\sigma_a + 2(D_1+D_2)\cos\sigma_a \end{aligned}\right\} \tag{12}$$

Consider the scallops in the x_s, y_s, z_s coordinates as shown in Figure 4-a with the k^{th} surface closest to the sun, with its mid section ξ from the $x_s z_s$ plane where

$$0 \le \xi < \theta_1 = \frac{2\pi}{N} \tag{13}$$

where ξ is determined from σ_l by

$$k\theta_1 - \sigma_l = \xi \tag{14}$$

Therefore the k integer is defined from (13) and (14) as

$$\frac{\sigma_l}{\theta_1} \le k < 1 + \frac{\sigma_l}{\theta_1} \tag{15}$$

If σ_I is the angle around the z_s axis (from the x_s axis) to the intersection with the sun vector $\bar{S}$ then the j^{th} surface that this boom would most likely hit is

$$\frac{\sigma_I - \xi}{\theta_1} + k - \frac{1}{2} \le j_g < \frac{\sigma_I - \xi}{\theta_1} + k + \frac{1}{2} \tag{15a}$$

On the other hand, if j is known, then we may find σ the angle around z_s axis from x_s to the center of the j^{th} scallop from Figure 4-a or (15a)

$$\sigma = (j-k)\theta_1 + \zeta \tag{15b}$$

As shown in Figure 4-b, ϕ is the scallop included angle measured from its midpoint counterclockwise. The range of ϕ over its scallop is

$$-\phi_m \leq \phi \leq \phi_m \quad \text{or} \quad |\phi_m| \geq \phi \tag{16}$$

Since the scallops are separated slightly a looser geometry is needed. Considering the scallops to be circularly extended until adjacent ones intersect, we define a circumscribed circular cylinder of radius r_m, as mentioned before.

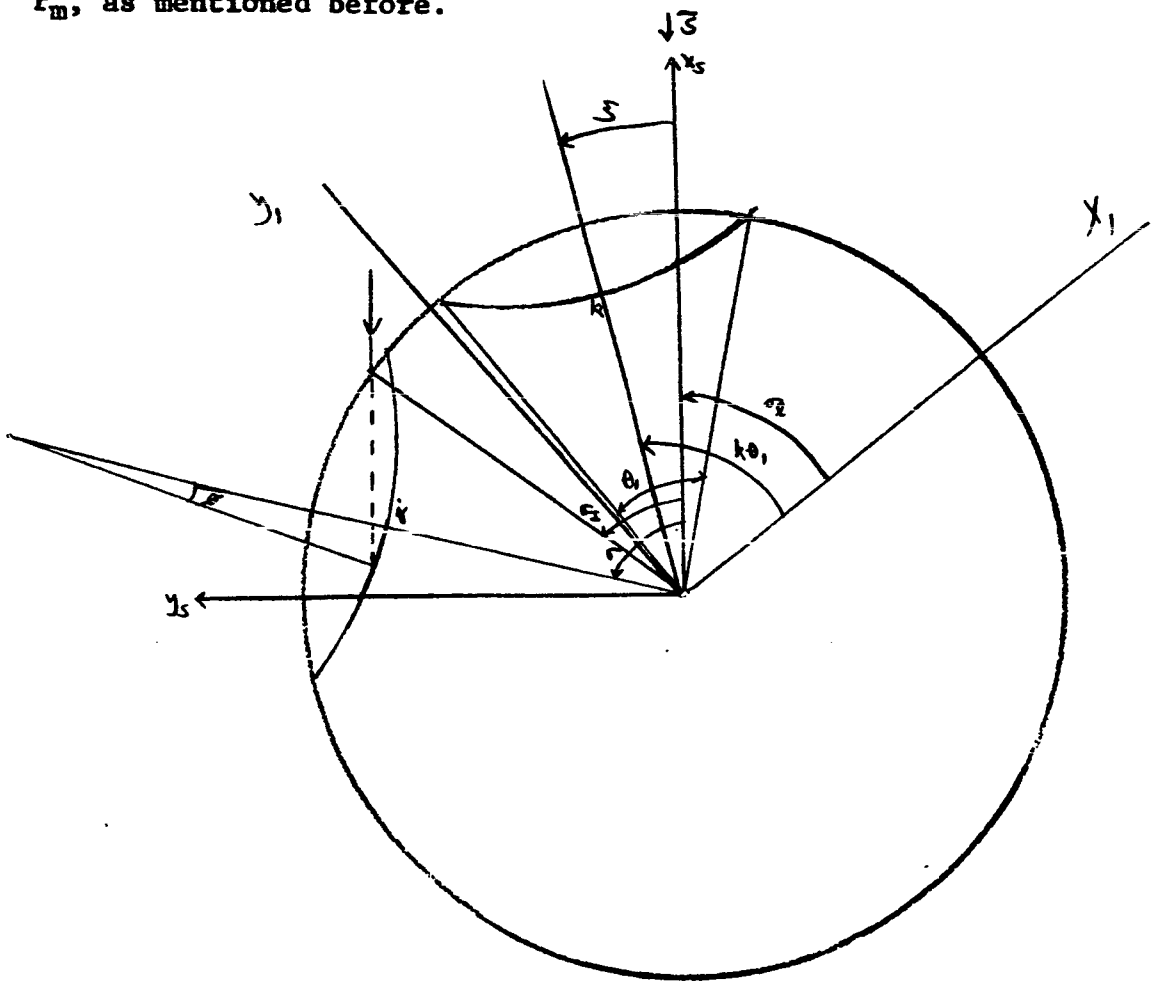
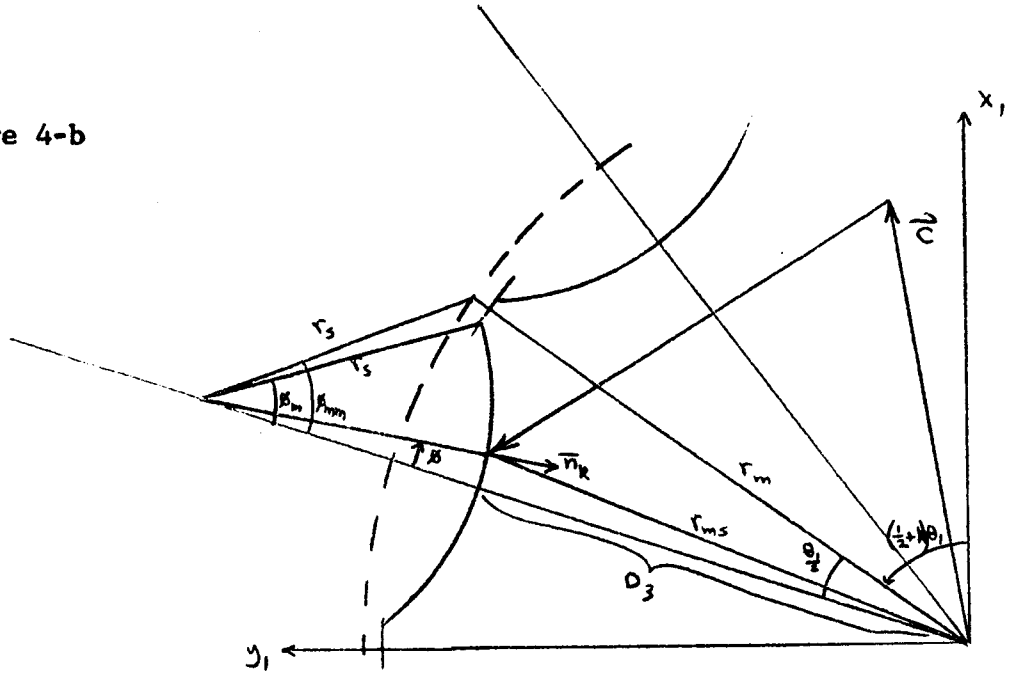


Figure 4-a

Figure 4-b



Assuming we know D_3, the distance from the vehicles central axis to the midpoint of each scallop and ϕ_m, the maximum half angle subtended by the scallop, ϕ_{mm} may be found by the low of sines

$$\frac{\pi}{2} < \phi_{mm} = \pi - \frac{\theta_1}{2} - \sin^{-1}\left(\frac{D_3+r_s}{r_s}\sin\frac{\theta_1}{2}\right) < 0 \qquad (17)$$

The inequality limits us to a unique solution. If the height of the triangle is imagined to be drawn normal to r_m we see

$$r_m = (r_s+D_3)\cos\frac{\theta_1}{2} - r_s\cos\phi_{mm} \qquad (18)$$

Also from the law of cosines

$$r_{ms} = \sqrt{r_s^2 + (D_3+r_s)^2 - 2r_s(D_3+r_s)\cos\phi} \qquad (18a)$$

The inside surfaces on either end of this vehicle and the outside surfaces of the scallops are more involved since these represent concave surfaces which give rise to shadowing and multiple reflections, both specular and diffuse.

In general multiple specular reflections with shadowing are the result of at least three (not necessarily different) surfaces and the law of reflection. First the light from the sun, $\bar{s}$ partially illuminates a surface, $f(x_f, y_f, z_f) = 0$ where a three dimensional curved (or straight) line $\mathcal{L}(x_\ell, y_\ell, z_\ell)$ acts as a shadow line, on one side of which no light reaches the f surface. Line $\mathcal{L}$ is either formed by the physical edges and/or the sun tangent curve on a shadowing surface. The light may then be specularly reflected, $\bar{s}_1$ where $\bar{s}_1$ depends on the f surface normal vector. Figure 5 illustrates

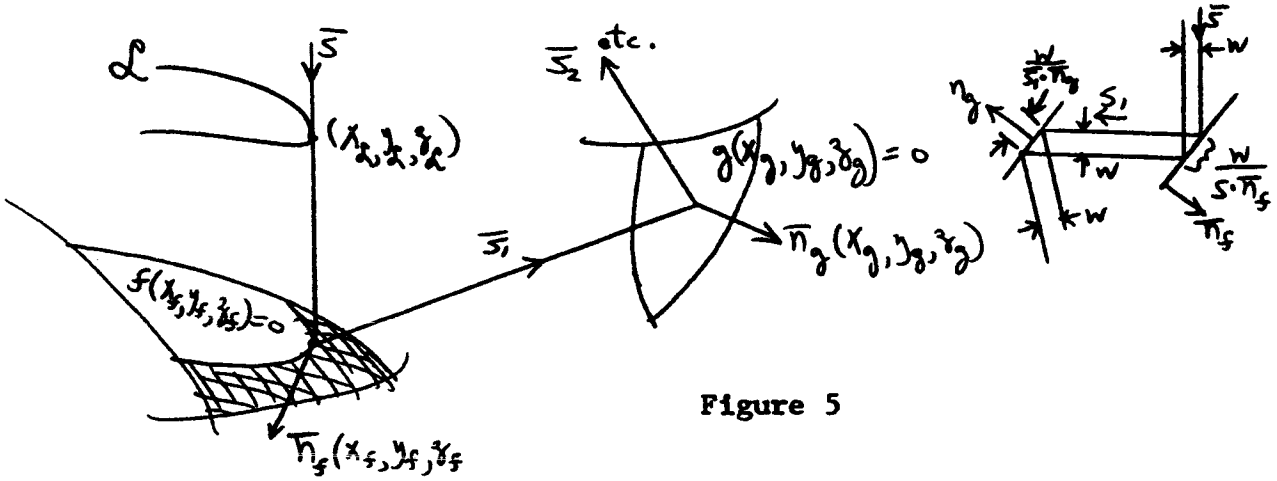


Figure 5

these surfaces with their arbitrary points. If (x_f, y_f, z_f) is an arbitrary point on the f surface, its normal vector, $\bar{n}_f$ is

$$\bar{n}_f = N_f \begin{bmatrix} f_{xf} \\ f_{yf} \\ f_{zf} \end{bmatrix} \tag{19}$$

where the subscripted f's represent the partial derivative of f with respect to the subscripting variable, and N_f normalizes $\bar{n}_f$ so $|\bar{n}_f| = 1$ and is away from the sun. To find the reflected $\bar{s}_1$ vector we write $\bar{s}$ in components parallel to the surface normal and to the surface itself:

$$\bar{s} = (\bar{s}\cdot\bar{n}_f)\bar{n}_f + [\bar{s} - (\bar{s}\cdot\bar{n}_f)\bar{n}_f]$$

The reflection $\bar{s}_1$ has the same surface component but the negative normal component, thus

$$s_1 = -(\bar{s}\cdot\bar{n}_f)\bar{n}_f + [\bar{s} - (\bar{s}\cdot\bar{n}_f)\bar{n}_f]$$

or

$$\bar{s}_1 = \bar{s} - 2(\bar{s}\cdot\bar{n}_f)\bar{n}_f \quad \text{if} \quad \bar{s}\cdot\bar{n}_f > 0 \tag{20}$$

If $\bar{s}\ \bar{n} \leq 0$ no reflection takes place from this side of the surface. Now the beam of light leaving some point on f travels along $\bar{s}_1$ to its intersection on g surface, thus an analytic description of this line is

$$\frac{x_g - x_f}{s_{1x1}} = \frac{y_g - y_f}{s_{1y1}} = \frac{z_g - z_f}{s_{1z1}} \tag{21}$$

so

$$y_g = y_f + \frac{s_{1y1}}{s_{1x1}}(x_g - x_f)$$
$$z_g = z_f + \frac{s_{1z1}}{s_{1x1}}(x_g - x_f) \tag{22}$$

then x_g is found from

$$g\left[x_g, y_f + \frac{s_{1y1}}{s_{1x1}}(x_g - x_f), z_f + \frac{s_{1z1}}{s_{1x1}}(x_g - x_f)\right] = 0 \tag{23}$$

Thus, a beam of light is reflected from a point (to be integrated) on surface f at (x_f, y_f, z_f) to a point on surface g determined by equations (23) and (22) respectively. Now, since the surface, g is known, its normal,

$$\bar{n}_g = N_g \begin{bmatrix} g_{xg} \\ g_{yg} \\ g_{zg} \end{bmatrix} \tag{24}$$

may be determined as in equation (19). Now $\bar{s}_2$ is found from rewriting equation (20) to be

$$\bar{s}_2 = \bar{s}_1 - 2(\bar{s}_1\cdot\bar{n}_g)\bar{n}_g \quad \text{if} \quad \bar{s}\cdot\bar{n}_f > 0 \text{ and } \bar{s}_1\cdot\bar{n}_g > 0$$

Equations (22) and (23) are then written for the new surface (if there is one). If a reflected beam fails to strike another surface, its torque computation halts and a new beam on f is chosen. This is the integration over the illuminated portion of f. The shadow line on from f is determined by rewriting (23) and (22) as

$$\left.\begin{aligned} & f\left[x_f, y_g + \frac{S_{y1}}{S_{x1}}(x_f - x_g), z_g + \frac{S_{z1}}{S_{x1}}(x_f - x_g)\right] = 0 \\ & y_f = y_g + \frac{S_{y1}}{S_{x1}}(x_f - x_g) \\ & z_f = z_g + \frac{S_{z1}}{S_{x1}}(x_f - x_g) \end{aligned}\right\} \quad (25)$$

The force vector ducts light reflected from f is multiplied by the specular reflection coefficient for surface f and in general, the solar properties of the reflected beam on surface g are considered different from those if $\bar{s}$ illuminates g directly. Often a surface, illuminated by a light vector, may be such that the vector mathematically intersects the surface more than once. This is the case for a circular cylinder if a vector intersects it and is not tangent to it. For surfaces such that there are more than two intersections, a more elegant procedure is needed to determine which intersection is actually sought. However, here we deal with planes which have unique intersections and simple surfaces of revolution with at most two intersections. There are two simple means to determine which intersection.

Let the intersection point to be tested as a physical possibility be represented by the vector $\vec{I}$. Also let the light vector be $\bar{s}_{k_s}$ where k_s may be zero for direct illumination or k_s represents the number of previous reflections. And let the surface normal vector at $\vec{I}$ be $\bar{n}$ where we now assume we know whether the light is inside or outside of the closed surface. This determines $\bar{n}$ to be out of or into the surface respectively to make the desired choice give

$$\bar{s} \cdot \bar{n} > 0 \quad (25a)$$

Another method is needed if the light vector originates inside a closed surface. Mathematically it will determine two intersections, one in the direction of the light and the other in the opposite direction. To rule out the second possibility we impose the condition

$$(\vec{I} - \vec{u}) \cdot \bar{s} > 0 \quad (25b)$$

where $\vec{u}$ represents the position vector of the light source inside the closed surface. We may note if the light is originated on a circular cylindrical surface to reflect on the same surface that the best test is (25a).

To compare the relative magnitudes of the incremental areas on each surface, consider light of area dA directly from the sun. Then the area this light illuminates on surface ζ of Figure 5 is $dA/\bar{n}_\zeta \cdot \bar{s}$. Its reflection then again has the cross-sectional area dA. Then the area illuminated on the g surface is $W/\bar{s}_1 \cdot \bar{n}_g$ where $\bar{s}_1$ is the reflection of $\bar{s}$ from $\bar{n}_\zeta$ given by Equation (20). Also if the intensity is 1 for $\bar{s}$ then the intensity for $\bar{s}_1$ is $\rho_{s\zeta}$ where $\rho_{s\zeta}$ is the specular reflection coefficient of $\bar{n}_\zeta$ surface for direct illumination. Also the intensity of $\bar{s}_2$ is $\rho_{s\zeta}\rho'_{sg}$ where ρ'_{sg} is the coefficient of specular reflection of the surface $\bar{n}_g$ for the first indirectly illuminated ray (as indicated by one prime), and so on. This more fully explains Equation (2) and how it is to be used.

Next is the consideration of logic as to which surface is illuminated, and which shadows another. This is simple to understand in theory. As in Figure 5 we consider $\bar{s}$ passing throughaa given point (on the grid in Figure 2-b) and intersecting a surface. We then, as efficiently as possible, determine which surface this reflection crosses first.

To find the intersections given a surface, a vector and a point through which it passes we resort to analytic geometry. In Figure 2-b, we may generalize the vehicle as consisting entirely of planes parallel to $x_s y_s$, a frustum of circular cone whose axis is parallel to z and translated cylinders with all axes parallel to z_s (note the cylinders may be considered as cones however their solution is less efficient. Let, in general a light unit vector passing through (u_1, u_2, u_3) (in the direction of advancing light) be $(s_1; s_2; s_3)$ and let (r, σ, γ) be the cylindrical (or polar) coordinate of the surface-vector intersection of the planes and cylinders and cone except for the scallops. Also let (r, ϕ, z_γ) be the intersection on the scallop cylinders with σ now reserved for determining which scallop.

In particular we find the intersection of $\begin{pmatrix} s_1 \\ s_2 \\ s_3 \end{pmatrix}$ on a plane (or disk) described by

$$z_s = k_z \tag{26}$$

Then the equation of the line joining (u_1, u_2, u_3) and (r, σ, k) is

$$\frac{r\cos\sigma - u_1}{s_1} = \frac{r\sin\sigma - u_2}{s_2} = \frac{k_z - u_3}{s_3} \tag{27}$$

Therefore we have

$$\sin\sigma = \frac{1}{r}\left[u_2 + \frac{s_2}{s_3}(k-u_3)\right]$$

$$\cos\sigma = \frac{1}{r}\left[u_1 + \frac{s_1}{s_3}(k-u_3)\right] \tag{28}$$

where

$$r = \sqrt{\left[u_1+\frac{s_1}{s_3}(k-u_3)\right]^2 + \left[u_2+\frac{s_2}{s_3}(k-u_3)\right]^2} \tag{29}$$

and

$$\vec{I} = \begin{bmatrix} r\cos\sigma \\ r\sin\sigma \\ k \end{bmatrix} \tag{29a}$$

Next consider the intersection of $\begin{pmatrix} s_1 \\ s_2 \\ s_3 \end{pmatrix}$ passing through (u_1, u_2, u_3) with the cylinders of the scallops and main vehicle. If the cylinder radius is r, and it may be translated as indicated in Figure 4, it may have a parametric representation given by

$$x = (r+D_3)\cos\sigma - r\cos(\phi+\sigma)$$

$$y = (r+D_3)\sin\sigma - r\sin(\phi+\sigma)$$

The equation of the line joining the intersection and (u_1, u_2, u_3) along $\begin{pmatrix} s_1 \\ s_2 \\ s_3 \end{pmatrix}$ is

$$\frac{(r+D_3)\cos\sigma - r\cos(\sigma+\phi) - u_1}{s_1} = \frac{(r+D_3)\sin\sigma - r\sin(\phi+\sigma) - u_2}{s_2} = \frac{g-u_3}{s_3} \tag{30}$$

The first two members are independent of z can be written

$$r\left[s_1\sin(\phi+\sigma) - s_2\cos(\phi+\sigma)\right] = (r+D_3)(s_1\sin\sigma - s_2\cos\sigma) + (u_1 s_2 - u_2 s_1) \tag{31}$$

We now define the temporary quantity, ψ by

$$\cos\psi = \frac{s_1}{\sqrt{s_1^2+s_2^2}} \qquad \sin\psi = \frac{s_2}{\sqrt{s_1^2+s_2^2}} \tag{32}$$

Equations (32) and (31) give the solution

$$\phi = \psi - \sigma + \sin^{-1} \frac{1}{r}\left[(r+D_3)\sin(\sigma-\psi) + (u_1 \sin\psi - u_2 \cos\psi)\right] \tag{33}$$

if

$$\frac{1}{r^2}\left[(r+D_3)\sin(\sigma-\psi) + (u_1\sin\psi - u_2\cos\psi)\right]^2 \leq 1 \tag{33a}$$

and (30) now gives z to be

$$z_0 = u_3 + \frac{S_3}{S_2}\left[(r+D_3)\sin\sigma - r\sin(\phi+\sigma) - u_2\right] \tag{34}$$

$$\vec{I} = \left((r+D_3)\cos\sigma - r\cos(\phi+\sigma),\ (r+D_3)\sin\sigma - r\sin(\phi+\sigma),\ u_3 + \frac{S_3}{S_2}\left[(r+D_3)\sin\sigma - r\sin(\phi+\sigma) - u_2\right]\right)$$

If we are working with one of the scallops,

$$|\phi| \leq \phi_m \tag{35}$$

If (35) is not satisfied or, in the case of the other cylinders, we may have chose the wrong solution of ϕ in (33). The other soluation ϕ of (33),

$$\phi = \psi - \sigma + \pi - \sin^{-1}\frac{1}{r}\left[(r+D_3)\sin(\sigma-\psi) + (u_1\sin\psi - u_2\cos\psi)\right] \tag{36}$$

This new value of ϕ is then used. This happens since a light ray intersects a cylinder in two places but physically the light is stopped at the first intersection, and the second beocmes extraneous. The conditions that must be met to determine the correct solution are either (25a) or (25b).

The same type of thing happens for the frustum of a cone whose equation is

$$x = r_{Nd_z}\cos\sigma \qquad y = r_{Nd_z}\sin\sigma \tag{37}$$

where

$$r_{Nd_z} = M_c z_s + r_1 \tag{37a}$$

and where M_c is the slope of the cone edge,

$$M_c = \frac{r_{Nd} - r_N}{h_4 + h_N} \tag{38}$$

where r_{Nd} is the small radius of the cone nozzle and r_N is the larger as shown in Figure 2-b. The height of the cone is implied in Figure 1 where h_4 is the distance to the r_3 cylinder from the x_1y_1 plane and h_N is the distance (negative) from x_1y_1 plane to the circle end of the nozzle. Again the equation of intersection is

$$\frac{r_{Nd_\gamma}\cos\sigma - u_1}{s_1} = \frac{r_{Nd_\gamma}\sin\sigma - u_2}{s_2} = \frac{z_s - u_3}{s_3}$$

This time for simplicity we choose to find z first. The first and last members give

$$\cos\sigma = \left[u_1 + \frac{s_1}{s_3}(z_s - u_3)\right]\frac{1}{r_{Nd_\gamma}} \tag{39}$$

while the second and last members give

$$\sin\sigma = \left[u_2 + \frac{s_2}{s_3}(z_s - u_3)\right]\cdot\frac{1}{r_{Nd_\gamma}} \tag{39a}$$

The sum of the squares of these equations gives a quadratic in z_s only, if r_{Nd_γ} is taken from (37a). Let

$$\begin{aligned} c_{\gamma 2} &= 1-(M_c^2+1)s_3^2 \\ c_{\gamma 1} &= s_3^2 M_c r_1 - s_2(s_3u_2 - s_2u_3) - s_1(s_3u_1 - s_1u_3) \\ c_{\gamma 0} &= (s_3u_1 - s_1u_3)^2 + (s_3u_2 - s_2u_3)^2 - s_3^2 r_1^2 \end{aligned} \tag{40}$$

$$\vec{I} = \begin{bmatrix} r_{Nd_\gamma}\cos\sigma \\ r_{Nd_\gamma}\sin\sigma \\ z_s \end{bmatrix} \tag{40a}$$

then

$$z_s = \frac{1}{c_{\gamma 0}}\left(c_{\gamma 1} - \sqrt{c_{\gamma 1}^2 - c_{\gamma 0}c_{\gamma 2}}\right) \tag{41}$$

or

$$z_s = \frac{1}{c_{\gamma 0}}\left(c_{\gamma 1} + \sqrt{c_{\gamma 1}^2 - c_{\gamma 0}c_{\gamma 2}}\right) \tag{41a}$$

The surface normals are not listed in terms of their respective coordinates. Note a surface may have a normal each direction when light may illuminate it on each side. Figure 1 shows all surfaces and their respective area unit normal vectors. However we are interested in writing them in the s-coordinates (as in Figure 2-b). The normal for the cylinder of radius r_3 is into the cylinder since the light strikes the convex surface,

$$\bar{n}_{c3} = \begin{pmatrix} -\cos\sigma \\ -\sin\sigma \\ 0 \end{pmatrix}_s \tag{42}$$

The end of the cylinder of radius r_1 may be illuminated outside and in so we write normal vectors for these cases respectively

$$\bar{n}_{c1} = \begin{pmatrix} -\cos\sigma \\ -\sin\sigma \\ 0 \end{pmatrix}_s \qquad \bar{n}_{c1p} = \begin{pmatrix} \cos\sigma \\ \sin\sigma \\ 0 \end{pmatrix}_s \tag{43}$$

The scallops likewise may be illuminated on their concave or convex surfaces. The surface normals for these cases are respectively for the j^{th} surface

$$\bar{n}_{j} = \begin{pmatrix} -\cos(\phi+\sigma) \\ -\sin(\phi+\sigma) \\ 0 \end{pmatrix}_s \qquad \bar{n}_{jp} = \begin{pmatrix} \cos(\phi+\sigma) \\ \sin(\phi+\sigma) \\ 0 \end{pmatrix}_s \tag{44}$$

The plane surfaces or disks over the end of the nozzle cone base, over the vehicle end (with the protruding nozzle cone), and over the $+z_s$ end have normal unit vectors respectively

$$\bar{n}_N = \begin{pmatrix} 0 \\ 0 \\ 1 \end{pmatrix}_s \quad \bar{n}_d = \begin{pmatrix} 0 \\ 0 \\ 1 \end{pmatrix}_s \quad \bar{n}_e = \begin{pmatrix} 0 \\ 0 \\ -1 \end{pmatrix}_s \tag{45}$$

Also the frustum of the cone has a unit normal of

$$\bar{n}_{Nd} = \begin{pmatrix} -\cos\eta_c\cos\sigma \\ -\cos\eta_c\sin\sigma \\ -\sin\eta_c \end{pmatrix} \tag{45a}$$

where η_c is the half angle at the vertex of the cone frustum if it were extended into the vehicle. This angle is found by the frustum's dimensions to be

$$\eta_c = \tan^{-1}\frac{r_N - r_{Nd}}{h_N + h_4} = \tan^{-1}(-M_c) \tag{45b}$$

and is considered always positive acute.

In all cases we choose the normal such that the dot product with the illumination light vector in the direction of propagation is positive. The primes represent illumination of the inside of the surface.

The general torque for the summation in Equation (3) is found from Equations (2), (6) and (8), the paragraph following Equation (25), and the general intersection vector $\vec{I}$ for each surface

$$\vec{\Delta L} = (\vec{I} - \vec{c}) \times P_o \prod_{i=0}^{k_s} \rho_{ss_i}^{[k]} \frac{2r_2(D_1+D_2)}{m_1 m_2 (\bar{s}_{k_s} \cdot \bar{n}_{s_{k_s}})} \cdot (\bar{s}_{k_s} \cdot \bar{n}_{s_{k_s}}) \left\{ (\alpha_{s_{k_s}} + \rho_{ds_{k_s}}) \bar{s}_{k_s} + \right. \tag{46}$$

$$\left. + \left[2(\bar{s}_{k_s} \cdot \bar{n}_{s_{k_s}}) + \tfrac{2}{3} \rho_{ds_{k_s}} \right] \bar{n}_{s_{k_s}} \right\}$$

In this equation, the subscript s_{k_s} designates the k_s reflection strikes. Also there are i primes $[i]$ since physically each reflection may be different wave length distributions and consequently different reflection ratios. Mathematically we must define $\rho_{ss_o} = 1$ for all surfaces which would mean physically that all light strikes the first surface. Note the sequence of subscripts s_i and consequently $\rho_{ss_i}^{[k]}$ depends upon the path the multiply-reflected light takes and is determined by the intersection procedure that describes Equations (19) to (25).

From the procedure of finding the vectors involved in Equation (46), we know $\bar{I}$, $\bar{s}_{k_s}$ and $\bar{n}_{s_{k_s}}$ are in the s-coordinates while $\vec{c}$ is given in 1-coordinates by Equation (1). However (5) implies

$$\begin{bmatrix} x_1 \\ y_1 \\ z_1 \end{bmatrix} = \begin{pmatrix} \cos\sigma_2 & -\sin\sigma_2 & 0 \\ \sin\sigma_2 & \cos\sigma_2 & 0 \\ 0 & 0 & 1 \end{pmatrix} \begin{bmatrix} x_s \\ y_s \\ z_s \end{bmatrix}_s \tag{47}$$

In general let

$$\overrightarrow{\bar{I}} = \begin{bmatrix} I_1 \\ I_2 \\ I_3 \end{bmatrix}_S \qquad \overrightarrow{S_{k_s}} = \begin{pmatrix} S_1 \\ S_2 \\ S_3 \end{pmatrix}_S \qquad \overrightarrow{n_{S_{k_s}}} = \begin{pmatrix} n_1 \\ n_2 \\ n_3 \end{pmatrix}_S \tag{48}$$

Then we have (49)

$$\overrightarrow{\bar{I}} = \begin{bmatrix} I_1\cos\sigma_l - I_2\sin\sigma_l \\ I_1\sin\sigma_l + I_2\cos\sigma_l \\ I_3 \end{bmatrix}_1 \quad \overrightarrow{S_{k_s}} = \begin{pmatrix} S_1\cos\sigma_l - S_2\sin\sigma_l \\ S_1\sin\sigma_l + S_2\cos\sigma_l \\ S_3 \end{pmatrix}_1 \quad \overrightarrow{n_{S_{k_s}}} = \begin{pmatrix} n_1\cos\sigma_l - n_2\sin\sigma_l \\ n_1\sin\sigma_l + n_2\cos\sigma_l \\ n_3 \end{pmatrix}_1$$

Performing the indicated cross product in (45) with the vectors in (1) and (48) give the 1-coordinate components of an incremental solar torque about C as follows:

(50)

$$\Delta L_1 = P_0 \prod_{i=0}^{k_s} {}^{[i]}P_{SS_i} \cdot \frac{2r_2(D_1+D_2)}{m_1 m_2} \Big\{ (\alpha_{S_{k_s}} + P d s_{k_s}) \Big[(I_1\sin\sigma_l + I_2\cos\sigma_l - y_{CB}) S_3 - (I_3 - z_{CB}) \cdot$$

$$\cdot (S_1\sin\sigma_l + S_2\cos\sigma_l) \Big] + \Big[2(S_1 n_1 + S_2 n_2 + S_3 n_3) + \tfrac{2}{3} P d s_{k_s} \Big] \cdot \Big[(I_1\sin\sigma_l + I_2\cos\sigma_l - y_{CB}) \cdot n_3 -$$

$$- (I_3 - z_{CB}) \cdot (n_1\sin\sigma_l + n_2\cos\sigma_l) \Big] \Big\}$$

$$\Delta L_2 = P_0 \prod_{i=0}^{k_s} {}^{[j]}P_{SS_i} \cdot \frac{2r_2(D_1+D_2)}{m_1 m_2} \Big\{ (\alpha_{S_{k_s}} + P d s_{k_s}) \Big[(I_3 - z_{CB})(S_1\cos\sigma_l - S_2\sin\sigma_l) - (I_1\cos\sigma_l -$$

$$- I_2\sin\sigma_l - x_{CB}) \cdot S_3 \Big] + \Big[2(S_1 n_1 + S_2 n_2 + S_3 n_3) + \tfrac{2}{3} P d s_{k_s} \Big] \cdot \Big[(I_3 - z_{CB}) \cdot (n_1\cos\sigma_l -$$

$$- n_2\sin\sigma_l) - (I_1\cos\sigma_l - I_2\sin\sigma_l - x_{CB}) n_3 \Big] \Big\}$$

$$\Delta L_3 = P_0 \prod_{i=0}^{k_s} {}^{[l]}P_{SS_i} \cdot \frac{2r_2(D_1+D_2)}{m_1 m_2} \Big\{ (\alpha_{S_{k_s}} + P d s_{k_s}) \Big[(I_1\cos\sigma_l - I_2\sin\sigma_l - x_{CB}) \cdot (S_1\sin\sigma_l + S_2\cos\sigma_l) -$$

$$- (I_1\sin\sigma_l + I_2\cos\sigma_l - y_{CB}) \cdot (S_1\cos\sigma_l - S_2\sin\sigma_l) \Big] + \Big[2(S_1 n_1 + S_2 n_2 + S_3 n_3) + \tfrac{2}{3} P d s_{k_s} \Big] \cdot$$

$$\cdot \Big[(I_1\cos\sigma_l - I_2\sin\sigma_l - x_{CB})(n_1\sin\sigma_l + n_2\cos\sigma_l) - (I_1\sin\sigma_l + I_2\cos\sigma_l - y_{CB}) \cdot$$

$$\cdot (n_1\cos\sigma_l - n_2\sin\sigma_l) \Big] \Big\}$$

This torque represents the additional torque on the vehicle due to an incremental area of a surface illuminated by the k_s^{th} reflected ray. This is then added to the torques previously summed, thus

$$\vec{L}_T = \vec{L}_T + \vec{\Delta L} \tag{51}$$

Reflection Coefficient Versus Angle of Incidence

The surface boundary conditions of the electromagnetic wave entering a piece of dielectric (glass) has the property that the $\vec{E}$ and $\vec{B}$ vectors are refracted and reflected differently for different polarizations. Chapter 7 of Optics by F. W. Sears indicates that for natural (unpolarized) light, the relfection coefficient is

$$\rho_s(\eta) = \frac{1}{2}\cdot\frac{\tan^2(\eta-\eta')}{\tan^2(\eta+\eta')} + \frac{1}{2}\cdot\frac{\sin^2(\eta-\eta')}{\sin^2(\eta+\eta')} \tag{52}$$

where η is the angle of incidence and η' is the refraction angle, where

$$\eta_0 \sin\eta = \eta' \sin\eta' \tag{53}$$

Snell's law determines this angle from the angle of incidence and the indicies of refraction for both media. This function gives about .05 from normal to almost 60°. Then this value climbs up to 1 at 90° (tangent to the surface). Equation (52) assumes all light incident on a surface is either specularly reflected or absorbed and refracted. However, our work assumes another possibility is present. That is, the light is diffusely reflected according to Lambert's law. If we consider a surface model composed of tiny specular reflecting hemispheres, we find most of the wanted properties. The reflections at shallow angles are statistically cancelled by shadowing while the overall plane between the hemispheres will give a statistical specular reflection. We assume therefore that the absorption is

$$\alpha = 1 - \rho_s(\eta) \tag{54}$$

and that the diffuse reflection is a certain percentage of the specular reflection

$$\rho_d = \delta \rho_s \tag{55}$$

where δ is approximated by laboratory imperical measurements.

Therefore from (52) and (55),

$$\rho_s = \frac{\rho_s(\eta)}{1+\delta} \tag{56}$$

The values of α, ρ_d and ρ_s are then placed in Equations (50) for the solar torque determination, where η is determined for each surface by

$$0 \leq \eta = \cos^{-1}\left(\overline{S}_{R_s} \cdot \overline{n}_{S_i}\right) < \frac{\pi}{2} \tag{57}$$

and η' is found from Equation (53)

$$0 \leq \eta' = \sin^{-1}\left(\frac{n_o}{n'} \sin\eta\right) < \frac{\pi}{2} \tag{58}$$

APPENDIX E

STIFFNESS MATRIX FOR AN ELEMENT OF THE GRAVITY GRADIENT ROD, PRELIMINARY

1 - INTRODUCTION

OBJECTIVE - To obtain a stiffness matrix for the gravity gradient rod which would reflect the behaviour of the rod more accurately than the assumption that the rod behaves like a beam.

METHOD

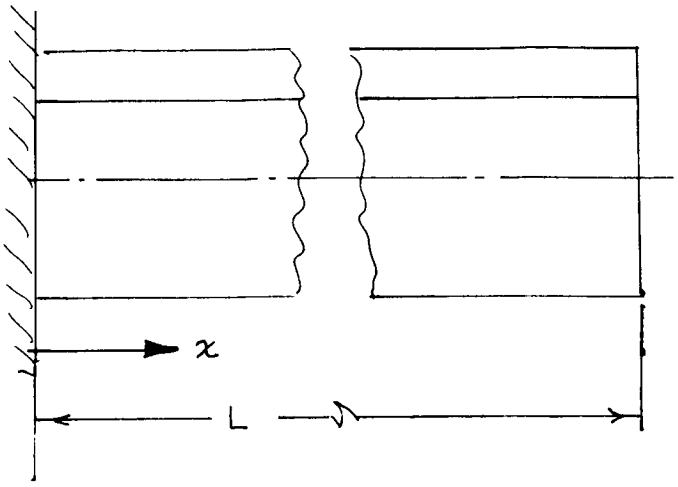
Procedures and formulae as given by Reference (1) shall be fully utilized where applicable. A rod of length "L" shall be considered. One end of the rod shall be considered to be clamped so that the boundary conditions as given by Equation 36 of Reference 1 apply for this end. The other end of the rod shall be given unit deflections and rotations "A" through "H" and the resulting edge loads shall be calculated. The resultants of these edge loads shall be calculated to obtain the stiffness coefficients.

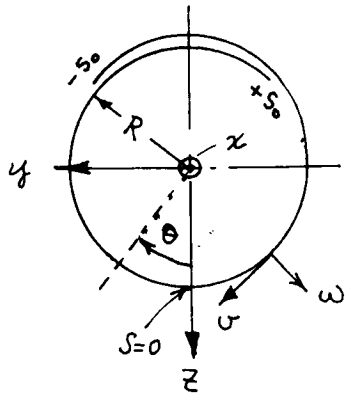
Reference Used in this appendix:

(1) "Gravity Gradient Thermal Bending Test Report," GE Document No. 64SD368, dated October 23, 1964

(2) "Gravity Gradient Thermal Bending Test Report," GE Document No. 63SD725, dated July 10, 1963

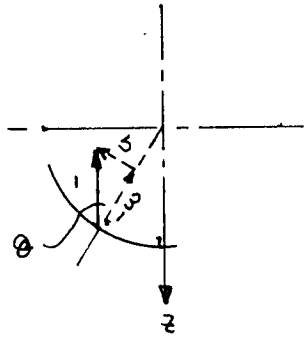
SIGN CONVENTION





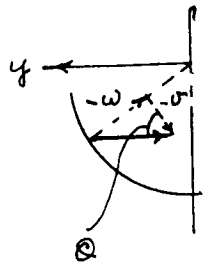
A - UNIT DEFLECTION IN -z DIRECTION

$$(1\text{-}1)\quad \begin{cases} u = 0 \\ v = \sin\theta \\ \omega = -\cos\theta \\ \frac{\partial w}{\partial x} = 0 \end{cases}$$



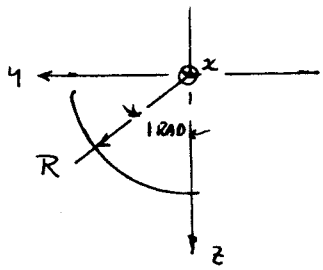
B - UNIT DEFLECTION IN -y DIRECTION

$$(1\text{-}2)\quad \begin{cases} u = 0 \\ v = -\cos\theta \\ \omega = -\sin\theta \\ \frac{\partial w}{\partial x} = 0 \end{cases}$$



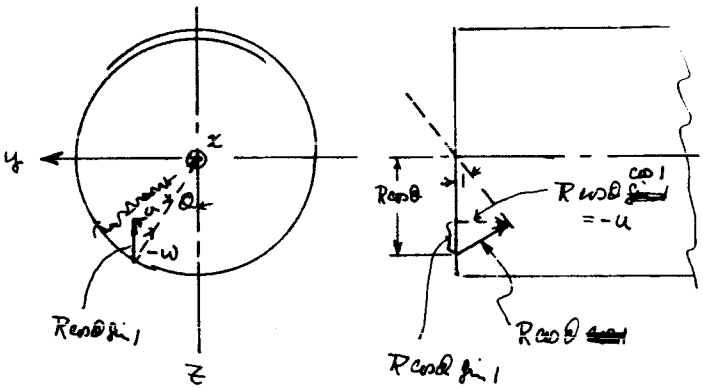
D - UNIT ROTATION ABOUT -x AXIS

$$(1\text{-}3)\begin{cases} u = 0 \\ v = R \\ \omega = 0 \\ \frac{\partial w}{\partial x} = 0 \end{cases}$$



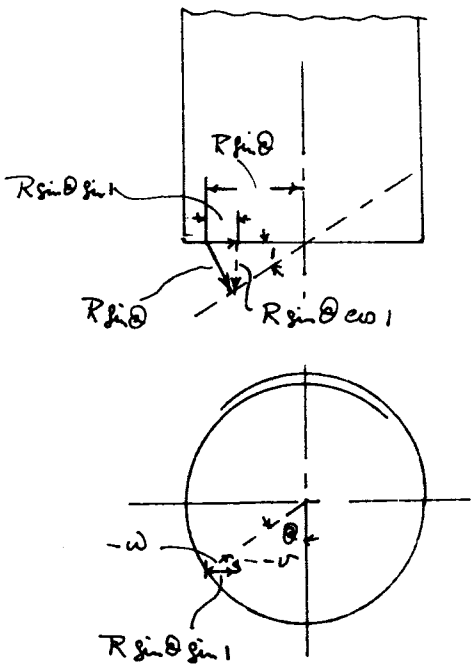
E - UNIT ROTATION ABOUT -y AXIS

$$(1\text{-}4)\begin{cases} u = -R\cos\theta\,\cos(1\,\text{RAD}) \\ v = R\sin(1\,\text{RAD})\sin\theta\cos\theta \\ \omega = -R\sin(1\,\text{RAD})\cos^2\theta \\ \frac{\partial w}{\partial x} = 0 \end{cases}$$



F - UNIT ROTATION ABOUT -z AXIS

$$(1\text{-}5)\begin{cases} u = R\sin\theta\,\cos(1\,\text{RAD}) \\ v = -R\sin(1\,\text{RAD})\sin\theta\cos\theta \\ \omega = -R\sin(1\,\text{RAD})\sin^2\theta \\ \frac{\partial w}{\partial x} = 0 \end{cases}$$



C - UNIT DISPLACEMENT ALONG $-x$ AXIS

$$(1\text{-}6)\quad \begin{cases} u = -1 \\ v = 0 \\ w = 0 \\ \frac{\partial w}{\partial x} = 0 \end{cases}$$

REMEMBERING HOWEVER THAT:

$$(1\text{-}7)\quad \begin{cases} \sin\theta\cos\theta = \sin 2\theta \\ \cos^2\theta = \frac{1}{2} + \frac{1}{2}\cos 2\theta \\ \sin^2\theta = \frac{1}{2} - \frac{1}{2}\cos 2\theta \end{cases}$$

AND LETTING:

$$\theta = \lambda s \qquad \text{WHERE} \qquad \lambda = \frac{1}{R}$$

WE MAY SUMMARIZE BOUNDARY CONDITIONS "A" THROUGH "F" AS FOLLOWS:

A]

$$(1\text{-}8)\quad \begin{cases} u = 0 \\ v = \sin\lambda s \\ w = -\cos\lambda s \\ \frac{\partial w}{\partial x} = 0 \end{cases}$$

B]

$$(1\text{-}9)\quad \begin{cases} u = 0 \\ v = -\cos\lambda s \\ w = -\sin\lambda s \\ \frac{\partial w}{\partial x} = 0 \end{cases}$$

C]

$$(1\text{-}10)\quad \begin{cases} u = -1 \\ v = 0 \\ w = 0 \\ \frac{\partial w}{\partial x} = 0 \end{cases}$$

D]

$$(1\text{-}11)\quad \begin{cases} u = 0 \\ v = R \\ w = 0 \\ \frac{\partial w}{\partial x} = 0 \end{cases}$$

E]

$$(1\text{-}12)\quad \begin{cases} u = & 0 & + a_{1E}\cos\lambda S & + 0 \\ v = & 0 & + \ 0 & + b_{2E}\sin 2\lambda S \\ w = & C_{0E} & + \ 0 & + C_{2E}\cos 2\lambda S \\ \frac{\partial w}{\partial x} = & 0 & + \ 0 & + 0 \end{cases}$$

F]

$$(1\text{-}13)\quad \begin{cases} u = & 0 & + a_{1F}\sin\lambda S & + 0 \\ v = & 0 & + 0 & + b_{2F}\sin 2\lambda S \\ w = & C_{0F} & + 0 & + C_{2F}\cos 2\lambda S \\ \frac{\partial w}{\partial x} = & 0 & + 0 & + 0 \end{cases}$$

WHERE:

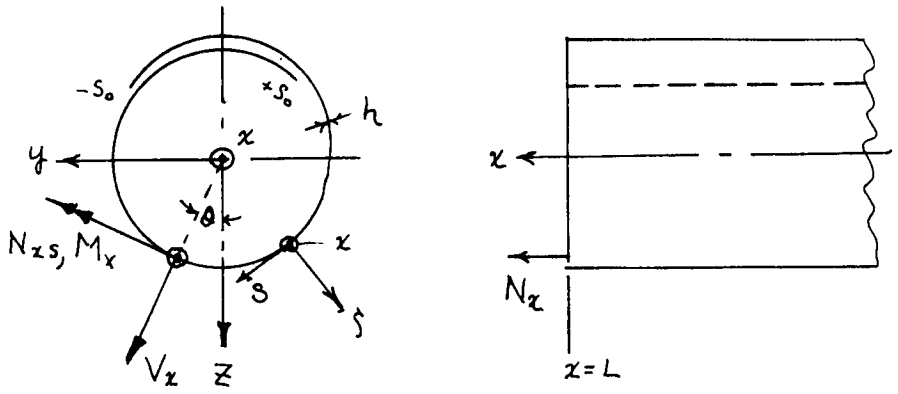
$$(1\text{-}14)\quad \begin{cases} a_{1E} = -R\cos(1RAD) \\ b_{2E} = R\sin(1RAD) \\ C_{0E} = -\tfrac{1}{2}R\sin(1RAD) = -\tfrac{1}{2}b_{2E} \\ C_{2E} = -\tfrac{1}{2}R\sin(1RAD) = -\tfrac{1}{2}b_{2E} \end{cases}$$

AND:

$$(1\text{-}15)\quad \begin{cases} a_{1F} = R\cos(1RAD) = -a_{1E} \\ b_{2F} = -R\sin(1RAD) = -b_{2E} \\ C_{0F} = -\tfrac{1}{2}R\sin(1RAD) = -\tfrac{1}{2}b_{2E} \\ C_{2F} = \tfrac{1}{2}R\sin(1RAD) = \tfrac{1}{2}b_{2E} \end{cases}$$

2- END LOADS IN TERMS OF EDGE LOADS

IN ORDER TO DEVELOP "BEAM" LOADS IN TERMS OF THE SHELL EDGE LOADS IT WILL BE HELPFUL TO INDICATE THE SHELL EDGE LOADS ORIENTED IN POSITIVE DIRECTIONS AS FOLLOWS:



EDGE LOADS

- N_x IS THE EDGE LOAD PER UNIT LENGTH IN THE x DIRECTION
- V_x " " " " " " " " " ŝ "
- N_{xs} " " " " " " " " " s "
- M_x " " " MOMENT " " " " " s "

"BEAM" LOADS ARE DESIGNATED AS FOLLOWS:

END LOADS

- F_1 - FORCE ALONG x AXIS
- F_2 - " " y "
- F_3 - " " z "
- F_4 - TORSION ABOUT x "
- F_5 - MOMENT " y "
- F_6 - " " z "

GENERALIZED SHELL END LOADS ARE DESIGNATED AS FOLLOWS:

F_{13} - FORCE ASSOCIATED WITH Ω (BREATHING)

F_{14} - FORCE ASSOCIATED WITH Ψ (WARPING)

WHENCE:

$$(2\text{-}1) \qquad F_1 = \int_{-S_0}^{S_0} N_x \, ds$$

$$(2\text{-}2) \qquad F_2 = \int_{-S_0}^{S_0} (V_x \sin\theta + N_{xs} \cos\theta) \, ds$$

$$(2\text{-}3) \qquad F_3 = \int_{-S_0}^{S_0} (V_x \cos\theta - N_{xs} \sin\theta) \, ds$$

$$(2\text{-}4) \qquad F_4 = -\int_{-S_0}^{S_0} N_{xs} R \, ds$$

$$(2\text{-}5) \qquad F_5 = \int_{-S_0}^{S_0} (M_x \cos\theta + N_x R \cos\theta) \, ds$$

$$(2\text{-}6) \qquad F_6 = -\int (M_x \sin\theta + N_x R \sin\theta) \, ds$$

THE EDGE LOADS MAY BE CALCULATED ON THE BASIS OF DISPLACEMENTS AS FOLLOWS:

$$(2\text{-}7) \qquad N_x = K \left(\frac{\partial u}{\partial x} + \nu \frac{\partial v}{\partial s} + \frac{\nu}{R} w \right)$$

$$(2\text{-}8) \qquad M_x = (-D) \left[\frac{\partial^2 w}{\partial x^2} + \nu \frac{\partial^2 w}{\partial s^2} - \frac{\nu}{R} \frac{\partial v}{\partial s} \right]$$

$$(2\text{-}9) \qquad N_{xs} = \left(\frac{1-\nu}{2} \right) \left[K \left(\frac{\partial u}{\partial s} + \frac{\partial v}{\partial x} \right) - \frac{D}{R} \left(2 \frac{\partial^2 w}{\partial x \partial s} - \frac{1}{R} \frac{\partial v}{\partial x} \right) \right]$$

$$(2\text{-}10) \qquad V_x = (-D) \left[\frac{\partial^3 w}{\partial x^3} + (2-\nu) \frac{\partial^3 w}{\partial x \partial s^2} - \frac{1}{R} \frac{\partial^2 v}{\partial x \partial s} \right]$$

CASE - A

WE MUST SATISFY THE SHELL EQUATIONS (1), (2), (3) OF REF 1 AND BOUNDARY CONDITIONS AS FOLLOWS:

@ $x = 0$:

I
(1) $u = 0$
(2) $v = 0$
(3) $w = 0$
(4) $\frac{\partial w}{\partial x} = 0$

@ $x = L$:

II-A
(1) $u = 0$
(2) $v = \sin \lambda s$
(3) $w = -\cos \lambda s$
(4) $\frac{\partial w}{\partial x} = 0$

THESE CONDITIONS WILL BE SATISFIED BY THE FUNCTIONS:

(2-11)
$$\begin{cases} u = U(x) \cos \lambda s \\ v = V(x) \sin \lambda s \\ w = W(x) \cos \lambda s \end{cases}$$

WHICH CORRESPOND TO "SOLUTION FOR LOAD II" OF REF 1.

ASSUME THAT U, V, W HAVE BEEN FOUND; ~~ACCORDING~~ THEN THE EDGE LOADS MAY BE FOUND AS FOLLOWS:

REQUIRED PARTIAL DERIVATIVES OF u, v, w:

(2-12)
$$\begin{cases} u = U(x) \cos \lambda s \qquad v = V(x) \sin \lambda s \\ \frac{\partial u}{\partial x} = U' \cos \lambda s \qquad \frac{\partial v}{\partial x} = V' \sin \lambda s \\ \frac{\partial u}{\partial s} = -\lambda U \sin \lambda s \qquad \frac{\partial v}{\partial s} = \lambda V \cos \lambda s \qquad \frac{\partial^2 v}{\partial x \partial s} = \lambda V' \cos \lambda s \\ w = W(x) \cos \lambda s \\ \frac{\partial w}{\partial x} = W' \cos \lambda s \qquad \frac{\partial w}{\partial s} = -\lambda W \sin \lambda s \qquad \frac{\partial^2 w}{\partial x \partial s} = -\lambda W' \sin \lambda s \\ \frac{\partial^2 w}{\partial x^2} = W'' \cos \lambda s \qquad \frac{\partial^2 w}{\partial s^2} = -\lambda^2 W \cos \lambda s \qquad \frac{\partial^3 w}{\partial x \partial s^2} = -\lambda^2 W' \cos \lambda s \\ \frac{\partial^3 w}{\partial x^3} = W''' \cos \lambda s \end{cases}$$

WHERE ' INDICATES $\frac{d}{dx}$

CASE A CONT'D

WHENCE:

$$(2-13)\quad N_x = K\left(U' + \nu\lambda V + \frac{\nu}{R}W\right)\cos\lambda s$$

$$(2-14)\quad M_x = (-D)\left(W'' - \nu\lambda^2 W - \frac{\nu\lambda}{R}V\right)\cos\lambda s$$

$$(2-15)\quad N_{xs} = \left(\frac{1-\nu}{2}\right)\left[K\left(-\lambda U + V'\right) - \frac{D}{R}\left(-2\lambda W' - \frac{1}{R}V'\right)\right]\sin\lambda s$$

$$(2-16)\quad V_x = (-D)\left(W''' - (2-\nu)\lambda^2 W' - \frac{\lambda}{R}V'\right)\cos\lambda s$$

AND SUBSTITUTING APPRORIATELY IN 2-1 THROUGH 2-6 WE OBTAIN:

$$(2-17)\begin{cases} F_{1A} = \left[K\left(U' + \nu\lambda V + \frac{\nu}{R}W\right)\right]\left[\frac{2}{\lambda}\sin\lambda s_0\right] \\ F_{2A} = 0 \\ F_{3A} = (-D)\left[W''' - (2-\nu)\lambda^2 W' - \frac{\lambda}{R}V'\right]\left[s_0 + \frac{1}{2\lambda}\sin 2\lambda s_0\right] \\ \qquad + \left(\frac{1-\nu}{2}\right)\left[K\left(\lambda U - V'\right) - \frac{D}{R}\left(2\lambda W' + \frac{1}{R}V'\right)\right]\left[s_0 - \frac{1}{2\lambda}\sin 2\lambda s_0\right] \\ F_{4A} = 0 \\ F_{5A} = \left[-DW'' + \left(K\frac{\nu}{R} + \nu D\lambda^2\right)W + \left(\frac{\nu\lambda}{R}D + \nu\lambda K\right)V + KU'\right]\left[s_0 + \frac{1}{2\lambda}\sin 2\lambda s_0\right] \\ F_{6A} = 0 \end{cases}$$

LET US DESIGNATE DISPLACEMENT COORDINATES AS FOLLOWS:

MOTION	CASE	COORDINATE @ $x = L$	COORDINATE @ $x = 0$
DISPLACEMENT ALONG x AXIS	C	1	7
" " y "	B	2	8
" " z "	A	3	9
ROTATION ABOUT x "	D	4	10
" " y "	E	5	11
" " z "	F	6	12
BREATHING, Ω	G	13	15
WARPING, Ψ	H	14	16

TABLE - 2-1

CASE A - CONT'D

IF WE DESIGNATE THE STIFFNESS COEFFICIENT BY k_{ij} SUCH THAT k_{ij} IS THE FORCE (OR MOMENT) IN THE DIRECTION OF THE i th COORDINATE DUE TO A UNIT DEFLECTION (OR ROTATION) IN THE NEGATIVE DIRECTION OF THE j th COORDINATE, THEN IT CAN BE SEEN THAT:

$$(2\text{-}18)\quad \begin{cases} F_{1A}(L) = k_{13} & F_{4A}(L) = k_{43} \\ F_{2A}(L) = k_{23} & F_{5A}(L) = k_{53} \\ F_{3A}(L) = k_{33} & F_{6A}(L) = k_{63} \end{cases}$$

$$(2\text{-}19)\quad \begin{cases} F_{1A}(0) = k_{73} & F_{4A}(0) = k_{10,3} \\ F_{2A}(0) = k_{83} & F_{5A}(0) = k_{11,3} \\ F_{3A}(0) = k_{93} & F_{6A}(0) = k_{12,3} \end{cases}$$

CASE - B

BOUNDARY CONDITIONS

@ $x=0$:

$$I \begin{cases} u=0 \\ v=0 \\ w=0 \\ \frac{\partial w}{\partial x}=0 \end{cases}$$

@ $x=L$:

$$II\text{-}B \begin{cases} u=0 \\ v=-\cos\lambda s \\ w=-\sin\lambda s \\ \frac{\partial w}{\partial x}=0 \end{cases}$$

THE SHELL EQUATIONS AND THESE BOUNDARY CONDITIONS WILL BE SATISFIED BY THE FUNCTIONS:

$$(2\text{-}20) \quad \begin{cases} u = U(x)\sin\lambda s \\ v = V(x)\cos\lambda s \\ w = W(x)\sin\lambda s \end{cases}$$

WHICH CORRESPONDS TO "SOLUTION FOR LOAD I" OF REF. 1.

TAKING THE APPROPRIATE PARTIAL DERIVATIVES AND SUBSTITUTING IN (2-7) THROUGH (2-10) WE OBTAIN:

$$(2\text{-}21) \quad N_x = K\left(U' - \nu\lambda V + \frac{\nu}{R}W\right)\sin\lambda s$$

$$(2\text{-}22) \quad M_x = \left(W'' - \nu\lambda^2 W + \frac{\nu\lambda}{R}V\right)(-D)\sin\lambda s$$

$$(2\text{-}23) \quad N_{xs} = \left(\frac{1-\nu}{2}\right)\left[K(\lambda U + V') - \frac{D}{R}\left(2\lambda W' - \frac{1}{R}V'\right)\right]\cos\lambda s$$

$$(2\text{-}24) \quad V_x = (-D)\left[W''' - (2-\nu)\lambda^2 W' + \frac{\lambda}{R}V'\right]\sin\lambda s$$

WHICH WHEN SUBSTITUTED IN (2-1) THROUGH (2-6) GIVE

$$(2\text{-}25) \quad \begin{cases} F_{1B} = F_{3B} = F_{5B} = 0 \\ F_{2B} = (-D)\left[W''' - (2-\nu)\lambda^2 W' + \frac{\lambda}{R}V'\right]\left[s_o - \frac{1}{2\lambda}\sin 2\lambda s_o\right] \\ \qquad + \left(\frac{1-\nu}{2}\right)\left[K(\lambda U + V') - \frac{D}{R}\left(2\lambda W' - \frac{1}{R}V'\right)\right]\left[s_o + \frac{1}{2\lambda}\sin 2\lambda s_o\right] \\ F_{4B} = -\left(\frac{1-\nu}{2}\right)\left[K(\lambda U + V') - \frac{D}{R}\left(2\lambda W' - \frac{1}{R}V'\right)\right]\frac{2R}{\lambda}\sin\lambda s_o \\ F_{6B} = -\left[(-D)W'' + \left(\frac{\nu}{R}K + \nu\lambda^2 D\right)W - \left(\nu\lambda K + \frac{\nu\lambda}{R}D\right)V + KU'\right]\left[s_o - \frac{1}{2\lambda}\sin 2\lambda s_o\right] \end{cases}$$

CASE - B CONT'D

EQUATION (2-25) GIVES ADDITIONAL COEFFICIENTS DUE TO DISPLACEMENTS ALONG THE L COORDINATE AS FOLLOWS:

$$(2\text{-}26)\quad \begin{cases} F_{1B}(L) = k_{12} & F_{4B}(L) = k_{42} \\ F_{2B}(L) = k_{22} & F_{5B}(L) = k_{52} \\ F_{3B}(L) = k_{32} & F_{6B}(L) = k_{62} \end{cases}$$

$$(2\text{-}27)\quad \begin{cases} F_{1B}(0) = k_{72} & F_{4B}(0) = k_{10,2} \\ F_{2B}(0) = k_{82} & F_{5B}(0) = k_{11,2} \\ F_{3B}(0) = k_{92} & F_{6B}(0) = k_{12,2} \end{cases}$$

CASE - C

BOUNDARY CONDITIONS:

@ $x=0$:

$$I \begin{cases} u = 0 \\ v = 0 \\ w = 0 \\ \frac{\partial w}{\partial x} = 0 \end{cases}$$

@ $x=L$:

$$II\text{-}C \begin{cases} u = -1 \\ v = 0 \\ w = 0 \\ \frac{\partial w}{\partial x} = 0 \end{cases}$$

THE SHELL EQUATIONS AND THESE BOUNDARY CONDITIONS MAY BE SATISFIED BY THE FUNCTIONS:

$$(2\text{-}28)\quad \left.\begin{cases} u = U(x)\cos\lambda_0 s \\ v = V(x)\sin\lambda_0 s \\ w = W(x)\cos\lambda_0 s \end{cases}\right\} \text{WHERE } \lambda_0 = 0$$

THIS SOLUTION CORRESPONDS TO "SOLUTION FOR LOAD-II" WHEN $m=0$ AS INDICATED BY REF 1, P. C-36

CASE-D CONT'D

EQUATIONS 2-35 GIVE ADDITIONAL STIFFNESS COEFICIENTS AS FOLLOWS:

$$(2\text{-}36)\quad \begin{cases} F_{1D}(L) = k_{14} & F_{4D}(L) = k_{44} \\ F_{2D}(L) = k_{24} & F_{5D}(L) = k_{54} \\ F_{3D}(L) = k_{34} & F_{6D}(L) = k_{64} \end{cases}$$

$$(2\text{-}37)\quad \begin{cases} F_{1D}(0) = k_{74} & F_{4D}(0) = k_{10,4} \\ F_{2D}(0) = k_{84} & F_{5D}(0) = k_{11,4} \\ F_{3D}(0) = k_{94} & F_{6D}(0) = k_{12,4} \end{cases}$$

CASE-E

NOTE THAT FROM EQUATION (1-12) THE BOUNDARY CONDITIONS @ $x=L$ ARE MADE UP OF A SERIES WITH 3 PARTS AS FOLLOWS:

$$\text{II-}E_0 \begin{cases} u = 0 \\ v = 0 \\ w = C_{0E} \\ \frac{\partial w}{\partial x} = 0 \end{cases} \qquad \text{II-}E_1 \begin{cases} u = a_{1E} \cos \lambda s \\ v = 0 \\ w = 0 \\ \frac{\partial w}{\partial x} = 0 \end{cases} \qquad \text{II-}E_2 \begin{cases} u = 0 \\ v = b_{2E} \sin 2\lambda s \\ w = C_{2E} \cos 2\lambda s \\ \frac{\partial w}{\partial x} = 0 \end{cases}$$

SO THAT THE SOLUTION IS MADE UP IN 3 PARTS.

CASE - E CONT'D

FOR $\text{II}\text{-}E_0$ LET:

$$\left.\begin{aligned} u &= U(x)\cos\lambda_0 s \\ v &= V(x)\sin\lambda_0 s \\ w &= W(x)\cos\lambda_0 s \end{aligned}\right\} \text{WHERE} \quad \lambda_0 = 0$$

WHENCE APPLYING (2-13) THROUGH (2-16); WITH $\lambda = \lambda_0 = 0$:

$$(2\text{-}38)\quad \begin{cases} N_{x_0} = K\left(U' + \frac{\nu}{R}W\right) \\ M_{x_0} = W'' \\ N_{xs_0} = 0 \\ V_{x_0} = W''' \end{cases}$$

WHICH GIVES:

$$(2\text{-}39)\quad \begin{cases} F_{1E_0} = 2K\left(U' + \frac{\nu}{R}W\right)s_0 \\ F_{2E_0} = F_{4E_0} = F_{6E_0} = 0 \\ F_{3E_0} = 2RW'''\sin\frac{1}{R}s_0 \\ F_{5E_0} = 2R\left[W'' + RK\left(U' + \frac{\nu}{R}W\right)\right]\sin\frac{1}{R}s_0 \end{cases}$$

FOR $\text{II}\text{-}E_1$ LET:

$$\begin{aligned} u &= U(x)\cos\lambda s \\ v &= V(x)\sin\lambda s \\ w &= W(x)\cos\lambda s \end{aligned}$$

CASE-E CONT'D

WHENCE APPLYING (2-13) THROUGH (2-16) AND (2-1) THROUGH (2-6):

$$(2\text{-}40)\quad \begin{cases} F_{1E_1} = \left[K\left(U' + \nu\lambda V + \frac{\nu}{R}W\right)\right]\left[\frac{2}{\lambda}\sin\lambda s_0\right] \\ F_{2E_1} = F_{4E_1} = F_{6E_1} = 0 \\ F_{3E_1} = (-D)\left[W''' - (2-\nu)\lambda^2 W' - \frac{\lambda}{R}V'\right]\left[s_0 + \frac{1}{2\lambda}\sin 2\lambda s_0\right] \\ \qquad + \left(\frac{1-\nu}{2}\right)\left[K(\lambda U - V') - \frac{D}{R}(2\lambda W' + \frac{1}{R}V')\right]\left[s_0 - \frac{1}{2\lambda}\sin 2\lambda s_0\right] \\ F_{5E_1} = \left[-DW'' + \left(K\frac{\nu}{R} + \nu\lambda^2 D\right)W + \left(\frac{\nu\lambda}{R}D + \nu K\lambda\right)V + KU'\right]\left[s_0 + \frac{1}{2\lambda}\sin 2\lambda s_0\right] \end{cases}$$

NOTE THAT ALTHOUGH (2-40) APPEARS TO BE THE SAME AS (2-17) THEY ARE QUITE DIFFERENT SINCE U, V, W IN (2-40) MUST BE EQUAL TO $a_{1E}, 0, 0$ RESPECTIVELY @ $x = L$ THE U, V, W IN (2-17) MUST BE EQUAL TO $0, 1, -1$ RESPECTIVELY @ $x = L$.

FOR II-E_2 LET:

$$u = U(x)\cos 2\lambda s$$
$$v = V(x)\sin 2\lambda s$$
$$w = W(x)\cos 2\lambda s$$

WHENCE APPLYING (2-13) THROUGH (2-16) AND (2-1) THROUGH (2-6) AND REPLACING λ BY 2λ WE OBTAIN:

$$(2\text{-}41)\quad \begin{cases} F_{1E_2} = \left[K\left(U' + 2\nu\lambda V + \frac{\nu}{R}W\right)\right]\left[\frac{1}{\lambda}\sin 2\lambda s_0\right] \\ F_{2E_2} = F_{4E_2} = F_{6E_2} = 0 \\ F_{3E_2} = (-D)\left[W''' - (2-\nu)4\lambda^2 W' - \frac{2\lambda}{R}V'\right]\left[s_0 + \frac{1}{4\lambda}\sin 4\lambda s_0\right] \\ \qquad + \left(\frac{1-\nu}{2}\right)\left[K(2\lambda U - V') - \frac{D}{R}(4\lambda W' + \frac{1}{R}V')\right]\left[s_0 - \frac{1}{4\lambda}\sin 4\lambda s_0\right] \\ F_{5E_2} = \left[-DW'' + \left(K\frac{\nu}{R} + 4\nu\lambda^2 D\right)W + \left(\frac{2\nu\lambda}{R}D + 2\nu K\lambda\right)V + KU'\right]\left[s_0 + \frac{1}{4\lambda}\sin 4\lambda s_0\right] \end{cases}$$

THE TOTAL "BEAM" LOADS MAY BE OBTAINED FROM THE RELATIONSHIP:

$$(2\text{-}42)\qquad F_{iE} = F_{iE_0} + F_{iE_1} + F_{iE_2} \qquad (i = 1, \ldots 6)$$

CASE - E CONT'D

FINALLY THE ASSOCIATED STIFFNESS COEFFICIENTS ARE GIVEN BY:

$$(2\text{-}43)\quad \begin{cases} F_{1E}(L) = k_{15} & F_{4E}(L) = k_{45} \\ F_{2E}(L) = k_{25} & F_{5E}(L) = k_{55} \\ F_{3E}(L) = k_{35} & F_{6E}(L) = k_{65} \end{cases}$$

$$(2\text{-}44)\quad \begin{cases} F_{1E}(0) = k_{75} & F_{4E}(0) = k_{10,5} \\ F_{2E}(0) = k_{85} & F_{5E}(0) = k_{11,5} \\ F_{3E}(0) = k_{95} & F_{6E}(0) = k_{12,5} \end{cases}$$

CASE - F

NOTE THAT THE BOUNDARY CONDITIONS @ $x = L$ FOR CASE F AS GIVEN BY (1-13) ARE MADE UP OF A SERIES $\mathrm{II}F_0$, $\mathrm{II}F_1$, $\mathrm{II}F_2$ SUCH THAT $\mathrm{II}F_0$ AND $\mathrm{II}F_2$ ARE SIMILAR IN FORM TO $\mathrm{II}E_0$ AND $\mathrm{II}E_2$ BUT THAT II-F_1 IS SIMILAR TO II-B SO THAT WE MAY WRITE DIRECTLY:

$$(2\text{-}45)\quad \begin{cases} F_{1F_0} = 2K\left(U' + \frac{\nu}{R}W\right)S_0 \\ F_{2F_0} = F_{4F_0} = F_{6F_0} = 0 \\ F_{3F_0} = -2R\,DW'''\sin\frac{1}{R}S_0 \\ F_{5F_0} = 2R\left[-DW'' + RK\left(U' + \frac{\nu}{R}W\right)\right]\sin\frac{1}{R}S_0 \end{cases}$$

CASE F - CONT'D

$$(2\text{-}46)\quad \begin{cases} F_{1F_1} = F_{3F_1} = F_{5F_1} = 0 \\ F_{2F_1} = (-D)\left[W''' - (2-\nu)\lambda^2 W' + 0 + \frac{\lambda}{R}V'\right]\left[S_0 - \frac{1}{2\lambda}\sin 2\lambda S_0\right] \\ \qquad\qquad + \left(\frac{1-\nu}{2}\right)\left[K(\lambda U + V') - \frac{D}{R}(2\lambda W' - \frac{1}{R}V')\right]\left[S_0 + \frac{1}{2\lambda}\sin 2\lambda S_0\right] \\ F_{4F_1} = -\left(\frac{1-\nu}{2}\right)\left[K(\lambda U + V') - \frac{D}{R}(2\lambda W' - \frac{1}{R}V')\right]\left[\frac{2R}{\lambda}\sin\lambda S_0\right] \\ F_{6F_1} = -\left[(-D)W'' + \left(\frac{\nu}{R}K + \nu\lambda^2 D\right)W - \left(\nu\lambda K + \frac{\nu\lambda}{R}D\right)V + \bar{K}U'\right]\left[S_0 - \frac{1}{2\lambda}\sin 2\lambda S_0\right] \end{cases}$$

$$(2\text{-}47)\quad \begin{cases} F_{1F_2} = \left[K(U' + 2\nu\lambda V + \frac{\nu}{R}W)\right]\left[\frac{1}{\lambda}\sin 2\lambda S_0\right] \\ F_{2F_2} = F_{4F_2} = F_{6F_2} = 0 \\ F_{3F_2} = (-D)\left[W''' - (2-\nu)4\lambda^2 W' - \frac{2\lambda}{R}V'\right]\left[S_0 + \frac{1}{4\lambda}\sin 4\lambda S_0\right] \\ \qquad\qquad + \left(\frac{1-\nu}{2}\right)\left[K(2\lambda U - V') - \frac{D}{R}(4\lambda W' + \frac{1}{R}V')\right]\left[S_0 - \frac{1}{4\lambda}\sin 4\lambda S_0\right] \\ F_{5F_2} = \left[(-D)W'' + \left(K\frac{\nu}{R} + 4\nu\lambda^2 D\right)W + \left(2\nu\frac{\lambda}{R}D + 2\nu K\lambda\right)V + \bar{K}U'\right]\left[S_0 + \frac{1}{4\lambda}\sin 4\lambda S_0\right] \end{cases}$$

THE TOTAL BEAM LOADS ARE GIVEN BY:

$$(2\text{-}48)\qquad F_{iF} = F_{iF_0} + F_{iF_1} + F_{iF_2} \qquad (i = 1, \cdots 6)$$

THE STIFFNESS COEFFICIENTS ARE GIVEN BY:

$$(2\text{-}49)\quad \begin{cases} F_{1F}(L) = k_{16} & F_{4F}(L) = k_{46} \\ F_{2F}(L) = k_{26} & F_{5F}(L) = k_{56} \\ F_{3F}(L) = k_{36} & F_{6F}(L) = k_{66} \end{cases}$$

$$(2\text{-}50)\quad \begin{cases} F_{1F}(0) = k_{76} & F_{4F}(0) = k_{10,6} \\ F_{2F}(0) = k_{86} & F_{5F}(0) = k_{11,6} \\ F_{3F}(0) = k_{96} & F_{6F}(0) = k_{12,6} \end{cases}$$

3- MODIFICATIONS TO REF-1

CASE-A

BOUNDARY CONDITIONS:

@ $x=0$:

$$\text{I} \begin{cases} u=0 \\ v=0 \\ w=0 \\ \frac{\partial w}{\partial x}=0 \end{cases}$$

@ $x=L$:

$$\text{II-A} \begin{cases} u=0 \\ v=\sin\lambda s \\ w=-\cos\lambda s \\ \frac{\partial w}{\partial x}=0 \end{cases}$$

ASSUMED FORM OF SOLUTION TO EQUATIONS (1), (2), (3) OF REF-1:

$$u = U(x)\cos\lambda s$$
$$v = V(x)\sin\lambda s$$
$$w = W(x)\cos\lambda s$$

THIS PROPOSED SOLUTION WILL BE VALID PROVIDED THAT:

$$(3\text{-}1) \quad U'' - c_1 U + c_2 V' + c_3 W' = 0$$

$$(3\text{-}2) \quad -c_2 U' + c_4 V'' - c_5 V + c_6 W'' - c_7 W = 0$$

$$(3\text{-}3) \quad c_8 U' + c_{10} V - c_9 V'' + c_{12} W - c_{11} W'' + W^{IV} = 0$$

WHERE c_1 THROUGH c_{12} ARE GIVEN BY (10) OF REF-1

AS INDICATED ON P.16 OF REF-1 THE SOLUTION TO 3-1, 3-2, 3-3 IN TERMS OF REAL CONSTANTS IS GIVEN BY:

$$(3\text{-}4) \quad U(x) = e^{\rho x}\left(C_1 \sin qx + C_2 \cos qx\right) + e^{-\rho x}\left(C_3 \sin qx + C_4 \cos qx\right)$$

$$(3\text{-}5) \quad V(x) = e^{\rho x}\left(\bar{C}_1 \sin qx + \bar{C}_2 \cos qx\right) + e^{-\rho x}\left(\bar{C}_3 \sin qx + \bar{C}_4 \cos qx\right)$$
$$+ B_0 + B_1 x + B_2 x^2 + B_3 x^3$$

$$(3\text{-}6) \quad W(x) = e^{\rho x}\left(\bar{\bar{C}}_1 \sin qx + \bar{\bar{C}}_2 \cos qx\right) + e^{-\rho x}\left(\bar{\bar{C}}_3 \sin qx + \bar{\bar{C}}_4 \cos qx\right)$$
$$+ c\left(B_0 + B_1 x + B_2 x^2 + B_3 x^3\right)$$

WHERE C_i, $\bar{C}_i$, $\bar{\bar{C}}_i$, B_j ARE TO BE DETERMINED

CASE-A (CONT'D)

p AND q ARE GIVEN BY (55a) OF REF-1

c IS GIVEN BY (87) OF REF-1

IMPOSING BOUNDARY CONDITION, I LEADS TO:

(3-7) $$C_2 + C_4 = 0$$

(3-8) $$\bar{C}_2 + \bar{C}_4 + \bar{B}_0 = 0$$

(3-9) $$\bar{\bar{C}}_2 + \bar{\bar{C}}_4 + c\bar{B}_0 = 0$$

(3-10) $$q\bar{\bar{C}}_1 + p\bar{\bar{C}}_2 + q\bar{\bar{C}}_3 - p\bar{\bar{C}}_4 + c\bar{B}_1 = 0$$

IMPOSING BOUNDARY CONDITION II-A LEADS TO:

(3-11) $$e^{pL}(C_1 \sin qL + C_2 \cos qL) + e^{-pL}(C_3 \sin qL + C_4 \cos qL) = 0$$

(3-12) $$e^{pL}(\bar{C}_1 \sin qL + \bar{C}_2 \cos qL) + e^{-pL}(\bar{C}_3 \sin qL + C_4 \cos qL) + \bar{B}_0 + \bar{B}_1 L + \bar{B}_2 L^2 + \bar{B}_3 L^2 = 1$$

(3-13) $$e^{pL}(\bar{\bar{C}}_1 \sin qL + \bar{\bar{C}}_2 \cos qL) + e^{-pL}(\bar{\bar{C}}_3 \sin qL + \bar{\bar{C}}_4 \cos qL) + c(\bar{B}_0 + \bar{B}_1 L + \bar{B}_2 L^2 + \bar{B}_3 L^3) = -1$$

(3-14) $$e^{pL}\{(q\bar{\bar{C}}_1 + p\bar{\bar{C}}_2)\cos qL + (p\bar{\bar{C}}_1 - q\bar{\bar{C}}_2)\sin qL\} + e^{-pL}\{(q\bar{\bar{C}}_3 - p\bar{\bar{C}}_4)\cos qL - (p\bar{\bar{C}}_3 + q\bar{\bar{C}}_4)\sin qL\} + c(\bar{B}_1 + 2\bar{B}_2 L + 3\bar{B}_3 L^2) = 0$$

CASE-A CONT'D

IN ADDITION TO THE BOUNDARY CONDITIONS WE HAVE THE DEPENDENCY RELATIONS (SEE REF-1, EQUATION 109 & 111a):

$$(3\text{-}15) \quad C_1 = C_1 x_B - C_2 y_B$$

$$(3\text{-}16) \quad \bar{C}_2 = C_1 y_B + C_2 x_B$$

$$(3\text{-}17) \quad \bar{C}_3 = C_3 \bar{x}_B + C_4 \bar{y}_B$$

$$(3\text{-}18) \quad \bar{C}_4 = -C_3 \bar{y}_B + C_4 \bar{x}_B$$

$$(3\text{-}19) \quad \bar{\bar{C}}_1 = C_1 x_C - C_2 y_C$$

$$(3\text{-}20) \quad \bar{\bar{C}}_2 = C_1 y_C + C_2 x_C$$

$$(3\text{-}21) \quad \bar{\bar{C}}_3 = C_3 \bar{x}_C + C_4 \bar{y}_C$$

$$(3\text{-}22) \quad \bar{\bar{C}}_4 = -C_3 \bar{y}_C + C_4 \bar{x}_C$$

WHERE $x_B, y_B, \bar{x}_B, \bar{y}_B, x_C, y_C, \bar{x}_C, \bar{y}_C$ MAY BE DETERMINED FROM EQUATIONS (70) AND (71) OF REF-1

EQUATIONS (3-7) THROUGH (3-22) CONSTITUTE A SET OF 16 SIMULTANEOUS LINEAR EQUATIONS WITH 16 UNKNOWNS, $C_1, \ldots C_4$; $\bar{C}_1, \ldots \bar{C}_4$; $\bar{\bar{C}}_1, \ldots \bar{\bar{C}}_4$; B_0, B_1, B_2, B_3 WHICH CAN BE REPRESENTED MORE COMPACTLY BY:

CASE A - CONT'D

$$(3-23)\qquad \begin{bmatrix} \alpha_1 & \alpha_2 & \alpha_3 & \alpha_4 \\ \beta_1 & \beta_2 & \beta_3 & \beta_4 \\ \gamma_1 & \gamma_2 & \gamma_3 & \gamma_4 \\ \delta_1 & \delta_2 & \delta_3 & \delta_4 \end{bmatrix} \begin{Bmatrix} C \\ \bar{C} \\ \bar{\bar{C}} \\ B \end{Bmatrix} = \begin{Bmatrix} k_1 \\ k_2 \\ k_3 \\ k_4 \end{Bmatrix}$$

WHERE :

$$(3-24)\qquad C = \begin{Bmatrix} C_1 \\ C_2 \\ C_3 \\ C_4 \end{Bmatrix} \qquad \bar{C} = \begin{Bmatrix} \bar{C}_1 \\ \bar{C}_2 \\ \bar{C}_3 \\ C_4 \end{Bmatrix} \qquad \bar{\bar{C}} = \begin{Bmatrix} \bar{\bar{C}}_1 \\ \bar{\bar{C}}_2 \\ \bar{\bar{C}}_3 \\ \bar{\bar{C}}_4 \end{Bmatrix} \qquad B = \begin{Bmatrix} B_0 \\ B_1 \\ B_2 \\ B_3 \end{Bmatrix}$$

$$(3-25)\qquad k_1 = k_2 = k_3 = \begin{Bmatrix} 0 \\ 0 \\ 0 \\ 0 \end{Bmatrix} \qquad k_4 = \begin{Bmatrix} 0 \\ 1 \\ -1 \\ 0 \end{Bmatrix}$$

AND:

α_i, β_i, γ_i $(i=1,\cdots 4)$ ARE 4 x 4 MATRICES AS SHOWN ON TABLE C-1 (PC-31) OF REF-1.

AND δ_i ARE GIVEN BY:

$$(3-26)\qquad \delta_1 = \begin{bmatrix} (e^{\rho L}\sin qL) & (e^{\rho}\cos qL) & (e^{-\rho L}\sin qL) & (e^{-\rho L}\cos qL) \\ 0 & 0 & 0 & 0 \\ 0 & 0 & 0 & 0 \\ 0 & 0 & 0 & 0 \end{bmatrix}$$

CASE A - CONT'D

$$(3-27)\quad \delta_2 = \begin{bmatrix} 0 & 0 & 0 & 0 \\ (e^{pL}\sin qL) & (e^{pL}\cos qL) & (e^{-pL}\sin qL) & (e^{-pL}\cos qL) \\ 0 & 0 & 0 & 0 \\ 0 & 0 & 0 & 0 \end{bmatrix}$$

$$(3-28)\quad \delta_3 = \begin{bmatrix} 0 & 0 & 0 & 0 \\ 0 & 0 & 0 & 0 \\ (e^{pL}\sin qL) & (e^{pL}\cos qL) & (e^{-pL}\sin qL) & (e^{-pL}\cos qL) \\ \left(e^{pL}(q\cos qL + p\sin qL)\right) & \left(e^{pL}(p\cos qL - q\sin qL)\right) & \left(e^{-pL}(q\cos qL - p\sin qL)\right) & \left(e^{-pL}(-p\cos qL - q\sin qL)\right) \end{bmatrix}$$

$$(3-29)\quad \delta_4 = \begin{bmatrix} 0 & 0 & 0 & 0 \\ 1 & L & L^2 & L^3 \\ c & cL & cL^2 & cL^3 \\ 0 & c & 2cL & 3cL^2 \end{bmatrix}$$

CASE-B

BOUNDARY CONDITIONS

@ $x=0$: I $\begin{cases} u=0 \\ v=0 \\ \omega=0 \\ \frac{\partial w}{\partial x}=0 \end{cases}$ @ $x=L$: II-B $\begin{cases} u=0 \\ v=-\cos\lambda s \\ \omega=-\sin\lambda s \\ \frac{\partial w}{\partial x}=0 \end{cases}$

ASSUMED FORM OF SOLUTION:

$$u = U(x)\sin\lambda s$$
$$v = V(x)\cos\lambda s$$
$$\omega = W(x)\sin\lambda s$$

WE ARE LED TO A SET OF ORDINARY DIFFERENTIAL EQUATIONS WITH A CHARACTERISTIC EQUATION WITH IDENTICAL COEFFICIENTS AS FOR CASE-A SO THAT THE FORM OF U, V, W IS IDENTICAL WITH (3-4), (3-5), (3-6). AS BEFORE THE CONSTANTS ARE DETERMINED BY (3-23) EXCEPT THAT FOR CASE B:

(3-30) $$k_4 = \begin{Bmatrix} 0 \\ -1 \\ -1 \\ 0 \end{Bmatrix}$$

WHICH WILL LEAD TO A DIFFERENT SET OF CONSTANTS.

CASE-C

BOUNDARY CONDITIONS

@ $x=0$: I $\begin{cases} u=0 \\ v=0 \\ w=0 \\ \frac{\partial w}{\partial x}=0 \end{cases}$ @ $x=L$: II-C $\begin{cases} u=-1 \\ v=0 \\ w=0 \\ \frac{\partial w}{\partial x}=0 \end{cases}$

ASSUMED FORM OF SOLUTION:

$$\left.\begin{aligned} u &= U(x)\cos\lambda_0 s \\ v &= V(x)\sin\lambda_0 s \\ w &= W(x)\cos\lambda_0 s \end{aligned}\right\} \text{WHERE } \lambda_0 = 0$$

AS BEFORE THE CONSTANTS MAY BE DETERMINED FROM (3-23) EXCEPT THAT FOR CASE C:

(3-31) $$R_4 = (-1, 0, 0, 0)^T$$ (T- INDICATES - TRANSPOSE)

CASE-D

BOUNDARY CONDITIONS:

@ $x=0$: I $\begin{cases} u=0 \\ v=0 \\ w=0 \\ \frac{\partial w}{\partial x}=0 \end{cases}$ @ $x=L$: II-D $\begin{cases} u=0 \\ v=R \\ w=0 \\ \frac{\partial w}{\partial x}=0 \end{cases}$

ASSUMED FORM OF SOLUTION:

$$\left.\begin{aligned} u &= U(x)\sin\lambda_0 s \\ v &= V(x)\cos\lambda_0 s \\ w &= W(x)\sin\lambda_0 s \end{aligned}\right\} \text{WHERE } \lambda_0 = 0$$

AS BEFORE THE CONSTANTS MAY BE DETERMINED FROM (3-23) EXCEPT THAT FOR CASE D:

(3-32) $$R_4 = (0, P, 0, 0)^T$$

CASE - E

BOUNDARY CONDITIONS :

$$@\ x=0:\ I\begin{cases} u=0 \\ v=0 \\ \omega=0 \\ \frac{\partial w}{\partial x}=0 \end{cases} \qquad @\ x=L:\ \text{II-E}\begin{cases} u = \overbrace{0}^{\text{II-E}_0} + \overbrace{a_{1E}\cos\lambda s}^{\text{II-E}_1} + \overbrace{0}^{\text{II-E}_2} \\ v = 0 + 0 + b_{2E}\sin 2\lambda s \\ \omega = C_{0E} + 0 + C_{2E}\cos 2\lambda s \\ \frac{\partial \omega}{\partial x} = 0 + 0 + 0 \end{cases}$$

ASSUMED FORM OF SOLUTION ($\lambda_0 = 0$):

$$u = U_0(x)\cos\lambda_0 s + U_1(x)\cos\lambda s + U_2(x)\cos 2\lambda s$$

$$v = V_0(x)\sin\lambda_0 s + V_1(x)\sin\lambda s + V_2(x)\sin 2\lambda s$$

$$\omega = W_0(x)\cos\lambda_0 s + W_1(x)\cos\lambda s + W_2(x)\cos 2\lambda s$$

AGAIN WE APPLY (3-23) THREE TIMES TO OBTAIN THE APPROPRIATE CONSTANTS FOR U, V, W WITH THE FOLLOWING MODIFICATIONS :

(3-33) $$(k_4)_0 = \begin{Bmatrix} 0 \\ 0 \\ C_{0E} \\ 0 \end{Bmatrix} \qquad (k_4)_1 = \begin{Bmatrix} a_{1E} \\ 0 \\ 0 \\ 0 \end{Bmatrix} \qquad (k_4)_2 = \begin{Bmatrix} 0 \\ b_{2E} \\ C_{2E} \\ 0 \end{Bmatrix}$$

WHERE $a_{1E}, b_{2E}, C_{0E}, C_{2E}$ ARE GIVEN BY (1-14)

CASE-F

BOUNDARY CONDITIONS:

			II-F_0		II-F_1		II-F_2
@ $x=0$: I	$u=0$	@ $x=L$:	$u=$ 0	+	$a_{1F}\sin\lambda s$	+	0
	$v=0$		$v=$ 0	+	0	+	$b_{2F}\sin 2\lambda s$
	$w=0$		$w=$ C_{0F}	+	0	+	$C_{2F}\cos 2\lambda s$
	$\frac{\partial w}{\partial x}=0$		$\frac{\partial w}{\partial x}=$ 0	+	0	+	0

ASSUMED FORM OF SOLUTION:

$$u = U_0(x)\cos\lambda_0 s + U_1(x)\sin\lambda s + U_2(x)\cos 2\lambda s$$
$$v = V_0(x)\sin\lambda_0 s + V_1(x)\cos\lambda s + W_2(x)\sin 2\lambda s$$
$$w = W_0(x)\cos\lambda_0 s + V_1(x)\sin\lambda s + W_2(x)\cos 2\lambda s$$

APPLY (3-23) THREE TIMES TO OBTAIN THE APPROPRIATE CONSTANTS FOR U, V, W WITH THE FOLLOWING MODIFICATIONS:

(3-34)
$$(k_4)_0 = \begin{Bmatrix} 0 \\ 0 \\ C_{0F} \\ 0 \end{Bmatrix} \qquad (k_4)_1 = \begin{Bmatrix} a_{1F} \\ 0 \\ 0 \\ 0 \end{Bmatrix} \qquad (k_4)_2 = \begin{Bmatrix} 0 \\ b_{2F} \\ C_{2F} \\ 0 \end{Bmatrix}$$

WHERE a_{1F}, b_{2F}, C_{0F}, C_{2F} ARE GIVEN BY (1-15)

CASE-G

IN THIS APPENDIX WE CONSIDER THE FORCES IN THE GRAVITY GRADIENT ROD RESULTING FROM A "BREATHING" DISPLACEMENT AS SHOWN IN FIG A-1 @ $x = L$, WHERE $\omega(L,s) = \Omega s^2$, ALL OTHER DISPLACEMENTS BEING FIXED. OUR OBJECTIVE IS TO FIND THE SET OF STIFFNESS COEFICIENTS ASSOCIATED WITH THIS ADDITIONAL SHELL MOTION WHERE THE VALUE Ω COMPLETELY CHARACTERIZES THE DISPLACEMENT

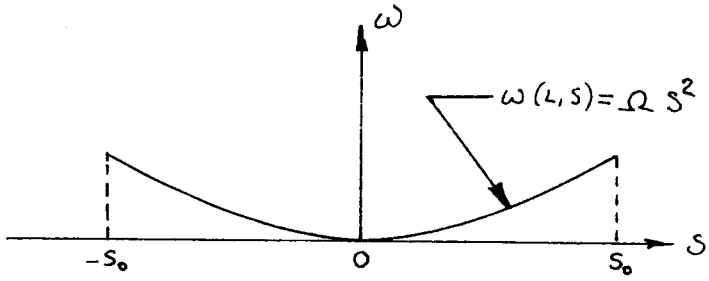


FIG-A-1

$\omega(L,s)$ MAY BE APPROXIMATED BY:

(A-1) $$\omega = A_0 + A_1 \cos\frac{\pi}{s_0}s + A_2 \cos\frac{2\pi}{s_0}s + \cdots A_m \cos\frac{m\pi}{s_0}s + \cdots$$

WHERE:

(A-2) $$A_0 = \frac{1}{s_0}\int_0^{s_0} \Omega s^2 ds = \frac{1}{3}\Omega s_0^2$$

(A-3) $$A_m = \frac{2}{s_0}\int_0^{s_0} \Omega s^2 \cos\frac{m\pi}{s_0}s\, ds = \frac{2\Omega}{s_0\lambda_m^3}\left[2\lambda_m s\cos\lambda_m s + (\lambda_m^2 s^2 - 2)\sin\lambda_m s\right]_0^{s_0}$$

WHICH GIVES:

(A-4) $$A_m = 4\Omega\left(\frac{s_0}{\pi}\right)^2\frac{(-1)^m}{m^2}$$

SUBSTITUTING A-2 AND A-4 INTO A-1 AND LIMITING OUR EXPANSION TO 5 TERMS WE OBTAIN:

$$(A\text{-}5) \qquad \omega = \left(\frac{S_0}{\pi}\right)^2 \Omega \left\{ \frac{\pi^2}{3} - 4\cos\frac{\pi}{S_0}S + \cos\frac{2\pi}{S_0}S - \frac{4}{9}\cos\frac{3\pi}{S_0}S + \frac{1}{4}\cos\frac{4\pi}{S_0}S \right\}$$

@ $x = L$.

OR:

$$(A\text{-}5a) \qquad \omega(L,S) = \left(\frac{S_0}{\pi}\right)^2 \Omega \sum_{m=0}^{4} a_m \cos\lambda_m S$$

WHERE:

$$(A\text{-}5b) \qquad \lambda_m = \frac{m\pi}{S_0}$$

AND a_m IS GIVEN BY TABLE A-1

m	0	1	2	3	4
a_m	$\pi^2/3$	-4	1	$-4/9$	$1/4$

TABLE A-1

IT IS RESONABLE THEN TO ASSUME SOLUTIONS:

$$(A\text{-}6) \qquad \begin{cases} u = \left(\frac{S_0}{\pi}\right)^2 \Omega \sum U_m(x) \cos\lambda_m S \\ v = \left(\frac{S_0}{\pi}\right)^2 \Omega \sum V_m(x) \sin\lambda_m S \\ \omega = \left(\frac{S_0}{\pi}\right)^2 \Omega \sum W_m(x) \cos\lambda_m S \end{cases}$$

BOUNDARY REQUIREMENTS

@ $x = L$:	@ $x = 0$:
$u = 0$	$u = 0$
$v = 0$	$v = 0$
$\omega = \left(\frac{S_u}{\pi}\right)^2 \Omega \sum a_m \cos \lambda_m S$	$\omega = 0$
$\frac{\partial \omega}{\partial x} = 0$	$\frac{\partial \omega}{\partial x} = 0$

(A-7)

SO THAT :

$$(A\text{-}8) \quad U_m(L) = V_m(L) = W_m'(L) = U_m(0) = V_m(0) = W_m'(0) = 0, \quad W_m(L) = a_m$$

IF THE POTENTIAL ENERGY OF THE SYSTEM IS GIVEN IS $\mathcal{U}$ THEN A GENERALIZED STIFFNESS COEFICIENT $k_{13,13}$ IS GIVEN BY :

$$F_{13G}(L) = k_{13,13} = \frac{\partial^2 \mathcal{U}}{\partial \Omega^2}$$

WHERE F_{13G} IS THE GENERALIZED FORCE @ $x=L$ DUE TO THE GENERALIZED DISPLACEMENT G SHOWN IN FIG A-1.

$$(A\text{-}9) \quad \mathcal{U} = -\int_A W \, dA + \oint_C T_i \, u_i \, dc$$

WHERE :

W IS THE STRAIN ENERGY DENSITY PER UNIT AREA
T_i ARE TRACTIONS ON THE PERIMETER "C" BOUNDING THE AREA "A"
u_i ARE DISPLACEMENTS ON THE PERIMETER

BUT BY CLAPEYRON'S THEOREM : $\int_A W \, dA = \frac{1}{2} \oint_C T_i \, u_i \, dc$

HENCE :

$$(A\text{-}10) \qquad \mathcal{U} = \frac{1}{2} \oint_C T_i u_i \, dc$$

FOR OUR SYSTEM :

$$(A\text{-}11) \qquad T_i = V_x = \frac{\partial^3 \omega}{\partial x^3} + (2-\nu) \frac{\partial^3 \omega}{\partial x \partial s^2} - \frac{1}{R} \frac{\partial^2 v}{\partial x \partial s}$$

$$(A\text{-}12) \qquad u_i = \omega(L,s)$$

$$(A\text{-}13) \qquad dc \Leftrightarrow ds \qquad @ \; x = L$$

HENCE :

$$(A\text{-}14) \qquad \mathcal{U} = \frac{1}{2} \int_{-s_0}^{s_0} [V_x \, \omega]_{x=L} \, ds$$

$$v = \left(\frac{s_0}{\pi}\right)^2 \Omega \sum V_m(x) \sin \lambda_m s$$

$$(A\text{-}15) \qquad \frac{\partial^2 v}{\partial x \partial s} = \left(\frac{s_0}{\pi}\right)^2 \Omega \sum V_m'(x) \lambda_m \cos \lambda_m s$$

$$\omega = \left(\frac{s_0}{\pi}\right)^2 \Omega \sum W_m(x) \cos \lambda_m s$$

$$(A\text{-}16) \qquad \frac{\partial^3 \omega}{\partial x^3} = \left(\frac{s_0}{\pi}\right)^2 \Omega \sum W_m'''(x) \cos \lambda_m s$$

$$(A\text{-}17) \qquad \frac{\partial^3 \omega}{\partial x \partial s^2} = \left(\frac{s_0}{\pi}\right)^2 \Omega \sum -\lambda_m^2 \, W_m'(x) \cos \lambda_m s$$

HENCE :

$$(A\text{-}18) \qquad V_x = \left(\frac{s_0}{\pi}\right)^2 \Omega \sum_m \left[W_m''' - (2-\nu) \lambda_m^2 W_m' - \frac{1}{R} \lambda_m V_m'\right] \cos \lambda_m s$$

BUT @ $x = L$ $\quad W_m'(L) = 0$ $\quad$ SO THAT :

$$(A\text{-}19) \qquad V_x\Big]_{x=L} = \left(\frac{s_0}{\pi}\right)^2 \Omega \sum_m \left[W_m''' - \frac{1}{R} \lambda_m V_m'\right] \cos \lambda_m s$$

AND :

$$(A\text{-}20)\quad \left[V_x\,\omega\right]_{x=L} = \left(\frac{S_0}{\pi}\right)^4 \Omega^2 \sum_n \left[W_n''' - \frac{\lambda_n}{R} V_n'\right] \cos\lambda_n s \sum_m a_m \cos\lambda_m s$$

OR :

$$(A\text{-}21)\quad \left[V_x\,\omega\right]_{x=L} = \left(\frac{S_0}{\pi}\right)^4 \Omega^2 \sum_{m\,n} [a_m]\left[W_n''' - \frac{\lambda_n}{R} V_n'\right] \cos\lambda_n s \cos\lambda_m s$$

SUBSTITUTING INTO (A-14) :

$$(A\text{-}22)\quad \mathcal{U} = \frac{1}{2}\left(\frac{S_0}{\pi}\right)^4 \Omega^2 \sum_{m\,n} [a_m]\left[W_n''' - \frac{\lambda_n}{R} V_n'\right]_{x=L} \int_{-S_0}^{S_0} \cos\lambda_m s \cos\lambda_n s \, ds$$

DUE TO SYMMETRY ABOUT $S=0$:

$$(A\text{-}23)\quad \int_{-S_0}^{S_0} \cos\lambda_m s \cos\lambda_n s \, ds = 2\int_0^{S_0} \cos\lambda_m s \cos\lambda_n s \, ds$$

IF $\lambda_m = \lambda_n = \lambda \neq 0$, THEN :

$$(A\text{-}24)\quad 2\int_0^{S_0} \cos^2\lambda s \, ds = \frac{2}{\lambda}\left[\frac{1}{2}\lambda s + \frac{1}{4}\sin 2\lambda s\right]_0^{S_0} = S_0$$

IF $\lambda_m \neq \lambda_n$, THEN :

$$(A\text{-}25)\quad 2\int_0^{S_0} \cos\lambda_m s \cos\lambda_n s \, ds = 2\left[\frac{\sin(\lambda_m-\lambda_n)s}{2(\lambda_m-\lambda_n)} + \frac{\sin(\lambda_m+\lambda_n)s}{2(\lambda_m+\lambda_n)}\right]_0^{S_0} = 0$$

IF $\lambda_m = \lambda_n = 0$, THEN :

$$(A\text{-}26)\quad 2\int_0^{S_0} ds = 2S_0$$

SO THAT:

$$(A\text{-}27)\quad \mathcal{U} = \frac{1}{2}\left(\frac{S_o}{\pi}\right)^4 \Omega^2 \left\{ 2 S_o a_o W_o''' + S_o \sum_{j=1}^{4} [a_j]\left[W_j''' - \frac{\lambda_j}{R} V_j'\right] \right\}_{x=L}$$

THE STIFFNESS COEFFICIENT IS GIVEN BY:

$$(A\text{-}28)\quad \frac{\partial^2 \mathcal{U}}{\partial \Omega^2} = \left(\frac{S_o}{\pi}\right)^4 \left\{ 2 S_o a_o W_o''' + S_o \sum_{j=1}^{4} [a_j]\left[W_j''' - \frac{\lambda_j}{R} V_j'\right] \right\}_{x=L} = F_{13G}(L)$$

WHERE a_o, a_j MAY BE FOUND FROM TABLE A-1.

NOTE THAT (A-28) PROVIDES THE EXPRESSION FOR THE STIFFNESS COEFFICIENT $F_{13G}(L) = k_{13,13}$.

OFF DIAGONAL TERMS

NOTE THE ANALOGY BETWEEN DEFLECTION "G" AND "A" AS SHOWN ON P. 1-2. WE MAY IMMEDIATELY DEDUCE THAT:

$$F_{2G} = F_{4G} = F_{6G} = 0$$

TO FIND THE REMAINING BEAM LOADS F_{1G}, F_{3G}, F_{5G} WE ASSUME THE BOUNDARY REQUIREMENTS AS GIVEN BY (A-7) EXCEPT THAT Ω TAKES ON THE VALUE $\Omega = -1$, THUS:

@ $x=L$:

II-G
$$\begin{cases} u = 0 \\ v = 0 \\ \omega = -\left(\frac{S_0}{\pi}\right)^2 \sum_{m=0}^{4} a_m \cos \lambda_m s \\ \frac{\partial \omega}{\partial x} = 0 \end{cases}$$

@ $x=0$:

I
$$\begin{cases} u = 0 \\ v = 0 \\ \omega = 0 \\ \frac{\partial \omega}{\partial x} = 0 \end{cases}$$

THESE CONDITIONS MAY BE SATISFIED BY THE FUNCTIONS:

(A-29)
$$\begin{cases} u = -\left(\frac{S_0}{\pi}\right)^2 \sum_m U_m(x) \cos \lambda_m s \\ v = -\left(\frac{S_0}{\pi}\right)^2 \sum_m V_m(x) \sin \lambda_m s \\ \omega = -\left(\frac{S_0}{\pi}\right)^2 \sum_m W_m(x) \cos \lambda_m s \end{cases}$$

BY ANALOGY WITH 2-13 THROUGH (2-16) WE MAY WRITE

(A-30) $$N_x = -\left(\frac{S_0}{\pi}\right)^2 K \sum_m \left(U_m' + \nu \lambda_m V_m + \frac{\nu}{R} W_m\right) \cos \lambda_m s$$

(A-31) $$M_x = -\left(\frac{S_0}{\pi}\right)^2 \sum_m \left[W_m'' - \nu \lambda_m^2 W_m + \frac{\nu}{R} \lambda_m V_m\right) \cos \lambda_m s$$

(A-32) $$N_{xs} = -\left(\frac{S_0}{\pi}\right)^2 \sum_m \left[K\left(-\lambda_m U_m + V_m'\right) + \frac{D}{R}\left(-2\lambda_m W_m' - \frac{1}{R} V_m'\right)\right] \sin \lambda_m s$$

(A-33) $$V_x = -\left(\frac{S_0}{\pi}\right)^2 \sum_m \left[W_m''' - (2-\nu)\lambda_m^2 W_m' - \frac{\lambda_m}{R} V_m'\right] \cos \lambda_m s$$

FROM (2-1) :

$$F_1 = \int_{-S_0}^{S_0} N_x \, ds = -\left(\frac{S_0}{\pi}\right)^2 K \sum_m \left(U_m' + \nu \lambda_m V_m + \frac{1}{R} W_m\right) \int_{-S_0}^{S_0} \cos \lambda_m s \, ds$$

(A-34) $$F_{1G} = -\left(\frac{S_0}{\pi}\right)^2 K \sum_m \left(U_m' + \nu \lambda_m V_m + \frac{\nu}{R} W_m\right) \frac{1}{\lambda_m} \left[\sin \lambda_m s\right]_{-S_0}^{S_0} = 0$$

FROM (2-3):

$$F_3 = \int_{-S_0}^{S_0} (V_x \cos \tfrac{1}{R} s - N_{xs} \sin \tfrac{1}{R} s)\, ds$$

$$(A\text{-}35) \quad F_{3G} = -\left(\frac{S_0}{\pi}\right)^2 \sum_m \left[W_m''' - (2-\nu)\lambda_m^2 W_m' - \frac{\lambda_m}{R} V_m\right] \int_{-S_0}^{S_0} \cos \lambda_m s \cos \tfrac{1}{R} s\, ds$$

$$-\left(\frac{S_0}{\pi}\right)^2 \sum_m \left[K(-\lambda_m U_m + V_m') + \frac{D}{R}(-2\lambda_m W_m' - \tfrac{1}{R} V_m')\right] \int_{-S_0}^{S_0} \sin \lambda_m s \sin \tfrac{1}{R} s\, ds$$

BUT:

$$(A\text{-}36) \quad \int_{-S_0}^{S_0} \cos \lambda_m s \cos \tfrac{1}{R} s\, ds = \left[\frac{\sin(\lambda_m - \frac{1}{R}) S_0}{(\lambda_m - \frac{1}{R})} + \frac{\sin(\lambda_m + \frac{1}{R}) S_0}{(\lambda_m + \frac{1}{R})}\right]$$

AND:

$$\sin(\lambda_m - \tfrac{1}{R}) S_0 = \sin \lambda_m S_0 \cos \tfrac{1}{R} S_0 - \cos \lambda_m S_0 \sin \tfrac{1}{R} S_0$$

$$\sin(\lambda_m + \tfrac{1}{R}) S_0 = \sin \lambda_m S_0 \cos \tfrac{1}{R} S + \cos \lambda_m S_0 \sin \tfrac{1}{R} S_0$$

$$\sin \lambda_m S_0 = 0, \quad \cos \lambda_m S_0 = (-1)^m$$

HENCE:

$$(A\text{-}37) \quad \int_{-S_0}^{S_0} \cos \lambda_m s \cos \tfrac{1}{R} s\, ds = \left[\frac{(-1)^{m+1}}{(\lambda_m - \frac{1}{R})} + \frac{(-1)^m}{(\lambda_m + \frac{1}{R})}\right] \sin \frac{S_0}{R}$$

SIMILARLY:

$$(A\text{-}38) \quad \int_{-S_0}^{S_0} \sin \lambda_m s \sin \tfrac{1}{R} s\, ds = \left[\frac{(-1)^{m+1}}{(\lambda_m - \frac{1}{R})} - \frac{(-1)^m}{(\lambda_m + \frac{1}{R})}\right] \sin \frac{S_0}{R}$$

BEFORE SUBSTITUTING A-37, A-38 INTO A-35 NOTE THAT DUE TO THE BOUNDARY CONDITIONS I & II-G U, V, W' ARE ZERO @ $x = 0, L$ SO THAT :

$$(A\text{-}39)\quad F_{3G} = -\left(\frac{S_0}{\pi}\right)^2 \sum_m \left[W_m'''\right] \int_{-S_0}^{S_0} \cos\lambda_m s \cos\tfrac{1}{R}s \, ds$$

$$- \left(\frac{S_0}{\pi}\right)^2 \sum_m \left[K V_m'\right] \int_{-S_0}^{S_0} \sin\lambda_m s \sin\tfrac{1}{R}s \, ds$$

SUBSTITUTING A-37 & A-38 INTO A-39 WE OBTAIN:

$$(A\text{-}40)\quad F_{3G} = -\left(\frac{S_0}{\pi}\right)^2 \sin\frac{S_0}{R} \left\{ \sum_m W_m''' \left[\frac{(-1)^{m+1}}{(\lambda_m - \frac{1}{R})} + \frac{(-1)^m}{(\lambda_m + \frac{1}{R})}\right] \right.$$

$$\left. + K V_m' \left[\frac{(-1)^{m+1}}{\lambda_m - \frac{1}{R}} - \frac{(-1)^m}{(\lambda_m + \frac{1}{R})}\right] \right\}$$

FROM (2-5):

$$F_{5G} = \int_{-S_0}^{S_0} \left(M_x \cos\tfrac{1}{R}s + N_x R \cos\tfrac{1}{R}s\right) ds$$

$$(A\text{-}41)\quad F_{5G} = -\left(\frac{S_0}{\pi}\right)^2 \sum_m \left(W_m'' - \nu\lambda_m^2 W_m\right) \int_{-S_0}^{S_0} \cos\lambda_m s \cos\tfrac{1}{R}s \, ds$$

$$- \left(\frac{S_0}{\pi}\right)^2 \sum_m K \left(U_m' + \frac{\nu}{R} W_m\right) \int_{-S_0}^{S_0} \cos\lambda_m s \cos\tfrac{1}{R}s \, ds$$

$$(A\text{-}42)\quad F_{5G} = -\left(\frac{S_0}{\pi}\right)^2 \sin\frac{S_0}{R}\sum_m \left\{\left[W_m'' - \nu\lambda_m^2 W_m\right] + K\left[U_m' + \frac{\nu}{R}W_m\right]\right\}\left\{\frac{(-1)^{m+1}}{\left(\lambda_m - \frac{1}{R}\right)} + \frac{(-1)^m}{\left(\lambda_m + \frac{1}{R}\right)}\right\}$$

OUR RESULTS THUS FAR MAY BE SUMMARIZED AS FOLLOWS:

$$(A\text{-}43)\quad \begin{cases} F_{1G} = F_{2G} = F_{4G} = F_{6G} = 0 \\ F_{3G} = -\left(\frac{S_0}{\pi}\right)^2 \sin\frac{S_0}{R}\left\{\sum_m W_m'''\left[\frac{(-1)^{m+1}}{\left(\lambda_m - \frac{1}{R}\right)} + \frac{(-1)^m}{\left(\lambda_m + \frac{1}{R}\right)}\right] + K V_m'\left[\frac{(-1)^{m+1}}{\left(\lambda_m - \frac{1}{R}\right)} - \frac{(-1)^m}{\left(\lambda_m + \frac{1}{R}\right)}\right]\right\} \\ F_{5G} = -\left(\frac{S_0}{\pi}\right)^2 \sin\frac{S_0}{R}\left\{\sum_m \left[\left(W_m'' - \nu\lambda_m^2 W_m\right) + K\left(U_m' + \frac{\nu}{R}W_m\right)\right]\left[\frac{(-1)^{m+1}}{\left(\lambda_m - \frac{1}{R}\right)} + \frac{(-1)^m}{\left(\lambda_m + \frac{1}{R}\right)}\right]\right\} \\ F_{13G} = \left(\frac{S_0}{\pi}\right)^4\left\{2S_0 a_0 W_0''' + S_0\sum_{j=1}^{4} a_j\left(W_j''' - \frac{\lambda_j}{R}V_j'\right)\right\}_{x=L} \end{cases}$$

A-43 PROVIDES US WITH THE FOLLOWING STIFFNESS COEFFICIENTS:

$$(A\text{-}44)\quad \begin{cases} F_{1G}(L) = k_{1,13} & F_{4G}(L) = k_{4,13} & F_{13G}(L) = k_{13,13} \\ F_{2G}(L) = k_{2,13} & F_{5G}(L) = k_{5,13} & \\ F_{3G}(L) = k_{3,13} & F_{6G}(L) = k_{6,13} & \end{cases}$$

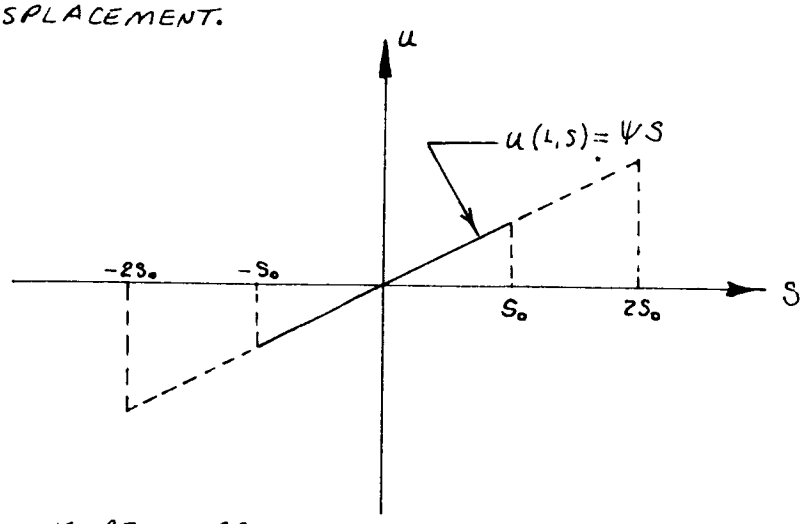
$$(A\text{-}45)\quad \begin{cases} F_{1G}(0) = k_{7,13} & F_{4G}(0) = k_{10,13} \\ F_{2G}(0) = k_{8,13} & F_{5G}(0) = k_{11,13} \\ F_{3G}(0) = k_{9,13} & F_{6G}(0) = k_{12,13} \end{cases}$$

THERE REMAINS THE PROBLEM OF FINDING:

$$F_{14G}(L) = k_{14,13}\,;\quad F_{15G}(0) = k_{15,13}\,;\quad F_{16G}(0) = k_{16,13}$$

CASE-H

IN THIS APPENDIX WE CONSIDER THE FORCES IN THE GRAVITY GRADIENT ROD RESULTING FROM A "WARPING" DISPLACEMENT, H @ $x=L$ AS SHOWN IN FIGURE B-1, WHERE $u(L,s)=\psi s$, ALL OTHER DISPLACEMENTS BEING FIXED. OUR OBJECTIVE IS TO FIND THE SET OF STIFFNESS COEFFICIENTS ASSOCIATED WITH THIS SHELL MOTION WHERE THE VALUE ψ COMPLETELY CHARACTERIZES THE DISPLACEMENT.



$u(L,s)$ MAY BE APPROXIMATED BY:

(B-1) $$u = A_1 \sin\frac{\pi}{2s_0}s + A_2 \sin\frac{2\pi}{2s_0}s + \cdots A_m \sin\frac{m\pi}{2s_0}s + \cdots$$

LET:

(B-1a) $$\lambda_m = \frac{m\pi}{2s_0}$$

THEN:

$$(B-2) \qquad A_m = \frac{1}{S_0}\int_0^{2S_0} \psi S \sin \lambda_m S \, dS = \frac{\psi}{S_0 \lambda_m^2}\left[\sin \lambda_m S - \lambda_m S \cos \lambda_m S\right]_0^{2S_0}$$

SO THAT:

$$(B-3) \qquad A_m = \frac{4S_0\psi}{\pi}\,\frac{(-1)^{m+1}}{m}$$

LIMITING OUR EXPANSION TO 4 TERMS:

$$(B-4) \qquad u(L,S) = \frac{4S_0}{\pi}\psi\left\{\sin\frac{\pi}{2S_0}S - \frac{1}{2}\sin\frac{2\pi}{2S_0}S + \frac{1}{3}\sin\frac{3\pi}{2S_0}S - \frac{1}{4}\sin\frac{4\pi}{2S_0}S\right\}$$

NOTE THAT OUR REGION OF INTEREST IS FROM $-S_0$ TO $+S_0$, HOWEVER THE EXPANSION WAS TAKEN OVER TWICE THIS REGION IN ORDER TO GIVE A BETTER REPRESENTATION OF THE FUNCTION, ψS @ $\pm S_0$.

CONSIDER SOLUTIONS IN THE FORM:

$$(B-5) \begin{cases} u = \frac{4S_0}{\pi}\psi \sum_m U_m(x)\sin\lambda_m S \\ v = \frac{4S_0}{\pi}\psi \sum_m V_m(x)\cos\lambda_m S \\ w = \frac{4S_0}{\pi}\psi \sum_m W_m(x)\sin\lambda_m S \end{cases}$$

BOUNDARY REQUIREMENTS:

@ $x=L$:		@ $x=0$:
$u = \frac{4S_0}{\pi}\psi \sum_m a_m \sin \lambda_m s \Rightarrow U_m(L) = a_m = \frac{(-1)^{m+1}}{m}$		$u=0$
$v = 0$		$v=0$
$w = 0$		$w=0$
$\frac{\partial w}{\partial x} = 0$		$\frac{\partial w}{\partial x}=0$

(B-6)

SO THAT:

$$(B-7)\quad U_m(L) = \frac{(-1)^{m+1}}{m}, \quad V_m(L) = W_m(L) = W_m'(L) = 0$$

AS SHOWN IN APPENDIX-A, THE POTENTIAL ENERGY IN THE SYSTEM IS GIVEN BY:

$$\mathcal{U} = \frac{1}{2}\oint_C T_i u_i \, dC$$

WHICH FOR OUR CASE IS:

$$(B-8)\quad \mathcal{U} = \frac{1}{2}\int_{-S_0}^{S_0} \left[N_x u\right]_{x=L} ds$$

BUT:

$$N_x = K\left(\frac{\partial u}{\partial x} + \nu\frac{\partial v}{\partial s} + \frac{\nu}{R}w\right)$$

AND SINCE $w(L,s) = 0$,

(B-9) $$N_x\Big]_{x=L} = K\left(\frac{\partial u}{\partial x} + \nu\frac{\partial v}{\partial s}\right)_{x=L}$$

(B-10) $$\frac{\partial u}{\partial x} = \frac{4\delta_0}{\pi}\psi\sum U_m'(x)\sin\lambda_m s$$

(B-11) $$\frac{\partial v}{\partial s} = -\frac{4\delta_0}{\pi}\psi\sum \lambda_m V_m(x)\sin\lambda_m s$$

BUT FROM (B-7) $V_m(L) = 0$ SO THAT:

(B-12) $$N_x\Big]_{x=L} = K\frac{4\delta_0}{\pi}\psi\sum U_m'(L)\sin\lambda_m s$$

AND

(B-13) $$u(L,s) = \frac{4\delta_0}{\pi}\psi\sum_m a_m\sin\lambda_m s$$

WHENCE:

(B-14) $$\mathcal{U} = \tfrac{1}{2}K\left(\frac{4\delta_0}{\pi}\right)^2\psi^2\sum_{mn}\int_{-s_0}^{s_0} U_m'(L)\,a_m\sin\lambda_m s\sin\lambda_n s\,ds$$

OR:

(B-14a) $$\mathcal{U} = \tfrac{1}{2}K\left(\frac{4\delta_0}{\pi}\right)^2\psi^2\sum_{mn} U_m'(L)\,I_{mn}$$

WHERE:

(B-14b) $$I_{mn} = \int_{-s_0}^{s_0}\sin\lambda_m s\sin\lambda_n s\,ds$$

BUT IF $\lambda_m \neq \lambda_n$

$$(B\text{-}15) \quad \int_{-S_0}^{S_0} \sin \lambda_m s \sin \lambda_n s \, ds = \frac{\sin(\lambda_m - \lambda_n) S_0}{(\lambda_m - \lambda_n)} - \frac{\sin(\lambda_m + \lambda_n) S_0}{(\lambda_m + \lambda_n)}$$

AND :

$$(B\text{-}15a) \quad \lambda_m - \lambda_n = \frac{m-n}{2} \frac{\pi}{S_0}$$

HENCE :

$$(B\text{-}16) \quad \int_{-S_0}^{S_0} \sin \lambda_m s \sin \lambda_n s \, ds = \frac{2S_0}{\pi} \left[\frac{\sin\left(\frac{m-n}{2}\right)\pi}{m-n} - \frac{\sin\left(\frac{m+n}{2}\right)\pi}{m+n} \right]$$

IF $\lambda_m \neq \lambda_n$

AND :

$$(B\text{-}17) \quad \int_{-S_0}^{S_0} \sin \lambda_m s \sin \lambda_n s \, ds = \frac{1}{\lambda} \left[\frac{1}{2} \lambda s - \frac{1}{4} \sin 2\lambda s \right]_{-S_0}^{S_0} = S_0$$

IF $\lambda_m = \lambda_n = \lambda$

UTILIZING (B-16) AND (B-17) WE MAY CONSTRUCT

I_{mn} AS SHOWN IN TABLE B-1.

①	②	③	④	⑤	⑥	⑦
m	n	$\frac{1}{2}(m-n)$	$\frac{1}{2}(m+n)$	$\frac{\sin ③\pi}{③}$	$\frac{\sin ④\pi}{④}$	$I_{mn} = \begin{cases} [⑤ \cdot ⑥]\frac{S_0}{\pi} & \text{FOR } m \neq n \\ S_0 & \text{FOR } m = n \end{cases}$
1	1	—	—	—	—	S_0
1	2	$-\frac{1}{2}$	$3/2$	2	$-2/3$	$8/3\ S_0/\pi$
1	3	-1	2	0	0	0
1	4	$-3/2$	$5/2$	$-2/3$	$2/5$	$-16/15\ S_0/\pi$
2	1					$8/3\ S_0/\pi$
2	2	—	—	—	—	S_0
2	3	$-1/2$	$5/2$	2	$2/5$	$8/5\ S_0/\pi$
2	4	-1	3	0	0	0
3	1					0
3	2					$8/5\ S_0/\pi$
3	3	—	—	—	—	S_0
3	4	$-1/2$	$7/2$	2	$-2/7$	$12/7\ S_0/\pi$
4	1					$-16/15\ S_0/\pi$
4	2					0
4	3					$12/7\ S_0/\pi$
4	4	—	—	—	—	S_0

TABLE B-1

SUBSTITUTING I_{mn}. WE HAVE

$$\sum_{mn} U_m'(L)\, a_m I_{mn} = U_1' S_0 + U_2' \frac{8 S_0}{3\pi} - \frac{16 S_0}{15\pi} U_4' - \frac{1}{2}\frac{8}{3}\frac{S_0}{\pi} U_1' - \frac{1}{2} S_0 U_2' - \frac{1}{2}\frac{8}{5}\frac{S_0}{\pi} U_3' + \frac{1}{3}\frac{8}{5}\frac{S_0}{\pi} U_2' + \frac{1}{3} S_0 U_3' + \frac{1}{3}\frac{12}{7}\frac{S_0}{\pi} U_4' + \frac{1}{4}\frac{16}{5}\frac{S_0}{\pi} U_1' - \frac{1}{4}\frac{12}{7}\frac{S_0}{\pi} U_3' - \frac{1}{4} S_0 U_4'$$

WHICH UPON COMBINING TERMS:

$$(B\text{-}18) \quad \sum_{mn} U_m'(L)\, a_m I_{mn} = S_0 U_1' \left(1 - \frac{4}{3\pi} + \frac{4}{15\pi}\right) + S_0 U_2' \left(\frac{8}{3\pi} - \frac{1}{2} + \frac{8}{15\pi}\right) + S_0 U_3' \left(\frac{1}{3} - \frac{4}{5\pi} - \frac{3}{7\pi}\right) + S_0 U_4' \left(-\frac{1}{4} - \frac{16}{15\pi} + \frac{4}{7\pi}\right)$$

THE STIFFNESS COEFFICIENT IS GIVEN BY:

$$(B\text{-}19) \quad \frac{\partial^2 \mathcal{U}}{\partial \psi^2} = K \left(\frac{4 S_0}{\pi}\right)^2 \sum_{mn} U_m'(L)\, a_m I_{mn}$$

AND SUBSTITUTING (B-18) INTO (B-19):

$$(B\text{-}20) \quad \frac{\partial^2 \mathcal{U}}{\partial \psi^2} - K \left(\frac{4}{\pi}\right)^2 S_0^3 \left\{ U_1' \left[1 - \frac{16}{15\pi}\right] + U_2' \left[-\frac{1}{2} + \frac{16}{5\pi}\right] - U_3' \left[-\frac{1}{3} + \frac{43}{35\pi}\right] - U_4' \left[\frac{1}{4} + \frac{52}{105\pi}\right] \right\}_{x=L} = F_{14H}(L)$$

OFF DIAGONAL TERMS

TO THE FORM OF SOLUTION GIVEN BY (B-5) THERE CORRESPONDS THE FOLLOWING EXPRESSIONS FOR EDGE LOADS, SETTING $\psi = -1$:

$$(B\text{-}21)\quad N_x = -\frac{4S_0}{\pi} K \sum_m \left(U_m' - \nu \lambda_m V_m + \frac{\nu}{R} W_m \right) \sin \lambda_m s$$

$$(B\text{-}22)\quad M_x = -\frac{4S_0}{\pi} K \sum_m \left(W_m'' - \nu \lambda_m^2 W_m - \frac{\nu \lambda_m}{R} V_m \right) \sin \lambda_m s$$

$$(B\text{-}23)\quad N_{xs} = -\frac{4S_0}{\pi} \sum_m \left[K (\lambda_m U_m + V_m') + \frac{D}{R} \left(2\lambda_m W_m' - \frac{1}{R} V_m' \right) \right] \cos \lambda_m s$$

$$(B\text{-}24)\quad V_x = -\frac{4S_0}{\pi} \sum_m \left[W_m''' - (2-\nu) \lambda_m^2 W_m' + \frac{\lambda_m}{R} V_m' \right] \sin \lambda_m s$$

IN ACCORDANCE WITH THE BOUNDARY CONDITIONS (B-6), $V_m, W_m, W_m' = 0$ @ $x = 0, L$ SO THAT THE END "BEAM" LOADS ARE GIVEN BY :

$$(B\text{-}25)\quad F_{1H} = -\frac{4S_0}{\pi} K \sum_m (U_m') \int_{-S_0}^{S_0} \sin \lambda_m s \, ds = 0$$

$$F_{2H} = \int_{-S_0}^{S_0} \left(V_x \sin \tfrac{1}{R} s + N_{xs} \cos \tfrac{1}{R} s \right) ds$$

$$(B\text{-}26)\quad F_{2H} = -\frac{4S_0}{\pi} \left\{ \sum_m \left[W_m''' + \frac{\lambda_m}{R} V_m' \right] \int_{-S_0}^{S_0} \sin \lambda_m s \sin \tfrac{1}{R} s \, ds \right.$$

$$\left. + \sum_m \left[K (\lambda_m U_m + V_m') - \frac{D}{R^2} V_m' \right] \int_{-S_0}^{S_0} \sin \lambda_m s \cos \tfrac{1}{R} s \, ds \right.$$

$$F_{3H} = \int_{-S_0}^{S_0} \left(V_x \cos \tfrac{1}{R} s - N_{xs} \sin \tfrac{1}{R} s \right) ds$$

$$(B\text{-}27) \quad F_{3H} = -\left(\frac{4S_0}{\pi}\right) \sum_m \left[W_m''' + \frac{\lambda_m}{R} V_m' \right] \int_{-S_0}^{S_0} \sin \lambda_m s \cos \tfrac{1}{R} s \, ds$$

$$-\left(\frac{4S_0}{\pi}\right) \sum_m \left[K \left(\lambda_m U_m + V_m' \right) - \frac{D}{R^2} V_m' \right] \int_{-S_0}^{S_0} \sin \lambda_m s \sin \tfrac{1}{R} s \, ds$$

$$(B\text{-}28) \quad F_{4H} = -\int_{-S_0}^{S_0} N_{xs} R \, ds = -\left(\frac{4S_0}{\pi}\right) \sum_m \left[K \left(\lambda_m U_m + V_m' \right) + \frac{D}{R} \left(-\tfrac{1}{R} V_m \right) \right] R \int_{-S_0}^{S_0} \cos \lambda_m s \, ds$$

$$F_{5H} = \int_{-S_0}^{S_0} \left(M_x \cos \tfrac{1}{R} s + N_x R \cos \tfrac{1}{R} s \right) ds$$

$$(B\text{-}29) \quad F_{5H} = -\left(\frac{4S_0}{\pi}\right) \sum_m \left[W_m'' \right] \int_{-S_0}^{S_0} \sin \lambda_m s \cos \tfrac{1}{R} s \, ds - \frac{4S_0}{\pi} \sum_m \left[U_m' R \right] \int_{-S_0}^{S_0} \sin \lambda_m s \cos \tfrac{1}{R} s \, ds$$

$$F_{6H} = -\int_{-S_0}^{S_0} \left(M_x \sin \tfrac{1}{R} s + N_x R \sin \tfrac{1}{R} s \right) ds$$

$$= \frac{4S_0}{\pi} \sum_m \left[W_m'' \right] \int_{-S_0}^{S_0} \sin \lambda_m s \cos \tfrac{1}{R} s \, ds + \frac{4S_0}{\pi} \sum_m \left[U_m' R \right] \int_{-S_0}^{S_0} \sin \lambda_m s \cos \tfrac{1}{R} s \, ds$$

$$(B\text{-}30) \quad F_{6H} = \frac{4S_0}{\pi} \sum_m \left[W_m'' + R U_m' \right] \int_{-S_0}^{S_0} \sin \lambda_m s \cos \tfrac{1}{R} s \, ds$$

BUT:

$$(B\text{-}31)\qquad \int_{-S_0}^{S_0} \sin\lambda_m s \sin\tfrac{1}{R} s \, ds = \left[\frac{\sin(\lambda_m - \frac{1}{R})S_0}{(\lambda_m - \frac{1}{R})} - \frac{\sin(\lambda_m + \frac{1}{R})S_0}{(\lambda_m + \frac{1}{R})} \right]$$

$$(B\text{-}32)\qquad \int_{-S_0}^{S_0} \sin\lambda_m s \cos\tfrac{1}{R} s \, ds = \left[-\frac{\cos(\lambda_m - \frac{1}{R})s}{2(\lambda_m - \frac{1}{R})} - \frac{\cos(\lambda_m + \frac{1}{R})s}{2(\lambda_m + \frac{1}{R})} \right]_{-S_0}^{S_0} = 0$$

$$(B\text{-}33)\qquad \int_{-S_0}^{S_0} \cos\lambda_m s \, ds = \frac{1}{\lambda_m}\left[\sin\lambda_m s\right]_{-S_0}^{S_0} = \frac{2}{\lambda_m}\sin\lambda_m S_0$$

SUBSTITUTING (B-31), (B-32), (B-33) INTO (B-25) THROUGH (B-30)

WE OBTAIN:

$$(B\text{-}34)\qquad \begin{cases} F_{1H} = F_{5H} = F_{6H} = 0 \\ F_{2H} = -\frac{4S_0}{\pi} \sum_m \left[W_m''' + \frac{\lambda_m}{R} V_m' \right] \left[\frac{\sin(\lambda_m - \frac{1}{R})S_0}{(\lambda_m - \frac{1}{R})} - \frac{\sin(\lambda_m + \frac{1}{R})S_0}{(\lambda_m + \frac{1}{R})} \right] \\ F_{3H} = -\frac{4S_0}{\pi} \sum_m \left[K(\lambda_m U_m + V_m') - \frac{D}{R^2} V_m' \right] \left[\frac{\sin(\lambda_m - \frac{1}{R})S_0}{(\lambda_m - \frac{1}{R})} - \frac{\sin(\lambda_m + \frac{1}{R})S_0}{(\lambda_m + \frac{1}{R})} \right] \\ F_{4H} = -\frac{4S_0}{\pi} \sum_m \left[K(\lambda_m U_m + V_m') - \frac{D}{R^2} V_m' \right] \left[\frac{2R}{\lambda_m} \sin\lambda_m S_0 \right] \end{cases}$$

(B-34) PROVIDES US WITH THE FOLLOWING STIFFNESS COEFFICIENTS:

(B-35)
$$\begin{cases} F_{1H}(L) = k_{1,14} & F_{4H}(L) = k_{4,14} \\ F_{2H}(L) = k_{2,14} & F_{5H}(L) = k_{5,14} \\ F_{3H}(L) = k_{3,14} & F_{6H}(L) = k_{6,14} \end{cases}$$

(B-36)
$$\begin{cases} F_{1H}(0) = k_{7,14} & F_{4H}(0) = k_{10,14} \\ F_{2H}(0) = k_{8,14} & F_{5H}(0) = k_{11,14} \\ F_{3H}(0) = k_{9,14} & F_{6H}(0) = k_{12,14} \end{cases}$$

$F_{14H}(L) = k_{14,14}$ IS GIVEN BY (B-20). $F_{14H}(0) = k_{16,14}$ IS TO BE FOUND SUBSEQUENTLY.

APPENDIX F

SIGNAL-TO-NOISE CALCULATIONS FOR THE TV CAMERA SUBSYSTEM

1. Summary

SNR calculations for the TV Sensor are given in Tables F-1 and F-2, based on link parameters obtained from NASA/GSFC. The results show that when a 40-foot ground antenna is employed, TV pictures of good quality can be expected only when a medium-altitude satellite is near zenith. For other cases involving either medium or synchronous-altitude satellites, performance ranges from marginal to poor, depending on weather conditions.

The use of an 85-foot antenna results in TV pictures that range in quality from good to excellent under all conditions.

2. Technical Discussion

The down-link calculations of IF signal-to-noise ratio are shown in Table F-1, assuming a synchronous-altitude satellite at maximum range and a 40-foot ground antenna. The IF signal-to-noise ratio of 6.8 db requires the use of the phase-lock demodulator in the ground receiver, since this SNR is below the threshold of a conventional FM demodulator. Even assuming a phase-lock demodulator, the resulting margin of 0.8 db does not provide an adequate safety factor to account for further reduction in signal strength due to variation in satellite attitude, or for increased attenuation and receiver noise resulting from bad weather conditions. The atmospheric attenuation at 4Gc will probably not exceed 1 db, except for a very small fraction of the time, at a minimum elevation angle of 5 deg. (See Item 7 of Section 4). This attenuation would also produce an increase in the apparent

TABLE F-1. SNR CALCULATIONS (DOWN-LINK)

	Loss (db)	Gain (db)	Power Level (dbm)
Transmitter power (1)			36
Satellite antenna gain (2)		14.7	
System losses (3)	4		
Range attenuation (4)	197		
Receiving antenna gain (5)		52	
Received power			-98.3
Receiver noise (6)			-105.1
SNR (7)		6.8	
Margin (8)		0.8	

Notes:

(1) Transmitter power output = 4 watts preceding diplexer.

(2) Includes gain reduction at low elevation angles, but no allowance for variation in satellite attitude.

(3) 1 db loss for ground receiver and 3 db loss for satellite (Includes transmission line losses, diplexer loss, polarization loss, etc.)

(4) Slant range = 22,000 nm for min. elevation angle of 5 deg. at synchronous altitude. Clear weather conditions.

(5) 40 ft. parabolic antenna, efficiency = 60 percent, frequency = 4 gc.

(6) $N = \eta B$
$\eta = kT = 1.38 \times 10^{-23} \times 90^{\circ}K = 1.24 \times 10^{-21}$ watt/cps.
$\eta = -179$ dbm/cps
For B = 25 mc,
N = 3.1×10^{-14} w.
N = -105.1 dbm

(7) With an 85-foot dish having a $50^{\circ}K$ noise temperature, the SNR, will be about 9 db higher (6.5 db increase in antenna gain and 2.5 db reduction in noise temperature).

(8) Assuming 6 db threshold for a phase-lock demodulator.

TABLE F-2. OUTPUT SNR[1,2] FOR TV SENSOR

	85-foot dish, 50°K noise temp. in clear weather		40-foot dish, 90°K noise temp. in clear weather	
	5° Elev.	Zenith	5° Elev.	Zenith
Synchronous altitude				
Clear weather (typical) summer conditions)	37.6[3] db	40.7[4] db	28.6[3] db	31.7[4] db
Bad weather (heavy rain and clouds)	33.6[5]	~40.7[6]	below threshold	~31.7[6]
Medium altitude				
Clear weather	38.7[7]	44.7[8]	29.7[7]	35.7[8]
Bad weather	34.7[5]	~44.7[6]	below threshold	~35.7[6]

Notes:

(1) All results include 2.7 db preemphasis improvement.

(2) No allowance for satellite antenna gain reduction due to attitude variation.

(3) Range = 22,000 nm, satellite antenna gain = 14.7 db

(4) Range = 19,300 nm, satellite antenna gain = 16.7 db

(5) Atmospheric loss = 1 db, noise temp. increased to 100°K.

(6) Effects of bad weather should be almost negligible at zenith.

(7) Range = 8500 nm, satellite antenna gain = 7.5 db.

(8) Range = 6000 nm, satellite antenna gain = 10.5 db.

receiver noise temperature of as much as 50°K, however. According to Figure 6 of Ref. 7*, the sky temperature (T_o) in clear weather at 4 Gc is about 25°K, for a 5 deg. elevation angle. For heavy rain or clouds having a physical temperature (T_1) of 290°K and a loss of 1 db ($\alpha = 0.8$), the sky temperature is

$$T_s = (1 - \alpha)\, T_1 + \alpha\, T_o$$

$$= 78^{\circ}K$$

*See Item 7 of Section 4.

or an increase of 53°K. This order of increase in the noise temperature of a low-noise receiver is substantiated by measurements made on the Bell System Antenna at Andover (See Item 8 of Section 4).

The overall result of bad weather effects, in the present case, would therefore be to increase the range attenuation by 1 db and to increase the receiver noise from 90°K to about 143°K (2 db). The margin of 0.8 db shown in Table F-1, therefore, disappears completely in bad weather, and the received signal is below the threshold even of the phase-lock demodulator.

To compute the output SNR of the TV signal, clear weather will be assumed, with the demodulator operating above threshold as shown in Table F-1. Since frequency modulation is to be employed at the transmitter, the receiver is assumed to be suitably filtered to recover the FM signal. The noise voltage spectrum will therefore be triangular. The average signal-to-noise ratio at the output of an FM receiver is given by:

$$\frac{S_o}{N_o} = 3\left(\frac{\Delta f}{fm}\right)^2 \frac{C}{2\eta fm}$$

where Δf = peak frequency deviation

fm = baseband cutoff frequency

C = received carrier power

η = IF noise spectral density

For TV, the SNR is usually specified in terms of the ratio of peak-to-peak signal power to rms noise power. The peak-to-peak signal power (S_p) is proportional to $(2\Delta f)^2$, while S_o is proportional to $\frac{(\Delta f)^2}{2}$. Hence $S_p = 8\, S_o$, and the above equation can be rewritten as

$$\frac{S_p}{N_o} = 12\left(\frac{\Delta f}{fm}\right)^2 \frac{C}{\eta fm}$$

for

$$\Delta f = 5 \text{ mc peak (10 mc peak-to-peak) and } f_m = 4.5 \text{ mc},$$

$$\frac{S_p}{N_o} \text{ (db)} = 11.7 - 98.3 \text{ dbm} + 179 \text{ dbm/cps} - 66.5$$

$$= 25.9 \text{ db}$$

According to NASA/GSFC, the use of the preemphasis and deemphasis circuits recommended by CCIR (see Item 9 of Section 4) will result in an SNR improvement of about 2.7 db. The resulting SNR is therefore

$$\frac{S_p}{N_o} = 25.9 + 2.7 = 28.6 \text{ db}$$

It is recognized here that the SNR requirements for detecting the location of the boom tip target against varying earth and sky backgrounds have not yet been established. Tests in the laboratory have indicated that detection of the target is sometimes possible with a 20 db SNR and at other times is not possible at a 35 db SNR, depending on the background and illumination characteristics. However, since it was stated by representatives of NASA/GSFC at the interface meeting of 30 July 1964 that the TV transmission system would meet the recommendations of the CCIR for active communication satellites, these standards are used here as a basis of comparison.

The Report of the Television Allocations Study Organization (Ref. 10) states that a SNR of 29 db* results in a picture quality that is regarded as "passable" or better by 70% of the observers, where the qualitative rating implies that noise is perceptible but not objectionable. For a picture to be rated as "fine" or better (noise virtually imperceptible) by 90% or more of the viewers, an SNR of 38 to 40 db would be required. This is just the improvement in SNR that is afforded by the use of an 85-foot dish having a receiver noise temperature of 50°K in clear weather. The achievement of a 40 db SNR is probably satisfactory for the present application, although this still does not quite meet the CCIR recommendation for active

*The SNR specified in Item 10 of Section 4 is the ratio of rms carrier power at sync peak to rms noise power. This is about 1 db higher than the ratio of black-to-white video signal power to rms noise power, which is the ratio employed here.

communication satellite systems (see Item 11 of Section 4). This recommendation states that the peak-to-peak signal to weighted rms noise ratio should be at least 55 db for 99% of the time. Since weighting attenuates noise by about 10 db (Item 12 of Section 4) for "triangular" noise, the recommended peak-to-peak signal to unweighted noise ratio would be 45 db.

These results for synchronous altitude have been extended to cover the medium altitude case, and the SNR to be expected in the various cases of interest is summarized in Table F-2.

High-quality performance can be expected using the 85-foot antenna except in very bad weather at low elevation angles, and even here the performance is such that most viewers would regard typical scenes to be "fine" quality.

This quality is only achieved for a 40-foot antenna when the medium-altitude satellite is near zenith. At low elevation angles, the performance is marginal even in clear weather, and in bad weather the signal falls below the threshold of the ground receiver.

APPENDIX G

RF ATTITUDE SENSOR
SYSTEM ERROR ANALYSIS

System Performance Without Modification

To evaluate the measurement performance of the RF Attitude Sensor system as presently conceived it becomes necessary to locate and evaluate all sources of error in the system.

Receiver Noise

With a received signal (minimum) level of -84 dbm and assuming a 3 db power loss in the microwave coupler the signal to noise ratio can be calculated as:

KT = -174

B +40 (10 kc)

F +10

= -174 + 50 = -124 dbm receiver noise power

Signal level = -84 dbm -3 db = -87 dbm

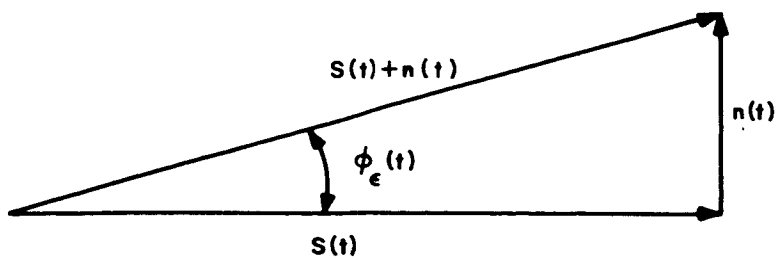
S/N ratio = 124 - 87 = 37 db

Assuming the noise is completely uncorrelated the rms phase error can be calculated in the following manner.

Let

$S(t) = A \cos \omega_o t$ (Signal)

The phase error due to quadrature noise is $\phi_\epsilon(t)$ as shown:



for small angles

$$\phi_\epsilon\ (t) = \tan^{-1} \frac{n(t)}{A} \simeq \frac{n(t)}{A}$$

$$(\phi_\epsilon)^2 = \frac{[n(t)]^2}{A^2}$$

For gaussian noise of n(t), $[n(t)]^2$ is proportional to the noise power.

The signal power is proportional to $A^2/2$

$\therefore$ The ratio $[n(t)]^2/A^2 = N/2S$

Where N is the noise power and S the signal power

$$S/N = 1/2\phi_\epsilon{}^2$$

For 37 db:

$$S/N = 5 \times 10^3$$

$$2(\phi_\epsilon)^2 = 0.2 \times 10^{-3};\ (\phi_\epsilon)^2 = 10^{-4}$$

$$\phi_\epsilon = 10^{-2} \text{ rad} = 0.58 \text{ degrees}$$

Quantizing Error

This error (since the phase-locked loop keeps the central channel phase-coherent with the counted 2.56 mc signal) occurs only on one end of the counting period and can have a peak to peak value of $\pm$ one count. Since one count equals 0.705 electrical degrees the peak to peak error equals 1.41 degrees or an rms value of 0.4 degrees.

Signal Leakage

Leakage of signals in the microwave assembly could cause system errors provided the phase of the undesired signal changes as a function of time. Since the design of the microwave assembly has been specified to minimize these effects, the expected leakage of any importance is due to reflection of the received and pilot tone signals off the mixers, out the antenna to another antenna and to the "wrong" channel. Assuming a 20 db (VSWR 1.225:1) loss in reflection from the mixer and utilizing the directivity and spurious coupling factors specified by the microwave

subcontractor the signal leakage becomes -49 db and -52 db for the received and pilot tone signals respectively. The leakage error then would be:

Pilot tone	0.1^{o} rms
Received Signal	0.14^{o} rms

Video Signal Processing

The time delay incorporated from the envelope detector to the signal count gate can contribute to system error if the time delay of one channel with respect to another changes as a function of time. By the use of wideband components except for a well controlled video filter in each channel, this effect should be controllable to less than 0.2 degree. For purposes of calculation one degree is assumed.

The system errors exclusive of pilot tone and received signal stability and other unknowns add to:

Receiver Noise	0.6^{o}
Quantizing error	0.4^{o}
Leakage (Signal)	0.14^{o}
Leakage (Pilot Tone)	0.1^{o}
Video Processing	1.0^{o}
RMS sum	1.25 degrees

Thus it appears that an rms error of ~ 6.5 degrees ($\sqrt{43}$) due to stability and other unknowns would be allowable before the system error specification (6.7^{o}) would be exceeded.

A quantity that will probably contribute some system error will be differential phase changes due to the incident polarization angle upon the antennas. This quantity will probably contribute a phase error on the order of one degree. Since the antennas will be close wound archimedean spirals precisely placed and oriented by a photographic process, it is expected that this contribution will be well controlled. Since at this time there is no way to measure and evaluate a completed microwave assembly, assume a contribution of 3 degrees.

The above measured and assumed values of system phase error leave a contribution of $\cong \sqrt{34} = 5.8$ degrees error allowable for oscillator and multiplier noise before the specification value of 6.72 degrees (electrical) is exceeded.

Oscillator Noise

In consideration of oscillator noise it is becoming clear that there are a number of different phenomena affecting the instantaneous phase (and thus frequency) of the oscillator. According to the currently published data these phenomena affect the oscillator performance over different time spans to various degrees. Depending upon the oscillator design and measuring apparatus these effects may or may not be separable. Over the time of interest in this system, however, the effects of importance can be reduced to two.

There is an FM type of effect which can be explained intuitively as the occurrence of a step function in oscillator phase within the feedback loop of the oscillator. This disturbance will cause the oscillator to proceed oscillating on its new phase point independent of its past history. This type of noise will, if uncorrected, result in a random walk of phase to a new phase arbitrarily far from the original phase as time elapses.

The second type of noise of interest is that of additive phase noise of zero mean. This noise will be relatively broad band, limited only by the noise bandwidth of the oscillator and/or the following multiplier stages. Since this noise is of zero mean, if removed the oscillator will revert to its unperturbed state. This noise will affect the system in exactly the same manner as noise originating in the multiplier or receiver front end and in the complete system will be inseparable from these other noise sources.

For the FM type of noise, since it is introduced in all three channels the correlation of the noise over the time of measurement interest is important and the error can be evaluated as follows.

Since the phase-locked loop proposed for the RF Altitude Sensor system has negligible effect upon the stability of the oscillator over the time of interest, the oscillator noise will be considered on a free-running basis.

To limit the rms error to 2 degrees over the measurement time of 10^{-4} seconds the necessary coherence time can be calculated as

$$\phi_\epsilon \text{ rms} = \sqrt{t/Tc}$$

where ϕ_ϵ rms is the desired maximum error; t the maximum data sample time and T_c the coherence time for the oscillator.

Thus

$$Tc = t/\phi_\epsilon^2 = 10^{-4}/(0.035)^2 = 0.08 \text{ sec.}$$

The required stability (minimum) for the oscillator would then be:

$$S^2 = \frac{t'/Tc}{\omega^2 t'^2} = \frac{1}{\omega^2 Tc\, t'}$$

Where S is the stability factor of the oscillator over the time t'

$$S^2 = \frac{1}{(2\pi \times 6.2 \times 10^9)^2 (0.08)}$$

$$= .83 \times 10^{-20}$$

and

$$S = .93 \times 10^{-10} \text{ (1 second)}$$

if the allowable ϕ_ϵ were 4^o then

$$S = 1.8 \times 10^{-10} \text{ (1 second)}$$

The oscillator additive phase noise and the noise introduced in the system by multiplication of the VCO to obtain the pilot tone are both additive noises whose mean remains zero.

As a result the performance of the system due to these effects can be related to the signal-to-noise ratio at the output of the multiplier. (To separate this from the random walk of phase due to oscillator noise, an ideal oscillator is assumed.) Further the noise is assumed completely uncorrelated over 10^{-4} second.

To limit the oscillator and multiplier phase noise contribution to two degrees rms, the noise is assumed to be all quadrature to the signal and considering both turn on and turn off of the counter:

$$\text{for } \phi_\epsilon = \frac{2^o}{\sqrt{2}} = \frac{0.035 \text{ rad.}}{\sqrt{2}}$$

$$\frac{S}{N} = \frac{1}{\frac{2\,(0.035)^2}{2}} = 8.12 \times 10^2 = 29 \text{ db}$$

This then is the minimum signal-to-noise ratio (out of the multiplier) allowable for a 2 degrees rms error contribution.

Expected RF Attitude Sensor System Performance

Oscillator Noise:

A number of examples of short term stabilities for various oscillators, both fixed and variable, are given in TIS # R63RG027, pages 2-10 and 2-11. This data indicates that short term stability of 1×10^{-10} is reasonable for a controlled (variable) crystal oscillator.

A more pertinent oscillator is that used for the last 3-1/2 years on production MISTRAM-A transponders. This oscillator is constructed as a single potted assembly in a total metal enclosure making an extremely rigid structure. A production module was tested in a phase-locked loop to determine the capability of the oscillator. The basic frequency of the oscillator was 4 mc; the loop operating frequency was 8216 mc (multiplication factor of 2054) and the closed loop noise bandwidth was tested down to 1 kc. (This bandwidth was as low as current interest justified at the time.)

Under these conditions there was no discernable phase jitter on the loop due to oscillator noise. Allowing for measurement inaccuracies the rms phase error was certainly less than three degrees.

Calculating the stability factor of the oscillator from equation (2-9) (pg 2-13 R63RG027)

$$(\Delta\phi)^2 = \frac{2\pi (ST^{1/2})^2 f_o^2}{Bo} \qquad (\Delta\phi = 3^o)$$

$$(.052)^2 = \frac{2\pi S^2 (8 \times 10^9)^2}{10^3} \qquad (T = 1 \text{ sec})$$

$$S^2 = \frac{(27.1) \times 10^{-4} \times 10^3}{1.28\pi \times 10^{20}} = 67.5 \times 10^{-22}$$

$$S = 8.2 \times 10^{-11} \text{ (1 second)}$$

The equivalent coherence time (referred to a frequency of 6.2 Gc) would be

$$T_c = \frac{1}{\omega_o^2 S^2 T}$$

$$= \frac{1}{(2\pi \times 6.2 \times 10^9 \times 8.2 \times 10^{-11})^2 \times 1 \text{ sec}}$$

$$= 0.1 \text{ second.}$$

The corresponding phase error due to FM noise, in a data sample time of 10^{-4} seconds, is

$$\phi_\epsilon = \sqrt{\frac{T}{T_c}} = \sqrt{\frac{10^{-4}}{10^{-1}}} \text{ rad}$$

$$\simeq 1.8^o$$

The above calculation assumes that the measured/estimated phase jitter seen in the phase-locked loop was due entirely to FM type noise and its random walk result. In

actuality it is nearly certain that there was considerable additive phase noise present also. It will now be assumed that all of the phase jitter in the phase-locked loop is due to phase (additive) noise, rather than to FM noise, and the phase error caused by this noise in the RF Attitude Sensor receiver will be computed. To be conservative, contributions from both noise sources will then be included in the overall evaluation of phase errors in the system.

Recognizing the fact that the oscillator-multiplier must have had significant phase noise, its upper bound can be estimated in the following manner. If it is assumed that the additive phase noise constituted all the error, and further assuming the bandwidth prior to the phase detector was wide with respect to the sampling interval of interest in RF Attitude Sensor, then it can be said that the phase jitter seen was all the phase jitter that will affect the system. In this case the minimum possible bandwidth prior to the phase detector was 100 kc. This satisfies the second condition. Since the frequency of interest in the measurement was 8.2 Gc and the RF Attitude Sensor frequency of interest is 6.2 Gc the phase jitter seen can be related to the RF Attitude Sensor case by the ratio of frequencies:

$$\phi_\epsilon \leq \frac{3 \times 6.2}{8.2} = 2.27^o$$

Thus, making the assumption that the FM noise is insignificant, a worst case signal-to-noise ratio can be calculated.

$$\frac{S}{N} = \frac{1}{2\,(\phi_\epsilon)^2} = \frac{1}{2\,(0.04)^2} = 3.12 \times 10^2$$

In db the worst case S/N ratio is:

$$S/N \geq 10 \log (3.12 \times 10^2) = 24.4 \text{ db}$$

In this case with the previous mentioned assumptions this is the minimum signal to noise ratio for an rms combination of the contributions of two oscillators and two multiplier chains.

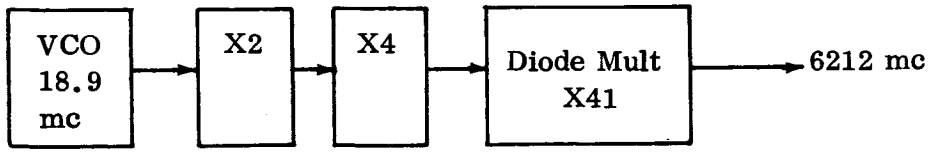
There is insufficient data to apportion this error to the individual contributors so if a worst case is assumed, namely that all this noise was due only to the one oscillator under test, then the following prediction of RF Attitude Sensor system error can be made.

For both turn on and turn off

$$\phi_{\epsilon_T} = \left[(2.27^2 + 2.27)^2\right]^{1/2} = 3.6 \text{ degrees rms.}$$

It is felt that these calculations represent a reasonable and conservative value of stability for a rigidly potted, crystal variable oscillator. In fact it is seriously doubted that when this oscillator was designed (4-1/2 years ago) that it was optimized in any way for short term stability since its intended use was in a loop whose noise bandwidth was 40 kc. As a result even better stability may well be obtainable.

To evaluate the phase noise contribution of the multiplier for RF Attitude Sensor the following was done. The multiplier for the pilot tone can be shown as:



The active section of the multiplier which multiplies the signal from 18.9 mc to 151 mc and generates the power to drive the step recovery diode was disconnected from the oscillator and its input properly terminated. The output noise power was then measured. The oscillator signal was reapplied and the signal output power measured. At this point, the signal to noise ratio was found to be 82 db.

Since the S/N ratio due to phase noise will degrade as the square of the multiplication factor the signal-to-noise ratio at C band can be expected to be 82 - 32.3 = 49.7 db.

Since all active stages (which can amplify thermal noise) of the multiplier for RF Attitude Sensor were included in this measurement, and since the noise induced after the first "times 8" multiplication must be 18 db higher to yield the same contribution it is felt that all significant sources of multiplier phase noise have been included. As a result the rms phase error expected from the pilot tone multiplier is:

For 49.7 db: $S/N = .93 \times 10^5$

$2 (\phi_\epsilon)^2 = 1.075 \times 10^{-5}$

$(\phi_\epsilon)^2 \simeq 5 \times 10^{-6}$

$\phi_\epsilon = 2.2 \times 10^{-3}$ rad $\simeq$ 0.13 degrees rms

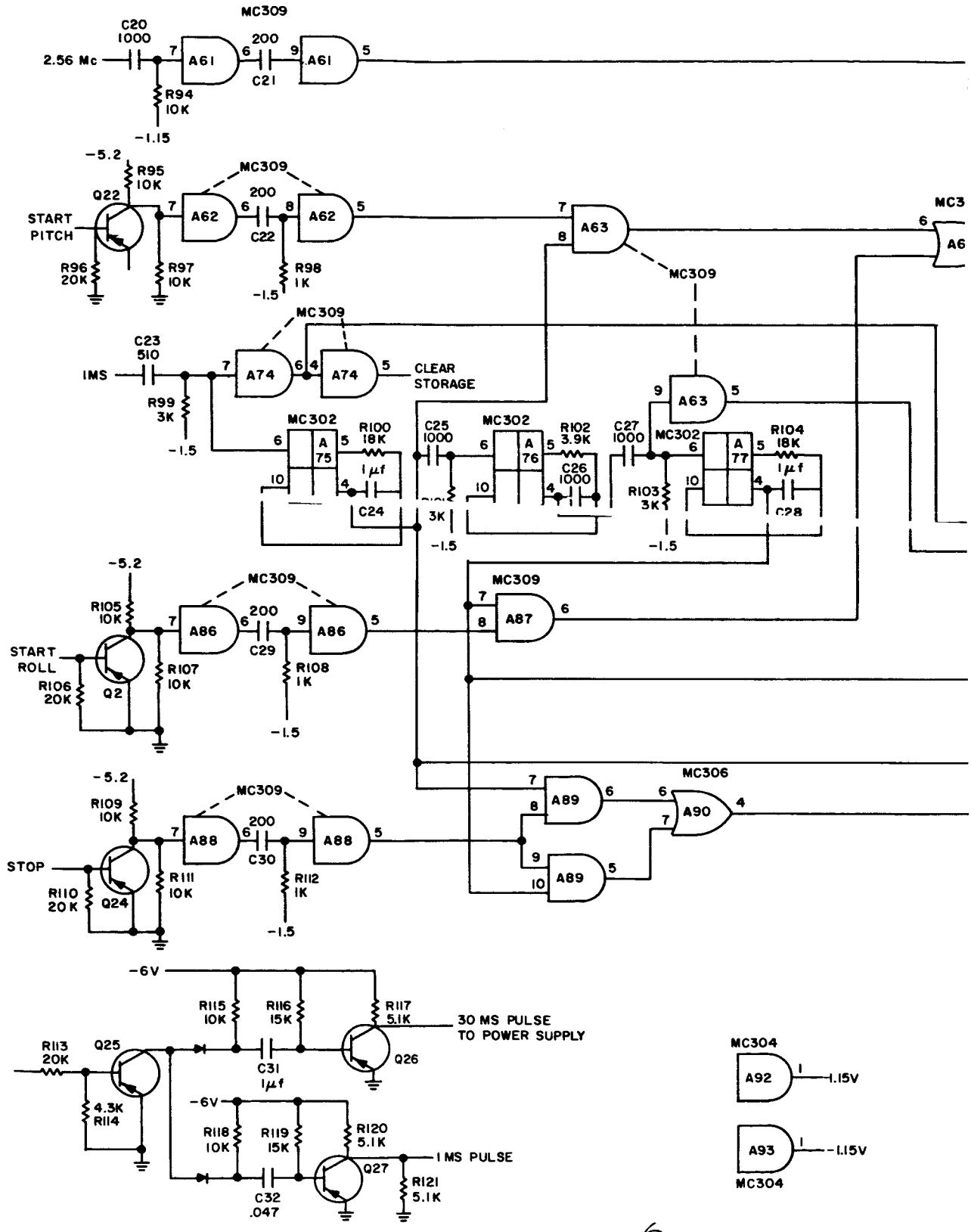
Adding up all the important sources of phase error for the system an rms sum is obtained.

Receiver Noise	0.6^o
Quantizing Error	0.4^o
Leakage (signal)	0.14^o
Leakage (pilot tone)	0.1^o
Video Processing	1.0^o
Antenna effects	3.0^o
FM noise (Oscillator)	1.8^o
Phase Noise (Oscillator)	3.6^o
Multiplier Noise	0.13^o
RMS Sum	5.17 degrees

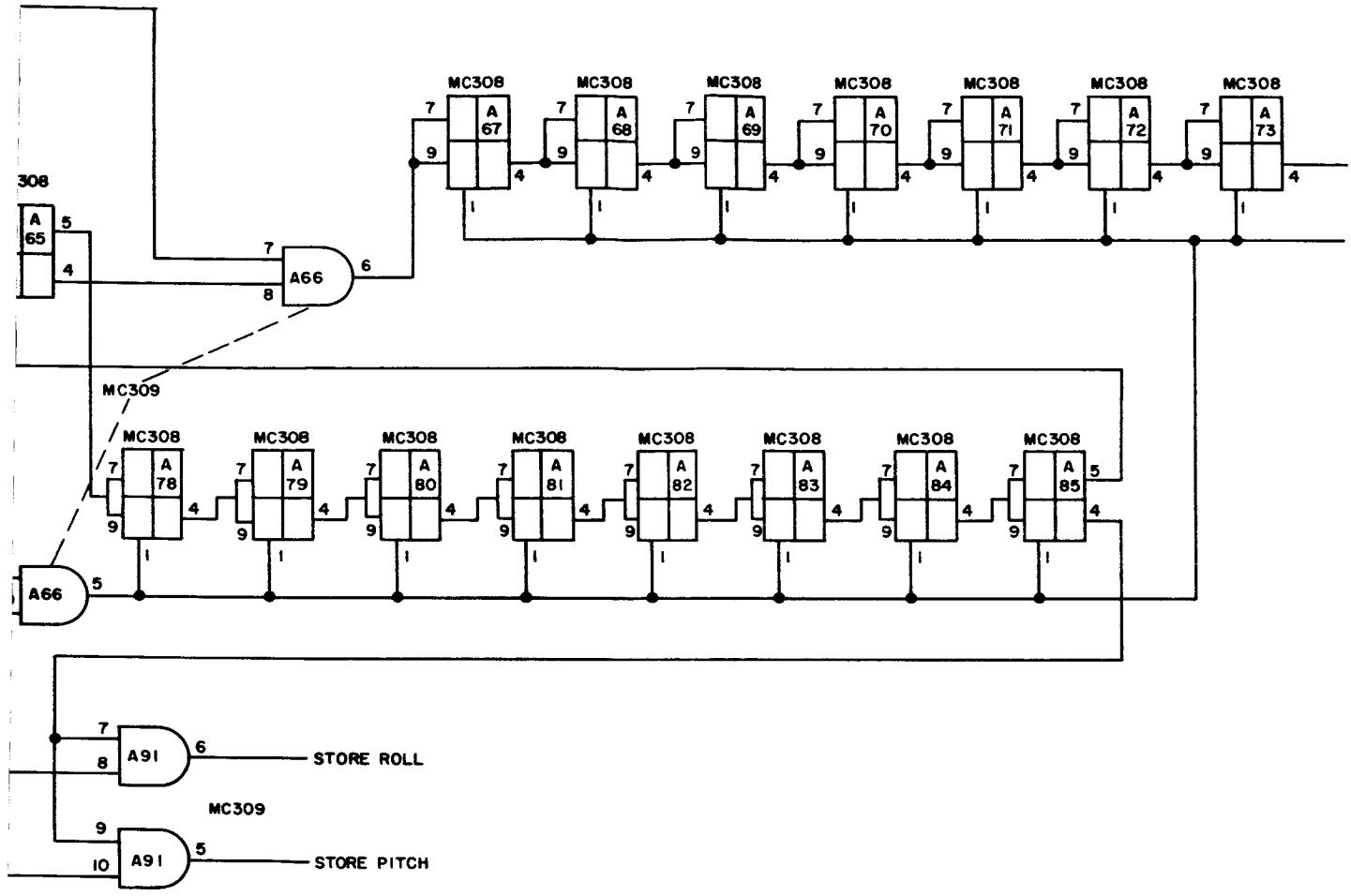
Due to the very pessimistic nature of some of the above assumptions it appears that the specification of 6.7 degrees rms for the entire system can be met with ample safety margin. This leaves a total of 4^o rms of unknowns to be allotted to the ground station and to other factors of lesser importance.

System Modification

Should additional performance in the presence of noise be needed or desired a data processing scheme that takes an average can be rather easily incorporated. The present concept is to take one data point every three seconds or when ever requested by the telemetry subsystem. With this arrangement total data gathering time is less than two msec per read pulse. With averaging circuits a total of 128 data points per read pulse would be accumulated and upon read to buffer storage the seven least significant bits would be discarded, thus reading the data average to storage. This would increase the data gathering time to about 22 msec per read pulse and increase average power input on the order of 100 milliwatts. This approach would decrease the effect of rapidly varying errors by an order of magnitude.


MC309
C20
1000
2.56 Mc
A61
200
C21
A61
R94
10K
-1.15
-5.2
R95
10K
Q22
START
PITCH
A62
200
C22
A62
R96
20K
R97
10K
R98
1K
-1.5
A63
MC309
MC3
A6
MC309
C23
510
1MS
A74
A74
CLEAR
STORAGE
R99
3K
-1.5
MC302
A
75
R100
18K
1μf
C24
C25
1000
MC302
A
76
R102
3.9K
C26
1000
3K
-1.5
C27
1000
MC302
A
77
R104
18K
1μf
C28
R103
3K
-1.5
A63
MC309
-5.2
R105
10K
START
ROLL
R106
20K
Q2
A86
200
C29
A86
R107
10K
R108
1K
-1.5
MC309
A87
-5.2
R109
10K
STOP
R110
20K
Q24
A88
200
C30
A88
R111
10K
R112
1K
-1.5
MC309
A89
A89
MC306
A90
-6V
R115
10K
R116
15K
R117
5.1K
30 MS PULSE
TO POWER SUPPLY
R113
20K
Q25
4.3K
R114
C31
1μf
Q26
-6V
R118
10K
R119
15K
R120
5.1K
1 MS PULSE
Q27
R121
5.1K
C32
.047
MC304
A92
1
-1.15V
A93
1
-1.15V
MC304

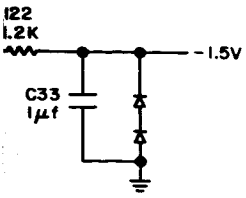
130



PIN NO. 1 OF ALL MC303,306 AND 309 = −1.15V

PIN NO. 2 OF ALL INTEGRATED CIRCUITS = −5.2 V

PIN NO. 3 OF ALL INTEGRATED CIRCUITS = GRD



NOTE: This circuit would replace the 8-Bit Counter (Figure 2.4.6-18) if averaging were employed.

Figure G-1. Averaging Logic

APPENDIX H

RF ATTITUDE SENSOR
EFFECTS OF SHORT TERM STABILITY
ON DIGITAL PHASE MEASUREMENT

THE SYSTEM

The portions of the RF Attitude Sensor system that are significant to this analysis are illustrated in Figure H-1. Only two channels are shown, and the other channel would be treated in the same way and would produce similar results. The mixer is not shown in detail because its action does not affect the analysis. Also the fact that the local oscillator signal is derived from the VCO is of no consequence to this analysis and is not shown.

The received signals are indicated in Figure H-1. The frequency ω_g is the ground transmitter frequency and $\phi_g(t)$ represents phase perturbations caused by oscillator short term stability. The phases ϕ_a and ϕ_b represent the information, and the quantity to be measured, from which the attitude can be obtained, is the difference $\phi_a - \phi_b$.

The voltage controlled oscillator is controlled by the phase detector which compares $\phi_1(t)$, the output of Channel 1, with the local reference signal (this reference is at 10 kc). The phase detector output is filtered before being applied to the VCO, and the frequency $\dot{\phi}_o(t)$ of the output is proportional to this filtered voltage. The phase $\phi_s(t)$ represents the phase perturbations caused by the short term stability of the VCO, and this phase is added to the output phase.

The output of the detector on channel 1 is given by

$$\phi_1(t) = \phi_g(t) - m\,\phi_s(t) + \phi_a - \phi_o(t) \qquad (1)$$

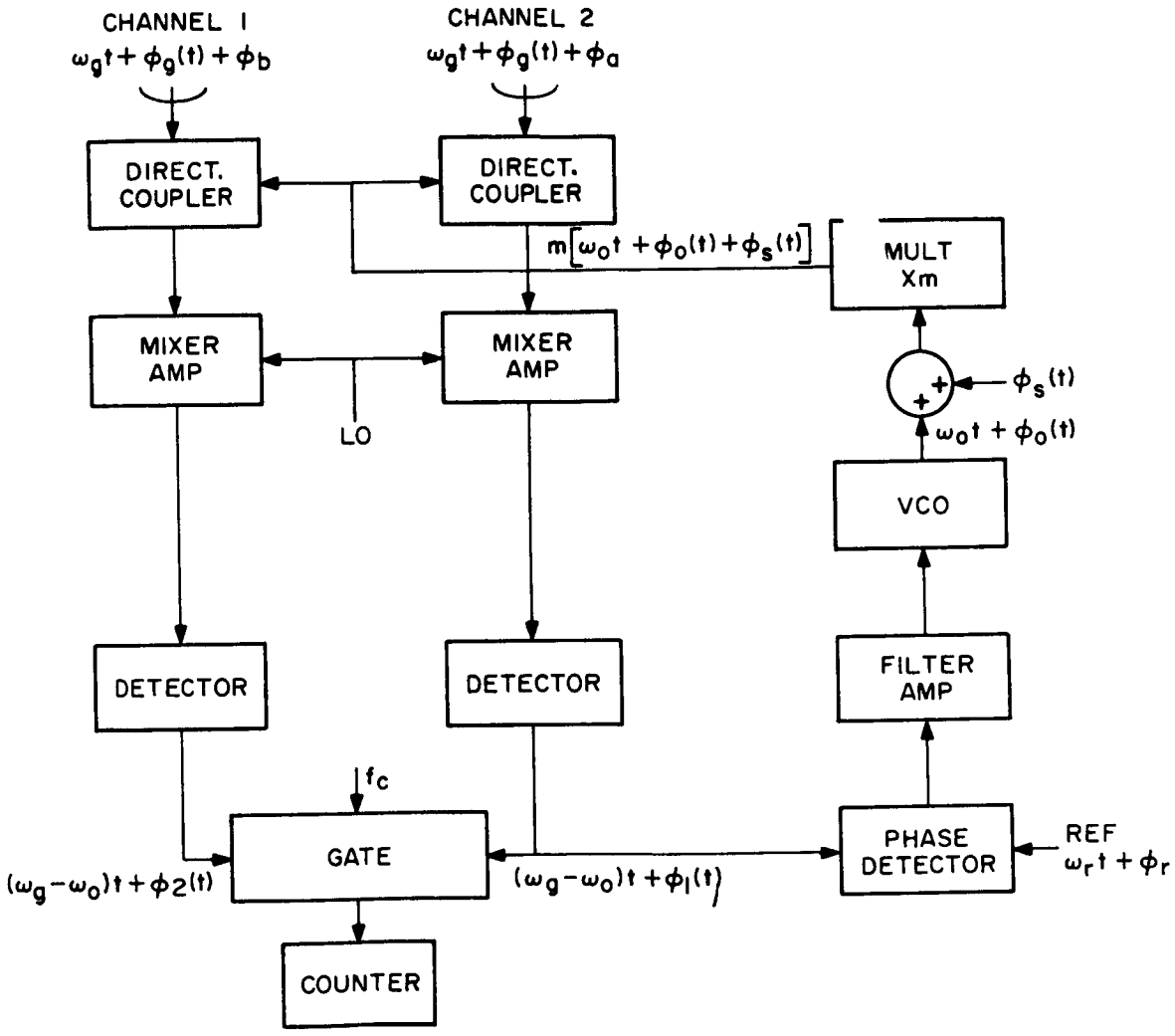

CHANNEL 1
$\omega_g t + \phi_g(t) + \phi_b$
CHANNEL 2
$\omega_g t + \phi_g(t) + \phi_a$
DIRECT. COUPLER
DIRECT. COUPLER
$m[\omega_o t + \phi_o(t) + \phi_s(t)]$
MULT Xm
MIXER AMP
MIXER AMP
LO
$\phi_s(t)$
$\omega_o t + \phi_o(t)$
VCO
DETECTOR
DETECTOR
FILTER AMP
f_c
GATE
PHASE DETECTOR
REF
$\omega_r t + \phi_r$
$(\omega_g - \omega_o)t + \phi_2(t)$
$(\omega_g - \omega_o)t + \phi_1(t)$
COUNTER

Figure H-1

The action of the control loop causes the relation among the frequencies to be

$$\omega_g + \omega_o = \omega_r \tag{2}$$

Now, solving the control loop equations, the outputs of the two channels may be computed for the closed loop situation. The results, in operator notation, are

$$\phi_1(s) = \frac{\phi_g(s) - m\,\phi_s(s)}{1 + KH\,(s)} + \frac{\phi_a}{1 + KH\,(s)} + \frac{KH\,(s)}{1 + KH\,(s)}\,\phi_r \tag{3}$$

$$\phi_2(s) = \frac{\phi_g(s) - m\,\phi_s(s)}{1 + KH\,(s)} + \frac{\phi_a}{1 + KH\,(s)} + \frac{KH\,(s)}{1 + KH\,(s)}\,\phi_r + \phi_b - \phi_a \tag{4}$$

K is the open loop gain and H (s) is the response of the filter.

THE MEASUREMENT

From Equations (3) and (4) it is evident that the measurement required is $\phi_1 - \phi_2$ which gives the desired phase difference $\phi_a - \phi_b$. If this were done instantaneously, as in an analog phase detector, the effect of oscillator stability ϕ_g and ϕ_s would cancel out and would not cause error in the result. However in the proposed system the measurement is extended over a time up to the period of the reference (0.1 msec), and the oscillator errors can be significant.

The phase measurement is made by measuring the time between the instants that ϕ_1 and ϕ_2 have the same value. Since multiples of π are easy to sense (these are zero crossings), this is the value of those used. Said in another way, the phase difference is measured by measuring the time between a zero crossing of ϕ_1 and a zero crossing of ϕ_2.

This is expressed analytically as follows: At some time t the output of channel 1 has the value

$$\phi_1(t) + \omega_r t = \omega_r t + \phi_r\,(t) + \phi_i \tag{5}$$

where $\phi_n(t)$ represents the net phase error caused by the ground and spacecraft oscillators. The angle ϕ_i is some initial value which is almost equal to ϕ_r. In any case, this initial value is fixed.

At a time T later, the output of Channel 2 has the same value as is given by Equation (5). This value is

$$\phi_2(t + T) + \omega_r(t + T) = \omega_r(t + T) + \phi_n(t + T) + \phi_i + \phi_b - \phi_a \tag{6}$$

Equating (5) and (6) gives the result

$$\phi_a - \phi_b = \omega_r T + \phi_n(t + T) - \phi_n(t) \tag{7}$$

The average result of this measurement is

$$\overline{\phi_a - \phi_b} = \omega_r t \tag{8}$$

where the bar represents ensemble average. The rms value of the error caused by short term stability is σ_ϕ given by

$$\sigma_\phi^2 = \overline{\left[\phi_n(t + T) - \phi_n(t)\right]^2} \tag{9}$$

Thus σ_ϕ is the rms phase error accumulated in the time T, where T can be as large as 0.1 msec.

This may be expressed in terms of the short term stability for the oscillator that causes the phase error ϕ_n. The stability is generally defined as

$$S(T) = \frac{\sigma_\phi}{\omega T} \tag{10}$$

where σ_ϕ is the phase error accumulated in the time T (exactly as defined in Eq. 9) and ω is the radian frequency at which this phase is accumulated. Thus the phase error is given by

$$\sigma_\phi = \omega T S(T) \quad \text{radians} \tag{11}$$

Stability is generally not known for intervals as short as 0.1 msec. However, the stability generally behaves according to $1/\sqrt{T}$. Using this relation the accumulated phase is

$$\sigma_\phi = k\sqrt{T} \tag{12}$$

The correlation time T_c is the time for the accumulated phase to equal 1 radian.

Thus, the constant k is

$$k = 1/\sqrt{T_c} \tag{13}$$

and Eq. 12 becomes

$$\sigma_\phi = \sqrt{\frac{T}{T_c}} \quad \text{radians} \tag{14}$$

Results using Equations (11) and (14) are as follows. Suppose σ_ϕ is 2 degrees, the radio frequency is C-band (6 Gc), and the time interval is 0.1 msec. Then, according to Equation (11) the stability required is about one part in 10^8 for 0.1 msec. Since the stability behaves as $1/\sqrt{T}$, the required stability based on one second is about one part in 10^{10}. From Equation (14) the required correlation time is approximately 0.1 second.

In arriving at Equation (9) the effect of the phase locked loop on the short term stability has been neglected. To take this into account we may consider the phase error $\phi_n'(t)$ which is the result of modifying $\phi_n(t)$ by the term $(1 + KH)^{-1}$ in Eq. 3 and 4. Then

$$\begin{aligned} \sigma_\phi^2 &= \overline{\left[\phi_n'(t+T) - \phi_n'(t)\right]^2} \\ &= 2\left[R_{\phi_n'}(0) - R_{\phi_n'}(T)\right] \\ &= 2\int_0^\infty \left|E(\omega)\right|^2 G_\phi(\omega)\,(1 - \cos \omega T)\, df \end{aligned} \tag{15}$$

$R_{\phi_n'}(T)$ is the autocorrelation of the phase error as modified by the loop. $G_\phi(\omega)$ is the spectrum of the unmodified phase error and $\left|E(\omega)\right|$ is the appropriate loop response.

Using typical values for the loop filter and integrating Equation (15) gives the result

$$\sigma_{\phi}^2 = \frac{2}{B_o T_c}\left[1 - e^{-\frac{B_o T}{2}}\left(\cos\frac{\sqrt{3}}{2}B_o T - \frac{1}{\sqrt{3}}\sin\frac{\sqrt{3}}{2}B_o T\right)\right] \tag{16}$$

where B_o is the loop noise bandwidth in cycles per second. Since the product $B_o T$ is small (B_o = 1 kc and T = 0.1 msec), Equation (16) may be approximated by

$$\sigma_{\phi}^2 = \frac{T}{T_c} \tag{17}$$

which is the same as Equation (14). This shows that the loop has negligible effect.

ACCURACY IMPROVEMENT BY SMOOTHING

One way to improve the accuracy is to average a large number of measurements. To determine the accuracy improvement, rewrite Equation (7) in the form

$$\omega_r T_i = (\phi_a - \phi_b)_i - \left[\phi_n(t_i + T_i) - \phi_n(t_i)\right] \tag{18}$$

Summing up N of these measurements yields:

$$S = \omega_r \sum_{i=1}^{N} T_i = \sum_{i=1}^{N} (\phi_a - \phi_b)_i - \sum_{i=1}^{N}\left[\phi_n(t_i + T_i) - \phi_n(t_i)\right] \tag{19}$$

The average value is

$$\begin{aligned} \overline{S} &= \omega_r \sum_{i=1}^{N} \overline{T}_i = \omega_r N \overline{T}_i \\ &= \sum_{i=1}^{N} \overline{(\phi_a - \phi_b)_i} = N (\phi_a - \phi_b) \end{aligned} \tag{20}$$

Thus, the desired output is

$$\phi_a - \phi_b = \frac{S}{N} \tag{21}$$

and it is assumed that $\phi_a - \phi_b$ does not change over the time interval.

The rms error in S is σ_s as given by

$$\sigma_s^2 = \overline{\left[\sum_{i=1}^{N} \phi_n (t_i + T_i) - \phi_n(t_i) \right]^2} \tag{22}$$

To be conservative, assume that the measurement intervals are adjacent to one another and that the time intervals T_i are equal ($T_i = T$). Then the phase error sum becomes

$$\sum_{i=1}^{N} \left[\phi_n (t_i + T_i) - \phi_n(t_i) \right] = \phi_n (t_i + N\,T) - \phi_n(t_i) \tag{23}$$

The RMS error is given by

$$\sigma_s^2 = \overline{\left[\phi_n(t_i + N\,T) - \phi_n(t_i) \right]^2} \tag{24}$$

The RMS error in $\phi_a - \phi_b$ is σ_ϕ which is

$$\sigma_\phi = \frac{\sigma_s}{N} = \sqrt{\frac{T}{N\,T_c}} \tag{25}$$

According to Equation (25), average has the effect of increasing the correlation time. Without average the required correlation time was given as 0.1 second. If an average is taken over one hundred measurements, the required correlation time is only 1 msec. Only 10 msec would be required to make the one hundred measurements.

FREQUENCY MULTIPLIER NOISE

For good oscillators, and for very short measuring intervals, the phase error caused by frequency multiplier noise often swamps out the phase error caused by short term stability. This is illustrated in Figure H-2. The oscillator stability goes as $1/\sqrt{T}$ as indicated. The effect of multiplier noise goes as 1/T, and this predominates at small T. The crossover point depends on the relative quality of the oscillator and of the multiplier.

The accumulated phase for small values of T, when the multiplier dominates, is given by

$$\begin{aligned} \sigma_{\phi} &= \omega T\, S\,(T) \\ &= \omega K \end{aligned} \tag{25}$$

where we have written

$$S\,(T) = \frac{K}{T} \tag{26}$$

which corresponds to the behavior of the multiplier. Thus the rms phase error is constant for very small T. A typical range of values for K is 10^{-12} to 10^{-11}. The corresponding phase error is between 2.1 and 21 degrees. Of course this error will be improved by averaging in the same way as the oscillator induced error.

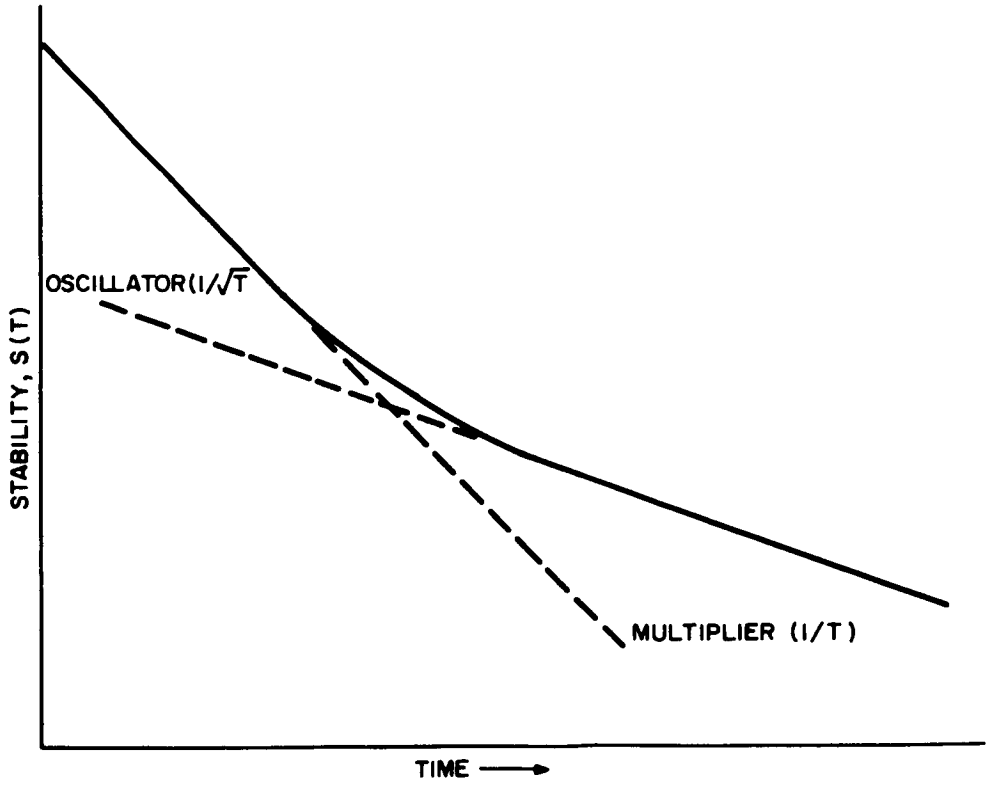


Figure H-2. Typical Stability

APPENDIX I

RF ATTITUDE SENSOR APPLICATION OF ATS PROJECT APPROVED PARTS

The initial Radio Guidance Operation (RGO) proposal and design of the Radio Frequency Attitude Sensor was based largely upon the use of component parts which had been qualified for use in other equipments. Failure rates used in prediction of equipment MTBF were based upon actual field experience with the parts. Parts which had not previously been in use were to have been qualified based upon the RF Attitude Sensor application. Design of the circuitry, subassemblies, assemblies and the sensor was, of course, dictated to a large extent by the component parts selected.

Direction to apply, as completely as possible, parts from the ATS Approved Parts List, 490L106, was interpreted as utilization only to the extent that the mechanical configuration and module construction (Modular Weldment) would not have to be altered. In the preliminary review of the Hughes Aircraft Company part specifications, several parts were determined to be not usable for the following reasons:

1. Several capacitors, in particular parts 988503, 988529 and 988541, were found to be too large for module use. Their use would necessitate either increased module cross-section area or a significant increase in module length with the components mounted longitudinal, contrary to the normal transverse mounting. A substantial penalty would be paid in size and weight as well as assembly cost.
2. Some of the parts (such as diodes 988701 and 988723, in the specific applications) would not permit a derating of 4.
3. The crystals defined by Specification 988660 were not considered to be satisfactory for the intended application. It was considered that another satisfactory vendor, with whom the RGO has had extensive experience in the servo loop application of voltage tuned crystals, would be capable of supplying the required crystals.

4. The 988826 transistor would not provide the necessary power output at frequencies up to 227 megacycles without a considerable increase in the required number of stages.

In addition to the above specific factor, there were other general reasons for not desiring to use HAC approved parts. These were as follows:

1. Many newer and improved parts are available. It was suspected that a substantial amount of time and effort had gone into attempting to qualify the parts and establish vendor approvals; and, as a result, other improved parts were continually becoming available.
2. No specific consideration appeared to be given to radiation environment in spite of the satellite application.
3. Modular connections were intended to be welded. The part specifications do not consider weldable lead materials.
4. Many of the approved vendors initially contacted appeared to be, to some extent, unfamiliar with the specifications and reluctant to quote on providing the parts.

Following some preliminary redesign effort and selection of the approved parts which were considered to be usable without significantly affecting the general electrical and mechanical design approach, quotations were requested for the appropriate quantities from approved vendors. There was experienced immediate reluctance on the part of many vendors to quote to the specifications and receipt of even verbal quotations was exceedingly slow.

As verbal and written quotations were received, the impact upon the program schedule and cost became very evident. Specific and general effects are given below.

1. The majority of the vendors provided a list of exceptions to the specifications. This would necessitate an extensive coordination effort.
2. Delivery promises on items normally considered to be "off-the-shelf" were on the order of sixteen weeks for flight items and ten weeks for prototype items. In the case of long lead items with normal delivery of ten to twelve weeks, deliveries on flight items were as long as six months with four months for prototype items.

3. A great deal of variation in costs on the same items from different vendors has been evidenced. The basic prices received were generally four to five times the commercial price; and, particularly with items required in small quantities, the lot charge results in an overall unit price of ten times or more greater than the commercial price.

The application of approved parts necessitated modifications to the design; and, as a result, it is not possible to present a full comparison of commercial versus approved parts costs. However, some typical costs of like items are presented below in order to indicate the impact on cost. In most cases, the commercial price is the actual cost of the approved part without aging and is greater than a true commercial cost. The prices used are based upon the quantities which were required for the attitude sensor.

Item Type	Commercial Equivalent	Unit Cost	Approved Part	Prototype Unit Cost	Flight Unit Cost	Lot Charge
Transistor	2N2977	$33.00	988851-1	$ 33.00	$ 37.70	$1149.00
Transistor	2N2907	$17.00	988853-1	$ 20.45	$ 23.05	$1927.30
Diode	-	$ 3.13	988704	$ 53.91	$ 80.53	
Resistor	-	$ 1.00	988611	$ 2.50	$ 3.50	
Varactor	-	$50.00	988903-2	$100.00	$100.00	$3000.00
Capacitor	-	$15.01	988500-144	$ 16.07	$ 18.88	
Choke	-	$ .69	988670	$ 6.88	$ 6.88	$ 51.00

A conservative estimate of the increase in direct material cost for the attitude sensor due to the use of approved parts is that it would be greater by a factor of five. This does not take into account the associated costs which could be incurred in the process of resolving specification difficulties and working out delivery problems.

A modification of the approach to achieve high reliability should be given consideration. A reduced component part activity coupled with aging of sub-assemblies, assemblies and units could provide greater assurance in other areas which contribute to failures. This type of program would verify not only that satisfactory component parts have been received but that the parts are properly applied and that potential

failures have not been introduced through the assembly and test process. A program of this nature, with a modified component part approach, could be less costly to implement than use of the ATS approved parts.